



Final Report  
ONR Contract Number N00014-88-K-0475

**EXTENSION OF ON-SURFACE RADIATION  
CONDITION (OSRC) THEORY TO FULL-VECTOR  
ELECTROMAGNETIC WAVE SCATTERING BY  
THREE-DIMENSIONAL CONDUCTING,  
DIELECTRIC, AND COATED TARGETS**

**Principal Investigator:**

**Allen Taflove, Professor**  
Department of Electrical Engineering and Computer Science  
McCormick School of Engineering, Northwestern University  
2145 Sheridan Rd., Evanston, IL 60208  
(708) 491-4127 (office), -8887 (lab), -4455 (fax)  
taflove@eecs.nwu.edu (email)

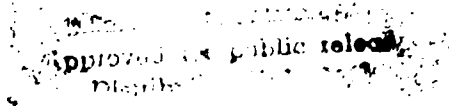


**Co-Investigator:**

**Korada R. Umashankar, Professor**  
Department of Electrical Engineering and Computer Science  
University of Illinois at Chicago  
P.O. Box 4348, Chicago, IL 60680

December, 1993

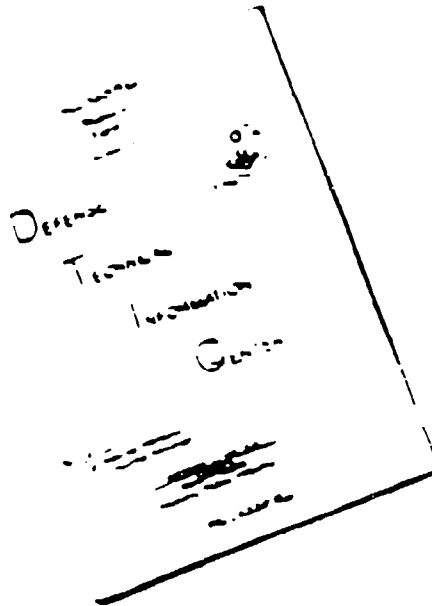
93-30621



# REPORT DOCUMENTATION PAGE

1a. REPORT SECURITY CLASSIFICATION <b>UNCLASSIFIED</b>		1b. RESTRICTIVE MARKINGS	
2a. SECURITY CLASSIFICATION AUTHORITY		3. DISTRIBUTION / AVAILABILITY OF REPORT  <b>UNLIMITED</b>	
2b. DECLASSIFICATION / DOWNGRADING SCHEDULE			
4. PERFORMING ORGANIZATION REPORT NUMBER(S)		5. MONITORING ORGANIZATION REPORT NUMBER(S)	
6a. NAME OF PERFORMING ORGANIZATION <b>Northwestern University McCormick School of Engineering</b>	6b. OFFICE SYMBOL (If applicable)	7a. NAME OF MONITORING ORGANIZATION <b>Office of Naval Research Electronics Division</b>	
6c. ADDRESS (City, State, and ZIP Code) <b>EECS Department 2145 Sheridan Rd. Evanston, IL 60208</b>		7b. ADDRESS (City, State, and ZIP Code) <b>Code 1114 800 N. Quincy St. Arlington, Virginia 22217-5000</b>	
8a. NAME OF FUNDING / SPONSORING ORGANIZATION <b>Same as 7a</b>	8b. OFFICE SYMBOL (If applicable)	9. PROCUREMENT INSTRUMENT IDENTIFICATION NUMBER <b>N00014-88-K-0475</b>	
8c. ADDRESS (City, State, and ZIP Code) <b>Same as 7b</b>		10. SOURCE OF FUNDING NUMBERS	
		PROGRAM ELEMENT NO	PROJECT NO
		TASK NO	WORK UNIT ACCESSION NO.
11. TITLE (Include Security Classification) <b>Extension of OSRC to Full-Vector Electromagnetic Wave Scattering (UNCLASSIFIED)</b>			
12. PERSONAL AUTHOR(S) <b>Taflove, Allen (Northwestern University) Umashankar, Korada Renu (University of Illinois at Chicago)</b>			
13a. TYPE OF REPORT <b>Final</b>	13b. TIME COVERED <b>FROM 88/7/1 TO 93/3/31</b>	14. DATE OF REPORT (Year, Month, Day) <b>93/8/27</b>	15. PAGE COUNT <b>262</b>
16. SUPPLEMENTARY NOTATION			
17. COSATI CODES		18. SUBJECT TERMS (Continue on reverse if necessary and identify by block number)  <b>Electromagnetic wave scattering, radiation boundary conditions, finite-difference time-domain (FD-TD)</b>	
FIELD	GROUP		
19. ABSTRACT (Continue on reverse if necessary and identify by block number)  This project introduced radiation boundary condition (RBC) and absorbing boundary condition (ABC) theory to the engineering electromagnetics community. A novel approximate method for obtaining the scattering of 2-D and 3-D bodies, the on-surface radiation condition (OSRC) method, was formulated and validated. RBCs and ABCs were shown to work well at points closer to scatterers than anyone had expected. Finite-difference time-domain (FD-TD) methods exploiting these ABCs were pursued for applications in scattering, radiation, penetration, biomedical studies, and nonlinear optics. Multiprocessing supercomputer software was developed for FD-TD, leading to the largest scale detailed electromagnetic wave interaction models ever conducted, including entire jet fighter aircraft modeled for radar cross section (RCS) at UHF frequencies up to 500 MHz.			
20. DISTRIBUTION / AVAILABILITY OF ABSTRACT <input checked="" type="checkbox"/> UNCLASSIFIED/UNLIMITED <input type="checkbox"/> SAME AS RPT <input type="checkbox"/> DTIC USERS		21. ABSTRACT SECURITY CLASSIFICATION <b>UNCLASSIFIED</b>	
22a. NAME OF RESPONSIBLE INDIVIDUAL <b>Dr. Arthur Jordan</b>		22b. TELEPHONE (Include Area Code) <b>(703) 696-4217</b>	22c. OFFICE SYMBOL <b>Code 1114</b>

# DISCLAIMER NOTICE



THIS DOCUMENT IS BEST  
QUALITY AVAILABLE. THE COPY  
FURNISHED TO DTIC CONTAINED  
A SIGNIFICANT NUMBER OF  
PAGES WHICH DO NOT  
REPRODUCE LEGIBLY.

**Final Report**  
**ONR Contract Number N00014-88-K-0475**

**Extension of On-Surface Radiation Condition (OSRC) Theory  
to Full-Vector Electromagnetic Wave Scattering by Three-  
Dimensional Conducting, Dielectric, and Coated Targets**

This document provides a concise final report of technical progress and accomplishments for ONR Contract N00014-88-K-0475. The format is a narrative description of the research followed by a compilation of reproductions of journal articles resulting in whole or in part from this funding.

**Research Accomplishments- OSRC**

1. We completed the OSRC analysis of TM scattering by PEC wedges of arbitrary angle, showing that the proper current singularity at the edge (and associated scattering effects) naturally arises out of the Bayliss-Turkel  $B_2$  operator.
2. We applied  $B_2$  OSRC to analyze full-vector EM scattering by a PEC sphere using radial potentials, and obtained excellent agreement with the exact solution.
3. We applied  $B_2$  OSRC to PEC bodies of revolution, in one case applying  $B_2$  to surface potentials, and in the other case applying  $B_2$  directly to the surface E and H fields.
4. We applied the Rayleigh hypothesis and high-frequency asymptotic analyses to the PEC wedge and the cavity-backed aperture to develop an understanding of the differences between these approaches and OSRC.
5. We applied  $B_3$  and  $B_4$  OSRC to analyze full-vector EM scattering by a PEC sphere, and found monotonic improvement in the accuracy of the computed surface currents at all points along the surface, especially the shadow region, as the order of the radiation boundary operator increased from 2 to 3 to 4.

An important direct result of this ONR-sponsored research is that our publications sparked interest in radiation boundary condition (RBC) and absorbing boundary condition (ABC) theory in the engineering electromagnetics community. As late as the publication of our first OSRC paper in 1987, this community was unaware of the importance of RBC and ABC theory and applications, and unaware of the existence of a substantial body of work on these topics in the applied mathematics literature. Since 1987, the number of RBC and ABC papers published at international engineering electromagnetics symposia (and in related journals) has risen from a level of zero to a level today where special sessions on RBC/ABC theory and applications are routinely held, and the topic is absolutely mainstream.

DTIC ( )

DTIC ( )	
Dist	Avail and or specify
<b>A-1</b>	



### Research Accomplishments by Students Funded in Part by the ONR Grant

1. We completed (in 2-D) the formulation and testing of our new spatial decomposition technique for MoM, a unique analytical approach that retains the fundamental basis, accuracy, and robustness of MoM, but profoundly reduces the required computer memory and running time.
2. We constructed the world's largest 3-D finite-difference time-domain (FD-TD) computational electromagnetics models. The first was an FD-TD model of a  $30\lambda_0$  U-shaped jet engine inlet, having 25-million vector field unknowns. We solved this problem in only 3 minutes, 40 seconds on a Cray Y-MP/8, achieving the fastest computational rate (1.6 GFlops) and highest degree of Cray-processor concurrency (7.97/8) attained for such a model up to the date of publication. We later extended our FD-TD modeling to a complete fighter aircraft, the General Dynamics/Lockheed VFY-218, at illumination frequencies from 100 MHz to 500 MHz. Currently, our 3-D FD-TD codes can solve for up to 500-million vector field unknowns (in core) when implemented on the Cray M-90 supercomputer. Peak processing rates on the Cray C90 are at about 10 GFlops.
3. Using FD-TD, we completed the first grid-based analyses of radiation by 2-D and 3-D horn antennas and horn-fed parabolic dishes, and demonstrated high modeling accuracy.
4. We completed a patient-specific EM hyperthermia model for cancer treatment, using artificial intelligence techniques to semi-automatically process computed tomography (CT) images of patients, thereby assembling a 3-D biological tissue dielectric medium data base for FD-TD EM analysis on the Cray. Using FD-TD, we completed the first grid-based Maxwell's equations models of optical imaging and holography for diffraction-limited structures.
5. We made a significant advance in computational physics that permits for the first time the numerical modeling of the operation of femtosecond optical devices directly from the full-vector nonlinear Maxwell's equations. Here, we learned how to rigorously incorporate linear and nonlinear dispersion -- the key optical physics of glass and semiconductor optical materials -- into the FD-TD direct time integration of Maxwell's equations. We obtained for the first time direct Maxwell's equations models of temporal solitons in 1-D and 2-D, spatial solitons in 2-D, and mutual deflection of spatial solitons in 2-D (light switching light). Our models can treat engineering features in optical microchips down to the 10-nanometer distance scale, incorporating such quantum effects as Kerr nonlinearity, Raman interactions, and two-photon absorption.

An important direct result of these aspects of our ONR-sponsored research is that our publications sparked interest in FD-TD and related grid-based Maxwell's equations solvers in the engineering electromagnetics community. As late as the publication of our Wave Motion review paper in 1988, this community was largely unaware of the power of such solvers in the context of the emergence of capable supercomputers, and largely unaware of the existence of a substantial body of work on these topics in the computational fluid dynamics literature. Since 1988, the number of FD-TD and related finite-element and finite-volume papers published at international engineering electromagnetics symposia and in related journals has risen from a level of less than 10 per year (published primarily by my group) to a level today where a *single conference* (for example, both the 1992 and 1993 IEEE International Antennas and Propagation Society Symposia) has more than 90 presented by research teams worldwide. We hope that our new nonlinear Maxwell's equations FD-TD work will have eventually have a similar impact upon the worldwide nonlinear optics community.

Office of Naval Research  
Final Publication / Patents / Presentations / Honors Report  
for ONR Contract Number N00014-88-K-0475  
1 July 1988 through 31 March 1993

Contract / Grant Number: N00014-88-K-0475

Contract / Grant Title: Extension of On-Surface Radiation Condition Theory to Full-Vector Electromagnetic Wave Scattering by Three-Dimensional Conducting, Dielectric, and Coated Targets

Principal Investigator: Allen Taflove

Mailing Address: Department of Electrical Engineering and Computer Science  
McCormick School of Engineering  
Northwestern University  
Evanston, Illinois 60208

Phone Numbers: (708) 491-4127 (office), -8887 (lab), -4455 (fax)

E-Mail Address: taflove@eecs.nwu.edu

a. Number of Papers Submitted to Refereed Journals but not yet published: 4

b. Number of Papers Published in Refereed Journals: 25 (reproduced in this report in Appendix A)

1. G. A. Kriegsmann, A. Taflove and K. R. Umashankar, "A new formulation of electromagnetic wave scattering using an on-surface radiation boundary condition approach," IEEE Trans. Antennas and Propagation, vol. 35, Feb. 1987, pp. 153-161. (See pp. A1 - A9 of this report.)

NOTE: This paper was published before the award of this ONR contract. However, because it launched the entire topic of RBC, ABC, and OSRC theory in the engineering electromagnetics community, it is important to use it to lead off the publications list.

2. T. G. Moore, G. A. Kriegsmann and A. Taflove, "An application of the WKBJ technique to the on-surface radiation condition," IEEE Trans. Antennas and Propagation, vol. 36, Sept. 1988, pp. 1329-1331. (See pp. A10 - A12 of this report.)
3. T. G. Moore, J. G. Blaschak, A. Taflove and G. A. Kriegsmann, "Theory and application of radiation boundary operators," invited review paper, IEEE Trans. Antennas and Propagation, vol. 36, Dec. 1988, pp. 1797-1812. (See pp. A13 - A28 of this report.)
4. A. Taflove, "Review of the formulation and applications of the finite-difference time-domain method for numerical modeling of electromagnetic wave interactions with arbitrary structures," invited paper, Wave Motion, vol. 10, Dec. 1988, pp. 547-582. (See pp. A29 - A64 of this report.)

5. F. A. Harfoush, A. Taflove and G. A. Kriegsmann, "A numerical technique for analyzing electromagnetic wave scattering from moving surfaces," IEEE Trans. Antennas and Propagation, vol. 37, Jan. 1989, pp. 55-63. (See pp. A65 - A73 of this report.)
6. J. G. Blaschak, G. A. Kriegsmann and A. Taflove, "A study of wave interactions with flanged waveguides and cavities using the on-surface radiation condition method," Wave Motion, vol. 11, March 1989, pp. 65-76. (See pp. A74 - A85 of this report.)
7. A. Taflove and K. R. Umashankar, "Review of FD-TD numerical modeling of electromagnetic wave scattering and radar cross section," invited paper, Proc. IEEE, vol. 77 (Special Issue on Radar Cross Section of Complex Objects), May 1989, pp. 682-699. (See pp. A86 - A103 of this report.)
8. A. Taflove and K. R. Umashankar, "The finite-difference time-domain method for numerical modeling of electromagnetic scattering," invited paper, IEEE Trans. Magnetics, vol. 25 (Special Issue on Field Computation), July 1989, pp. 3086-3091. (See pp. A104 - A109 of this report.)
9. A. T. Perlik, A. Taflove and T. Opsahl, "Predicting scattering of electromagnetic fields using FD-TD on a Connection Machine," IEEE Trans. Magnetics, vol. 25 (Special Issue on Field Computation), July 1989, pp. 2910-2912. (See pp. A110 - A112 of this report.)
10. B. Beker, K. R. Umashankar and A. Taflove, "Numerical analysis and validation of the combined-field surface integral equations for electromagnetic scattering by arbitrary shaped two-dimensional anisotropic objects," IEEE Trans. Antennas and Propagation, vol. 37, Dec. 1989, pp. 1573-1581. (See pp. A113 - A121 of this report.)
11. A. Taflove and K. R. Umashankar, "The finite-difference time-domain method for numerical modeling of electromagnetic wave interactions," invited paper, Electromagnetics, vol. 10 (Special Issue on Three-Dimensional Electromagnetic Computation), Jan. - June 1990, pp. 105-126. (See pp. A122 - A133 of this report.)
12. M. A. Strickel and A. Taflove, "Time-domain synthesis of broadband absorptive coatings for two-dimensional conducting targets," IEEE Trans. Antennas and Propagation, vol. 38, July 1990, pp. 1084-1091. (See pp. A134 - A141 of this report.)
13. F. A. Harfoush, G. A. Kriegsmann and A. Taflove, "Numerical implementation of relativistic electromagnetic field boundary conditions in a laboratory-frame grid," J. Computational Physics, vol. 89, July 1990, pp. 80-94. (See pp. A142 - A149 of this report.)
14. S. Arendt, K. R. Umashankar, A. Taflove and G. A. Kriegsmann, "Extension of on-surface radiation condition theory to scattering by two-dimensional homogeneous dielectric objects," IEEE Trans. Antennas and Propagation, vol. 38, Oct. 1990, pp. 1551-1558. (See pp. A150 - A157 of this report.)
15. F. A. Harfoush and A. Taflove, "Scattering of electromagnetic waves by a material half-space with a time-varying conductivity," IEEE Trans. Antennas and Propagation, vol. 39, July 1991, pp. 898-906. (See pp. A162 - A170 of this report.)
16. D. S. Katz, M. J. Piket-May, A. Taflove and K. R. Umashankar, "FD-TD analysis of electromagnetic wave radiation from systems containing horn antennas," IEEE Trans. Antennas and Propagation, vol. 39, August 1991, pp. 1203-1212. (See pp. A171 - A180 of this report.)
17. R. M. Joseph, S. C. Hagness and A. Taflove, "Direct time integration of Maxwell's equations in linear dispersive media with absorption for scattering and propagation of femtosecond electromagnetic pulses," Optics Letters, 16, Sept. 15, 1991, pp. 1412-1414. (See pp. A181 - A183 of this report.)

18. K. R. Umashankar, W. Chun, and A. Taflove, "Simple analytical solution to electromagnetic scattering by two-dimensional conducting objects with edges and corners. Part I - TM polarization," IEEE Trans. Antennas and Propagation, 39, December 1991, pp. 1665-1671. (See pp. A184 - A190 of this report.)
19. P. M. Goorjian and A. Taflove, "Direct time integration of Maxwell's equations in nonlinear dispersive media for propagation and scattering of femtosecond electromagnetic solitons," Optics Letters, 17, Feb. 1, 1992, pp. 180-182. (See pp. A191 - A193 of this report.)
20. M. J. Piket-May, A. Taflove, W. - C. Lin, D. S. Katz, V. Sathiseelan, and B. B. Mittal, "Initial results for automated computational modeling of patient-specific electromagnetic hyperthermia," IEEE Trans. Biomedical Engineering, 39, March 1992, pp. 226-237. (See pp. A194 - A205 of this report.)
21. T. G. Jurgens, A. Taflove, K. R. Umashankar, and T. G. Moore, "Finite-difference time-domain modelling of curved surfaces," IEEE Trans. Antennas and Propagation, 40, April 1992, pp. 357-366. (See pp. A206 - A215 of this report.)
22. K. R. Umashankar, S. Nimmagadda, and A. Taflove, "Numerical analysis of electromagnetic scattering by electrically large objects using spatial decomposition technique," IEEE Trans. Antennas and Propagation, 40, August 1992, pp. 867-877. (See pp. A216 - A226 of this report.)
23. P. M. Goorjian, A. Taflove, R. M. Joseph, and S. C. Hagness, "Computational modeling of femtosecond optical solitons from Maxwell's equations," IEEE J. Quantum Electronics, 28, October 1992, pp. 2416-2422. (See pp. A227 - A233 of this report.)
24. A. Taflove, "Re-inventing electromagnetics: supercomputing solution of Maxwell's equations via direct time integration on space grids," Computing Systems in Engineering, vol. 3 (Special Issue on High-Performance Computing for Flight Vehicles), Dec. 1992, pp. 153-168. (See pp. A234 - A249 of this report.)
25. M. J. Piket-May, A. Taflove and J. B. Troy, "Electrodynamics of visible-light interactions with the vertebrate retinal rod," Optics Letters, 18, April 15, 1993, pp. 568-570. (See pp. A250 - A252 of this report.)

c. Number of Books or Chapters Submitted but not yet Published: 2

d. Number of Books or Chapters Published: 3, as follows-

1. A. Taflove and K. R. Umashankar, "The finite-difference time-domain method for numerical modeling of electromagnetic wave interactions with arbitrary structures," Chapter 8 in Progress in Electromagnetics Research 2: Finite Element and Finite Difference Methods in Electromagnetic Scattering, M. A. Morgan, ed., J. A. Kong, chief ed., Elsevier, 1990.
2. A. Taflove and K. R. Umashankar, "Review of FD-TD numerical modeling of electromagnetic wave scattering and radar cross section," in Radar Cross Sections of Complex Objects, W. R. Stone, ed., IEEE Press, New York, 1990.
3. A. Taflove, "State of the art and future directions in finite-difference and related techniques in supercomputing computational electromagnetics," in Directions in Electromagnetic Wave Modeling, H. L. Bertoni and L. B. Felsen, eds., Plenum, 1991.

e. Number of Printed Technical Reports and Non-Refereed Papers: 3, as follows-

1. D. S. Katz, A. Taflov, J. P. Brooks and E. Harrigan, "Large-scale methods in computational electromagnetics," Cray Channels, Spring 1991, pp. 16-19. (See pp. A158 - A161 of this report.)
2. FD-TD Computational Modeling of Vivaldi Flare Antennas, Final Report to Northrop Defense Systems Division, Rolling Meadows, IL, July 1992.
3. Basis and Application of FD-TD Techniques for Electromagnetic Wave Interactions, Course Notes for IEEE Antennas and Propagation Society Short Course, Chicago, IL, July 1992.

e'. Major Computer Software Contribution: 1, as follows-

1. Cray Research proprietary user-friendly, CAD-based FD-TD electromagnetic wave interaction software, EMDS, which is capable of conformal surface modeling of entire fighter-sized aircraft for radar cross section up to 1 - 2 GHz. Released for beta testing in Sept. 1992, EMDS is a joint development of Cray Research, A. Taflov, and his students. No government funding is involved.

f. Number of Patents Filed: 0

g. Number of Patents Granted: 0

h. Number of Invited Presentations at Workshops or Professional Society Meetings: 31, listed as follows-

1. "Computational electromagnetics," Lockheed Aeronautical Systems Co., Burbank, CA, Sept. 1989.
2. "Applications of supercomputing computational electromagnetics," Illinois Institute of Technology EECS Department, Chicago, IL, Oct. 1989.
3. "Supercomputing computational electromagnetics," DARPA, Arlington, VA (on behalf of the DOD EM Computer Code Consortium), Nov. 1989.
4. "Computational electromagnetics," (all-day seminar), U. S. Naval Weapons Center, China Lake, CA, Jan. 1990.
5. "Time-domain solutions in computational electromagnetics using finite-difference and finite-volume methods," Ultra-Wideband Radar Symposium, Los Alamos National Laboratory, March 1990.
6. "State of supercomputing computational electromagnetics for scattering and radar cross section," U.S. Department of Defense, Crystal City, D.C., April 1990.
7. "The role of analysis in an age of computers: View from the numerical side," Special Session on the Role of Analysis in an Age of Computers (Leo Felsen, Chairman), IEEE 1990 AP-S International Meeting, Dallas, TX, May 1990.
8. "Software validation for FD-TD," Code Validation Workshop (Ed Miller, Chairman), IEEE 1990 AP-S International Meeting, Dallas, TX, May 1990.
9. "Preparation for careers in science and engineering: High school college, and graduate school," Midwest Talent Search, Northwestern University Dept. of Education, Evanston, IL, May 1990.

10. "From B-2 bombers to very high speed integrated circuits and beyond: Supercomputing computational electromagnetics in the 1990's," given to John Rollwagen, Chairman and Chief Executive Officer, Cray Research, Inc., Minneapolis, Minn., June 1990.
  11. "State of the art and future directions in finite-difference and related techniques in supercomputing computational electromagnetics," International Conference on Directions in Electromagnetic Wave Modeling, Polytechnic University, New York, NY, Oct. 1990.
  - 12 - 23. IEEE Antennas and Propagation Society (AP-S) National Lecture, "Where is engineering electromagnetics going?" 135-minute talk presented from Oct. 1990 - May 1991 at twelve locations: (1) Grumman Aerospace Corporation, Bethpage, NY; (2) IEEE AP-S, Santa Clara, CA; (3) University of California at Davis; (4) University of Arizona at Tucson; (5) Arizona State University, Tempe, AZ; (6) IEEE AP-S, Phoenix, AZ; (7) Los Alamos National Laboratory, Los Alamos, NM; (8) IEEE AP-S, Chicago, IL; (9) IEEE AP-S, Dallas, TX; (10) ABB Impell Corporation, Lincolnshire, IL (in honor of National Engineers' Week); (11) IEEE AP-S, Atlanta, GA; and (12) IEEE AP-S, Boston, MA.
  24. "Finite-difference time-domain solution of Maxwell's equations," Progress in Electromagnetics Research (PIERS) Symposium, MIT, Boston, MA, July 1991.
  25. "Supercomputing simulation of femtosecond pulse propagation," Superconducting Digital Circuits and Systems Conference, George Washington University, Washington, DC, Sept. 1991.
  26. A. Taflov, "Re-inventing electromagnetics: Supercomputing solution of Maxwell's equations via direct time integration on space grids," One-hour invited talk at the American Institute of Aeronautics and Astronautics (AIAA) 30th Aerospace Sciences Mtng. (AIAA Paper No. 92-0333), Reno, NV, Jan. 1992.
  27. A. Taflov, "Mathematical developments in grid-based time-domain algorithms for Maxwell's equations," 50-minute keynote talk at Electromagnetic Code Consortium/U.S. Army Missile Command Symposium on the Solution of Maxwell's Equations for the 90's and Beyond, Redstone Arsenal, Huntsville, AL, April 1992.
  28. A. Taflov, "Re-inventing electromagnetics: Supercomputing solution of Maxwell's equations via direct time integration on space grids," Two-hour lecture at the Electromagnetics Laboratory and the Electromagnetic Communications Laboratory, University of Illinois at Urbana-Champaign, May 1992.
  29. A. Taflov, "Re-inventing electromagnetics: Supercomputing solution of Maxwell's equations via direct time integration on space grids," 45-minute invited talk at the National Engineering Consortium ComForum, Chicago, IL, June 1992.
  30. A. Taflov, "Re-inventing electromagnetics: Supercomputing solution of Maxwell's equations via direct time integration on space grids," 50-minute invited talk at the Symposium on Computational Electromagnetics, Computer-Aided Design and Supercomputing, sponsored by the Office of Research and Development, Central Intelligence Agency, McLean, Virginia, July 1992.
  31. A. Taflov, "Re-inventing electromagnetics: Supercomputing solution of Maxwell's equations via direct time integration on space grids," 3-hour invited lecture at Air Force Institute of Technology, Wright-Patterson AFB, Ohio, Sept. 1992.
- i. Number of Other Presentations at Workshops or Professional Society Meetings: 10

j. Honors / Awards / Prizes / Offices

1. Fellow, IEEE (1990)
2. Member, Electromagnetics Academy (1990)
3. Distinguished National Lecturer, IEEE Antennas and Propagation Society (1990-91)
4. Adviser of the Year (\$1700 cash award), Northwestern's McCormick School of Engineering (1991)
5. Chairman, Technical Program Committee, IEEE Antennas and Propagation Society International Symposium, Chicago, IL (1991-92)
6. First listed in Who's Who in Engineering, Eighth Edition (1991)
7. Member, Search Committee, Dean of the McCormick School of Engineering (1991-92).
8. First listed in Who's Who in America, Forty-Seventh Edition (1992-3)
9. Chairman, Graduate Committee, Dept. of Electrical Engineering and Computer Science (ended 6/92).
10. Member, Search Committee, Dean of the McCormick School (ended 3/92)
11. Member, Promotion and Tenure Committee, McCormick School (ongoing)
12. Faculty adviser to Eta Kappa Nu and Tau Beta Pi honor societies' student chapters at the McCormick School (ongoing)
13. Originator of, and faculty adviser to, the McCormick School Undergraduate Design Competition (ongoing).
14. Re-builder of, and faculty adviser to, the McCormick School amateur radio club/station, W9BGX (ongoing).
15. Originator of, and principal faculty adviser to, McCormick School outreach program to three local high schools (New Trier, Evanston Township, and Niles North (ongoing).

k. Total number of Graduate Students and Post-Docs Supported at least 25% on this contract/grant:

Graduate Students   4   Post-Docs   0  

Of these, 2 are female. None are Blacks, Aleuts, Amindians, etc.

## **Appendix A**

### **Reproductions of Journal Articles Resulting in Whole or in Part From This Project**



# A New Formulation of Electromagnetic Wave Scattering Using an On-Surface Radiation Boundary Condition Approach

GREGORY A. KRIEGSMANN, ALLEN TAFLOVE, SENIOR MEMBER, IEEE, AND KORADA R. UMASHANKAR, SENIOR MEMBER, IEEE

**Abstract**—A new formulation of electromagnetic wave scattering by convex, two-dimensional conducting bodies is reported. This formulation, called the on-surface radiation condition (OSRC) approach, is based upon an expansion of the radiation condition applied directly on the surface of a scatterer. Past approaches involved applying a radiation condition at some distance from the scatterer in order to achieve a nearly reflection-free truncation of a finite-difference time-domain lattice. However, it is now shown that application of a suitable radiation condition directly on the surface of a convex conducting scatterer can lead to substantial simplification of the frequency-domain integral equation for the scattered field, which is reduced to just a line integral. For the transverse magnetic (TM) case, the integrand is known explicitly. For the transverse electric (TE) case, the integrand can be easily constructed by solving an ordinary differential equation around the scatterer surface contour. Examples are provided which show that OSRC yields computed near and far fields which approach the exact results for canonical shapes such as the circular cylinder, square cylinder, and strip. Electrical sizes for the examples are  $ka = 5$  and  $ka = 10$ . The new OSRC formulation of scattering may present a useful alternative to present integral equation and uniform high-frequency approaches for convex cylinders larger than  $ka = 1$ . Structures with edges or corners can also be analyzed, although more work is needed to incorporate the physics of singular currents at these discontinuities. Convex dielectric structures can also be treated using OSRC. These will be the subject of a forthcoming paper.

## I. INTRODUCTION

THE APPROACH PRESENTED here is a high-frequency technique for modeling electromagnetic scattering, radically different from the geometric theory of diffraction (GTD). This new technique, which we call the on-surface radiation condition (OSRC) approach, converts the usual surface integral equation for the scattering problem into either an integration of known quantities or a simple ordinary differential equation for convex two-dimensional targets. It is currently applicable to convex conducting cylinders of arbitrary cross section, yielding codes for both the transverse electric (TE) and transverse magnetic (TM) cases that are

suitable for rapid processing by computers in the class of the VAX 11/780. The OSRC approach has been extended to two-dimensional homogeneous dielectric targets, yielding similar analyses. These will be reported in a separate paper [1].

The OSRC approach was motivated by numerical experiments conducted over the past twenty years aimed at simulating scalar or vector wave propagation and scattering using a finite-difference time-domain (FD-TD) model of the governing wave equation. This type of simulation results in numerical analogs of the incident and scattered waves propagating within a finite, two- or three-dimensional data space of field components positioned at distinct points in a lattice. To bound the numerical domain, but not disturb the simulation of a scatterer embedded in an infinite space, it has been found necessary to introduce a suitable radiation boundary condition at the outermost lattice planes. This boundary condition should allow outgoing scattered waves to exit the numerical data domain without undergoing nonphysical reflection.

Several early investigators employed the Sommerfeld condition (in the time domain) as a local radiation boundary condition to truncate the numerical domain [2]–[5]. Later workers identified and exploited higher order differential operators for this purpose [6]–[11]. These operators appear to fall into two categories. The first, exemplified by the work of Kriegsmann and Morawetz [8] and Bayliss and Turkel [9], uses the asymptotic behavior of the scattered field in cylindrical or spherical coordinate systems to establish a series  $B_n$  of operators that, when applied to the scattered field, annihilate the first  $n$  terms of the asymptotic series. Bayliss and Turkel further demonstrated that the series  $B_n$  can be conveniently generated using a recursive formula. The second category, exemplified by the work of Trefethen and Halpern [11], derives an approximate one-way wave equation in Cartesian coordinates by factoring the dispersion relation of the full wave equation, and providing a rational polynomial interpolation of the resulting square root at selected wave propagation angles. This results in a reflection-free passage of plane waves propagating at these angles through the lattice truncation plane. The number of reflection-free angles and their values can be selected in a systematic manner.

A recent series of numerical experiments involving FD-TD modeling of Maxwell's equations in Cartesian coordinates and two and three space dimensions has been reported [12]–[14]. These experiments utilized the radiation boundary operator

Manuscript received May 31, 1985; revised August 1, 1986. This work was supported in part by NASA Lewis Research Center Grant NAG 3-63\* and by National Science Foundation Grant MCS-8300578.

G. A. Kriegsmann is with the Department of Engineering Sciences and Applied Mathematics, Technological Institute, Northwestern University, Evanston, IL 60201.

A. Taflov is with the Department of Electrical Engineering and Computer Science, Technological Institute, Northwestern University, Evanston, IL 60201.

K. R. Umashankar is with the Department of Electrical Engineering and Computer Science, University of Illinois, Chicago, IL 60680.

published by Mur [10], which is now known to be a Pade (2, 0) approximant as defined by Trefethen and Halpern [11]. For continuous, sinusoidal excitation, it was observed that, if the Mur condition were applied only eight space cells from the outer surfaces of structures spanning up to 96 cells (with each cell spanning approximately 0.1 wavelength), the radar cross section could be modeled with an accuracy of 1 dB or better over a 40 dB dynamic range [14]. The robustness of the numerical experimental data suggested that it might be possible to apply a suitable radiation condition even closer to a scatterer to further reduce the required FD-TD lattice size.

In preparing for the new series of FD-TD numerical experiments, an analysis revealed unexpectedly that substantial simplification of the overall scattering problem would occur for the important class of convex-shaped, two-dimensional, conducting scatterers if the radiation condition were applied *directly on the surface* of a scatterer in this class. Essentially, the original frequency-domain integral equation for the scattered field would be reduced to just a line integral about the scatterer surface contour, where the integrand is either known explicitly (for the TM case) or can be easily constructed via solution of an ordinary differential equation about the surface contour (for the TE case). The prior application of this concept, which we call the OSRC approach, is not evident in the literature.

Subsequent sections of this paper will develop the OSRC theory for two-dimensional, convex-shaped, conducting scatterers for the TM and TE cases. Radiation boundary conditions published by Kriegsmann and Morawetz [8], similar to  $B_1$  and  $B_2$  published by Bayliss and Turkel [9], will be used in this development. (It should be understood that OSRC theory might be developed for the full range of Cartesian or circular coordinate radiation operators, and that operators other than  $B_1$  and  $B_2$  may present specific advantages.) It will be demonstrated that use of a higher order OSRC can yield computed near and far scattered fields which approach the exact solution for several canonical conducting geometries having electrical sizes  $ka = 5$  and  $ka = 10$ . The results indicate that OSRC may present a useful alternative to present integral equation and uniform high-frequency methods for electrically large convex cylinders of arbitrary cross section shape.

## II. FORMULATION OF THE OSRC APPROACH (TM POLARIZATION)

We shall consider a plane electromagnetic wave illuminating a two-dimensional, perfectly conducting, convex-shaped cylinder for the transverse magnetic polarization case. The incident wave, propagating at an angle  $\alpha$  with respect to the  $-x$  axis, is given by

$$\vec{E}_{inc} = U_{inc} e^{-j\omega t} \hat{z}; \quad U_{inc} = e^{jk(x \cos \alpha - y \sin \alpha)} \quad (1)$$

where the unit vector  $\hat{z}$  is parallel to the cylinder axis. The parameter  $\omega$  is the frequency of the incident wave;  $k = \omega a/c$ ;  $a$  is a characteristic dimension of the cylinder's cross section; and  $c$  is the speed of light in free space. The variables  $x$  and  $y$  are the corresponding dimensionless Cartesian coordinates in the plane orthogonal to  $\hat{z}$ . They are scaled with respect to the length  $a$ .

The scattered electric field  $\vec{E}_s$  is given by

$$\vec{E}_s = U_s(\vec{x}) e^{-j\omega t} \hat{z} \quad (2a)$$

$$U_s(\vec{x}) = \int_C \left[ G(\vec{x}|\vec{x}') \frac{\partial U_s(\vec{x}')}{\partial \nu'} - U_s(\vec{x}') \frac{\partial G(\vec{x}|\vec{x}')}{\partial \nu'} \right] ds' \quad (2b)$$

where  $C$  represents the boundary of the cylinder's cross section;  $\partial/\partial \nu'$  denotes an outward normal derivative on  $C$ ; and  $G$  is the free-space Green's function given by

$$G(\vec{x}|\vec{x}') = \frac{j}{4} H_0^{(1)}(kR) \quad (2c)$$

$$R = |\vec{x} - \vec{x}'| = \sqrt{(x - x')^2 + (y - y')^2} \quad (2d)$$

The vectors  $\vec{x}$  and  $\vec{x}'$  appearing above are just normalized ( $x, y$ ) and  $(x', y')$ , respectively. Since the cylinder is perfectly conducting, the function  $U_s(\vec{x}')$  can be replaced by  $-U_{inc}(\vec{x}')$  in (2b) to obtain

$$U_s(\vec{x}) = \int_C \left[ G(\vec{x}|\vec{x}') \frac{\partial U_s(\vec{x}')}{\partial \nu'} + U_{inc}(\vec{x}') \frac{\partial G(\vec{x}|\vec{x}')}{\partial \nu'} \right] ds' \quad (3a)$$

Thus, the scattered field is completely determined when  $\partial U_s(\vec{x}')/\partial \nu'$  is found. The  $z$ -directed surface electric current  $J$  is related to this normal derivative by

$$J = \frac{j}{\eta_0 k} \left( \frac{\partial U_s}{\partial \nu'} + \frac{\partial U_{inc}}{\partial \nu'} \right) \quad (3b)$$

where  $\eta_0 = \sqrt{\mu_0/\epsilon_0}$ . An expression for the normal derivative will be derived shortly.

First, the far-field expansion of (3) can be obtained by using the asymptotic expansion of  $H_0^{(1)}$  as  $r = |\vec{x}| \rightarrow \infty$ :

$$U_s(\vec{x}) = \left[ \sum_0^{\infty} A_n(\varphi, \alpha, k) r^{-n} \right] \cdot \frac{e^{jkr}}{\sqrt{r}} \quad (4)$$

where  $r$  and  $\varphi$  are the cylindrical coordinates of  $\vec{x}$ . The term  $A_0$  in (4) is given explicitly by

$$A_0(\varphi, \alpha, k) = \frac{e^{j\pi/4}}{\sqrt{8k\pi}} \int_C \left[ \frac{\partial U_s}{\partial \nu'} - jk \cos \delta U_{inc} \right] e^{-jk\psi} ds' \quad (5a)$$

where  $\psi = \vec{x}' \cdot \vec{x}$  and  $\cos \delta = \hat{\nu}' \cdot \hat{x}$ , for  $\hat{x} = (\cos \varphi, \sin \varphi)$  and  $\hat{\nu}'$  = unit normal to the curve  $C$  at  $s'$ . The bistatic radar cross section (RCS) is related to  $A_0$  by the expression:

$$\text{RCS} = 2\pi a |A_0|^2 \quad (5b)$$

Next, a sequence of radiation boundary operators  $\{B_n\}$ ,  $n = 1, 2, \dots$  can be constructed which, for any  $n$ , annihilates the first  $n$  terms in the asymptotic expansion of (4). This can be considered as a way of matching the solution on the

radiation boundary to the first  $n$  terms of the expansion of the solution exterior to the boundary. When  $B_n$  is applied to  $U_s$  at a fixed radius  $r = R$ , the annihilation relationship can be expressed as

$$B_n U_s = O(R^{-2n-1/2}); \quad n = 1, 2, 3, \dots \quad (6)$$

In this expression, the symbol  $O(R^{-m})$  denotes a quantity which decays like  $R^{-m}$  as  $R \rightarrow \infty$ . The first two operators, which are used in this paper, are

$$B_1 = \partial/\partial r + 1/2r - jk \quad (7a)$$

$$B_2 = \partial/\partial r + 1/2r - jk - \left( \partial^2/\partial \varphi^2 + \frac{1}{4} \right) / [2r^2(1/r - jk)] \quad (7b)$$

These operators appeared in [8], and differ from those in [9] by the inclusion of the  $1/r$  term in the denominator of the last term in (7b). The  $1/r$  term may be neglected for the TM case, but must be retained for the TE case. Equation (6) has been previously used (with  $n = 1, 2$ ) in conjunction with finite-difference time-marching schemes to close the computational space at some distance from the scatterer while permitting only an acceptably small level of nonphysical wave reflection [8], [9]. Excellent results have been obtained for radiation boundary surfaces only a few space cells from the scatterer for a wide variety of problems.

Now, however,  $B_n$  will be applied to  $U_s$  directly on the surface of the scatterer, instead of at some distance off the scatterer. This permits formal expressions for the normal derivative of the scattered field  $\partial U_s/\partial \nu'$  to be obtained via application of (6) on contour  $C$ , and setting the right hand side of (6) equal to zero. First, the following replacements are made:

$$\frac{\partial}{\partial r'} \rightarrow \frac{\partial}{\partial \nu'}; \quad \frac{1}{r'} \rightarrow \zeta(s'); \quad \frac{1}{r'^2} \frac{\partial^2}{\partial \varphi'^2} \rightarrow \frac{\partial^2}{\partial s'^2} \quad (8)$$

where  $\zeta(s')$  is the curvature of the cylinder's surface at  $s'$ , and  $\partial^2/\partial s'^2$  is the second derivative with respect to the arc length of  $C$ . Essentially, these replacements are motivated by approximating  $C$  at a point  $\mathcal{R}(s')$  by its osculating circle [15] and locally defining the operator  $B_n$ . Then,  $B_1 U_s = 0$  implies

$$\frac{\partial U_s}{\partial \nu'} = [jk - \zeta(s')/2] U_s \quad (9a)$$

while  $B_2 U_s = 0$  gives

$$\frac{\partial U_s}{\partial \nu'} = \left\{ jk - \frac{\zeta(s')}{2} + \frac{j\zeta^2(s')}{8[k + j\zeta(s')]} \right\} U_s + \frac{j}{2[k + j\zeta(s')]} \frac{\partial^2 U_s}{\partial s'^2} \quad (9b)$$

Since the cylinder is perfectly conducting,  $U_s$  is replaced by  $-U_{inc}$  on the right hand side of (9). This gives, for  $B_1$  and  $B_2$ ,

respectively,

$$\frac{\partial U_s}{\partial \nu'} = \left[ \frac{\zeta(s')}{2} - jk \right] U_{inc}, \quad \text{for } B_1 \quad (10a)$$

$$\frac{\partial U_s}{\partial \nu'} = \left\{ \frac{\zeta(s')}{2} - jk - \frac{j\zeta^2(s')}{8[k + j\zeta(s')]} \right\} U_{inc} - \frac{j}{2[k + j\zeta(s')]} \frac{\partial^2 U_{inc}}{\partial s'^2}, \quad \text{for } B_2. \quad (10b)$$

Inserting either of these results into (3a) gives an analytical formula for the scattered field. The corresponding surface electric current expressions are obtained by combining (3b) with either (10a) or (10b).

We observe that the term  $-jkU_{inc}$ , which appears in both (10a) and (10b), is the leading-order Kirchhoff term. In the OSRC formulation, however, this term as well as the others is valid in both the lit and shadow regions of a convex scatterer.

### III. APPLICATION TO THE CIRCULAR CYLINDER: TM POLARIZATION

This section will discuss the application of the on-surface radiation condition formulation to the first of three canonical, two-dimensional, convex conducting geometries, the circular cylinder for TM polarization of the incident wave. For this problem,  $C$  is the circle  $r = 1$ , with  $\partial/\partial \nu' = \partial/\partial r'$ ,  $\zeta = 1$ , and the  $s'$  derivatives in (10b) are just  $\varphi'$  derivatives. Without loss of generality,  $\alpha$  is taken as zero in (1) so that (10a) and (10b) become

$$\frac{\partial U_s}{\partial r'} = \left( \frac{1}{2} - jk \right) e^{jk \cos \varphi'}, \quad \text{for } B_1 \quad (11a)$$

$$\frac{\partial U_s}{\partial r'} = \left( \frac{1}{2} - jk - \frac{j}{8k} - \frac{1}{2} \cos \varphi' + \frac{jk}{2} \sin^2 \varphi' \right) e^{jk \cos \varphi'}, \quad \text{for } B_2. \quad (11b)$$

In (11b), the term  $(k + j\zeta)$  in (10b) has been replaced by  $k$ . Computed results for the surface current obtained using these expressions and (3b) are shown in Fig. 1(a) for  $k = 5$ , and in Fig. 1(b) for  $k = 10$ , along with the results obtained by using a cylindrical mode summation. As is evident, (11b) agrees with the modal sum more closely than (11a). In general, the use of the higher order  $B_2$  operator implied by (11b) results in agreement of the surface current to within 1 dB of the exact solution for the  $k = 10$  case.

Inserting (11a) and (11b) into (5) gives, after some manipulation, the following respective formulas for bistatic radar cross section:

$$\frac{RCS}{\lambda} = \frac{k^2 \pi}{2} \cdot \left| \left( j - \frac{1}{2k} \right) J_0(\xi) + \sin(\varphi/2) J_1(\xi) \right|^2, \quad \text{for } B_1 \quad (12a)$$

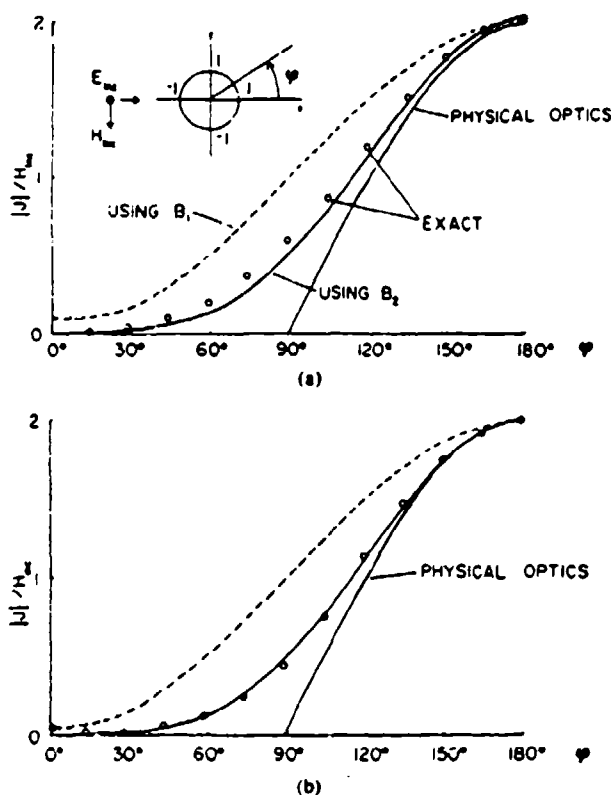


Fig. 1. Surface electric current on conducting circular cylinder, TM case, computed using OSRC method, showing convergence to exact solution for higher order radiation boundary operator. (a)  $k = 5$ . (b)  $k = 10$ .

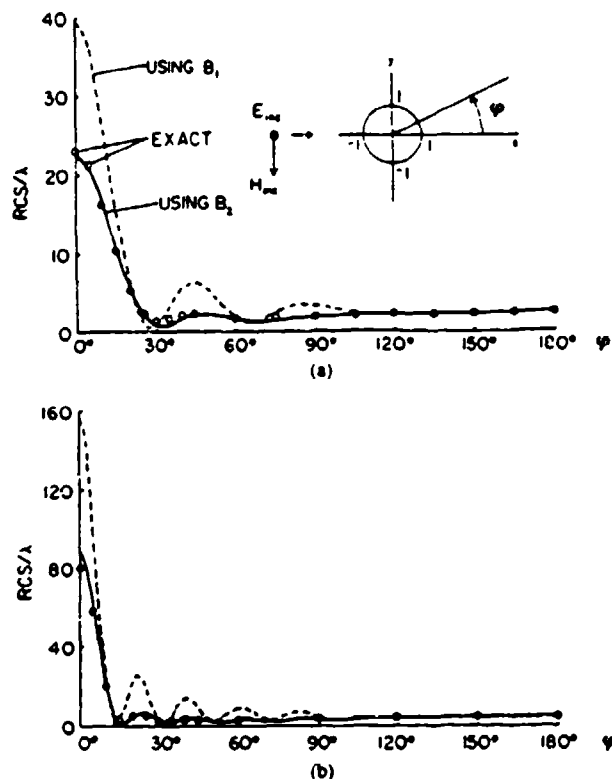


Fig. 2. Bistatic radar cross section of conducting circular cylinder, TM case, computed using OSRC method, showing convergence to exact solution for higher order radiation boundary operator. (a)  $k = 5$ . (b)  $k = 10$ .

$$\frac{RCS}{\lambda} = \frac{k^2 \pi}{2} \cdot \left| \left[ j - \frac{1}{2k} - \frac{j}{2} \cos^2(\varphi/2) \right] J_0(\xi) + g(\varphi) J_1(\xi) \right|^2, \text{ for } B_2 \quad (12b)$$

where

$$g(\varphi) = \left( 1 + \frac{j}{2k} \right) \sin(\varphi/2) + \frac{\cos \varphi}{2\xi} \quad (12c)$$

$$\xi = 2k \sin(\varphi/2). \quad (12d)$$

Note that the evaluation of only two Bessel functions is required for the RCS computation, regardless of the electrical size of the cylinder.

Fig. 2(a) shows the magnitudes of the radar cross section computed using (12a) and (12b) for the  $k = 5$  cylinder case, along with the exact solution. Fig. 2(b) plots corresponding data for the  $k = 10$  cylinder case. Just as observed in Figs. 1(a) and 1(b) (cylinder surface currents), the radar cross section obtained using the formula corresponding to the higher order radiation condition  $B_2$ , is in much better agreement with the exact solution than that corresponding to  $B_1$ . Here, the higher order formula, (12b), results in agreement to within 0.5 dB of the exact radar cross section, in general.

#### IV. APPLICATION TO THE CONDUCTING STRIP: TM POLARIZATION

In this example, the scatterer surface contour  $C$  is composed of the upper and lower halves of the line segment  $y = 0, |x|$

$\leq 1$ . On the upper half of the strip,  $\partial/\partial\nu' = \partial/\partial y'$ ,  $\zeta = 0$ , and  $\partial^2/\partial s'^2 = \partial^2/\partial x'^2$ ; while on the lower half of the strip,  $\partial/\partial\nu' = -\partial/\partial y'$ . No special attention or care is paid to the edges,  $x' = \pm 1, y' = 0$  although the edges are points of infinite curvature. For brevity, only the higher order normal derivative expression, (10b), will be used in this example. Inserting (1) into (10b) gives

$$\frac{\partial U_s}{\partial \nu'} = -jk \left( 1 - \frac{1}{2} \cos^2 \alpha \right) e^{jkx' \cos \alpha}, \text{ for } B_2. \quad (13a)$$

Using (13a) and (3b), the  $z$ -directed surface electric current is given by

$$J = \frac{1}{\eta_0} \left( \pm \sin \alpha + 1 - \frac{1}{2} \cos^2 \alpha \right) e^{jkx' \cos \alpha}, \quad \text{for } B_2 \text{ (at } y = 0 \pm). \quad (13b)$$

Note that for a given wave angle of incidence  $\alpha$ , the magnitude of  $J$  is independent of position  $x'$  on the strip, similar to the physical optics case. However, a nonzero value of  $J$  is computed in the shadow region  $y = 0^-$ .

Inserting (13a) into (5) with  $\varphi = \pi - \alpha$  gives

$$\frac{RCS}{\lambda} = \frac{1}{2\pi} \cdot \left| \left( 1 - \frac{1}{2} \cos^2 \alpha \right) \frac{\sin(2k \cos \alpha)}{\cos \alpha} \right|^2; \text{ for } B_2 \quad (14)$$

as the monostatic radar cross section of the conducting strip.

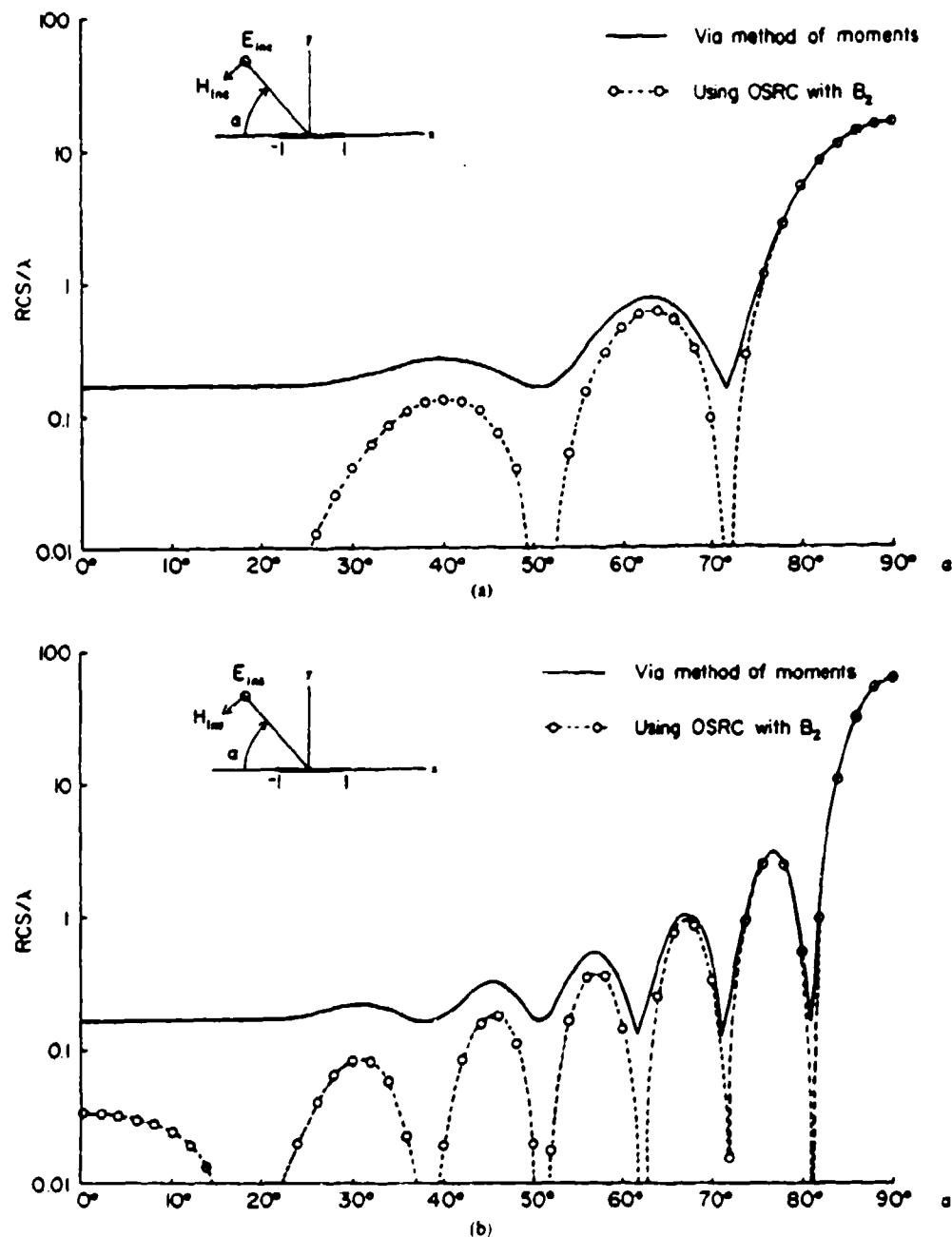


Fig. 3. Monostatic radar cross section of conducting strip, TM case, computed using OSRC method with the  $B_2$  radiation boundary operator. (a)  $k = 5$ . (b)  $k = 10$ .

Fig. 3(a) compares the results of this analysis to those of the moment method [16] for a  $k = 5$  strip; and Fig. 3(b) contains the same information for  $k = 10$ . In general, the agreement is within 1 dB for look angle,  $\alpha$ , between  $60^\circ$  and  $90^\circ$ , except at nulls. Disagreement at smaller  $\alpha$  is probably due to edge currents.

#### V. APPLICATION TO THE SQUARE CONDUCTING CYLINDER: TM POLARIZATION

In this example, the scatterer surface contour  $C$  is a square with the four corners  $(\pm\sqrt{2}, \pm\sqrt{2})$ . The determination of the surface current distribution follows the same line of analysis as

used in Section IV. In particular, (10b) directly gives

$$\frac{\partial U_s}{\partial \nu'} = -jk \left( 1 - \frac{1}{2} \cos^2 \alpha \right) e^{jk(x' \cos \alpha - y' \sin \alpha)}, \quad \text{for } B_2 \quad (15a)$$

for  $|x| \leq 1, y = \pm 1$ ; and

$$\frac{\partial U_s}{\partial \nu'} = -jk \left( 1 - \frac{1}{2} \sin^2 \alpha \right) e^{jk(z \cos \alpha - y' \sin \alpha)}; \quad \text{for } B_2 \quad (15b)$$

for  $x = \pm 1$ , and  $|y| \leq 1$ . The  $z$ -directed surface electric current follows from (15a), (15b), and (3b). It is given by

$$J = \frac{1}{\eta_0} \left( \pm \sin \alpha + 1 - \frac{1}{2} \cos^2 \alpha \right) e^{jk(x' \cos \alpha \mp y' \sin \alpha)}, \quad \text{for } B_2 \quad (16a)$$

for  $|x| \leq 1$ ,  $y = \pm 1$ ; and

$$J = \frac{1}{\eta_0} \left( \mp \cos \alpha + 1 - \frac{1}{2} \sin^2 \alpha \right) e^{jk(\pm x \cos \alpha - y' \sin \alpha)}, \quad \text{for } B_2 \quad (16b)$$

for  $x = \pm 1$ , and  $|y| \leq 1$ . Similar to the strip case of Section IV, it is noted that, for a given wave angle of incidence  $\alpha$  the magnitude of  $J$  is independent of position,  $x'$  or  $y'$ , on each side of the cylinder. It is also noted that nonzero values of  $J$  are computed in the shadow regions of the cylinder.

To compute the monostatic radar cross section, (15a) and (15b) are inserted into (5) with  $\varphi = \pi - \alpha$ :

$$\frac{\text{RCS}}{\lambda} = \frac{1}{2\pi} \cdot |g_1(\alpha) + g_2(\alpha) + g_3(\alpha)|^2 \quad (17a)$$

where

$$g_1(\alpha) = \left( 1 - \frac{1}{2} \sin^2 \alpha \right) \frac{\sin(2k \sin \alpha)}{\sin \alpha} \cos(2k \cos \alpha) \quad (17b)$$

$$g_2(\alpha) = \left( 1 - \frac{1}{2} \cos^2 \alpha \right) \frac{\sin(2k \cos \alpha)}{\cos \alpha} \cos(2k \sin \alpha) \quad (17c)$$

$$g_3(\alpha) = \frac{-j \sin(2k \sin \alpha) \sin(2k \cos \alpha)}{\sin \alpha \cos \alpha} \quad (17d)$$

The formula for the monostatic radar cross section versus  $\alpha$  is now given by (17a). Results using this formula are shown in Figs. 4(a) and 4(b) in comparison with the method of moments [16] for the  $k = 5$  and  $k = 10$  cylinder cases. Agreement is within about 0.5 dB at all points (except for  $\alpha = 12^\circ$  and  $\alpha = 14^\circ$  for the  $k = 10$  case).

#### VI. FORMULATION OF THE OSRC APPROACH (TE POLARIZATION)

For the case of TE polarization, (2b) is still valid if  $U_s$  is identified as the scattered  $z$ -directed magnetic field. Now, however, the surface current is given in terms of the incident field, i.e.,  $\partial U_s / \partial \nu'$  is known in (2b). If  $B_1$  is used, (9a) would then give  $U_s$  on  $C$ , and (2b) would be an analytic formula for  $U_s(\vec{x})$ . If the higher order  $B_2$  expression of (9b) is used, then  $U_s(\vec{x}'(s'))$  satisfies a linear second-order differential equation.

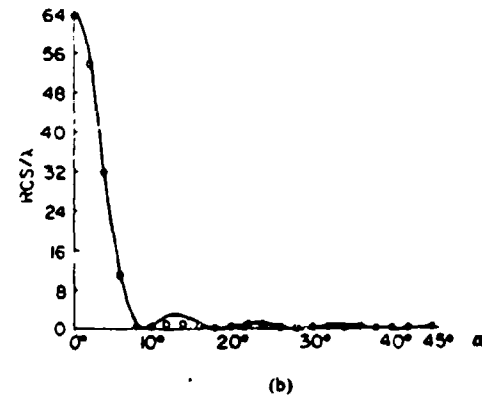
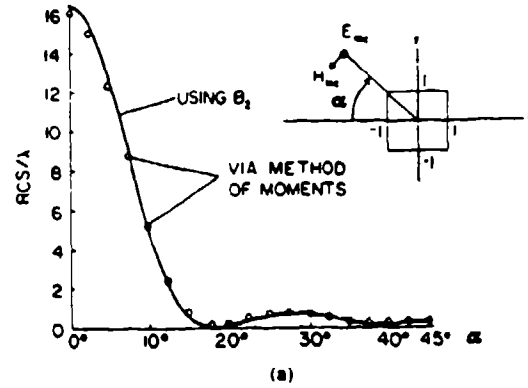


Fig. 4. Monostatic radar cross section of conducting square cylinder, TM case, computed using OSRC method with the  $B_2$  radiation boundary operator. (a)  $k = 5$ . (b)  $k = 10$ .

tion. By requiring that the solution be  $L$ -periodic ( $L$  is the dimensionless length of  $C$ ;  $L$ -periodic means that the solution must be observed to repeat itself upon successive complete walks around  $C$ ), and noting that the coefficient of  $U_s$  is not purely complex, a unique solution of (9b) can be found. When this is inserted into (2b), once again an analytic formula for  $U_s(\vec{x})$  can be obtained.

Let us now apply the above to the case of the circular conducting cylinder. For convenience, the definitions of Section III will again be used. For TE polarization, we have

$$J_s = -(U_s + U_{inc}) \quad (18a)$$

and

$$\frac{\partial U_s}{\partial \nu'} = -\frac{\partial U_{inc}}{\partial \nu'} \quad (18b)$$

On substituting (18a) and (18b) into (9a), the total surface electric current on the circular cylinder is obtained as

$$J_s = -U_{inc} \cdot (1 - \cos \varphi), \quad \text{for } B_1. \quad (19)$$

Note that the use of  $B_1$  provides an explicit expression for the current.

The case for  $B_2$  is more involved. Substituting (18a) and (18b) into (9b) yields the following second-order differential

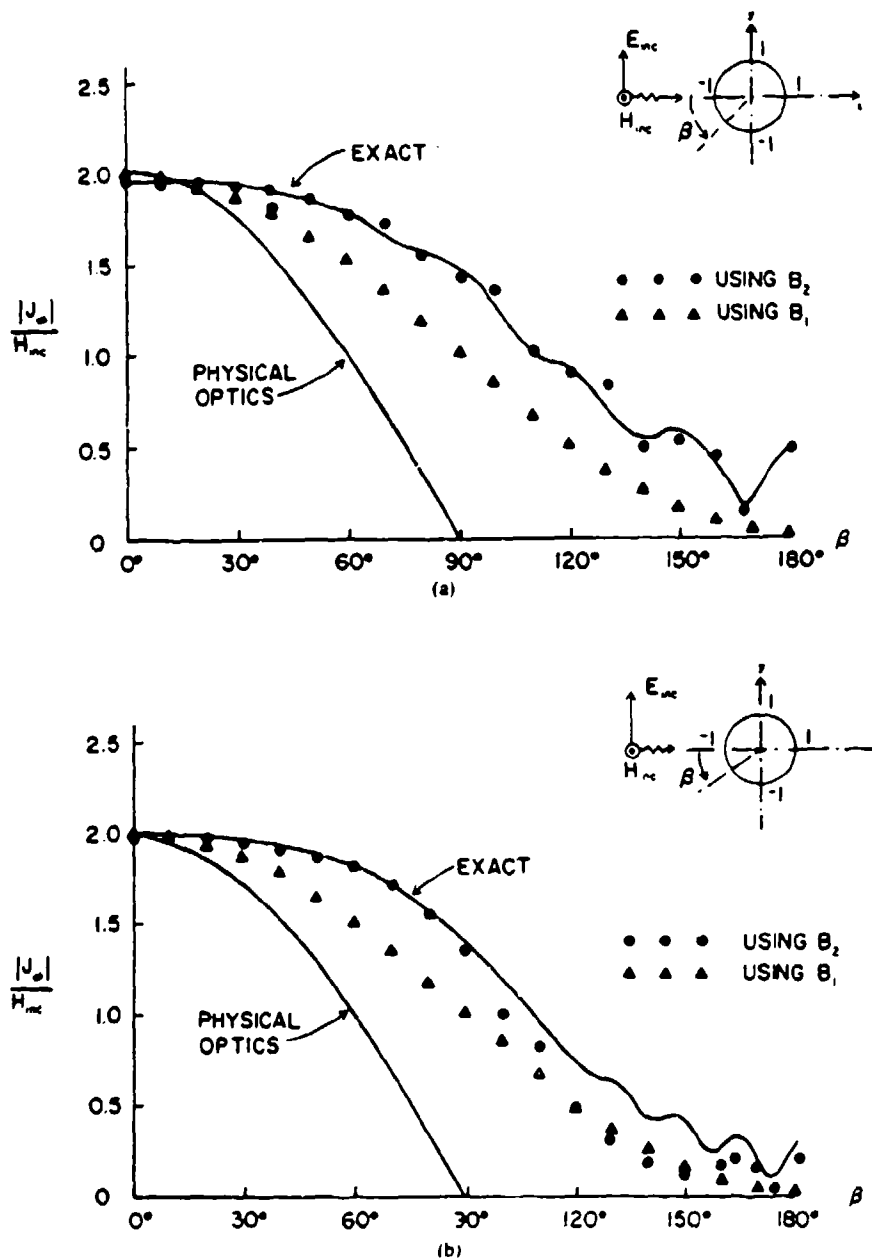


Fig. 5. Surface electric current on conducting circular cylinder, TE case, computed using OSRC method, showing convergence to exact solution for higher order radiation boundary operator. (a)  $k = 5$ . (b)  $k = 10$ .

equation for the current:

$$C_2 \frac{d^2 J_s}{d\varphi^2} - J_s = U_{inc} \cdot (1 - C_1 \cos \varphi) - C_2 \frac{\partial^2 U_{inc}}{\partial \varphi^2}, \quad \text{for } B_2 \quad (20a)$$

where

$$C_1 = \frac{8k^2 + j8k}{-3 + 8k^2 + j12k}; \quad C_2 = \frac{-4}{-3 + 8k^2 + j12k} \quad (20b)$$

and  $J_s$  is  $2\pi$ -periodic. We note that this system is linear with constant coefficients, and can be solved using standard analytical or numerical methods. We also note from (20) that, in the high-frequency limit (large  $k$ ),  $C_1$  approaches 1 and  $C_2$

approaches  $-1/2k^2$ . However, (20) does not reduce to (19) because the  $\varphi$  derivatives introduce  $k^2$  factors multiplying the  $C_2$  terms.

Fig. 5 graphs the  $B_1$  OSRC solution (from (19)), the  $B_2$  OSRC solution (from the system of (20)), and the method of moments solution for the current distribution on a  $k = 5$  and  $k = 10$  cylinder. Note that the use of the  $B_2$  operator extends the range of essential agreement between OSRC and the method of moments result over most of the circumference of the cylinder. In particular, we observe the evolution of an oscillatory behavior (identified as the result of the creeping wave) in the shadow region.

When the scattering cylinder is convex but not circular, the system of (20) no longer has constant coefficients. Again,

there are standard solution techniques. In particular, a simple, and very promising approach is the following iterative scheme, illustrated for (20) as

$$J_{\phi}^{(n+1)} = C_2 \frac{d^2 J_{\phi}^{(n)}}{d\phi^2} - U_{inc} \cdot (1 - C_1 \cos \phi) + C_2 \frac{\partial^2 U_{inc}}{\partial \phi^2} \quad (21)$$

where  $J_{\phi}^{(n)}$  denotes the  $n$ th iteration for the current. A convenient selection for  $J_{\phi}^{(0)}$  is the  $B_1$  result given by (19). This scheme would be conveniently implemented for arbitrary convex bodies on conventional computers.

## VII. RELATION TO PREVIOUS HIGH-FREQUENCY APPROACHES

The OSRC approach provides an approximate asymptotic high-frequency result which is convenient for engineering applications. This new approach is valid both for fields directly at the surface and exterior to the surface of a smooth, perfectly conducting, convex cylinder when it is illuminated by a plane wave. As was seen for the  $k = 5$  and  $k = 10$  circular cylinders, the computed surface current result is uniform in the sense that it remains essentially valid within the transition region between lit and shadow regions, and even in deep shadow regions. As observed earlier, the OSRC results contain the leading-order Kirchhoff term, as well as others, which are valid in both lit and shadow regions.

Previous work in this area [17], [18] also developed uniform-theory solutions for convex, conducting, two-dimensional cylinders. However, the previous work required a complicated analysis. In fact, a separate analysis was needed close to the cylinder surface. The new approach discussed in this paper has the advantages of simplicity and a consistent ease of application for arbitrary convex cylinders, for both on-surface and off-surface fields. Further, the new approach appears to permit good treatment of convex scatterers that do not have smooth surface contours, i.e., have edges or corners, as exemplified by the strip and square-cylinder results reported in this paper. Shadow-region currents with OSRC are nonzero for such structures. However, OSRC does not currently provide edge-current singularity behavior.

## VIII. SUMMARY AND CONCLUSION

A new formulation of electromagnetic wave scattering by two-dimensional conducting bodies of convex shape has been presented. This formulation is based upon a series expansion of the radiation condition which is applied directly on the scatterer surface. Substantial simplification of the overall scattering formulation is achieved since the original integral equation for the scattered field is reduced to just a line integral whose integrand is either known (for the TM case) or can be easily constructed (for the TE case). Results presented for TM illumination of the circular cylinder, square cylinder, and infinitely thin strip scatterers are simple analytical expressions for the surface electric current distribution and radar cross section. Results presented for TE illumination of the circular cylinder are obtained via solution of a simple second-order differential equation. Comparison of these OSRC results with benchmark computations for scatterer sizes of  $ka = 5$  and  $ka = 10$  indicates good agreement for the  $B_2$  radiation operator.

The ability to easily construct a sequence of higher order OSRC operators may ultimately lead to new approaches in modeling reentrant scatterers (as well as convex) and three-dimensional scatterers. This may present a useful alternative to present integral equation and uniform high-frequency approaches for such structures. A forthcoming paper will consider the application of OSRC to convex dielectric scatterers [1].

## ACKNOWLEDGMENT

The authors wish to thank the referees for their constructive remarks. They also wish to thank Mr. Thomas Moore for his careful checking of the analysis and numerical implementation.

## REFERENCES

- [1] K. R. Umashankar, A. Taflov, and G. A. Kriegsmann, "Extension of on-surface radiation condition theory to scattering by two-dimensional homogeneous dielectric objects," *IEEE Trans. Antennas Propagat.*, submitted for publication.
- [2] A. C. Vastano and R. O. Reid, "Tsunami response for islands: verification of a numerical procedure," *J. Marine Research*, vol. 25, pp. 129-139, 1967.
- [3] D. E. Merewether, "Transient currents induced on a metallic body of revolution by an electromagnetic pulse," *IEEE Trans. Electromagn. Compat.*, vol. EMC-13, pp. 41-44, May 1971.
- [4] K. S. Kunz and K.-M. Lee, "A three-dimensional finite-difference solution of the external response of an aircraft to a complex transient EM environment: Part I—The method and its implementation," *IEEE Trans. Electromagn. Compat.*, vol. EMC-20, pp. 328-333, May 1978.
- [5] G. A. Kriegsmann and C. S. Morawetz, "Numerical solutions of exterior problems with the reduced wave equation," *J. Comp. Phys.*, vol. 28, pp. 181-197, 1978.
- [6] E. L. Lindman, "Free-space boundary conditions for the time dependent wave equation," *J. Comp. Phys.*, vol. 18, pp. 66-78, 1975.
- [7] B. Engquist and A. Majda, "Absorbing boundary conditions for the numerical simulation of waves," *Math. Comp.*, vol. 31, pp. 629-651, July 1977.
- [8] G. A. Kriegsmann and C. Morawetz, "Solving the Helmholtz equation for exterior problems with variable index of refraction: I," *SIAM J. Sci. Stat. Comput.*, vol. 1, pp. 371-385, Sept. 1980.
- [9] A. Bayliss and E. Turkel, "Radiation boundary conditions for wave-like equations," *Commun. Pure Appl. Math.*, vol. 33, pp. 707-725, 1980.
- [10] G. Mur, "Absorbing boundary conditions for the finite-difference approximation of the time-domain electromagnetic field equations," *IEEE Trans. Electromagn. Compat.*, vol. EMC-23, pp. 377-382, Nov. 1981.
- [11] L. N. Trefethen and L. Halpern, "Well-posedness of one-way wave equations and absorbing boundary conditions," *Inst. Comput. Appl. Sci. and Eng. (ICASE)*, NASA Langley Res. Center, Hampton, VA, Rep. 85-30, June 1985.
- [12] K. R. Umashankar and A. Taflov, "A novel method to analyze electromagnetic scattering of complex objects," *IEEE Trans. Electromagn. Compat.*, vol. EMC-24, pp. 397-405, Nov. 1982.
- [13] A. Taflov and K. R. Umashankar, "Radar cross section of general three-dimensional scatterers," *IEEE Trans. Electromagn. Compat.*, vol. EMC-25, pp. 433-440, Nov. 1983.
- [14] A. Taflov, K. R. Umashankar, and T. G. Jurgens, "Validation of FD-TD modeling of the radar cross section of three-dimensional structures spanning up to nine wavelengths," *IEEE Trans. Antennas Propagat.*, vol. AP-33, pp. 662-666, June 1985.
- [15] J. J. Stoker, *Differential Geometry*. New York: Wiley, 1969.
- [16] R. F. Harrington, *Field Computation by Moment Methods*. New York: Macmillan, 1968.
- [17] R. Kouyoumjian, "Asymptotic high-frequency methods," *Proc. IEEE*, vol. 53, pp. 864-876, Aug. 1965.
- [18] P. H. Pathak, "An asymptotic analysis of the scattering of plane waves by a smooth convex cylinder," *Radio Sci.*, vol. 14, pp. 419-435, May-June 1979.





Gregory A. Kriegsmann received the M.S. degree in electrical engineering and the Ph.D. degree in applied mathematics from the University of California, Los Angeles, in 1970 and 1974, respectively.

He was a Courant Instructor in Applied Mathematics at New York University from 1974 to 1976. He is currently Professor of Applied Mathematics in the Department of Engineering Sciences and Applied Mathematics at Northwestern University, Evanston, IL. His research interests include the development of asymptotic and numerical methods

for solving wave propagation problems.

Dr. Kriegsmann is a member of Tau Beta Pi, the Society of Industrial and Applied Mathematicians, and the Acoustical Society of America.

Allen Tafflove (M'75-SM'84), for a photograph and biography please see page 766 of the June 1986 issue of this TRANSACTIONS.

Kerada R. Umashankar (S'69-M'75-SM'81), for a photograph and biography please see pages 765 and 766 of the June 1986 of this TRANSACTIONS.

by an incident field other than a plane wave. However, the uniform high-frequency solution (1) is valid only for broadside plane-wave incidence.

#### ACKNOWLEDGMENT

The authors are indebted to James L. Schmitz and Ernest J. Yasso for their help in performing the bistatic scattering cross section measurements.

#### REFERENCES

- [1] A. D. Yaghjian and R. V. McGahan, "Broadside radar cross section of the perfectly conducting cube," *IEEE Trans. Antennas Propagat.*, vol. AP-33, pp. 321-329, Mar. 1985.
- [2] A. D. Yaghjian, "Augmented electric- and magnetic-field integral equations," *Radio Sci.*, vol. 16, pp. 987-1001, Nov.-Dec. 1981.
- [3] M. G. Cote, "A spatial filtering technique for removing phase errors in automated bistatic scattering measurements," in *Digest Nat. Radio Science Meeting*, Boulder, CO, Jan. 1988, p. 73.
- [4] A. R. Tobin, A. D. Yaghjian, and M. M. Bell, "Surface integral equations for multi-wavelength, arbitrarily shaped, perfectly conducting bodies," in *Digest Nat. Radio Science Meeting*, Boulder, CO, Jan. 1987, p. 9.
- [5] J. J. Bowman, T. B. A. Senior, and P. L. E. Uslenghi, *Electromagnetic and Acoustic Scattering by Simple Shapes*. Amsterdam: North-Holland, 1969, ch. 6.
- [6] A. Michaeli, "Equivalent edge currents for arbitrary aspects of observation," *IEEE Trans. Antennas Propagat.*, vol. AP-32, pp. 252-258, Mar. 1984.
- [7] —, "Contribution of a single face to the wedge diffracted field," *IEEE Trans. Antennas Propagat.*, vol. AP-33, pp. 221-223, Feb. 1985.
- [8] —, "Equivalent currents for second-order diffraction by edges of perfectly conducting polygonal surfaces," *IEEE Trans. Antennas Propagat.*, vol. AP-35, pp. 183-190, Feb. 1987.
- [9] T. K. Sarker and E. Arvas, "On a class of finite step iterative methods (conjugate directions) for the solution of an operator equation arising in electromagnetics," *IEEE Trans. Antennas Propagat.*, vol. AP-33, pp. 1058-1066, Oct. 1985.
- [10] R. G. Kouyoumjian, "The geometrical theory of diffraction and its application," in *Numerical and Asymptotic Techniques in Electromagnetics, Topics in Applied Physics*, vol. 3, R. Mittra, Ed. New York: Springer-Verlag, 1975, p. 180.
- [11] F. A. Sikta, W. D. Burnside, T. Chu, and L. Peters, Jr., "First order equivalent current and corner diffraction scattering from flat plate structures," *IEEE Trans. Antennas Propagat.*, vol. AP-31, pp. 584-589, July 1983.
- [12] A. C. Ludwig, "Backscattering from a cube," *Appl. Computational Electromagn. Soc. J., Newsletter*, vol. 2, pp. 55-74, Fall 1987.

### An Application of the WKJB Technique to the On-Surface Radiation Condition

THOMAS G. MOORE, STUDENT MEMBER, IEEE,  
GREGORY A. KRIEGSMANN, AND  
ALLEN TAFLOVE, SENIOR MEMBER, IEEE

**Abstract**—The on-surface radiation condition (OSRC) method and the WKJB method are used to derive an analytic formula for the surface currents on a two-dimensional perfectly conducting convex target. The

Manuscript received August 4, 1987; revised January 21, 1988. This work was supported in part by the NASA Lewis Research Center under Grant NAG 3-635 and in part by the National Science Foundation under Grants MCS-8300578 and DMS-870094.

T. G. Moore and A. Taflove are with the Department of Electrical Engineering and Computer Science, Technological Institute, Northwestern University, Evanston, IL 60208.

G. A. Kriegsmann is with the Department of Engineering Sciences and Applied Mathematics, Technological Institute, Northwestern University, Evanston, IL 60208.

IEEE Log Number 8821482.

currents are induced by an incident TE-polarized plane wave. The case of a circular cylinder is used to demonstrate the usefulness of the combined methods. It is shown that a two-term expansion yields good results for the surface currents and excellent results for the ensuing bistatic radar cross section.

#### I. INTRODUCTION

Recently, Kriegsmann *et al.* have introduced a new method for solving scattering problems for two-dimensional convex cylinders [1]. By applying a radiation boundary condition on the surface of the scatterer (OSRC) they obtained a simple analytic expression for the surface current when the incident wave was transverse magnetic (TM) polarized. When the incident wave was TE polarized, the method yielded an ordinary differential equation for the surface current. This equation contains variable coefficients which depend upon the geometry of the cylinder and the nature of the incident wave. In general, it cannot be solved exactly.

In this communication, we shall derive an approximate solution to this differential equation by using the WKJB technique [2]. The motivation for such an approximation is twofold. First, it affords an accurate analytical approximation to the surface current without recourse to the numerical solution of a boundary value problem for arbitrary convex shapes. Secondly, and perhaps more importantly, a recent work by Jones [3] suggests that the approximate "surface current" for a three-dimensional convex acoustic target (hard) satisfies a second-order partial differential equation on the target's surface. We believe that a similar situation will occur when the OSRC method is extended to handle three-dimensional electromagnetic scattering problems. It seems plausible that the method presented herein could be extended to handle such situations.

The remainder of this work is organized in three additional sections. In Section II the scattering problem is formulated, and the OSRC method is used to derive an ordinary differential equation for the surface current. An approximate solution to this equation is deduced by the WKJB method in Section III. Finally, in Section IV the results for a circular cylinder are presented.

#### II. FORMULATION

We shall consider a transverse electric plane wave illuminating a two-dimensional perfectly conducting convex cylinder. The incident wave, propagating at an angle  $\alpha$  with respect to the  $-x$  axis, is given by

$$\vec{H}_{inc} = U_{inc} e^{-j\omega t} \hat{z} \quad U_{inc} = e^{jk(x \cos \alpha - y \sin \alpha)} \quad (1)$$

where the unit vector  $\hat{z}$  is parallel to the axis of the cylinder. The parameter  $\omega$  is the frequency of the incident wave,  $k = \omega a/c$ ,  $c$  is the speed of light in free space, and  $a$  is a characteristic dimension of the cylinder's cross section. The variables  $x$  and  $y$  are the corresponding dimensionless Cartesian coordinates in the plane orthogonal to  $\hat{z}$ . They are scaled with respect to the length  $a$ .

The scattered magnetic field  $\vec{H}_s$  is given by

$$\vec{H}_s(\vec{x}) = U(\vec{x}) e^{-j\omega t} \hat{z} \quad (2a)$$

$$U(\vec{x}) = \int_C J(\vec{x}) \frac{\partial G}{\partial \nu'}(\vec{x}, \vec{x}') ds' \quad (2b)$$

where  $C$  represents the boundary of the cylinder's cross section,  $\partial/\partial \nu'$  denotes an outward normal derivative on  $C$ , and  $G$  is the free-space Green's function given by

$$G(\vec{x}|\vec{x}') = \frac{j}{4} H_0^{(1)}(kR) \quad (2c)$$

$$R = |\vec{r} - \vec{r}'| = \sqrt{(x - x')^2 + (y - y')^2}. \quad (2d)$$

The vectors  $\vec{r}$  and  $\vec{r}'$  appearing above are just normalized  $(x, y)$  and  $(x', y')$ , respectively. The tangential surface current  $J$  appearing in (2b) is related to  $U_{inc}$  and  $U$  by

$$J(\vec{r}) = -[U_{inc}(\vec{r}) + U(\vec{r})]. \quad (3)$$

The tangential current is unknown, because  $U$  is not prescribed for the TE polarization. The OSRC method provides a means of generating an approximation to  $U$  in terms of known geometric quantities and  $U_{inc}$ . The motivation for this method, and its complete description are explained in [1]. Here, we present a single second-order approximation which is the one most often used in practice. <sup>1</sup>

$$\frac{d^2}{ds^2} U + A(s)U = B(s) \frac{\partial U_{inc}}{\partial \nu} \quad (4a)$$

$$A(s) = 2k^2 + 3jk\zeta(s) - \frac{3}{4}\zeta^2(s) \quad (4b)$$

$$B(s) = 2j(k + j\zeta(s)) \quad (4c)$$

where  $\zeta(s)$  is the curvature of the cylinder's surface at  $s$  and  $d^2/ds^2$  is the second derivative with respect to the arclength of  $C$ . Combining (3), (4), and the definition of  $U_{inc}$  from (1), we find that  $J$  satisfies

$$\frac{d^2 J}{ds^2} + A(s)J = -F(s)e^{jk\phi} \quad (5a)$$

$$F(s) = k^2 \left\{ 2 - \left( \frac{d\phi}{ds} \right)^2 - 2a(s) \right\} + jk \left\{ \frac{d^2 \phi}{ds^2} + 3\zeta(s) - 2a(s)\zeta(s) \right\} - \frac{3}{4}\zeta^2(s) \quad (5b)$$

$$a(s) = \hat{n}(s) \cdot (\cos \alpha, -\sin \alpha) \quad (5c)$$

$$\phi(s) = \vec{x}_0(s) \cdot (\cos \alpha, -\sin \alpha) \quad (5d)$$

where  $\vec{x}_0(s)$  is the vector representation of the curve  $C$ . In addition to satisfying (5)  $J$  must also be periodic, i.e.,

$$J(s+L) = J(s), \quad \frac{dJ}{ds}(s+L) = \frac{dJ}{ds}(s), \quad 0 \leq s \leq L \quad (6)$$

where  $L$  is the length of  $C$ . Thus the OSRC method has reduced the determination of the surface current to the problem of solving an ordinary second-order linear differential equation with variable coefficients and periodic boundary conditions.

We note here that the coefficient  $A(s)$  in (5a) has a nonzero complex component. Thus the homogeneous solution of (5), (6), i.e.,  $F = 0$  in (5a), has only the zero solution. From this we deduce that (5), (6) has a unique solution [4].

### III. WKBJ ANALYSIS

The actual computation of the surface current  $J$  which satisfies (5), (6) is impossible to perform analytically for an arbitrary convex cylinder. In general, it must be done numerically. However, it is quite easy to obtain a WKBJ approximation of  $J$  which yields an analytic formula.

According to this procedure we express  $J$  as

$$J(s) = V(s, k)e^{jk\psi(s)} \quad (7a)$$

where the amplitude  $V(s, k)$  has the asymptotic expansion

$$V(s, k) \sim \sum_{n=0}^{\infty} V_n(s)k^{-n}. \quad (7b)$$

Since the phase  $\phi(s)$  defined in (5d) satisfies (6), the function  $J$  will too, as long as the amplitudes  $V_n(s)$  also satisfy these conditions. Inserting (7) into (5) and equating to zero the coefficients of the powers of  $k$ , we deduce an infinite number of algebraic equations which sequentially determine the  $V_n(s)$ . The first two amplitudes, which suffice for our purpose here, are given by

$$V_0(s) = -1 + \frac{a(s)}{D(s)} \quad (8a)$$

$$V_1(s) = -j \left\{ \frac{\ddot{\phi} + (\ddot{\phi} + 3\dot{\zeta})V_0 + 2\dot{\phi}\dot{V}_0 - \zeta(2a-3)}{2D} \right\} \quad (8b)$$

$$D = 1 - \frac{1}{2}\dot{\phi}^2 \quad (8c)$$

where the dots denote differential with respect to the arclength  $s$ . We note that the denominator  $D$  does not vanish because  $\dot{\phi}$  is the projection of the unit tangent vector onto  $(\cos \alpha, -\sin \alpha)$  and is thus less than one in modulus. We also observe that  $V_0$  and  $V_1$  satisfy (6) because the curvature  $\zeta(s)$  and  $\phi(s)$  are periodic functions.

Inserting the first two terms of (7b) into (7a) we formally deduce that

$$J \sim \left[ V_0 + \frac{1}{k} V_1 + O(1/k^2) \right] e^{jk\psi(s)} \quad (9)$$

where  $O(1/k^2)$  represents the remaining terms. This is the WKBJ approximation of the periodic solution of (5), (6).

The approximate surface current given by (9) can be inserted into (2) to determine the scattered field. This expression simplifies in the far field,  $r \gg 1$ , to

$$U \sim A(\Theta, k) \frac{e^{jkr}}{\sqrt{r}} \quad (10a)$$

$$A(\Theta, k) = -\sqrt{\frac{k}{8\pi}} e^{-j\pi/4} \int_C \left[ V_0(s) + \frac{1}{k} V_1(s) \right] e^{jk\psi(s)} \cos \delta(s) ds \quad (10b)$$

where  $\psi(s) = -\vec{x}_0(s) \cdot \hat{\rho} + \phi(s)$ ,  $\cos \delta = \hat{n} \cdot \hat{\rho}$ ,  $\hat{n}$  is the unit normal of  $C$  at  $s$ , and  $\hat{\rho} = (\cos \Theta, \sin \Theta)$  is the unit vector in the observation direction.

### IV. EXAMPLE: THE CIRCULAR CYLINDER

In this example  $C$  is a circle of unit radius so that  $\zeta = 1$  in all the preceding formulas. Without loss of generality, the angle  $\alpha$  defined in (1) is set to zero in the subsequent equations. The exact boundary value problem for the Helmholtz equation can be solved exactly using a Fourier series representation. In Fig. 1 we have graphed the results predicted by (9) versus the Fourier series solution for the  $k = 5$  circular cylinder. Thirty terms were taken in the Fourier series to obtain an accurate answer. As can be seen in this diagram, the results given by (9) are quite close to the exact answer. Similarly, Fig. 2 shows our results for the  $k = 10$  circular cylinder. Here again 30 terms were used in the partial sum to insure accuracy. The agreement between (9) and the exact solution is even better than before: this is to be expected since the WKBJ method is a high-frequency approximation.

Fig. 3 compares the bistatic radar cross section predicted by (10b) for a  $k = 5$  circular cylinder versus the exact answer computed by a

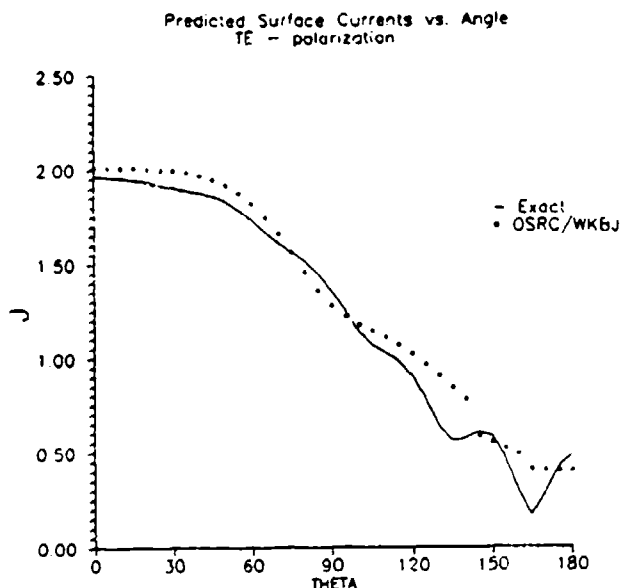


Fig. 1. OSRC predicted surface currents using a two-term asymptotic expansion for  $k = 5$  circular cylinder.

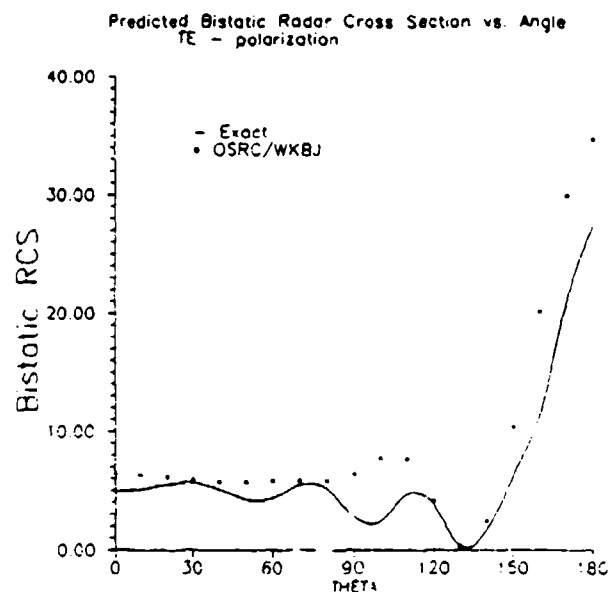


Fig. 3. Predicted RCS for  $k = 5$  circular cylinder (RCS is scaled with respect to  $k$ ).

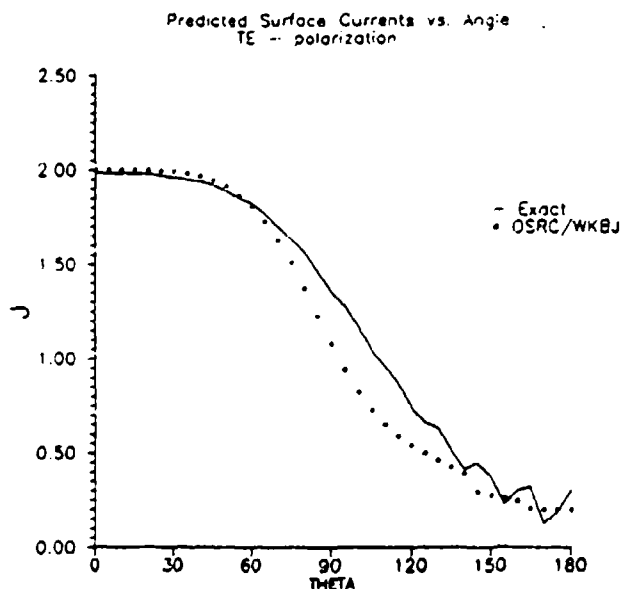


Fig. 2. OSRC predicted surface currents using a two-term asymptotic expansion for  $k = 10$  circular cylinder.

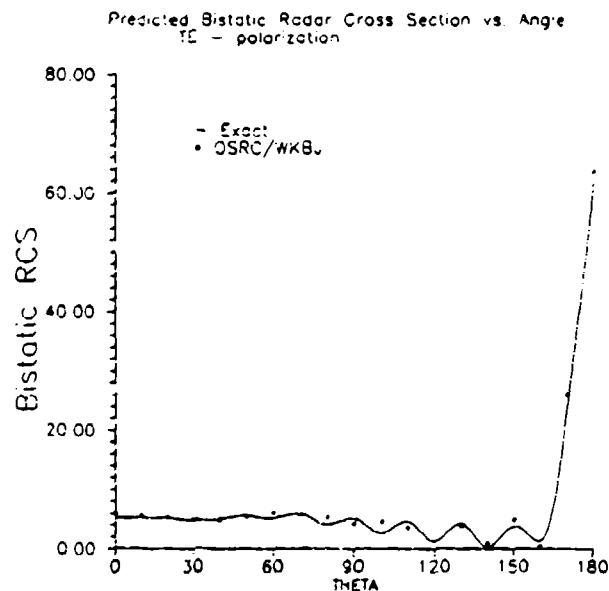


Fig. 4. Predicted RCS for  $k = 10$  circular cylinder (RCS is scaled with respect to  $k$ ).

Fourier series. Fig. 4 shows the bistatic radar cross section for a  $k = 10$  circular cylinder. We can see that the agreement between the predicted and the exact RCS is very good over the entire range of angles, and as before, the error is even smaller for the larger cylinder. This is to be expected since the integration process tends to remove small errors introduced by the asymptotic expansion. The most significant errors are in the deep shadow where the phase of our approximate currents differs from the exact answer. This is not a deficiency in the WKBJ method but rather the OSRC approximation.

In conclusion we see that the asymptotic expansion (9) does a good job of estimating the surface current over a wide range of frequencies while even better agreements can be seen in the bistatic radar cross section results. Thus, for convex objects being illuminated by a TE

polarized wave, the combination of the OSRC and WKBJ methods provides a powerful tool for analyzing scattering problems.

#### REFERENCES

- [1] G. A. Kriegsmann, A. Taflov, and K. R. Umashankar, "A new formulation of electromagnetic wave scattering using a on-surface radiation boundary condition approach," *IEEE Trans. Antennas Propagat.*, vol. AP-35, pp. 153-161, Feb. 1987.
- [2] D. S. Jones, *The Theory of Electromagnetism*. Oxford, England: Pergamon, 1964.
- [3] —, "An approximated boundary condition in acoustics," *J. Sound and Vibration*, vol. 121, pp. 37-45, 1988.
- [4] I. Stakgold, *Boundary Value Problems of Mathematical Physics*, vol. 1. New York: Macmillan, 1967.

## Tutorial

# Theory and Application of Radiation Boundary Operators

THOMAS G. MOORE, STUDENT MEMBER, IEEE, JEFFREY G. BLASCHAK, STUDENT MEMBER, IEEE,  
ALLEN TAFLOVE, SENIOR MEMBER, IEEE, AND GREGORY A. KRIEGSMANN

*Invited Review Paper*

**Abstract**—A succinct unified review is provided of the theory of radiation boundary operators which has appeared principally in the applied mathematics and computational physics literature over the last ten years. With the recent introduction of the on-surface radiation condition (OSRC) method and the continued growth of finite-difference and finite-element techniques for modeling electromagnetic wave scattering problems, the understanding and use of radiation boundary operators has become increasingly important to the engineering community. In the OSRC method, specific radiation boundary operators are applied directly on the surface of an arbitrary convex target, substantially simplifying the usual integral equation for the scattered field. In the finite-difference and finite-element techniques, radiation boundary operators are used to truncate the computational domain near the target, while accurately simulating an infinite modeling space. Results are presented to illustrate the application of radiation boundary operators in both of these areas. Recent OSRC results include analysis of the scattering behavior of both electrically small and electrically large cylinders, a reactively loaded acoustic sphere, and a simple resonant duct. New radiation boundary operator results include the demonstration of the effectiveness of higher order operators in truncating finite-difference time-domain grids.

## I. INTRODUCTION

WITH THE RECENT introduction of the on-surface radiation condition (OSRC) method [1] and the continued growth of finite-difference time-domain (FD-TD) [2] and finite-element [3] techniques for modeling electromagnetic wave scattering problems, the understanding and use of radiation boundary operators has become increasingly important to the engineering community. Radiation boundary operators have fundamentally different uses in the OSRC and finite-difference/finite-element methods. Finite techniques use radiation boundary operators in either the time domain or frequency domain to create a radiation boundary condition (RBC) which truncates a volumetric computational domain electrically close to a modeled target, and yet effectively

simulates the extension of the computational domain to infinity. In contrast, the OSRC method uses the radiation boundary operator directly on the surface of the target to reduce the usual frequency-domain integral equation for the scattered field to either an integration of known quantities or a second-order ordinary differential equation. Each is simply implemented on the target surface. Although the OSRC and finite methods use radiation boundary operators in different manners, both techniques can be greatly enhanced by more effective radiation boundary operators.

The purpose of this paper is to provide a succinct unified review of key research that has been performed in the area of radiation boundary operators. Because much of this research has appeared in the applied mathematics and computational physics literature over the past ten years, its results and implications are generally not well known by the engineering electromagnetics community. This paper will also present some recent results from the application of these operators to engineering problems. In particular, we will examine two basic types of radiation boundary operators and give examples showing their use in both the FD-TD and OSRC methods. Specifically, in Section II we will discuss the theory behind radiation boundary operators. In Section III the radiation boundary operators will be used to construct new radiation boundary conditions for a two-dimensional FD-TD grid of higher order than those currently used; and the effectiveness of the new radiation boundary conditions will be tested. In Section IV, the radiation boundary operators will be used in the OSRC method to approximately solve the problem of scattering from a perfectly conducting cylinder. Section V concludes with a discussion of the research activities that are ongoing in the areas of radiation boundary operators and their applications.

## II. THEORY

There are two basic types of radiation boundary operators: mode annihilating and one-way wave equation approximations. Each of these radiation boundary operators possesses different characteristics and forms. In this section, the two different types of radiation boundary operators are examined in detail.

Manuscript received October 15, 1987; revised January 18, 1988. This work was supported in part by NASA Lewis Research Center Grant NAG 3-635 and in part by the National Science Foundation Grant MCS-8300578.

T. G. Moore and A. Taflov are with the Department of Electrical Engineering and Computer Science, Technological Institute, Northwestern University, Evanston, IL 60201.

J. G. Blaschak is with the Lincoln Laboratory, Massachusetts Institute of Technology, Lexington, MA 02173.

G. A. Kriegsmann is with the Department of Engineering Sciences and Applied Mathematics, Technological Institute, Northwestern University, Evanston, IL 60201.

IEEE Log Number 8823652.

### A. Mode-Annihilating Operators

The first type of radiation boundary operator to be discussed is the mode-annihilating differential operator. This type of operator is based on the idea of killing the terms (herein referred to as "modes") of the far-field expansion of outward propagating solutions to the wave equation. One can view the idea of killing modes of the scattered fields as first being proposed by Sommerfeld in the form of the Sommerfeld radiation condition [4] which annihilates the first mode in the expansion. Later, researchers [5] extended the Sommerfeld theory and created an operator that annihilates the next mode in the expansion. Independently, other researchers created a general operator that kills an arbitrary number of modes in the expansion as derived and presented in [6]. It is the theory that appeared in [6] that will be reviewed in this section.

For this section we will proceed as follows. In Section II-A1) the scattered fields are written in terms of a far-field expansion, and the effect that the Sommerfeld radiation condition has on the expansion is presented. The operators derived in [6], are presented in Section II-A2) for the full three-dimensional case and are specialized to two dimensions in Section II-A3).

1) *Far-Field Expansions and the Sommerfeld Radiation Condition:* We consider here solutions  $U(R, \theta, \phi, t)$  to the scalar wave equation

$$\nabla^2 U - U_t = 0 \quad (1)$$

and the associated Helmholtz equation for time-harmonic waves

$$\nabla^2 U + k^2 U = 0 \quad (2)$$

where the wave speed  $c$  has been scaled to unity and the harmonic wave is assumed to have time dependency  $e^{-j\omega t}$ . The radiating solutions of the scalar wave equation (i.e., solutions propagating in directions which are outward from the origin of a spherical coordinate system) can be expanded in a convergent series of the form [7],

$$U(R, \theta, \phi, t) = \sum_{i=1}^{\infty} \frac{f_i(t-R, \theta, \phi)}{R^i} \quad (3)$$

This result was extended to the time-harmonic case for both vector and scalar fields [8]. For the scalar Helmholtz equation, it is proved in [8] that

$$U(R, \theta, \phi) = \frac{e^{jkR}}{R} \sum_{i=0}^{\infty} \frac{f_i(\theta, \phi)}{R^i} \quad (4)$$

is a convergent expansion for scalar wave functions that satisfy the Sommerfeld radiation condition.

The Sommerfeld radiation condition [4], given by

$$\lim_{R \rightarrow \infty} R(U_R - jkU) = 0 \quad (5a)$$

where  $U_R$  denotes a derivative respect to  $R$ , is satisfied by the each term of (4). By using the correspondence  $-jk = \partial/\partial t$ , the Sommerfeld condition is extended to

$$\lim_{R \rightarrow \infty} R(U_R + U_t) = 0 \quad (5b)$$

which is satisfied by each term of the expansion in (3). The

Sommerfeld radiation condition can be viewed as an operator on the far-field expansion of  $U$  giving the asymptotic result,

$$\left( \frac{\partial}{\partial R} - jk \right) U = O(R^{-2}) \quad (6)$$

in the limit  $R \rightarrow \infty$ . In other words, the Sommerfeld condition retains terms that are no greater than  $O(R^{-2})$  in the expansion.

2) *Higher Order Operators:* With the goal of devising operators that annihilate terms up to any order in the far-field expansion of  $U$ , a sequence of operators  $B_n$  was proposed [6] for the expansion in (3). A similar sequence of operators was independently developed for the Helmholtz equation in two dimensions [5]. The former were extended [9] for the Helmholtz equation in both two and three dimensions. We restrict our review here to operators for the time-harmonic case [9], keeping in mind that results for waves of arbitrary time variation can be obtained by a simple substitution of  $\partial/\partial t$  for the term  $-jk$ .

The derivation of  $B_n$  begins by multiplying a slightly rewritten version of (4) by  $R^n$  and then splitting the sum as shown:

$$R^n U(R, \theta, \phi) = \sum_{i=1}^n R^{n-i} e^{jkR} F_i(\theta, \phi) + \sum_{i=n+1}^{\infty} R^{n-i} e^{jkR} F_i(\theta, \phi). \quad (7)$$

Now define the intermediate operator,

$$L = \frac{\partial}{\partial R} - jk \quad (8a)$$

and observe that applying  $L^n$  to both sides of (7) annihilates the first sum and makes the leading order term of the second sum be  $O(R^{-n-1})$ . We have

$$L^n (R^n U) = O(R^{-n-1}) \quad (8b)$$

which accomplishes the goal of annihilating the first  $n$  terms of the far-field expansion. A more useful way to express this result is as a single operator acting on  $U$  only. This is achieved by inductive arguments [9]. For  $n = 1$ ,

$$L(RU) = \left( \frac{\partial}{\partial R} - jk \right) RU = O(R^{-2}) \quad (9a)$$

$$\left( \frac{\partial}{\partial R} - jk + \frac{1}{R} \right) U + U = O(R^{-2}) \quad (9b)$$

which can be written as

$$\left( \frac{\partial}{\partial R} - jk + \frac{1}{R} \right) U = O(R^{-2}). \quad (9c)$$

The first operator in the sequence is then

$$B_1 = L + \frac{1}{R} \quad (10a)$$

which, when applied to both sides of (4), annihilates the first term of the expansion. Similarly,

$$B_2 = \left( L + \frac{3}{R} \right) \left( L + \frac{1}{R} \right) \quad (10b)$$

annihilates the first two terms. In general, the recursion relation,

$$B_n = \left( L + \frac{2n-1}{R} \right) B_{n-1} \quad (11)$$

produces an operator which annihilates the first  $n$  terms of the expansion in (4). The sequence of operators gives

$$B_n U = O(R^{-2n-1}) \quad (12)$$

for any function  $U$  satisfying the expansion in (4).

In the literature,  $B_n$  has been utilized as a boundary condition

$$B_n U = 0 \quad (13)$$

for the wave function  $U$ . This condition becomes more accurate, in powers of  $R^{-1}$ , as the order of the operator  $n$  increases. The original application of (13) was to truncate a computational domain while accurately modeling the outward propagation of waves to infinity. Further application of  $B_n$ , particularly  $B_2$ , is found in the OSRC method for computing scattering from two-dimensional, convex, conducting and homogenous dielectric bodies.

3) *Operators for Two-Dimensional Wave Propagation:* Extension of  $B_n$  for use with wave functions  $U(r, \theta, t)$  in two space dimensions proceeds in the time harmonic case from an expansion presented in [10],

$$U(r, \theta) = H_0(kr) \sum_{i=0}^{\infty} \frac{F_i(\theta)}{r^i} + H_1(kr) \sum_{i=0}^{\infty} \frac{G_i(\theta)}{r^i} \quad (14)$$

which has the far-field result [9],

$$U(r, \theta) = \sqrt{\frac{2}{\pi kr}} e^{j(kr - (\pi/2))} \sum_{i=0}^{\infty} \frac{f_i(\theta)}{r^i} \quad (15)$$

that is analogous to (4). A sequence of boundary operators is defined [6] by the recursion relationship

$$B_n = \left( L + \frac{4n-3}{2r} \right) B_{n-1} \quad (16)$$

where

$$B_1 = L + \frac{1}{r} \quad (17a)$$

and

$$L = \frac{\partial}{\partial r} - jk. \quad (17b)$$

The operator  $B_n$  annihilates the first  $n$  terms of the expansion (16) and yields

$$B_n U = O(r^{-2n-1/2}). \quad (18)$$

The utility of these operators will be demonstrated in Section IV in the OSRC calculation of electromagnetic

scattering from a conducting circular cylinder illuminated by a TE polarized plane wave. The first two operators used there are

$$B_1 = \frac{\partial}{\partial r} + \frac{1}{2r} - jk \quad (19a)$$

and

$$B_2 = \frac{\partial}{\partial r} + \frac{1}{2r} - jk - \left( \frac{\partial^2}{\partial \theta^2} + \frac{1}{4} \right) / \left[ 2r^2 \left( \frac{1}{r} - jk \right) \right]. \quad (19b)$$

In the derivation of (19b) the recursion relation, (16) produces a second-order  $r$  derivative. It is conveniently eliminated by the substitution from the Helmholtz equation,

$$\frac{\partial^2}{\partial r^2} = -\frac{1}{r^2} \frac{\partial^2}{\partial \theta^2} - \frac{1}{r} \frac{\partial}{\partial r} - k^2. \quad (20)$$

## B. One-Way Wave Equations

A partial differential equation which permits wave propagation only in certain directions is called a "one-way wave equation." Fig. 1 shows a finite two-dimensional Cartesian domain  $\Omega$  on which the time-dependent wave equation is to be simulated. In the interior of  $\Omega$ , a numerical scheme which models wave propagation in all directions is applied. On the outer boundary  $\partial\Omega$ , only numerical wave motion that is outward from  $\Omega$  is permitted. The boundary must permit outward propagating numerical waves to exit  $\Omega$  just as if the simulation were performed on a computational domain of infinite extent. A scheme which enacts a one-way wave equation on  $\partial\Omega$  for this purpose is called a radiation boundary condition (RBC).

1) *Derivation by Wave Equation Factoring<sup>1</sup>:* The derivation of an RBC whose purpose is to absorb numerical waves incident upon the outer boundary of a finite-difference or finite-element grid can be explained in terms of operator factoring. Consider the two-dimensional wave equation in Cartesian coordinates,

$$U_{xx} + U_{yy} - U_{tt} = 0. \quad (21)$$

The partial differential operator here is

$$L = D_x^2 + D_y^2 - D_t^2 \quad (22a)$$

which uses the notation,

$$D_x^2 = \frac{\partial^2}{\partial x^2} \quad D_y^2 = \frac{\partial^2}{\partial y^2} \quad D_t^2 = \frac{\partial^2}{\partial t^2}. \quad (22b)$$

The wave equation is then compactly written as

$$LU = 0. \quad (23)$$

The wave operator  $L$  can be factored in the following manner:

$$LU = L^+ L^- U = 0 \quad (24a)$$

<sup>1</sup> It can be demonstrated that wave equation factoring can generate  $B_1$  and  $B_2$  described in Section II-A. However, this has not been shown for  $n > 2$ .

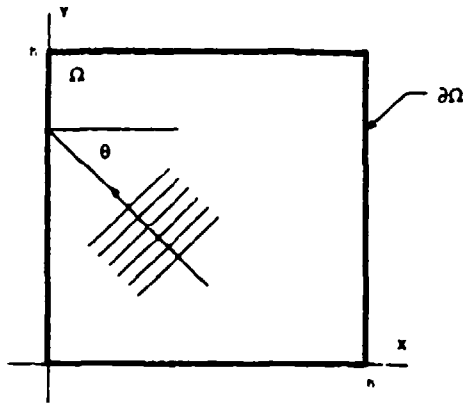


Fig. 1. Two-dimensional Cartesian computational domain.

where  $L^-$  is defined as

$$L^- = D_x - D_t \sqrt{1 - S^2} \quad (24b)$$

with

$$S = \frac{D_y}{D_t} \quad (24c)$$

the operator  $L^+$  is similarly defined except for a "+" sign before the radical.

In [11] it is shown that at a boundary, say at  $x = 0$ , the application of  $L^-$  to the wave function  $U$  will exactly absorb a plane wave incident at any angle and traveling in the  $-x$  direction. Thus

$$L^- U = 0 \quad (25)$$

applied at  $x = 0$  functions as an exact analytical RBC which absorbs wave motion from the interior of the spatial domain  $\{ \Omega = (x, y): 0 < x < h, 0 < y < h \}$ . The operator  $L^+$  performs the same function for waves traveling in the  $+x$  direction that impact the other  $x$  boundary in Fig. 1 at  $x = h$ . The presence of the radical in (24b) classifies  $L^-$  as a pseudodifferential [11] operator that is nonlocal in both the space and time variables. This is an undesirable characteristic in that it prohibits the direct numerical implementation of (25) as an RBC.

Approximation of the radical in (24b) produce RBC's that can be implemented numerically and are useful in FD-TD simulations of the wave equation. The numerical implementation of an RBC is not exact in that a small amount of reflection does develop as numerical waves pass through the grid boundary. However, it is possible to design an RBC which minimizes the reflection as much as possible over a range of incident angles [12]. The RBC derived in [13] and applied in the simulation of electromagnetic scattering [14], uses a two-term Taylor series approximation to the radical in (24b).

$$\sqrt{1 - S^2} \approx 1 - \frac{1}{2} S^2. \quad (26a)$$

This leads to the following approximate analytical RBC which

can be numerically implemented at the  $x = 0$  boundary:

$$U_{xx} - U_{tt} + \frac{1}{2} U_{yy} = 0. \quad (26b)$$

A generalization of (26) presented in [15] showed that the construction of numerically useful absorbing boundary conditions reduces to approximation of  $\sqrt{1 - S^2}$  on the interval  $[-1, 1]$  by the rational function,

$$r(s) = \frac{p_m(s)}{q_n(s)} \quad (27)$$

where  $p$  and  $q$  are polynomials of degree  $m$  and  $n$ , and  $r(s)$  is said to be of type  $(m, n)$ . By specifying  $r(s)$  as a general type  $(2, 0)$  approximant, the radical is approximated by an interpolating polynomial of the form

$$\sqrt{1 - S^2} \approx p_0 + p_2 S^2 \quad (28a)$$

resulting in the general second-order approximate analytical RBC,

$$U_{xx} - p_0 U_{tt} - p_2 U_{yy} = 0. \quad (28b)$$

The choice of the coefficients  $p_0$  and  $p_2$  is determined by the method of interpolation. Standard techniques such as Chebyshev, least-squares, or Padé approximation are applied with the goal of producing an approximate RBC whose performance is good over a wide range of incident wave angles. Expressions similar to (28) can be derived and applied at the other three boundaries of a two-dimensional FD-TD grid.

High order approximations to the radical in (24b) were proposed in [15] as a means to derive a more accurate approximate RBC. Use of the general type  $(2, 2)$  rational function,

$$\sqrt{1 - S^2} \approx \frac{p_0 + p_2 S^2}{q_0 + q_2 S^2} \quad (29a)$$

gives the general third-order approximate analytical RBC,

$$q_0 U_{xx} + q_2 U_{yy} - p_0 U_{tt} - p_2 U_{yy} = 0. \quad (29b)$$

Appropriate selection of the  $p$  and  $q$  coefficients in (29) produces various families of RBC's, as suggested in [12] and [15]. For example,  $q_0 = p_0 = 1$ ,  $p_2 = -3/4$ , and  $q_2 = -1/4$  gives a Padé  $(2, 2)$  approximation in (29a) with the resulting RBC function better than (26b) for numerical waves impacting the grid boundary at near normal incidence. This results in the third-order RBC originally proposed in [11]. Other types of approximating polynomials "tune" the RBC to absorb numerical waves incident at specified angles other than normal, and are considered to be a means to improve wide-angle performance [12]. Results from a comparative study [16] of the performance of various families of RBC's are presented in Section III.

2) *Derivation by Dispersion Relation:* An alternate procedure for obtaining one-way wave equations is presented in the literature [12], [15]. We summarize the technique here for completeness. It is well known that if the dispersion



relation for a linear constant-coefficient partial differential equation is known, then the equation itself is specified [17]. Thus if one can obtain the dispersion relation for a one-way wave equation, then an RBC appropriate for use on  $\partial\Omega$  is obtained.

If a plane wave solution

$$U(x, y, t) = e^{j(\omega t + \xi x + \eta y)} \quad (30)$$

is substituted into (21), then

$$\omega^2 = \xi^2 + \eta^2 \quad (31)$$

is the dispersion relation for the wave equation which permits wave propagation in all directions of the  $x$ - $y$  plane. The wave in (30) has velocity

$$\mathbf{v} = v_x \hat{\mathbf{x}} + v_y \hat{\mathbf{y}} \quad (32a)$$

where

$$v_x = -\frac{\xi}{\omega} = -\cos \theta \quad (32b)$$

$$v_y = -\frac{\eta}{\omega} = -\sin \theta \quad (32c)$$

and  $\theta$  is the counterclockwise angle measured from the the negative  $x$  axis. By rewriting (31) as

$$\frac{\xi}{\omega} = \pm \sqrt{1 - s^2} \quad (33a)$$

with

$$s = \frac{\eta}{\omega} \quad (33b)$$

a dispersion relation can be identified which corresponds to an equation that admits plane wave solutions propagating only in the  $-x$  direction. This is obtained by choosing the positive branch of the square root in (33a) which corresponds to waves having velocity component  $v_x$ , in the  $-x$  direction. Wave motion from the interior of  $\Omega$  will be absorbed at the  $x = 0$  grid boundary if an equation having the dispersion relation,

$$\xi = \omega \sqrt{1 - s^2} \quad (34)$$

is applied at that boundary.

Equation (34) is a dispersion relation for a pseudodifferential equation [11] and cannot be identified with a linear partial differential equation which can be implemented numerically on the  $x = 0$  boundary. By approximating the radical in (34), it is possible to obtain a dispersion relation which can be identified with a partial differential equation that functions as an approximate analytical RBC. The same methods of approximation for the radical used in Section II-A1) can be applied here; however,  $s$  is now defined by (33b). Once a dispersion relation is obtained with approximates the exact relation in (34), the same RBC's are derived as in Section II-A1). We illustrate here application of the two-term Taylor

series approximation to the radical. Equation (34) becomes

$$\xi = \omega \left( 1 - \frac{1}{2} \frac{\eta^2}{\omega^2} \right) \quad (35a)$$

which is equivalent to

$$\xi \omega = \omega^2 - \frac{1}{2} \eta^2 \quad (35b)$$

which is the dispersion relation of

$$U_{xx} = U_{xx} - \frac{1}{2} U_{yy} \quad (35c)$$

This is the same expression as the approximate analytical RBC given in (26b). Higher order RBC's follow directly.

### III. APPLICATION OF ONE-WAY WAVE EQUATIONS: FD-TD RADIATION BOUNDARY CONDITIONS

In the simulation of electromagnetic wave scattering by finite techniques, one-way wave equations are used to truncate the computational domain in a manner which accurately models the propagation of scattered waves to infinity [13], [14]. This section summarizes recent results in applying the theory of one-way wave equations to the simulation of electromagnetic scattering by the FD-TD method. In particular, the promise of higher order RBC's is quantified by a reflection coefficient analysis and by numerical experiments. It is demonstrated that a reduction in grid boundary reflection is realized when a third-order RBC is applied on the boundary of a two-dimensional FD-TD grid.

#### A. Reflection Coefficient Analysis

Numerical radiation boundary conditions derived from approximate analytical one-way wave equations are not exact in that a small amount of reflection will be realized from numerical wave striking the grid boundary. For a numerical plane wave striking the  $x = 0$  boundary in Fig. 1, the amount of reflection is dependent upon the angle of incidence  $\theta$ . Now, scattered waves from a complex body can be viewed as a superposition of plane waves striking the computational boundaries over a wide range of incident angles. Therefore, the performance of a given RBC can be assessed by deriving a reflection coefficient  $R$ , which quantifies the amount of nonphysical reflection a plane wave produces as a function of  $\theta$  when it interacts with the grid boundary. Clearly, a good RBC gives a small value of  $R$  over a wide range of  $\theta$ . Such an RBC should perform well in the simulation of a realistic scattering situation because the grid boundaries would permit most of the scattered energy to exit the computational domain.

Consider the outgoing plane wave in Fig. 1. The wave has the form,

$$U_{inc} = e^{j(kx \cos \theta - ky \sin \theta)} \quad (36)$$

The total field at the boundary of the computational domain must satisfy the specific RBC in effect there. Postulating the existence of a reflected wave launched from the boundary, the

TABLE I  
COEFFICIENTS FOR THIRD-ORDER RBC'S

Type of Approximation	$p_0$	$p_1$	$q_1$	Angles of Exact Absorption (°)
Padé	1.00000	-0.75000	-0.25000	0.00
$L^\infty$	0.99973	-0.80864	-0.31657	11.7, 31.9, 43.5
Chebyshev points	0.99650	-0.91296	-0.47258	15.0, 45.0, 75.0
$L^2$	0.99250	-0.92233	-0.51084	18.4, 51.3, 76.6
C-P	0.99030	-0.94314	-0.5556	18.4, 53.1, 81.2
Newman points	1.00000	-1.00000	-0.66976	0.0, 60.5, 90.0
$L^\infty$	0.95651	-0.94354	-0.70355	26.9, 66.6, 87.0

$q_0 = 1.00000$  for each technique.

TABLE II  
COEFFICIENTS FOR SECOND-ORDER RBC'S

Type of Approximation	$p_0$	$p_1$	Angles of Exact Absorption (°)
Padé	1.00000	-0.50000	0.00
$L^\infty$	1.00023	-0.51555	7.6, 18.7
Chebyshev points	1.03597	-0.76537	22.5, 67.5
$L^2$	1.03084	-0.73631	22.1, 64.4
C-P	1.06103	-0.84883	25.8, 73.9
Newman points	1.00000	-1.00000	0.0, 90.0
$L^\infty$	1.12500	-1.00000	31.4, 81.6

total field at the  $x = 0$  boundary has the form,

$$U = ej(kl + kx \cos \theta - ky \sin \theta) + R ej(kl - kx \cos \theta - ky \sin \theta) \quad (37)$$

where  $R$  can be determined by substituting  $U$  directly into the equation for the RBC used at the  $x = 0$  boundary.

By substituting (37) into (28b) and (29b), reflection coefficient expressions as a function of incident angle are obtained for the general second- and third-order RBC's. They are, respectively,

$$R = \frac{\cos \theta - p_0 - p_1 \sin^2 \theta}{\cos \theta + p_0 + p_1 \sin^2 \theta} \quad (38)$$

and

$$R = \frac{q_0 \cos \theta + q_1 \cos \theta \sin^2 \theta - p_0 - p_1 \sin^2 \theta}{q_0 \cos \theta + q_1 \cos \theta \sin^2 \theta + p_0 + p_1 \sin^2 \theta} \quad (39)$$

where the coefficients  $p$  and  $q$  correspond to the approximating function used in the derivation of the RBC. Seven techniques of approximation are developed in [15] for this purpose. The techniques are: Padé; Chebyshev on a subinterval ( $L^\infty$ ); interpolation in Chebyshev points; least-squares ( $L^2$ ); Chebyshev-Padé (or C-P); interpolation in Newman points; and Chebyshev ( $L^\infty$ ). Tables I and II show  $p$  and  $q$  coefficients for approximating functions of both second and third order. The mechanics of their derivation can be found in [15]. A type (2, 2) approximant produces a third-order RBC. Second-order RBC's are obtained from type (2, 0) approximants. Also shown in Tables I and II are angles of incidence at which the RBC's are designed to exactly absorb numerical plane waves. The Padé family concentrates absorption near  $\theta = 0^\circ$ . The others distribute absorption angles through the

range  $[0, \pi/2]$  as a means to improve wide-angle performance [15]. A more general approach, which permits the design of boundary conditions for plane waves incident at arbitrary angles, is presented in [18] and [19].

Figs. 2 and 3 show the behavior of the reflection coefficient for the two best-performing RBC's as a function of incident angle on the range  $[0, \pi/2]$ . In all cases studied, the behavior of reflection coefficient for third-order RBC's is better than that of second-order RBC's. Fig. 2(a) shows  $R$  less than one percent for  $0 < \theta < 45^\circ$  for the third-order Padé RBC. Note that the Padé RBC's have a very low reflection coefficient for normal incidence. The distribution of exact absorption angles away from  $\theta = 0^\circ$  is illustrated in Fig. 2(b) for the  $L^\infty$  RBC. The nulls in the behavior of  $R$  are as predicted by the analysis presented in [15]. Fig. 3 compares the third-order Padé and the third-order  $L^\infty$  RBC's. By sacrificing performance near  $\theta = 0^\circ$ , the  $L^\infty$  RBC extends the point at which  $R$  is less than one percent to about  $\theta = 60^\circ$ .

### B. Numerical Experiments

Numerical experiments are now reported which clearly measure the amount of nonphysical reflection a given RBC produces as a pulse propagates through a grid boundary. Fig. 4(a) shows two domains on which the two-dimensional FD-TD algorithm is computed simultaneously for the transverse magnetic (TM) case. On the boundary of the test domain  $\Omega_T$  a test RBC is applied. Each point in  $\Omega_T$  has a corresponding member in the substantially larger domain  $\Omega_B$ . A line source is located at grid position (50, 25) in both domains. The source produces outward propagating, cylindrical waves which are spatially coincident in both domains up until time steps when the waves interact with the boundary of  $\Omega_T$ . Any reflection from the boundary of  $\Omega_T$  makes the solution at points within  $\Omega_T$  differ from the solution at corresponding points within  $\Omega_B$ . The wave solution at points within  $\Omega_B$  represents the desired numerical modeling of free-space propagation up until time steps when reflections from its own boundary enter the region of  $\Omega_B$  corresponding to  $\Omega_T$ . By calculating the difference in the solutions in  $\Omega_B$  and  $\Omega_T$  at each point at each time step, a measure of the spurious reflection caused by the boundary of  $\Omega_T$  is obtained.

We define at the  $n$ th time step

$$D(l, j) = E_l^T(l, j) - E_l^B(l, j) \quad (40a)$$

for all  $(l, j)$  within the test domain, where  $E_l^T$  is the solution

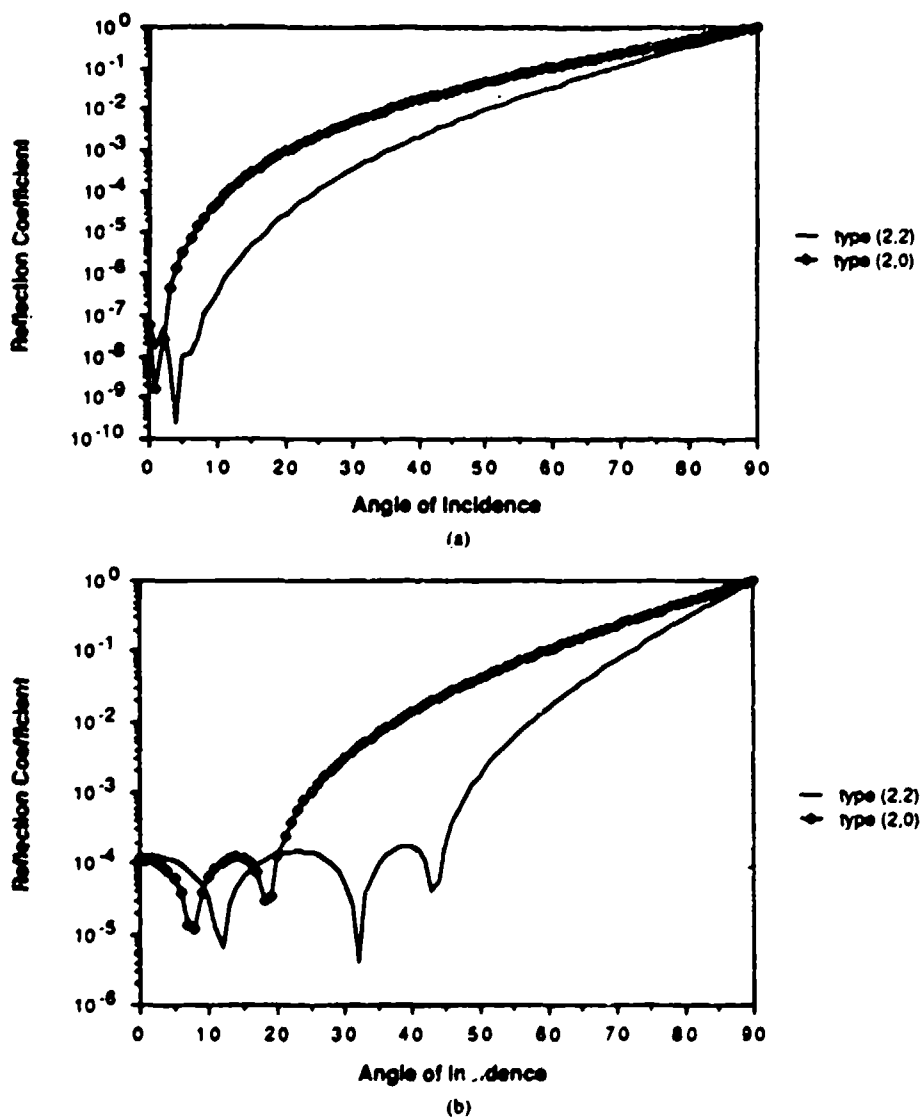


Fig. 2. Reflection coefficient versus wave angle of incidence. (a) Padé RBC. (b) Chebyshev on subinterval RBC.



Fig. 3. Comparison of third-order RBC's.

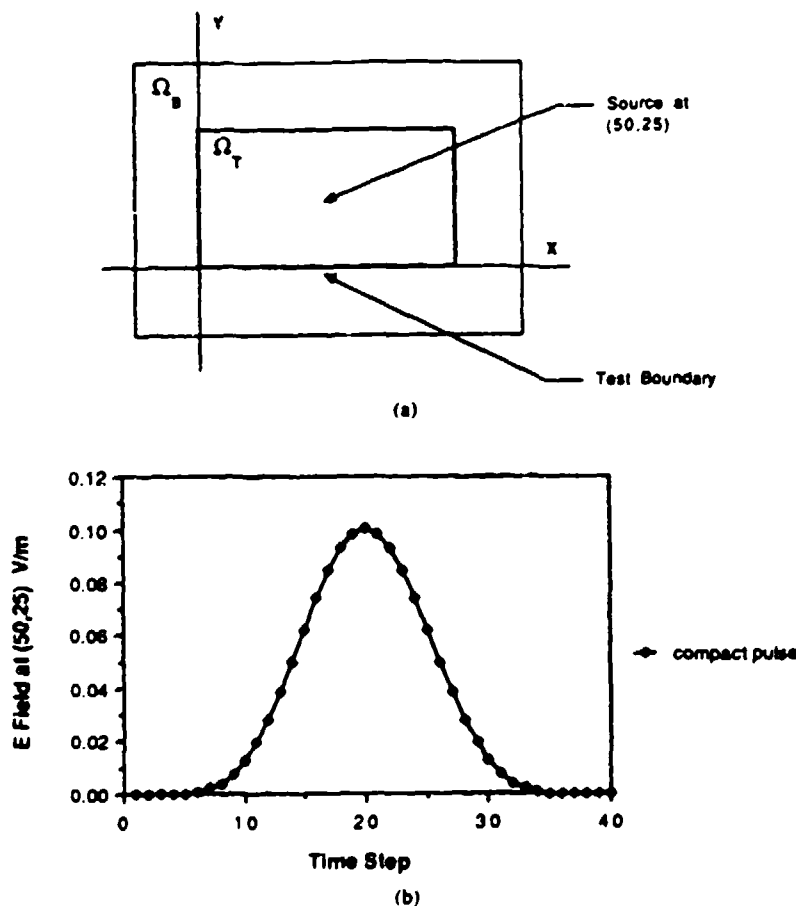


Fig. 4. Pulse studies. (a) Computational domains. (b) Wave source.

within  $\Omega_T$  and  $E_t^B$  is the solution at points in  $\Omega_B$ .  $D(i, j)$  is the local error in the test domain caused by its grid boundary reflections. We also define a global reflected error measure,

$$E = \sum_i \sum_j D^2(i, j) \quad (40b)$$

for all  $(i, j)$  within  $\Omega_T$ , which measures the total reflected error within the test grid at the  $n$ th time step.

The source used in the numerical experiments is the pulse obtained from [20] and is defined as follows:

$$E_z(50, 25, n) = \begin{cases} \alpha(10 - 15 \cos \omega_1 \xi + 6 \cos \omega_2 \xi - \cos \omega_3 \xi), & \xi \leq \tau \\ 0, & \xi > \tau \end{cases} \quad (41a)$$

where

$$\begin{aligned} \alpha &= \frac{1}{320} \\ \omega_m &= \frac{2\pi m}{\tau}, \quad m = 1, 2, 3 \\ \xi &= n\delta t \\ \tau &= 10^{-9} \end{aligned} \quad (41b)$$

and  $\delta t$  is the time step used in the simulation. In all experiments we maintained  $\delta t = 2.5 \times 10^{-11}$  sec and  $\Delta = 2c \delta t$ , where  $c$  is the speed of light in free-space and  $\Delta$  is the space increment of the finite difference grid. The time profile of the pulse defined in (41a) is shown in Fig. 4(b). This pulse was selected because it has an extremely smooth transition to zero. As discussed in [20], the pulse has its first five derivatives vanish at  $\xi = 0, \tau$  and is a good approximation to a smooth compact pulse.

This pulse has very little high-frequency content which is important because of the deleterious effects of grid dispersion (dependence of numerical wave phase velocity upon spatial wavenumber). Grid dispersion and its relation to RBC's is discussed in [21], and [22]. This problem is compounded in higher dimensions by anisotropies of the numerical wave phase velocity with wave vector angle in the grid [3], [23] and is a subject of current research aimed at further reduction of grid boundary reflection coefficients.

The source point in Fig. 4(a) is 25 cells from the boundary of  $\Omega_T$  at  $y = 0$ . With the specification  $\Delta = 2c \delta t$ , disturbances at the source point require 50 time steps to propagate to the boundary at  $y = 0$ . At time step 70, the peak of the pulse just starts to pass through the boundary. We choose to observe the reflection at the first row of grid points away from the  $y = 0$  boundary (along  $J = 1$ ) at time step  $n = 100$ . This permits the bulk of the outgoing pulse to pass through the boundary and excite the largest observable reflection.

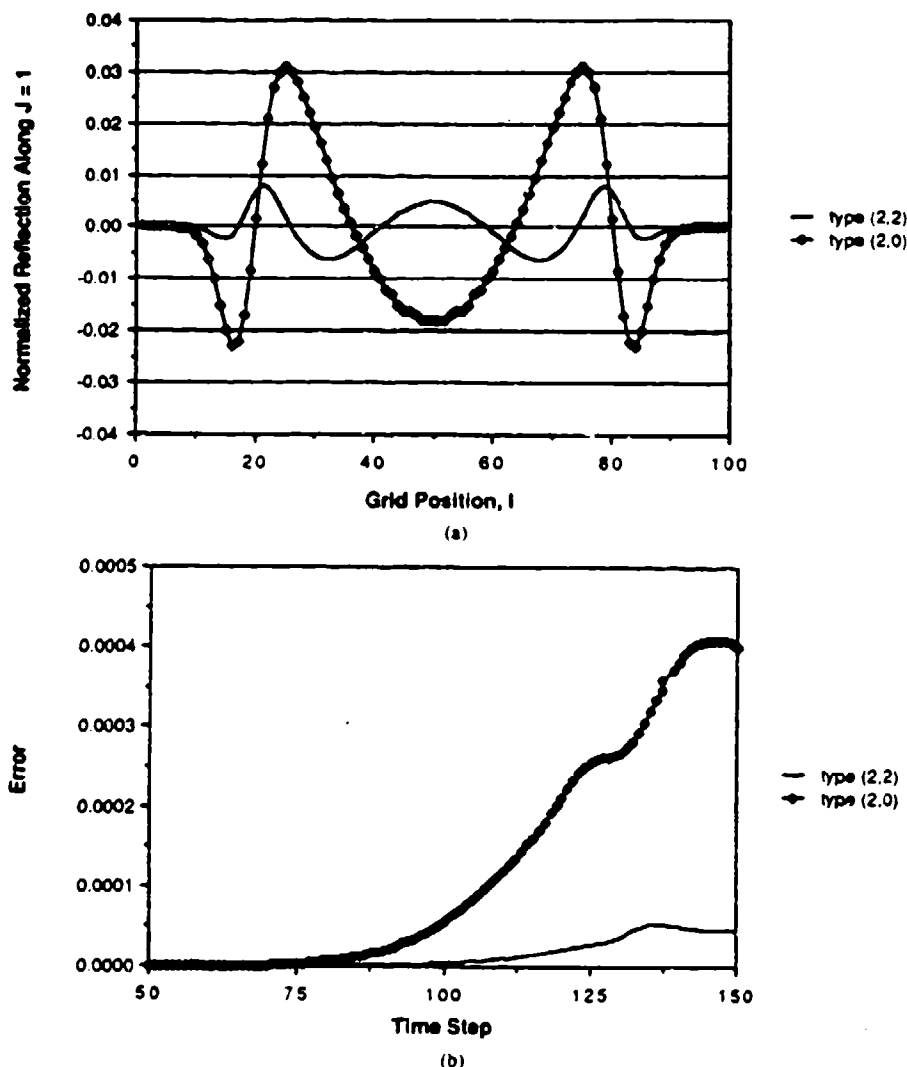


Fig. 5. Error measures, Padé RBC. (a) Local error at  $n = 100$ . (b) Global error.

Figs. 5 and 6 show the local and global reflection errors observed for the Padé and  $L_\sigma^\infty$  RBC's. Fig. 7 compares the third-order conditions. In Figs. 5(a), 6(a), and 7(a),  $D(i, 1)$  has been normalized with the peak value of the incident pulse which strikes the  $y = 0$  boundary at time step  $n = 70$  at grid position (50, 0). The pulse experiment results are in agreement with the reflection coefficient analysis by showing that higher order RBC's do perform better than lower order RBC's in actual simulations. However, comparison of the third-order  $L_\sigma^\infty$  RBC to the third-order Padé RBC does not indicate any particular performance advantage. The improved wide-angle performance suggested in [15] is not evident in these experiments.

#### IV. APPLICATION OF MODE-ANNIHILATING OPERATORS: OSRC

The on-surface radiation condition method [1] is a new analytical technique by which it is possible to construct accurate approximation of two- and three-dimensional scattering problems involving convex and simple reentrant targets. In this section, two areas of application will be examined. In the first application, the OSRC method will be applied to compute

the scattering cross section of two canonical convex targets: 1) a circular cylinder illuminated by both a transverse electric (TE) and transverse magnetic polarized plane wave; and 2) an acoustic sphere with a constant surface impedance. In the second application, the OSRC method will be applied to the scattering of a plane wave by a canonical reentrant geometry: the open end of a semi-infinite flanged parallel-plate waveguide. Before either of the cases is examined, some background discussion on the OSRC method is necessary.

##### A. Background

The OSRC method is based upon the application of a radiation boundary operator, such as those discussed in Section II, directly on the surface of the target. The effect of this is to relate the surface currents to known field quantities through a simple expression; thus the problem reduces to solving an equation along the contour of the target. Only second-order operators will be considered here because they are the most widely used. The method used in this paper will be the same one used in [1]. For completeness, recently proposed variations will be reviewed as well.

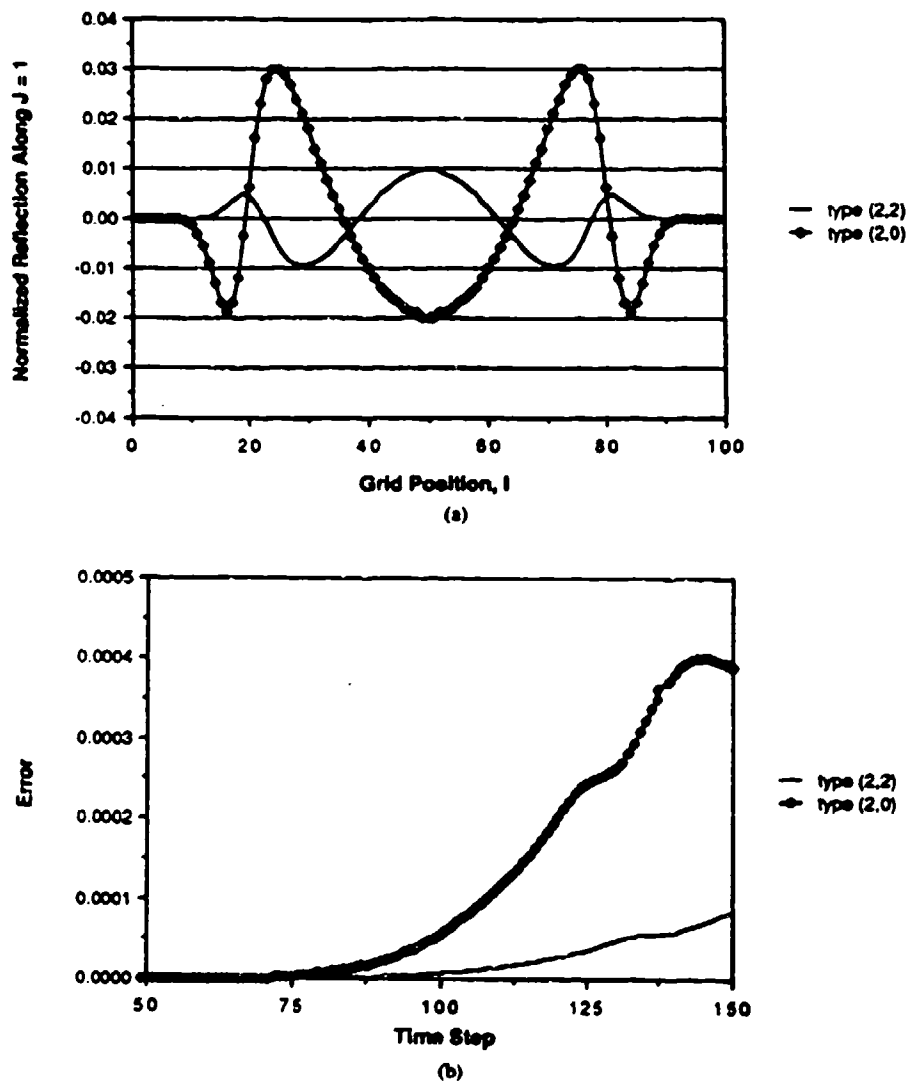


Fig. 6. Error measures, Chebyshev on subinterval RBC. (a) Local error at  $n = 100$ . (b) Global error.

The original method developed for two-dimensional electromagnetic targets is to apply a mode-annihilating radiation boundary operator locally at each point on the surface of the target [1]. This is conveniently done by noting that an osculating circle can approximate the target's surface locally at each point. The operator then works on the fields as if they were emanating from within the local osculating circle. In two dimensions, this is accomplished by making the following substitutions:

$$\frac{\partial}{\partial r} \rightarrow \frac{\partial}{\partial n} \quad (42a)$$

$$\frac{1}{r} \rightarrow \kappa(s) \quad (42b)$$

$$\frac{1}{r^2} \frac{\partial^2}{\partial \theta^2} \rightarrow \frac{\partial^2}{\partial s^2} \quad (42c)$$

second-order two-dimensional surface boundary operator [1]

$$2(\kappa - jk) \frac{\partial}{\partial n} U = \frac{\partial^2}{\partial s^2} U + \left[ 2k^2 - \frac{3}{4} \kappa^2 + 3jk\kappa \right] U. \quad (42d)$$

A three-dimensional surface boundary operator developed for acoustic targets is presented in [24]. There, the following substitutions are made in the three-dimensional mode-annihilating radiation boundary operator:

$$\frac{\partial}{\partial R} \rightarrow \frac{\partial}{\partial n} \quad (43a)$$

$$\frac{1}{R} \rightarrow H(s) \quad (43b)$$

$$\frac{\nabla^2 s}{R^2} \rightarrow \nabla \cdot \nabla \quad (43c)$$

where  $n$  is the outward normal,  $s$  is an arc length parameter, and  $\kappa(s)$  is the curvature of the target at  $s$ . This produces the

where  $\nabla \cdot \nabla$  is the surface Laplacian and  $H$  is the mean curvature. This produces the second-order three-dimensional

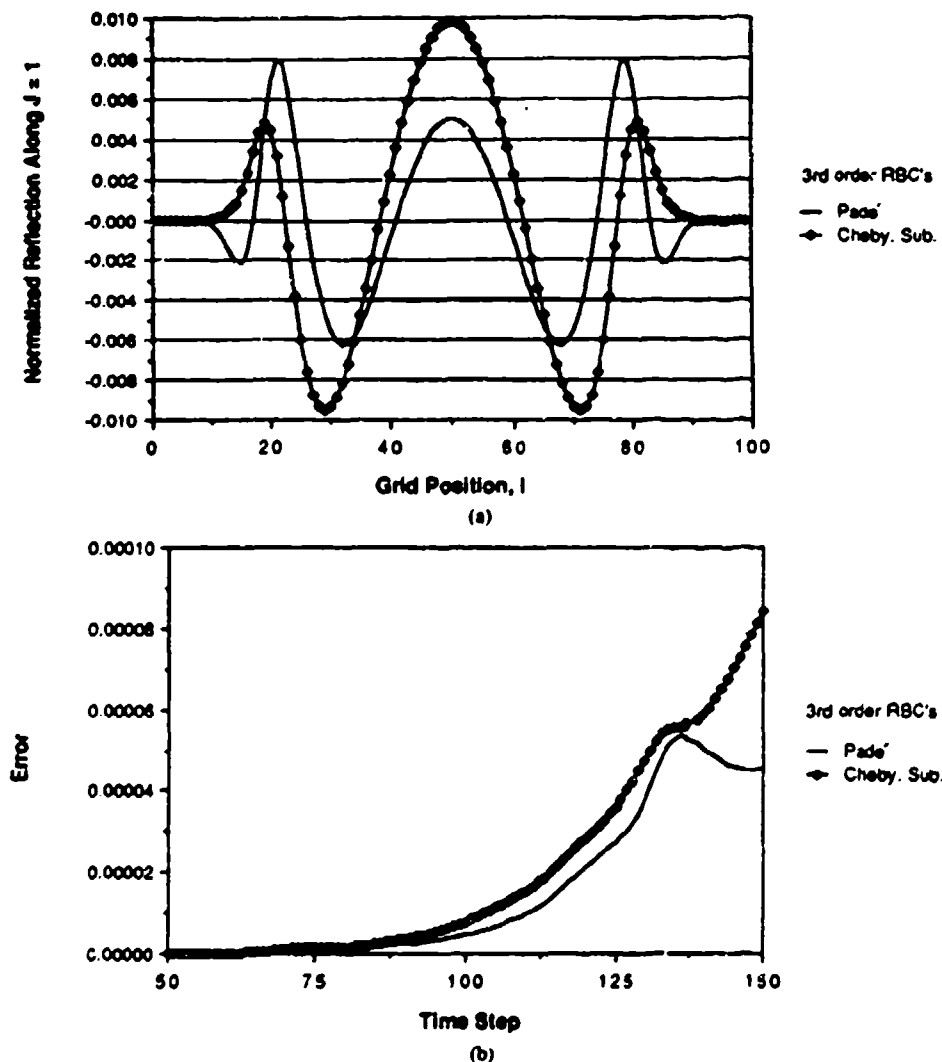


Fig. 7. Comparison of Padé to Chebyshev on subinterval. (a) Local error at  $n = 100$ . (b) Global error.

surface boundary operator,

$$-2jk \frac{\partial}{\partial n} U = \nabla \cdot \nabla U + 2(-k^2 - jkH)U. \quad (43d)$$

A variation of this surface boundary condition is presented in [25] in which a slightly different radiation boundary operator is used. It is

$$2(H - jk) \frac{\partial}{\partial n} U = \nabla \cdot \nabla U + 2(H^2 - k^2 - 2jkH)U. \quad (43e)$$

The fundamental difference between (43d) and (43e) is that the latter annihilates terms of order  $(kR)^{-3}$  as compared to  $(kR)^{-2}$  for the former.

Other methods have recently been presented for deriving a general surface boundary condition for OSRC. A sequence of surface boundary operators is derived in [26] by directly factoring the wave equation, as in Section II-B but in a general coordinate system based on the local properties of the target's surface. These results differ from (42d), (43d), and (43e) by a

term proportional to the derivative of the curvature multiplied by  $k^{-2}$ . No published evidence exists at this time to indicate that this term has any beneficial effects. The most recent derivation of surface boundary conditions for OSRC was presented in [27], which demonstrates that the surface boundary condition can be derived directly from geometrical acoustics/optics by making the assumption that the surface of the target is a phase front. The resulting boundary condition in three dimensions is

$$2jk \frac{\partial}{\partial n} U = \nabla \cdot \nabla U + (2k^2 + H^2 - \kappa_0 - jkH)U \quad (44a)$$

where  $\kappa_0$  is the Gaussian curvature. The corresponding surface boundary condition in two dimensions is

$$2(\kappa - jk) \frac{\partial}{\partial n} U = \frac{\partial^2}{\partial s^2} U + \left[ 2k^2 - \frac{3}{4} \kappa^2 + 3jk\kappa \right] U - \frac{j}{4k} \frac{\partial^2 \kappa}{\partial s^2} U - \frac{j}{k} \frac{\partial \kappa}{\partial s} \frac{\partial U}{\partial s}. \quad (44b)$$

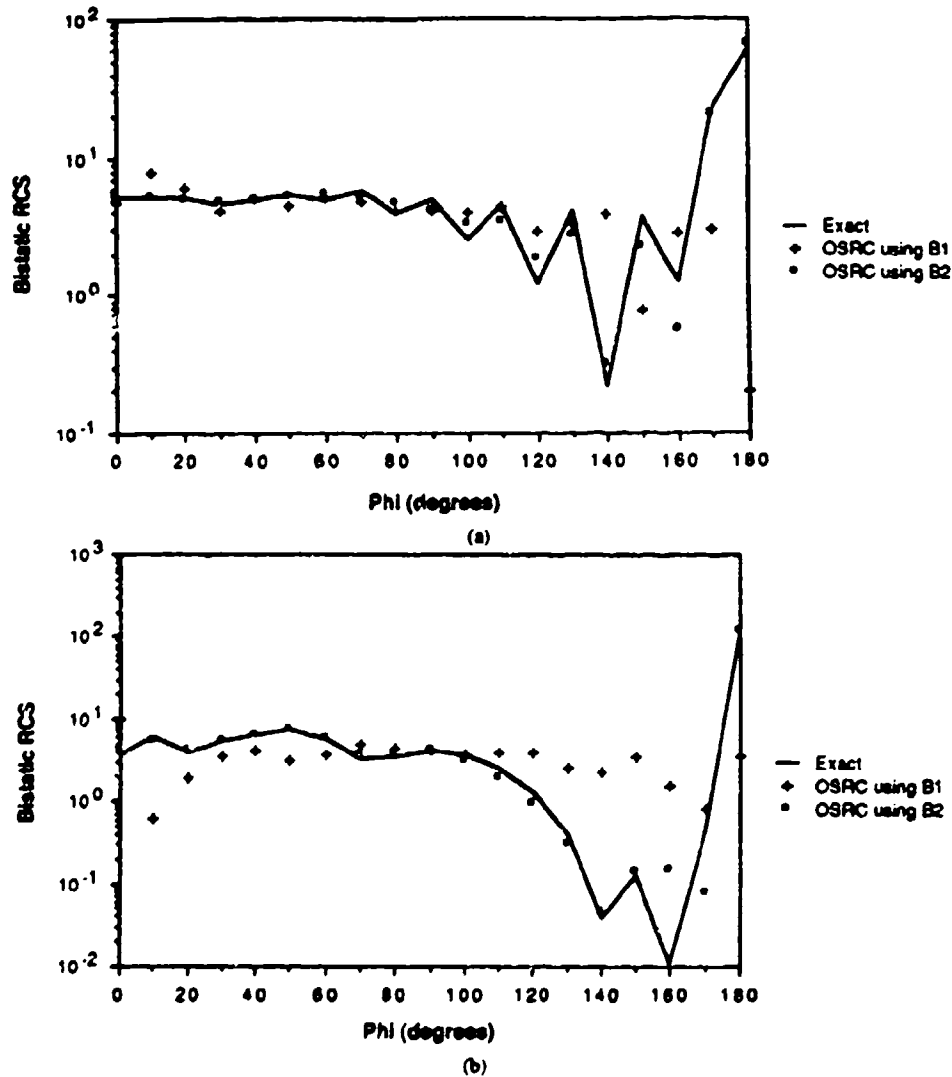


Fig. 8. OSRC computed bistatic RCS of conducting circular cylinder, TE case. (a)  $ka = 10$ . (b)  $ka = 20$ .

We note that (44b) also differs from (42d) in the terms proportional to the derivative of the target's curvature (which are formally  $O(k^{-3})$  corrections), but, in turn, differs slightly from the operator derived in [26]. More importantly, [27] shows how this method is deriving surface boundary operators can be applied to the vector scattering case of OSRC. However, no validations have been published to date.

Now that the surface boundary conditions have been derived, the application of the OSRC method to scalar problems is straightforward. We set

$$B_n' / j\omega = 0 \quad (45)$$

on the surface of the target, where  $B_n'$  is one of the surface boundary conditions described above. What results is an expression that relates the scattered field to its normal derivative at each point on the surface of the target. This is now combined with the usual relation between the incident and scattered field (or the normal derivative of the scattered field), as dictated by the problem.

#### B. Application to Scattering from Convex Targets

The use of OSRC is first illustrated by modeling scattering by a perfectly conducting circular cylinder of radius  $a$ . The

cylinder is illuminated by either a transverse electric or transverse magnetic polarized plane wave. For either polarization, the second-order surface boundary condition (42d) is applied to the surface of the cylinder.

For TE polarization, with the magnetic field tangent to the target's surface, the OSRC method results in an ordinary differential equation (ODE) for the azimuthal surface current density  $J_\phi$ :

$$C_2 \frac{d^2 J_\phi}{d\phi^2} - J_\phi = U_{inc} (1 - C_1 \cos \phi) - C_2 \frac{\partial^2 U_{inc}}{\partial \phi^2} \quad (46a)$$

where

$$C_1 = \frac{(8k^2 + j8k)}{-3 + 8k^2 + j12k} \quad C_2 = \frac{-4}{-3 + 8k^2 + j12} \quad (46b)$$

This is a very simple ODE since it has constant coefficients and thus may be solved analytically. The bistatic radar cross section patterns for a  $ka = 10$  and  $ka = 20$  cylinder, computed via a modal solution of (46), are plotted in Figs. 8(a) and (b). The OSRC results for the  $B_2$  operator are seen to demonstrate excellent agreement with the exact solution over a



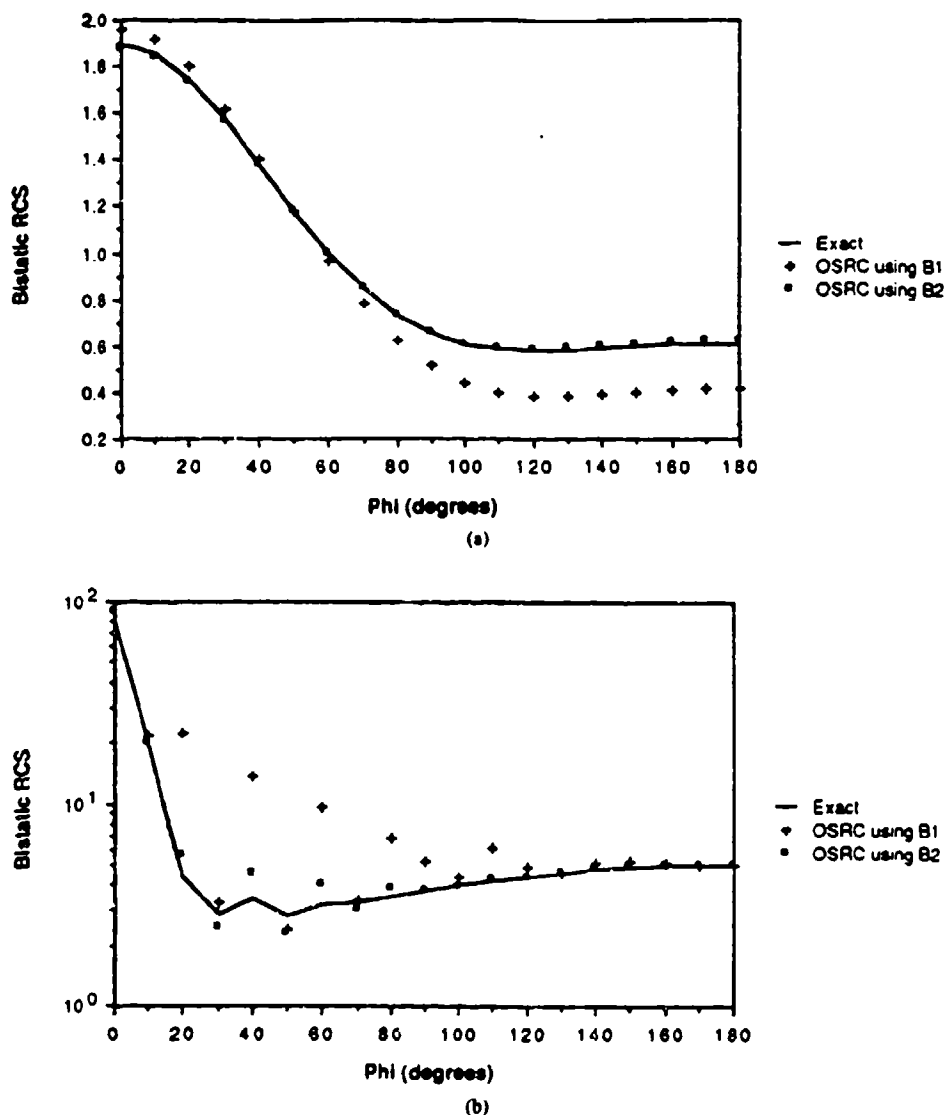


Fig. 9. OSRC computed bistatic RCS of conducting circular cylinder, TM case. (a)  $ka = 1$ . (b)  $ka = 10$ .

wide (30 dB) dynamic range. The solution to (46) can be accurately approximated by using the WKBJ method for  $k \geq 5$  [28]. There an approximate formula for an arbitrary convex target is derived by the same technique.

For TM polarization, the electric field is tangent to the target's surface and thus the OSRC method gives a simple algebraic expression for the longitudinal surface current density  $J_z$ :

$$J_z = \frac{j}{\eta_0 k} \left[ \frac{1}{2} + jk (\cos \phi - 1) - jk - \frac{j}{8k} \right. \\ \left. - \frac{1}{2} \cos \phi + \frac{jk}{2} \sin^2 \phi \right] e^{jk \cos \phi}. \quad (47)$$

The OSRC predicted bistatic radar cross section patterns for a  $ka = 1$  and  $ka = 10$  cylinder are plotted in Fig. 9(a) and (b). The OSRC results for the  $B_2$  operator are again seen to demonstrate excellent agreement with the exact solution over a substantial dynamic range.

The application of OSRC to a basic three-dimensional

convex target was first illustrated by modeling scattering by a soft acoustic sphere [24]. It was next applied to an acoustic sphere loaded with a constant impedance. Because this problem is solved in [25], only one example is presented here. In this example, an acoustic plane wave propagating in the  $-z$  direction impinges upon a spherical target of radius  $a$  having a constant normalized surface impedance of  $Z = 10$ . Condition (43e) is applied to the surface of the sphere. After inserting (43e) into (45), a second-order partial differential equation results for the surface currents, whose solution is approximated by a simple two-term asymptotic expansion and is then used to determine the far fields. Fig. 10 shows the backscattered cross section versus  $k$ . Again, there is excellent agreement with the exact solution.

### C. Application to Scattering from Reentrant Structures

The second area of application illustrates using OSRC to model scattering by simple reentrant structures. We consider the problem of a plane wave impinging on the open end of a semi-infinite flanged parallel-plate waveguide [29], shown in Fig. 11. A plane wave, at an angle  $\alpha$  measured counterclock-

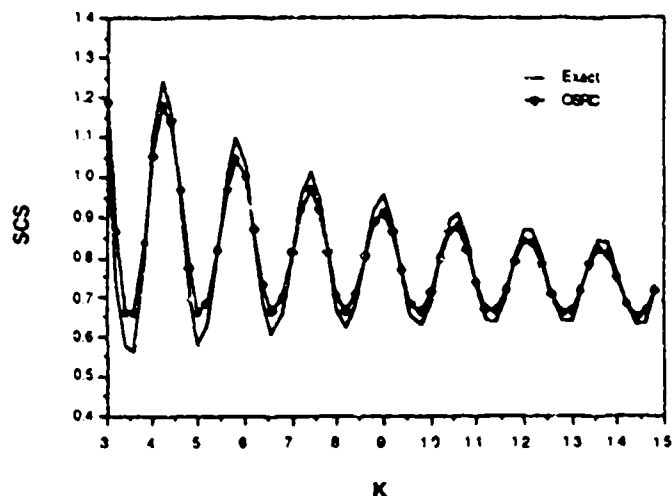


Fig. 10. Normalized back scattering cross section versus  $K$  for reactively loaded sphere ( $Z = 10$ ). Exact solution is calculated from modal series representation. Dotted line is two-term OSRC solution.

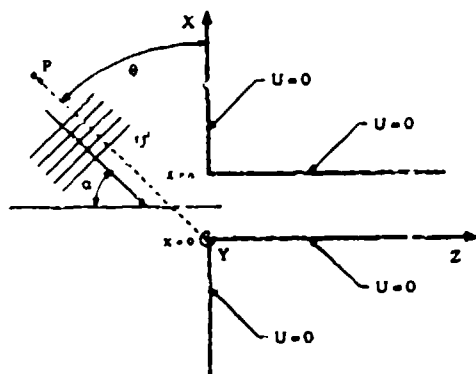


Fig. 11. Plane wave incident on open end of flanged, semi-infinite parallel-plate waveguide.  $a = 1.5$  m,  $f = 250$  MHz.

wise with reference to the  $-z$  axis, illuminates the mouth of the waveguide. The flange and the walls of the guide are assumed to be perfectly conducting. The incident wave  $U^i$  is considered to be the  $y$  component  $E_y$  of the incident electric field vector. Thus, for the boundary conditions shown, TE modes are excited inside the guide. The operator (42d), with  $\kappa = 0$ , is applied to the field representations valid in the guide aperture and yields an expression for the coefficients in the modal representation of the waveguide fields. Knowledge of the modal coefficients then permits the derivation of a simple expression for the bistatic radar cross section of the field scattered by the aperture, and the fields penetrating into the waveguide. Results of calculations using this approach are presented in Figs. 12 and 13. Fig. 12 shows the bistatic cross section for a plane wave at  $\alpha = 0^\circ$ . Fig. 13 shows the magnitude and phase distribution of the field penetrating the guide at a distance of  $z = 2$  m from the aperture. The OSRC results are compared to results obtained by FD-TD simulations. Excellent agreement is observed. The value of the OSRC solution is striking in its simple form and negligible computational requirements.

#### V. FUTURE RESEARCH

Research on radiation boundary operators is presently directed at two basic goals. The first is the development of

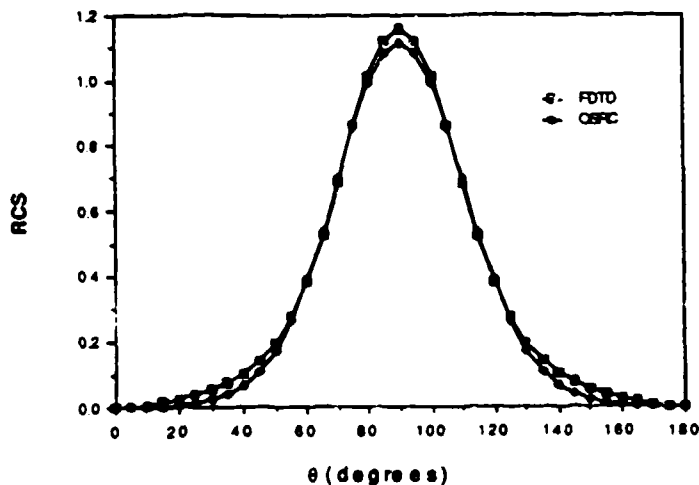


Fig. 12. Bistatic cross section for scattering from waveguide aperture due to plane wave at  $\alpha = 0^\circ$  and  $f = 250$  MHz. Angle  $\theta$  is as shown in Fig. 11.

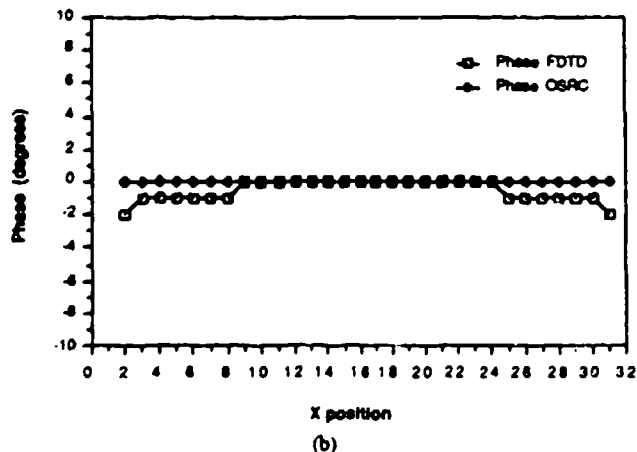
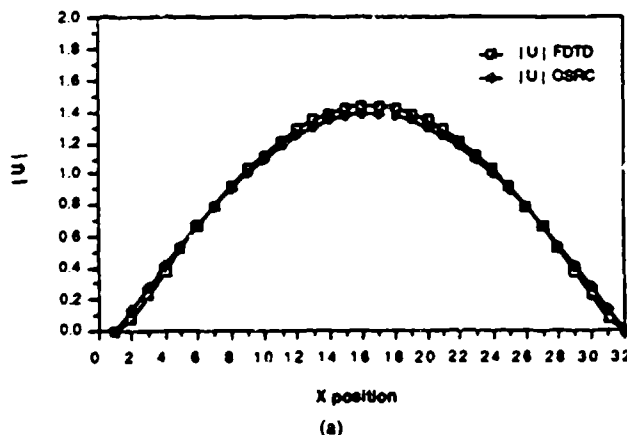


Fig. 13. Field penetration into waveguide at  $z = 2$  m for plane wave at  $\alpha = 0^\circ$  and  $f = 250$  MHz. (a)  $E$ -field magnitude. (b)  $E$ -field phase.

better truncation conditions for finite-difference and finite-element grids. This is aimed at reducing nonphysical reflections from the outer grid boundary which contribute to the numerical noise floor of the modeling procedure. Reducing the numerical noise floor will allow the simulation of scatterers with wider dynamic range. The second goal is the development of optimal mode-annihilating radiation boundary operators for the OSRC method.

The work on operators for truncating FD-TD and FE-TD grids fall into two basic categories. The first category is the synthesis of wide-angle radiation boundary operators. Although there are two basic types of radiation boundary operators, the main thrust of the research is directed towards one-way wave equation approximations. Here, work is proceeding in deriving approximations to the dispersion relation that will absorb waves over a wide range of angles properly taking into account anisotropy and dispersion of numerical mode phase velocities. The second category concerns the difference approximation for the operator. This is crucial for the operation of the boundary condition, because a perfectly valid operator which is not properly converted to a finite-difference equation, may cause instabilities in the simulation.

In contrast to the work on the grid truncation operators, the work on surface boundary conditions for the OSRC method is based on the optimization of the mode-annihilating radiation boundary operators. A key goal of this research is to produce a surface boundary condition which can better predict tangential energy propagation along the target's surface. Presently, two methods are being investigated for this purpose. The first method postulates a special multiplicative operator that models tangential propagating waves. The second method depends upon the application of the OSRC in the time domain to obtain a target impulse response [30]. The idea is to adjust the coefficients in the operator to match the exact response over a wide frequency range. Finally, the operators are also being examined to assess their ability to predict the correct current singularities on targets with edges.

#### ACKNOWLEDGMENT

The authors wish to acknowledge the contributions of Professor Korada R. Umashankar of the University of Illinois at Chicago in the development of the OSRC theory.

#### REFERENCES

- [1] G. A. Kriegsmann, A. Taflov, and K. R. Umashankar, "A new formulation of electromagnetic wave scattering using an on-surface radiation boundary condition approach," *IEEE Trans. Antennas Propagat.*, vol. AP-35, pp. 152-161, Feb. 1987.
- [2] A. Taflov and K. R. Umashankar, "The finite-difference time-domain (FD-TD) method for electromagnetic scattering and interaction problems," *J. Electromagn. Waves Appl.*, vol. 1, no. 4, pp. 363-387, 1987.
- [3] A. C. Cangellaris, C. C. Lin, and K. K. Mei, "Point-matched time-domain finite-element methods for electromagnetic radiation and scattering," *IEEE Trans. Antennas Propagat.*, vol. AP-35, pp. 1160-1173, Oct. 1987.
- [4] A. Sommerfeld, *Partial Differential Equations in Physics*. New York: Academic, 1949.
- [5] G. A. Kriegsmann and C. S. Morawetz, "Numerical solutions of exterior problems with the reduced wave equation," *J. Comput. Phys.*, vol. 28, pp. 181-197, 1979.
- [6] A. Bayliss and E. Turkel, "Radiation boundary conditions for wave-like equations," *Commun. Pure Appl. Math.*, vol. 23, pp. 707-725, 1980.
- [7] F. G. Friedlander, "On the radiation field of pulse solutions of the wave equation," *Proc. Royal Soc. London Ser. A*, vol. 269, pp. 53-69, 1962.
- [8] C. H. Wilcox, "An expansion theorem for electromagnetic fields," *Commun. Pure Appl. Math.*, vol. 9, pp. 115-132, 1956.
- [9] A. Bayliss, M. Gunzburger, and E. Turkel, "Boundary conditions for the numerical solution of elliptic equations in exterior regions," *SIAM J. Appl. Math.*, vol. 42, pp. 430-451, Apr. 1982.
- [10] S. N. Karp, "A convergent far-field expansion for two-dimensional radiation functions," *Commun. Pure Appl. Math.*, vol. 14, pp. 427-434, 1961.
- [11] B. Engquist and A. Majda, "Absorbing boundary conditions for the numerical simulation of waves," *Math. Comput.*, vol. 31, pp. 629-651, July 1977.
- [12] L. Halpern and L. N. Trefethen, "Wide-angle one-way wave equations," Dept. Math., Mass. Inst. Technol., Cambridge, Numerical Analysis Rep. 86-5, July 1986.
- [13] G. Mur, "Absorbing boundary conditions for the finite-difference approximation of time-domain electromagnetic field equations," *IEEE Trans. Electromagn. Compat.*, vol. EMC-23, pp. 377-382, Nov. 1981.
- [14] K. R. Umashankar and A. Taflov, "A novel method to analyze electromagnetic scattering of complex objects," *IEEE Trans. Electromagn. Compat.*, vol. EMC-24, pp. 392-405, Nov. 1982.
- [15] L. N. Trefethen and L. Halpern, "Well-posedness of one-way wave equations and absorbing boundary conditions," *Math. Comput.*, vol. 47, pp. 421-435, Oct. 1986.
- [16] J. G. Blaschak and G. A. Kriegsmann, "A comparative study of absorbing boundary conditions," *J. Comput. Phys.*, vol. 77, pp. 109-139, July 1988.
- [17] G. B. Whitham, *Linear and Nonlinear Waves*. New York: Wiley, 1974.
- [18] R. L. Higdon, "Absorbing boundary conditions for difference approximations to the multidimensional wave equation," *Math. Comput.*, vol. 47, pp. 437-459, 1986.
- [19] —, "Numerical absorbing boundary conditions for the wave equation," *Math. Comput.*, vol. 49, pp. 65-90, 1987.
- [20] G. A. Kriegsmann, A. N. Norris, and E. L. Reiss, "Acoustic pulse scattering by baffled membranes," *J. Acoust. Soc. Amer.*, vol. 79, Jan. 1986.
- [21] L. N. Trefethen, "Group velocity in finite difference schemes," *SIAM Rev.*, no. 24, pp. 114-136, 1982.
- [22] —, "Group velocity interpretation of stability theory of Gustafsson, Kreiss, and Sundstrom," *J. Comput. Phys.*, no. 49, pp. 199-217, 1983.
- [23] A. Taflov and K. R. Umashankar, "Advanced numerical modeling of microwave penetration and coupling for complex structures—Final report," Lawrence Livermore National Lab., VCRL-15960, Contract 6599805, Sept. 1987.
- [24] D. S. Jones, "An approximate boundary condition in acoustics," submitted to *J. Sound Vibration*, 1987.
- [25] G. A. Kriegsmann and T. G. Moore, "An application of the on-surface radiation condition to the scattering of acoustic waves by a reactively loaded sphere," *Wave Motion*, vol. 10, pp. 277-284, 1988.
- [26] W. F. Richards, D. R. Wilton, and J. X. Jiang, "Factorization of the three-dimensional Helmholtz equation with applications to the on surface radiation condition method," submitted to *IEEE Trans. Antennas Propagat.*, 1987.
- [27] D. S. Jones, "Surface radiation conditions," submitted to *IMA J. Appl. Math.*, 1987.
- [28] T. G. Moore, G. A. Kriegsmann, and A. Taflov, "An application of the WKBJ technique to the on-surface radiation condition," *IEEE Trans. Antennas Propagat.*, vol. 36, pp. 1329-1331, Sept. 1988.
- [29] J. G. Blaschak, G. A. Kriegsmann, and A. Taflov, "A study of wave interactions with flanged waveguides and cavities using the on-surface radiation condition method," *Wave Motion*, in press.
- [30] T. G. Moore, G. A. Kriegsmann, and A. Taflov, "An application of the OSRC method to time dependent problems," submitted to *IEEE Trans. Antennas Propagat.*, 1988.



Thomas G. Moore (S'84) received the B.S. and M.S. degrees in 1986 and 1987, respectively, from Northwestern University, Evanston, IL, where he is currently working toward the Ph.D. degree.

His research interests include computational electromagnetics, electromagnetic theory, and nonlinear wave propagation.

Mr. Moore is a member of Tau Beta Pi and Eta Kappa Nu.



Jeffrey G. Blaschak (S'84) received the B.S. degree from the University of Pittsburgh, Pittsburgh, PA, the M.S. degree from Purdue University, Lafayette, IN, and the Ph.D. degree in electrical engineering from Northwestern University, Evanston, IL, in 1988.

He has worked for AT&T Bell Laboratories, Lockheed Missiles and Space Company, and the Pennsylvania State University. Currently, he is a Member of the Technical Staff at MIT Lincoln Laboratory, Lexington, MA. His research interests

include various numerical techniques for the computation of electromagnetic wave propagation, radiation and scattering.



Allen Taflové (M'75-SM'84) was born in Chicago, IL, on June 14, 1949. He received the B.S. (with highest distinction), M.S. and Ph.D. degrees in electrical engineering from Northwestern University, Evanston, IL, in 1971, 1972, and 1975, respectively.

From 1975 to 1984, he was a staff member at IIT Research Institute in Chicago, IL, holding the positions of Associate Engineer, Research Engineer, and Senior Engineer. There, his research was concerned with computational modeling of electro-

magnetic wave penetration and scattering interactions with complex structures, power-frequency coupling of earth-return transmission systems, and

development of novel techniques for recovery of oil from oil shale, tar sand, and slowly producing conventional wells based upon *in situ* radio-frequency heating. He was the principal investigator on eight externally funded programs in these areas, including five which contributed to the early development of the finite-difference time-domain numerical modeling approach for complex electromagnetic wave interaction problems. He also provided technical leadership for major field experiments in radio frequency heating applied to oil recovery and is one of three principal co-inventors of technology in this area that is now covered by more than ten U.S. patents. In 1984, he returned to Northwestern where he is now Professor of Electrical Engineering and Computer Science. He has continued research in computational electromagnetics and related areas, including inverse scattering and target synthesis; propagation and scattering of waves within dispersive, nonlinear, and time-varying media; and applications of vector and concurrent-processing supercomputers to numerical electromagnetics. A recent research topic of great interest is the on-surface radiation condition approach for scattering.

Dr. Taflové is a member of Tau Beta Pi, Eta Kappa Nu, and Sigma Xi, and is a member of Commission B of URSI. He was senior author of a paper awarded the Best Paper prize at the IEEE 1983 International Symposium on Electromagnetic Compatibility, Washington, DC.

Gregory A. Kriegsmann, for a photograph and biography see page 161 of the February 1987 issue of this TRANSACTIONS.

## REVIEW OF THE FORMULATION AND APPLICATIONS OF THE FINITE-DIFFERENCE TIME-DOMAIN METHOD FOR NUMERICAL MODELING OF ELECTROMAGNETIC WAVE INTERACTIONS WITH ARBITRARY STRUCTURES

Allen TAFLOVE

*Department of Electrical Engineering and Computer Science, Technological Institute, Northwestern University, Evanston, IL 60201, U.S.A.*

Received 1 April 1988, Revised 15 May 1988

This paper reviews the basis and applications of the finite-difference time-domain (FD-TD) numerical modeling approach for Maxwell's equations. FD-TD is very simple in concept and execution. However, it is remarkably robust, providing highly accurate modeling predictions for a wide variety of electromagnetic wave interaction problems. The accuracy and breadth of FD-TD applications will be illustrated by a number of two- and three-dimensional examples. The objects modeled range in nature from simple geometric shapes to extremely complex aerospace and biological systems. In all cases where rigorous analytical, code-to-code, or experimental validations are possible, FD-TD predictive data for penetrating and scattered near fields as well as radar cross sections are in excellent agreement with the benchmarks. It will also be shown that opportunities are arising in applying FD-TD to model rapidly time-varying systems, microwave circuits, and inverse scattering. With continuing advances in FD-TD modeling theory as well as continuing advances in supercomputer technology, there is a strong possibility that FD-TD numerical modeling will occupy an important place in high-frequency engineering electromagnetics as we move into the 1990s.

### 1. Introduction

Accurate numerical modeling of full-vector electromagnetic wave interactions with arbitrary structures is difficult. Typical structures of engineering interest have shapes, apertures, cavities, and material compositions or surface loadings which produce near fields that cannot be resolved into finite sets of modes or rays. Proper numerical modeling of such near fields requires sampling at sub-wavelength resolution to avoid aliasing of magnitude and phase information. The goal is to provide a self-consistent model of the mutual coupling of the electrically-small cells comprising the structure.

This paper reviews the formulation and applications of a candidate numerical modeling approach for this purpose: the finite-difference time-domain (FD-TD) solution of Maxwell's curl equations.

FD-TD is analogous to existing finite-difference solutions of scalar wave propagation and fluid-flow problems in that the numerical model is based upon a direct solution of the governing partial differential equation. Yet, FD-TD is a nontraditional approach to numerical electromagnetic wave modeling of complex structures for engineering applications, where frequency-domain integral equation approaches such as the method of moments have dominated for 25 years (see the article by Umashankar in this issue).

One of the goals of this paper is to demonstrate that recent advances in FD-TD modeling concepts and software implementation, combined with advances in computer technology, have expanded the scope, accuracy, and speed of FD-TD modeling to the point where it may be the preferred choice for certain types of electromagnetic wave penetration, scattering, guiding, and inverse scattering

problems. With this in mind, this paper will succinctly review the following FD-TD modeling validations and examples:

- (1) electromagnetic wave scattering, two dimensions:
  - (a) square metal cylinder, TM polarization,
  - (b) circular muscle-fat layered cylinder, TE polarization,
  - (c) homogeneous, anisotropic, square material cylinder, TM polarization,
  - (d) circular metal cylinder, conformally modeled, TE and TM polarization,
  - (e) flanged metal open cavity,
  - (f) relativistically vibrating mirror, oblique incidence;
- (2) electromagnetic wave scattering, three dimensions:
  - (a) metal cube, broadside incidence,
  - (b) flat conducting plate, multiple monostatic looks,
  - (c) T-shaped conducting target, multiple monostatic looks;
- (3) electromagnetic wave penetration and coupling, two and three dimensions:
  - (a) narrow slots and lapped joints in thick screens,
  - (b) wires and wire bundles in free space and in a metal cavity;
- (4) very complex three-dimensional structures:
  - (a) missile seeker section,
  - (b) inhomogeneous tissue model of the entire human body;
- (5) microstrip and microwave circuit models,
- (6) inverse scattering reconstructions in one and two dimensions.

Finally, this paper will conclude with a discussion of computing resources for FD-TD and the potential impact of massively concurrent machines.

## 2. General characteristics of FD-TD

As stated, FD-TD is a direct solution of Maxwell's time-dependent curl equations. It employs

no potential. Instead, it applies simple, second-order accurate central-difference approximations [1] for the space and time derivatives of the electric and magnetic fields directly to the respective differential operators of the curl equations. This achieves a sampled-data reduction of the continuous electromagnetic field in a volume of space, over a period of time. Space and time discretizations are selected to bound errors in the sampling process, and to ensure numerical stability of the algorithm [2]. Electric and magnetic field components are interleaved in space to permit a natural satisfaction of tangential field continuity conditions at media interfaces. Overall, FD-TD is a marching-in-time procedure which simulates the continuous actual waves by sampled-data numerical analogs propagating in a data space stored in a computer. At each time step, the system of equations to update the field components is fully explicit, so that there is no need to set up or solve a set of linear equations, and the required computer storage and running time is proportional to the electrical size of the volume modeled.

Figure 1(a) illustrates the time-domain wave tracking concept of the FD-TD method. A region of space within the dashed lines is selected for field sampling in space and time. At time = 0, it is assumed that all fields within the numerical sampling region are identically zero. An incident plane wave is assumed to enter the sampling region at this point. Propagation of the incident wave is modeled by the commencement of time-stepping, which is simply the implementation of the finite-difference analog of the curl equations. Time-stepping continues as the numerical analog of the incident wave strikes the modeled target embedded within the sampling region. All outgoing scattered wave analogs ideally propagate through the lattice truncation planes with negligible reflection to exit the sampling region. Phenomena such as induction of surface currents, scattering and multiple scattering, penetration through apertures, and cavity excitation are modeled time-step by time-step by the action of the curl equations analog. Self-consistency of these modeled phenomena is gen-

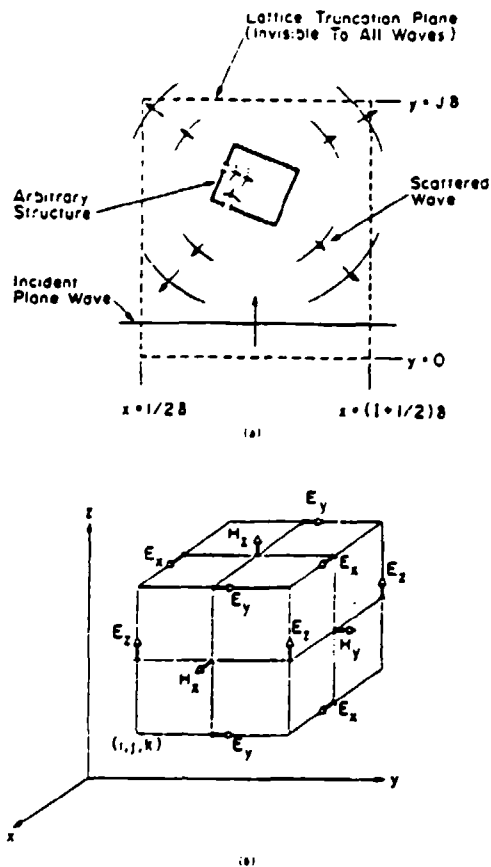


Fig. 1. Basic elements of the FD-TD space lattice: (a) time-domain wave tracking concept; (b) lattice unit cell in Cartesian coordinates.

erally assured if their spatial and temporal variations are well resolved by the space and time sampling process.

Time-stepping is continued until the desired late-time pulse response or steady-state behavior is observed. An important example of the latter is the sinusoidal steady state, wherein the incident wave is assumed to have a sinusoidal dependence, and time-stepping is continued until all fields in the sampling region exhibit sinusoidal repetition. This is a consequence of the limiting amplitude principle [3]. Extensive numerical experimentation with FD-TD has shown that the number of complete cycles of the incident wave required to be time-stepped to achieve the sinusoidal steady

state is approximately equal to the Q-factor of the structure or phenomenon being modeled.

Figure 1(b) illustrates the positions of the electric and magnetic field components about a unit cell of the FD-TD lattice in Cartesian coordinates [1]. Note that each magnetic field vector component is surrounded by four circulating electric field vector components, and vice versa. This arrangement permits not only a centered-difference analog to the space derivatives of the curl equations, but also a natural geometry for implementing the integral form of Faraday's Law and Ampere's Law at the space-cell level. This integral interpretation permits a simple but effective modeling of the physics of thin-slot coupling, thin-wire coupling, and smoothly curved target surfaces, as will be seen later.

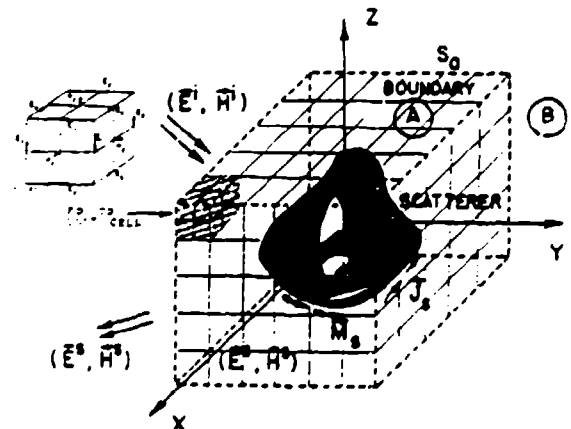


Fig. 2. Arbitrary three-dimensional scatterer embedded in an FD-TD lattice.

Figure 2 illustrates how an arbitrary three-dimensional scatterer is embedded in an FD-TD space lattice comprised of the unit cells of Fig. 1(b). Simply, the desired values of electrical permittivity and conductivity are assigned to each electric field component of the lattice. Correspondingly, desired values of magnetic permeability and equivalent conductivity are assigned to each magnetic field component of the lattice. The media parameters are interpreted by the FD-TD program as local coefficients for the time-stepping

algorithm. Specification of media properties in this component-by-component manner results in a stepped-edge, or staircase approximation of curved surfaces. Continuity of tangential fields is assured at the interface of dissimilar media with this procedure. There is no need for special field matching at media interface points. Stepped-edge approximation of curved surfaces has been found to be adequate in the FD-TD modeling problems studied in the 1970s and early 1980s, including wave interactions with biological tissues [4], penetration into cavities [5, 6], and electromagnetic pulse (EMP) interactions with complex structures [7-9]. However, recent interest in wide dynamic range models of scattering by curved targets has prompted the development of surface-conforming FD-TD approaches which eliminate stair-casing. These will be summarized later in this paper.

### 3. Basic FD-TD algorithm details

#### 3.1. Maxwell's equations

Consider a region of space which is source-free and has constitutive electrical parameters that are independent of time. Then, using the MKS system of units, Maxwell's curl equations are given by

$$\frac{\partial \mathbf{H}}{\partial t} = -\frac{1}{\mu} \nabla \times \mathbf{E} - \frac{\rho'}{\mu} \mathbf{H}, \quad (1)$$

$$\frac{\partial \mathbf{E}}{\partial t} = \frac{1}{\epsilon} \nabla \times \mathbf{H} - \frac{\sigma}{\epsilon} \mathbf{E} \quad (2)$$

where  $\mathbf{E}$  is the electric field in volts/meter;  $\mathbf{H}$  is the magnetic field in amperes/meter;  $\epsilon$  is the electrical permittivity in farads/meter;  $\sigma$  is the electrical conductivity in mhos/meter (siemens/meter);  $\mu$  is the magnetic permeability in henrys/meter; and  $\rho'$  is an equivalent magnetic resistivity in ohms/meter. (The magnetic resistivity term is provided to yield symmetric curl equations, and allow for the possibility of a magnetic field loss mechanism.) Assuming that  $\epsilon$ ,  $\sigma$ ,  $\mu$ , and  $\rho'$  are isotropic, the following system of scalar equations is equivalent to Maxwell's curl equations

in the rectangular coordinate system ( $x, y, z$ ):

$$\frac{\partial H_x}{\partial t} = \frac{1}{\mu} \left( \frac{\partial E_z}{\partial y} - \frac{\partial E_y}{\partial z} - \rho' H_x \right), \quad (3a)$$

$$\frac{\partial H_y}{\partial t} = \frac{1}{\mu} \left( \frac{\partial E_z}{\partial x} - \frac{\partial E_x}{\partial z} - \rho' H_y \right), \quad (3b)$$

$$\frac{\partial H_z}{\partial t} = \frac{1}{\mu} \left( \frac{\partial E_y}{\partial x} - \frac{\partial E_x}{\partial y} - \rho' H_z \right); \quad (3c)$$

$$\frac{\partial E_x}{\partial t} = \frac{1}{\epsilon} \left( \frac{\partial H_z}{\partial y} - \frac{\partial H_y}{\partial z} - \sigma E_x \right), \quad (4a)$$

$$\frac{\partial E_y}{\partial t} = \frac{1}{\epsilon} \left( \frac{\partial H_z}{\partial x} - \frac{\partial H_x}{\partial z} - \sigma E_y \right), \quad (4b)$$

$$\frac{\partial E_z}{\partial t} = \frac{1}{\epsilon} \left( \frac{\partial H_y}{\partial x} - \frac{\partial H_x}{\partial y} - \sigma E_z \right). \quad (4c)$$

The system of six coupled partial differential equations of (3) and (4) forms the basis of the FD-TD algorithm for electromagnetic wave interactions with general three-dimensional objects. Before proceeding with the details of the algorithm, it is informative to consider one important simplification of the full three-dimensional case. Namely, if we assume that neither the incident plane wave excitation nor the modeled geometry has any variation in the  $z$ -direction (i.e., all partial derivatives with respect to  $z$  equal zero), Maxwell's curl equations reduce to two decoupled sets of scalar equations. These decoupled sets, termed the transverse magnetic (TM) mode and the transverse electric (TE) mode, describe two-dimensional wave interactions with objects. The relevant equations for each case follow:

- TM case ( $E_z$ ,  $H_x$ , and  $H_y$  field components only)

$$\frac{\partial H_x}{\partial t} = -\frac{1}{\mu} \left( \frac{\partial E_z}{\partial y} + \rho' H_x \right), \quad (5a)$$

$$\frac{\partial H_y}{\partial t} = \frac{1}{\mu} \left( \frac{\partial E_z}{\partial x} - \rho' H_y \right), \quad (5b)$$

$$\frac{\partial E_z}{\partial t} = \frac{1}{\epsilon} \left( \frac{\partial H_y}{\partial x} - \frac{\partial H_x}{\partial y} - \sigma E_z \right); \quad (5c)$$



- TE case ( $H_z$ ,  $E_x$ , and  $E_y$  field components only)

$$\frac{\partial E_x}{\partial t} = \frac{1}{\epsilon} \left( \frac{\partial H_z}{\partial y} - \sigma E_x \right), \quad (6a)$$

$$\frac{\partial E_y}{\partial t} = -\frac{1}{\epsilon} \left( \frac{\partial H_z}{\partial x} + \sigma E_y \right), \quad (6b)$$

$$\frac{\partial H_z}{\partial t} = \frac{1}{\mu} \left( \frac{\partial E_x}{\partial y} - \frac{\partial E_y}{\partial x} - \rho' H_z \right). \quad (6c)$$

### 3.2. The Yee algorithm

In 1966, Yee [1] introduced a set of finite-difference equations for the system of (3) and (4). Following Yee's notation, we denote a space point in a rectangular lattice as

$$(i, j, k) = (i \Delta x, j \Delta y, k \Delta z) \quad (7a)$$

and any function of space and time as

$$F^n(i, j, k) = F(i \Delta x, j \Delta y, k \Delta z, n \Delta t) \quad (7b)$$

where  $\Delta x$ ,  $\Delta y$ , and  $\Delta z$  are, respectively, the lattice space increments in the  $x$ -,  $y$ -, and  $z$ -coordinate directions;  $\Delta t$  is the time increment; and  $i$ ,  $j$ ,  $k$ , and  $n$  are integers. Yee used centered finite-difference expressions for the space and time derivatives that are both simply programmed and second-order accurate in the space and time increments respectively:

$$\begin{aligned} \frac{\partial F^n(i, j, k)}{\partial x} &= \frac{F^n(i + \frac{1}{2}, j, k) - F^n(i - \frac{1}{2}, j, k)}{\Delta x} + O(\Delta x^2), \\ & \quad (8a) \end{aligned}$$

$$\begin{aligned} \frac{\partial F^n(i, j, k)}{\partial t} &= \frac{F^{n+1/2}(i, j, k) - F^{n-1/2}(i, j, k)}{\Delta t} + O(\Delta t^2). \\ & \quad (8b) \end{aligned}$$

To achieve the accuracy of (8a), and to realize all of the required space derivatives of the system of (3) and (4), Yee positioned the components of  $E$  and  $H$  about a unit cell of the lattice as shown

in Fig. 1(b). To achieve the accuracy of (8b), he evaluated  $E$  and  $H$  at alternate half time steps. The following are sample finite-difference time-stepping expressions for a magnetic and an electric field component resulting from these assumptions:

$$\begin{aligned} H_z^{n+1/2}(i, j + \frac{1}{2}, k + \frac{1}{2}) &= \frac{1 - \frac{\rho'(i, j + \frac{1}{2}, k + \frac{1}{2}) \Delta t}{2\mu(i, j + \frac{1}{2}, k + \frac{1}{2})}}{1 + \frac{\rho'(i, j + \frac{1}{2}, k + \frac{1}{2}) \Delta t}{2\mu(i, j + \frac{1}{2}, k + \frac{1}{2})}} \cdot H_z^{n-1/2}(i, j + \frac{1}{2}, k + \frac{1}{2}) \\ &+ \frac{\Delta t}{\mu(i, j + \frac{1}{2}, k + \frac{1}{2})} \cdot \left[ 1 + \frac{\rho'(i, j + \frac{1}{2}, k + \frac{1}{2}) \Delta t}{2\mu(i, j + \frac{1}{2}, k + \frac{1}{2})} \right]^{-1} \\ &\times \{ [E_y^n(i, j + \frac{1}{2}, k + 1) - E_y^n(i, j + \frac{1}{2}, k)] / \Delta z \\ &+ [E_x^n(i, j, k + \frac{1}{2}) - E_x^n(i, j + 1, k + \frac{1}{2})] / \Delta y \}, \quad (9) \end{aligned}$$

$$\begin{aligned} E_x^{n+1}(i, j, k + \frac{1}{2}) &= \frac{1 - \frac{\sigma(i, j, k + \frac{1}{2}) \Delta t}{2\epsilon(i, j, k + \frac{1}{2})}}{1 + \frac{\sigma(i, j, k + \frac{1}{2}) \Delta t}{2\epsilon(i, j, k + \frac{1}{2})}} \cdot E_x^n(i, j, k + \frac{1}{2}) \\ &+ \frac{\Delta t}{\epsilon(i, j, k + \frac{1}{2})} \cdot \left[ 1 + \frac{\sigma(i, j, k + \frac{1}{2}) \Delta t}{2\epsilon(i, j, k + \frac{1}{2})} \right]^{-1} \\ &\times \{ [H_y^{n+1/2}(i + \frac{1}{2}, j, k + \frac{1}{2}) - H_y^{n+1/2}(i - \frac{1}{2}, j, k + \frac{1}{2})] / \Delta x \\ &+ [H_z^{n+1/2}(i, j - \frac{1}{2}, k + \frac{1}{2}) - H_z^{n+1/2}(i, j + \frac{1}{2}, k + \frac{1}{2})] / \Delta y \}. \quad (10) \end{aligned}$$

With the system of finite-difference equations represented by (9) and (10), the new value of a field vector component at any lattice point depends only on its previous value and on the previous values of the components of the other field vector at adjacent points. Therefore, at any given time step, the computation of a field vector can proceed

either one point at a time; or, if  $p$  parallel processors are employed concurrently,  $p$  points at a time.

### 3.3. Numerical stability

To ensure the stability of the time-stepping algorithm exemplified by (9) and (10),  $\Delta t$  is chosen to satisfy the inequality [2, 10]

$$c_{\max} \Delta t \leq \left\{ \frac{1}{\Delta x^2} + \frac{1}{\Delta y^2} + \frac{1}{\Delta z^2} \right\}^{-1/2} \quad (11)$$

where  $c_{\max}$  is the maximum electromagnetic wave phase velocity within the media being modeled. Note that the corresponding numerical stability criterion set forth in (7) and (8) of reference [1] is incorrect (cf. [2]). For the TM and TE two-dimensional modeling cases, it can be shown [10] that the modified time-step limit for numerical stability is obtained from (11) simply by setting  $\Delta z = \infty$ .

### 3.4. Numerical dispersion

The numerical algorithm for Maxwell's curl equations represented by (9) and (10) causes dispersion of the simulated wave modes in the computational lattice. That is, the phase velocity of numerical modes in the FD-TD lattice can vary with modal wavelength, direction of propagation, and lattice discretization. This numerical dispersion can lead to nonphysical results such as pulse distortion, artificial anisotropy, and pseudorefraction. Numerical dispersion is a factor in FD-TD modeling that must be accounted to understand the operation of the algorithm and its accuracy limits.

Following the analysis in [10], it can be shown that the numerical dispersion relation for the three-dimensional case represented by (9) and (10) is given by

$$\begin{aligned} \left( \frac{1}{c \Delta t} \right)^2 \sin^2(\tfrac{1}{2} \omega \Delta t) &= \frac{1}{\Delta x^2} \sin^2(\tfrac{1}{2} k_x \Delta x) \\ &+ \frac{1}{\Delta y^2} \sin^2(\tfrac{1}{2} k_y \Delta y) + \frac{1}{\Delta z^2} \sin^2(\tfrac{1}{2} k_z \Delta z) \end{aligned} \quad (12)$$

where  $k_x$ ,  $k_y$ , and  $k_z$  are, respectively, the  $x$ -,  $y$ -, and  $z$ -components of the wavevector;  $\omega$  is the wave angular frequency; and  $c$  is the speed of light in the homogeneous material being modeled.

In contrast to the numerical dispersion relation, the analytical dispersion relation for a plane wave in a continuous, lossless medium is just

$$\omega^2 / c^2 = k_x^2 + k_y^2 + k_z^2 \quad (13)$$

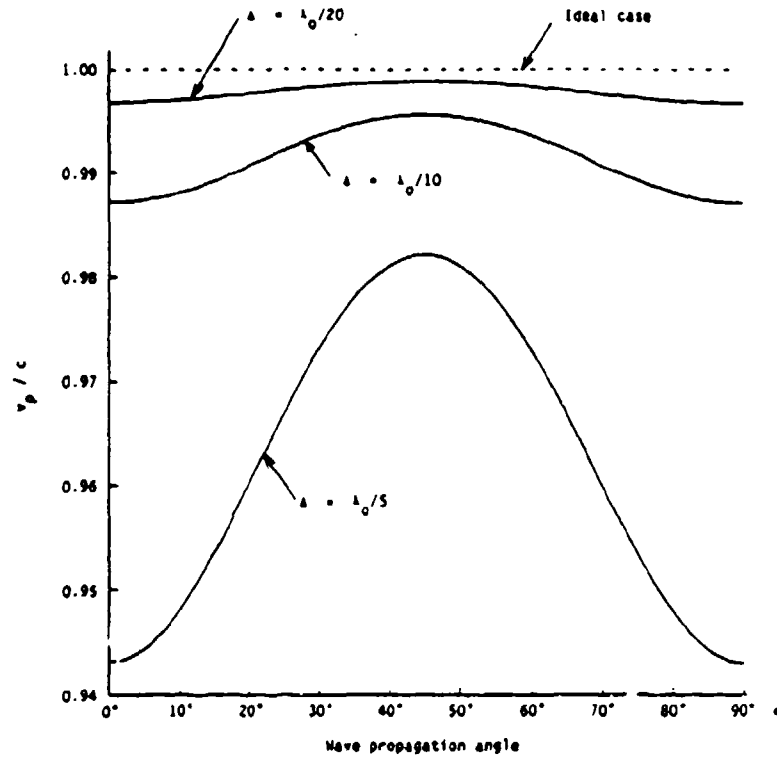
for the three-dimensional case. Although, at first glance, (12) bears little resemblance to the ideal case of (13), we can easily show that (12) reduces to (13) in the limit as  $\Delta t$ ,  $\Delta x$ ,  $\Delta y$ , and  $\Delta z$  all go to zero. Qualitatively, this suggests that numerical dispersion can be reduced to any degree that is desired if we only use a fine-enough FD-TD gridding.

To quantitatively illustrate the dependence of numerical dispersion upon FD-TD grid discretization, we shall take as an example the two-dimensional TM case ( $\Delta z = \infty$ ), assuming for simplicity square unit cells ( $\Delta x = \Delta y = \Delta$ ) and wave propagation at an angle  $\alpha$  with respect to the positive  $x$ -axis ( $k_x = k \cos \alpha$ ;  $k_y = k \sin \alpha$ ). Then, dispersion relation (12) simplifies to

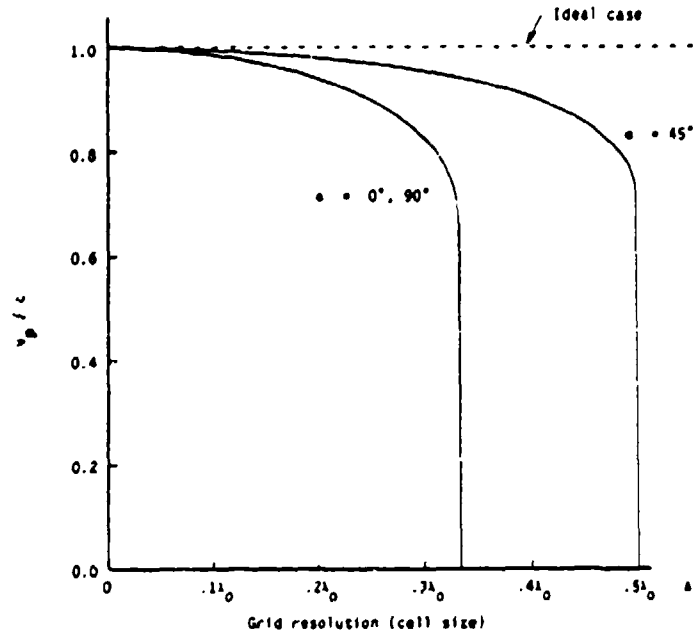
$$\begin{aligned} \left( \frac{\Delta}{c \Delta t} \right)^2 \sin^2(\tfrac{1}{2} \omega \Delta t) \\ = \sin^2(\tfrac{1}{2} k \cos \alpha \Delta) + \sin^2(\tfrac{1}{2} k \sin \alpha \Delta). \end{aligned} \quad (14)$$

Equation (14) can be conveniently solved for the wavevector magnitude,  $k$ , by applying Newton's method. This process is especially convenient if  $\Delta$  is normalized to the free-space wavelength.

Figure 3(a) provides results using this procedure which illustrate the variation of numerical phase velocity with wave propagation angle in the FD-TD grid. Three different grid resolutions of the propagating wave are examined: coarse ( $\lambda_0/5$ ); normal ( $\lambda_0/10$ ); and fine ( $\lambda_0/20$ ). For each resolution, the relation  $c \Delta t = \tfrac{1}{2} \Delta$  was maintained. This relation is commonly used in two- and three-



(a)



(b)

Fig. 3. Variation of FD-TD numerical wave phase velocity (dispersion): (a) with wave propagation angle in the grid for three different grid discretizations; (b) with grid resolution for three different wave propagation angles.

dimensional FD-TD codes to satisfy the numerical stability criterion of (11) with ample safety margin. From Fig. 3(a), it is seen that the numerical phase velocity is maximum at  $45^\circ$  (oblique incidence), and minimum at  $0^\circ$  and  $90^\circ$  (incidence along either Cartesian grid axis) for all grid resolutions. This represents a numerical anisotropy that is inherent in the Yee algorithm. However, the velocity error relative to the ideal case diminishes by approximately a 4:1 factor each time that the grid cell size is halved, so that the worst-case velocity error for the normal resolution case is only  $-1.3\%$ , and only  $-0.31\%$  for the fine resolution case.

Figure 3(b) graphs the variation of numerical phase velocity with grid resolution at the fixed incidence angles,  $45^\circ$  and  $0^\circ$  ( $90^\circ$ ). Again, the relation  $c\Delta t = \frac{1}{2}\Delta$  was maintained for each resolution. Here, it is seen that the numerical phase velocity at each angle of incidence diminishes as the propagating wave is more coarsely resolved, eventually reaching a sharp threshold where the numerical phase velocity goes to zero and the wave can no longer propagate in the FD-TD grid. This represents a numerical low-pass filtering effect that is inherent in the Yee algorithm, wherein the wavelength of propagating numerical modes has a lower bound of 2 to 3 space cells, depending upon the propagation direction. As a result, FD-TD modeling of pulses having finite duration (and thus, infinite bandwidth) can result in progressive pulse distortion as higher spatial frequency components propagate more slowly than lower spatial frequency components, and very high spatial frequency components with wavelengths less than 2 to 3 cells are rejected. This numerical dispersion causes broadening of finite-duration pulses, and leaves a residue of high-frequency ringing on the trailing edges due to the relatively slowly propagating high-frequency components. From Figs. 3(a) and 3(b), we see that pulse distortion can be bounded by obtaining the Fourier spatial frequency spectrum of the desired pulse, and selecting a grid cell size so that the principal spectral components are resolved with at least 10 cells

per wavelength. This would limit the spread of numerical phase velocities of the principal spectral components to less than 1%, regardless of the wave propagation angle in the grid.

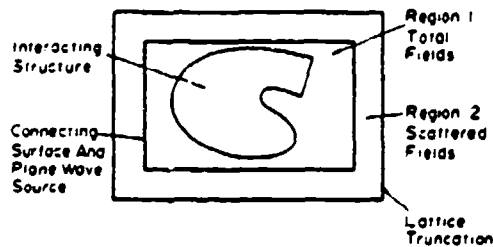
In addition to numerical phase velocity anisotropy and pulse distortion effects, numerical dispersion can lead to pseudorefraction of propagating modes if the grid cell size is a function of position in the grid. Such variable-cell gridding would also vary the grid resolution of propagating numerical modes, and thereby perturb the modal phase velocity distribution. This would lead to nonphysical reflection and refraction of numerical modes at interfaces of grid regions having different cell sizes (even if these interfaces were located in free space), just as physical waves undergo reflection and refraction at interfaces of dielectric media having different indices of refraction. The degree of nonphysical refraction is dependent upon the magnitude and abruptness of the change of the modal phase velocity distribution, and can be estimated using conventional theory for wave refraction at dielectric interfaces.

We have stated that, in the limit of infinitesimal  $\Delta t$  and  $\Delta$ , (12) reduces to (13), the ideal dispersion case. This reduction also occurs if  $\Delta t$ ,  $\Delta$ , and the direction of propagation are suitably chosen. For example, in a three-dimensional cubic lattice, reduction to the ideal dispersion case can be demonstrated for wave propagation along a lattice diagonal ( $k_x = k_y = k_z = k/\sqrt{3}$ ) and  $\Delta t = \Delta/c\sqrt{3}$  (exactly the limit set by numerical stability). Similarly, in a two-dimensional square grid, the ideal dispersion case can be demonstrated for wave propagation along a grid diagonal ( $k_x = k_y = k/\sqrt{2}$ ) and  $\Delta t = \Delta/c\sqrt{2}$  (again the limit set by numerical stability). Finally, in one dimension, the ideal case is obtained for  $\Delta t = \Delta/c$  (again the limit set by numerical stability) for all propagating modes.

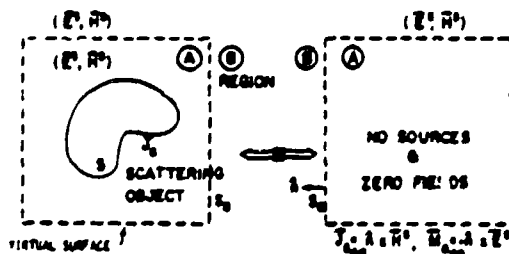
### 3.5. Lattice zoning and plane wave source condition

The numerical algorithm for Maxwell's curl equations defined by the finite-difference system reviewed above has a linear dependence upon the

components of the electromagnetic field vectors. Therefore, this system can be applied with equal validity to either the incident-field vector components, the scattered-field vector components, or the total-field vector components (the sum of incident plus scattered). Present FD-TD codes utilize this property to zone the numerical space lattice into two distinct regions, as shown in Fig. 4(a), separated by a rectangular virtual surface which serves to connect the fields in each region [11, 12].



(a)



(b)

Fig. 4. Zoning of the FD-TD lattice: (a) total field and scattered field regions; (b) near-to-far field integration surface located in the scattered field region.

Region 1, the inner region of the FD-TD lattice, is denoted as the total-field region. Here, it is assumed that the finite-difference system for the curl equations operates on total-field vector components. The interacting structure of interest is embedded within this region.

Region 2, the outer region of the FD-TD lattice, is denoted as the scattered-field region. Here, it is assumed that the finite-difference system for the curl equations operates only on scattered-field vector components. This implies that there is no

incident wave in Region 2. The outer lattice planes bounding Region 2, called the lattice truncation planes, serve to implement the free-space radiation condition (discussed in the next section) which simulates the field sampling space extending to infinity.

The total-field/scattered-field lattice zoning illustrated in Fig. 4(a) provides a number of key features which enhance the computational flexibility and dynamic range of the FD-TD method:

**Arbitrary incident wave.** The connecting condition provided at the interface of the inner and outer regions, which assures consistency of the numerical space derivative operations across the interface, simultaneously generates an arbitrary incident plane wave in Region 1 having a user-specified time waveform, angle of incidence, and angle of polarization. This connecting condition, discussed in detail in [10], almost completely confines the incident wave to Region 1 and yet is transparent to outgoing scattered wave modes which are free to enter Region 2.

**Simple programming of inhomogeneous structures.** The required continuity of total tangential  $E$  and  $H$  fields across the interface of dissimilar media is automatically provided by the original Yee algorithm if the media are located in a zone (such as Region 1) where total fields are time-marched. This avoids the problems inherent in a pure scattered-field code, where enforcement of the continuity of total tangential fields is a separate process requiring the incident field to be computed at all interfaces of dissimilar media, and then added to the values of the time-marched scattered fields at the interfaces. Clearly, computation of the incident field at numerous points along possibly complex, structure-specific loci is likely to be much more involved than computation of the incident field only along the simple connecting surface between Regions 1 and 2 (needed to implement the total-field/scattered-field zoning). The latter surface has a fixed locus that is independent of the shape or complexity of the interaction structure that is embedded in Region 1.

**Wide computational dynamic range.** Low levels of the total field in deep shadow regions or cavities of the interaction structure are computed directly by time-marching total fields in Region 1. In a pure scattered-field code, however, the low levels of total field are obtained by computing the incident field at each desired point, and then adding to the values of the time-marched scattered fields. Thus, it is seen that a pure scattered-field code relies upon near cancellation of the incident and scattered field components of the total field to obtain accurate results in deep shadow regions and cavities. An undesirable hallmark of this cancellation is contamination of the resultant low total-field levels by subtraction noise, wherein slight percentage errors in calculating the scattered fields result in possibly very large percentage errors in the residual total fields. By time-marching total fields directly, the zoned FD-TD code avoids subtraction noise in Region 1 and achieves a computational dynamic range more than 30 dB greater than that for a pure scattered-field code.

**Far-field response.** The provision of a well-defined scattered-field region in the FD-TD lattice permits the near-to-far-field transformation illustrated in Fig. 4(b). The dashed virtual surface shown in Fig. 4(b) can be located along convenient lattice planes in the scattered-field region of Fig. 4(a). Tangential scattered  $E$  and  $H$  fields computed via FD-TD at this virtual surface can then be weighted by the free-space Green's function and then integrated (summed) to provide the far-field response and radar cross section (full bistatic response for the assumed illumination angle) [12-14]. The near-field integration surface has a fixed rectangular shape, and thus is independent of the shape or composition of the enclosed structure being modeled.

### 3.6. Radiation condition

A basic consideration with the FD-TD approach to solve electromagnetic wave interaction problems is that most computational domains of interest are ideally unbounded or "open". Clearly, no

computer can store an unlimited amount of data, and therefore, the field computation zone must be limited in size. A suitable boundary condition on the outer perimeter of the computation zone must be used to simulate the extension of the computation zone to infinity. This boundary condition must be consistent with Maxwell's equations in that an outgoing vector scattered-wave numerical analog striking the lattice truncation must exit the lattice without appreciable nonphysical reflection, just as if the lattice truncation was invisible.

Now, the vector field components at the lattice truncation planes cannot be computed using the centered-differencing approach discussed earlier because of the assumed absence of known field data at points outside of the lattice truncation (which are needed to form the central differences). It has been shown that a suitable lattice truncation is provided by implementing a near-field radiation condition separately for each of the Cartesian tangential electric (or magnetic) vector components present in the truncation planes [11-13]. In FD-TD codes to date, the radiation condition used is a Pade (2,0) interpolant of the factored (one-way) wave equation [15, 16] as differenced in [11]. Higher-order Pade (2,2) and Chebyshev (2,2) interpolants are currently under study for numerical implementation in the FD-TD computer programs [17].

## 4. FD-TD modeling validations for electromagnetic wave scattering, two dimensions

Analytical and code-to-code validations have been obtained relative to FD-TD modeling of electromagnetic wave scattering for a wide variety of canonical two-dimensional structures. Both convex and re-entrant (cavity-type) shapes have been studied; and structure material compositions have included perfect conductors, homogeneous and inhomogeneous lossy dielectrics, and anisotropic dielectric and permeable media. Selected validations will be reviewed here.

#### 4.1. Square metal cylinder, TM polarization [12]

Here, we consider the scattering of a TM-polarized plane wave obliquely incident upon a square metal cylinder of electrical size  $k_0 s = 2$ , where  $s$  is the side width of the cylinder. The square FD-TD grid cell size is set equal to  $s/20$ , and the grid truncation (radiation boundary) is located at a uniform distance of 20 cells from the cylinder surface.

Figure 5 compares the magnitude and phase of the cylinder surface electric current distribution computed using FD-TD to that computed using a benchmark code which solves the frequency-domain surface electric field integral equation (EFIE) via the method of moments (MOM). The MOM code assumes target symmetry and discretizes one-half of the cylinder surface with 84 divisions. The FD-TD computed surface current is taken as  $\hat{n} \times \mathbf{H}_{tan}$ , where  $\hat{n}$  is the unit normal vector at the cylinder surface, and  $\mathbf{H}_{tan}$  is the FD-TD value of the magnetic field vector component in free space immediately adjacent to the cylinder surface. From Fig. 5, we see that the magnitude of the FD-TD computed surface current

agrees with the MOM solution to better than  $\pm 1\%$  ( $\pm 0.09$  dB) at all comparison points more than 2 FD-TD cells from the cylinder corners (current singularities). The phase of the FD-TD solution agrees with the MOM solution to within  $\pm 3^\circ$  at virtually every comparison point, including the shadow region.

#### 4.2. Circular muscle-fat layered cylinder, TE polarization [18]

Here, we consider the penetration of a TE-polarized plane wave into a simulated biological tissue structure represented by a 15 cm radius muscle-fat layered cylinder. The inner layer (radius = 7.9 cm) is assumed to be comprised of muscle having a relative permittivity of 72 and conductivity of 0.9 S/m. The outer layer is assumed to be comprised of fat having a relative permittivity of 7.5 and conductivity of 0.48 S/m. An illumination frequency of 100 MHz is modeled, with the FD-TD grid cell size set equal to 1.5 cm (approximately  $1/24$  wavelength within the muscle). A stepped-edge (staircase) approximation of the circular layer boundaries is used.

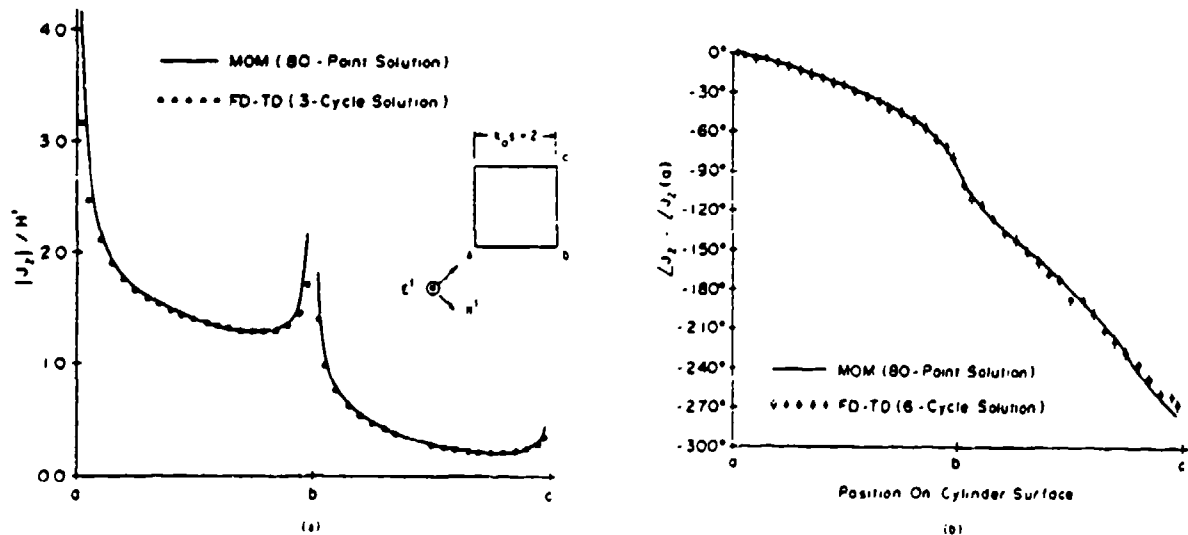


Fig. 5. Comparison of FD-TD and frequency-domain surface electric field integral equation results for longitudinal surface electric current distribution on a  $k_0 s = 2$  square metal cylinder, TM case: (a) magnitude; (b) phase [12].

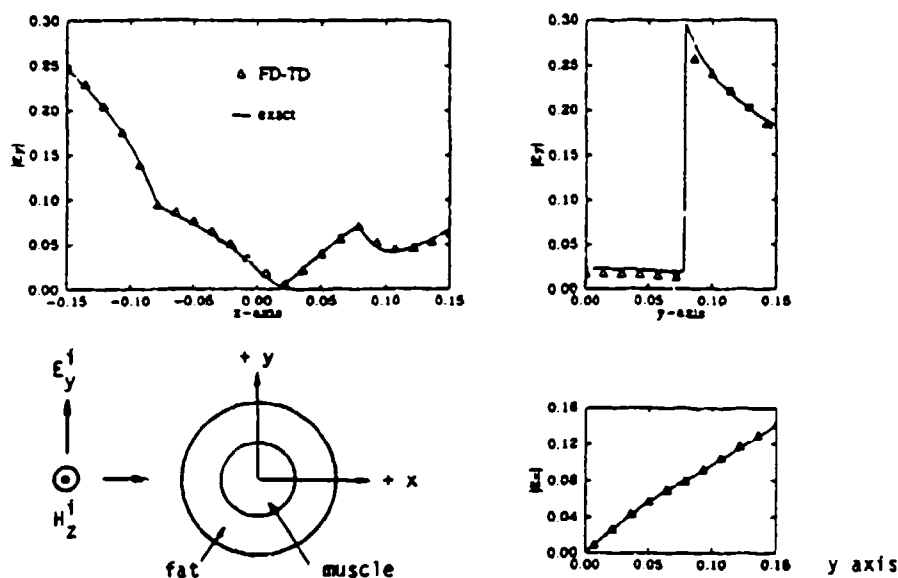


Fig. 6. Comparison of FD-TD and exact solutions for penetrating electric field vector components within a 15 cm radius, circular, muscle-fat layered cylinder, TE polarization, 100 MHz [18].

Figure 6, taken from [18], shows the analytical validation results for the magnitude of the penetrating electric field vector components along two cuts through the muscle-fat cylinder, one parallel to the direction of propagation of the incident wave, and one parallel to the incident electric field vector. The exact solution is obtained by summing sufficient terms of the eigenfunction expansion to assure convergence of the sum. Excellent agreement of the FD-TD and exact solutions is noted, even at jump discontinuities of the field (and at jump discontinuities of the slope of the field distribution) that occur at the layer boundaries. This fine agreement is observed despite the stepped-edge approximation of the circular layer boundaries.

#### 4.3. Homogeneous, anisotropic, square material cylinder, TM polarization [19]

The ability to independently specify electrical permittivity and conductivity for each  $E$  vector component in the FD-TD lattice, and magnetic permeability and equivalent loss for each  $H$  vector

component, leads immediately to the possibility of using FD-TD to model material structures having diagonalizable tensor electric and magnetic properties. No alteration of the basic FD-TD algorithm is required. The more complicated behavior associated with off-diagonal tensor components can also be modeled, in principle, with some algorithm complications [20].

Recent development of coupled, surface, combined-field integral equation (CFIE) theory for modeling electromagnetic wave scattering by arbitrary-shaped, two-dimensional, anisotropic material structures [19] has permitted detailed code-to-code validation studies of FD-TD anisotropic models. Figure 7 illustrates one such study. Here, the magnitude of the equivalent surface electric current induced by TM illumination of a square anisotropic cylinder is graphed as a function of position along the cylinder surface for both the FD-TD and CFIE models. The incident wave propagates in the  $+y$ -direction and has a  $+z$ -directed electric field. The cylinder has an electrical size  $k_0 s = 5$ , permittivity  $\epsilon_{xx} = 2$ , and diagonal permeability tensor  $\mu_{xx} = 2$  and  $\mu_{yy} = 4$ . For the



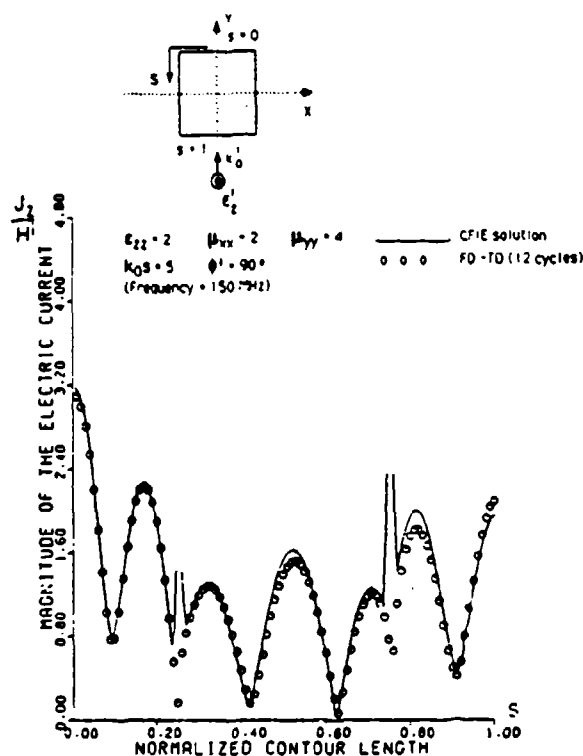


Fig. 7. Comparison of FD-TD and frequency-domain surface combined-field integral equation results for longitudinal surface electric current distribution on a  $k_{oz} = 5$  square anisotropic cylinder, TM case [19].

case shown, the FD-TD grid cell size is set equal to  $s/50$ , and the radiation boundary is located at a uniform distance of 20 cells from the cylinder surface.

From Fig. 7, we see that the FD-TD and CFIE results agree very well almost everywhere on the cylinder surface, despite the presence of a complicated series of peaks and nulls. Disagreement is noted at the cylinder corners where CFIE predicts sharp local peaks, but FD-TD predicts local nulls. Studies are continuing to resolve this corner physics issue.

#### 4.4. Circular metal cylinder, conformally modeled, TE and TM polarization

A key flaw in previous FD-TD models of conducting structures with smooth curved surfaces has

been the need to use stepped-edge (staircase) approximations of the actual structure surface. Although not a serious problem for modeling wave penetration and scattering for low- $Q$  metal cavities, recent FD-TD studies have shown that stepped approximations of curved walls and aperture surfaces can shift center frequencies of resonant responses by 1% to 2% for  $Q$  factors of 30 to 80, and can possibly introduce spurious nulls [21]. In the area of scattering, the use of stepped surfaces has limited application of FD-TD for modeling the important class of targets where surface roughness, exact curvature, and dielectric or permeable loading is important in determining the radar cross section.

Recently, two different types of FD-TD conformal surface models have been proposed and examined for two-dimensional problems:

(1) *Faraday's Law contour path models* [22]. These preserve the basic Cartesian grid arrangement of field components at all space cells except those adjacent to the structure surface. Space cells adjacent to the surface are deformed to conform with the surface locus. Slightly modified time-stepping expressions for the magnetic field components adjacent to the surface are derived from the integral form of Faraday's Law implemented around the perimeters of the deformed cells.

(2) *Stretched, conforming mesh models* [23, 24]. These employ available numerical mesh generation schemes to construct non-Cartesian grids which are continuously and globally stretched to conform with smoothly shaped structures. Time-stepping expressions are either adapted from the Cartesian FD-TD case [23] or obtained via analogy to the computational fluid dynamics formalism [24].

Research is ongoing for each of these types of conformal surface models. Key questions include: ease of mesh generation; suppression of numerical artifacts such as instability, dispersion, pseudorefraction, and subtraction noise limitation of computational dynamic range; coding complexity; and computer execution time. (See also the paper by Madsen and Ziolkowski in this issue.)

The accuracy of the Faraday's Law contour path models for smoothly curved structures subjected to TE and TM illumination is illustrated in Figs. 8(a) and 8(b) respectively. Here, a moderate-resolution Cartesian FD-TD grid (having  $1/20$  wavelength cell size) is used to compute the azimuthal or longitudinal electric current distribution on the surface of a  $k_0 a = 5$  circular metal cylinder. For both polarizations, the contour path FD-TD model achieves an accuracy of 1.5% or better at most surface points relative to the exact series solution. Running time for the conformal FD-TD model is essentially the same as for the old staircase FD-TD model since only a few  $H$  components immediately adjacent to the target surface require a slightly modified time-stepping relation.

#### 4.5. Flanged metal open cavity [25]

Here, we consider the interaction of a TM-polarized plane wave obliquely incident upon a flanged metal open cavity. The open cavity is formed by a flanged parallel-plate waveguide having a plate spacing,  $a$ , of 1 m, short-circuited by a terminating plate located at a distance,  $d$ , of 1 m from the aperture. At the assumed illumination frequency of 382 MHz,  $k_0 a = k_0 d \approx 8$ , and only the first two TE waveguide modes propagate within the open cavity. An oblique angle of incidence,  $\alpha = 30^\circ$ , is assumed for this case.

Figure 9 compares the magnitude and phase of the penetrating electric field within the cavity  $\frac{1}{2}$  m from the aperture computed using FD-TD to that computed using a cavity modal expansion and OSRC [25]. Good agreement is seen. Figure 10 shows a similar comparison for the bistatic radar cross section due to the induced aperture field distribution. Again, good agreement is noted.<sup>1</sup>

<sup>1</sup> It should be noted that the results obtained using the cavity modal expansion and OSRC represent a good approximation, but not a rigorous solution.

#### 4.6. Relativistically vibrating mirror, oblique incidence [26]

Analytical validations have been recently obtained for FD-TD models of reflection of a monochromatic plane wave by a perfectly conducting surface either moving at a uniform relativistic velocity or vibrating at a frequency and amplitude large enough so that the surface attains relativistic speeds [26]. The FD-TD approach of [26] is novel in that it does not require a system transformation where the conducting surface is at rest. Instead, the FD-TD grid is at rest in the laboratory frame, and the computed field solution is given directly in the laboratory frame. This is accomplished by implementing the proper relativistic boundary conditions for the fields at the surface of the moving conductor.

Figure 11 shows results for one of the more interesting problems of this type modeled so far, that of oblique plane wave incidence on an infinite vibrating mirror. This case is much more complicated than the normal incidence case, in that it has no closed-form solution. An analysis presented in the literature [27] writes the solution in an infinite-series form using plane-wave expansions, where the unknown coefficients in the series are solved numerically. This analysis serves as the basis of comparison for the FD-TD model results for the time variation of the scattered field envelope at points near the mirror.

Since it is difficult to model exactly an infinite plane mirror in a finite two-dimensional grid, a long, thin, rectangular perfectly-conducting slab is used as the mirror model, as shown in Fig. 11(a). Relativistic boundary conditions for the fields are implemented on the front and back sides of the slab. The other two sides, parallel to the velocity vector, are insensitive to the motion of the slab, and therefore no relativistic boundary conditions are required there. To minimize the effect of edge diffraction, the slab length is carefully selected so that the slab appears to be infinite in extent at observation point,  $P$ , during a well-defined early-time response when the edge effect has not yet

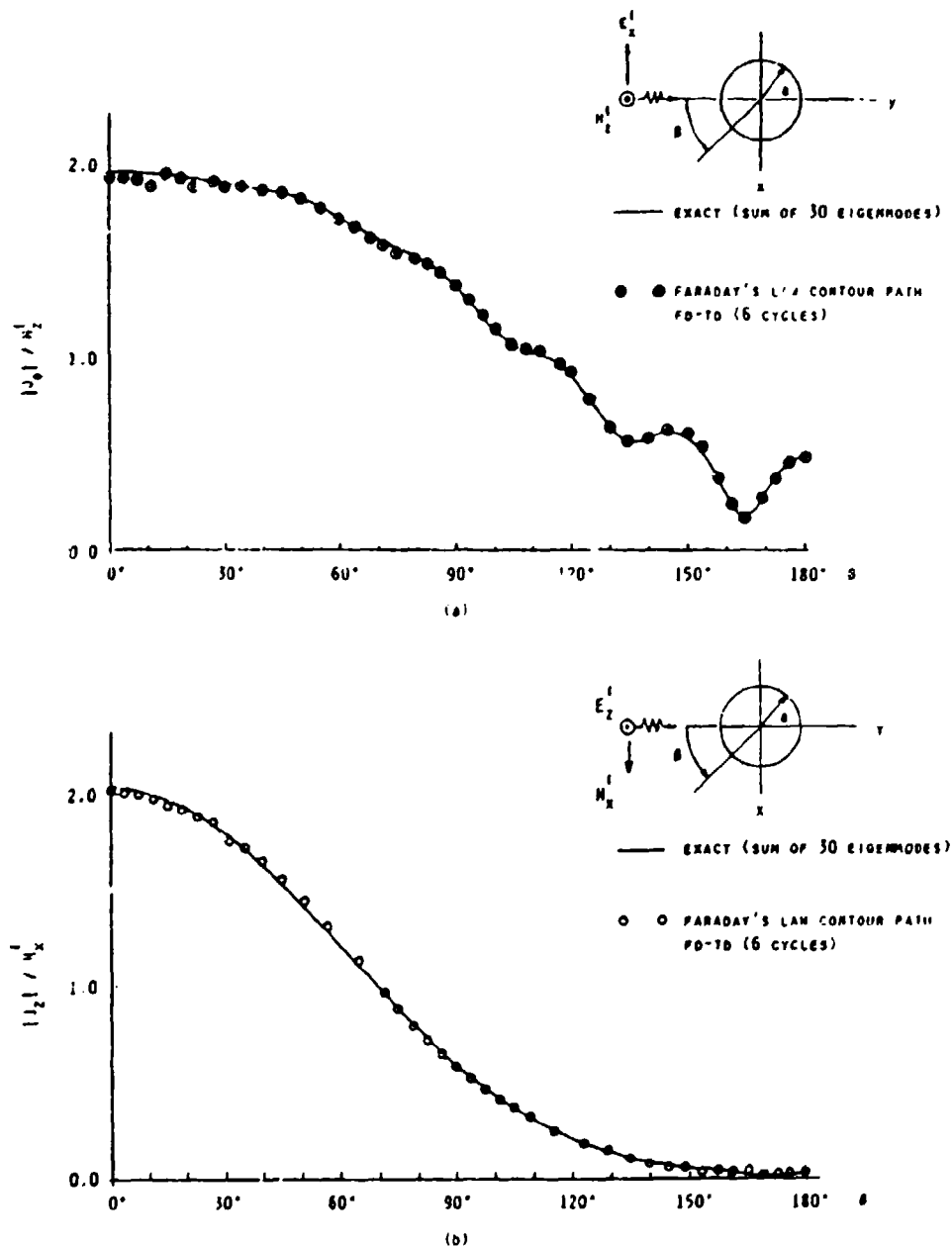


Fig. 8. Comparison of Faraday's Law contour-path FD-TD and exact solutions for surface electric current distribution on a  $k_0 a = 5$  circular metal cylinder: (a) TE case, azimuthal current; (b) TM case, longitudinal current [22].

propagated to  $P$ . Since the TM case does not provide appreciably different results than the TE case [27], only the TE case is considered. From Fig. 11(b), we see good agreement between the FD-TD

and analytical results obtained from [27] for the envelope of the scattered  $E$  field vs. time for an incident angle of  $30^\circ$ , peak mirror speed 20% that of light, and observation points  $z/d = -5$  and

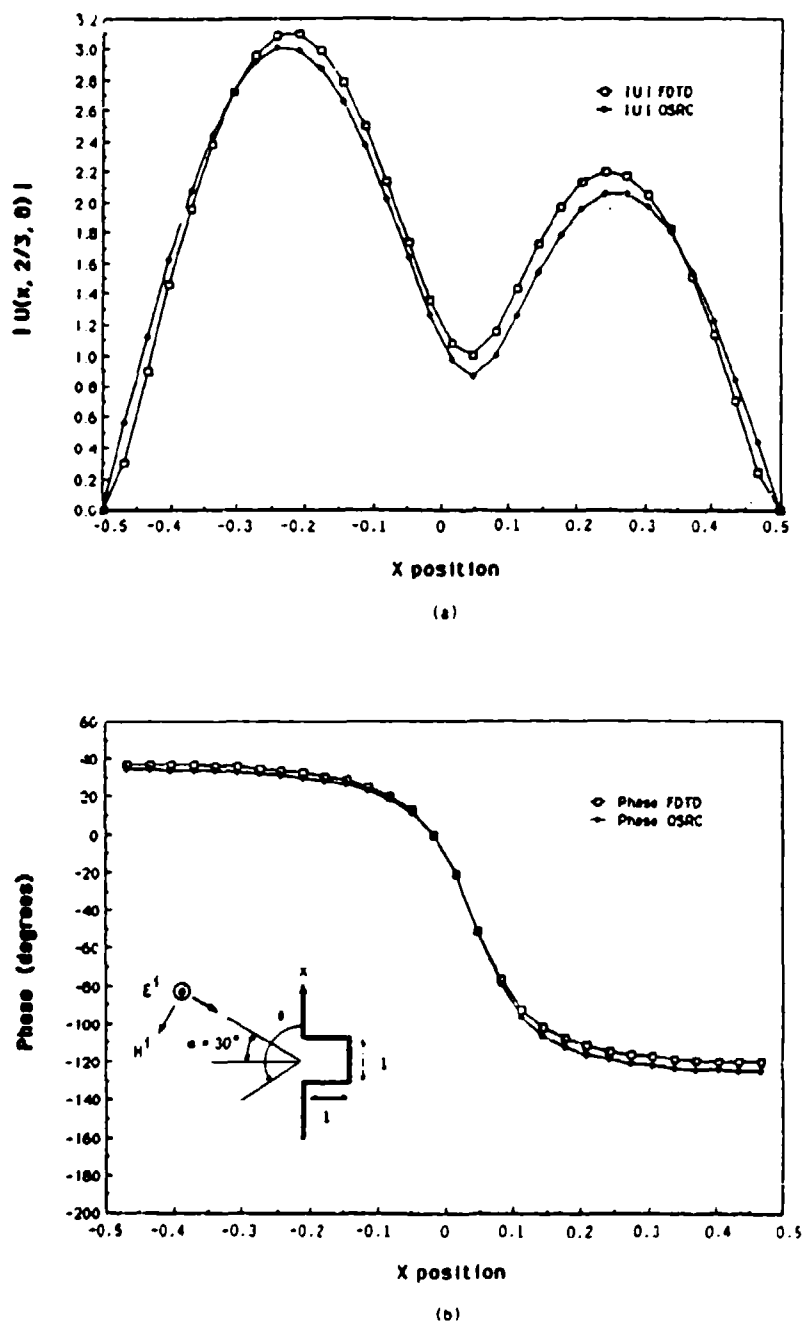


Fig. 9. Comparison of FD-TD and frequency-domain modal/OSRC approximate solution for the penetrating electric field distribution  $\frac{1}{2}$  meter within the flanged open cavity: (a) magnitude; (b) phase [25].

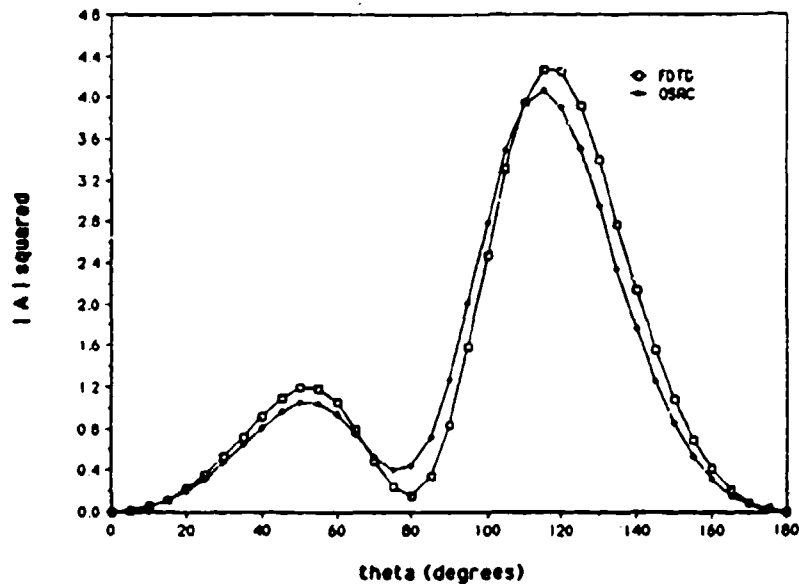
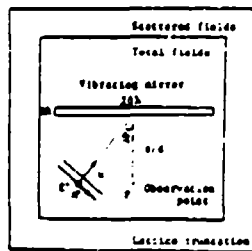
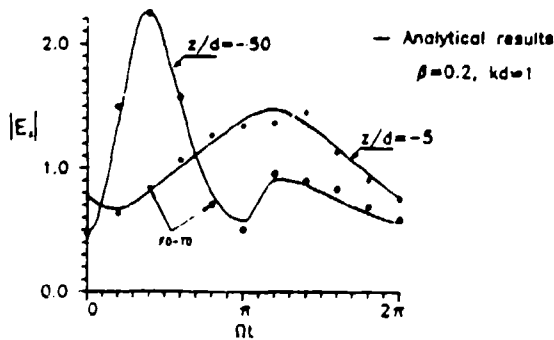


Fig. 10. Comparison of FD-TD and frequency-domain modal/OSRC approximate solution for the bistatic radar cross section due to the induced aperture field distribution of the flanged open cavity [25].



(a)



(b)

Fig. 11. Comparison of FD-TD and analytical results for the envelope of the scattered electric field vs. time for a monochromatic plane wave illuminating a relativistically vibrating mirror at a 30° oblique angle: (a) problem geometry; (b) comparative solutions at two distances from the mirror surface [26].

$z/d = -50$ , where  $kd = 1$ . Similar agreement is found for an even more oblique angle, 60° [26]. This agreement is satisfying since the action of the relativistically vibrating mirror is so complicated, generating a reflected wave having a spread both in frequency and spatial reflection angle, as well as evanescent modes.

### 5. FD-TD modeling validations for electromagnetic wave scattering, three dimensions

Analytical, code-to-code, and experimental validations have been obtained relative to FD-TD modeling of electromagnetic wave scattering for a wide variety of canonical three-dimensional structures, including cubes, flat plates, and crossed plates. Selected validations will be reviewed here.

#### 5.1. Metal cube, broadside incidence [13]

Results are now shown for the FD-TD computed surface electric current distribution on a metal cube subject to plane-wave illumination at broadside incidence. The electric current distribution is com-

pared to that computed by solving a frequency-domain surface EFIE using a standard triangular surface-patching MOM code [13]. It is shown that a very high degree of correspondence exists between the two sets of predictive data.

The detailed surface current study involves a cube of electrical size  $k_0 s = 2$ , where  $s$  is the side width of the cube. For the FD-TD model, each face of the cube is spanned by 400 square cells ( $20 \times 20$ ), and the radiation boundary is located at a uniform distance of 15 cells from the cube surface. For the MOM model, each face of the cube is spanned by either 18 triangular patches or 32 triangular patches (to test the convergence of the MOM model). Comparative results for surface current are graphed along two straight-line loci along the cube:  $\overline{abcd}$ , which is in the plane of the incident magnetic field; and  $\overline{ab'c'd'}$ , which is in the plane of the incident electric field.

Figure 12 compares the FD-TD and MOM results for the magnitude and phase of the surface current along  $\overline{ab'c'd'}$ . The FD-TD values agree with the high-resolution MOM data to better than  $\pm 2.5\%$  ( $\pm 0.2$  dB) at all comparison points. Phase agreement for the same sets of data is better than  $\pm 1^\circ$ . (The low-resolution MOM data have a phase anomaly in the shadow region.) In Fig. 13, comparably excellent agreement is obtained along  $\overline{abcd}$ , but only after incorporation of an edge-correction term in the MOM code [28] to enable it to properly model the current singularities at the cube corners,  $b$  and  $c$ .

### 5.2. Flat conducting plate, multiple monostatic looks [14, 20]

We next consider a  $30 \text{ cm} \times 10 \text{ cm} \times 0.65 \text{ cm}$  flat conducting plate target. At 1 GHz, where the plate spans 1 wavelength, a comparison is made between FD-TD and MOM results for the monostatic radar cross section (RCS) vs. look-angle azimuth (keeping a fixed elevation angle), as shown in Fig. 14(a). Here, the FD-TD model uses a uniform cell size of  $0.625 \text{ cm}$  ( $\lambda_0/48$ ), forming the plate by  $48 \times 16 \times 1$  cells. The radiation boundary is located at a

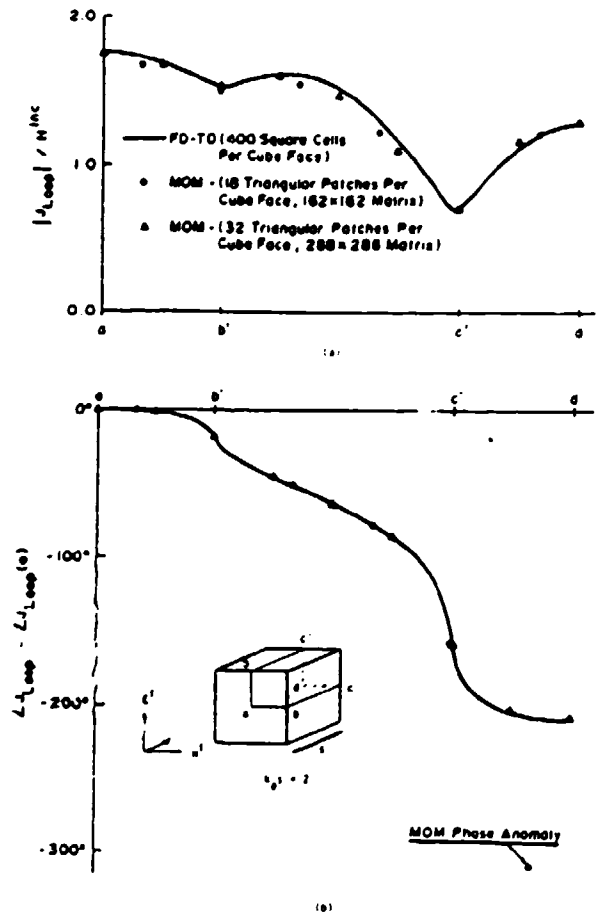


Fig. 12. Comparison of FD-TD and frequency-domain surface electric field integral equation results for surface electric current distribution along the E-plane locus,  $\overline{ab'c'd'}$ , of the  $k_0 s = 2$  metal cube: (a) magnitude; (b) phase [13].

uniform distance of only 8 cells from the plate surface. For the MOM model, study of the convergence of the computed broadside RCS indicates that the plate thickness must be accounted by using narrow side patches, and the space resolution of each surface patch should be finer than approximately 0.2 wavelength. As a result, the MOM model forms the plate by  $10 \times 3 \times 1$  divisions, yielding a total of 172 triangular surface patches. Figure 14(a) shows excellent agreement between the two models (within about  $\pm 0.2$  dB).

At 5 GHz, the plate spans 9 wavelengths, and the use of the MOM model is virtually precluded.

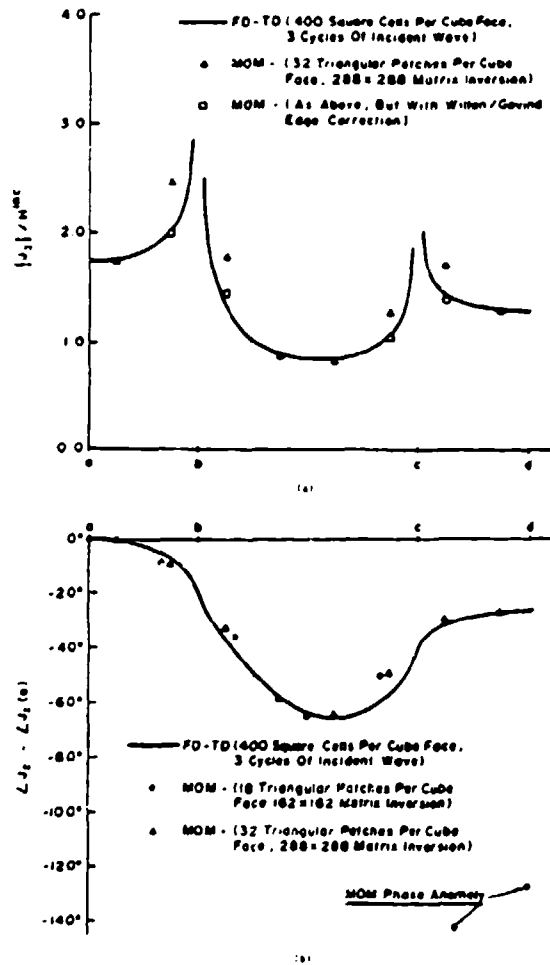


Fig. 13. Comparison of FD-TD and frequency-domain surface electric field integral equation results for surface electric current distribution along the  $H$ -plane locus,  $abcd$ , of the  $k_0s = 2$  metal cube: (a) magnitude; (b) phase [13].

If we follow the convergence guidelines discussed above, the plate would require approximately  $50 \times 15 \times 1$  divisions to properly converge, yielding a total of 3260 triangular surface patches, and requiring the generation and inversion of a  $4890 \times 4890$  complex-valued system matrix. On the other hand, FD-TD remains feasible for the plate at 9 GHz. Choosing a uniform cell size of 0.3125 cm ( $\lambda_0/10.667$ ), the plate is formed by  $96 \times 32 \times 2$  cells. With the radiation boundary again located only 8 cells from the plate surface, the overall lattice size

is  $112 \times 48 \times 18$ , containing 580,608 unknown field components (real numbers). Figure 14(b) shows excellent agreement between the FD-TD results and measurements of the monostatic RCS vs. look angle performed in the anechoic chamber facility operated by SRI International. The observed agreement is within about 1 dB and  $1^\circ$  of look angle. As will be seen next, this level of agreement is maintained for more complicated targets having corner reflector properties.

### 5.3. T-shaped conducting target, multiple monostatic looks [14, 20]

We last consider the monostatic RCS pattern of a T-shaped target comprised of two flat conducting plates electrically bonded together. The main plate has the dimensions  $30 \text{ cm} \times 10 \text{ cm} \times 0.33 \text{ cm}$ , and the bisecting fin has the dimensions  $10 \text{ cm} \times 10 \text{ cm} \times 0.33 \text{ cm}$ .<sup>2</sup> The illumination is a 9.0 GHz plane wave at  $0^\circ$  elevation angle and TE polarization relative to the main plate. Thus, the main plate spans 9.0 wavelengths. Note that look-angle azimuths between  $90^\circ$  and  $180^\circ$  provide substantial corner reflector physics, in addition to the edge diffraction, corner diffraction, and other effects found for an isolated flat plate.

For this target, the FD-TD model uses a uniform cell size of 0.3125 cm ( $\lambda_0/10.667$ ), forming the main plate by  $32 \times 96 \times 1$  cells and the bisecting fin by  $32 \times 32 \times 1$  cells. With the radiation boundary again located only 8 cells from the target's maximum surface extensions, the overall lattice size is  $48 \times 112 \times 48$ , containing 1,548,288 unknown field components (212.6 cubic wavelengths). Starting with zero-field initial conditions, 661 time steps are used, equivalent to 31 cycles of the incident wave at 9.0 GHz.

Figure 15 compares the FD-TD predicted monostatic RCS values at 32 key look angles between  $0^\circ$  and  $180^\circ$  with measurements performed by SRI International. These look angles are selec-

<sup>2</sup> The center line of the "bisecting" fin is actually positioned 0.37 cm to the right of the center line of the main plate. This is accounted for in the FD-TD model.

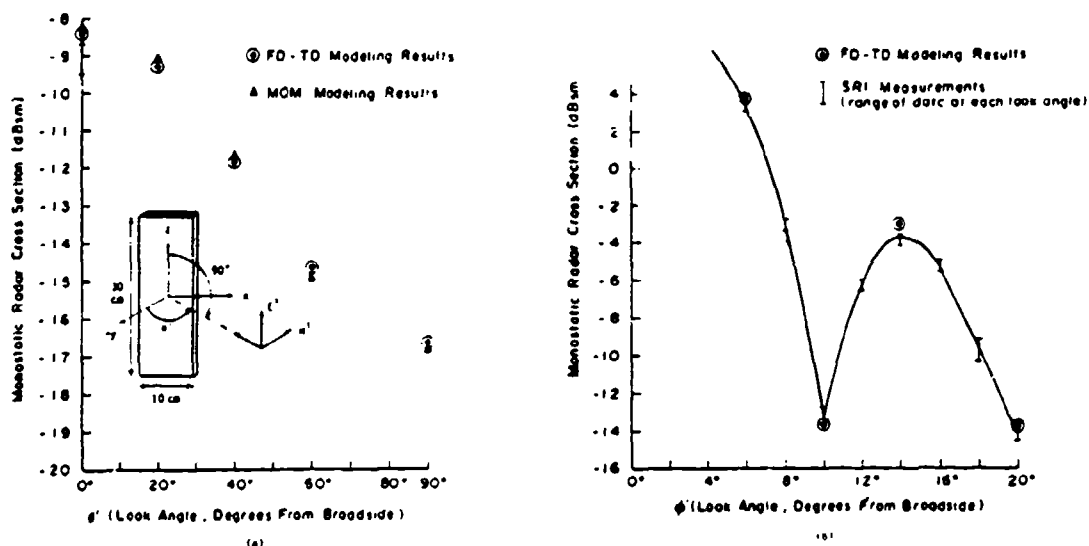


Fig. 14. Validation of FD-TD results for the monostatic radar cross section of a rectangular, flat conducting plate: (a) versus frequency-domain surface electric field integral equation results at 1 GHz (plate size =  $1 \times 1$  wavelengths); (b) versus anechoic chamber measurements at 9 GHz (plate size =  $9 \times 3$  wavelengths) [14, 20].

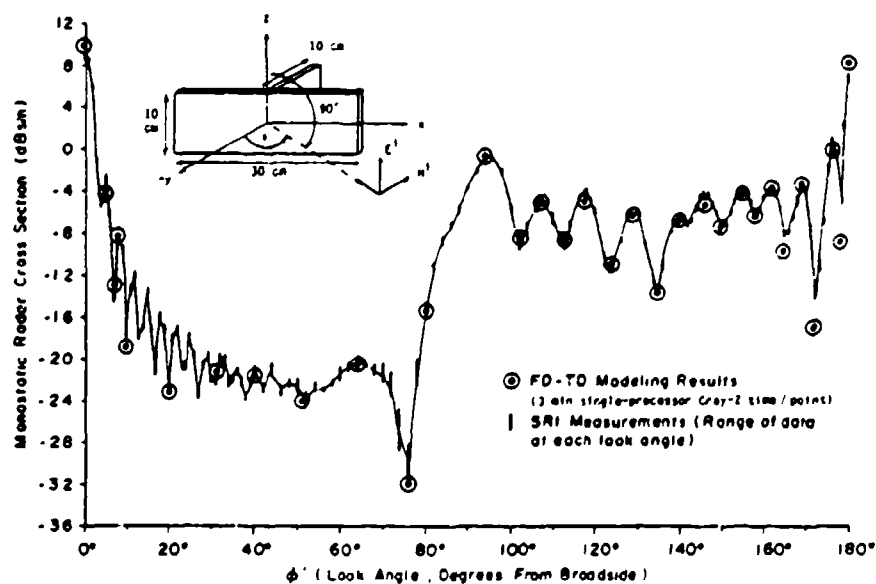


Fig. 15. Comparison of FD-TD modeling predictions with anechoic chamber measurements of monostatic radar cross section for a T-shaped conducting target at 9 GHz (target span =  $9 \times 3 \times 3$  wavelengths) [14, 20].



ted to define the major peaks and nulls of the monostatic RCS pattern. It is seen that the agreement is again excellent: in amplitude, within about 1 dB over a total RCS-pattern dynamic range of 40 dB; and in azimuth, within  $1^\circ$  in locating the peaks and nulls of the RCS pattern. Note especially the fine agreement for look-angle azimuths greater than  $90^\circ$ , where there is a pronounced corner reflector effect.

## 6. FD-TD modeling validations for electromagnetic wave penetration and coupling, two and three dimensions

### 6.1. Penetration models for narrow slots and lapped joints in thick screens

The physics of electromagnetic wave transmission through narrow slots and lapped joints in shielded enclosures must be accurately understood to permit good engineering design of equipment to meet specifications for performance concerning electromagnetic pulse, lightning, high-power microwaves, electromagnetic interference and compatibility, undesired radiated signals, and RCS. In many cases, slots and joints can have very narrow gaps filled by air, oxidation films, or layers of anodization. Joints can be simple (say, two metal sheets butted together); more complex (a lapped or "furniture" joint); or even more complex (a threaded screw-type connection with random points of metal-to-metal contact, depending upon the tightening). Extra complications arise from the possibility of electromagnetic resonances within the joint, either in the transverse or longitudinal (depth) direction.

Clearly, to make any headway with this complicated group of problems using the FD-TD approach, it is necessary to develop and validate FD-TD models which can simulate the geometric features of generic slots and joints. Since a key geometric feature is likely to be the narrow gap of the slot or joint relative to one FD-TD space cell,

it is important to understand how subcell gaps can be efficiently modeled.

Three different types of FD-TD subcell models have been proposed and examined for modeling narrow slots and joints:

(1) *Equivalent slot loading* [29]. Here, rules are set to define an equivalent permittivity and permeability in a slot formed by a single-cell gap to effectively narrow the gap to the desired degree.

(2) *Subgridding* [30]. Here, the region within the slot or joint is provided with a sufficiently fine grid. This grid is properly connected to the coarser grid outside of the slot.

(3) *Faraday's Law contour path model* [31]. Here, space cells adjacent to and within the slot or joint are deformed to conform with the surface locus (in a manner similar to the conformal curved surface model). Slightly modified time-stepping expressions for the magnetic field components in these cells are derived from the integral form of Faraday's Law implemented about the perimeters of the deformed cells.

The accuracy of the Faraday's Law contour path model for narrow slots and joints is illustrated in Figs. 16 and 17 by direct comparison of the computed gap electric field distribution against high-resolution numerical benchmarks. Figure 16 models a 0.1 wavelength thick conducting screen which extends 0.5 wavelength to each side of a straight slot which has a gap of 0.025 wavelength. Broadside TE illumination is assumed. Three types of predictive data are compared: (1) the low-resolution ( $0.1 \lambda_0$ ) FD-TD model using the contour path approach to treat the slot as a  $\frac{1}{2}$ -cell gap; (2) a high-resolution ( $0.025 \lambda_0$ ) FD-TD model treating the slot as a 1-cell gap; and (3) a very-high-resolution frequency-domain EFIE model, solved via MOM (having  $0.0025 \lambda_0$  sampling in the slot) which treats the slotted screen as a pure scattering geometry. From Fig. 16, we see that there is excellent agreement between all three sets of predictive data in both magnitude and phase. Of particular interest is the ability of the low-resolution FD-TD model, using the contour path approach, to accurately compute the peak electric field in the slot.

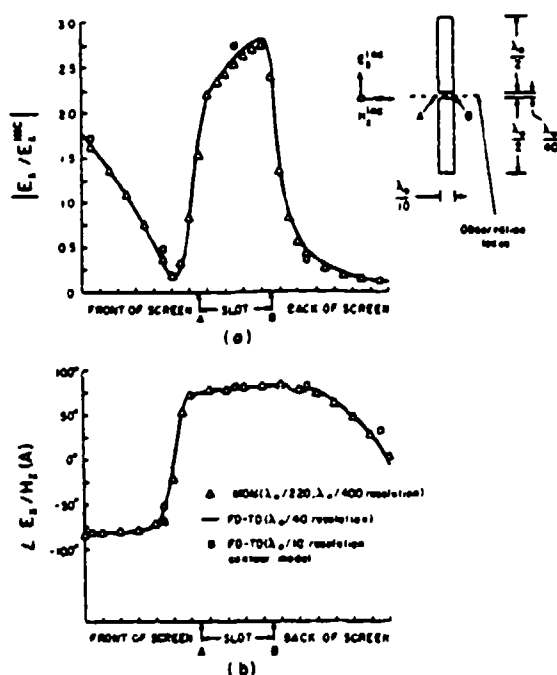


Fig. 16. Comparison of FD-TD and frequency-domain surface electric field integral equation results for the gap electric field distribution in a slotted conducting screen, straight slot case, TE illumination: (a) magnitude; (b) phase [31].

Figure 17 shows the geometry of a U-shaped lapped joint which was selected for detailed study of path-length (depth) power transmission resonances. The U shape of the joint permits adjustment of the overall joint path length without disturbing the positions of the input and output ports at A and F. A uniform gap of 0.025 wavelength is assumed, as is a screen thickness of 0.3 wavelength

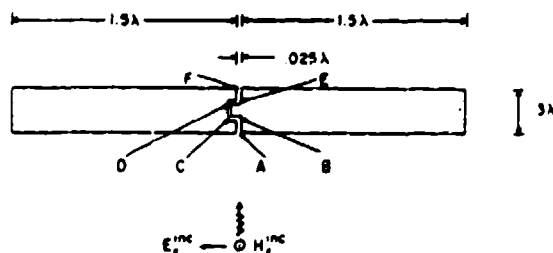


Fig. 17. Geometry of U-shaped lapped joint in a conducting screen, TE illumination (shown to scale) [31].

and width of 3 wavelengths. Figure 18 compares the gap electric field distribution within the joint as computed by: (1) a low-resolution ( $0.09 \lambda_0$ ) contour path FD-TD model treating the gap as 0.28 cell; and (2) a high-resolution ( $0.025 \lambda_0$ ) FD-TD model treating the gap as 1 cell. The total path length  $ABCDEF$  within the lapped joint is adjusted to equal 0.45 wavelength, which provides a sharp power transmission peak to the shadow side of the screen. From Fig. 18, we see a very good agreement between the low- and high-resolution FD-TD models, even though this is a numerically stressful resonant penetration case.

An implication of these results is that coarse ( $0.1 \lambda_0$ ) FD-TD gridding can be effectively used to model the fine-grained physics of wave penetration through subcell slots and joints if simple algorithm modifications are made in accordance with the contour path approach. This can substantially reduce computer resource requirements and coding complexity for FD-TD models of complex structures, without sacrificing appreciable accuracy in the results.

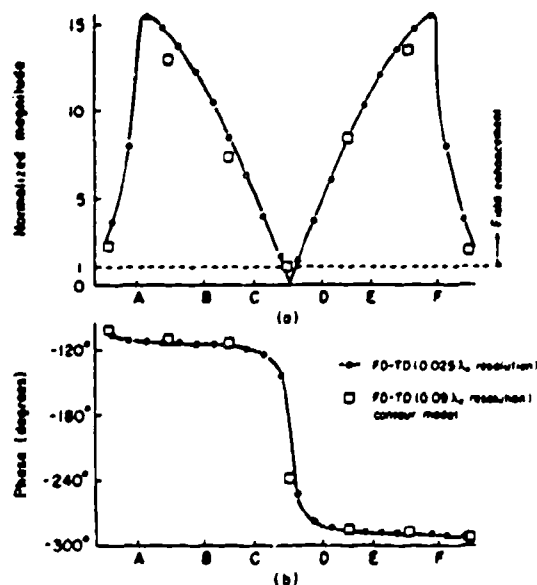


Fig. 18. FD-TD computed gap electric field distribution within the lapped joint at the first transmission resonance: (a)  $|E_{gp}/E_{inc}|$ ; (b)  $\angle E_{gp}/H_2(A)$  [31].

## 6.2. Coupling models for wires and wire bundles

In equipment design for threats represented by electromagnetic pulse, high-power microwaves, and electromagnetic interference, understanding electromagnetic wave coupling to wires and cable bundles located within shielding enclosures is a problem that is complementary to that of wave penetration through apertures of the shield (such as narrow slots and joints). Similar to the narrow slot problem, a key dimension of the interacting structure, in this case the wire or bundle diameter, may be small relative to one FD-TD space cell. Thus, it is important to understand how thin, sub-cell, wires and bundles can be efficiently modeled if FD-TD is to have much application to coupling problems.

Two different types of FD-TD subcell models have been proposed and examined for modeling thin wires:

(1) *Equivalent inductance* [32]. Here, an equivalent inductance is defined for a wire within a space cell, permitting a lumped-circuit model of the wire to be set up and computed in parallel with the field solution.

(2) *Faraday's Law contour path model* [21]. Here, space cells adjacent to the wire are deformed to conform with the surface locus (in a manner similar to the conformal curved surface model).  $1/r$  singularities of the azimuthal magnetic field and radial electric field are assumed to exist within the deformed cells. Slightly modified time-stepping expressions for the azimuthal magnetic field components in these cells are derived from the integral form of Faraday's Law implemented around the perimeter of the deformed cells.

The accuracy of the Faraday's Law contour path model for thin wires in free space is illustrated in Figs. 19(a) and 19(b). Figure 19(a) graphs the scattered azimuthal magnetic field at a fixed distance of  $1/20$  wavelength from the center of an infinitely long wire having a radius ranging between  $1/30,000$  and  $1/30$  wavelength. TM illumination is assumed. We see that there is excellent agreement between the exact series solution and

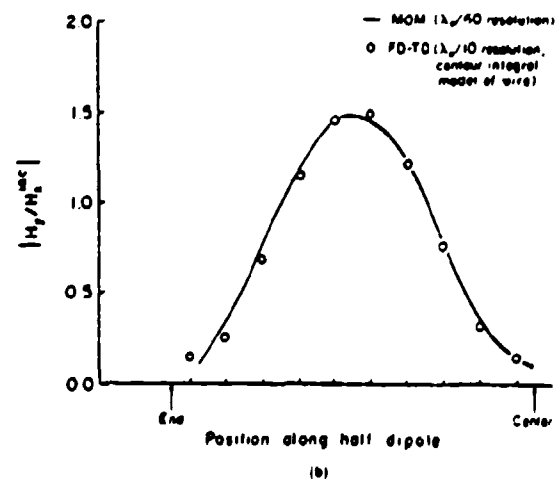
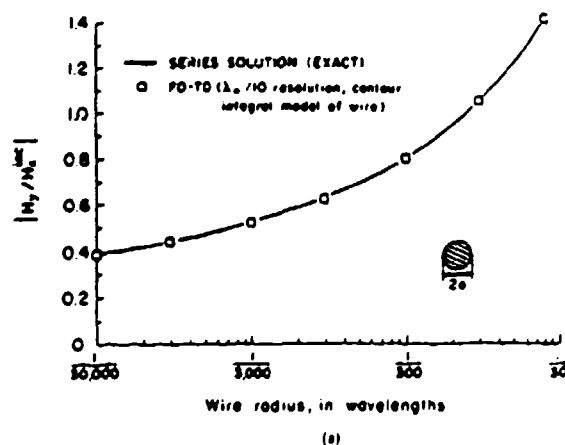


Fig. 19. Validation studies for the Faraday's Law contour path FD-TD model for thin wires in free space: (a) comparison of FD-TD and exact solutions for the scattered azimuthal magnetic field at a fixed distance of  $1/20$  wavelength from the center of an infinitely long wire (as a function of wire radius); (b) comparison of FD-TD and MOM results for the scattered azimuthal magnetic field distribution along a  $2.0$  wavelength (antiresonant) wire of radius  $1/300$  wavelength [21].

the low-resolution ( $0.1 \lambda_0$ ) FD-TD contour path model over the entire 3-decade range of wire radius. Figure 19(b) graphs the scattered azimuthal magnetic field distribution along a  $2.0$  wavelength (antiresonant) wire of radius  $1/300$  wavelength. Broadside TM illumination is assumed, and the field is observed at a fixed distance of  $1/20$  wavelength from the wire center. We see that there

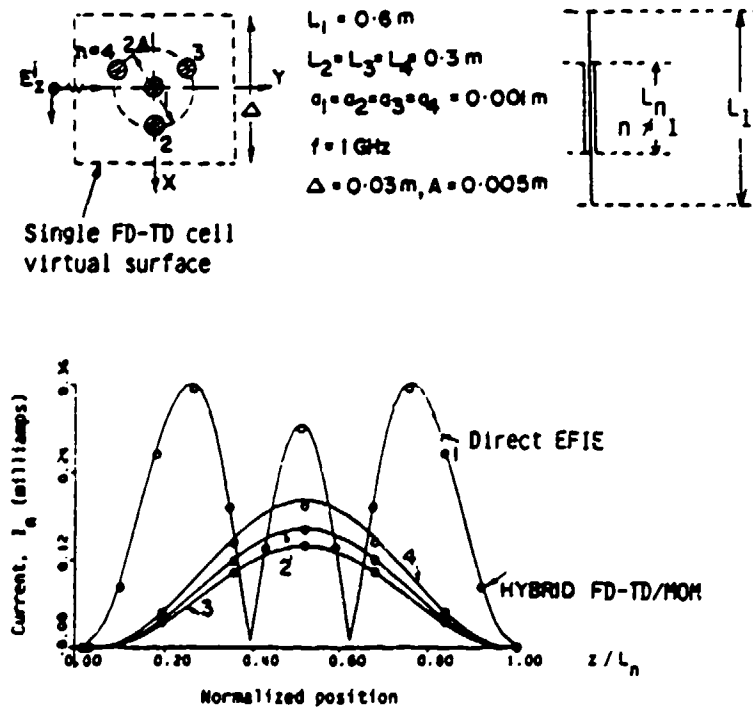


Fig. 20. Comparison of hybrid FD-TD/MOM modeling predictions with direct frequency-domain electric field integral equation results for induced currents on a wire bundle [21].

is excellent agreement between a frequency-domain EFIE (MOM) solution sampling the wire current at  $1/60$  wavelength increments, and the low-resolution ( $0.1 \lambda_0$ ) FD-TD contour path model.

The FD-TD contour path model can be extended to treat thin wire bundles, as well as single wires. Figure 20 shows the code-to-code validation results for the induced currents on a bundle comprised of 4 wires, where 3 are of equal length. Here, a wire of length 60 cm (2.0 wavelengths) is assumed to be at the center of the bundle, and three parallel wires of length 30 cm (1.0 wavelength) are assumed to be located at  $120^\circ$  angular separations on a concentric circle of radius 5 mm ( $1/60$  wavelength). The radii of all wires in the bundle are equal and set to 1 mm ( $1/300$  wavelength). The assumed excitation is in free space, provided by a 1 GHz broadside TM plane wave. Following the technique of [21], the bundle is replaced by a single

wire having varying equivalent radius corresponding to the three sections along the bundle axis. The physics of the single wire of varying equivalent radius is incorporated in a low-resolution ( $0.1 \lambda_0$ ) FD-TD contour path model, as discussed above. The FD-TD model is then run to obtain the tangential  $E$  and  $H$  fields at a virtual surface conveniently located at the cell boundary containing the equivalent wire (shown as a dashed line in Fig. 20). These fields are then utilized as excitation to obtain the currents induced on the individual wires of the original bundle. This last step is performed by setting up an EFIE and solving via MOM. Figure 20 shows an excellent correspondence between the results of the hybrid FD-TD/MOM procedure described above and the usual direct EFIE (MOM) solution for the induced current distribution on each wire of the bundle.

The hybrid FD-TD/MOM procedure for modeling thin wire bundles is most useful when the

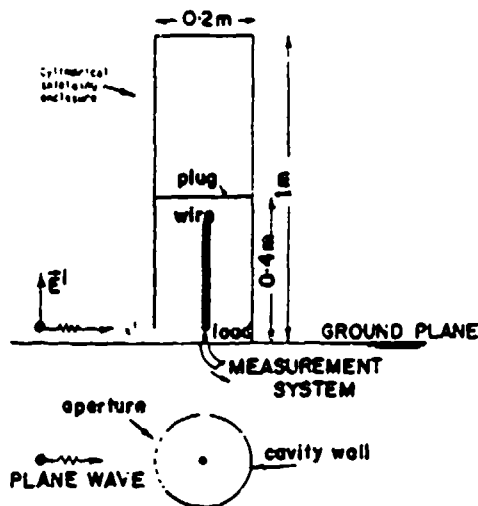


Fig. 21. Geometry of the cylindrical metal shielding enclosure and internal wire or wire-pair [21].

bundle is located within a shielding enclosure. Figures 21 and 22 show the geometry and test results for such a model involving the variation of induced load current with illumination frequency for a single wire and a wire-pair located at the center of a cylindrical metal enclosure. The enclosure is 1.0 m high, 0.2 m in diameter, and referenced to a large metal ground plane. Approximate plane wave illumination is provided by an electrically-large conical monopole referenced to the same ground plane. Wave penetration into the interior of the enclosure is through a circumferential slot aperture (12.5 cm arc length, 1.25 cm gap) at the ground plane. For the cases studied, an internal shorting plug is located 40 cm above the ground plane. For the single-wire test, a wire of length 30 cm and radius 0.495 mm is centered within the interior and connected to the ground plane with a lumped 50-ohm load. For the wire-pair test, parallel wires of these dimensions are located 1 cm apart, with one wire shorted to the ground plane and the other connected to the ground plane with a lumped 50-ohm load. All results are normalized to a 1 V/m incident wave electric field.

From Fig. 22, we see that there is a good correspondence between the measured and numerically

modeled wire load current for both test cases. The two-wire test proved to be especially challenging since the observed  $Q$  factor of the coupling response (center frequency divided by the half-power bandwidth) is quite high, about 75. Indeed, it is found that the FD-TD code has to be stepped through as many as 80 cycles to approximately reach the sinusoidal steady state for illumination frequencies near the resonant peak [21]. However, substantially fewer cycles of time-stepping are needed away from the resonance, as indicated in the figure.

## 7. Use of FD-TD for modeling very complex three-dimensional structures

Two characteristics of FD-TD cause it to be very promising for numerical modeling of electromagnetic wave interactions with very complex objects: (1) Dielectric and permeable media can be specified independently for each electric and magnetic field vector component in the three-dimensional volume being modeled. Since there may be tens of millions of such vector components in large FD-TD models, inhomogeneous media of enormous complexity can be specified in principle. (2) The required computer resources for this type of detailed volumetric modeling are dimensionally low, only of order  $N$ , where  $N$  is the number of space cells in the FD-TD lattice.

The emergence of supercomputers has recently permitted FD-TD to be seriously applied to a number of very complex electromagnetic wave interaction problems. Two of these will now be briefly reviewed.

### 7.1. UHF wave penetration into a missile seeker section [6, 33]

Here, FD-TD is applied to model the penetration of an axially incident 300 MHz plane wave into a metal-coated missile guidance section. The FD-TD model, shown in Fig. 23, contains the following elements: (1) magnesium fluoride

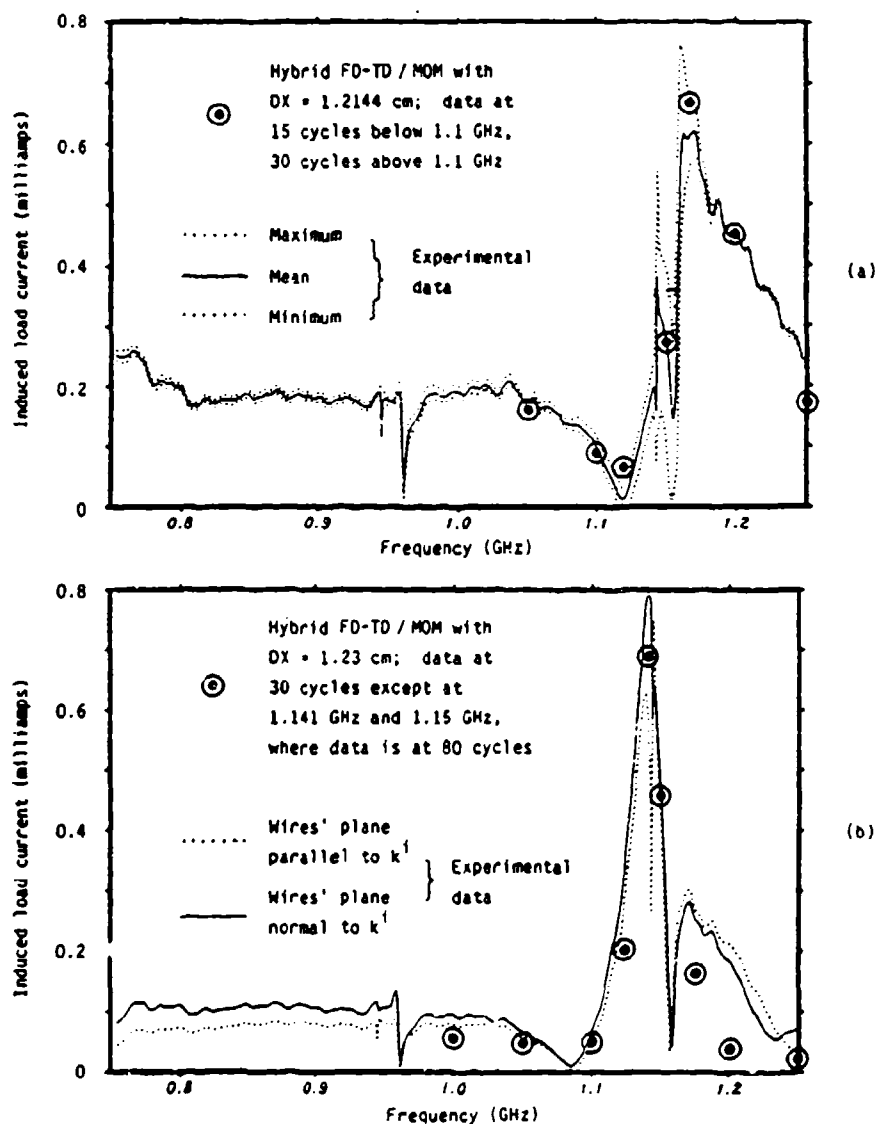


Fig. 22. Comparison of hybrid FD-TD/MOM modeling predictions with experimental data for induced load current: (a) single wire in shielding enclosure; (b) wire pair in shielding enclosure [21].

infrared dome; (2) circular nose aperture; (3) circumferential sleeve-fitting aperture 23 cm aft (loaded with fiberglass); (4) head-coil assembly; (5) cooled detector unit with enclosing phenolic ring; (6) pre-amp can; (7) wire bundle connecting the detector unit to the pre-amp can; (8) wire bundle connecting the pre-amp can to the metal

backplane; and (9) longitudinal metal support rods. The fiberglass structure of the nose cone and its metalization are approximated in a stepped-surface manner, as is the infrared dome.

For this structure, the FD-TD model uses a uniform cell size of  $\frac{1}{3}$  cm ( $\lambda_0/300$ ), with an overall lattice size of  $24 \times 100 \times 48$  cells containing

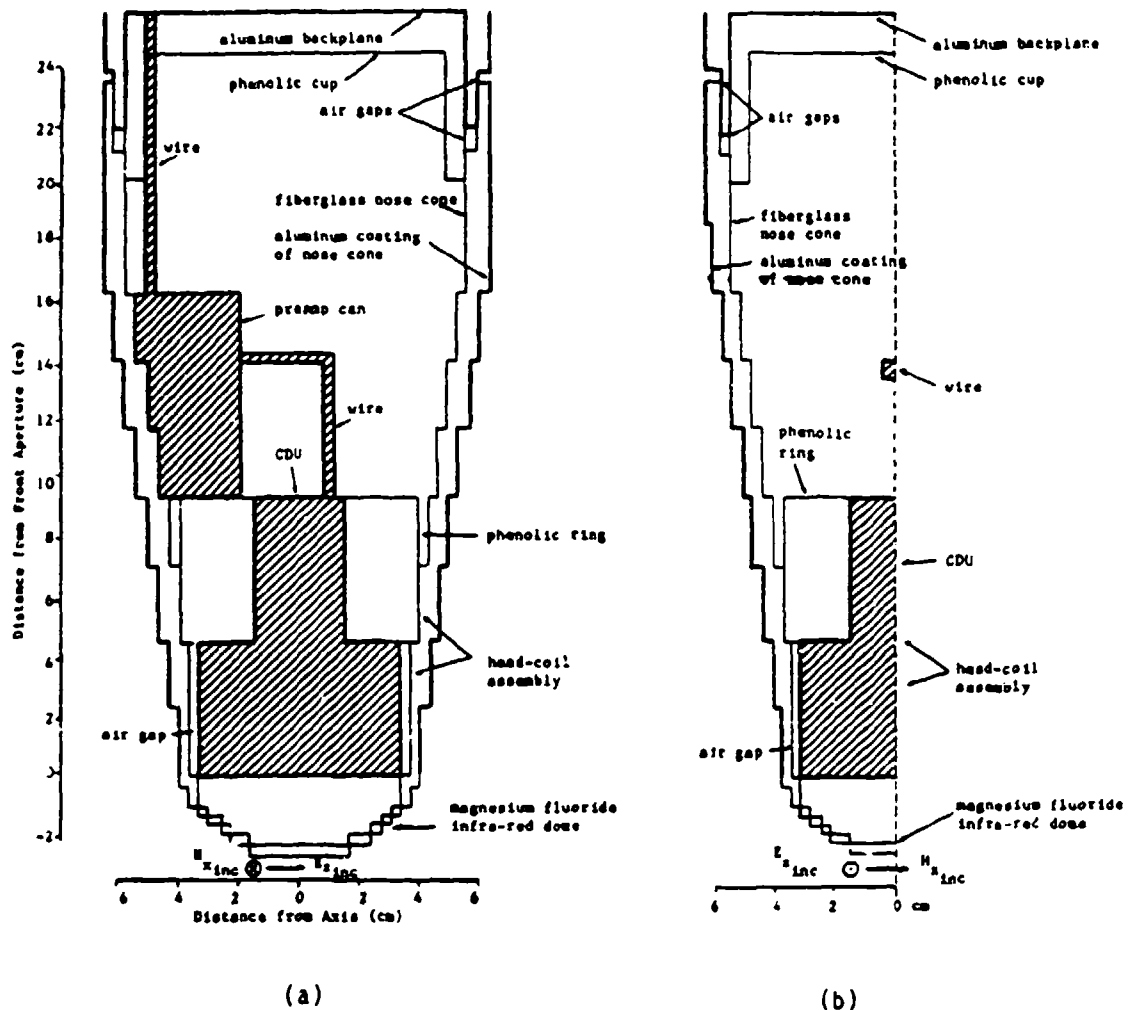
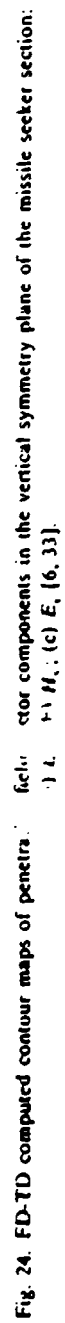


Fig. 23. FD-TD model of the missile seeker section, showing component materials: (a) at the vertical symmetry plane; (b) at the horizontal observation plane [6, 33].

690,000 unknown field components. (A single symmetry plane is used, giving an effective lattice size of  $48 \times 100 \times 48$ .) The model is run for 1800 time steps, equivalent to 3.0 cycles of the incident wave at 300 MHz.

Figure 24 plots contour maps of the FD-TD computed field vector components at the symmetry plane of the model. An important observation is that the simulated wire bundles connecting the cooled detector unit, pre-amp can, and metal back-

plane are paralleled by high-level magnetic field contours (Fig. 24(b)). This is indicative of substantial, uniform current flow along each bundle. Such current flow would generate locally a magnetic field looping around the wire bundle which, when "cut" by the symmetry plane, shows up as parallel field contours spaced equally on each side of the bundle. Using a simple Ampere's Law argument, the common-mode bundle currents can be calculated, thus obtaining a key transfer function



factor components in the vertical symmetry plane of the missile seeker section:

14.  $H_0: (c) E, [6, 33]$ .



between free-field incident UHF plane wave power density and coupled wire currents [33]. As stated earlier, this information is useful for studies of vulnerability of electronic systems to upset due to both natural and man-made electromagnetic phenomena.

Although this missile seeker model was composed to demonstrate the capability of FD-TD to map fields penetrating into a complex structure having multiple apertures and realistic internal engineering details, it should be understood that the full bistatic radar cross section pattern of the structure is available as a byproduct with virtually no additional effort. Further, with the  $\frac{1}{2}$  cm space resolution used, the FD-TD radar cross section model would be useful up to 9 GHz.

### 7.2. Whole-body human dosimetry at VHF and UHF frequencies [34, 35]

Here, FD-TD is applied to model the penetration of plane waves at VHF and UHF frequencies into the entire human body. Directly exploiting the ability of FD-TD to model media inhomogeneities down to the space-cell level, highly realistic three-dimensional FD-TD tissue models of the complete body have been constructed. Specific electrical parameters are assigned to each of the electric field vector components at the 16,000 to 40,000 space cells comprising the body model. Assignments are based upon detailed cross-section tissue maps of the body (as obtained via cadaver studies available in the medical literature), and cataloged measurements of tissue dielectric properties. Uniform FD-TD space resolutions as fine as 1.3 cm throughout the entire human body have proven feasible with the Cray-2.

Figure 25, taken from [35], shows the FD-TD computed contour maps of the specific absorption rate (SAR) distribution along horizontal cuts through the head and liver of the three-dimensional inhomogeneous man model. In Fig. 25(a), the incident wave has a power density of  $1 \text{ mW/cm}^2$  at 350 MHz, while in Fig. 25(b), the incident wave has the same power density but is

at 100 MHz. These contour maps illustrate the high level of detail of local features of the SAR distribution that is possible via FD-TD modeling for highly realistic tissue models.

### 8. FD-TD microstrip and microwave circuit models

Recently, FD-TD modeling has been extended to provide detailed characterizations of microstrips, resonators, finlines, and two-dimensional microwave circuits. In [36], FD-TD is used to calculate the dispersive characteristics of a typical microstrip on a gallium arsenide substrate. A Gaussian pulse excitation is used, and the effective dielectric constant and characteristic impedance vs. frequency is efficiently obtained over a broad frequency range via Fourier transform of the time-domain field response.

In [37], FD-TD is first used to obtain resonant frequencies of several three-dimensional cavities loaded by dielectric blocks. Next, the resonant frequency of a finline cavity is computed. Last, the resonant frequencies of a microstrip cavity on anisotropic substrate are obtained, and the dispersion characteristics of the microstrip used in the cavity are calculated. FD-TD modeling results are compared primarily to those obtained using the transmission line matrix (TLM) approach, and the two methods are found to give practically the same results. (See also the paper by Johns in this issue [pp. 597-610].)

In [38], a modified version of FD-TD is presented which provides central-difference time-stepping expressions for distributions of voltage and surface current density along arbitrary-shaped two-dimensional microwave circuits. This approach is quite different from that of [36, 37], which utilize the original volumetric field sampling concept for FD-TD. As a result, the method of [38] requires fewer unknowns to be solved, and avoids the need for a radiation boundary condition. However, an auxiliary condition is required to describe the loading effects of the fringing fields

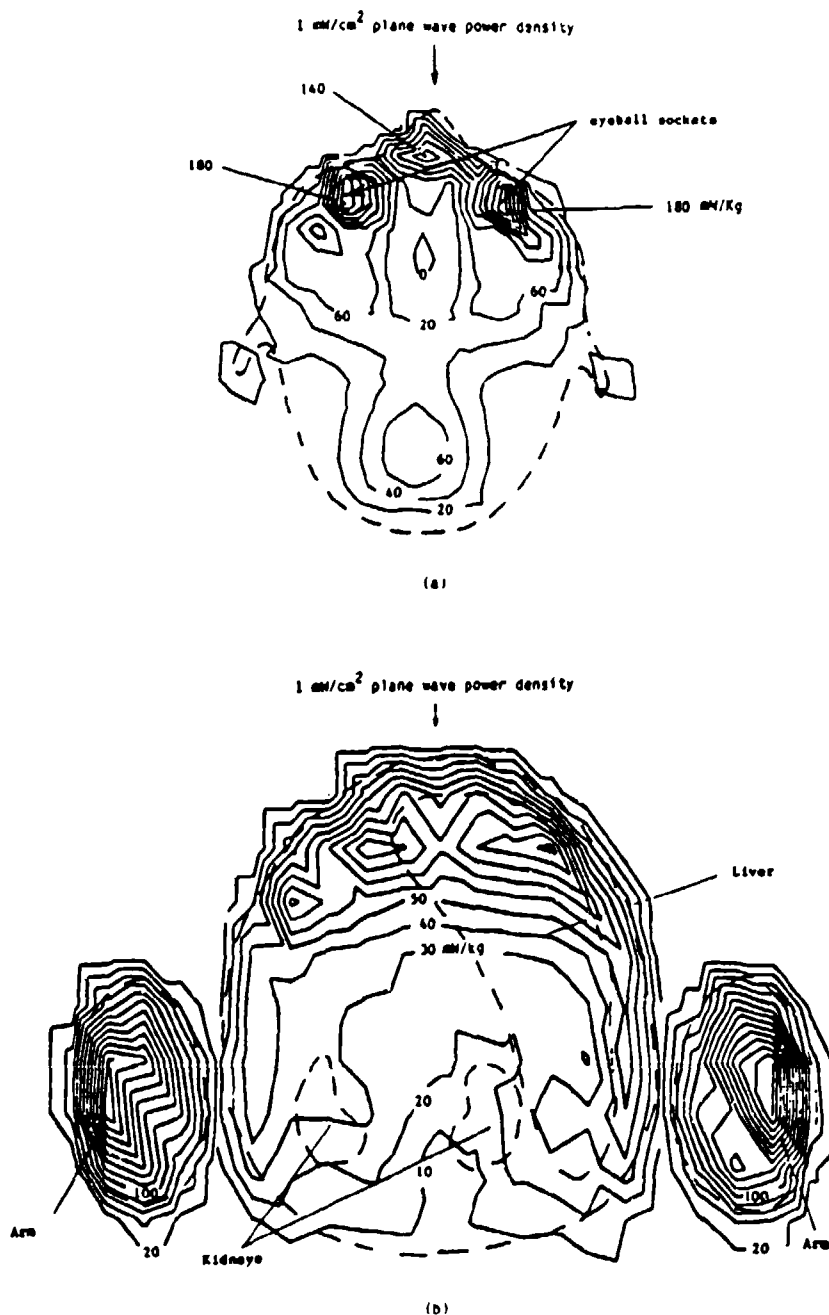


Fig. 25. FD-TD computed contour maps of the specific absorption rate due to penetrating electromagnetic fields within a highly realistic, three-dimensional model of the entire human body: (a) along a horizontal cut through the head at 350 MHz; (b) along a horizontal cut through the liver at 100 MHz [35].

at the edges of the microstrip conducting paths. Figure 26, taken from [38], shows the FD-TD computed  $S$ -parameter,  $|S_{21}|$ , as a function of frequency for a two-port microstrip ring circuit. The ring circuit, gridded as shown in the figure, has an inner radius of 4 mm, outer radius of 7 mm, substrate relative permittivity of 10 and relative permeability of 0.93 (simulating duroid), and is connected to two 50-ohm lines making a  $90^\circ$  angle. The broadband response of the circuit is obtained

using a single FD-TD run for an appropriate pulse excitation, followed by Fourier transformation of the desired response time-domain waveform. From Fig. 26, we see good agreement of the predicted and measured circuit response over the 2–12 GHz frequency band and a dynamic range of about 30 dB. Reference [38] concludes that the application of its FD-TD approach to arbitrarily-shaped microstrip circuits is encouraging, but more work is needed to determine the modeling limitations,

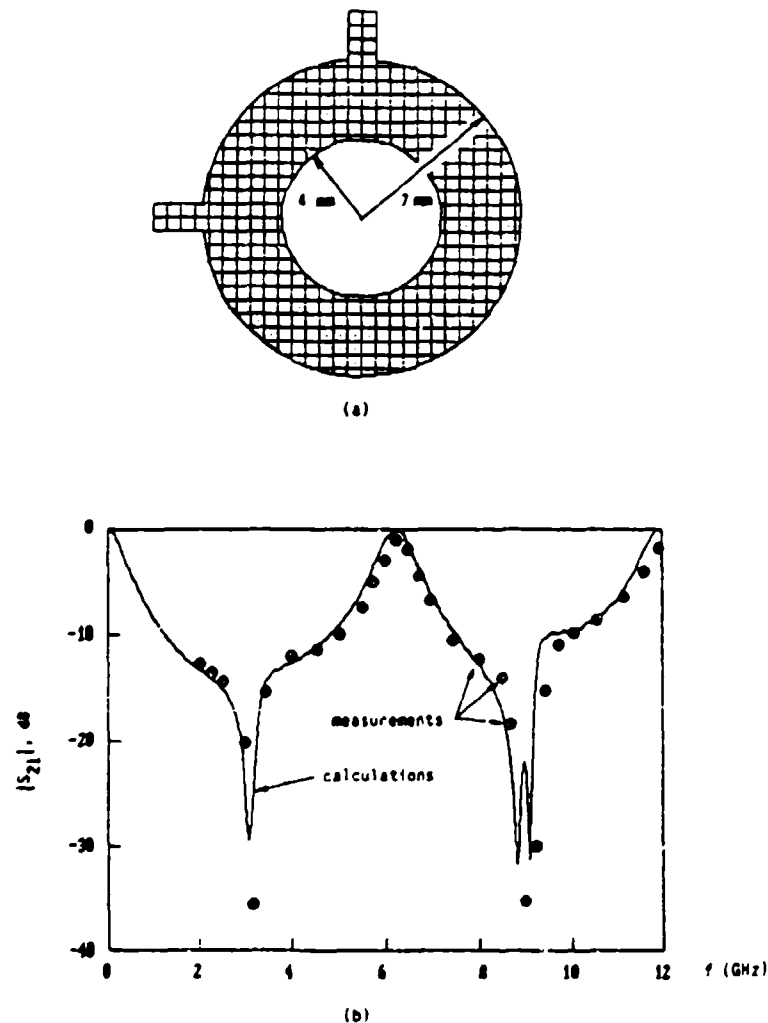


Fig. 26. Comparison of FD-TD modeling predictions with measurements of  $|S_{21}|$  for a two-port microstrip ring circuit: (a) geometry and gridding of microstrip circuit; (b) comparative results over 2–12 GHz [38].

especially at higher frequencies where media dispersion can become important.

### 9. FD-TD inverse scattering reconstructions in one and two dimensions

Initial work has demonstrated the possibility of accurately reconstructing one-dimensional profiles of permittivity and conductivity [39], and the shape and dielectric compositions of two-dimensional targets [40, 41] from minimal scattered field pulse response data. The general approach involves setting up a numerical feedback loop which uses a one- or two-dimensional FD-TD code as a forward-scattering element, and a specially constructed non-linear optimization code as the feedback element. FD-TD generates a test pulse response for a trial layering or target shape/composition. The test pulse is compared to the measured pulse, and an error signal is developed. Working on this error signal, the nonlinear optimization element perturbs the trial layering or target shape/composition in a manner to drive down the error. Upon repeated iterations, the proposed layering or target ideally converges to the actual one, a strategy similar to that of [42].

The advantage of working in the time domain is that a layered medium or target shape can be reconstructed sequentially in time as the wavefront of the incident pulse sweeps through, taking advantage of causality. This reduces the complexity of reconstruction since only a portion of the layering or target shape is being generated at each iteration. Advanced strategies for reconstruction in the presence of additive noise may involve the use of prediction/correction, where the trial layer or target shape is considered to be a predictor of the actual case, which is subsequently corrected by optimization of the entire layered medium or target shape using the complete scattered pulse waveform.

Figure 27 shows the application of the basic FD-TD feedback strategy to a one-dimensional

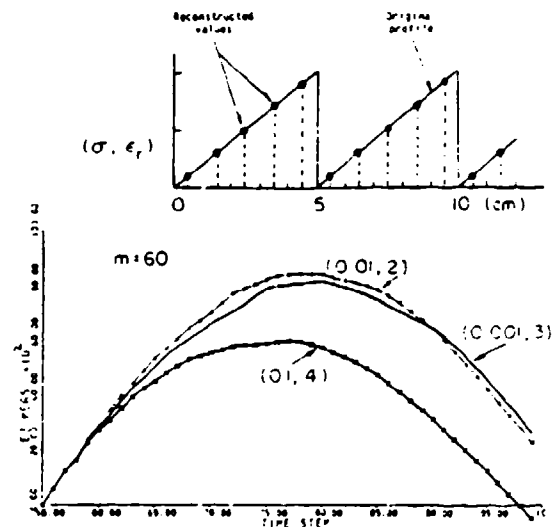


Fig. 27. Application of the FD-TD-feedback strategy to reconstruct a one-dimensional "sawtooth" variation of electrical permittivity and conductivity in the absence of noise [39].

layered medium in the absence of noise. Both the electrical permittivity and conductivity of the medium vary in a "sawtooth" manner with depth. The curves show simulated measured data for the reflected pulse for three cases defined by the peak values of the conductivity (0.001 S/m, 0.01 S/m, and 0.1 S/m) and the corresponding spatially coincident peak values of relative permittivity (3, 2, and 4) of the medium. In each case, the incident pulse is assumed to be half-sinusoid spanning 50 cm between zero crossings. Noting that the dark dots superimposed on the "sawtooth" represent the reconstructed values of permittivity and conductivity, we see that the basic FD-TD feedback strategy is quite successful in the absence of noise [39].

Figure 28 shows the application of the FD-TD feedback strategy to reconstruct a two-dimensional lossy dielectric target. The target is a 30 cm × 30 cm square cylinder having a uniform conductivity of 0.01 S/m, and a tent-like relative permittivity profile which starts at 2.0 at the front and left sides and increases linearly to a peak value of 4.0 at the back corner on the right side. These profiles are

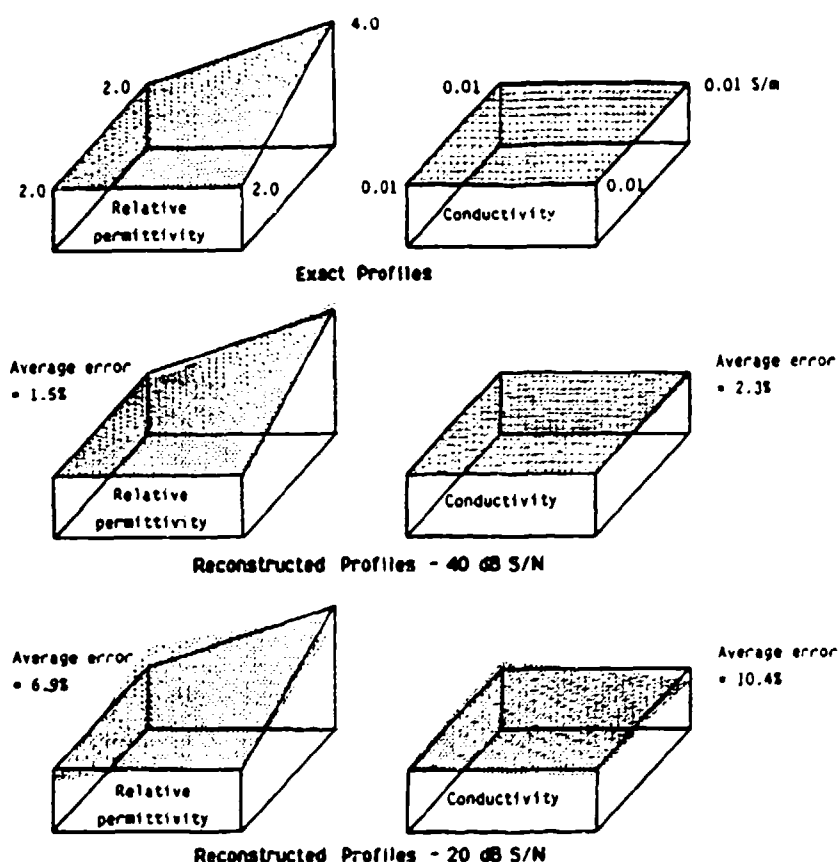


Fig. 28. Application of the FD-TD/feedback strategy to reconstruct a two-dimensional lossy dielectric target in the presence of noise [41].

illustrated in a perspective manner at the top of Fig. 28. The target is assumed to be illuminated by a TM polarized plane wave that is directed toward the front of the target (as visualized at the top of Fig. 28). The incident waveform is a 3-cycle sinusoidal tone burst having a 60 MHz carrier frequency. For the reconstruction, the only data utilized is the time-domain waveform of the scattered electric field as observed at two points. These points are located 1 m from the front of the target, and are positioned 15 cm to either side of the target center line. To simulate measured data, the FD-TD computed scattered field waveforms are contaminated with additive Gaussian noise. In all of the

reconstructions, the target shape and location is assumed to be known.

From Fig. 28, we see that for a signal/noise ratio of 40 dB, the average error in the reconstructed permittivity and conductivity profiles is 1.5% and 2.3% respectively. If the signal/noise ratio is reduced to 20 dB, the average errors increase to 6.9% and 10.4%, respectively [41]. Research is ongoing to determine means of improving the noise performance, especially using predictor/corrector techniques briefly discussed earlier. Given the relatively small amount of scattered field data utilized, the FD-TD feedback strategy appears promising for future development.

## 10. Very large-scale computer software

The FD-TD method is naturally suited for large-scale processing by state-of-the-art vector supercomputers and concurrent processors. This is because essentially all of the arithmetic operations involved in a typical FD-TD run can be vectorized or cast into a highly concurrent format. Further, the  $O(N)$  demand for computer memory and clock cycles (where  $N$  is the number of lattice space cells) is dimensionally low, and permits three-dimensional FD-TD models of structures spanning  $50\text{--}100 \lambda_0$  to be anticipated by the early 1990s.

Table 1  
Computation times

Machine	10-wavelength model present FD-TD code*
VAX 11/780 (no floating-point accelerator)	40.0 h
Cray-2 (single processor, using the VAX Fortran)	12.0 min
Cray-2 (single processor, some code optimization)	3.0 min
Cray-2 (four processors, some code optimization)	1 min (est.)
True 10 Gflop machine	2 sec (est.)

\*  $1.55 \cdot 10^6$  unknown field vector components, 661 time steps (T-shaped target). The complete bistatic RCS pattern is obtained for a single illumination angle at a single frequency. Times are increased by 50%–100% if an impulsive illumination/Fourier transform is used to obtain the bistatic RCS pattern at a multiplicity of frequencies within the spectrum of the impulsive illumination.

Let us now consider computation times of present FD-TD codes. Table 1 lists computation times (derived either from benchmark runs or based on analysts' estimates) for modeling one illumination angle of a  $10 \lambda_0$  three-dimensional structure using the present FD-TD code. Note that the fourth computing system listed in the table is a hypothetical next-generation machine operating at an average rate of 10 Gflops. This capability is generally expected to be available in the early 1990s.

From Table 1, it is fairly clear that steadily advancing supercomputer technology will permit

routine engineering usage of FD-TD for modeling electromagnetic wave interactions with electrically-large structures by 1995.

An interesting prospect that has recently arisen is the reduction of the  $O(N)$  computational burden of FD-TD to  $O(N^{1/3})$ . This possibility is a consequence of the appearance of the Connection Machine (CM), which has tens of thousands of simple processors and associated memories arranged in a highly efficient manner for processor-to-processor communication. With the CM, a single processor could be assigned to store and time-step a single row of vector field components in a three-dimensional FD-TD space lattice. For example,  $1.5 \cdot 10^6$  processors would be sufficient to store the 6 Cartesian components of  $E$  and  $H$  for each of the  $500 \times 500$  rows of a cubic lattice spanning  $50 \lambda_0$  (assuming 10 cells/ $\lambda_0$  resolution). FD-TD time-stepping would be performed via row operations mapped onto the individual CM processors. These row operations would be performed concurrently. Thus, for a fixed number of time steps, the total running time would be proportional to the time needed to perform a single row operation, which in turn would be proportional to the number of field vector components in the row, or  $O(N^{1/3})$ .

For the  $50 \lambda_0$  cubic lattice noted above, this would imply a dimensional reduction of the computational burden from  $O(500^3)$  to  $O(500)$ , a tremendous benefit. As a result, it is conceivable that a suitably scaled CM could model one illumination angle of a  $50 \lambda_0$  three-dimensional structure in only a few seconds, achieving effective floating-point rates in the order of 100 Gflops. For this reason, FD-TD software development for the CM is a promising area of research for developing ultralarge numerical models of electromagnetic wave interactions with complex structures.

## 11. Conclusion

This paper has reviewed the basic formulation of the FD-TD numerical modeling approach for Maxwell's equations. A number of two- and three-

dimensional examples of FD-TD modeling of electromagnetic wave interactions with structures were provided to indicate the accuracy and breadth of FD-TD applications. The objects modeled range in nature from simple geometric shapes to extremely complex aerospace and biological systems. In all cases studied to date where rigorous analytical, code-to-code, or experimental validations were possible, FD-TD predictive data for penetrating and scattered near fields as well as radar cross section were in excellent agreement with benchmark data. It was also shown that opportunities are arising in applying FD-TD to rapidly time-varying systems, microwave circuits, and inverse scattering. With continuing advances in FD-TD modeling theory, as well as continuing advances in vector and concurrent supercomputer technology, there is a strong possibility that FD-TD numerical modeling will occupy an important place in high-frequency engineering electromagnetics as we move into the 1990s.

#### Acknowledgment

The author wishes to acknowledge the research contributions of his colleagues, Prof. K.R. Umashankar of the University of Illinois at Chicago and Prof. G.A. Kriegsmann of Northwestern University. Contributions of graduate students at these two institutions, especially Mr. Ben Beker, Mr. Jeffrey Blaschak, Mr. Fady Harfoush, Mr. Thomas Jurgens, Mr. Thomas Moore, and Mr. Mark Strickel are also gratefully acknowledged. The author also wishes to acknowledge the support of his sponsors, past and present, including the U.S. Air Force Rome Air Development Center (Contracts F30602-77-C-0163, F30602-79-C-0039, F30602-80-C-0302, and F19628-82-C-0140); Lawrence Livermore National Laboratory (Contract 6599805); NASA Lewis Research Center (Grant NAG 3-635); National Science Foundation (Grants ECS-8515777 and ASC-8811273); and Office of Naval Research Contract N00014-88-K-0475.

#### References

- [1] K.S. Yee, "Numerical solution of initial boundary value problems involving Maxwell's equations in isotropic media", *IEEE Trans. Antennas Propagat.* 14, 302-307 (1966).
- [2] A. Taflové and M.E. Brodwin, "Numerical solution of steady-state electromagnetic scattering problems using the time-dependent Maxwell's equations", *IEEE Trans. Microwave Theory Tech.* 23, 623-630 (1975).
- [3] G.A. Kriegsmann, "Exploiting the limiting amplitude principle to numerically solve scattering problems", *Wave Motion* 4, 371-380 (1982).
- [4] A. Taflové and M.E. Brodwin, "Computation of the electromagnetic fields and induced temperatures within a model of the microwave-irradiated human eye", *IEEE Trans. Microwave Theory Tech.* 23, 888-896 (1975).
- [5] A. Taflové, "Application of the finite-difference time-domain method to sinusoidal steady state electromagnetic penetration problems", *IEEE Trans. Electromagn. Compat.* 22, 191-202 (1980).
- [6] A. Taflové and K.R. Umashankar, "A hybrid moment method/finite-difference time-domain approach to electromagnetic coupling and aperture penetration into complex geometries", *IEEE Trans. Antennas Propagat.* 30, 617-627 (1982).
- [7] R. Holland, "Threde: a free-field EMP coupling and scattering code", *IEEE Trans. Nuclear Sci.* 24, 2416-2421 (1977).
- [8] K.S. Kunz and K.M. Lee, "A three-dimensional finite-difference solution of the external response of an aircraft to a complex transient EM environment I: The method and its implementation", *IEEE Trans. Electromagn. Compat.* 20, 328-333 (1978).
- [9] D.E. Menwether, R. Fisher and F.W. Smith, "On implementing a numeric Huygen's source scheme in a finite-difference program to illuminate scattering bodies", *IEEE Trans. Nuclear Sci.* 27, 1819-1833 (1980).
- [10] A. Taflové and K.R. Umashankar, "Advanced numerical modeling of microwave penetration and coupling for complex structures", Final Report No. UCRL-15960, Contract 6599805, Lawrence Livermore Nat. Lab. (1987).
- [11] G. Mur, "Absorbing boundary conditions for the finite-difference approximation of the time-domain electromagnetic field equations", *IEEE Trans. Electromagn. Compat.* 23, 377-382 (1981).
- [12] K.R. Umashankar and A. Taflové, "A novel method to analyze electromagnetic scattering of complex objects", *IEEE Trans. Electromagn. Compat.* 24, 397-405 (1982).
- [13] A. Taflové and K.R. Umashankar, "Radar cross section of general three-dimensional scatterers", *IEEE Trans. Electromagn. Compat.* 25, 433-440 (1983).
- [14] A. Taflové, K.R. Umashankar and T.G. Jurgens, "Validation of FD-TD modeling of the radar cross section of three-dimensional structures spanning up to nine wavelengths", *IEEE Trans. Antennas Propagat.* 33, 662-666 (1985).

- [15] B. Engquist and A. Majda, "Absorbing boundary conditions for the numerical simulation of waves", *Math. Comput.* 31, 629-651 (1977).
- [16] L.N. Trefethen and L. Halpern, "Well-posedness of one-way wave equations and absorbing boundary conditions", Rept. 85-30, Inst. Comput. Appl. Sci. and Eng. (ICASE), NASA Langley Res. Center, Hampton, VA (1985).
- [17] J.G. Blaschak and G.A. Kriegsmann, "A comparative study of absorbing boundary conditions", *J. Comput. Physics* 77, 109-139 (1988).
- [18] D.T. Borup, D.M. Sullivan and O.P. Gandhi, "Comparison of the FFT conjugate gradient method and the finite-difference time-domain method for the 2-D absorption problem", *IEEE Trans. Microwave Theory Tech.* 35, 383-395 (1987).
- [19] B. Beker, K.R. Umashankar and A. Taflové, "Numerical analysis and validation of the combined field surface integral equations for electromagnetic scattering by arbitrary shaped two-dimensional anisotropic objects", *IEEE Trans. Antennas Propagat.*, submitted.
- [20] A. Taflové and K.R. Umashankar, "Analytical models for electromagnetic scattering", Final Report RADC-TR-85-87 on contract F19628-82-C-0140, Electromagn. Sci. Div., Rome Air Dev. Center, Hanscom AFB, MA (1985).
- [21] K.R. Umashankar, A. Taflové and B. Beker, "Calculation and experimental validation of induced currents on coupled wires in an arbitrary shaped cavity", *IEEE Trans. Antennas Propagat.* 35, 1248-1257 (1987).
- [22] T.G. Jurgens, A. Taflové, K.R. Umashankar and T.G. Moore, "FD-TD conformal modeling of smoothly curved targets", *IEEE Trans. Antennas Propagat.*, submitted.
- [23] M. Fusco, "FD-TD algorithm in curvilinear coordinates", *IEEE Trans. Antennas Propagat.*, submitted.
- [24] V. Shankar and W. Hall, "A time-domain differential solver for electromagnetic scattering problems", *Proc. IEEE* 77 (1989).
- [25] J.G. Blaschak, G.A. Kriegsmann and A. Taflové, "A study of wave interactions with flanged waveguides and cavities using the on-surface radiation condition method", *Wave Motion* 11 (1989).
- [26] F. Harfoush, A. Taflové and G.A. Kriegsmann, "A numerical technique for analyzing electromagnetic wave scattering from moving surfaces in one and two dimensions", *IEEE Trans. Antennas Propagat.* 37 (1989).
- [27] D. De Zutter, "Reflections from linearly vibrating objects: plane mirror at oblique incidence", *IEEE Trans. Antennas Propagat.* 30, 898-903 (1982).
- [28] D.R. Wilton and S. Govind, "Incorporation of edge conditions in moment method solutions", *IEEE Trans. Antennas Propagat.* 25, 845-850 (1977).
- [29] J. Gilbert and R. Holland, "Implementation of the thin-slit formalism in the finite-difference EMP code THREDII", *IEEE Trans. Nuclear Sci.* 28, 4269-4274 (1981).
- [30] K.S. Yee, "A numerical method of solving Maxwell's equations with a coarse grid bordering a fine grid", SGEMP Note #9, Document D-DV-86-0008, D Division, Lawrence Livermore Nat. Lab. (1986).
- [31] A. Taflové, K.R. Umashankar, B. Beker, F. Harfoush and K.S. Yee, "Detailed FD-TD analysis of electromagnetic fields penetrating narrow slots and lapped joints in thick conducting screens", *IEEE Trans. Antennas Propagat.* 36, 247-257 (1988).
- [32] R. Holland and L. Simpson, "Finite-difference analysis of EMP coupling to thin struts and wires", *IEEE Trans. Electromagn. Compat.* 23, 88-97 (1981).
- [33] A. Taflové and K.R. Umashankar, "Evaluation of time-domain electromagnetic coupling techniques. Vol. I: Theory and numerical results", Final Report RADC-TR-80-251 on contract F30602-79-C-0039, Rome Air Dev. Center, Griffiss AFB, NY (1980).
- [34] D.M. Sullivan, D.T. Borup and O.P. Gandhi, "Use of the finite-difference time-domain method in calculating EM absorption in human tissues", *IEEE Trans. Biomed. Eng.* 34, 148-157 (1987).
- [35] D.M. Sullivan, O.P. Gandhi and A. Taflové, "Use of the finite-difference time-domain method in calculating EM absorption in man models", *IEEE Trans. Biomed. Eng.* 35, 179-186 (1988).
- [36] X. Zhang, J. Fang, K.K. Mei and Y. Liu, "Calculations of the dispersive characteristics of microstrips by the time-domain finite-difference method", *IEEE Trans. Microwave Theory Tech.* 36, 263-267 (1988).
- [37] D.H. Choi and W.J. Hofer, "The finite-difference time-domain method and its application to eigenvalue problems", *IEEE Trans. Microwave Theory Tech.* 34, 1464-1470 (1986).
- [38] W.K. Gwarek, "Analysis of arbitrarily-shaped two-dimensional microwave circuits by the finite-difference time-domain method", *IEEE Trans. Microwave Theory Tech.* 36, 738-744 (1988).
- [39] K.R. Umashankar, S.K. Chaudhuri and A. Taflové, "Finite-difference time-domain formulation of an inverse scattering scheme for remote sensing of inhomogeneous lossy layered media", *IEEE Trans. Antennas Propagat.*, submitted.
- [40] M.A. Strickel, A. Taflové and K.R. Umashankar, "Accurate reconstruction of two-dimensional conducting and homogeneous dielectric target shapes from a single-point TM scattered field pulse response", *IEEE Trans. Antennas Propagat.*, submitted.
- [41] M.A. Strickel and A. Taflové, "Reconstruction of one- and two-dimensional inhomogeneous dielectric targets using the FD-TD/feedback method", *IEEE Trans. Antennas Propagat.*, submitted.
- [42] C.L. Bennett and G.F. Ross, "Time-domain electromagnetics and its applications", *Proc. IEEE* 66, 299-318 (1978).



# A Numerical Technique for Analyzing Electromagnetic Wave Scattering from Moving Surfaces in One and Two Dimensions

FADY HARFOUSH, STUDENT MEMBER, IEEE, ALLEN TAFLOVE, SENIOR MEMBER, IEEE, AND GREGORY A. KRIEGSMANN

**Abstract**—The electromagnetic wave scattering properties of a moving, perfectly conducting mirror are analyzed using a new numerical technique based on the finite-difference time domain (FD-TD) method. This numerical technique is unique in that it does not require a system transformation where the object is at rest but gives a solution to the problem directly in the laboratory frame. First, two canonical one-dimensional cases are considered, the uniformly moving and the uniformly vibrating mirror. Numerical results for the scattered field spectrum are compared to available analytical results, and an excellent agreement is demonstrated. The ability of the FD-TD model to obtain the physics of the double-Doppler effect (for the uniform translation case), and FM-like reflected spectrum (for the uniform vibration case) is highlighted. Second, the method is extended to two-dimensions where a plane wave at oblique incidence on an infinite vibrating mirror is considered. A good agreement with published results is demonstrated for this case. This new approach based on FD-TD provides a potentially strong tool to numerically model a variety of problems involving moving and vibrating scatterers where alternative analytical or numerical modeling means are not available.

## I. INTRODUCTION

THE ANALYTICAL THEORY of electromagnetic wave scattering by moving bodies has been developed principally for canonical one-, two-, and three-dimensional structures [1], [2], [3]. Canonical problems considered include planar conducting and dielectric interfaces in uniform translation or vibration [4], uniformly moving random rough surfaces [5], uniformly moving or vibrating cylindrical and spherical shapes [6], [7], [8], and simple rotating shapes [9]. Motivation for pursuing such analyses has been provided in part by research in the generation of millimeter and submillimeter waves using the interaction of microwaves with relativistically moving ionization (plasma) fronts or electron beam fronts [10], [11].

Existing analytical theory in this area models the physics of a reflecting surface in uniform translation or vibration by employing system transformations where the surface is at rest.

Manuscript received November 3, 1986; revised May 5, 1988. This work was supported in part by National Science Foundation Grant ECS-8515777. F. Harfoush is with Fermilab National Accelerator Laboratory, Batavia, IL 60501.

A. Taflové is with the Department of Electrical Engineering and Computer Science, Technological Institute, Northwestern University, Evanston, IL 60201.

G. A. Kriegsmann is with the Department of Engineering Sciences and Applied Mathematics, Technological Institute, Northwestern University, Evanston, IL 60201.

EE Log Number 8824118.

Difficulties arise when attempting such analyses for general two- or three-dimensional scatterers, since closed-form solutions cannot be obtained when the scatterer shape, composition, translation, and surface vibration are arbitrary. Yet, such general problems arise as more detailed information is required concerning microwave interactions with moving or oscillating charged particle beams of finite cross section.

This paper introduces a purely numerical approach for modeling scattering by relativistically moving perfectly conducting bodies based upon the finite-difference time-domain (FD-TD) method [12]–[24]. This approach uses no system transformation and gives the solution directly in the laboratory frame. It exploits the detailed time-domain modeling characteristics of FD-TD, and has the potential to permit computation of accurate solutions for moving/vibrating rigid body problems of substantially more complexity than existing analytical approaches. The work presented here includes derivation of the necessary modifications of FD-TD for the relativistic body case, and validations for uniform translation and vibration in one and two dimensions against existing analytical theory. The ability of the FD-TD model to obtain the physics of the double-Doppler effect (for uniform translation), and FM-like reflected spectrum (for vibration), will be highlighted. A subsequent paper will address the extension of the new approach to treat convex, conducting, two-dimensional bodies subject to uniform relativistic translation and/or vibration.

The present paper is organized as follows. Section II briefly summarizes the background of the basic FD-TD method, and then describes the basis and FD-TD numerical implementation of the required relativistic electromagnetic field boundary conditions. Section III discusses validation studies for the uniformly moving mirror in one dimension. Section IV discusses validation studies for the uniformly vibrating mirror also in one dimension. Section V presents a two-dimensional case study of the oblique incidence with comparative results. Last, Section VI provides the summary and conclusions.

## II. DESCRIPTION OF THE NUMERICAL METHOD

### A. Background of the Basic FD-TD Method

In the mid-1960's, Yee introduced a computationally efficient means of directly solving Maxwell's time-dependent

curl equations using finite differences [12], now designated as the finite-difference time domain method. With this approach, the continuous electromagnetic field in a finite volume of space is sampled at discrete points in a space lattice and at discrete points in time. Wave propagation, scattering, and penetration phenomena are modeled in a self-consistent manner by marching in time, that is, repeatedly implementing the finite-difference analog of the curl equations at each lattice point. This results in a simulation of the continuous actual waves and sampled-data numerical analogs propagating in a data space stored in a computer. Space and time sampling increments are selected to avoid aliasing of the continuous field distribution, and to guarantee stability of the time-marching algorithm [13]. Time marching is completed when the desired steady-state field behavior is observed.

The basic FD-TD method permits the modeling of electromagnetic wave interactions with a level of detail comparable to that of the widely used method of moments [25]. Further, its explicit nature leads to overall computer storage and running time requirements that are linearly proportional to  $N$ , the number of field unknowns in the finite volume of space being modeled. These two attributes permit FD-TD to provide detailed numerical models of wave interactions with structures having volumetric complexity, such as biological tissues [14] and loaded cavities [15], [16].

For the present work, it has been necessary to modify the basic FD-TD formulation to model moving, perfectly conducting, scatterers. The most simple, "brute-force" approach would be to simply let the scatterer occupy slightly different positions in the space lattice at each time step. This corresponds to the quasi-steady-state method [4], which has been adopted in certain analytical solution approaches. Although this method gives an approximate answer when applied to FD-TD, as will be seen in Section III, it does not completely provide the proper physics. An appropriate relativistic electromagnetic field boundary condition, discussed next, must also be incorporated into the FD-TD code at the surface of the scatterer. Fortunately, this condition is easy to derive in a form suitable for FD-TD implementation.

### B. The Relativistic Boundary Conditions in the FD-TD Code

There are a number of ways to solve for the scattered field from a moving object. In general, the desired analytical solution for the scattered field can be obtained by a Lorentz transformation of the incident field to the moving system, and solution for the scattered field in the frame of reference of the moving system [26]. In this reference frame, the scatterer surface is stationary and the electromagnetic boundary conditions are well defined. The inverse Lorentz transformation then provides the final answer in the laboratory frame. However, a direct solution that is more straightforward (and shorter in some cases) is possible in the laboratory frame without a Lorentz transformation if one uses what is defined as the "relativistic boundary conditions" at a moving interface between medium 1 and medium 2. The derivation of these conditions, in its general form, is well presented in [3] and yields

$$\hat{u}_n \times (\vec{E}_2 - \vec{E}_1) - (\hat{u}_n \cdot \vec{v})(\vec{B}_2 - \vec{B}_1) = 0 \quad (1a)$$

$$\hat{u}_n \cdot (\vec{D}_2 - \vec{D}_1) = \rho_s \quad (1b)$$

$$\hat{u}_n \times (\vec{H}_2 - \vec{H}_1) + (\hat{u}_n \cdot \vec{v})(\vec{D}_2 - \vec{D}_1) = \vec{J}_s \quad (1c)$$

$$\hat{u}_n \cdot (\vec{B}_2 - \vec{B}_1) = 0 \quad (1d)$$

where  $\vec{E}_i$ ,  $\vec{D}_i$ ,  $\vec{H}_i$ , and  $\vec{B}_i$  are, respectively, the electric field, electric flux density, magnetic field, and magnetic flux density in medium 1 and 2;  $\rho_s$  and  $\vec{J}_s$  denote the surface-charge and current densities;  $\vec{v}$  is the velocity of the moving interface (assumed to be uniform), and  $\hat{u}_n$  is the unit vector normal to the interface.

It is important to note from (1) that a scatterer motion transverse to the surface plane (perpendicular to the surface normal) results in boundary conditions similar to that of a fixed object, simply because the term  $\hat{u}_n \cdot \vec{v}$  is now equal to 0. It should further be noted that (1) implies that the tangential  $E$ -field at the surface of a perfectly conducting moving boundary can be finite. However, this does not result in an infinite surface current density because the usual expression,  $\vec{J} = \sigma \vec{E}$ , for current density in a material of conductivity  $\sigma$  is no longer valid. Instead, for a uniformly moving object, the total induced current is the result of a conduction current plus an extra term. Defining  $\beta$  as the ratio  $v/c$ ,  $c$  being the velocity of light in free space, the total current is given by

$$\vec{J} = \sigma(\vec{E} + \vec{v} \times \vec{B}) \frac{1}{\sqrt{1 - \beta^2}} \quad (2)$$

where, for a perfect conductor,  $\vec{E} + \vec{v} \times \vec{B} = 0$  from (1); and therefore the surface current density  $\vec{J}_s$  remains finite. In many references, only small velocities are considered and the term  $\beta^2$  is neglected compared to 1.

In the derivation of the above equations, no assumption is made on the speed  $v$  relative to the speed of light  $c$ , hence the name relativistic boundary conditions. The only assumption made is that the speed  $v$  is uniform. However, the same relativistic boundary conditions derived for uniform  $v$  have been widely applied to study accelerating bodies, under certain conditions where the acceleration is sufficiently low [4], [27]. Here, a new reference frame called the "co-moving frame" or "instantaneous frame" is introduced. The difference is that now the velocity  $v$  in (1) represents the instantaneous velocity instead of the uniform velocity. The term "Doppler approximation" [2] is also used to denote analyses wherein it is assumed that the instantaneous velocity equals a uniform velocity. It is not within the scope of this paper to discuss the details of this theory. Its validity in rotating coordinates has been investigated by Shiozawa [27]. The reader can also refer to the presentation given in [4] and [9].

For a perfectly conducting moving surface, the boundary condition (1a) relates linearly the local values of the instantaneous total tangential  $E$ - and  $H$ -fields at the surface of the conductor (lit side). This relation, similar in form to that of a surface impedance, presents a problem for implementing in the FD-TD code which computes  $E$  and  $H$  values separated by half-step intervals in time and space. It is necessary to derive an equivalent form of the relativistic boundary condition for perfectly conducting surfaces that is not contradictory with this half-step nonlocalization of field values in the FD-

TD code. Derivation of such an equivalent form is given in the Appendix.

Using the results of the Appendix, the relativistic boundary condition for a moving mirror (in a form appropriate for FD-TD implementations) is given by

$$E = 2 \frac{-\hat{u}_n \cdot \vec{v}}{c - \hat{u}_n \cdot \vec{v}} E' \quad (3)$$

or

$$B = \frac{2c}{c - \hat{u}_n \cdot \vec{v}} \cdot B' \quad (4)$$

where  $E$  and  $E'$  are, respectively, the total tangential electric field and the incident tangential electric field values at the mirror surface.  $B$  and  $B'$  are, respectively, the total tangential magnetic field and the incident tangential magnetic field values at the mirror surface.

Now, the value of the total tangential electric field at the mirror surface is given in terms of the incident electric field value at the boundary. The latter is easily obtained from a parallel one-dimensional grid already built into the FD-TD code as a look up table. Implementation of the boundary condition for a moving mirror now becomes a simple matter. At each half-time step when the  $E$ -field and the  $H$ -field are computed, respectively, the position of the reflecting mirror in the grid is first determined. Then, the relativistic boundary conditions (3) or (4) for the field values at the surface of the mirror are implemented.

### C. Approximation of $E$ and $H$ Adjacent to a Moving Surface

The question arises as to the value of the incident electric field when the position of the mirror does not coincide with a point in the grid. For this purpose, linear interpolation is used. From the geometry of Fig. 1,

$$E' \text{ at mirror} = \frac{(\delta_y - \Delta) \cdot E'(j+1) + \Delta \cdot E'(j)}{\delta_y} \quad (5)$$

The value of the total electric field at the mirror surface is stored at the total electric field grid point closest to the surface. No extra grid points are introduced. In Fig. 1 for example, the value of the total electric field at the boundary is stored at the  $E(j+1)$  point if  $\Delta < \delta_y - \Delta$  and at the  $E(j)$  point if  $\Delta > \delta_y - \Delta$ .

Next, a Faraday's law contour integral is used to compute the total  $H$ -field adjacent to the mirror surface. (The idea of contour integral subcell models has been previously used in the FD-TD analysis of wave penetration through narrow slots in thick conducting screens [22] and coupling to wires and wire bundles [23].) Applying Faraday's law, given by

$$\oint \vec{E} \cdot d\vec{l} = - \frac{\partial \int \vec{B} \cdot d\vec{S}}{\partial t} \quad (6)$$

along the path defined in Fig. 1, and assuming that the  $H$ -field is almost uniform in the shaded region, we obtain

$$(E(j+1) - E(j)) \cdot \delta_z = -\mu \frac{\partial B}{\partial t} \delta_z \cdot (\delta_y - \Delta) \quad (7)$$

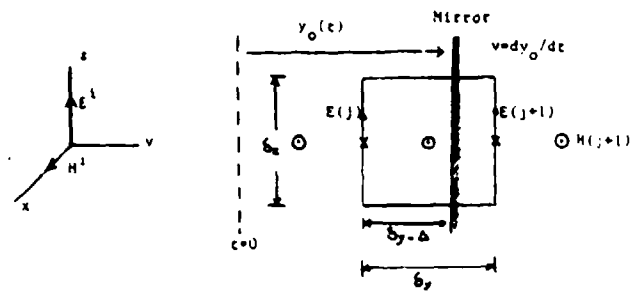


Fig. 1. FD-TD field component geometry for the moving mirror case in a one-dimensional FD-TD grid.

By applying Ampere's law, a similar contour integral can be derived to compute the total  $E$ -field adjacent to the mirror surface [22].

## III. THE CASE OF A UNIFORMLY MOVING MIRROR, NORMAL ILLUMINATION

### A. Existing Analytical Formulation

An incident sinusoidal plane wave of frequency  $\omega_i$  (illumination frequency) and unit amplitude is normally incident on a uniformly moving mirror. Referring to Fig. 1, a positive mirror velocity  $v$  means that the mirror is receding from the incident wave, and a negative mirror velocity means that the mirror is advancing toward the incident wave. The scattered electric field is given by [2]

$$E'_z(y, t) = - \left[ \frac{1 - \frac{v}{c}}{1 + \frac{v}{c}} \right] \exp j \left[ \left( \frac{1 - \frac{v}{c}}{1 + \frac{v}{c}} \right) (\omega_i t - ky) + 2jk \left( \frac{r_0 - vt_0}{1 - \frac{v}{c}} \right) \right] \quad (8)$$

where  $y_0 = v(t - t_0) + r_0$  is the position of the mirror boundary with respect to a reference point, and  $r_0$  and  $t_0$  are some initial values. (For simplicity, we set both  $r_0$  and  $t_0$  equal to 0.) A "double-Doppler" effect is apparent from (8) in that both the frequency and amplitude of the scattered field are transformed by the same multiplying factor defined as  $\alpha = [1 - (v/c)]/[1 + (v/c)]$ .

### B. FD-TD Modifications Considered

Three different FD-TD algorithm modifications for the electromagnetic boundary condition at a moving surface, discussed in Section II-B, have been considered in numerical tests of whether FD-TD can properly model the double-Doppler effect.

- 1) *The Quasi-Stationary Method*—Here, the mirror is assumed stationary for a complete one-time-step interval. The relativistic boundary conditions are not implemented. Only the position of the mirror is determined after each full time step. A contour integral model is used when necessary to compute more exactly the  $H$ - and/or  $E$ -field next to the mirror surface. Such a method

TABLE I  
DOUBLE-DOPPLER SHIFTS AS OBTAINED BY FD-TD AND  
ANALYTICALLY, FOR THREE DIFFERENT MODELS  
AND A GIVEN VELOCITY

Case	v/c	Reflected Amplitude		Reflected Frequency	
		Analytical	FD-TD	Analytical	FD-TD
Reference	0	1	1	1	1
Quasistatic	-1/3	1	0.9783	2	2
		0 at $\omega \neq 2$	0.0427 at $\omega = 9^*$		
Semi relativistic	-1/3	2	1.994	2	2
		0 at $\omega \neq 2$	0.1308 at $\omega = 9^*$		
Full relativistic	-1/3	2	1.994	2	2
		0 at $\omega \neq 2$	0.0523 at $\omega = 9^*$		

\* Spurious frequency components

will give the proper shift in frequency but leaves the amplitude unchanged as the theory predicts [2].

- 2) *The Semirelativistic Method*—Here, the relativistic boundary condition is implemented each time for the  $E$ -field only. In other words, only (3) is used. The value of the total  $E$ -field at the mirror surface is stored at the closest, total  $E$ -field, grid point to the mirror surface. No extra grid point is introduced. A contour integral model is used to compute the  $H$ -field next to the mirror surface. This method should be enough to model the proper physics of the problem. However, usage of a contour integral model makes the program more difficult to generalize for arbitrary mirror velocities.
- 3) *The Fully-Relativistic Method*—Here, the relativistic boundary condition is implemented each half-time step for both the  $E$ -field and the  $H$ -field using (3) and (4) respectively. This case does not require a contour integral model since now the  $H$ -field, next to the mirror, is computed from (4). This method was found to be more accurate and more general than the previous method.

In all the above three cases, the fields behind the mirror are set to zero.

#### C. Comparative FD-TD and Analytical Results

Let us consider the case of a mirror illuminated at normal incidence by a unit-amplitude sinusoidal plane wave having a normalized frequency,  $\omega_i = 1$ . The mirror is assumed to be advancing toward the incident wave at one-third the speed of light ( $v = -c/3$ ). Table I shows double-Doppler shifts as obtained analytically and by FD-TD for the three relativistic moving surface models. The spatial frequency spectrum of the reflected wave is obtained by taking the Fourier transform of the FD-TD computed field versus position sample after 20 cycles had been stepped. The spatial frequency is scaled such that a value,  $\omega = 10$ , corresponds to the FD-TD grid Nyquist frequency (the maximum spatial frequency that the FD-TD grid can support as a sampled-data system).

It is seen that the quasi-stationary boundary conditions cause the FD-TD code to generate a reflected-wave spatial frequency component with the proper upward Doppler frequency shift (to  $\omega = 2$ ) leaving the amplitude almost unchanged as predicted by the analytical theory of [2]. The semirelativistic

boundary condition provides the proper Doppler shifts in both the frequency and magnitude (again of a shift of 2:1) with a small spurious frequency component. The fully relativistic boundary condition, causes a further damping of the undesired frequency component. For both the semi-relativistic and fully-relativistic cases, the error in the computed amplitude of the properly shifted spectral component at  $\omega = 2$  is only 0.3 percent (0.026 dB). The FD-TD computed spurious frequency component near  $\omega = 9$  is limited to 6.54 percent (-23.7 dB) in the semirelativistic case and to 2.62 percent (-31.6 dB) in the fully relativistic case.

Table II shows double-Doppler results obtained for eight different mirror velocities using only the fully relativistic boundary condition. In all of these cases, FD-TD generates a reflected wave with the proper Doppler shifts in both frequency and amplitude. The error in the FD-TD computed amplitude of the properly shifted spectral component is limited to less than 1.5 percent (0.131 dB), and the generation of spurious frequency components is limited to less than 5 percent (-26 dB). These spurious components are numerical artifacts due to the interpolation process used in computing the incident field at the mirror surface (Section II-C), and the storing of the surface field values at the closest grid point (Section II-B). As observed in Table II, these artifacts disappear when the mirror velocity equals  $c/2$  where, at every time step, the mirror position corresponds exactly to a grid field point.

#### IV. THE UNIFORMLY VIBRATING MIRROR

##### A. Existing Analytical Formulation

Referring to Fig. 1, the exact form of the scattered field from a linearly vibrating mirror is given by a set of two equations [28], [29]:

$$t = t_0 + \frac{d}{c} \sin(\omega_i t_0) - \frac{y}{c} \quad (9a)$$

$$E_z^s(y,t) = -\frac{1 - \beta \cos(\omega_i t_0)}{1 + \beta \cos(\omega_i t_0)} \cos(\omega_i t_0 - kd \sin(\omega_i t_0)) \quad (9b)$$

where  $\omega_i$  is the frequency of the incident wave;  $y_0 =$

TABLE II  
DOUBLE-DOPPLER SHIFTS AS OBTAINED BY FD-TD AND  
ANALYTICALLY, FOR UNIFORM VELOCITIES

v/c	Reflected Amplitude		Reflected Frequency	
	Analytical	FD-TD	Analytical	FD-TD
1/3	2.000 0 at $\omega \neq 2$	1.9940 0.0523 at $\omega = 9^\circ$	2.000	2.000
1/5	1.5000 0 at $\omega \neq 1.5000$	1.4909 0.0660 at $\omega = 7^\circ$ 0.0751 at $\omega = 9^\circ$	1.5000	1.5000
1/7	1.3333 0 at $\omega \neq 1.3333$	1.3239 0.0613 at $\omega = 4^\circ$ 0.0465 at $\omega = 5^\circ$	1.3333	1.3333
1/2	0.3333 0 at $\omega \neq 0.3333$	0.3284 0 at $\omega \neq 0.3333$	0.3333	0.3333
1/3	0.5000 0 at $\omega \neq 0.5000$	0.4939 0.0410 at $\omega = 4^\circ$	0.5000	0.5000
1/4	0.6000 0 at $\omega \neq 0.6000$	0.5590 0.0081 at $\omega = 4^\circ$ 0.0021 at $\omega = 3^\circ$	0.6000	0.6000
1/5	0.6666 0 at $\omega \neq 0.6000$	0.6587 0.0560 at $\omega = 5^\circ$ 0.0164 at $\omega = 6^\circ$	0.5000	0.6000
1/7	0.7500 0 at $\omega \neq 0.7500$	0.7416 0.0514 at $\omega = 2^\circ$ 0.0153 at $\omega = 4^\circ$	0.7500	0.7500

\* Spurious frequency components

$d \sin(\omega_v t)$  describes the displacement of the mirror vibrating with a frequency,  $\omega_v$  and  $\beta = \omega_v d/c = v_{\max}/c$ . Equation (9b) can also be written in a Fourier series expansion,

$$E'_z(y, t) = -Re \sum_{m=-\infty}^{\infty} J_{-m}(\alpha_m) \cdot \left( 1 + \frac{m}{m + 2 \frac{\omega_i}{\omega_v}} \right) e^{j(\omega_i + m\omega_v)t + (y/c)} \quad (10a)$$

where

$$\alpha_m = m\beta + 2kd = \beta \left( m + 2 \frac{\omega_i}{\omega_v} \right). \quad (10b)$$

The scattered field spectrum thus contains the incident frequency  $\omega_i$  and an infinity of sidebands located at  $\omega_i + m\omega_v$  generated by the vibration of the mirror.

The scattered field spectrum for the vibrating mirror is very similar to the spectrum of an FM tone-modulated signal. In both cases, an infinity of sidebands located at  $\omega_{\text{cent}} + m\omega_\Delta$  is generated, where  $\omega_{\text{cent}}$  is a center frequency (the illuminating frequency for the vibrating mirror case, the carrier frequency for the FM case); and  $\omega_\Delta$  is the sideband separation (the vibration frequency for the mirror case, the modulating tone frequency for the FM case). Further, in both cases, the spectral amplitude of the  $m$ th sideband is proportional to  $J_m$ ; a Bessel function of order  $m$ . For the vibrating mirror, the argument of the Bessel function depends on the amplitude and frequency of vibration; for FM, the argument depends upon the amplitude and frequency of the modulating tone.

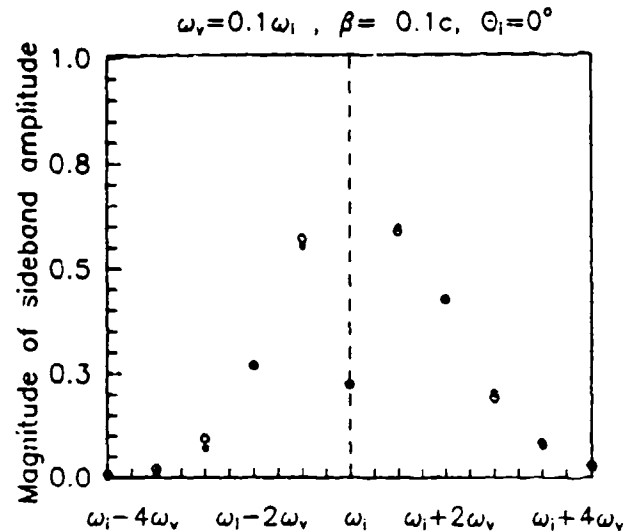


Fig. 2. Comparison of FD-TD and analytical results for the sidebands of the reflected spectrum. •: exact values; ○: FD-TD values.

### B. FD-TD Modeling Procedure

In modeling the vibration of the mirror with the FD-TD code, we follow the same procedure as for the uniformly moving mirror, but use only the fully relativistic boundary condition, and assume that we are in a region where the theory of the "co-moving frame" is still applicable [4]. Our interest will be mainly in the variation of the scattered field amplitude at the fundamental frequency  $\omega_i$ , as a function of mirror vibration frequency  $\omega_v$ , and amplitude  $d$ . It is clear from (10) that at the fundamental frequency, where  $m = 0$ , the exact solution for the magnitude of the scattered field leads to a  $J_0(2kd)$  dependence, where  $2kd = 2\beta(\omega_i/\omega_v)$ .

### C. Comparative FD-TD and Analytical Results

Fig. 2 shows the magnitudes of the sideband components of the reflected field spectrum for a vibrating mirror having a vibration frequency  $\omega_v$ , equal to 0.1 times the illumination frequency  $\omega_i$ ; and a maximum mirror surface velocity equal to 0.1 times the speed of light. The plotted values are computed using both the exact solution of (10) and the FD-TD method with fully relativistic boundary conditions and a spatial resolution of 20 cells per wavelength of the illuminating wave. An excellent correspondence is noted between the exact and FD-TD numerical data. The error in computing the magnitude of the reflected component at the illuminating frequency is only 0.27 percent (0.02 dB).

As mentioned earlier, an important test for the FD-TD approach is to compare the variation of the scattered field amplitude at the illuminating frequency with the exact solution as mirror vibration parameters are changed. Noting that the exact solution states that the argument of the Bessel function weight for this spectral component is dependent upon the product of maximum normalized mirror velocity,  $\beta$ , and  $\omega_i/\omega_v$ , the FD-TD modeling procedure should trace out the same Bessel function variation of the scattered field amplitude at the illuminating frequency regardless of whether  $\beta$  is

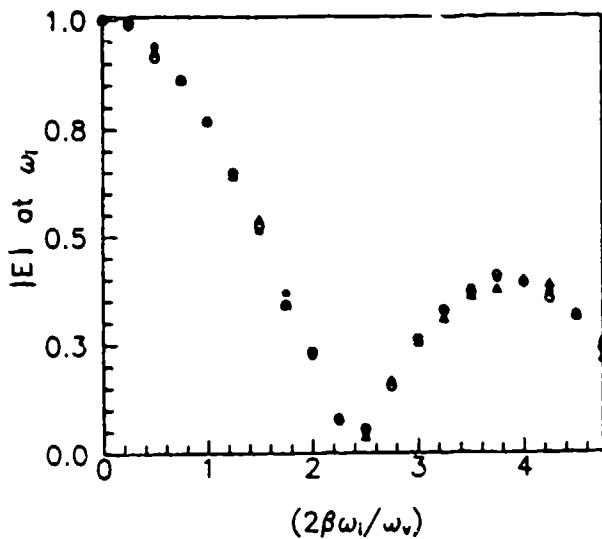


Fig. 3. Comparison of FD-TD and analytical results for the scattered field magnitude at the illumination frequency. •: exact values; ○: FD-TD values for  $\omega_i = 5\omega_v$ ; △: FD-TD values for  $\beta = 0.1c$ .

varied while keeping  $\omega_i/\omega_v$  fixed, or whether  $\omega_i/\omega_v$  is varied while keeping  $\beta$  fixed. Fig. 3 graphs the results of numerous trials of the FD-TD procedure wherein these parametric studies (and corresponding Fourier analyses) were conducted with the fully-relativistic boundary conditions incorporated into the FD-TD code. For the first case where  $\beta$  is varied from 0 to 0.5, the ratio of illumination frequency  $\omega_i$  to mirror vibration frequency  $\omega_v$  is fixed at 5; and the product of  $2\beta(\omega_i/\omega_v)$  varies between 0 and 5. For the second case where  $\beta$  is fixed at 0.1,  $\omega_i/\omega_v$  is varied from 0 to 25; and again the product of  $2\beta(\omega_i/\omega_v)$  varies between 0 and 5.

Fig. 3 shows that the FD-TD numerical predictions for the scattered field amplitude at the illuminating frequency are very close to the Bessel function  $J_0$  behavior given by the exact solution as the mirror vibrational parameters vary. The accuracy of the FD-TD predicted scattered field amplitude is essentially the same, regardless of whether  $\beta$  is fixed or  $\omega_i/\omega_v$  is fixed during the parametric study. These results indicate that the FD-TD code, with fully relativistic boundary conditions at the mirror surface, is properly modeling the physics of the vibrating mirror problem, including the interesting scattered field null at the first zero of the Bessel function.

## V. EXTENSION OF METHOD TO TWO-DIMENSIONS

### A. Problem Description: Oblique Incidence on a Vibrating Mirror

In this section we consider the case of oblique plane wave incidence on an infinite vibrating mirror. This case, analyzed by De Zutter [30], is much more complicated than the normal incidence case in that it has no closed-form solution. The solution is written in an infinite-series form using plane-wave expansions, where the unknown coefficients in the series are obtained numerically, as described in [30]. In that paper, the field amplitude versus time is calculated at different points along the symmetry axis of the mirror, and for various angles of incidence.

### B. FD-TD Modeling Procedure

An approach analogous to the one-dimensional case is adopted to implement the relativistic boundary conditions in a two-dimensional FD-TD code. The two-dimensional case approach is again based on the "Doppler approximation" [2], [28], [30], where it is assumed that the mirror moves with a uniform velocity equal to the instantaneous vibrational value. Propagation delays are accounted for by assuming that reflections are generated at the "precursor" position of the mirror. In [28], an analysis of the normal incidence case, the precursor positions coincide for all points of the mirror. In [30], an analysis of the oblique incidence case, this feature is lost, and a similar approximate solution ignores the propagation delays. However, propagation delays are automatically accounted for in the FD-TD code by virtue of its time-domain nature.

From the special theory of relativity, a wave reflected from a uniformly moving mirror has a reflected angle  $\theta_r$ , given as [26]

$$\cos \theta_r = \frac{\cos \theta_i (1 + \beta^2) - 2\beta}{1 - 2\beta \cos \theta_i + \beta^2} \quad (11)$$

A derivation similar to the one-dimensional case leads to the following relativistic boundary conditions suitable for FD-TD implementation:

$$E = \pm \frac{\beta(\cos \theta_r + \cos \theta_i)}{1 \pm \beta \cos \theta_r} \cdot E^i \quad (12)$$

$$H = \frac{(\cos \theta_r + \cos \theta_i)}{\cos \theta_i (1 \pm \beta \cos \theta_r)} \cdot H^i \quad (13)$$

where  $\beta = v/c$  and the fields refer to total tangential field values. The numerical steps involved are now only slightly more complicated because of the angular dependence of the incident field values at the mirror surface. From (11) it is clearly seen that  $\cos \theta_r$  is a function of  $v$ . Therefore, the reflected wave has a spread both in frequency and spatial reflection angle [30].

A validation is sought for the oblique incidence case of the infinite plane mirror modeled by De Zutter. Since it is impossible to exactly model an infinite mirror in a finite two-dimensional grid, we select a long, thin, rectangular, perfectly-conducting slab as the model for the infinite mirror, as shown in Fig. 4. The relativistic boundary conditions (12) and (13) are implemented on the front and back sides of the object. The other two sides, parallel to the velocity vector, are insensitive to the motion of the object, and therefore no relativistic boundary conditions are required there.

The use of a finite-length rectangular slab to model the infinite mirror introduces edge diffraction artifacts. To minimize the edge effect, we select a slab long enough to appear from the observation point as infinite during a well-defined early-time response when the edge effect has not yet reached the observation point. Since the transverse electric (TE) case does not provide substantially different results than the transverse magnetic (TM) case [30], only the TM case is considered. Such a test should provide us with good insight as to the ability of FD-TD to handle moving boundary problems in two dimensions.

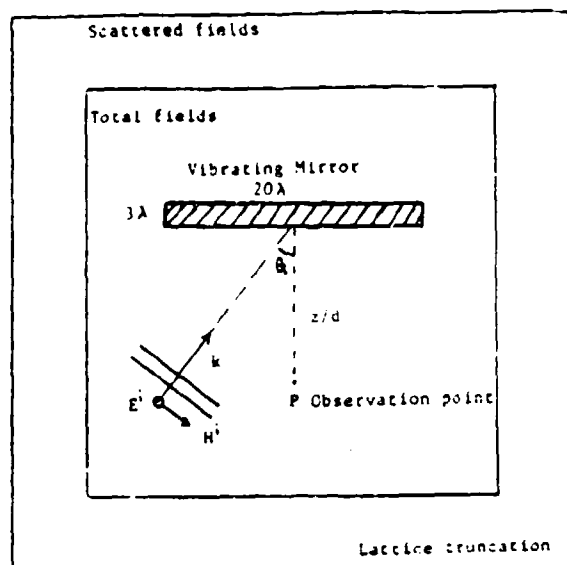


Fig. 4. Modeling of a vibrating mirror in a two-dimensional FD-TD grid

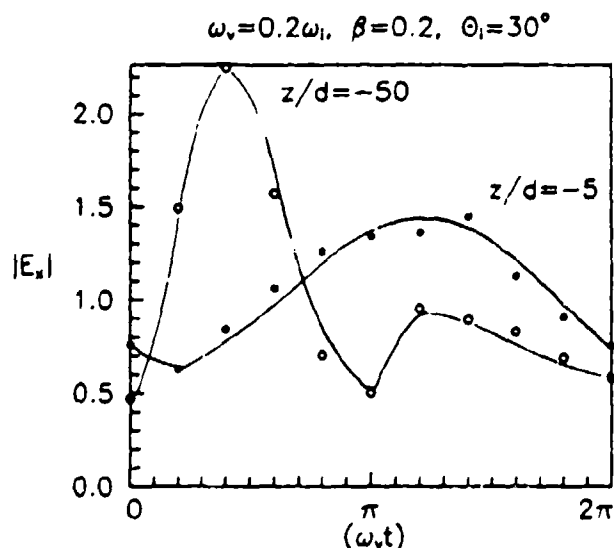


Fig. 5. Comparison of FD-TD and analytical results for the scattered field time envelope at oblique incidence. —: analytical results; o: FD-TD results.

### C. Comparative FD-TD and Analytical Results

Fig. 5 shows good agreement between the FD-TD results and the analytical results obtained from [30] for the envelope of the scattered  $E$  field versus time for  $\theta_i = 30^\circ$ ,  $\beta = 0.2$ ,  $kd = 1$ , and observation points  $z/d = -5$  and  $z/d = -50$ . Similar agreement is shown in Fig. 6 for  $\theta_i = 30^\circ$ ,  $\beta = 0.02$ , and  $kd = 0.1$ . Fig. 7 compares the FD-TD and analytical results for  $\theta_i = 60^\circ$ ,  $\beta = 0.2$ , and  $kd = 1$ . For both  $z/d = -5$  and  $z/d = -50$ , a good correspondence is noted between the analytical and FD-TD numerical data.

In general, the FD-TD method gives good results, and it is fair to claim that this technique, unique in its approach for numerically modeling moving boundaries, is a promising

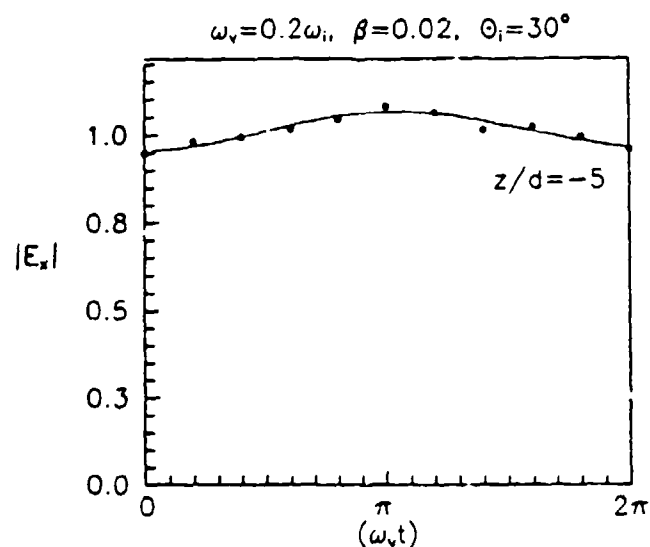


Fig. 6. Comparison of FD-TD and analytical results for the scattered field time envelope at oblique incidence. —: analytical results; o: FD-TD results.

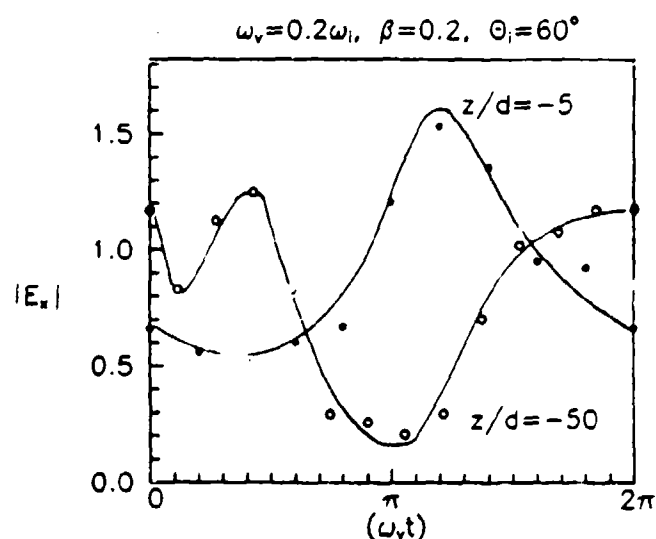


Fig. 7. Comparison of FD-TD and analytical results for the scattered field time envelope at oblique incidence. —: analytical results; o: FD-TD results.

strong tool to analyze more complicated problems involving arbitrary moving shapes.

### VI. SUMMARY AND CONCLUSION

A numerical approach based on the FD-TD technique, using fully relativistic electromagnetic field boundary conditions at the surface of a conductor, has been formulated to model scattering from perfectly conducting moving mirrors in one and two dimensions. The numerical approach is unique in that it requires no system transformation, contrary to other possible numerical methods where the problem is first solved in the moving frame and then transformed back to the rest frame. For nonuniform velocities, the concept of a "Doppler-approximation" was used. Since the stability of the FD-TD

code is assured by the proper selection of the space and time increments, and since no new iterative equation coupled to the original FD-TD equations is introduced, the method remains stable. Two types of one-dimensional relativistic mirror motion have been considered: uniform translation and sinusoidal vibration of the mirror surface. Comparison with the exact, analytical solutions for these types of mirror motion indicates that the new numerical approach accurately computes the magnitude and frequency of spectral components resulting from the scattering process. Physics that appears to be properly modeled includes the double-Doppler effect (uniform translation case) and FM-like spectral sidebands (sinusoidal vibration case). When extended to two dimensions, the code again shows good agreement with the available analytical results for the case of oblique incidence upon an infinite vibrating mirror. Here, the physics involved is much more complicated than in one dimension because both propagating and nonpropagating evanescent modes are generated at the mirror surface.

The FD-TD code that has been constructed can be directly adapted to model other types of moving-boundary problems involving two- and three-dimensional, perfectly conducting bodies of finite size and arbitrary shape. A logical extension of the existing approach involves developing more general, suitable relativistic boundary conditions to model scattering by moving objects having a finite conductivity without using a system to information.

#### APPENDIX

The following is a derivation of an equivalent relativistic boundary condition suitable for modeling moving perfect conductors in the FD-TD grid. The incident wave is assumed to be polarized in the positive  $z$ -direction and propagating in the positive  $y$ -direction with an amplitude of unity. Thus, the incident fields are given by

$$E_z^i = e^{j\omega_c(t-y/c)}$$

and

$$B_x^i = \frac{1}{c} E_z^i.$$

The reflected  $E$ -field will have the form

$$E_z^r = A e^{j\omega_c(t+y/c)}$$

so that the reflected  $B$ -field in free space will then be given by

$$B_x^r = -\frac{1}{c} E_z^r.$$

The total  $B$ -field is therefore

$$B_x = B_x^i + B_x^r = \frac{1}{c} (E_z^i - E_z^r)$$

but, since

$$E_z^t = E_z^i - E_z^r$$

therefore

$$B_x = \frac{1}{c} (2E_z^i - E_z^t).$$

For a mirror receding from the incident wave, the relativistic

boundary condition is given by

$$E_z^t - v \cdot B_x^t = 0.$$

Substituting for  $B_x^t$  in the above equation we get

$$E_z^t - \frac{v}{c} (2E_z^i - E_z^t) = 0.$$

Therefore, the final form for  $E_z^t$  is

$$E_z^t = 2 \frac{v}{c+v} E_z^i. \quad (14)$$

Similarly, for the total  $B$ -field at the boundary we have

$$B_x^t = \frac{1}{c} (2E_z^i - E_z^t).$$

Substituting for  $E_z^t$  in the above equation with  $E_z^t = cB_x^t$ , we get finally for the  $B$ -field

$$B_x^t = \frac{2c}{c+v} B_x^i. \quad (15)$$

Equations (14) and (15) are the ones used in our code to implement the proper relativistic boundary conditions at the surface of the mirror.

#### REFERENCES

- [1] B. L. Michelsen, G. C. Herman, A. T. de Hoop, and D. De Zutter, "Three-dimensional relativistic scattering of electromagnetic waves by an object in uniform translation motion," *J. Math. Phys.*, vol. 22, no. 11, pp. 2716-2722, Nov. 1981.
- [2] J. Cooper, "Scattering of electromagnetic fields by a moving boundary: the one-dimensional case," *IEEE Trans. Antennas Propagat.*, vol. AP-28, no. 6, pp. 791-795, Nov. 1980.
- [3] R. C. Costen and D. Adamson, "Three dimensional derivation of the electrodynamic jump conditions and momentum-energy laws at a moving boundary," *Proc. IEEE*, vol. 52, no. 9, Sept. 1965.
- [4] J. Van Bladel, *Relativity and Engineering*. New York: Springer-Verlag, 1984.
- [5] A. A. Tzikas, D. P. Christoulidis, and E. E. Kriezis, "Relativistic bistatic scattering by a uniformly moving random rough surface," *IEEE Trans. Antennas Propagat.*, vol. AP-34, no. 8, pp. 1046-1052, Aug. 1986.
- [6] S. W. Lee and R. Mittra, "Scattering of electromagnetic waves by a moving cylinder in free-space," *Can. J. Phys.*, vol. 45, no. 9, pp. 2999-3007, 1967.
- [7] V. Twersky, "Relativistic scattering of electromagnetic waves by moving obstacles," *J. Math. Phys.*, vol. 12, pp. 2326-2341, 1971.
- [8] D. Gensor, "Scattering by time varying obstacles," *J. Sound Vibration*, vol. 25, no. 1, pp. 101-110, 1977.
- [9] J. Van Bladel, "Electromagnetic fields in the presence of rotating bodies," *Proc. IEEE*, vol. 64, no. 3, pp. 301-317, Mar. 1976.
- [10] P. Sprangle, V. L. Granatstein, and L. Baker, "Stimulated collective scattering from a magnetized relativistic electron beam," *Physical Rev. A*, vol. 12, no. 4, pp. 1697-1701, Oct. 1975.
- [11] M. Lampe, E. Ott, W. M. Manheimer and S. Kainer, "Submillimeter wave production by upshifted reflection from a moving ionization front," *IEEE Trans. Microwave Theory Tech.*, vol. MTT-25, no. 6, June 1977.
- [12] K. S. Yee, "Numerical solution of initial boundary value problems involving Maxwell's equations in isotropic media," *IEEE Trans. Antennas Propagat.*, vol. AP-14, pp. 302-307, May 1966.
- [13] A. Taflov and M. E. Brodwin, "Numerical solution of steady-state electromagnetic scattering problems using the time-dependent Maxwell's equations," *IEEE Trans. Microwave Theory Tech.*, vol. MTT-23, pp. 623-630, Aug. 1975.
- [14] —, "Computation of the electromagnetic fields and induced temperatures within a model of the microwave-irradiated human eye," *IEEE Trans. Microwave Theory Tech.*, vol. MTT-23, pp. 888-896, Nov. 1975.
- [15] A. Taflov, "Application of the finite-difference time-domain method to sinusoidal steady-state electromagnetic penetration problems,"



- IEEE Trans. Electromagn. Compat.*, vol. EMC-22, pp. 191-202, Aug. 1980.
- [16] A. Taflové and K. R. Umashankar, "A hybrid moment/finite-difference time-domain approach to electromagnetic coupling and aperture penetration into complex geometries," *IEEE Trans. Antennas Propagat.*, vol. AP-30, pp. 617-627, July 1982.
  - [17] B. Engquist and A. Madja, "Radiation boundary conditions for acoustic and elastic wave calculations," *Comm. Pure Appl. Math.*, vol. 32, pp. 313-357, 1979.
  - [18] J. G. Blaschak and G. A. Kriegsmann, "A comparative study of absorbing boundary conditions," *J. Comput. Phys.*, vol. 77, pp. 109-139, July 1988.
  - [19] K. R. Umashankar and A. Taflové, "A novel method to analyze electromagnetic scattering of complex objectives," *IEEE Trans. Electromagn. Compat.*, vol. EMC-24, pp. 397-405, Nov. 1982.
  - [20] A. Taflové and K. R. Umashankar, "Radar cross section of general three-dimensional scatterers," *IEEE Trans. Electromagn. Compat.*, vol. EMC-25, pp. 433-440, Nov. 1983.
  - [21] A. Taflové, K. R. Umashankar, and T. G. Jurgens, "Validation of FD-TD modeling of the radar cross section of three-dimensional structures spanning up to 9 wavelengths," *IEEE Trans. Antennas Propagat.*, vol. AP-33, pp. 662-666, June 1985.
  - [22] A. Taflové, K. R. Umashankar, B. Beker, F. Harfoush, and K. S. Yee, "Detailed FD-TD analysis of electromagnetic field penetrating narrow slots and lapped joints in thick conducting screens," *IEEE Trans. Antennas Propagat.*, vol. 36, pp. 247-257, Feb. 1988.
  - [23] K. R. Umashankar, A. Taflové, and B. Beker, "Calculation and experimental validation of induced currents on coupled wires in arbitrary shaped cavity," *IEEE Trans. Antennas Propagat.*, vol. AP-35, pp. 1248-1257, Nov. 1987.
  - [24] A. Taflové and K. R. Umashankar, "The finite-difference time-domain (FD-TD) method for electromagnetic wave scattering and interaction problems," *J. Electromagn. Waves App.*, vol. 1, no. 3, pp. 243-267, 1987.
  - [25] R. F. Harrington, *Field Computation by Moment Methods*. New York: Macmillan, 1968.
  - [26] W. Pauli, *Theory of Relativity*. Elmsford, NY: Pergamon 1958.
  - [27] T. Shiozawa, "Phenomenological and electron-theoretical study of the electrodynamics of rotating systems," *Proc. IEEE*, vol. 61, pp. 1694-1702, 1973.
  - [28] J. Van Bladel and D. De Zutter, "Reflections from linearly vibrating objects: plane mirror at normal incidence," *IEEE Trans. Antennas Propagat.*, vol. AP-29, no. 4, pp. 629-636, July 1981.
  - [29] R. E. Kleinman, "Scattering by linearly vibrating objects," *IEEE Trans. Antennas Propagat.*, vol. AP-27, no. 3, pp. 344-352, May 1979.
  - [30] D. De Zutter, "Reflections from linearly vibrating objects: plane mirror at oblique incidence," *IEEE Trans. Antennas Propagat.*, vol. AP-30, no. 5, pp. 898-903, Sept. 1982.
- Fady Harfoush (S'86), for a photograph and biography please see page 257 of the February 1988 issue of this TRANSACTIONS.
- Allen Taflové (M'75-SM'84), for a photograph and biography please see page 1812 of the December 1988 issue of this TRANSACTIONS.
- Gregory A. Kriegsmann, for a photograph and biography please see page 161 of the February 1987 issue of this TRANSACTIONS.

## A STUDY OF WAVE INTERACTIONS WITH FLANGED WAVEGUIDES AND CAVITIES USING THE ON-SURFACE RADIATION CONDITION METHOD

Jeffrey BLASCHAK

*Department of Electrical Engineering, The Technological Institute, Northwestern University, Evanston, IL 60208, U.S.A.*

Gregory A. KRIEGSMANN

*Department of Engineering Sciences and Applied Mathematics, The Technological Institute, Northwestern University, Evanston, IL 60208, U.S.A.*

Allen TAFLOVE

*Department of Electrical Engineering, The Technological Institute, Northwestern University, Evanston, IL 60208, U.S.A.*

Received 29 January 1988

The scattering of a plane wave from the open end of a flanged, parallel plate waveguide is approximately solved using the On-Surface Radiation Condition method. Simple explicit formulae are given for the field within the waveguide and for the bistatic cross-section. In addition, our theory also gives an approximate solution to the associated open cavity problem, which is formed when the waveguide is terminated by a short circuit positioned a finite distance from the aperture. These problems serve as prototypes for receiving antennae and open resonators respectively. Numerical results are presented which confirm the accuracy of the OSRC method. An interesting byproduct of our analysis is the approximate prediction of the complex eigenfrequencies of the open resonator.

### 1. Introduction

In this paper, we study the interaction of waves with an infinitely flanged, parallel-plate waveguide which is either infinite in extent or short-circuited at a finite distance along its length. (See Fig. 1.) The former case serves as a prototype for both receiving antennae and simple re-entrant structures while the second models a basic Helmholtz resonator. We restrict our attention here to scalar waves so that the results obtained are applicable to acoustics and electromagnetics in two dimensions.

The method we develop is approximate and is based upon the On-Surface Radiation Condition method (OSRC) which has been recently developed to analytically model the scattering of waves by convex targets [1, 2, 3]. In this method a differential operator (radiation boundary operator) which annihilates the scattered field as

$r \rightarrow \infty$  is applied directly on the surface of a target. Then, both the field and its normal derivative can be deduced from this approximate condition and the given boundary condition for the scatterer.

In this paper, we apply an annihilating operator to the scattered field in the aperture of a parallel-plate waveguide and again obtain a relationship between the field and its normal derivative. Combining this result with the continuity of the total field and its normal derivative in the aperture, we effectively decouple the waveguide region from the half-space  $z < 0$ . This allows us to explicitly determine the field within the waveguide without recourse to matrix inversion [4], ray tracing [5, 6], or hybrid method [7]. From this result, we also obtain (with the aid of a Green's function representation) the scattered field in the region  $z < 0$ .

The results of our approximate OSRC theory for penetrating and scattered fields compare extremely well with detailed numerical computa-

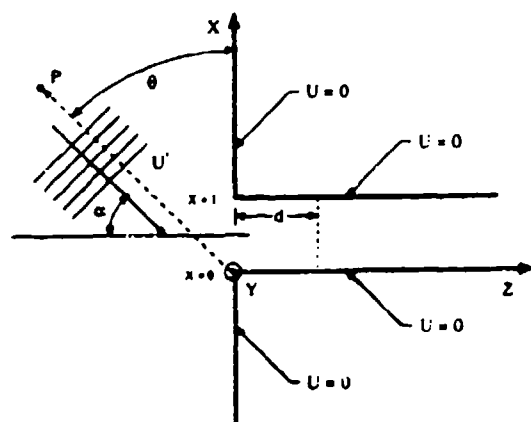


Fig. 1. Plane wave at angle  $\alpha$  illuminates the open end of a flanged, infinite, parallel plate waveguide. The cavity problem is created by placing a short at the position  $z = d$ .

tions obtained using a time-dependent finite difference scheme (FD-TD) [8, 9] applied directly to the field equations. Excellent agreement is found for both the infinite waveguide case and the short-circuited waveguide. In the former case a key OSRC result shows that the scattered field exhibits "resonant" frequency behavior. This is again verified by the FD-TD scheme. Moreover, we are able to use our approximate results to obtain an estimate of the open resonator's "eigenfrequencies". These are complex numbers whose imaginary parts dictate the rate at which energy leaks away from the open cavity.

The remainder of this paper will now be outlined. Section 2 contains the formulation of the scattering problem and Section 3 includes the extension of the OSRC method that is required to handle the present problem. Section 4 contains the results of several illustrative examples which clearly indicate the accuracy of our approximate method. And finally, Section 5 includes a derivation of the approximate "eigenfrequencies" of our prototype Helmholtz resonator.

## 2. Formulation

The geometry of the flanged parallel-plate waveguide is shown in Fig. 1. Here  $x$  and  $z$  rep-

resent nondimensional variables which have been scaled with respect to the guide's physical width  $a$ . The total field,  $U(x, z, k)$  satisfies the Helmholtz equation

$$\Delta U + k^2 U = 0; \quad z < 0 \text{ with } |x| < \infty, \quad (2.1a)$$

$$\text{and } z > 0 \text{ with } 0 < x < 1,$$

where  $k = \omega a/c$  and  $c$  is the wave's speed, and the boundary condition

$$U = 0, \quad (x, z) \in R \quad (2.1b)$$

where  $R$  represents the boundary composed of the flange and the waveguide's walls. A time dependence of  $\exp(i\omega t)$  has been assumed and will be suppressed in the subsequent equations.

An incident plane wave given by

$$U_{inc}(x, z, k) = \exp[-ik(z \cos \alpha - x \sin \alpha)] \quad (2.2)$$

impinges upon this target and scatters from it. Accordingly, the total field  $U^-$  in the region  $z < 0$  is given by

$$U^- = U_{inc}(x, z, k) + U_{sc}(x, z, k); \quad z < 0, \quad (2.3)$$

where the second term in (2.3) is the wave reflected by the flange and  $u$  is the scattered field caused by the waveguide. The latter satisfies the Helmholtz equation (2.1a) for  $z < 0$  and the Sommerfeld radiation condition

$$\lim_{r \rightarrow \infty} \sqrt{r} \left[ \frac{\partial}{\partial r} + iku \right] = 0 \quad (2.4)$$

where  $r = [x^2 + z^2]^{1/2}$ .

When the wall at  $z = d$  (the short circuit) is not present, the total field in the waveguide,  $U^+$ , is given by

$$U^+ = \sum T_n \exp(-ik_n z) \times \sin(n\pi x); \quad z > 0. \quad (2.5a)$$

When the wall at  $z = d$  is present, the total field in the waveguide is given by

$$U^+ = \sum T_n \{ \exp(-ik_n z) - \gamma_n \exp(ik_n z) \} \times \sin(n\pi x); \quad 0 < z < d. \quad (2.5b)$$

The sum  
integers  
reflection

$k_n$

$\gamma_n$

The tra-  
mined.

To co-  
value pr-  
contin-  
 $0 < x <$

$U^-$

$\frac{\partial}{\partial r}$

Finally,  
ments,  
terms of

$u(x, z, k)$

where  $k$   
Hankel

$R =$

Here we  
We co-  
problem  
In the el-  
tude of  
along t  
would  
case,  $L$   
and the  
cally

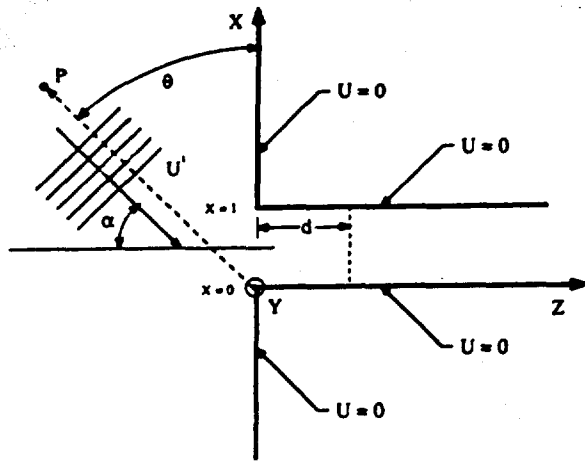


Fig. 1. Plane wave at angle  $\alpha$  illuminates the open end of a flanged, infinite, parallel plate waveguide. The cavity problem is created by placing a short at the position  $z = d$ .

tions obtained using a time-dependent finite difference scheme (FD-TD) [8, 9] applied directly to the field equations. Excellent agreement is found for both the infinite waveguide case and the short-circuited waveguide. In the former case a key OSRC result shows that the scattered field exhibits "resonant" frequency behavior. This is again verified by the FD-TD scheme. Moreover, we are able to use our approximate results to obtain an estimate of the open resonator's "eigenfrequencies". These are complex numbers whose imaginary parts dictate the rate at which energy leaks away from the open cavity.

The remainder of this paper will now be outlined. Section 2 contains the formulation of the scattering problem, and Section 3 includes the extension of the OSRC method that is required to handle the present problem. Section 4 contains the results of several illustrative examples which clearly indicate the accuracy of our approximate method. And finally, Section 5 includes a derivation of the approximate "eigenfrequencies" of our prototype Helmholtz resonator.

## 2. Formulation

The geometry of the flanged parallel-plate waveguide is shown in Fig. 1. Here  $x$  and  $z$  rep-

resent nondimensional variables which have been scaled with respect to the guide's physical width  $a$ . The total field,  $U(x, z, k)$  satisfies the Helmholtz equation

$$\Delta U + k^2 U = 0; \quad z < 0 \text{ with } |x| < \infty, \quad (2.1a)$$

$$\text{and } z > 0 \text{ with } 0 < x < 1,$$

where  $k = \omega a/c$  and  $c$  is the wave's speed, and the boundary condition

$$U = 0, \quad (x, z) \in R \quad (2.1b)$$

where  $R$  represents the boundary composed of the flange and the waveguide's walls. A time dependence of  $\exp(i\omega t)$  has been assumed and will be suppressed in the subsequent equations.

An incident plane wave given by

$$U_{inc}(x, z, k) = \exp[-ik(z \cos \alpha - x \sin \alpha)] \quad (2.2)$$

impinges upon this target and scatters from it. Accordingly, the total field  $U^-$  in the region  $z < 0$  is given by

$$U^- = U_{inc}(x, z, k) - U_{inc}(x, -z, k) + u(x, z, k); \quad z < 0, \quad (2.3)$$

where the second term in (2.3) is the wave reflected by the flange and  $u$  is the scattered field caused by the waveguide. The latter satisfies the Helmholtz equation (2.1a) for  $z < 0$  and the Sommerfeld radiation condition

$$\lim_{r \rightarrow \infty} \sqrt{-\left[\frac{\partial}{\partial r} + ikz\right]} = 0 \quad (2.4)$$

where  $r = [x^2 + z^2]^{1/2}$ .

When the wall at  $z = d$  (the short circuit) is not present, the total field in the waveguide,  $U^+$ , is given by

$$U^+ = \sum T_n \exp(-ik_n z) \times \sin(n\pi x); \quad z > 0. \quad (2.5a)$$

When the wall at  $z = d$  is present, the total field in the waveguide is given by

$$U^+ = \sum T_n \{\exp(-ik_n z) - \gamma_n \exp(ik_n z)\} \times \sin(n\pi x); \quad 0 < z < d. \quad (2.5b)$$

The summation in (2.5) runs over all positive integers  $n$ . The propagation constants  $k_n$  and the reflection coefficients  $\gamma_n$  are defined respectively by

$$k_n = [k^2 - (n\pi)^2]^{1/2}, \quad (2.6a)$$

$$\gamma_n = \exp(-2ik_n d). \quad (2.6b)$$

The transmission coefficients  $T_n$  are to be determined.

To complete the formulation of our boundary value problem, we demand that  $U$  and  $\partial/\partial z U$  be continuous along the waveguide aperture  $z = 0$  and  $0 < x < 1$ , that is,

$$U^-(x, 0, k) = U^+(x, 0, k), \quad 0 < x < 1, \quad (2.7a)$$

$$\frac{\partial}{\partial z} U^-(x, 0, k) = \frac{\partial}{\partial z} U^+(x, 0, k), \quad 0 < x < 1. \quad (2.7b)$$

Finally, using standard Green's function arguments, we find that the scattered field is given in terms of  $U(x, 0, k)$  by

$$u(x, z, k) = \int_0^1 U(x', 0, k) \dot{H}_0^{(1)}(kR) \frac{dx'}{R} \quad (2.8a)$$

where  $\dot{H}_0^{(1)}$  is the derivative of the zeroeth order Hankel function and  $R$  is defined by

$$R = [(x - x')^2 + z^2]^{1/2}. \quad (2.8b)$$

Here we note that  $U(x, 0, k) = u(x, 0, k)$  by (2.3).

We can physically interpret the above scattering problem in terms of electromagnetics or acoustics. In the electromagnetic case,  $U$  would be the amplitude of the electric field vector which is polarized along the  $y$ -axis, and the waveguide and flange would be perfectly conducting. In the acoustics case,  $U$  would be proportional to the pressure, and the waveguide and flange would be acoustically "soft".

### 3. Extension of the OSRC method

The scattered field  $u$  satisfies the radiation boundary condition [10, 11]

$$\frac{\partial}{\partial r} u + \left[ \frac{2}{r} + ik \right] u - \frac{Lu}{2r^2(ik + 1/r)} = O(r^{-5}) \quad (3.1a)$$

as  $r \rightarrow \infty$  where  $L$  is defined by

$$Lu = \left[ \frac{\partial^2}{\partial \theta^2} u + \frac{u}{4} \right]. \quad (3.1b)$$

In our previous work [1] we applied (3.1) directly on the surface of a two-dimensional convex target by setting the  $O(r^{-5})$  term equal to zero and replacing  $r^{-1}$  by  $\kappa$ ,  $r^{-2}\partial^2 u/\partial \theta^2$  by  $\partial^2 u/\partial s^2$ , and  $\partial u/\partial r$  by  $\partial u/\partial \nu$ . Here,  $\kappa$  is the curvature of the target's boundary curve,  $s$  is the arclength, and  $\partial/\partial \nu$  is the outgoing normal derivative.

We now apply the same operator to the scattered field  $u$  in the aperture of the flanged waveguide. We set  $\kappa$  equal to zero because the aperture is planar, replace  $s$  by  $x$  in the second tangential derivative, and  $\nu$  by  $-z$  in the normal derivative. This yields the approximate condition

$$Bu = \frac{\partial}{\partial z} u - iku - \frac{i}{2k} \frac{\partial^2}{\partial x^2} u = 0, \quad 0 < x < 1, z = 0. \quad (3.2)$$

We note here that the operator  $B$  can also be obtained by an approximate factoring of the Helmholtz equation in rectangular coordinates [12].

Next, we deduce from (2.7) and the definition of the operator  $B$  that

$$BU^+ = BU^-, \quad 0 < x < 1, z = 0. \quad (3.3)$$

Inserting (2.3) into the right-hand side of (3.3) and using (3.2), we find that

$$BU^+ = g(x), \quad 0 < x < 1, z = 0 \quad (3.4a)$$

where the function  $g(x)$  is defined by

$$g(x) = -2ik \cos \alpha \exp(ikx \sin \alpha), \quad 0 < x < 1. \quad (3.4b)$$

Applying the operator  $B$  to  $U^*$  given by (2.5) and combining this result with (3.4), we obtain

$$\sum G_n T_n \sin(n\pi x) = g(x), \quad 0 < x < 1, \quad (3.5a)$$

$$\sum J_n T_n \sin(n\pi x) = g(x), \quad 0 < x < 1, \quad (3.5b)$$

where the sums are again over integer  $n$  and

$$G_n = -i \left[ k_n + k - \frac{1}{2k} (n\pi)^2 \right], \quad (3.6a)$$

$$J_n = -i \left[ k_n(1 + \gamma_n) + k(1 - \gamma_n) - \frac{1}{2k} (1 - \gamma_n)(n\pi)^2 \right]. \quad (3.6b)$$

Finally, we use the Fourier inversion formula to solve (3.5) for the unknown coefficients  $T_n$ . We find that

$$T_n = 4ik \cos \alpha g_n(k \sin \alpha) / G_n \quad (3.7a)$$

for the flanged waveguide and

$$T_n = 4ik \cos \alpha g_n(k \sin \alpha) / J_n \quad (3.7b)$$

for the short-circuited waveguide (open resonator), where  $g_n(\zeta)$  is

$$g_n(\zeta) = - \begin{cases} \frac{n\pi}{(n\pi)^2 - \zeta^2} [1 - (-1)^n \exp(i\zeta)], & \zeta \neq n\pi, \\ \frac{i}{2}, & \zeta = n\pi. \end{cases} \quad (3.8)$$

The approximate field within the waveguide is obtained by combining (2.5a), (3.6a), (3.7a), and (3.8). The analogous expression for the field within the open resonator is given by (2.5b), (3.6b), (3.7b), and (3.8).

The scattered field is given by (2.7) with  $U(x, 0, k)$  replaced by either (2.5a) or (2.5b). By using standard far-field approximations in (2.8) we find that, as  $r \rightarrow \infty$ ,

$$u(x, z, k) \sim A(\theta, k) \frac{e^{-ikr}}{\sqrt{r}}, \quad (3.9a)$$

$$A(\theta, k) = k \sin \theta (2\pi k)^{-1/2} \times \exp(-i\pi/4) \sum T_n g_n(\cos \theta) \quad (3.9b)$$

where  $g_n(\zeta)$  is defined in (3.8) and  $\theta$  is measured

from the  $x$ -axis in a counter-clockwise direction (see Fig. 1).

#### 4. Illustrative examples

The accuracy of (2.5) and our approximations (3.7) is now demonstrated in two illustrative problems. In the first example, a flanged infinite waveguide is illuminated by a plane wave having  $k \approx 8$  and impinging at an incident angle  $\alpha$  as shown in Fig. 1. Two values of  $\alpha$  are chosen:  $\alpha = 0^\circ$  (normal incidence) and  $\alpha = 30^\circ$ . The second example is the associated cavity problem created by terminating the waveguide with a short circuit at a distance  $d$  from the aperture. For both examples, we compute the field distribution at  $z = \frac{2}{3}$  using (2.5) and the bistatic cross-section of the scattered field, in the region  $z < 0$ , using (3.9).

The accuracy of the OSRC method is assessed by comparing its results to those obtained using a finite difference scheme applied directly to the time-dependent field equations. The accuracy of finite difference time domain (FD-TD) methods on the problems we consider here is well established [8, 9]. In the first case, the infinite waveguide is modeled using FD-TD by a sufficiently long, finite waveguide which is terminated by a short. In the FD-TD simulation, this structure is illuminated by a sinusoidal incident plane wave and time-stepped for a sufficient number of wave cycles to allow the numerical solution within two wavelengths of the aperture to reach the time-harmonic steady-state. The waveguide length and number of time steps is carefully chosen to guarantee that reflections from the terminated end are not present in the aperture region of interest. For the second example, the depth of the cavity  $d$  is selected to be the same as the aperture width. The FD-TD cavity simulation is performed on a domain considerably smaller than that for the infinite waveguide. Here, however, more wave cycles are required to be time-stepped for the simulation to achieve the time-harmonic steady-state

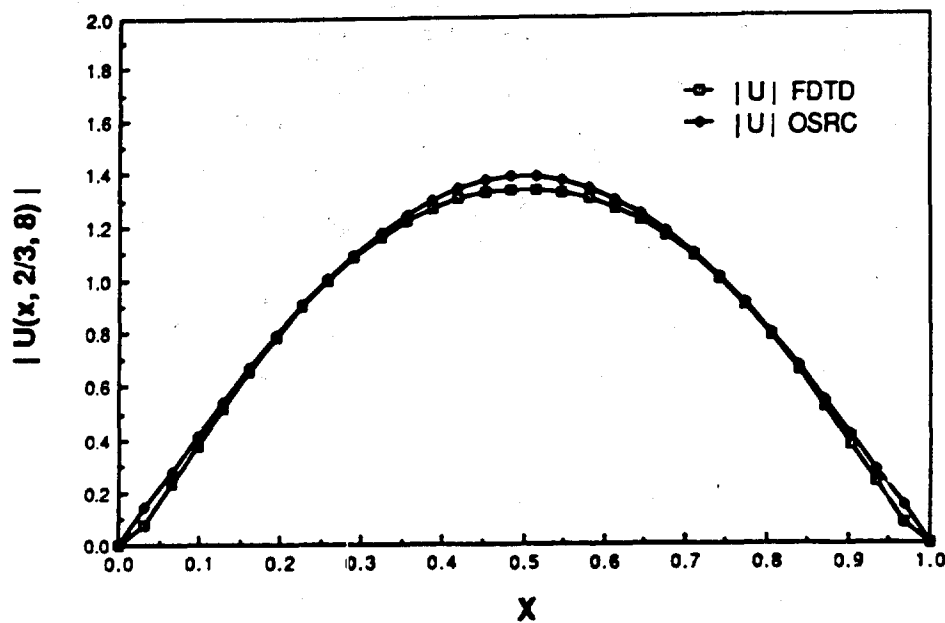


Fig. 2. Distribution of field magnitude inside infinite waveguide at  $z = \frac{2}{3}$  for  $\alpha = 0^\circ$ .

due to the structure's ability to trap energy for a period of time.

With  $k \approx 8$ , the dimensions of the infinite waveguide are such that only the first two modes propagate. The results of our OSRC and FD-TD calculations for the infinite waveguide example are

presented in Figs. 2 through 7. Figs. 2 and 3 show respectively the magnitude and phase of  $U^*(x, 0.666, 8)$  for  $\alpha = 0^\circ$ . For this case, only the first term in the sum (2.5) need be evaluated because  $T_2 = 0$ , by symmetry. The corresponding results for  $\alpha = 30^\circ$  are presented in Figs. 4 and 5

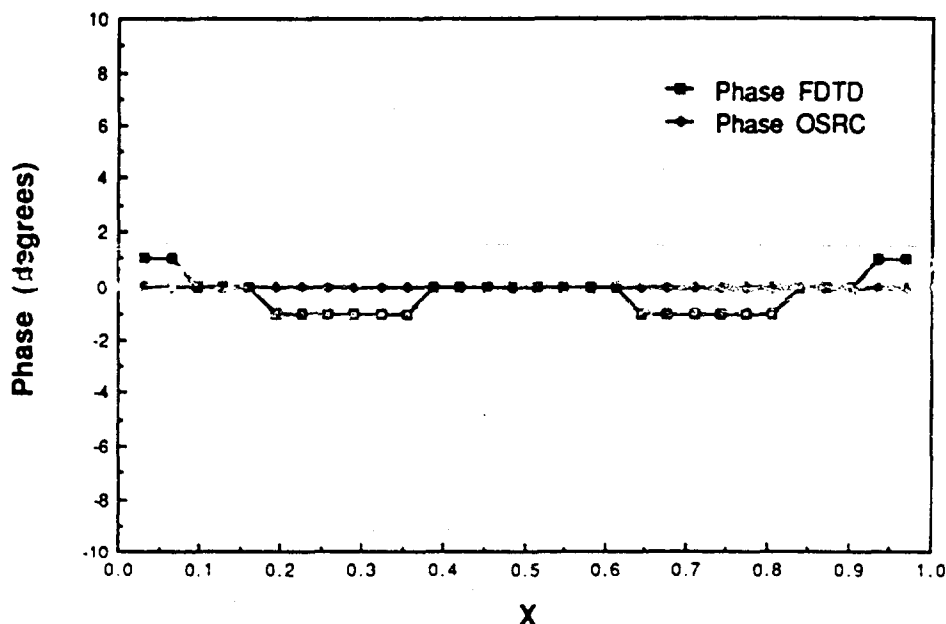
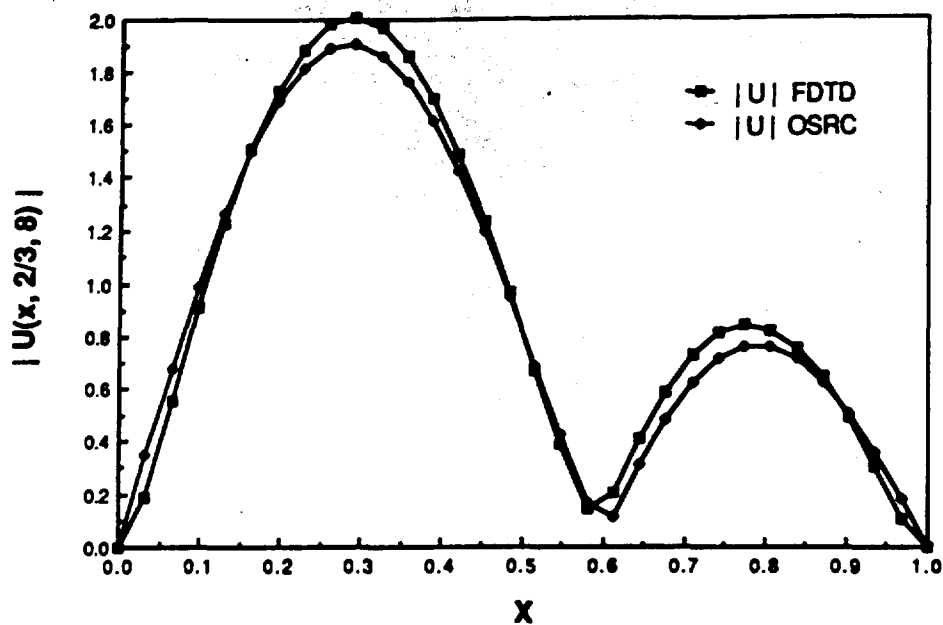


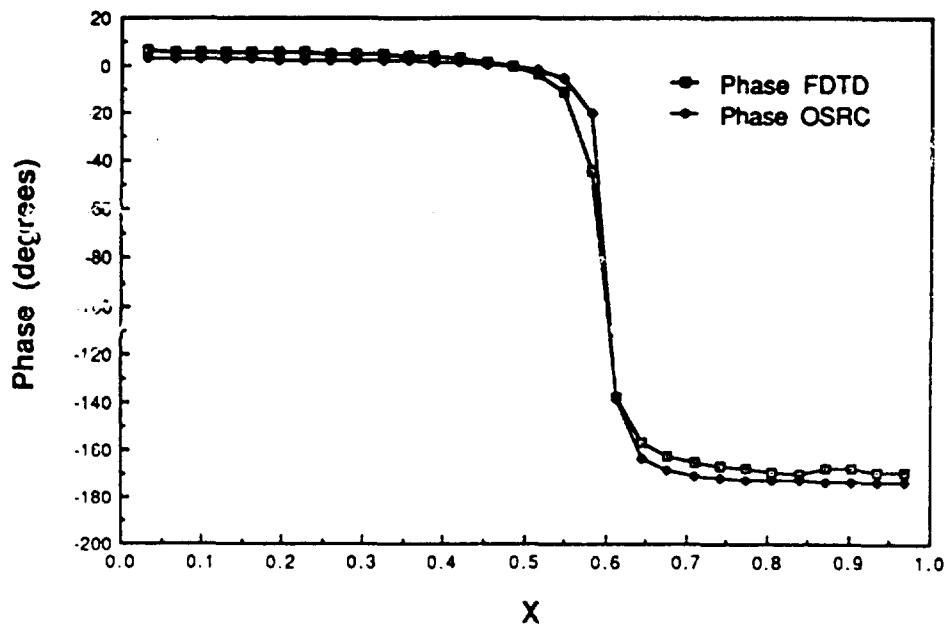
Fig. 3. Distribution of field phase inside infinite waveguide at  $z = \frac{2}{3}$  for  $\alpha = 0^\circ$ .

Fig. 4. Same as Fig. 2 except  $\alpha = 30^\circ$ .

respectively. Both propagating modes are excited for this case and thus, only the first two terms in (2.5) are needed for our approximate solution. These excellent results indicate that the on-surface radiation condition operator effectively couples the energy of the incident plane wave into the

propagating waveguide modes. We have also included several evanescent modes in (2.5) and found little change in the far field and a deleterious change in the aperture field.

The bistatic cross section of the scattered field in the region,  $z < 0$ , is shown in Figs. 6 and 7 for

Fig. 5. Same as Fig. 3 except  $\alpha = 30^\circ$ .



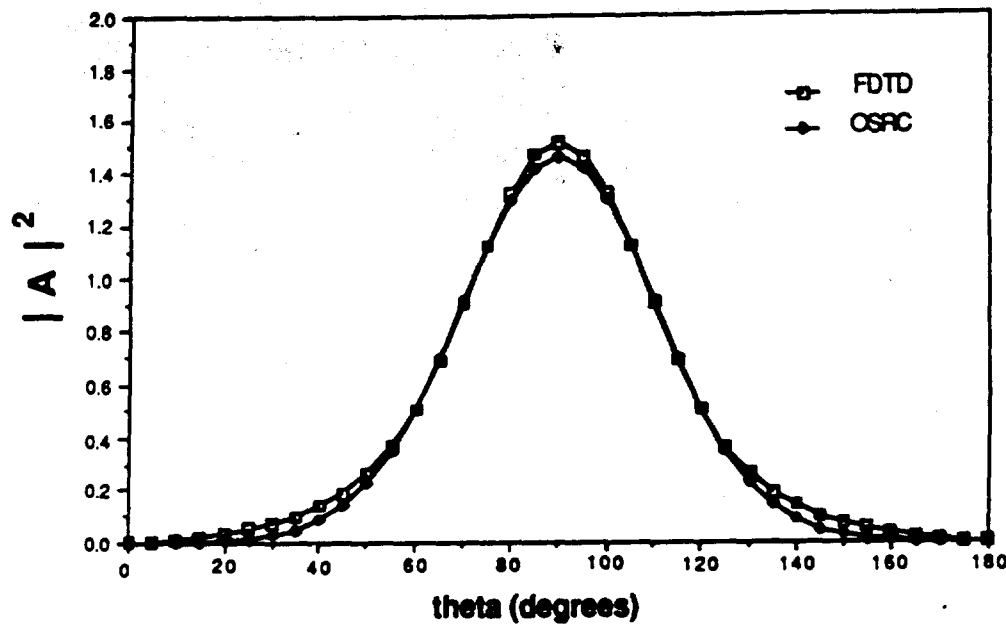


Fig. 6. Bistatic cross-section for the field scattered from the aperture of the infinite waveguide in the region  $z < 0$  for  $\alpha = 0^\circ$ . The angle  $\theta$  is as shown in Fig. 1.

each value of  $\alpha$ . Again, excellent agreement is observed between the results obtained using the on-surface radiation condition approach and those obtained by the FD-TD simulation. It should be noted that the amount of computer time required to evaluate the formulae generated by the OSRC

theory is negligible (less than 0.006%) compared to that of a typical FD-TD simulation for the idealized problems considered here.

The results of the companion calculations for the open resonator example are presented in Figs. 8 through 13. These results are for  $k \approx 8$  and

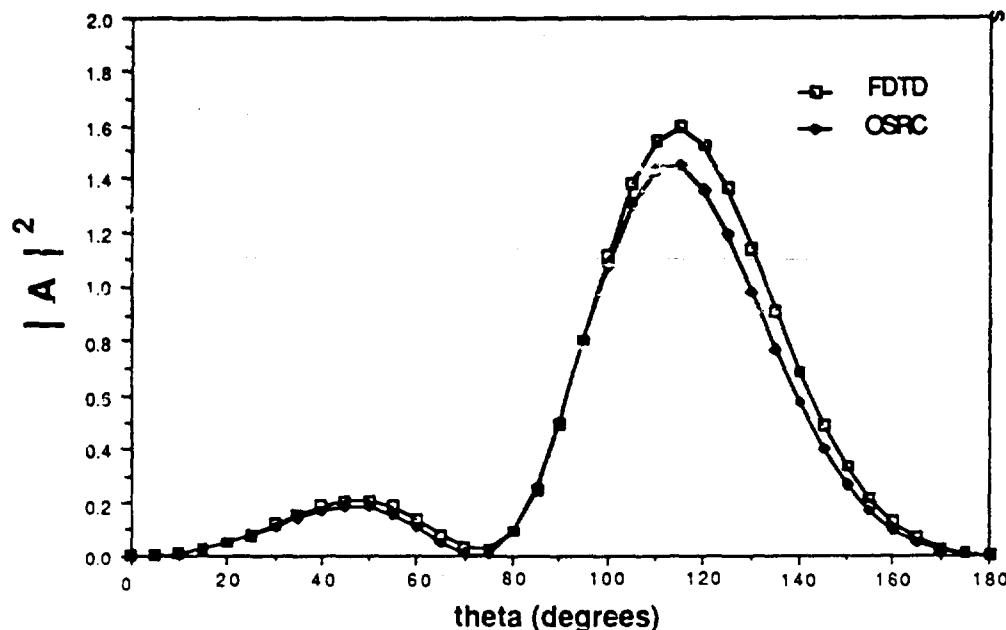


Fig. 7. Same as Fig. 6 except  $\alpha = 30^\circ$ .

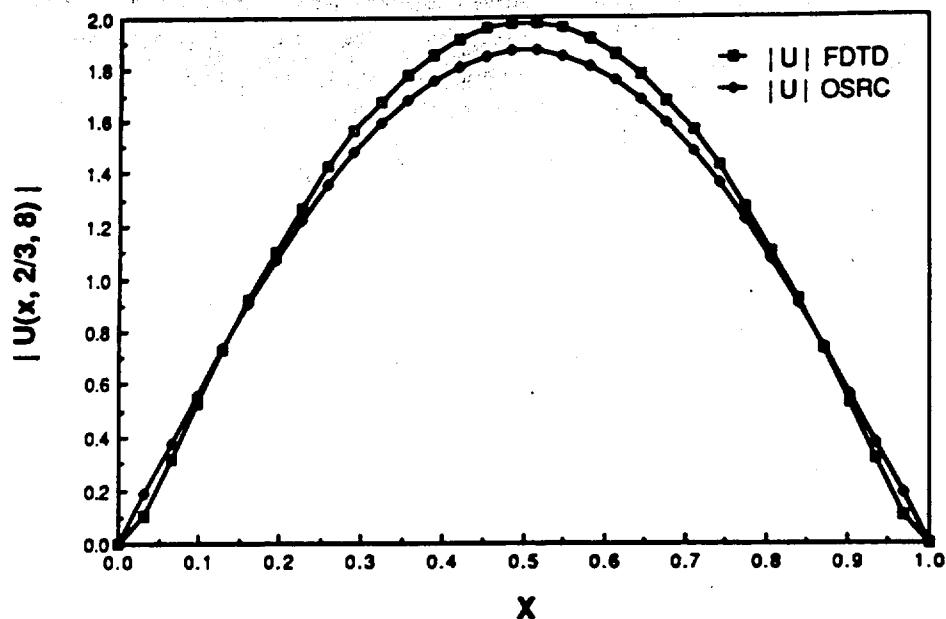


Fig. 8. Distribution of field magnitude inside the cavity at  $z = \frac{2}{3}$  for  $\alpha = 0^\circ$ .

$a = d = 1$ . Once again, good agreement between the OSRC results and the FD-TD simulations is observed.

Figure 14 shows the OSRC and FD-TD computed values for  $U^*(0.5, 0.0, k)$  as a function of  $k$ . The FD-TD result is obtained by simulating an

impulsive plane wave followed by an FFT. The agreement is good for  $3.5 < k < 8$  and deteriorates outside this band, which approximates the range of frequency components in the impulsive plane wave. The error at very low frequencies is caused by the OSRC method, which is consistent with our

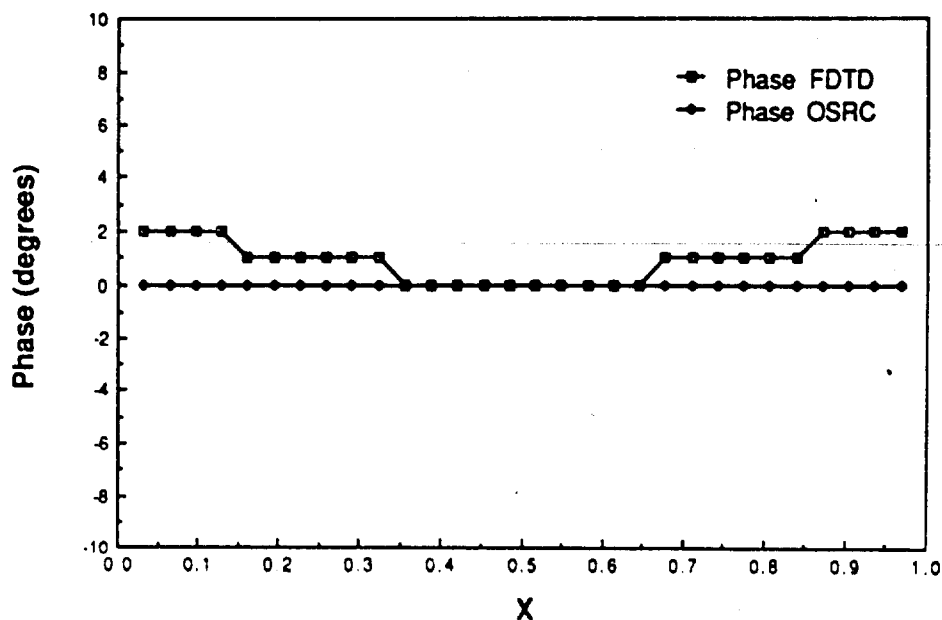
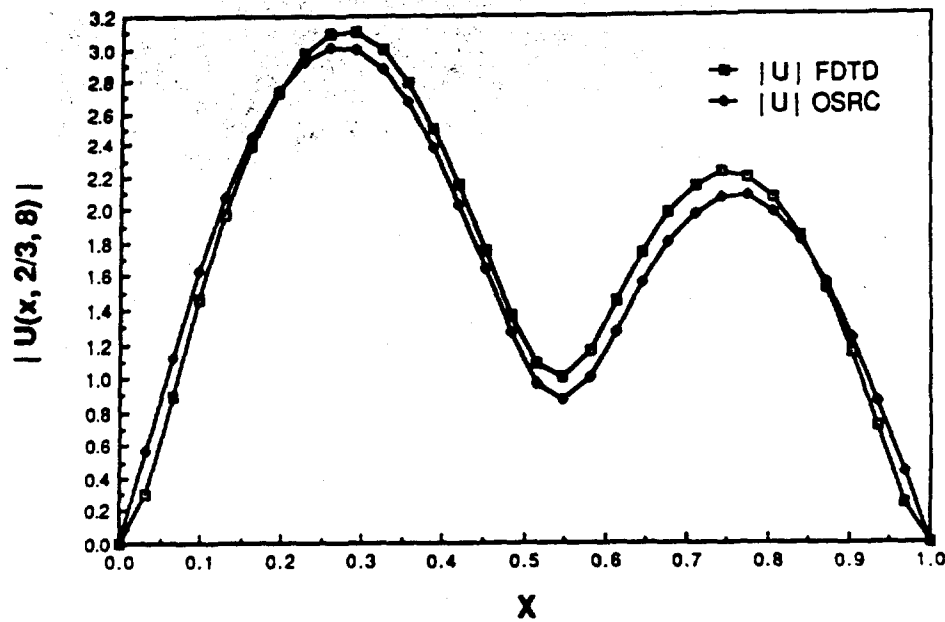


Fig. 9. Distribution of field phase inside the cavity at  $z = \frac{2}{3}$  for  $\alpha = 0^\circ$ .

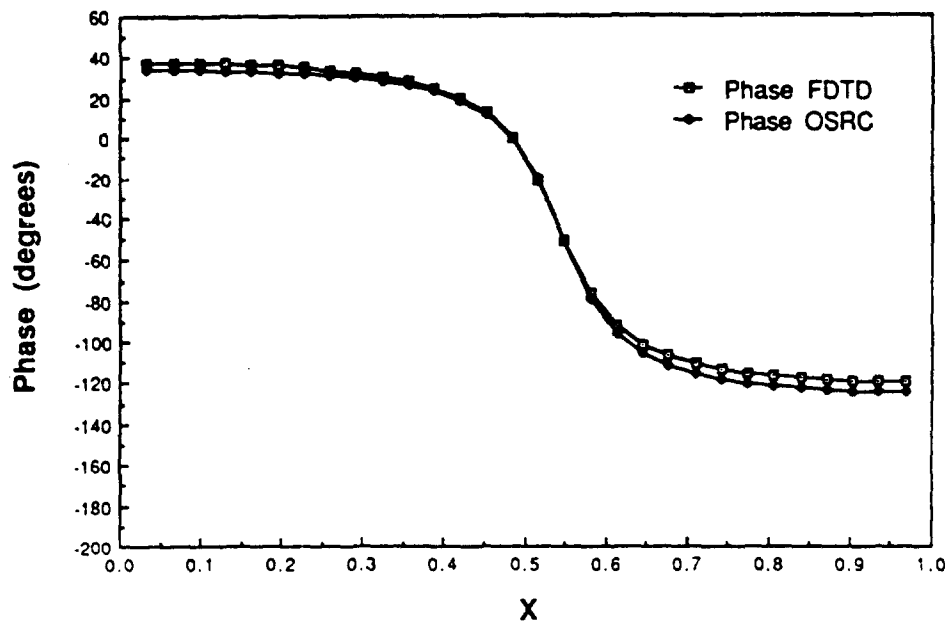
Fig. 10. Same as Fig. 8 except  $\alpha = 30^\circ$ .

previous observations [1], and the onset of cut-off which occurs at  $k = \pi$ . Additional errors can occur with the OSRC solution at other cut-off frequencies  $k = n\pi$  (if those modes are excited) because the energy is not out-going in the aperture. In the present case, the odd modes are excited while the

even ones are not. The peaks (except for the first one) and sharp nulls in the response occur roughly at the eigenfrequencies of the "closed" cavity

$$k_{n,m}^c = \pi[n^2 + m^2/d^2]^{1/2} \quad (4.1)$$

and show a resonance behavior for the open struc-

Fig. 11. Same as Fig. 9 except  $\alpha = 30^\circ$ .

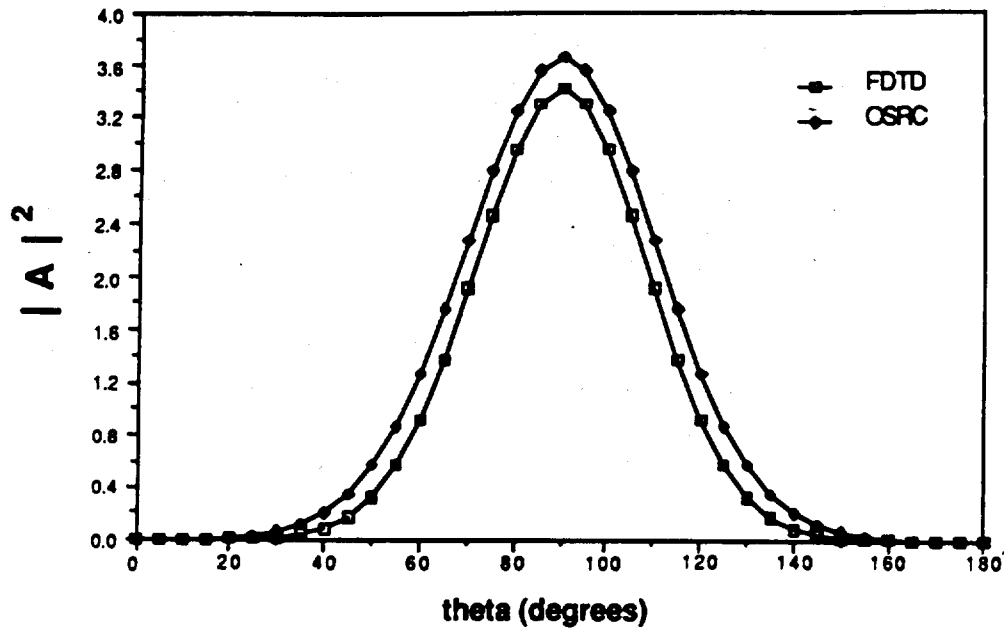


Fig. 12. Bistatic cross-section for the field scattered from the aperture of the cavity in the region  $z < 0$  for  $\alpha = 0^\circ$ . The angle  $\theta$  is as shown in Fig. 1.

ture. The deviation between the  $k_{n,m}^c$  and the real part of the complex eigenfrequency, as predicted by the OSRC method, will be discussed in the next section.

### 5. Complex eigenfrequencies of the open cavity

The complex eigenfrequencies for the open cavity can be approximated using our OSRC

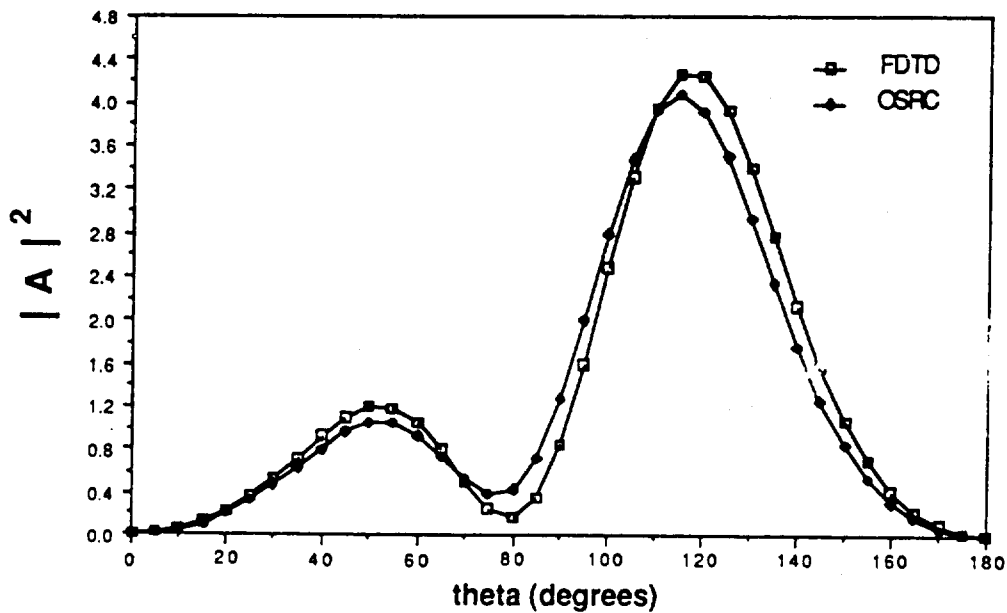


Fig. 13. Same as Fig. 12 except  $\alpha = 30^\circ$ .

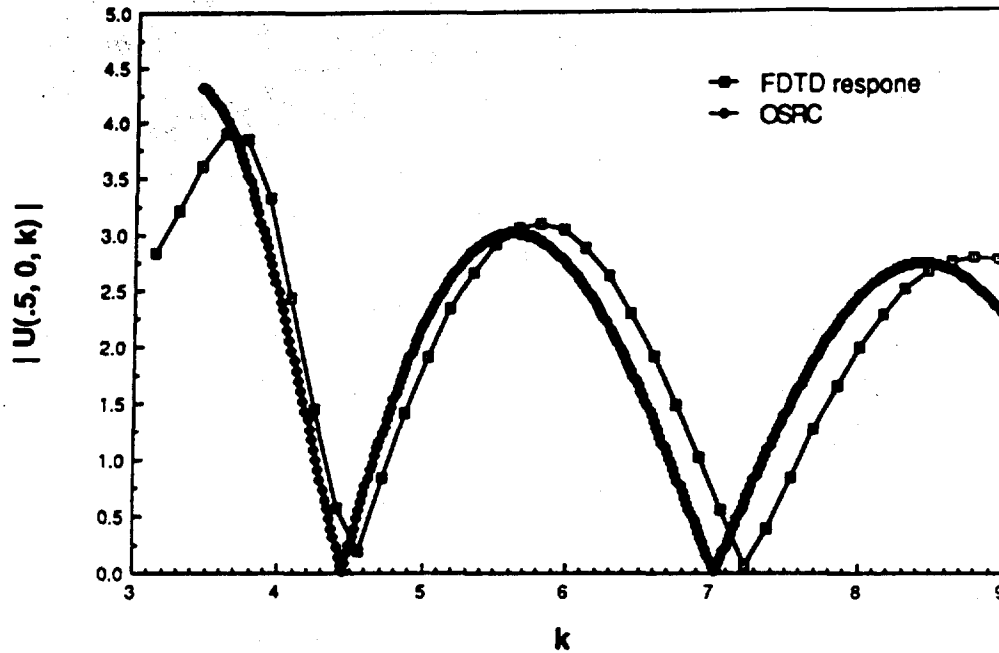


Fig. 14. Behavior of field magnitude as a function of wavenumber  $k$  at the mid-point of the cavity aperture ( $\alpha = 0^\circ$ ).

theory by setting the denominator of  $T_n$  equal to zero. Accordingly, setting  $J_n = 0$  in (3.6b), solving for  $\gamma_n$ , and simplifying the resulting expression we obtain

$$\gamma_n = (k + k_n)^4 / (n\pi)^4. \quad (5.1)$$

Inserting the change of variable

$$k = n\pi \cos \theta \quad (5.2)$$

into (2.6) and (5.1), we find that

$$\exp(\lambda \sin \theta) = \exp(4i\theta) \quad (5.3a)$$

where  $\lambda$  is defined by

$$\lambda = 2n\pi d. \quad (5.3b)$$

Equating the exponents in (5.3a), modulo  $2\pi$ , and setting  $\theta = x + iy$ , we deduce that  $x$  and  $y$  satisfy the simultaneous equations

$$\cos x \sinh y = \frac{4x + 2m\pi}{\lambda}, \quad (5.4a)$$

$$\sin x \cosh y = \frac{4y}{\lambda}. \quad (5.4b)$$

An approximate solution of the system (5.4) can be obtained when  $\lambda$  is large by observing that the

right-hand sides of (5.4) are formally small. Accordingly, we replace  $\sinh y$  by  $y$ ,  $\sin x$  by  $x$ ,  $\cos x$  by 1, and  $\cosh y$  by 1, and obtain a linear system whose solution is

$$x = -\frac{8m\pi}{16 + \lambda^2}, \quad (5.5a)$$

$$y = \frac{2m\pi\lambda}{16 + \lambda^2}. \quad (5.5b)$$

Combining these results with the definition of  $\theta$  and (5.2), and using the small argument approximation for the cosine, we deduce the approximation

$$k = n\pi \left\{ 1 - \frac{32\pi^2 m^2}{(16 + \lambda^2)^2} + \frac{2\pi^2 m^2 \lambda^2}{(16 + \lambda^2)^2} \right\} + in\pi \left\{ \frac{16m^2 \pi^2 \lambda}{(16 + \lambda^2)^2} \right\} \quad (5.6)$$

We have also solved the nonlinear system (5.4) by employing a Newton-Raphson scheme using the approximation (5.5) as an initial guess. Once the solution was obtained, we set  $\theta = x + iy$ , inserted this complex number into (5.2), and separated the real and imaginary parts of  $k$ . The results of

Table 1

$n$	Complex eigenfrequencies for $m = -1$	
	Iterative solution of (5.4)	Approximate solution using (5.6)
1	$3.773 + i0.9447$	$3.615 + i1.013$
2	$6.865 + i0.3758$	$6.865 + i0.4122$
3	$9.877 + i0.1923$	$9.883 + i0.2035$
4	$12.93 + i0.1148$	$12.93 + i0.1189$

Table 2

$n$	Complex eigenfrequencies for $m = -2$	
	Iterative solution of (5.4)	Approximate solution using (5.6)
1	$6.135 + i2.473$	$5.034 + i4.051$
2	$8.524 + i1.174$	$8.611 + i1.649$
3	$11.16 + i0.6620$	$11.26 + i0.8139$
4	$13.96 + i0.4161$	$14.02 + i0.4756$

our effort are shown in Table 1 for  $m = -1$ ,  $n = 1, 2, 3, 4$ , and in Table 2 for  $m = -2$ ,  $n = 1, 2, 3, 4$ . Negative values for  $m$  were chosen to ensure that the imaginary part of  $k$  was positive. The first column in each table contains the roots generated by the iterative scheme while the second lists those obtained from (5.6). The two columns agree well for  $m = -1$  but deviate, especially for  $n = 1$  and  $m = -2$ .

Finally, the deviation between the closed-cavity eigenfrequencies given by (4.1) and the real parts of  $k$  listed in Tables 1 and 2 differ by less than 2% for  $n = 2, 3, 4$  and by about 12% when  $n = 1$ . The imaginary part of the eigenfrequencies, which measures the rate at which energy leaks out of the open cavity, decreases as  $m$  increases. This indicates that the higher modes are trapped longer in the resonator and agrees with a ray interpretation.

## Acknowledgment

This work was sponsored in part by the National Science Foundation under Grant No. DMS-8700794.

## References

- [1] G.A. Kriegsmann, A. Taflove, and K.R. Umashankar, "A new formulation of electromagnetic wave scattering using an On-Surface Radiation Boundary Condition", *IEEE Trans. Antennas and Propagation AP-35*, 153-161 (1987).
- [2] J.G. Blaschak, T.G. Moore, G.A. Kriegsmann, and A. Taflove, "Theory and application of radiation boundary operators", *IEEE Trans. Antennas and Propagation*, in press.
- [3] G.A. Kriegsmann and T.G. Moore, "An application of the On-Surface Radiation Condition to the scattering of acoustic waves by a reactively loaded sphere", *Wave Motion* 10(3), 277-284 (1988).
- [4] A.Q. Howard, "On the mathematical theory of electromagnetic radiation from flanged waveguides", *J. Math. Phys.* 13(4), 482-490 (1972).
- [5] H.Y. Yee, L.B. Felsen, and J.B. Keller, "Ray theory of reflection from the open end of a waveguide", *SIAM J. Appl. Math.* 16(2), 268-300 (1968).
- [6] L. Grun and S.W. Lee, "Transmission into staggered parallel-plate waveguides", *IEEE Trans. Antennas and Propagation AP-30*, 35-43 (1982).
- [7] H. Shirai and L.B. Felsen, "Rays, modes, and beams for plane wave coupling into a wide parallel-plate waveguide", *Wave Motion* 9, 301-317 (1987).
- [8] A. Taflove, "Application of the finite-difference time-domain method to sinusoidal steady-state electromagnetic penetration problems", *IEEE Trans. Electromag. Compat. EMC-22*, 191-202 (1980).
- [9] A. Taflove, K.R. Umashankar, B. Beker, and F. Harfoush, "Detailed FD-TD analysis of electromagnetic field penetrating narrow slots and lapped joints in thick conducting screens", *IEEE Trans. Antennas Propag.*, in press.
- [10] G.A. Kriegsmann and C.S. Morawetz, "Solving the Helmholtz equation for exterior problems with a variable index of refraction", *SIAM J. Sci. Stat. Comput.* 1, 371-385 (1980).
- [11] A. Bayliss and E. Turkel, "Radiation boundary conditions for wave-like equations", *Comm. Pure Appl. Math.* 23, 707-725 (1980).
- [12] B. Enquist and A. Majda, "Absorbing boundary conditions for the numerical simulation of waves", *Math. Comput.* 31, 629-651 (1977).

# Review of FD-TD Numerical Modeling of Electromagnetic Wave Scattering and Radar Cross Section

ALLEN TAFLOVE, SENIOR MEMBER, IEEE, AND  
KORADA R. UMASHANKAR, SENIOR MEMBER, IEEE

*Invited Paper*

*Applications of the finite-difference time-domain (FD-TD) method for numerical modeling of electromagnetic wave interactions with structures are reviewed, concentrating on scattering and radar cross section (RCS). A number of two- and three-dimensional examples of FD-TD modeling of scattering and penetration are provided. The objects modeled range in nature from simple geometric shapes to extremely complex aerospace and biological systems. Rigorous analytical or experimental validations are provided for the canonical shapes, and it is shown that FD-TD predictive data for near fields and RCS are in excellent agreement with the benchmark data. It is concluded that, with continuing advances in FD-TD modeling theory for target features relevant to the RCS problem, and with continuing advances in vector and concurrent supercomputer technology, it is likely that FD-TD numerical modeling will occupy an important place in RCS technology in the 1990s and beyond.*

## I. INTRODUCTION

Accurate numerical modeling of the radar cross section (RCS) of complex objects is difficult. Typical structures of interest have shapes, apertures, cavities, and material compositions or loadings which produce near fields that cannot be resolved into finite sets of modes or rays. Proper numerical modeling of such near fields requires sampling at sub-wavelength resolution to avoid aliasing of magnitude and phase information. The goal is to provide a self-consistent model of the mutual coupling of electrically small regions (space cells) comprising the structure.

A candidate numerical modeling approach for this purpose is the finite-difference time-domain (FD-TD) solution

of Maxwell's curl equations. This approach is analogous to existing finite-difference solutions of fluid-flow problems encountered in computational aerodynamics, in that the numerical model is based on a direct solution of the governing partial differential equation. Yet FD-TD is a nontraditional approach to numerical electromagnetic modeling, where frequency-domain approaches have dominated.

FD-TD is very simple in concept and execution. Yet it is remarkably robust, providing highly accurate modeling predictions for a wide variety of electromagnetic wave interaction problems. One of the goals of this paper is to demonstrate that recent advances in FD-TD modeling concepts and software implementation, combined with advances in supercomputer technology, have expanded the scope, accuracy, and speed of FD-TD modeling to the point where it may be the preferred choice for scattering problems involving complex, electrically large, three-dimensional structures. With this in mind, this paper will succinctly review the following FD-TD modeling validations:

- 1) Canonical two-dimensional targets
  - a) Square metal cylinder, TM polarization
  - b) Circular muscle-fat-layered cylinder, TE polarization
  - c) Homogeneous, anisotropic, square material cylinder, TM polarization
  - d) Circular metal cylinder, conformally modeled, TE and TM polarization
  - e) Flanged metal open cavity
- 2) Canonical three-dimensional targets
  - a) Metal cube, broadside incidence
  - b) Flat conducting plate, multiple monostatic RCS observations
  - c) T-shaped conducting target, multiple monostatic RCS observations

The potential of FD-TD for modeling noncanonical, indeed very complex, three-dimensional objects will then be illustrated by reviewing published work which investigated the penetration of VHF and UHF plane-wave energy

Manuscript received April 12, 1988; revised October 4, 1988. This work was supported in part by the U.S. Air Force under RADC contracts F30602-79-C-0039 and F19628-82-C-0140; by NASA/Lewis under grant NAG 3-635, and by the National Science Foundation under grant ECS-8515777.

A. Taflov is with the Department of Electrical Engineering and Computer Science, Technological Institute, Northwestern University, Evanston, IL 60208, USA.

K. R. Umashankar is with the Department of Electrical Engineering and Computer Science, University of Illinois at Chicago, Chicago, IL 60680, USA.

IEEE Log Number 8927989.

0018-9219/89/0500-0686\$01.00 © 1989 IEEE

into 1) the infrared seeker section of a missile and 2) the entire human body. Finally, the paper will conclude with a discussion of large-scale computer software and the potential impact of massively concurrent machines.

## II. GENERAL CHARACTERISTICS OF FD-TD

As stated, FD-TD is a direct solution of Maxwell's time-dependent curl equations. It employs no potentials. Instead, it applies simple second-order accurate central-difference approximations [1] for the space and time derivatives of the electric and magnetic fields directly to the respective differential operators of the curl equations. This achieves a sampled-data reduction of the continuous electromagnetic field in a volume of space over a period of time. Space and time discretizations are selected to bound errors in the sampling process and to ensure numerical stability of the algorithm [2]. Electric and magnetic field components are interleaved in space to permit a natural satisfaction of tangential field continuity conditions at media interfaces. Overall, FD-TD is a marching-in-time procedure which simulates the continuous actual waves by sampled-data numerical analogs propagating in a data space stored in a computer. At each time step, the system of equations to update the field components is fully explicit, so that there is no need to set up or solve a system of linear simultaneous equations. As a consequence, the required computer storage and running time is dimensionally low, proportional only to  $N$ , where  $N$  is the number of electromagnetic field unknowns in the volume modeled.

Fig. 1(a) illustrates the time-domain wave tracking concept of the FD-TD method. A region of space (within the dashed line) is selected for field sampling in space and time. At time  $t = 0$ , it is assumed that all fields within the numerical sampling region are identically zero. An incident plane wave is assumed to enter the sampling region at this time. Propagation of the incident wave is modeled by the commencement of time-stepping, which is simply the implementation of the finite-difference analog of the curl equations. Time stepping continues as the numerical analog of the incident wave strikes the modeled target embedded within the sampling region. All outgoing scattered wave analogs ideally propagate through the lattice truncation planes with negligible reflection to exit the sampling region. Phenomena such as induction of surface currents, scattering and mul-

tipole scattering, penetration through apertures, and cavity excitation are modeled time step by time step by the action of the curl equations analog. Self-consistency of these modeled phenomena is generally assured if their spatial and temporal variations are well resolved by the space and time sampling process.

Time stepping is continued until the desired late-time pulse response or steady-state behavior is achieved. An important example of the latter is the sinusoidal steady state, wherein the incident wave is assumed to have a sinusoidal dependence, and time stepping is continued until all fields in the sampling region exhibit sinusoidal repetition. This is a consequence of the limiting amplitude principle [3]. Extensive numerical experimentation with FD-TD has shown that the number of complete cycles of the incident wave required to be time stepped to achieve the sinusoidal steady state is a function of two (possibly related) factors:

1) *Target electrical size.* Numerical wave analogs must be permitted time to propagate in the FD-TD computational lattice to causally connect the physics of all regions of the target. For many targets, this requires a number of time steps sufficient to permit at least two complete front-to-back-to-front traverses of the target by a wave analog traveling at the speed of light. For example, assuming a target spanning a maximum of 10 wavelengths, it is reasonable to assume that about 40 complete cycles of the incident wave should be time-stepped (as a minimum) to achieve the sinusoidal steady state. Using a space resolution of 10 lattice cells per wavelength, this corresponds to 800 time steps.

2) *Target Q factor.* Targets having well-defined low-loss cavities or low-loss dielectric compositions may require the number of complete cycles of the incident wave to be time-stepped to approach the Q factor of the cavity resonance. Because the Q factor can be large even for electrically small or moderate size cavities, this consideration can dictate how many time steps the FD-TD code must be run to achieve the sinusoidal steady state.

Table 1 summarizes the number of sinusoidal cycles needed to achieve the steady state for a wide range of structures modeled using FD-TD over the past 15 years. In the RCS area, it has been found that target electrical size has proven to be the dominant factor. Cavities for RCS-type problems tend to be open, and therefore low Q; and the use of radar-absorbing material (RAM) serves further to reduce Q factors of structural resonances.

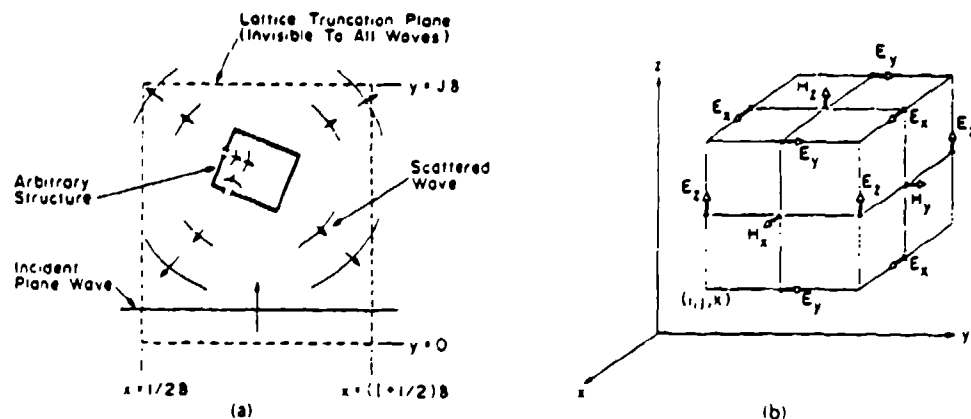


Fig. 1. Basic elements of FD-TD space lattice. (a) Time-domain wave tracking concept. (b) Lattice unit cell in Cartesian coordinates [1].



Table 1 Convergence of FD-TD to Sinusoidal Steady State

Number of Sinusoidal Cycles Needed	General Structure Type
$\leq 5$	Convex 2-D metal targets spanning less than $1 \lambda_0$ , TM case Lossy 3-D structures, especially those comprised of biological tissue media
5-20	Convex 2-D metal targets spanning $1-5 \lambda_0$ , TE case Convex 2-D dielectric targets spanning $1-5 \lambda_0$ , TM and TE cases Convex 3-D metal targets spanning $1-5 \lambda_0$
20-40	3-D metal wires and rods spanning on the order of $1 \lambda_0$ , excited near a resonance General 3-D metal targets spanning up to $10 \lambda_0$ , including corner reflectors and open cavities
$\geq 40$	Deeply reentrant 3-D metal targets (such as engine inlets) spanning $10 \lambda_0$ or more
$\geq 100$	3-D metal targets of arbitrary electrical size, but having aperture/cavity resonances of moderate to high $Q$ , and excited very near such a resonance

Fig. 1(b) illustrates the positions of the electric and magnetic field components about a unit cell of the FD-TD lattice in Cartesian coordinates [1]. Note that each magnetic field vector component is surrounded by four circulating electric field vector components, and vice versa. This arrangement permits not only a centered-difference analog to the space derivatives of the curl equations, but also a natural geometry for implementing the integral form of Faraday's law and Ampere's law at the space-cell level. This integral interpretation permits a simple but effective modeling of the physics of smoothly curved target surfaces, as will be seen later.

Fig. 2 illustrates how an arbitrary three-dimensional scatterer is embedded in an FD-TD space lattice comprised of the unit cells of Fig. 1(b). Simply, the desired values of electrical permittivity and conductivity are assigned to each

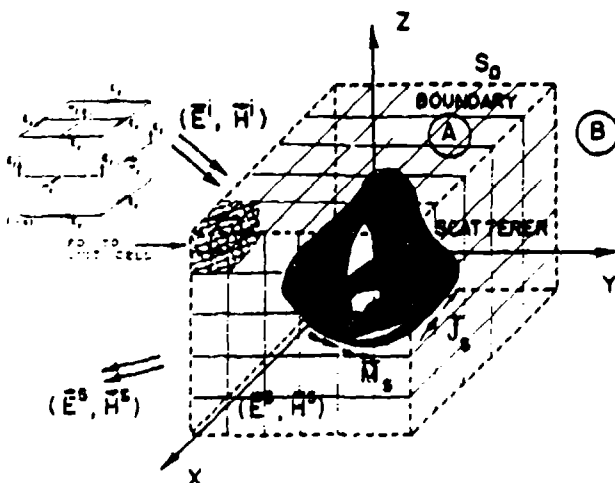


Fig. 2. Arbitrary three-dimensional scatterer embedded in FD-TD space lattice.

electric field component of the lattice. Correspondingly, desired values of magnetic permeability and equivalent conductivity are assigned to each magnetic field component of the lattice. The media parameters are interpreted by the FD-TD program as local coefficients for the time-stepping algorithm. Specification of media properties in this component-by-component manner results in a stepped-edge, or staircase, approximation of curved surfaces. Continuity of tangential fields is assured at the interface of dissimilar media with this procedure. There is no need for special field matching at media interface points. Stepped-edge approximation of curved surfaces has been found to be adequate in the FD-TD modeling problems studied in the 1970s and early 1980s, including wave interactions with biological tissues [4], penetration into cavities [5]-[7], and electromagnetic pulse (EMP) interactions with complex structures [8]-[10]. However, recent interest in wide-dynamic-range models of scattering by curved targets has prompted the development of surface-conforming FD-TD approaches which eliminate staircasing. These are summarized in a later section.

### III. REVIEW OF FD-TD ALGORITHM DETAILS

Table 2 lists the six coupled equations for the electric and magnetic fields which comprise Maxwell's equations in Cartesian coordinates. Table 3 lists the assumed space-time

Table 2 Maxwell's Curl Equations in Cartesian Coordinates

$$\frac{\partial H_z}{\partial t} = \frac{1}{\mu} \left( \frac{\partial E_y}{\partial x} - \frac{\partial E_x}{\partial y} - \rho' H_z \right) \quad (1a)$$

$$\frac{\partial H_y}{\partial t} = \frac{1}{\mu} \left( \frac{\partial E_x}{\partial z} - \frac{\partial E_z}{\partial x} - \rho' H_y \right) \quad (1b)$$

$$\frac{\partial H_x}{\partial t} = \frac{1}{\mu} \left( \frac{\partial E_z}{\partial y} - \frac{\partial E_y}{\partial z} - \rho' H_x \right) \quad (1c)$$

$$\frac{\partial E_z}{\partial t} = \frac{1}{\epsilon} \left( \frac{\partial H_y}{\partial x} - \frac{\partial H_x}{\partial y} - \sigma E_z \right) \quad (1d)$$

$$\frac{\partial E_y}{\partial t} = \frac{1}{\epsilon} \left( \frac{\partial H_z}{\partial z} - \frac{\partial H_z}{\partial x} - \sigma E_y \right) \quad (1e)$$

$$\frac{\partial E_x}{\partial t} = \frac{1}{\epsilon} \left( \frac{\partial H_z}{\partial x} - \frac{\partial H_x}{\partial y} - \sigma E_x \right) \quad (1f)$$

where

$E_x, E_y, E_z$  = Cartesian components of electric field, volts/meter  
 $H_x, H_y, H_z$  = Cartesian components of magnetic field, amperes/meter

$\epsilon$  = electric permittivity, farads/meter

$\sigma$  = electric conductivity, siemens/meter

$\mu$  = magnetic permeability, henrys/meter

$\rho'$  = equivalent magnetic loss, ohms/meter

Table 3 Central-Difference Approximations to Space and Time Partial Derivatives

$$(i, j, k) = (i\Delta x, j\Delta y, k\Delta z) \quad (2a)$$

$$F^n(i, j, k) = F(i\Delta x, j\Delta y, k\Delta z, n\Delta t) \quad (2b)$$

$$\frac{\partial F^n(i, j, k)}{\partial x} = \frac{F^n(i + \frac{1}{2}, j, k) - F^n(i - \frac{1}{2}, j, k)}{\Delta x} + \text{order } (\Delta x^2) \quad (3a)$$

$$\frac{\partial F^n(i, j, k)}{\partial t} = \frac{F^{n+1/2}(i, j, k) - F^{n-1/2}(i, j, k)}{\Delta t} + \text{order } (\Delta t^2) \quad (3b)$$

For a cubic space lattice:  $\Delta x = \Delta y = \Delta z = \delta$ .

**Table 4** Examples of Finite-Difference Expressions to Time-Step Field Vector Components

$$H_z^{n+1/2}(i, j + \frac{1}{2}, k + \frac{1}{2}) = \frac{1 - \frac{\rho'(i, j + \frac{1}{2}, k + \frac{1}{2})\Delta t}{2\mu(i, j + \frac{1}{2}, k + \frac{1}{2})}}{1 + \frac{\rho'(i, j + \frac{1}{2}, k + \frac{1}{2})\Delta t}{2\mu(i, j + \frac{1}{2}, k + \frac{1}{2})}} \cdot H_z^{n-1/2}(i, j + \frac{1}{2}, k + \frac{1}{2})$$

$$+ \frac{\Delta t}{\mu(i, j + \frac{1}{2}, k + \frac{1}{2})} \cdot \frac{1}{1 + \frac{\rho'(i, j + \frac{1}{2}, k + \frac{1}{2})\Delta t}{2\mu(i, j + \frac{1}{2}, k + \frac{1}{2})}} \left[ \frac{E_x^n(i, j + \frac{1}{2}, k + 1) - E_x^n(i, j + \frac{1}{2}, k)}{\Delta z} + \frac{E_y^n(i, j, k + \frac{1}{2}) - E_y^n(i, j + 1, k + \frac{1}{2})}{\Delta y} \right] \quad (4a)$$

$$E_x^{n+1}(i, j, k + \frac{1}{2}) = \frac{1 - \frac{\sigma(i, j, k + \frac{1}{2})\Delta t}{2\epsilon(i, j, k + \frac{1}{2})}}{1 + \frac{\sigma(i, j, k + \frac{1}{2})\Delta t}{2\epsilon(i, j, k + \frac{1}{2})}} \cdot E_x^n(i, j, k + \frac{1}{2})$$

$$+ \frac{\Delta t}{\epsilon(i, j, k + \frac{1}{2})} \cdot \frac{1}{1 + \frac{\sigma(i, j, k + \frac{1}{2})\Delta t}{2\epsilon(i, j, k + \frac{1}{2})}} \left[ \frac{H_z^{n+1/2}(i + \frac{1}{2}, j, k + \frac{1}{2}) - H_z^{n+1/2}(i - \frac{1}{2}, j, k + \frac{1}{2})}{\Delta x} + \frac{H_z^{n+1/2}(i, j - \frac{1}{2}, k + \frac{1}{2}) - H_z^{n+1/2}(i, j + \frac{1}{2}, k + \frac{1}{2})}{\Delta y} \right] \quad (4b)$$

notation for the field vector components sampled at discrete lattice locations and at discrete time steps. This table also provides the central-difference approximations to the space and time partial derivatives of Maxwell's equations, using the assumed sampled-field notation. Finally, Table 4 provides example finite-difference time-stepping expressions for a magnetic and an electric field component. As noted earlier, all quantities on the right-hand side of each time-stepping expression are known (stored in computer memory), so that the expressions are fully explicit.

The choice of  $\delta$  and  $\Delta t$  is motivated by reasons of accuracy and algorithm stability, respectively. To ensure the accuracy of the computed spatial derivatives of the electromagnetic fields,  $\delta$  must be small compared to a wavelength.  $\delta \leq \lambda/10$  is sufficient to realize less than  $\pm 7\%$  uncertainty ( $\pm 0.6$  dB) of the FD-TD solution of near fields due to the approximation of the spatial derivatives [5]. For  $\delta \leq \lambda/20$ , this uncertainty drops to less than  $\pm 2\%$  ( $\pm 0.2$  dB).  $\delta$  should also be small enough to permit resolution of the principal surfaces or volumetric details of the structure modeled.

To ensure the stability of the time-stepping algorithm exemplified by (4a) and (4b),  $\Delta t$  is chosen to satisfy the inequality [2]

$$\Delta t \leq \left( \frac{1}{\Delta x^2} + \frac{1}{\Delta y^2} + \frac{1}{\Delta z^2} \right)^{-1/2} c_{\max}^{-1}$$

$$\leq \frac{\delta}{c_{\max} \sqrt{3}} \quad \text{for a cubic lattice} \quad (5)$$

where  $c_{\max}$  is the maximum wave phase velocity within the model. Note that the corresponding stability criterion set forth in [1, eqs. (7) and (8)] is incorrect, as shown in [2].

Fig. 3(a) illustrates the division of the FD-TD lattice into total-field and scattered-field regions. This division has been found to be very useful since it permits the efficient sim-

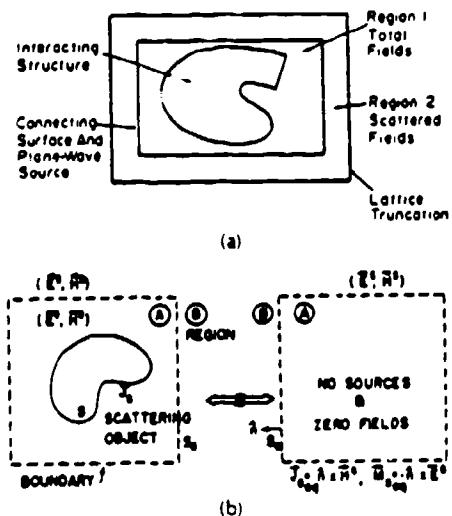


**Fig. 3.** Zoning of FD-TD space lattice. (a) Total-field and scattered-field regions [11], [12]. (b) Near-field to far-field integration surface located in the scattered-field region [12].

ulation of an incident plane wave in the total-field region with arbitrary angle of incidence, polarization, time-domain waveform, and duration [11], [12]. Three additional important benefits arise from this lattice division as follows.

1) *Large near-field computational dynamic range.* Because the target of interest is embedded in the total-field region, low total-field levels in shadow regions or within shielding enclosures are computed directly without suffering subtraction noise (as would be the case if scattered fields in such regions were time-stepped, and then added to a canceling incident field to obtain the low total-field levels). Avoidance of subtraction noise is the key to obtaining near-field computational dynamic ranges exceeding 60 dB [5].

2) *Natural satisfaction of electromagnetic boundary conditions.* Embedding the target in the total-field region permits a natural satisfaction of tangential field continuity across media interfaces, as discussed earlier, without having to compute the incident field at possibly thousands or tens of thousands of points along complicated media-interface loci that are unique to each target. The zoning arrangement of Fig. 3(a) requires computation of the incident field only along the rectangular connecting surface between total-field and scattered-field regions. This surface is fixed, that is, independent of the shape or composition of the enclosed target being modeled. A substantial benefit in computer running time arises as a result, a benefit that increases as the complexity of the target increases.

3) *Systematic computation of bistatic RCS.* The provision of a well-defined scattered-field region in the FD-TD lattice permits the near-field to far-field transformation illustrated in Fig. 3(b). The dashed virtual surface (field observation locus) shown in Fig. 3(b) can be located along convenient lattice planes in the scattered-field region of Fig. 3(a). Tangential scattered  $E$  and  $H$  fields computed via FD-TD at this virtual surface can then be weighted by the free-space Green's function and then integrated (summed) to provide the far-field response and RCS (full bistatic response for the assumed illumination angle) [12]–[14]. The near-field integration surface has a fixed rectangular shape and thus is independent of the shape or composition of the enclosed target being modeled.

Fig. 3(a) uses the term "lattice truncation" to designate the outermost lattice planes in the scattered-field region. The fields at these planes cannot be computed using the centered-differencing approach discussed earlier because of the assumed absence of known field data at points outside of the lattice truncation. These data are needed to form the central differences. Therefore, an auxiliary lattice truncation condition is necessary. This condition must be consistent with Maxwell's equations in that an outgoing scattered-wave numerical analog striking the lattice truncation must exit the lattice without appreciable nonphysical reflection, just as if the lattice truncation was invisible.

It has been shown that the required lattice truncation condition is really a radiation condition in the near field [15]–[17]. A very successful second-order accurate finite-difference approximation of the exact radiation condition in Cartesian coordinates was introduced in [11]. This approximation was subsequently used in a variety of two- and three-dimensional FD-TD scattering codes [12]–[14], yielding excellent results for both near and far fields. (For example, all FD-TD results in this paper, with the exception of the

missile seeker model of Section VI, were obtained using these codes.) However, recent interest in wide-dynamic-range models of scattering has prompted research in the construction of even more accurate near-field radiation conditions, including fixed third-order approximations [18], [19], adaptive conditions [20], and predictor-corrector conditions [21]. The goal here is to reduce the numerical lattice noise due to nonphysical reflections of wave analogs at the lattice truncations by at least one order of magnitude (20 dB) relative to that achieved by the second-order condition of [11].

#### IV. FD-TD MODELING VALIDATIONS FOR CANONICAL TWO-DIMENSIONAL TARGETS

Analytical and code-to-code validations have been obtained relative to FD-TD modeling of a wide variety of canonical two-dimensional targets. Both convex and reentrant (cavity-type) shapes have been studied. Further, target material compositions have included perfect conductors, homogeneous and inhomogeneous lossy dielectrics, and anisotropic dielectric and permeable media. Selected validations will be reviewed here.

##### A. Square Metal Cylinder, TM Polarization [12]

Here we consider the scattering of a TM-polarized plane wave obliquely incident upon a square metal cylinder of electrical size  $k_0 s = 2$ , where  $s$  is the side width of the cylinder. The FD-TD grid employs square unit cells of size  $s/20$ , and the grid truncation (radiation boundary) is located at a uniform distance of 20 cells from the cylinder surface.

Fig. 4 compares the magnitude and phase of the cylinder surface electric current distribution computed using FD-TD to that computed using a benchmark frequency-domain electric-field integral equation (EFIE) method-of-moments (MoM) code. The MoM code assumes target symmetry and discretizes one-half of the cylinder surface with 84 divisions. The FD-TD computed surface current is taken as  $\hat{n} \times \vec{H}_{tan}$ , where  $\hat{n}$  is the unit normal vector at the cylinder surface and  $\vec{H}_{tan}$  is the FD-TD value of the magnetic field vector component in free space immediately adjacent to the cylinder surface. From Fig. 4 we see that the magnitude of the FD-TD computed surface current agrees with the MoM solution to better than  $\pm 1\%$  ( $\pm 0.09$  dB) at all comparison points more than 2 FD-TD space cells from the cylinder corners (current singularities). The phase of the FD-TD solution agrees with the MoM solution to within  $\pm 3^\circ$  at virtually every comparison point, including the shadow region.

##### B. Circular Muscle-Fat-Layered Cylinder, TE Polarization [22]

Here we consider the penetration of a TE-polarized plane wave into a 15-cm-radius muscle-fat-layered cylinder. The inner layer (radius 7.9 cm) is assumed to be comprised of muscle having a relative permittivity of 72 and a conductivity of 0.9 S/m. The outer layer is assumed to be comprised of fat having a relative permittivity of 7.5 and a conductivity of 0.048 S/m. An illumination frequency of 100 MHz is modeled, with the FD-TD grid cell size set equal to 1.5 cm (approximately  $1/24$  wavelength within the muscle). A

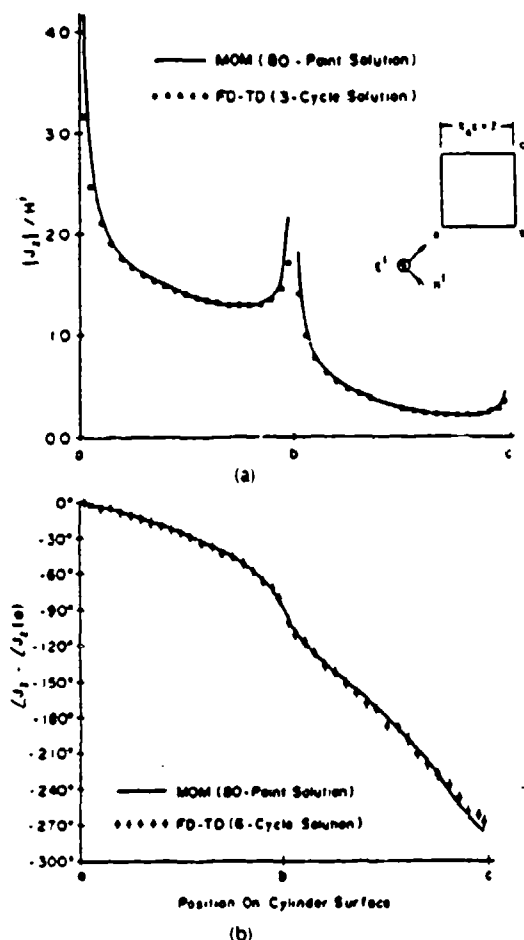


Fig. 4. Comparison of FD-TD and EFIE-MoM results for longitudinal surface electric current distribution induced on a perfectly conducting square cylinder of size  $k_0 s = 2$ . (a) Magnitude. (b) Phase [12].

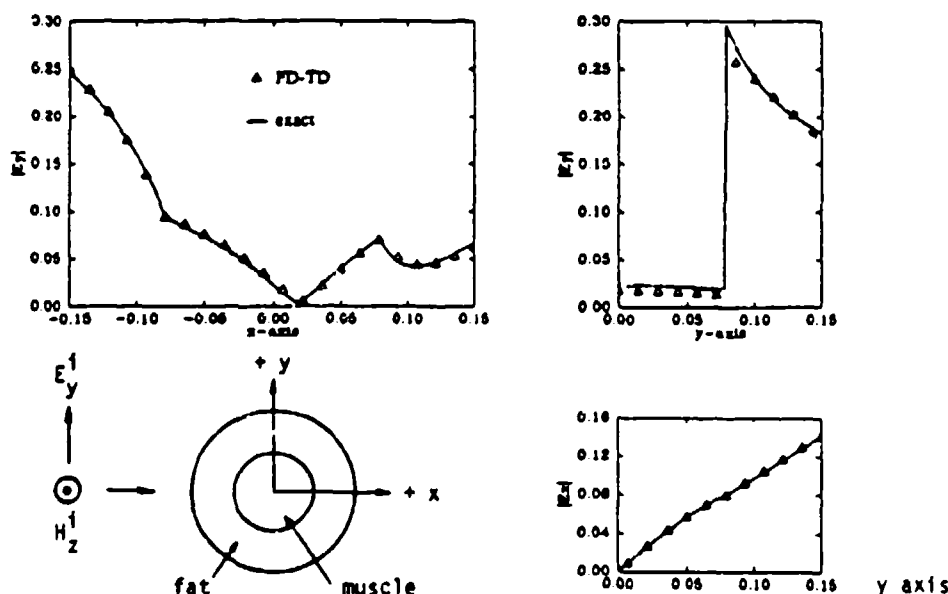


Fig. 5. Comparison of FD-TD and exact summed-eigenfunction solutions for distributions of penetrating electric field vector components within a circular muscle-fat-layered cylinder, TE polarization case at 100 MHz [22].

stepped-edge (staircase) approximation of the circular layer boundaries is used.

Fig. 5, taken from [22], shows the analytical validation results for the magnitude of the penetrating electric field vector components along two cuts through the muscle-fat cylinder, one parallel to the direction of propagation of the incident wave, and one parallel to the incident electric field vector. The exact solution is obtained by summing sufficient terms of the eigenfunction expansion to assure convergence of the sum. Excellent agreement of the FD-TD and exact solutions is noted, even at jump discontinuities of the field or the slope of the field distribution that occur at the layer boundaries. This fine agreement is observed despite the stepped-edge approximation of the circular layer boundaries.

### C. Homogeneous, Anisotropic, Square Material Cylinder, TM Polarization [23]

The ability to independently specify electrical permittivity and conductivity for each  $\hat{E}$  vector component in the FD-TD lattice, and magnetic permeability and equivalent conductivity for each  $\hat{H}$  vector component, leads immediately to the possibility of using FD-TD to model material targets having diagonal-tensor electric and magnetic properties. No alteration of the basic FD-TD algorithm is required. The more complicated behavior associated with off-diagonal tensor components can also be modeled, in principle, with some algorithm complications [24].

Recent development of analytical and numerical treatment of coupled surface combined-field integral equations (CFIE) for modeling scattering by arbitrarily shaped two-dimensional anisotropic targets [23] has permitted detailed tests of the accuracy of FD-TD anisotropic models. Fig. 6 illustrates the results of one such test. Here the magnitude of the equivalent surface electric current induced by TM illumination of a square anisotropic cylinder is graphed as a function of position along the cylinder surface for both

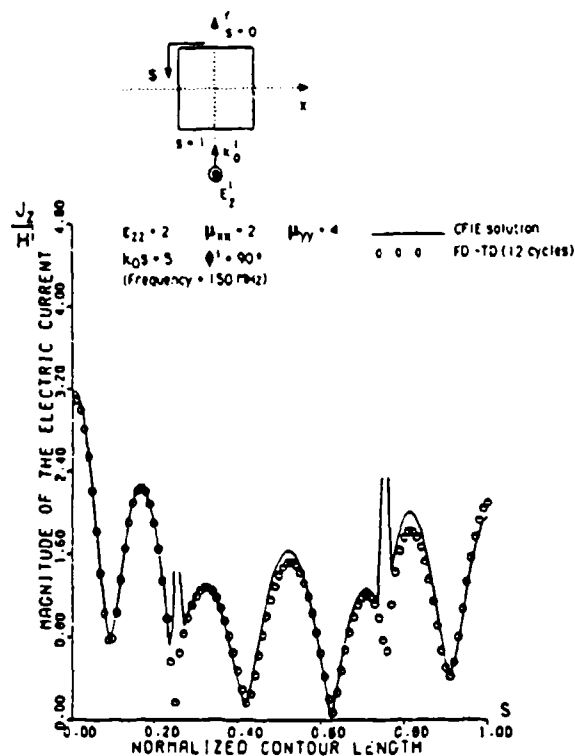


Fig. 6. Comparison of FD-TD and CFIE-MoM results for longitudinal surface electric current distribution induced on an anisotropic dielectric-permeable square cylinder of size  $k_0s = 5$ , TM case [23].

the FD-TD and the CFIE MoM models. The incident wave propagates in the  $+y$  direction and has a  $+z$ -directed electric field. The square cylinder has an electrical size  $k_0s = 5$ , permittivity  $\epsilon_{zz} = 2$ , and diagonal permeability tensor  $\mu_{zz} = 2$  and  $\mu_{yy} = 4$ . For the test shown, the FD-TD grid cell size is set equal to  $s/50$ , and the radiation boundary is located at a uniform distance of 20 cells from the cylinder surface.

From Fig. 6 we see that the FD-TD and CFIE results agree very well almost everywhere on the cylinder surface, despite the presence of a complicated series of peaks and nulls. Disagreement is noted at the cylinder corners where CFIE predicts sharp local peaks, but FD-TD predicts local nulls. Studies are continuing to resolve this corner physics issue.

#### D. Circular Metal Cylinder, TE and TM Polarization

A significant flaw in previous FD-TD models of conducting structures with smooth curved surfaces has been the need to use stepped-edge (staircase) approximations of the actual structure surface. Although not a serious problem for modeling wave penetration and scattering for low-Q metal cavities, recent FD-TD studies have shown that stepped approximations of curved walls and aperture surfaces can shift center frequencies of resonant responses by 1-2% for Q factors of 30 to 80, and can possibly introduce spurious nulls [25]. In the area of scattering by convex shapes, the use of stepped-surface approximations has limited application of FD-TD in modeling the important class of targets where surface roughness, exact curvature, and dielectric or permeable loading are important factors in determining the radar cross section.

Recently three different types of FD-TD conformal surface models have been proposed and examined for scattering problems:

1) *Locally distorted grid models*. These preserve the basic Cartesian grid arrangement of field components at all space cells except those immediately adjacent to the target surface. Space cells adjacent to the target surface are deformed to conform with the surface locus. Slightly modified time-stepping expressions for the field components in these cells are obtained by applying either a modified finite-volume technique [26] or the integral form of Faraday's law and Ampère's law about the perimeters of the deformed space cells [27].

2) *Globally distorted grid models, body fitted*. These employ available numerical mesh generation schemes to construct non-Cartesian grids which are continuously and globally stretched to conform with smoothly shaped targets. In effect, the Cartesian grid is mapped to a numerically generated coordinate system wherein the target surface contour occupies a locus of constant equivalent "radius." Time-stepping expressions are adapted either from the Cartesian FD-TD case [28] or from a characteristics-based method used in computational fluid dynamics [29].

3) *Globally distorted grid models, unstructured*. These employ available mesh generation schemes to construct non-Cartesian grids comprised of an unstructured array of space-filling cells. Target surface features are appropriately fit into the unstructured grid, with local grid resolution and cell shape selected to provide the desired geometric modeling aspects. An example of this class is the control-region approach discussed in [30].

Research is ongoing for each of these types of conformal surface models. Key questions concerning the usefulness of each model include the following:

- 1) Computer resources involved in mesh generation
- 2) Severity of numerical artifacts introduced by grid distortion, including numerical instability, dispersion, nonphysical wave reflection, and subtraction noise limitation of near-field computational dynamic range
- 3) Comparative computer resources for running the actual RCS models, especially for three-dimensional targets spanning more than 10 wavelengths

The accuracy of locally distorted grid models using the integral form of Faraday's law applied around the perimeters of the deformed space cells adjacent to a smoothly curved target is illustrated in Fig. 7 for TE and TM illumination cases. Here a moderate-resolution Cartesian FD-TD grid (having  $1/20$  wavelength cell size) is used to compute the azimuthal or longitudinal current distribution on the surface of a  $ka = 5$  circular metal cylinder. For both polarizations it is seen that the conformal FD-TD model achieves an accuracy of 1.5% or better at most surface points relative to the exact series solution. Computer running time for the conformal FD-TD model is essentially the same as for the old staircase FD-TD model since only a few  $H$  components immediately adjacent to the target surface require a slightly modified time-stepping relation.

#### E. Flanged Metal Open Cavity [20], [31]

Here we consider the interaction of a TM-polarized plane wave obliquely incident upon a flanged metal open cavity.

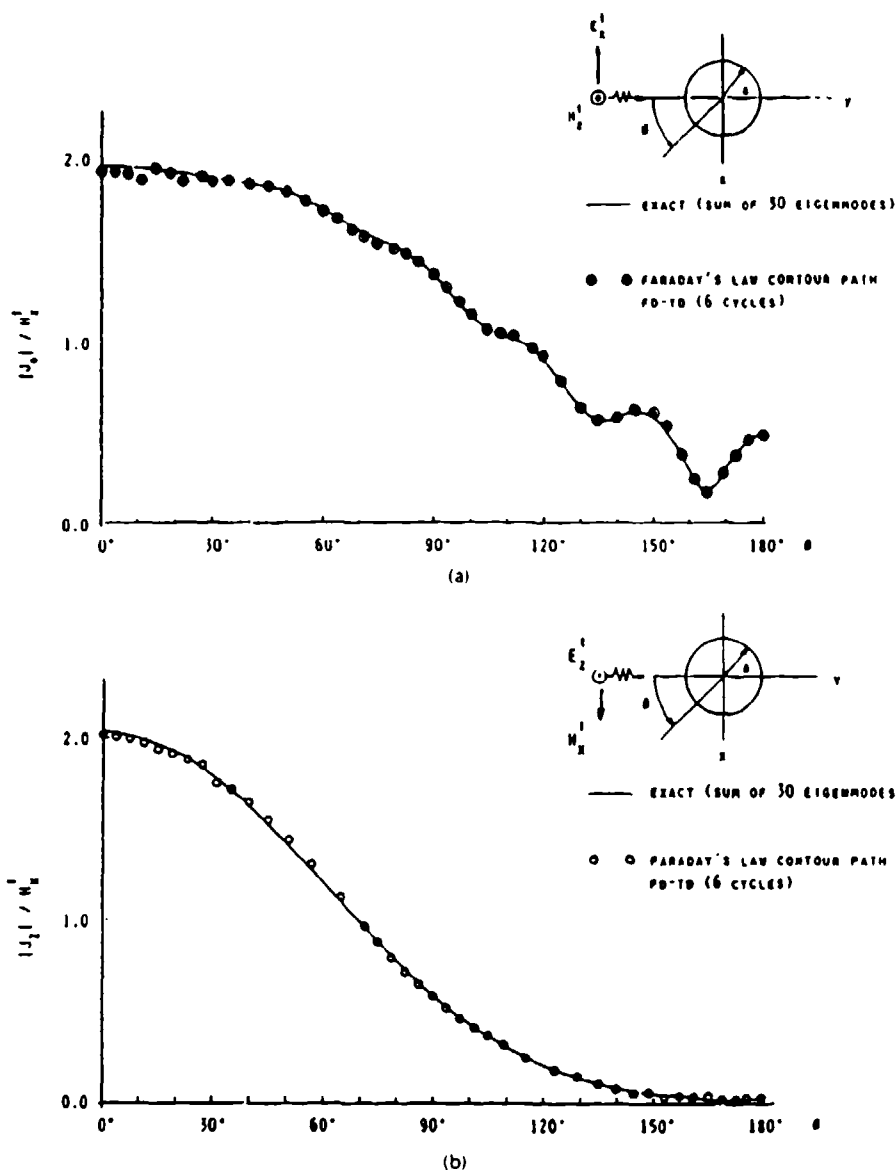


Fig. 7. Comparison of FD-TD and exact summed-eigenfunction solutions for surface electric current distribution induced on a  $k_0 a = 5$  circular conducting cylinder (conformal FD-TD model used, 0.05 wavelength grid cell size). (a) TE case, azimuthal current. (b) TM case, longitudinal current [27].

The open cavity is formed by a flanged parallel-plate waveguide having a plate spacing  $a = 1$  m, short-circuited by a metal plate located at a distance  $d = 1$  m from the aperture. At the assumed illumination frequency of 382 MHz,  $ka = kd = 8$ , and only the first two TE waveguide modes propagate within the open cavity. An oblique angle of incidence  $\alpha = 30^\circ$  is assumed for this case.

Fig. 8 compares the magnitude and phase of the penetrating electric field within the cavity 2/3 m from the aperture computed using FD-TD to that obtained analytically using a cavity modal expansion and on-surface radiation condition (OSRC) theory [31]. Good agreement is seen.<sup>1</sup> Fig.

<sup>1</sup>It should be noted that the results obtained using the cavity modal expansion and OSRC represent a good approximation, but not a rigorous solution.

9 shows a similar comparison for the bistatic RCS pattern due to the induced aperture field distribution. Again, good agreement is noted.

#### V. FD-TD MODELING VALIDATIONS FOR CANONICAL THREE-DIMENSIONAL TARGETS

Analytical, code-to-code, and experimental validations have been obtained relative to FD-TD modeling of a wide variety of canonical three-dimensional structures, including cubes, flat plates, corner reflectors, and aperture-perforated cavities. Selected validations will be reviewed here.

##### A. Metal Cube, Broadside Incidence [13]

Results are now shown for the FD-TD computed surface electric current distribution on a metal cube subject to

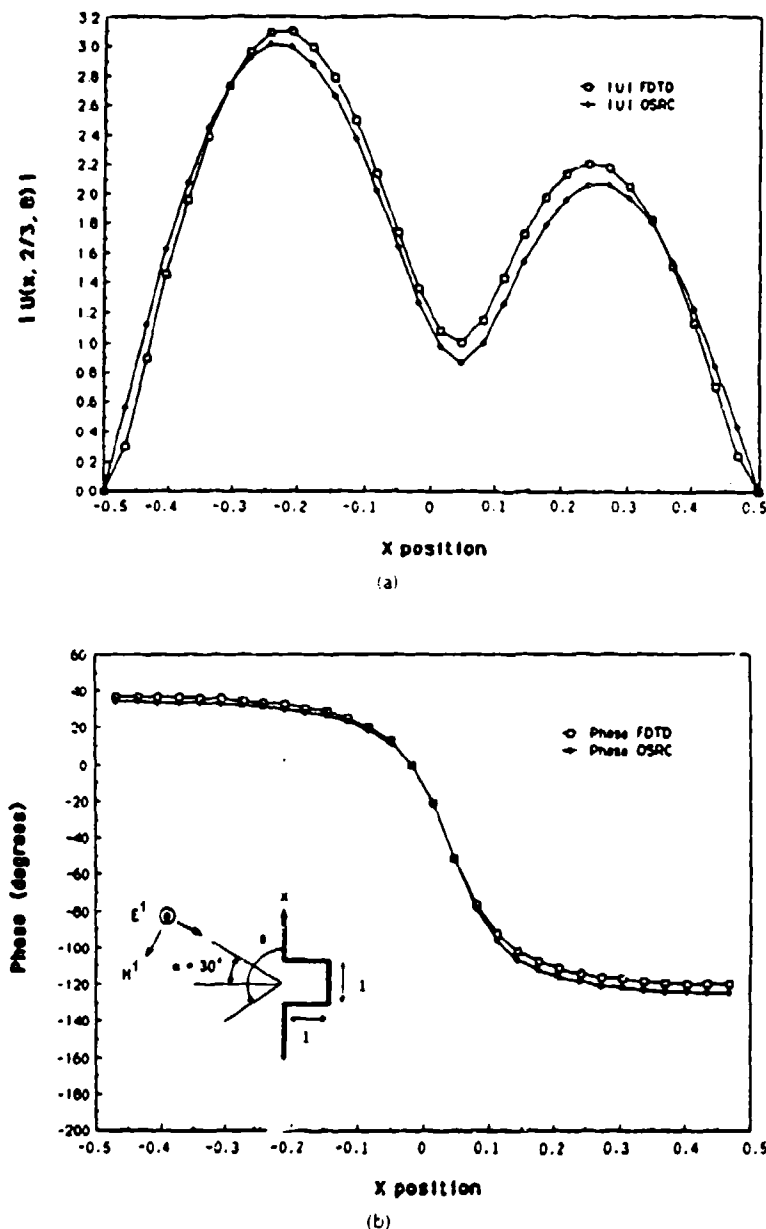


Fig. 8. Comparison of FD-TD and modal/OSRC approximate solution for penetrating electric field distribution 2/3 m within flanged open cavity. (a) Magnitude. (b) Phase [20], [31].

plane-wave illumination at broadside incidence. The electric current distribution is compared to that computed by a standard frequency-domain MoM code which discretizes target surfaces using triangular patches. It is shown that a very high degree of correspondence exists between the two sets of predictive data.

The detailed surface current study involves a cube of electrical size  $k_0 s = 2$ , where  $s$  is the side width of the cube. For the FD-TD model, each face of the cube is spanned by  $20 \times 20$  space cells, and the radiation boundary is located at a uniform distance of 15 cells from the cube surface. For the MoM model, each face of the cube is spanned by either 18 or 32 triangular patches to test the convergence of the MoM model. Comparative results for surface current are

graphed along two straight-line loci along the cube:  $\overline{abcd}$ , which is in the plane of the incident magnetic field, and  $\overline{a'b'c'd'}$ , which is in the plane of the incident electric field.

Fig. 10 compares the FD-TD and MoM results for the magnitude and phase of the "looping" current along  $\overline{ab'c'd'}$ . The FD-TD values agree with the high-resolution MoM data to better than  $\pm 2.5\%$  ( $\pm 0.2$  dB) at all comparison points. Phase agreement for the same sets of data is better than  $\pm 1^\circ$ . (The low-resolution MoM data have a phase anomaly in the shadow region.) In Fig. 11, comparably excellent agreement is obtained for the z-directed current along  $\overline{abcd}$ , but only after incorporation of an a priori edge-correction term in the MoM code [32] to enable it to properly model the current singularities at the cube corners  $b$  and  $c$ .

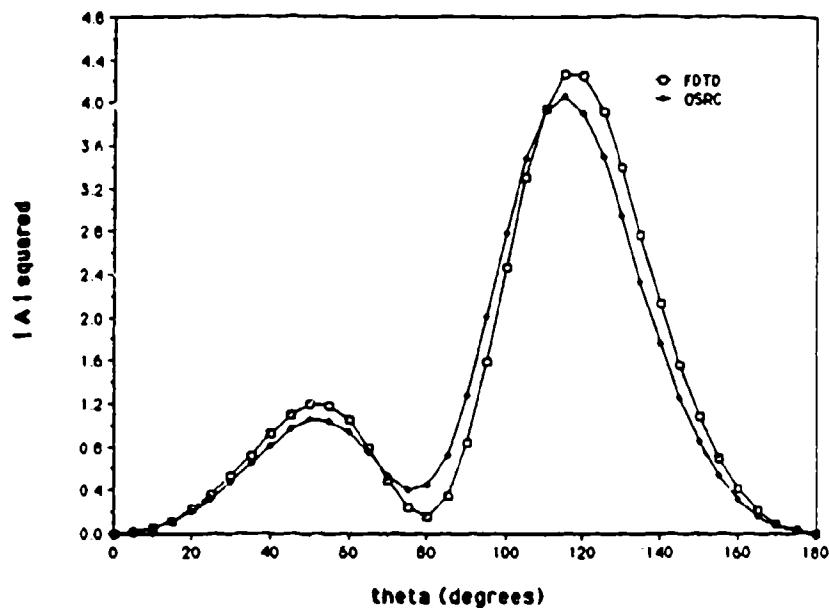


Fig. 9. Comparison of FD-TD and modal/OSRC approximate solution for bistatic radar cross section due to induced aperture field distribution of flanged open cavity [20], [31].

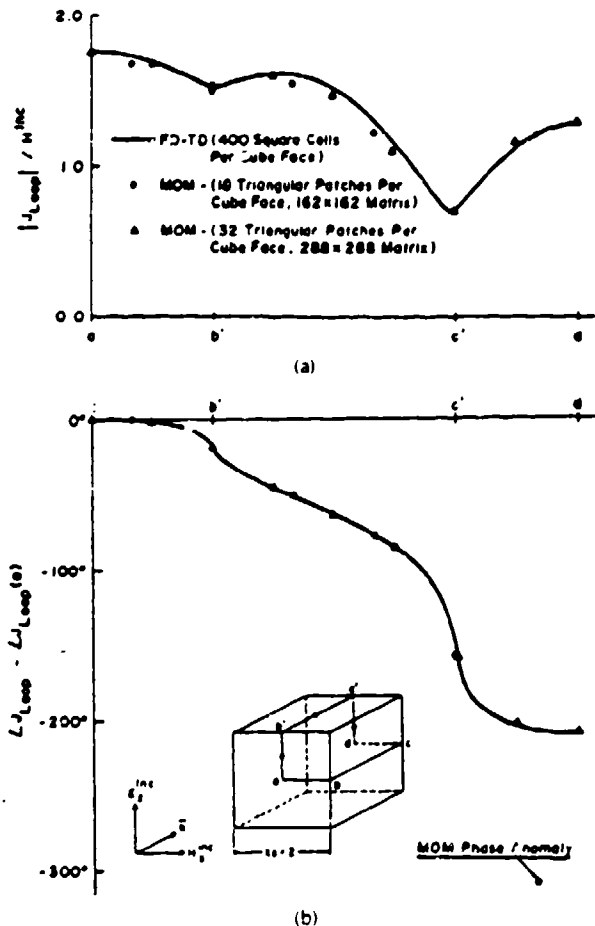


Fig. 10. Comparison of FD-TD and EFIE-MoM results for surface electric current distribution induced along  $E$ -plane locus of a perfectly conducting cube of size  $k_0 s = 2$ . (a) Magnitude. (b) Phase [13].

#### B. Flat Conducting Plate, Multiple Monostatic Observations [14], [24]

We next consider a  $30 \times 10 \times 0.65$  cm flat conducting plate target. At 1 GHz, where the plate spans  $1 \times 1.3 \lambda_0$ , a comparison is made between FD-TD and MoM results for the monostatic RCS versus observation-angle (look-angle) azimuth, keeping the elevation angle fixed at  $90^\circ$  as shown in Fig. 12(a). Here the FD-TD model uses a uniform cell size of 0.625 cm ( $\lambda_0/48$ ), forming the plate by  $48 \times 16 \times 1$  cells. The radiation boundary is located at a uniform distance of only 8 cells from the plate surface. For the MoM model, a study of the convergence of the computed broadside RCS indicates that the plate thickness must be accounted for by using narrow side patches, and the space resolution of each patch should be finer than approximately  $0.2 \lambda_0$ . As a result, the MoM model forms the plate by  $10 \times 3 \times 1$  divisions, yielding a total of 172 triangular surface patches. Fig. 12(a) shows excellent agreement between the two models, within about  $\pm 0.2$  dB.

At 9 GHz, the plate spans  $9 \times 3 \lambda_0$ , and the use of the MoM model is virtually precluded because of its large computational burden. If we follow the convergence guidelines discussed, the plate would require approximately  $50 \times 15 \times 1$  divisions to properly converge, yielding a total of 3260 triangular surface patches and requiring the generation and inversion of a  $4890 \times 4890$  complex-valued system matrix. On the other hand, FD-TD remains feasible for the plate at 9 GHz. Choosing a uniform cell size of 0.3125 cm ( $\lambda_0/10.667$ ), the plate is formed by  $96 \times 32 \times 2$  cells. With the radiation boundary again located only 8 cells from the plate surface, the overall lattice size is  $112 \times 48 \times 18$ , containing 580 608 unknown field components (real numbers). Fig. 12(b) shows excellent agreement between the FD-TD results and measurements of the monostatic RCS versus look-angle azimuth performed in the anechoic chamber facility operated by SRI International. The observed agreement is within



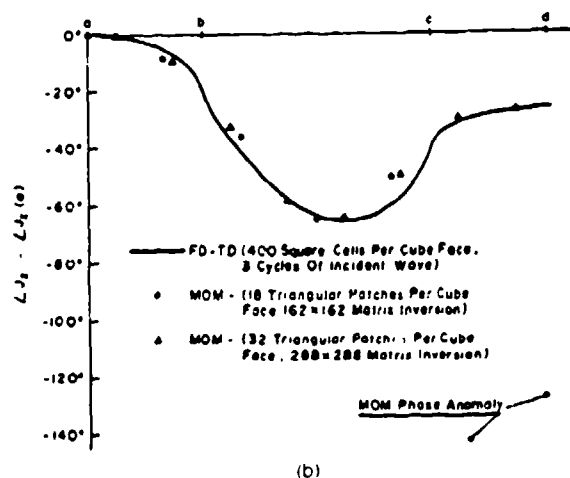
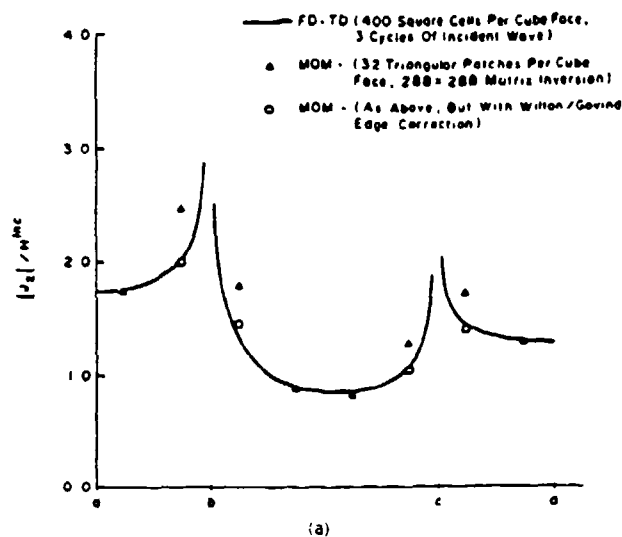


Fig. 11. Comparison of FD-TD and EFIE-MoM results for surface electric current distribution induced along  $H$ -plane locus of a perfectly conducting cube of size  $k_0 s = 2$ . (a) Magnitude. (b) Phase [13].

1 dB and  $1^\circ$  of look angle. As will be seen next, this level of agreement is maintained for more complicated three-dimensional targets having corner-reflector properties.

#### C. T-Shaped Target, Multiple Monostatic Observations [14], [24]

We last consider the monostatic RCS pattern of a crossed-plate target comprised of two flat conducting plates electrically bonded together to form the shape of a T. The main plate has the dimensions  $30 \times 10 \times 0.33$  cm and the "bisecting" fin has the dimensions  $10 \times 10 \times 0.33$  cm. (Due to a construction error, the centerline of the bisecting fin is actually positioned 0.37 cm to the right of the centerline of the main plate. This is accounted for in the FD-TD model.) The illumination is a 9.0-GHz plane wave at  $90^\circ$  elevation angle, polarized TE with respect to the main plate. Thus the entire T-shaped target spans  $9 \times 3 \times 3 \lambda_0$ . Note that monostatic RCS observations at azimuth angles  $\phi'$  between  $90^\circ$  and  $180^\circ$ , as defined in Fig. 13, are influenced by substantial

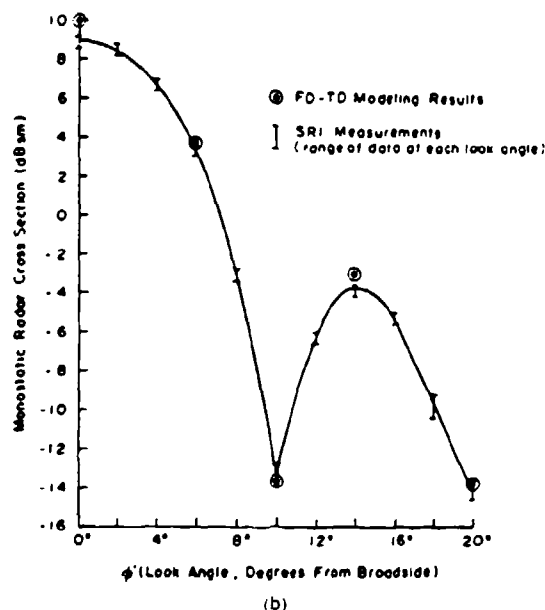
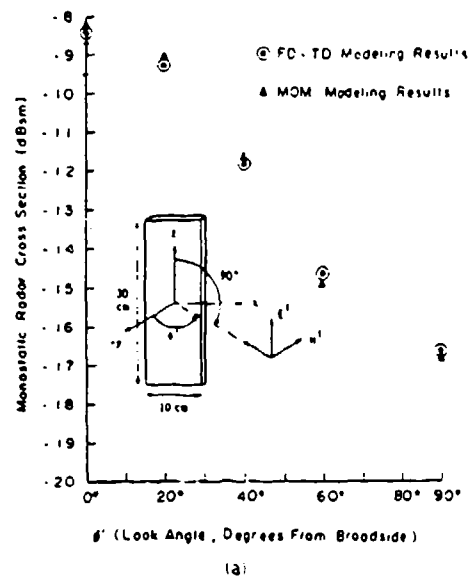


Fig. 12. Validation of FD-TD results for monostatic radar cross section of flat conducting plate. (a) Versus EFIE-MoM at 1 GHz (plate size  $1 \times 1/3$  wavelength). (b) Versus SRI measurements at 9 GHz (plate size  $9 \times 3$  wavelengths) [14], [24].

corner reflector physics. This is complicated by the fact that the sides of the corner reflector have unequal lengths ( $3\lambda_0$  versus  $4.5\lambda_0$ ), and further the target is not simply a single corner reflector, but actually two corner reflectors, back to back.

For this target, the FD-TD model uses a uniform cell size of 0.3125 cm ( $\lambda_0/10.667$ ), forming the main plate by  $96 \times 32 \times 1$  cells and the bisecting fin by  $32 \times 32 \times 1$  cells. With the radiation boundary again located *only 8 cells* from the target's maximum surface extensions, the overall lattice size is  $112 \times 48 \times 48$  cells, containing 1 548 288 unknown field components, and encompassing a total volume of 212.6 cubic wavelengths. Starting with zero-field initial conditions, 661 time steps are used per monostatic observation

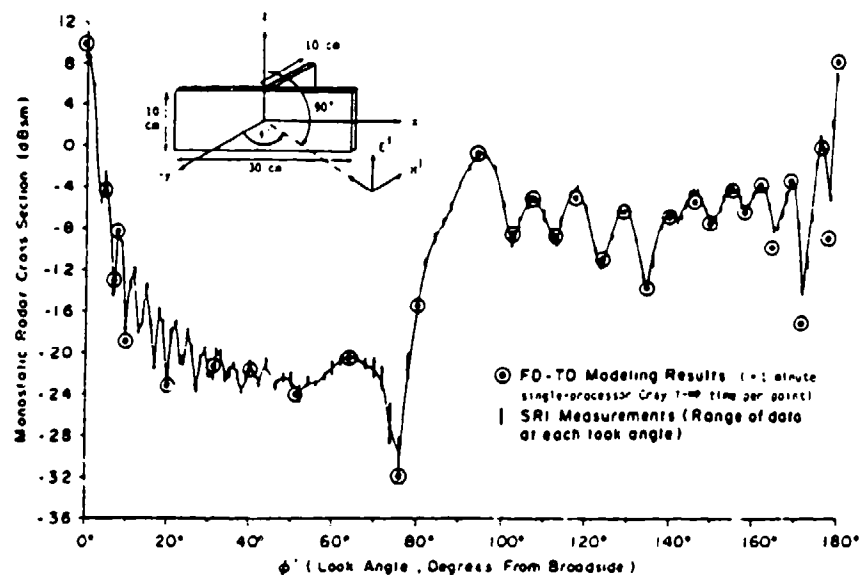


Fig. 13. Experimental validation of FD-TD modeling predictions of monostatic radar cross section versus azimuth for crossed-plate target at 9 GHz (main plate size  $9 \times 3$  wavelengths, bisecting fin size  $3 \times 3$  wavelengths) [14], [24].

to attain the sinusoidal steady state, equivalent to 31 cycles of the incident wave at 9.0 GHz.

Fig. 13 compares the FD-TD predicted monostatic RCS values at 32 key look-angle azimuths between  $0^\circ$  and  $180^\circ$  with measurements performed by SRI International. These azimuths are selected to define the major peaks and nulls of the monostatic RCS pattern. It is seen that the agreement is again excellent: in amplitude, within about 1 dB over a total RCS-pattern dynamic range exceeding 40 dB; and in azimuth, within  $1^\circ$  in locating the peaks and nulls of the RCS pattern. Note especially the fine agreement for azimuths greater than  $90^\circ$ , where the asymmetrical corner reflector induces an enhancement of the monostatic RCS response with substantial fine-grained detail in the RCS pattern. As of the publication of [14], this case (and similar cases studied in [24]) represented the largest detailed three-dimensional numerical scattering models of any type ever verified wherein a uniformly fine spatial resolution and the ability to treat nonmetallic composition are incorporated in the model.

#### VI. POTENTIAL OF FD-TD FOR MODELING VERY COMPLEX OBJECTS

Two characteristics of FD-TD cause it to be very promising for numerical modeling of electromagnetic wave interactions with very complex objects. 1) Dielectric and permeable media can be specified independently for each electric and magnetic field vector component in the three-dimensional volume being modeled. Since there may be tens of millions of such vector components in large FD-TD models, inhomogeneous media of enormous complexity can be specified in principle. 2) The required computer resources for this type of detailed volumetric modeling are dimensionally low, only of order  $N$ , where  $N$  is the number of space cells in the FD-TD lattice.

The emergence of supercomputers has recently permitted FD-TD to be seriously applied to a number of very com-

plex electromagnetic wave interaction problems. Two of these are reviewed briefly.

#### A. UHF Penetration into a Complex Missile Seeker Section [5], [7]

Here FD-TD is applied to model the penetration of an axially incident 300-MHz plane wave into a metal-coated missile guidance section. The FD-TD model, shown in Fig. 14, contains the following elements: 1) magnesium fluoride infrared dome, 2) fiberglass nose cone and its external metal coating, 3) circular nose aperture just back of the infrared dome, 4) head coil assembly, 5) cooled detector unit with enclosing phenolic ring, 6) preamplifier can, 7) wire bundle connecting the cooled detector unit to the preamplifier can, 8) wire bundle connecting the preamplifier can to the metal backplane, 9) longitudinal metal support rods, and 10) circumferential sleeve-fitting aperture, loaded with fiberglass, where the seeker section joins the thruster. The fiberglass structure of the nose cone and its metalization are approximated in a stepped-surface manner, as is the infrared dome.

For this target, the FD-TD model uses a uniform cell size of  $1/3$  cm ( $\lambda_0/300$ ), with an overall lattice size of  $100 \times 48 \times 24$  cells containing 690 000 unknown field components. (A single symmetry plane is used, giving an effective lattice size of  $100 \times 48 \times 48$ .) The model, implemented on a Control Data STAR-100 (the available supercomputer at the time), was run for 1800 time steps, equivalent to 3.0 cycles of the incident wave at 300 MHz.

Fig. 15 plots contour maps of the FD-TD computed field vector components at the symmetry plane of the model. An important observation is that the wire bundles connecting the cooled detector unit, preamplifier can, and metal backplane are paralleled by high-level magnetic field contours [Fig. 15(b)]. This is indicative of substantial uniform current flow along each bundle. Such current flow would generate locally a magnetic field looping around the wire bundle

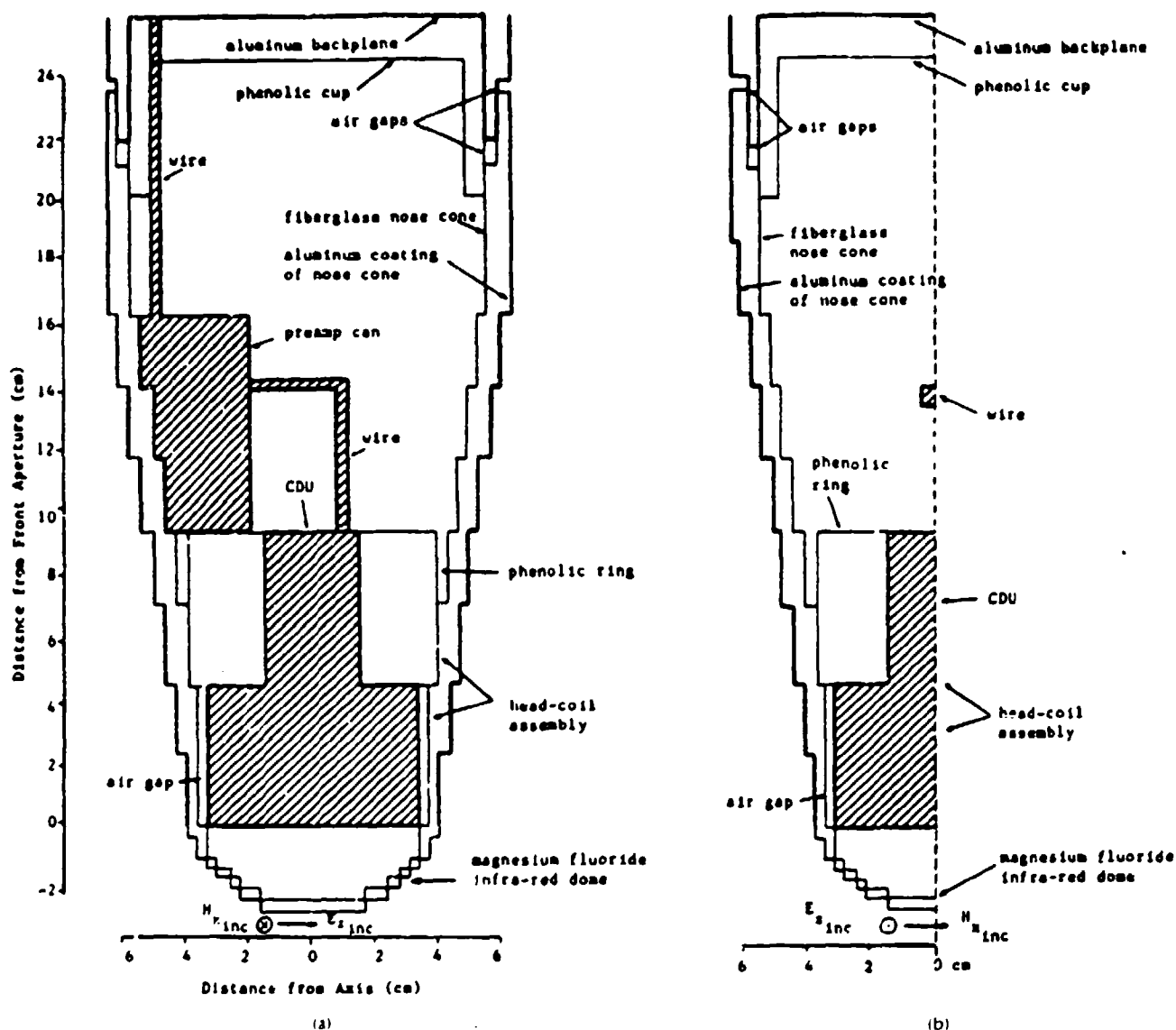


Fig. 14. Three-dimensional FD-TD model of missile seeker section showing component materials. (a) At vertical symmetry plane. (b) At horizontal observation plane [5], [7].

which, when "cut" by the symmetry plane, shows up as parallel field contours spaced equally on each side of the bundle. Using a simple Ampère's law argument, the common-mode bundle currents can be calculated, thus obtaining a key transfer function between free-field incident UHF plane-wave power density and coupled wire currents within the loaded seeker section [5]. This transfer function is useful for studies of intersystem electromagnetic compatibility and vulnerability to high-power microwaves.

Although this missile seeker model was structured to demonstrate the capability of FD-TD to map fields penetrating into a complex structure having multiple apertures and realistic internal engineering details, it should be understood that the full bistatic RCS pattern of the target is available as a "by-product" with virtually no additional effort. Further, with the 1.3-cm space resolution used, the FD-TD penetration/RCS model discussed is useful up to 9 GHz.

#### B. Whole-Body Human Dosimetry at VHF and UHF Frequencies [33], [34]

Here FD-TD is applied to model the penetration of plane waves at VHF and UHF frequencies into the entire human body. Directly exploiting the ability of FD-TD to model media inhomogeneities down to the space-cell level, highly realistic three-dimensional FD-TD tissue models of the complete body have been constructed. Specific electrical parameters are assigned to each of the electric field vector components at the 16 000 to 40 000 space cells comprising the body model. Assignments are based on detailed cross-section tissue maps of the body (as obtained via cadaver studies available in the medical literature), and cataloged measurements of tissue dielectric properties. Uniform FD-TD space resolutions as fine as 1.3 cm throughout the entire human body have proven feasible with the Cray-2 supercomputer.

Fig. 16, taken from [34], shows the FD-TD computed con-

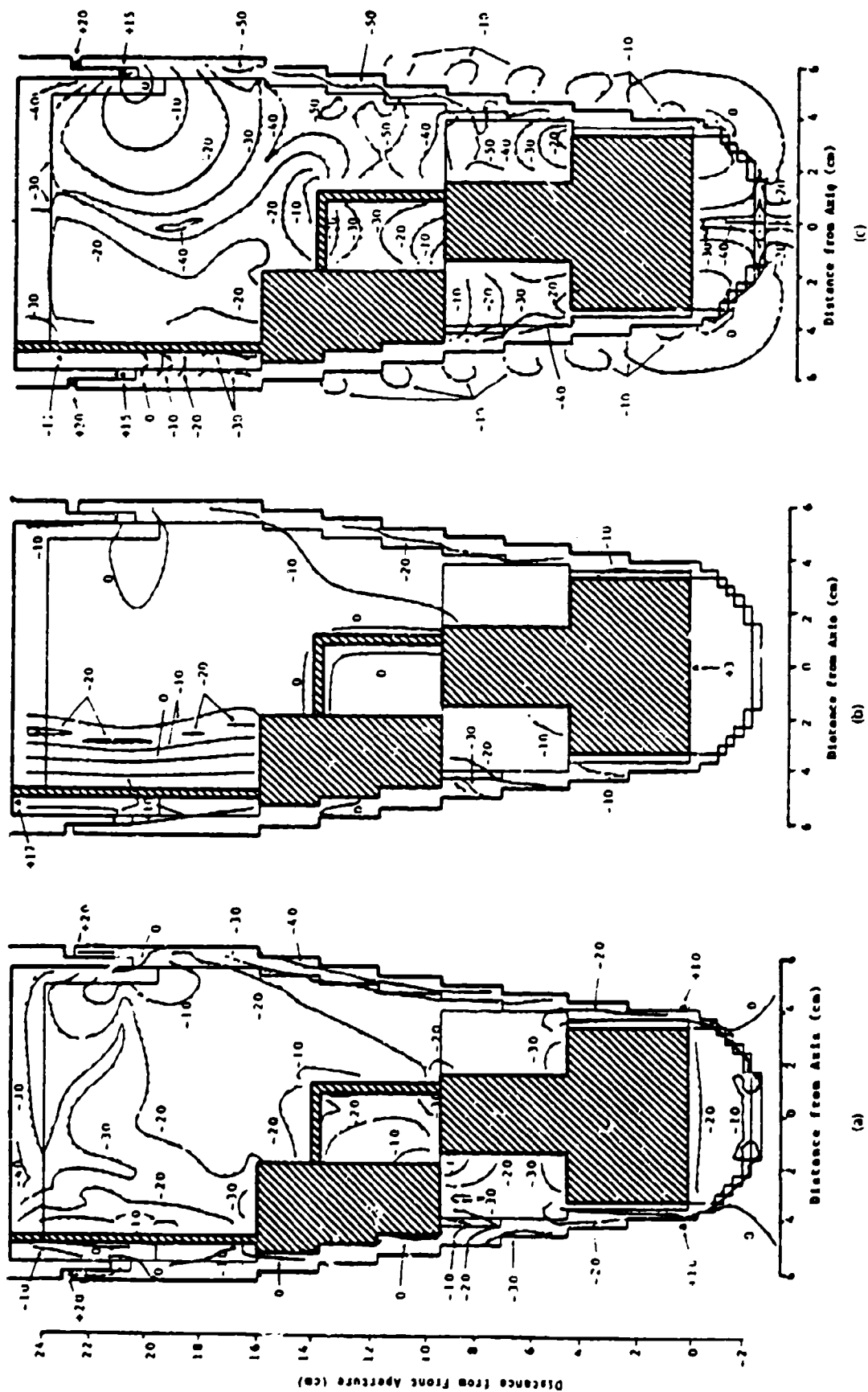


Fig. 15. FD-TD computed contour maps of penetrating field vector components in vertical symmetry plane of missile seeker section of Fig. 14. (a)  $E_z$ , (b)  $H_z$ , (c)  $H_x$ , [51, 57].

four maps of the specific absorption rate (SAR) distribution along horizontal cuts through the head and liver of the three-dimensional inhomogeneous human model. In Fig. 16(a) the incident wave has a power density of  $1 \text{ mW/cm}^2$  at 350 MHz, while in Fig. 16(b) the incident wave has the same power density but is at 100 MHz. These contour maps

illustrate the high level of detail of local features of the SAR distribution that is possible via FD-TD modeling for highly realistic tissue models. By implication, these results also show the applicability of FD-TD modeling to ultracomplex electromagnetic wave-absorbing media for RCS mitigation technology.

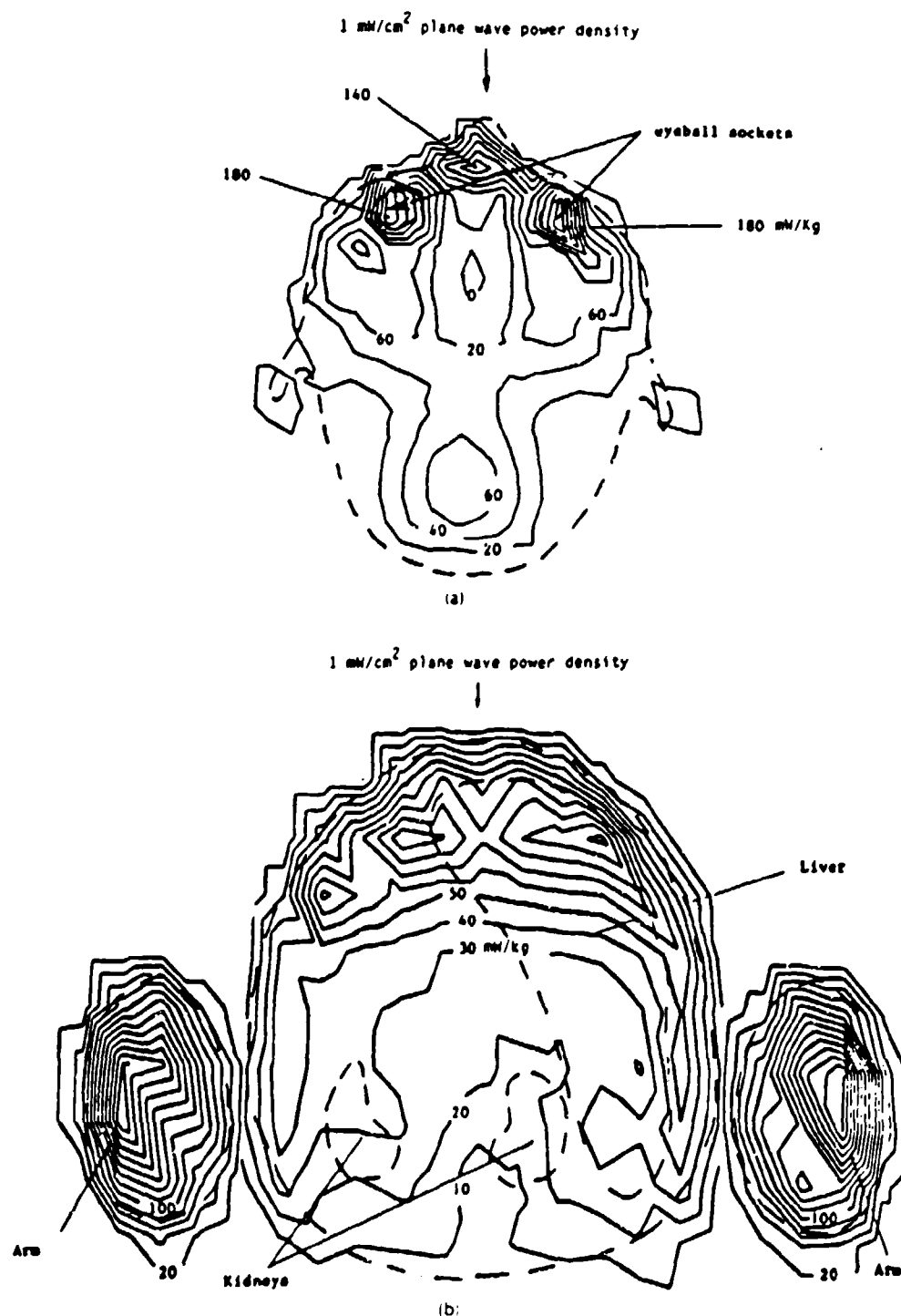


Fig. 16. FD-TD computed contour maps of specific absorption rate (SAR) due to penetrating electromagnetic fields within a highly realistic three-dimensional model of the entire human body. (a) Along horizontal cut through head at 350 MHz. (b) Along horizontal cut through liver at 100 MHz [34].

The FD-TD method is naturally suited for large-scale processing by state-of-the-art vector supercomputers and concurrent processors. This is because essentially all of the arithmetic operations involved in a typical FD-TD run can be vectorized or cast into a highly concurrent format. Further, the order( $N$ ) demand for computer memory and clock cycles (where  $N$  is the number of lattice space cells) is dimensionally low and permits three-dimensional FD-TD models of arbitrary targets spanning 50-100  $\lambda_0$  to be anticipated in the early 1990s.

#### A. Cray-Based Processing

Let us now consider running times of present FD-TD codes implemented on Cray supercomputers. Table 5 lists running times for modeling one monostatic RCS obser-

Table 5. Running Times of Present FD-TD Codes for  $9 \times 3 \times 3 \lambda_0$  T-Shaped Target

Machine	Running Time
VAX 11/780 (no floating-point accelerator)	40 hours
Cray-2 (single processor, using VAX Fortran code)	12 minutes
Cray-2 (single processor, some code optimization)	2 minutes
Cray Y-MP (single processor, optimized code)	72 seconds
Cray Y-MP (eight processors)	9 seconds
Cray-3 (sixteen processors)	3 seconds (est.)

- 1) 1.33-million unknown field components, 661 time steps
- 2) Complete time history of the near field is computed, from zero-field initial conditions to the sinusoidal steady state
- 3) Complete bistatic RCS pattern is obtained for a single illumination angle at a single frequency
- 4) Running times are increased by 50-100% if an impulsive excitation with fast Fourier transform is used to obtain the bistatic RCS pattern at a multiplicity of frequencies within the spectrum of the impulsive illumination

vation of the  $9 \times 3 \times 3 \lambda_0$  T-shaped target discussed in Section V-C. (Recall that this model involves an overall lattice volume of 212.6 cubic wavelengths containing 1 548 288 unknown field vector components time-stepped from zero-field initial conditions to the sinusoidal steady state over 661 time steps.) Five computing systems are listed in the table. The first is the Digital Equipment VAX 11/780 without floating-point accelerator. The second is a single processor of the Cray-2, using the VAX Fortran code either directly or after some optimization to take advantage of the vectorization and memory capabilities of the Cray-2. The third and fourth are, respectively, single-processor and eight-processor versions of the Cray Y-MP, using optimized Fortran.<sup>2</sup> The fifth is the 16-processor Cray-3, scheduled for initial usage in late 1989. (Running time for this case is estimated.)

Table 5 reveals an extraordinary reduction of FD-TD running time per monostatic RCS observation that has occurred

<sup>2</sup>Multiprocessing on the Cray Y-MP can be trivially accomplished for this (now) relatively small target by simultaneously placing eight individual processes, each representing one monostatic observation angle, on the eight individual processors of the machine. For the much larger targets of current and future interest, this procedure will not work because of memory conflicts between processors. Such targets will require only a single FD-TD process to be run on the machine, with the computational burden for this one process shared by the available processors. Analogous statements can be made for the 16 processor Cray-3.

during the past few years. Simple extrapolation of the Cray-3 running time indicated in the table to 50- $\lambda_0$  class three-dimensional targets containing on the order of 100 000 cubic wavelengths indicates essential feasibility with no further improvements in Cray technology beyond the Cray-3. It is clear that succeeding generations of such machines in the 1990s and beyond will permit routine engineering usage of FD-TD for modeling general electromagnetic wave interactions (including RCS) involving electrically large structures.

#### B. The Connection Machine

An interesting prospect that has recently arisen is the reduction of the order( $N$ ) computational burden of FD-TD to order( $N^{1/3}$ ). This possibility is a consequence of the appearance of the Connection Machine (CM), which has tens of thousands of simple processors and associated bit-wise memories arranged in a highly efficient manner for processor-to-processor communication. With the CM, a single processor could be assigned to store and time-step a single row of vector field components in a three-dimensional FD-TD space lattice. For example, 1 500 000 processors would be sufficient to store the six Cartesian components of  $E$  and  $H$  for each of the  $500 \times 500$  rows of a cubic lattice spanning 50  $\lambda_0$  (assuming 10 cells/ $\lambda_0$  resolution). FD-TD time stepping would be performed via row operations mapped onto the individual CM processors. These row operations would be performed concurrently. Thus for a fixed number of time steps, the total running time would be proportional to the time needed to perform a single row operation, which in turn would be proportional to the number of field vector components in the row, or order( $N^{1/3}$ ).

For the 50- $\lambda_0$  cubic lattice noted above, this would imply a dimensional reduction of the computational burden from order( $500^3$ ) to order(500), a tremendous benefit. As a result, it is conceivable that a suitably scaled CM could model one monostatic RCS observation angle of a 50- $\lambda_0$  three-dimensional target in only a few seconds, achieving effective floating-point rates on the order of 100 gigatlops (10 or more complete Cray-3s). For this reason, FD-TD algorithm development for the CM is a promising area of research for developing ultralarge numerical models of general electromagnetic wave interactions, including RCS.

#### VIII. CONCLUSION

This paper has presented a number of two- and three-dimensional examples of FD-TD numerical modeling of electromagnetic wave scattering and penetration. The objects modeled ranged in nature from simple geometric shapes to extremely complex aerospace and biological systems. In all cases studied to date where rigorous analytical, code-to-code, or experimental validations were possible, FD-TD predictive data for near fields and RCS were in excellent agreement with the benchmark data. With continuing advances in FD-TD modeling theory for target features relevant to the RCS problem, and with continuing advances in vector- and concurrent-processing supercomputer technology, it is likely that FD-TD numerical modeling will occupy an important place in RCS technology in the 1990s and beyond as the need for detailed models of three-dimensional complex material structures spanning 50  $\lambda_0$  or more becomes critical.

# REFERENCES

- [1] K. S. Yee, "Numerical solution of initial boundary value problems involving Maxwell's equations in isotropic media," *IEEE Trans. Antennas Propagat.*, vol. AP-14, pp. 302-307, May 1966.
- [2] A. Taflové and M. E. Brodwin, "Numerical solution of steady-state electromagnetic scattering problems using the time-dependent Maxwell's equations," *IEEE Trans. Microwave Theory Tech.*, vol. MTT-23, pp. 623-630, Aug. 1975.
- [3] G. A. Kriegsmann, "Exploiting the limiting amplitude principle to numerically solve scattering problems," *Wave Motion*, vol. 4, pp. 371-380, 1982.
- [4] A. Taflové and M. E. Brodwin, "Computation of the electromagnetic fields and induced temperatures within a model of the microwave-irradiated human eye," *IEEE Trans. Microwave Theory Tech.*, vol. MTT-23, pp. 888-896, Nov. 1975.
- [5] A. Taflové and K. R. Umashankar, "Evaluation of time-domain electromagnetic coupling techniques: vol. I: Theory and numerical results," Rome Air Development Center, Griffiss AFB, NY, Final Rep. RADC-TR-80-251, Contract F30602-79-C-0039, Apr. 1980.
- [6] A. Taflové, "Application of the finite-difference time-domain method to sinusoidal steady state electromagnetic penetration problems," *IEEE Trans. Electromag. Compat.*, vol. EMC-22, pp. 191-202, Aug. 1980.
- [7] A. Taflové and K. R. Umashankar, "A hybrid moment method/finite-difference time-domain approach to electromagnetic coupling and aperture penetration into complex geometries," *IEEE Trans. Antennas Propagat.*, vol. AP-30, pp. 617-627, July 1982.
- [8] R. Holland, "Threede: A free-field EMP coupling and scattering code," *IEEE Trans. Nuclear Sci.*, vol. NS-24, pp. 2416-2421, Dec. 1977.
- [9] K. S. Kunz and K. M. Lee, "A three-dimensional finite-difference solution of the external response of an aircraft to a complex transient EM environment. Part I—The method and its implementation," *IEEE Trans. Electromag. Compat.*, vol. EMC-20, pp. 328-333, May 1978.
- [10] D. E. Meriwether, R. Fisher, and F. W. Smith, "On implementing a numeric Huygen's source scheme in a finite-difference program to illuminate scattering bodies," *IEEE Trans. Nuclear Sci.*, vol. NS-27, pp. 1819-1833, Dec. 1980.
- [11] G. Mur, "Absorbing boundary conditions for the finite-difference approximation of the time-domain electromagnetic field equations," *IEEE Trans. Electromag. Compat.*, vol. EMC-23, pp. 377-382, Nov. 1981.
- [12] K. R. Umashankar and A. Taflové, "A novel method to analyze electromagnetic scattering of complex objects," *IEEE Trans. Electromag. Compat.*, vol. EMC-24, pp. 397-405, Nov. 1982.
- [13] A. Taflové and K. R. Umashankar, "Radar cross section of general three-dimensional scatterers," *IEEE Trans. Electromag. Compat.*, vol. EMC-25, pp. 433-440, Nov. 1983.
- [14] A. Taflové, K. R. Umashankar, and T. G. Jurgens, "Validation of FD-TD modeling of the radar cross section of three-dimensional structures spanning up to nine wavelengths," *IEEE Trans. Antennas Propagat.*, vol. AP-33, pp. 662-666, June 1985.
- [15] B. Engquist and A. Majda, "Absorbing boundary conditions for the numerical simulation of waves," *Math. Comp.*, vol. 31, pp. 629-651, July 1977.
- [16] G. A. Kriegsmann and C. Morawetz, "Solving the Helmholtz equation for exterior problems with variable index of refraction: I," *SIAM J. Sci. Stat. Comput.*, vol. 1, pp. 371-385, Sept. 1980.
- [17] A. Bayliss and E. Turkel, "Radiation boundary conditions for wave-like equations," *Commun. Pure Appl. Math.*, vol. 33, pp. 707-725, 1980.
- [18] L. N. Trefethen and L. Halpern, "Well-posedness of one-way wave equations and absorbing boundary conditions," *Inst. Computer Applications in Science and Engineering (ICASE), NASA Langley Research Center, Hampton, VA, Rep. 85-30*, June 1985.
- [19] J. C. Blaschak and G. A. Kriegsmann, "A comparative study of absorbing boundary conditions," *J. Comp. Phys.*, vol. 77, pp. 109-139, July 1988.
- [20] J. C. Blaschak, "Radiation boundary conditions: I. Absorbing boundary conditions for electromagnetic wave propagation; II. Application to on-surface radiation condition analysis of canonical reentrant structures," Ph.D. dissertation, Dep. Elec. Eng. and Comput. Sci., Northwestern University, Evanston, IL, Aug. 1988.
- [21] J. Fang and K. K. Mei, "A super-absorbing boundary algorithm for solving electromagnetic problems by time-domain finite-difference method," in *Proc. 1988 IEEE AP-S Int. Symp. (Syacuse, NY, June 1988)*, pp. 472-475.
- [22] D. T. Borup, D. M. Sullivan, and O. P. Gandhi, "Comparison of the FFT conjugate gradient method and the finite-difference time-domain method for the 2-D absorption problem," *IEEE Trans. Microwave Theory Tech.*, vol. MTT-35, pp. 383-395, Apr. 1987.
- [23] B. Beker, K. R. Umashankar, and A. Taflové, "Numerical analysis and validation of the combined field surface integral equations for electromagnetic scattering by arbitrary shaped two-dimensional anisotropic objects," *IEEE Trans. Antennas Propagat.*, vol. 37, Nov. 1989 (in press).
- [24] A. Taflové and K. R. Umashankar, "Analytical models for electromagnetic scattering," *Electromag. Sci. Div., Rome Air Development Center, Hanscom AFB, MA, Final Rep. RADC-TR-85-87, Contract F19628-82-C-0140*, May 1985.
- [25] K. R. Umashankar, A. Taflové, and B. Beker, "Calculation and experimental validation of induced currents on coupled wires in an arbitrary shaped cavity," *IEEE Trans. Antennas Propagat.*, vol. AP-35, pp. 1248-1257, Nov. 1987.
- [26] N. K. Madsen and R. W. Ziolkowski, "Numerical solution of Maxwell's equations in the time domain using irregular non-orthogonal grids," *Wave Motion*, vol. 10, pp. 583-596, Dec. 1988.
- [27] A. Taflové, T. G. Jurgens, T. G. Moore, and K. R. Umashankar, "FD-TD conformal modeling of smoothly curved targets," submitted to *IEEE Trans. Antennas Propagat.*
- [28] M. Fusco, "FD-TD algorithm in curvilinear coordinates," submitted to *IEEE Trans. Antennas Propagat.*
- [29] V. Shankar and W. Hall, "A time-domain differential solver for electromagnetic scattering problems," *Proc. IEEE*, vol. 77, this issue.
- [30] B. J. McCartin and J. F. DiCello, "Three-dimensional finite difference frequency domain scattering computations using the control region approximation," *IEEE Trans. Magn.*, vol. MAG-25, July 1989 (in press).
- [31] J. C. Blaschak, G. A. Kriegsmann, and A. Taflové, "A study of wave interactions with flanged waveguides and cavities using the on-surface radiation condition method," *Wave Motion*, vol. 11, pp. 65-76, Mar. 1989.
- [32] D. R. Wilton and S. Govind, "Incorporation of edge conditions in moment method solutions," *IEEE Trans. Antennas Propagat.*, vol. AP-25, pp. 845-850, Nov. 1977.
- [33] D. M. Sullivan, D. T. Borup, and O. P. Gandhi, "Use of the finite-difference time-domain method in calculating EM absorption in human tissues," *IEEE Trans. Biomed. Eng.*, vol. BME-34, pp. 148-157, Feb. 1987.
- [34] D. M. Sullivan, O. P. Gandhi, and A. Taflové, "Use of the finite-difference time-domain method in calculating EM absorption in man models," *IEEE Trans. Biomed. Eng.*, vol. 35, pp. 179-186, Mar. 1988.



Allen Taflové (Senior Member, IEEE) was born in Chicago, IL, on June 14, 1949. He received the B.S. (with highest distinction), M.S., and Ph.D. degrees in electrical engineering from Northwestern University, Evanston, IL, in 1971, 1972, and 1975, respectively.

From 1975 to 1984 he was a staff member in the Electronics Division, IIT Research Institute, Chicago, IL, holding the positions of Associate Engineer, Research Engineer, and Senior Engineer. During this time he was principal investigator on a number of externally funded research programs, including five that contributed to the early development of the finite-difference time-domain (FD-TD) method for computational modeling of electromagnetic wave interactions with complex structures. He was also a key contributor to large-scale programs involving the

application of radio-frequency heating to produce oil in place (without mining) from deposits of oil shale, tar sand, and heavy oil; to accelerate oil production from slowly producing conventional wells; and to decontaminate large sections of the ground permeated with toxic chemical wastes. In this technical area, he has been awarded 10 U.S. patents to date. In 1984, he returned to Northwestern University where he is currently Professor of Electrical Engineering and Computer Science. He is actively pursuing large-scale computational modeling of linear and nonlinear electromagnetic wave phenomena. Additional research interests include inverse scattering/target synthesis, the new on-surface radiation condition (OSRC) theory, computational optics, and applications of the most recent vector and concurrent supercomputers to large-scale electromagnetic modeling.

Dr. Tailore is a member of Tau Beta Pi, Eta Kappa Nu, Sigma Xi, and Commission B of URSI. He is coauthor of the Best Paper at the 1983 IEEE International EMC Symposium, Washington, DC.

Korada Umashankar (Senior Member, IEEE) received the B.E. degree from Mysore University, India, in 1962, the M.E. degree from the Indian Institute of Science, Bangalore, in 1964, and the Ph.D. degree



from the Indian Institute of Science, Bangalore, in 1964, and the Ph.D. degree from the University of Mississippi, University, in 1974, all in electrical engineering.

From 1964 to 1969 he was Assistant Professor and Head of the Department of Electrical Engineering, College of Engineering, Karnatak University, Hubli, India. During 1974-1975 he was a Post-Doctoral Research Associate, and during 1975-1977 Assistant Professor of Electrical Engineering at the University of Mississippi. From 1977 to 1979 he was a National Research Council Visiting Fellow at the Air Force Weapons Laboratory, Kirtland AFB, NM, involved with simulator studies and electromagnetic transients. From 1979 to 1984 he was Senior Engineer in the Electronics Division, IIT Research Institute, Chicago, IL, involved with the development of numerical models for electromagnetic interaction with complex objects. At present he is Associate Professor of Electrical Engineering, University of Illinois at Chicago, Chicago. His primary research work has been in the development of analytical and mathematical techniques in electromagnetic theory, EMP/EMC interaction, and EM simulation studies.

Dr. Umashankar is a member of Sigma Xi, Eta Kappa Nu, AAAS, and Commission B of URSI.



# THE FINITE-DIFFERENCE TIME-DOMAIN (FD-TD) METHOD FOR NUMERICAL MODELING OF ELECTROMAGNETIC SCATTERING

Allen Taflov, Senior Member, IEEE  
Department of Electrical Engineering  
and Computer Science  
The Technological Institute  
Northwestern University  
Evanston, IL 60201

Korada R. Umashankar, Senior Member, IEEE  
Department of Electrical Engineering  
and Computer Science  
University of Illinois at Chicago  
P. O. Box 4348  
Chicago, IL 60680

## Abstract

This paper reviews recent applications of the finite-difference time-domain (FD-TD) numerical modeling approach for Maxwell's equations. FD-TD is very simple in concept and execution. However, it is remarkably robust, providing highly accurate modeling predictions for a wide variety of electromagnetic wave interaction problems. The objects modeled to date range from simple 2-D geometric shapes to extremely complex 3-D aerospace and biological systems. Rigorous analytical or experimental validations are provided for the canonical shapes, and it is shown that FD-TD predictive data for near fields and radar cross section (RCS) are in excellent agreement with the benchmark data. It is concluded that, with continuing advances in FD-TD modeling theory for target features relevant to the RCS problem, and with continuing advances in vector- and concurrent-processing supercomputer technology, it is likely that FD-TD numerical modeling will occupy an important place in RCS technology in the 1990's and beyond.

## 1. Introduction

Accurate numerical modeling of the radar cross section (RCS) of complex electrically-large objects is difficult. Typical structures have shapes, apertures, cavities, and material compositions or coatings which produce near fields that cannot be resolved into finite sets of modes or rays. Proper numerical modeling of such near fields requires sampling at sub-wavelength resolution to avoid aliasing of magnitude and phase information. The goal is to provide a self-consistent model of the mutual coupling of all of the electrically small regions (cells) comprising the structure, even if the structure spans tens of wavelengths in three dimensions.

A candidate numerical modeling approach for this purpose is the finite-difference time-domain (FD-TD) solution of Maxwell's curl equations. This approach is analogous to existing finite-difference solutions of fluid-flow problems encountered in computational aerodynamics in that the numerical model is based upon a direct solution of the governing partial differential equation. Yet, FD-TD is a non-traditional approach to numerical electromagnetic modeling, where frequency-domain approaches have dominated.

One of the goals of this paper is to demonstrate that recent advances in FD-TD modeling concepts and software implementation, combined with advances in computer technology, have expanded the scope, accuracy, and speed of FD-TD modeling to the point where it may be the preferred choice for certain types of scattering problems. With this in mind, this paper will succinctly review the following FD-TD numerical modeling applications dealing with electromagnetic scattering by canonical two- and three-dimensional targets:

- Circular dielectric/permeable cylinder, conformally modeled
- Metal cube, broadside incidence

- Three-dimensional T-shaped conducting target, monostatic RCS pattern
- Trihedral metal corner reflector, monostatic RCS pattern
  - Bare metal case
  - Coated with a commercially available three-layer radar absorbing material (RAM)

Each of these examples compares the FD-TD modeling results with other data obtained via analysis, alternative numerical procedures, or actual measurements. Numerous other examples, including models of non-canonical aerospace and biological structures of great complexity, are available in the references.

## 2. General Characteristics of FD-TD

As stated, FD-TD is a direct solution of Maxwell's time-dependent curl equations. It employs no potentials. Instead, it applies simple, second-order accurate central-difference approximations [1] for the space and time derivatives of the electric and magnetic fields directly to the respective differential operators of the curl equations. This achieves a sampled-data reduction of the continuous electromagnetic field in a volume of space, over a period of time. Space and time discretizations are selected to bound errors in the sampling process, and to insure numerical stability of the algorithm [2]. Electric and magnetic field components are interleaved in space to permit a natural satisfaction of tangential field continuity conditions at media interfaces. Overall, FD-TD is a marching-in-time procedure which simulates the continuous actual waves by sampled-data numerical analogs propagating in a data space stored in a computer. At each time step, the system of equations to update the field components is fully explicit, so that there is no need to set up or solve a system of linear equations, and the required computer storage and running time is proportional to the electrical size of the volume modeled.

Fig. 1a illustrates the time-domain wave tracking concept of the FD-TD method. A region of space within the dashed lines is selected for field sampling in space and time. At time = 0, it is assumed that all fields within the numerical sampling region are identically zero. An incident plane wave is assumed to enter the sampling region at this point. Propagation of the incident wave is modeled by the commencement of time-stepping, which is simply the implementation of the finite-difference analog of the curl equations. Time-stepping continues as the numerical analog of the incident wave strikes the modeled target embedded within the sampling region. All outgoing scattered wave analogs ideally propagate through the lattice truncation planes with negligible reflection to exit the sampling region. Phenomena such as induction of surface currents, scattering and multiple scattering, penetration through apertures, and cavity excitation are modeled time-step by time-step by the action of the curl equations analog. Self-consistency of these modeled phenomena is generally assured if their spatial

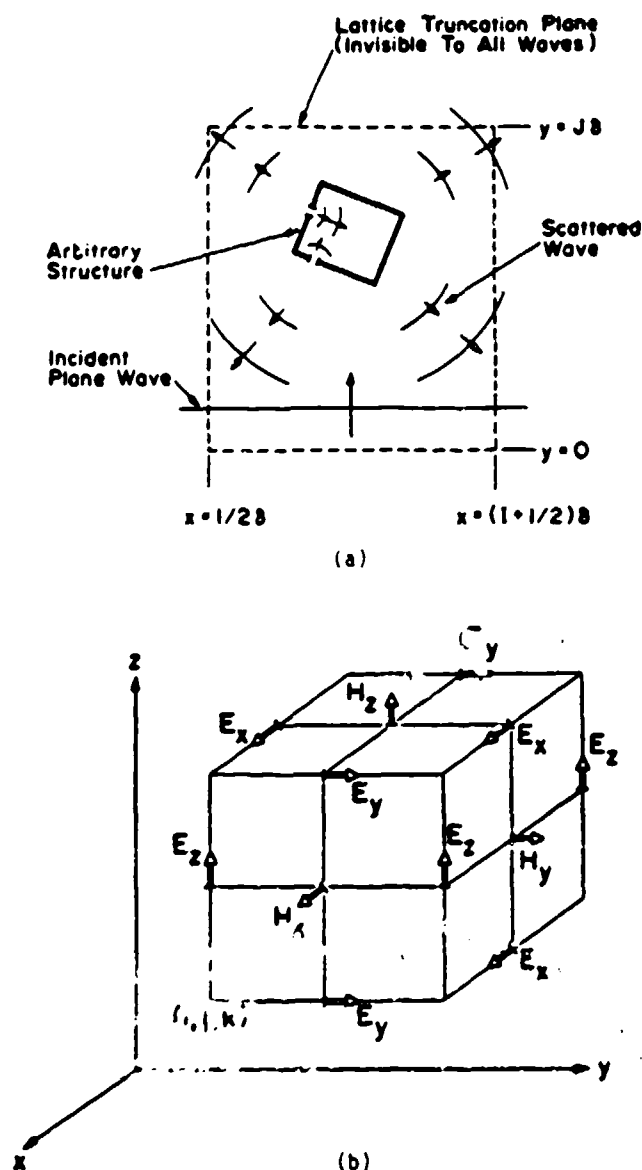


Fig. 1. Basic elements of the FD-TD space lattice: (a) time-domain wave tracking concept; (b) lattice unit cell in Cartesian coordinates [1].

and temporal variations are well resolved by the space and time sampling process.

Time-stepping is continued until the desired late-time pulse response or steady-state behavior is achieved. An important example of the latter is the sinusoidal steady state, wherein the incident wave is assumed to have a sinusoidal dependence, and time-stepping is continued until all fields in the sampling region exhibit sinusoidal repetition. This is a consequence of the limiting amplitude principle [3]. Extensive numerical experimentation with FD-TD has shown that the number of complete cycles of the incident wave required to be time-stepped to achieve the sinusoidal steady state is approximately equal to the Q factor of the structure or phenomenon being modeled.

Fig. 1b illustrates the positions of the electric and magnetic field components about a cubic lattice unit cell [1]. Note that each magnetic field vector component is surrounded by four circulating electric field

vector components, and vice versa. This arrangement permits not only a centered-difference analog to the space derivatives of the curl equations, but also a natural geometry for implementing the integral form of Faraday's Law and Ampere's Law at the space cell level. This integral representation permits a simple but effective modeling of the physics of smoothly curved target surfaces, as will be seen later.

Fig. 2 illustrates how an arbitrary three-dimensional scatterer is embedded in an FD-TD space lattice comprised of the unit cells of Fig. 1b. Simply, the desired values of electrical permittivity and conductivity are assigned to each electric field component of the lattice. Correspondingly, desired values of magnetic permeability and equivalent loss are assigned to each magnetic field component of the lattice. The media parameters are interpreted by the FD-TD program as local coefficients for the time-stepping algorithm. Specification of media properties in this component-by-component manner results in a stepped-edge approximation of curved surfaces. Continuity of tangential fields is assured at the interface of dissimilar media with this procedure. There is no need for special field matching at media interfaces. Stepped-edge approximation of curved surfaces has been found to be adequate in the FD-TD modeling problems studied in the 1970's and early 1980's, including wave interactions with biological tissues [4], penetration into cavities [5-7], and electromagnetic pulse interactions with complex structures [8-10]. However, recent interest in wide dynamic range models of scattering by curved targets has prompted the development of surface-conforming FD-TD approaches which eliminate staircasing. One such will be summarized later in this paper.

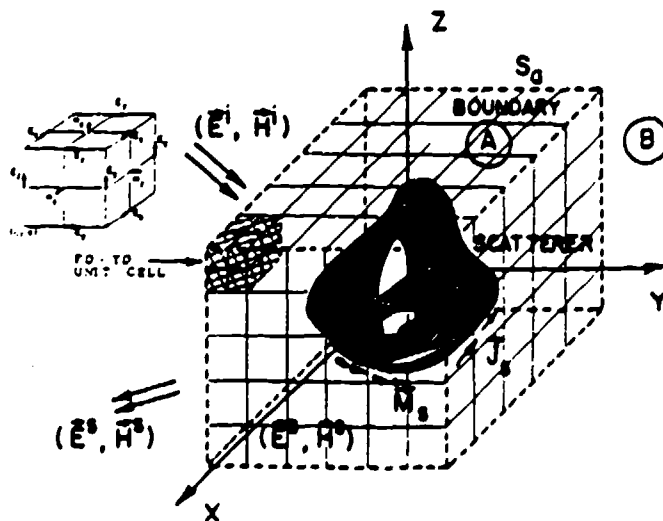


Fig. 2. Arbitrary 3-D scatterer embedded in the FD-TD space lattice.

Fig. 3a illustrates the division of the FD-TD lattice into total-field and scattered-field regions. This division has been found to be very useful since it permits the efficient simulation of an incident plane wave in the total-field region with arbitrary angle of incidence, polarization, time-domain waveform, and duration [11, 12]. Three additional important benefits arise from this lattice division, as follows:

a. A large near-field computational dynamic range is achieved since the scatterer of interest is embedded in the total-field region. Thus, low actual field levels

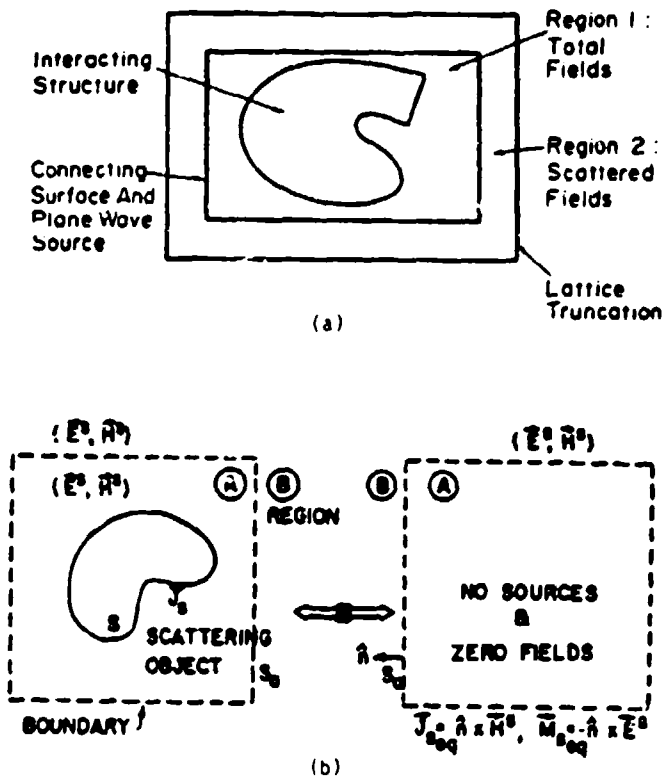


Fig. 3. Zoning of the FD-TD space lattice:  
(a) total-field and scattered-field regions [11, 12];  
(b) near-to-far field integration surface located  
in the scattered-field region [12].

in shadow regions or within shielding enclosures are computed directly without suffering subtraction noise (as would be the case if scattered fields in such regions were time-stepped via FD-TD, and then added to a canceling incident field to obtain the low total-field levels.)

b. Embedding the scatterer in the total-field region permits a natural satisfaction of tangential field continuity across media interfaces, as discussed earlier, without having to compute the incident field at possibly numerous points along a complex locus that is unique to each scatterer. The zoning arrangement of Fig. 3a requires computation of the incident field only along the rectangular connecting surface between the total-field and scattered-field regions. This surface is fixed, i.e., independent of the shape or composition of the enclosed scatterer being modeled.

c. The provision of a well-defined scattered-field region in the FD-TD lattice permits the near-to-far field transformation depicted in Fig. 3b. The dashed virtual surface shown here can be located along convenient lattice planes in the scattered-field region of Fig. 3a. Tangential scattered E and H fields computed via FD-TD at this virtual surface can then be weighted by the free-space Green's function and then integrated (summed) to provide the far-field response and RCS (full bistatic response for the assumed illumination angle) [12-14]. The near-field integration surface has a fixed rectangular shape, and thus is independent of the shape or composition of the enclosed scatterer being modeled.

Fig. 3a uses the term "lattice truncation" to designate the outermost lattice planes in the scattered-field region. The fields at these planes cannot be com-

puted using the centered-differencing approach because of the assumed absence of known field data at points outside of the lattice truncation. These data are needed to form the central differences. Therefore, an auxiliary lattice truncation condition is necessary. This condition must be consistent with Maxwell's equations in that an outgoing scattered-wave numerical analog striking the truncation must exit the lattice without appreciable non-physical reflection, just as if the lattice truncation was invisible.

It has been shown that the required lattice truncation condition is really a radiation condition in the near field [15-17]. A very successful second-order accurate finite-difference approximation of the exact radiation condition in Cartesian coordinates was introduced in [11]. This approximation was subsequently used in a variety of 2-D and 3-D FD-TD scattering codes [12-14], yielding excellent results for both near and far fields. (For example, all FD-TD results in this paper were obtained using this approximate radiation condition.) However, recent interest in wide dynamic range models of scattering has prompted research in the construction of even more accurate near-field radiation conditions, including fixed third-order accurate approximations [18, 19], adaptive conditions [20], and predictor-corrector conditions [21]. The goal here is to reduce the numerical lattice background noise due to non-physical reflections of wave analogs at the lattice truncations by at least 20 dB relative to that of [11].

### 3. Scattering Prediction for Canonical Targets

Analytical, code-to-code, and experimental validations have been obtained relative to FD-TD modeling of a wide variety of 2-D and 3-D structures [22]. Both convex and reentrant (cavity-type) shapes have been studied; and structure material compositions have included perfect conductors, homogeneous and inhomogeneous lossy dielectrics, and anisotropic dielectric and permeable media. Selected past and new validations will be reviewed here.

#### a. Circular Dielectric/Permeable Cylinder, Conformally Modeled

The interleaving of E and H field components in the FD-TD lattice permits the construction of generalized Faraday's Law and Ampere's Law contour paths which can be adjusted to exactly conform with a smoothly curved target surface. An example of this is shown in Fig. 4. In this manner, slightly modified time-stepping expressions for the field components at or adjacent to the target surface are derived from the integral form of Maxwell's equations. All other field components in the

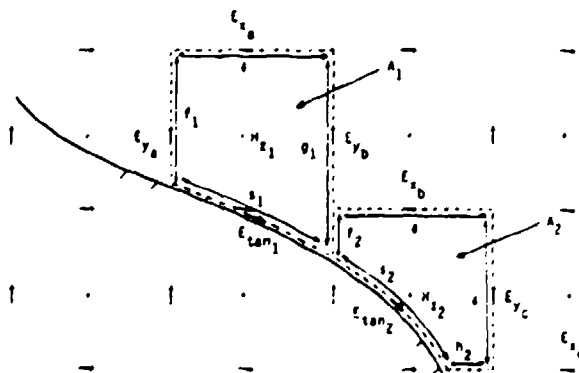


Fig. 4. Faraday's Law contour paths for conformal FD-TD modeling of a smoothly curved target, TE case

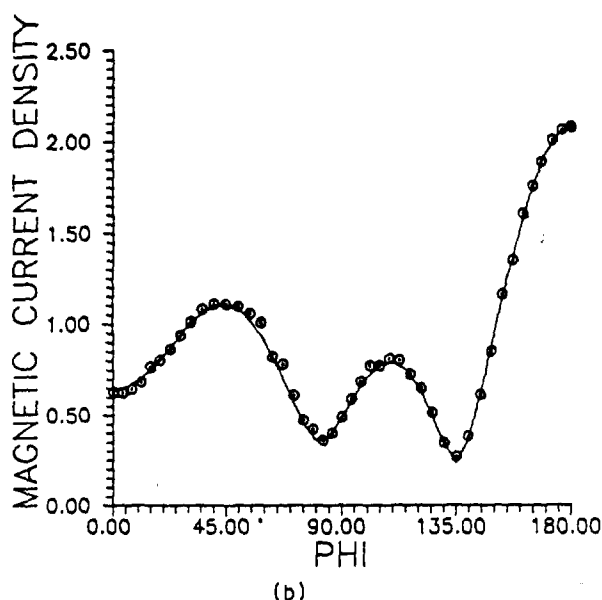
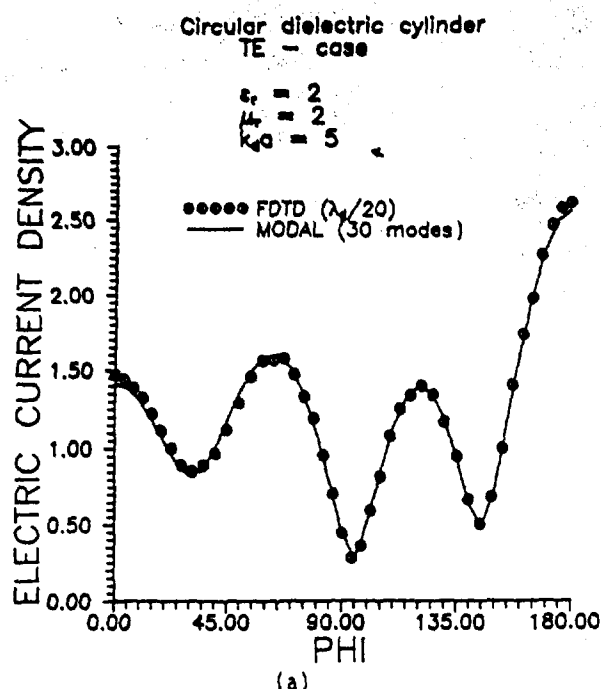


Fig. 5. Comparison of conformal FD-TD model and exact solution for TE illumination of a circular dielectric/permeable cylinder: (a) surface electric currents; (b) surface magnetic currents.

FD-TD lattice are time-stepped in the normal manner. In effect, only the space cells immediately adjacent to the target surface are deformed to conform with the surface.

The accuracy of the conformal FD-TD model is illustrated in Fig. 5. Here, a moderate-resolution Cartesian FD-TD grid (having  $1/20$  dielectric-wavelength cell size) is used to compute the surface electric and magnetic current distributions induced on a  $k_0 a = 5$  circular dielectric/permeable cylinder by a TE-polarized incident plane wave. Excellent agreement with the exact modal solution is seen. Note also that the computer running time for the conformal FD-TD model is essentially the same as for the old staircase FD-TD model since only a few field components immediately adjacent to the target

surface require a slightly modified time-stepping relation.

#### b. Metal Cube, Broadside Incidence [13]

Results are now shown for the FD-TD computed surface electric current distribution on a metal cube subject to plane-wave illumination at broadside incidence. The current distribution is compared to that computed by a standard frequency-domain, electric field integral equation (EFIE), triangular surface-patching, method of moments (MoM) code. It is shown that a very high degree of correspondence exists between the two sets of predictive data.

The detailed surface current study involves a metal cube of electrical size  $k_0 s = 2$ , where  $s$  is the side width of the cube. For the FD-TD model, each cube face is spanned by 400 square cells ( $20 \times 20$ ), and the radiation boundary is located at a uniform distance of 15 cells from the cube surface. For the MoM model, each cube face is spanned by either 18 or 32 triangular patches (to test its convergence). Fig. 6 graphs comparative results for the "looping" surface current along the E-plane locus  $ab'c'd$ . The FD-TD values agree with the high-resolution MoM data to better than  $\pm 2.5\%$  ( $\pm 0.2$  dB) in magnitude and  $\pm 1^\circ$  in phase at all comparison points.

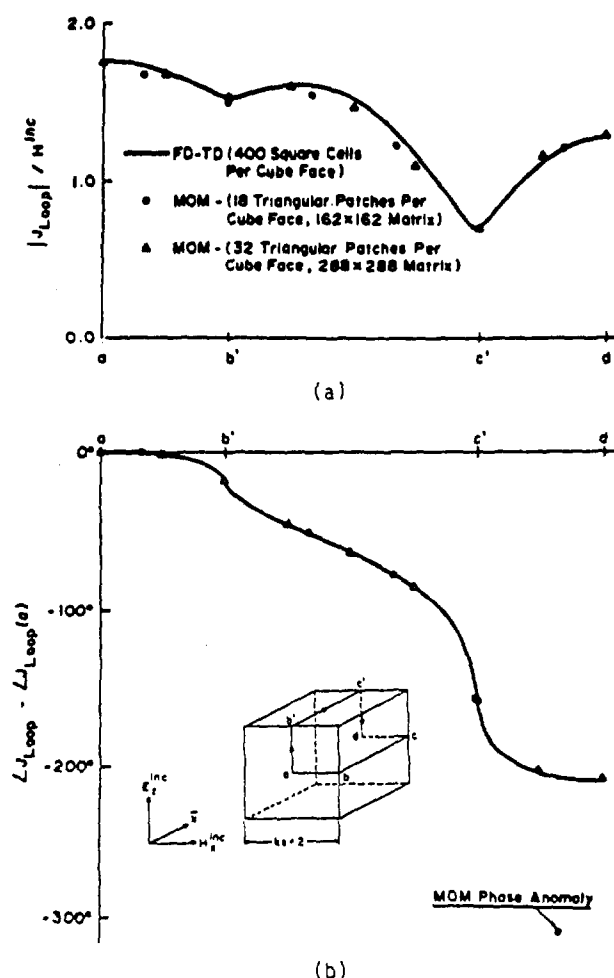


Fig. 6. Comparison of FD-TD and EFIE/MoM results for the "looping" surface electric current along the E-plane locus of a perfectly-conducting cube: (a) magnitude; (b) phase [13].

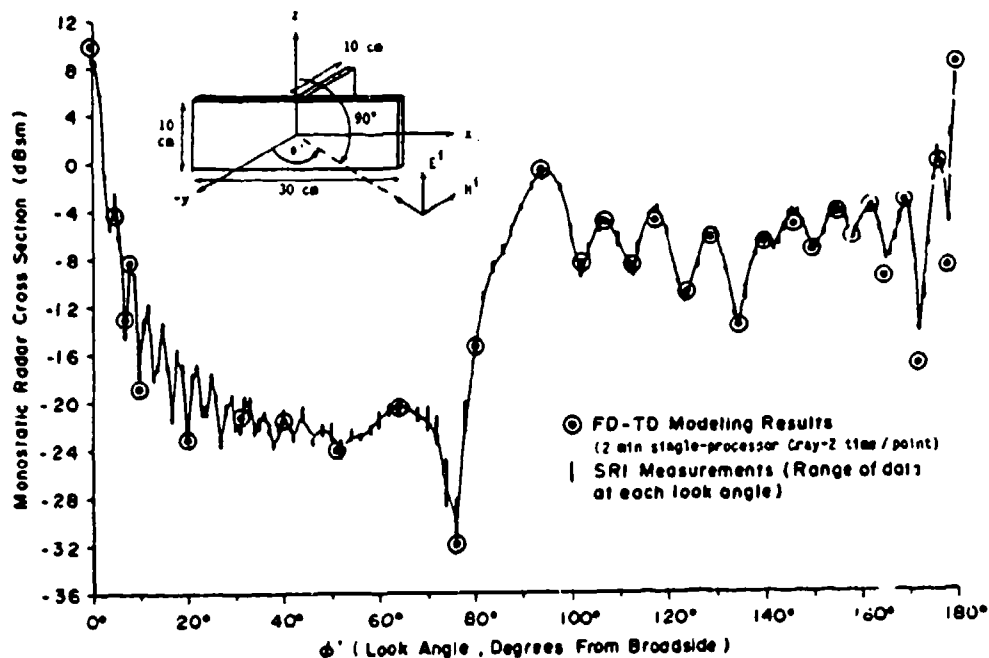


Fig. 7. Experimental validation of FD-TD modeling predictions of monostatic RCS vs. azimuth for the crossed-plate target at 9 GHz (main plate size =  $3 \times 9 \lambda_0$ , bisecting fin size =  $3 \times 3 \lambda_0$ ) [14, 22].

### c. Three-Dimensional T-Shaped Conducting Target [14, 22]

We next consider the monostatic RCS pattern of a T-shaped conducting target consisting of a  $10 \times 30 \times 0.33$  cm main plate and a  $10 \times 10 \times 0.33$  cm bisecting fin. The illumination is a 9.0-GHz plane wave at  $0^\circ$  elevation angle and TE polarization relative to the main plate. Thus, the main plate spans  $9.0 \lambda$ . Note that look angle azimuths (as defined in Fig. 7) between  $90^\circ$  and  $180^\circ$  provide substantial corner reflector physics in addition to the edge diffraction, corner diffraction, and other effects found for an isolated flat plate.

For this target, the FD-TD model uses a uniform cell size of  $0.3125$  cm ( $\lambda_0/10.667$ ), forming the main plate by

$32 \times 96 \times 1$  cells and the bisecting fin by  $32 \times 32 \times 1$  cells. The radiation boundary is located only 8 cells from the target's maximum surface extensions, so that the overall lattice size is  $48 \times 112 \times 48$  cells, containing 1,548,288 unknown field components (212.6 cubic wavelengths). Starting with zero-field initial conditions, 661 time steps are used, equal to 31 cycles of the incident wave.

Fig. 7 compares the FD-TD predicted monostatic RCS values at 32 key look angles with measurements performed by SRI International. These look angles are selected to define the major peaks and nulls of the monostatic RCS pattern. The agreement is excellent: in amplitude, within 1 dB over a 40-dB dynamic range; and in azimuth, within  $1^\circ$  in locating the pattern's peak and nulls.

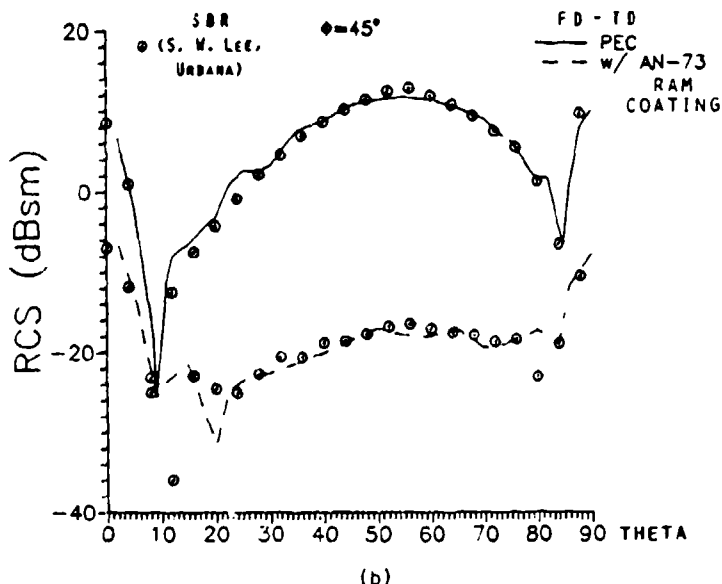
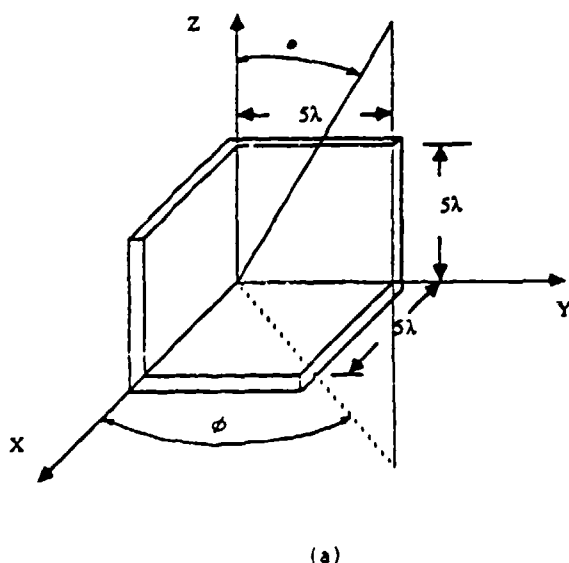


Fig. 8. Comparison of FD-TD and SDR results for the monostatic RCS vs. elevation angle of a trihedral corner reflector (both uncoated and with commercial RAM coating): (a) target geometry; (b) comparative RCS.

#### d. Trihedral Corner Reflector

We last consider the monostatic RCS pattern of a conducting trihedral corner reflector, both uncoated and with commercial radar absorbing material (RAM) coating. The reflector consists of three, thin, 15 x 15 cm flat plates mounted at mutual 90° angles, as shown in Fig. 8a. The illumination is a 10.0-GHz plane wave at 45° azimuth angle and  $\theta$ -directed E field. Thus, the reflector spans 5 x 5 x 5  $\lambda$ . For the coated case, the RAM is assumed to be Emerson & Cuming Type AN-73 (0.9525 cm thick, consisting of 3 distinct lossy layers of equal thickness).

For this target, the FD-TD model uses a uniform cell size of 0.25 cm ( $\lambda/12$ ), spanning each plate by 60 x 60 cells. The lattice radiation boundary is located only 12 cells from the target, so that the overall lattice size is 84 x 84 x 84 cells, containing 3,556,224 unknown field components (343 cubic wavelengths). Starting with zero-field initial conditions, 720 time steps are used, equal to 30 cycles of the incident wave.

Fig. 8b compares the FD-TD computed monostatic RCS pattern in the  $\theta$  plane ( $\phi$  fixed at 45°) with predictions made by a shooting and bouncing ray (SBR) code developed by Prof. S. W. Lee of the University of Illinois at Urbana. Excellent agreement is seen for the uncoated target case. For the RAM-coated case, both codes predict substantial reduction of the RCS response. It is seen that the predicted RCS patterns for this case are in good qualitative agreement.

#### 4. Potential for Modeling Ultra-Complex Targets

A graphic illustration of the potential of FD-TD for modeling structures comprised of ultra-complex electromagnetic wave absorbing media is provided by the whole-body dosimetry work reported by the University of Utah in [23]. Directly exploiting the ability of FD-TD to model media inhomogeneities down to the space-cell level, and fully utilizing the speed and memory capabilities of the Cray-2, highly realistic 3-D tissue models of the complete human body at a uniform space resolution in the order of 1 cm have been constructed for the first time. With capabilities of supercomputers expanding by at least one order of magnitude in the next decade, it is likely that FD-TD numerical modeling will occupy an important place in RCS technology in the 1990's and beyond.

#### Acknowledgement

This work was supported in part by ONR Contract N00014-88-K-0475, General Dynamics PO 4059045, and Cray Research, Inc. The help of Mr. Thomas Moore is gratefully acknowledged.

#### References

- [1] K. Yee, "Numerical solution of initial boundary value problems involving Maxwell's equations in isotropic media," *IEEE Trans. Antennas Propagat.*, AP-14, 302-307, May 1966.
- [2] A. Taflové and M. Brodwin, "Numerical solution of steady-state electromagnetic scattering problems using the time-dependent Maxwell's equations," *IEEE Trans. Microwave Theory Tech.*, MTT-23, 623-630, August 1975.
- [3] G. Kriegsmann, "Exploiting the limiting amplitude principle to numerically solve scattering problems," *Wave Motion* 4, 371-380, 1982.
- [4] A. Taflové and M. Brodwin, "Computation of the electromagnetic fields and induced temperatures within a model of the microwave irradiated human eye," *IEEE Trans. Microwave Theory Tech.*, MTT-23, 888-896, Nov. 1975.
- [5] A. Taflové and K. Umashankar, "Evaluation of time-domain electromagnetic coupling techniques," Final Report RADC-TR-80-251, Rome Air Dev. Ctr., Griffiss AFB, NY, April 1980.
- [6] A. Taflové, "Application of the finite-difference time-domain method to sinusoidal steady-state electromagnetic penetration problems," *IEEE Trans. Electromagn. Compat.*, EMC-22, 191-202, Aug. 1980.
- [7] A. Taflové and K. Umashankar, "A hybrid moment method/finite-difference time-domain approach to electromagnetic coupling and aperture penetration into complex geometries," *IEEE Trans. Antennas Propagat.*, AP-30, 617-627, July 1982.
- [8] R. Holland, "Threde: a free field EMP coupling and scattering code," *IEEE Trans. Nuclear Sci.*, NS-24, 2416-2421, Dec. 1977.
- [9] K. Kunz and K. Lee, "A three-dimensional finite-difference solution of the external response of an aircraft to a complex transient EM environment: Part I," *IEEE Trans. Electromagn. Compat.*, EMC-20, 328-333, May 1978.
- [10] D. Meriwether, R. Fisher, and F. Smith, "On implementing a numerical Huygen's source scheme in a finite-difference program to illuminate scattering bodies," *IEEE Trans. Nuclear Sci.*, NS-27, 1819-1833, Dec. 1980.
- [11] G. Mur, "Absorbing boundary conditions for the finite-difference approximation of the time-domain electromagnetic field equations," *IEEE Trans. Electromagn. Compat.*, EMC-23, 377-382, Nov. 1981.
- [12] K. Umashankar and A. Taflové, "A novel method to analyze electromagnetic scattering of complex objects," *IEEE Trans. Electromagn. Compat.*, EMC-24, 397-405, Nov. 1982.
- [13] A. Taflové and K. Umashankar, "Radar cross section of general three-dimensional scatterers," *IEEE Trans. Electromagn. Compat.*, EMC-25, 433-440, Nov. 1983.
- [14] A. Taflové, K. Umashankar, and T. Jurgens, "Validation of FD-TD modeling of the radar cross section of three-dimensional structures spanning up to nine wavelengths," *IEEE Trans. Antennas Propagat.*, AP-33, 652-666, June 1985.
- [15] B. Enquist and A. Majda, "Absorbing boundary conditions for the numerical simulation of waves," *Math. Comp.* 31, 629-651, July 1977.
- [16] G. Kriegsmann and C. Morawetz, "Solving the Helmholtz equation for exterior problems with variable index of refraction: I," *SIAM J. Sci. Stat. Comput.* 1, 371-385, Sept. 1980.
- [17] A. Bayliss and E. Turkel, "Radiation boundary conditions for wave-like equations," *Commun. Pure Appl. Math.* 33, 707-725, 1980.
- [18] L. Trefethen and L. Halpern, "Well-posedness of one-way wave equations and absorbing boundary conditions," *Inst. Comput. Appl. Sci. and Eng. (ICASE) NASA Langley Res. Center, Hampton, VA, Report 84-30, June 1985.*
- [19] J. Blaschak and G. Kriegsmann, "A comparative study of absorbing boundary conditions," *J. Comp. Physics* 77, 109-139, July 1988.
- [20] J. Blaschak, "Radiation boundary conditions: I. Absorbing boundary conditions for electromagnetic wave propagation," Ph.D. dissertation, Northwestern University, Evanston, IL, Aug. 1988.
- [21] J. Fang and K. Mei, "A super-absorbing boundary algorithm for solving electromagnetic problems by time-domain finite-difference method," *Proc. 1988 IEEE AP-S Symp.*, Syracuse, NY, June 1988, 472-475.
- [22] A. Taflové, "Review of the formulation and applications of the FD-TD method for numerical modeling of EM wave interactions," *Wave Motion* 10, Dec. 1989.
- [23] D. Sullivan, O. Gandhi, and A. Taflové, "Use of the finite-difference time-domain method in calculating EM absorption in man models," *IEEE Trans. Biomed. Eng.* 35, 179-186, March 1988.

# PREDICTING SCATTERING OF ELECTROMAGNETIC FIELDS USING FD-TD ON A CONNECTION MACHINE

Andrew T. Perlik, Member, IEEE  
MRJ, Inc.  
10455 White Granite Drive  
Gakton, Virginia 22124  
(703) 934-9232

Torstein Opsahl  
Center for Innovative Technology  
13873 Park Center Road  
Herndon, Virginia 22071

Allen Taflove, Senior Member, IEEE  
Department of Electrical Engineering and Computer Science  
Technological Institute, Northwestern University  
Evanston, Illinois 60201

## Abstract

The Finite Difference-Time Domain (FD-TD) numerical technique for solving Maxwell's equations is mapped onto a massively parallel Single Instruction Multiple Data (SIMD) architecture. A Connection Machine™ was chosen over other contemporary SIMD machines as the most promising candidate. The fundamental FD-TD algorithm developed by Taflove is decomposed into its serial and parallel segments. Connection Machine implementation is discussed in detail including processor assignment, processor utilization, run time, problem size, and future directions.

## Introduction

FD-TD is an explicit time stepping finite difference formulation of Maxwell's curl equations that was developed in the mid-1980's by Allen Taflove [1]. It has broad applicability to the study of electromagnetic scattering by three dimensional objects because the scatterers can be closed or open, conducting, dielectric, inhomogeneous, or anisotropic. The algorithm has been validated against experimental data on objects that exhibit scattering physics at edges, corners, and cavity penetration. Agreements to within 1 dB of experimental data have been reported for scatterers that physically span 9 wavelengths and have a bistatic scatter dynamic range of 40 dB [1]. Consequently, FD-TD is certainly among the most robust scattering predictive algorithms that are currently available. If a parallel computer algorithm could be developed that could handle larger scatterers than serial code and/or run faster than serial codes, then this new development could have broad applicability to the electromagnetics community.

## FD-TD Algorithm

FD-TD models the propagation of a plane wave in a finite volume of space containing the electromagnetic scatterer, Figure 1. A cubic cell spatial lattice grids the volume under study. Although simplistic, attempts to generalize the gridding procedure to a non-uniform, scatterer surface conformal one have not been totally satisfactory because both the computational dynamic range and algorithm run time degrade severely. Alternative gridding techniques still remain an area for continued research. An exploded view of a typical FD-TD cell appears in Figure 2, the well known Yee lattice. Note that the E and H field components are computed on a half cell staggered grid. This formulation guarantees second order accuracy in the difference equations that are being solved. Two computational regions are defined, a total field region and a scattered field region. The total field region completely encloses the scatterer. In it, the total field gets updated computationally in order to

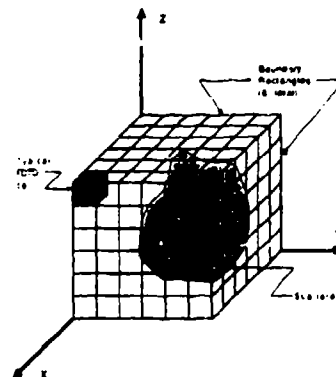


Figure 1. FD-TD Volumetric Grid Enclosing a Scatterer

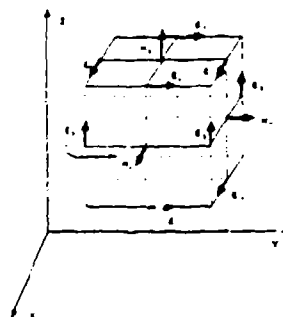


Figure 2. Yee FD-TD Lattice

preserve a large computational dynamic range. Scattered fields are needed to obtain far field information. The traveling wave incident fields get added at the interface of these two computational regions respecting causality.

A problem solution is obtained by time stepping the difference equations. As time evolves the incident wave travels through space exciting the scatterer. Time stepping continues until steady state is achieved for all field components in the grid. At steady state all field components are sinusoidal in time with converged magnitudes and converged relative phases.

Update equations for the volumetric grid decompose into four categories: discretized Maxwell's equations for grid interior points, Mur update equations for E components at the interior points of the boundary rectangles, interpolation and extrapolation equations for the edges of the boundary rectangles, and equations for the incident fields. Mur update equations [2] are

used to computationally terminate the volumetric grid. Basically, they are discrete versions of a one-way wave equation and are designed to "absorb" outgoing plane waves. In order to update a Mur boundary point to a new time, all nearest neighbor spatial values are needed. Consequently, the Mur updates do not apply for fields along the edges of the volumetric grid. Edges are updated heuristically using an interpolation and extrapolation scheme on nearest neighbor data.

#### The Connection Machine

The Connection Machine (CM) is a massively parallel SIMD computer manufactured by Thinking Machines Corporation in Cambridge, Massachusetts. CMs are hosted by serial computers that broadcast instructions to it, and the same instruction is executed by each processor on data in its own memory. A commercially available CM-2 contains a maximum of 65,536 processors, each having 65,536 bits of dedicated memory (63,995 bits are user addressable). Instructions are bit oriented giving the programmer the unusual, but extremely useful flexibility to match word length to suit desired dynamic range or to match interprocessor message lengths. Floating point coprocessors are available, but at the present time they support only 32 bit single precision arithmetic. An elapsed time for a complete cycle of arithmetic (i.e., retrieve operands, perform the arithmetic operation, and store the result) of 40  $\mu$ sec is easily achievable, using non-optimized non-pipelined code. Provided that all 65k processors are productively computing, 1.6 gigaflops (65k/40  $\mu$ s) establishes a lower limit on the machine capability. Typical performance for algorithms developed at MRI, Inc. is equivalent to a serial machine performance of 3 gigaflops, and peak performance rates equivalent to 28 gigaflops on a serial machine have been demonstrated.

General processor-to-processor communication is available; however, for the algorithm capabilities incorporated into the present model, only nearest neighbor processor communication is needed. All processors can get data from their nearest neighbors simultaneously. For a 32 bit message the elapsed time ranges from 30  $\mu$ sec to 140  $\mu$ sec depending on algorithm design implying that a net memory transfer rate of 70 gigabits is possible on a full machine.

On-line disk storage (data vault) is available up to 80 gigabytes for a 65k CM-2, but at present it is not compatible with all hosts. Software will be available in the near future to remedy the situation.

The host computer plays an integral part in executing algorithms. Not only does it broadcast instructions to the CM, but it can also read data out, perform computations, and write data back to selected processors. This affords the user with flexibility to use both serial and parallel computational capability, as needed.

Programs can be written on small (8k) machines and can be run on larger machines without changing the code. This is accomplished by using the good coding practice of exploiting the operating software supplied machine constants. The concept of virtual processors is also supported. Each physical processor can partition its memory by factors of 2 and assign to each partition a virtual processor ID. An 8k machine can, therefore, act like a 65k machine provided that each processor needs only 1/8 of a processor's physical memory. Run time degrades with virtualization.

#### Mapping FD-TD onto the CM

FD-TD was mapped onto the CM with two guiding principles: maximize the size of the volumetric grid that can be analyzed and minimize run time. Development took place under the constraints that no on-line disk storage was available and that all floating point arithmetic would be single precision (32 bit) so that the floating point coprocessors could be used. The first constraint arose because both development risk and time were high when the programming was started. Data vault software was new, unproven, and was available under an operating system that was less flexible than the one desired. Floating point arithmetic using the coprocessors reduced run time by a factor of 10--sufficiently attractive to warrant their use. Contrary to what might be expected, however, no compromise in desired accuracy is incurred. Single precision arithmetic was demonstrated to support a computational dynamic range of 40 dB and is believed to support a range of over 60 dB. The real trade was against volumetric grid size because using less than 32 bits would free memory for more grid points.

#### Step 1

The FD-TD algorithm is examined and broken into its algorithmic serial and parallel computational steps. Start by identifying the computational chronology at each time step:

- update incident fields
- update interior H fields
- update interior E fields
- update rectangular boundary edges
- update rectangular boundary interiors
- test for steady state

Each computational step above depends on the result of the previous one. Unless the basic algorithm is changed, these steps are sequential on both serial and parallel computers. All spatial points can theoretically be updated simultaneously in each computational step. In the second step, for example, all three components of H can be updated simultaneously as well.

#### Step 2

Identify the role(s) to be played by each processor for each parallel step. This step is critical for robust parallel code development. Performance both in run time and problem size could vary by orders of magnitude among implementations. Returning to the second computational step above, minimum execution time would result if each H field component and each E field component at a grid cell were assigned to individual processors. Such an assignment would greatly sacrifice problem size since each FD-TD cell would require six processors. Instead, the decision was made to assign each processor the role of updating the three H components and the three E components assigned to each FD-TD cell, Figure 3. The trade here was in favor of problem size at the expense of run time. Total storage requirements needed to support computations for each FD-TD cell sums to 1,536 bits, significantly less than the 63,995 user addressable bits. Each processor can, therefore, be virtualized by a factor of 39, the remaining storage being reserved for stack space.



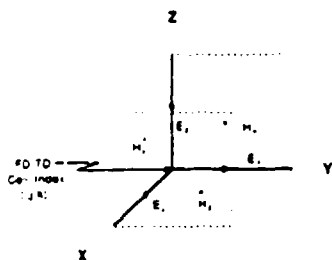


**Figure 3. Fields Assigned to a CM Processor**

Figure 4 summarizes the essential breakdown between the serial and parallel processing steps. Some steps have been left out for clarity, i.e., update of incident fields, convergence testing, and computation of peak and phase for scattered fields, but the breakdown in Figure 4 captures the philosophy.

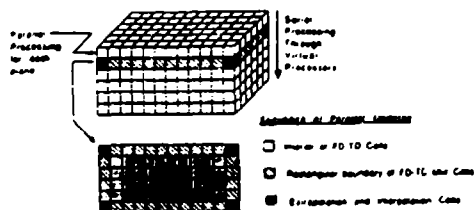


Figure 4. Overview of Essential Parallel and Serial Steps

### Assessment of Parallel Implementation

Each FD-ID cell needs only 1,536 bits for data storage. Creating virtual processors is clearly a good idea; otherwise, the excess memory per processor would not get used. Now consider processing for an individual plane. Let each plane be  $n$  cells by  $m$  cells. Then  $(n-2)(m-2)$  cells are interior ones, all getting updated simultaneously. Edge processors update next. Only four processors are active independent of grid size. Clearly, this is poor utilization of the processors since only a small number are being used. The true measure of its impact on overall performance is the relative amount of time consumed compared to the other grid update functions for each plane. Table 1 provides the data needed. Edge updates require nearly half as much time to compute as the interior points do. Updating the edges on the CM instead of the host was a poor choice, one that will be remedied in the next version of the software. Face updates are computed using  $2(n+m)-8$  processors, on the order of the square root of the number of available processors. Again referring to Table 1, the conclusion is drawn that a significant amount of time is required to update the face processors relative to the interior ones. This does not imply that face updates should be performed in the host, however, because the I/O between the host and the CM for the root of CM processors needed to service the faces may be too expensive. Algorithms for face update run time reductions are currently being examined.

Table 1. Normalized Elapsed Time for Major Parallel Program Segments

PROGRAM SEGMENT	NORMALIZED RUN TIME
interior update	1 unit
edge update	.496 units
face update	.402 units

The three program segments discussed above constitute the core code that gets executed for each plane in the PD-TD grid. The execution time required to service

those segments that employ only a fraction of the number of available processors, the edge and face updates, is approximately 47 percent of the total time required to service a plane. This suggests that the run time improvement for the current algorithm is at best a factor of 2. Run time improvements by factors of 10 or more will require a fundamental algorithm redesign.

### Assessment of Algorithm Performance

Performance assessment will touch on the following topics: problem size as a function of machine size, run time as a function of machine size, and comparison between serial and parallel codes. The most succinct method for conveying results is to express them in terms of the number of FD-TD cells that fit into the CM's random access memory (RAM). Otherwise, results would be coupled to scatterer size and the desired solution accuracy, since for fixed scatterer size solution accuracy is a function of the thickness of the scattered field computational region. With the present code an 8k processor CM can evaluate 38 planes of  $62 \times 126$  cells giving a total FD-TD volume of 296,856 cells. A 65k processor CM can evaluate 38 planes of  $254 \times 254$  cells for a total of 2,451,608 FD-TD cells. The same code will run on both machines at the same execution time of 0.045 seconds/time step/virtual plane. Total run time per time step is 38 times larger, 1.7 seconds/time step. Run time is flat with the increase in machine size because the architecture is SIMD. Run time does change as the number of virtual planes change because the physical processors serially service the virtual processors that they represent. Benchmarks were run to show that reducing the number of virtual planes by a factor of two also reduces the run time by a factor of two. The largest scatterer studied and reported in the literature as far as we are aware is the 9A cross tee plate reported by Taflov [1] using a Cray based code. It was embedded in a 258,048 cell lattice. By comparison the CM code can evaluate a computational lattice 9.5 times larger in volume on a full CM-2 in RAM. Furthermore, the CM code as currently written is somewhat more general because the lattice cells can be rectangular parallepipeds instead of just cubes. If the CM code is restructured in the same way, lattice size would double by another factor of two in volume and execution time per virtual level would fall by roughly 10 percent.

## Summary

The advent of massively parallel processors is still in its infancy; the CM, in particular, being commercially available for only two years and being based on technology that is 10 years old. Already, we are compiling data that suggests parallel codes are capable of exceeding lattice sizes and executing faster than even Cray based codes for lattice optimally matched to the CM's memory. The applicability of parallel processing to grid based techniques appears to have a bright future.

## References

- [1] A. Taflov and K. R. Umashankar, "Analytical Models for Electromagnetic Scattering," Final Technical Report RADC-TR-85-87 by ITT Research Institute, Chicago, IL, to Rome Air Development Center, Hanscom AFB, MA 01731 on Procurement Number F19628-82-C-0140, May 1985.
- [2] G. Mur, "Absorbing Boundary Conditions for the Finite-Difference Approximation of the Time-Domain Electromagnetic-Field Equations," IEEE Trans. Electromag. Compat., Vol. EMC-23, Nov. 1981, pp. 377-382.

A. Taflöv was supported in part for this research by NSF Grant No. ASC-8811273.

# Numerical Analysis and Validation of the Combined Field Surface Integral Equations for Electromagnetic Scattering by Arbitrary Shaped Two-Dimensional Anisotropic Objects

BENJAMIN BEKER, MEMBER, IEEE, KORADA R. UMASHANKAR, SENIOR MEMBER, IEEE, AND  
ALLEN TAFLOVE, SENIOR MEMBER, IEEE

**Abstract**—The numerical solution of coupled integral equations for arbitrary shaped two-dimensional homogeneous anisotropic scatterers is presented. The theoretical and the numerical approach utilized in the solution of the integral equations is based on the combined field formulation, and is specialized to both transverse electric (TE) and transverse magnetic (TM) polarizations. As opposed to the currently available methods for the anisotropic scatterers, this approach involves integration over the surface of the scatterer in order to determine the unknown surface electric and magnetic current distributions. The solution is facilitated by developing a numerical approach employing the method of moments. The various difficulties involved in the course of the numerical effort are pointed out, and the ways of overcoming them are discussed in detail. The results obtained for two canonical anisotropic structures, namely a circular cylinder and a square cylinder, are given along with validations obtained via alternative methods.

## I. INTRODUCTION

IN RECENT YEARS, the solution of physical problems involving anisotropic media has received a great deal of attention. In particular, volumetric approaches such as the finite-difference time-domain (FD-TD) method [1], [2] and the volumetric integral equation method [3]–[5] have already been addressed to solve scattering problems involving anisotropic materials. Also considered was another volumetric method based on the variational principle to solve problems involving anisotropic scatterers [6]. These methods can treat materials characterized by arbitrary permittivity and permeability tensors, thus giving a great deal of freedom in the types of media that can be analyzed by their use. However, the approaches and their numerical schemes [1]–[6] are completely volume dependent, requiring volumetric models even for ho-

mogeneous and isotropic cases. Further, their application to electrically large objects has not yet been established. Another approach to the solution of the scattering problem dealing with anisotropic scatterers is based on the plane wave representation of fields in the anisotropic medium [7]. The method discussed in [7] consists of using a superposition type integral to include all possible wave amplitudes and phases, and is applied to the circular cylinder excited at a normal incidence [7], and at an oblique incidence [8]. However, thus far this method has been applied only to the case of a circular cylindrical geometry.

In order to consider arbitrary shapes and computationally manageable sizes of the anisotropic scatterers, an alternative approach to the solution is presented. The method incorporates the surface boundary integrals instead of volume integrals, and is applicable to any arbitrary shaped two-dimensional homogeneous anisotropic scatterers, which can have discontinuities in their surface contour [9]. It involves extension to the formulation of the scattering problem for the isotropic bodies by utilizing the electromagnetic potential theory, and the subsequent derivation of the combined field surface integral equations [10]. However, the derivation of a complete set of consistent potentials for the anisotropic case is much more complicated than the same procedure for the isotropic medium. The detailed derivation of the combined field integral equations is discussed in a separate paper cited earlier [9]. The complete theoretical development is omitted here, and only the most relevant equations are stated to form the starting point for the numerical solution. Due to the complicated nature of these equations, it is practically useful to have a simple numerical scheme for analyzing anisotropic structures, and yet not compromising the accuracy of the numerical results.

The numerical results based on the surface formulation for the transverse magnetic (TM) polarized fields are presented for two canonical anisotropic structures. In general, however, these structures need not be restricted to any particular shape such as a smooth contour. They can include surface discontinuities in the form of sharp corner wedges. Also, in order to

Manuscript received November 19, 1987; revised June 22, 1988; October 26, 1988.

B. Beker and K. R. Umashankar are with the Department of Electrical Engineering and Computer Science, University of Illinois, Chicago, IL 60680.

A. Taflov is with the Department of Electrical Engineering and Computer Science, Technological Institute, Northwestern University, Evanston, IL 60201.

IEEE Log Number 8928391.

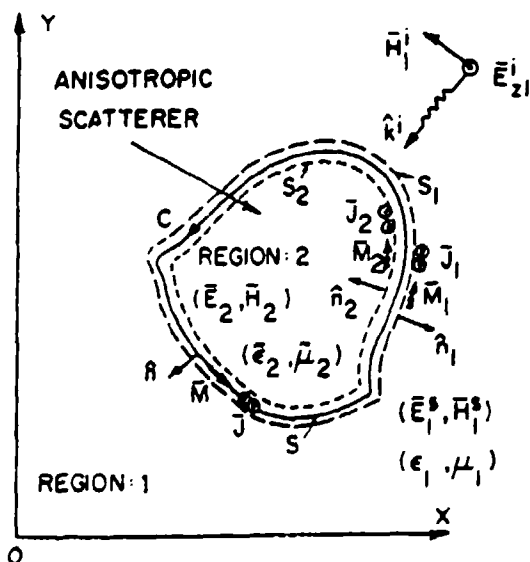


Fig. 1. Geometry of anisotropic scatterer with equivalent current sources.

demonstrate the feasibility of applying the developed method to compute the surface currents and the far fields, a relatively large object with its largest electrical dimension of  $k_0 s = 10$  will be considered. In particular, for validating the combined field formulation, the radar cross section (RCS) computed for a circular cylinder is compared to that available in the literature [7]. Also, the near surface current distributions and the RCS of the anisotropic square cylinder are validated against the results obtained based on the FD-TD algorithm [2], [10].

## II. INTEGRAL EQUATIONS FOR THE SURFACE FIELDS

Consider a two-dimensional anisotropic object for which there is no variation in its surface contour along the  $z$  axis of the coordinate system. It is located in a free-space medium and is excited by an externally incident, TM polarized, field with the time dependence of  $e^{-i\omega t}$  where  $\omega$  is the frequency of the excitation (see Fig. 1). Further, if the excitation is such that the  $z$  component of its propagation vector  $k_z^i$  is zero, then all scattered field quantities are independent of the  $z$  coordinate variation. In order to analyze the complete field distribution due to the presence of the anisotropic object, the equivalence principle [10], [11] can be invoked to obtain a set of coupled (combined field) integral equations for the unknown induced currents on the surface of the object. The full theoretical development leading to those integral equations is presented elsewhere [9], hence, only the key steps are repeated below. Referring to Fig. 1, the equations for the fields internal and external to the anisotropic object can be expressed in terms of the appropriate vector and scalar potentials as is done in [9]–[11]. If the space is separated into two regions, with region 1 occupied by the isotropic (free-space) medium, and the region 2 corresponding to the anisotropic scatterer, respectively, then the total electric  $E_{z1}^t$  and the magnetic  $H_{z1}^t$  field expressions in the region 1 are given by

$$E_{z1}^t = E_{z1}^i + i\omega A_{z1} - \frac{\hat{z} \cdot (\nabla \times \mathbf{F}_1)}{\epsilon_1 \epsilon_0} \quad (1a)$$

$$H_{z1}^t = H_{z1}^i + i\omega F_1 + \frac{i\omega}{k_1^2} \nabla(\nabla \cdot \mathbf{F}_1) + \frac{(\nabla \times \mathbf{A}_1)}{\mu_1 \mu_0} \quad (1b)$$

$$k_0^2 = \omega^2 \epsilon_0 \mu_0 \quad (1c)$$

$$k_1^2 = k_0^2 \epsilon_1 \mu_1 \quad (1d)$$

where  $k_1$ ,  $\epsilon_1$ ,  $\mu_1$  are the propagation constant, the relative permittivity, and the relative permeability of the isotropic medium. Similarly, the total electric  $E_{z2}^t$  and magnetic  $H_{z2}^t$  fields in the region 2 are given by

$$E_{z2}^t = i\omega A_{z2} - \hat{z} \cdot \frac{\hat{\epsilon}_2^{-1}}{\epsilon_0} \cdot (\nabla \times \mathbf{F}_2) \quad (2a)$$

$$H_{z2}^t = i\omega F_2 + \frac{i\omega}{k_a^2} \nabla(\nabla \cdot (\hat{\mu}_2 \cdot \mathbf{F}_2)) + \frac{\hat{\mu}_2^{-1}}{\mu_0} \cdot (\nabla \times \mathbf{A}_2) \quad (2b)$$

$$k_a^2 = k_0^2 \epsilon_{zz} (\mu_{xx} \mu_{yy} + \mu_{xy}^2) \quad (2c)$$

where the relative permittivity and permeability tensors for the anisotropic medium are defined by

$$\hat{\mu} = \begin{bmatrix} \mu_{xx} & \mu_{xy} & 0 \\ \mu_{yx} & \mu_{yy} & 0 \\ 0 & 0 & \mu_{zz} \end{bmatrix} \quad (3a)$$

$$\hat{\epsilon} = \begin{bmatrix} \epsilon_{xx} & \epsilon_{xy} & 0 \\ \epsilon_{yx} & \epsilon_{yy} & 0 \\ 0 & 0 & \epsilon_{zz} \end{bmatrix} \quad (3b)$$

It should be obvious from (1a), (1b) and (2a), (2b) that the appropriate Lorenz-type gauge condition has been utilized to eliminate the magnetic scalar potential, so that the field expressions could be cast in terms of the magnetic and the electric vector potentials only. The derivation leading to the Helmholtz equations and the final integral representation of the required components of the vector potentials  $\mathbf{A}$  and  $\mathbf{F}$  for the anisotropic medium is quite intricate [9]. A detailed account of the procedure taken to obtain them is discussed in [9], [15] and only their final forms are repeated below:

$$A_z(\mathbf{r}) = -\mu_0 \frac{\gamma}{4i\sqrt{\mu_{xx}\mu_{yy}}} \int_C J_z(\mathbf{r}') H_0^{(1)}(k_a R_m) ds' \quad (4a)$$

$$\Xi_x(\mathbf{r}) = -\epsilon_0 \epsilon_{zz} \frac{\gamma}{4i\sqrt{\mu_{xx}\mu_{yy}}} \int_C M_x(\mathbf{r}') H_0^{(1)}(k_a R_m) ds' \quad (4b)$$

$$\Xi_y(\mathbf{r}) = -\epsilon_0 \epsilon_{zz} \frac{\gamma}{4i\sqrt{\mu_{xx}\mu_{yy}}} \int_C M_y(\mathbf{r}') H_0^{(1)}(k_a R_m) ds' \quad (4c)$$

$$\gamma = (\mu_{xx}\mu_{yy} + \mu_{xy}^2) \quad (4d)$$

$$R_m = \sqrt{\frac{(x-x')^2}{\mu_{xx}} + \frac{(y-y')^2}{\mu_{yy}}} \quad (4e)$$

where  $J_z$ ,  $M_x$ ,  $M_y$  are the unknown electric and magnetic current distributions along the contour  $C$ ,  $H_0^{(1)}$  is the Hankel function of order zero and of first kind, and  $R_m$  is the scaled distance parameter [15], [16] between the integration and the observation points with  $C$  and  $ds'$  representing the contour of the scatterer and its differential element. The quantities  $\Xi_x$

and  $\Xi_j$  are the components of the auxiliary vector potential function defined by

$$\frac{\partial \mu}{\partial F} = f \quad (5)$$

which permits independent differential equations for  $\Xi_x$  and  $\Xi_y$ , so that eventually solutions for  $F_x$  and  $F_y$  can be determined [9]. It should be pointed out that in order to obtain the integral solutions for  $A_z$ ,  $\Xi_x$ ,  $\Xi_y$ , it was necessary to demand that the medium tensors possess antisymmetric properties, i.e.,  $\mu_{xy} = -\mu_{yx}$  for TM polarization, and  $\epsilon_{xy} = -\epsilon_{yx}$  for transverse electric (TE) polarization. The corresponding superposition integrals for the external isotropic medium can readily be obtained from (4a)–(4d) and (5) by setting the diagonal elements of the medium tensors (those in (3a) and (3b)) equal and the off-diagonal ones to zero.

Finally, application of the boundary conditions on the tangential components of the total electric and magnetic fields along  $C$ , yields the following set of two combined field (coupled) integral equations for the surface currents:

$$-\dot{n} \times E_1 = i\omega(\dot{n} \times \hat{z})(A_{z1} + A_{z2})$$

$$-\dot{n} \times \left( \frac{\nabla \times F_1}{\epsilon_0 \epsilon_1} + \frac{\hat{z}_2^{-1} \cdot (\nabla \times F_2)}{\epsilon_0} \right) \quad (6a)$$

$$-\dot{n} \times H_1 = \dot{n} \times \left\{ i\omega(F_1 + F_2) + i\omega \nabla \left( \nabla \cdot \left( \frac{F_1}{k_1^2} + \frac{\bar{\mu}_2 \cdot F_2}{k_2^2} \right) \right) + \left( \frac{(\nabla \times \bar{A}_1)}{\mu_1 \mu_0} + \frac{\bar{\mu}_2^{-1} \cdot (\nabla \times \bar{A}_2)}{\mu_0} \right) \right\} \quad (6b)$$

which are valid for the TM polarized incident field ( $E'_i, H'_i$ ). The same equations also apply to the TE polarization following appropriate substitutions of symbols as is dictated by the duality principle [11]. In particular, allowing  $E \rightarrow H$ ,  $H \rightarrow -E$ , and interchanging the roles of the permittivity and permeability tensors results in the desired combined field integral equations set for the TE polarization.

### III. NUMERICAL SOLUTION OF THE INTEGRAL EQUATIONS

The first step in the numerical solution of (6a) and (6b) based on the method of moments is the proper choice of the testing and the expansion functions. This choice is usually dictated by the complexity of the integrals and the scatterer contour. For example, if the integrands contain derivatives with respect to the observation coordinates along the tangential direction of the scatterer, then it is customary to use higher order testing functions, such as the triangles, to replace those derivatives by differences [12]. The use of the simpler testing functions, such as pulses, simplifies the testing scheme. On the other hand, it complicates the integrands, because the derivative operations due to the gradient, divergence, and the curl will now be taken inside the integrals. However, this approach has been found to speed up the convergence rate of the solution [13], and for this reason will be implemented here.

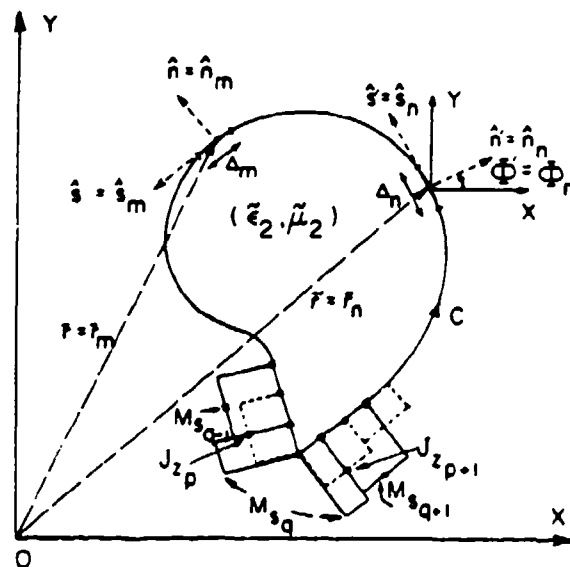


**Fig. 2. Segmented boundary contour.**

The expansion scheme for the unknown surface electric and magnetic currents is chosen to consist of the simplest possible functions, such as pulses. The only remaining task is to decide whether the pulses for each current expansion ought to be staggered or not. This, in fact, depends on the contour of the scatterer, i.e., if the contour is smooth (continuous), then there is no need to use the staggered distribution. However, if the contour includes surface discontinuities, such as the corners and arbitrary bends, then it is appropriate to stagger the pulses so as to enforce the continuity of the circumferential current, and to avoid expanding the axial current at the bend where it is singular [10]. For the problem at hand, i.e., for TM polarization, the axial electric current  $J_z$ , and the circumferential magnetic current  $M_\phi$ , are expanded in a staggered manner as shown in Fig. 2, because objects having both smooth and discontinuous contours can be considered for the solution using the same computer algorithm. These same expansion pulses are also employed as the testing functions for the two coupled integral equations. Thus, the unknown surface currents are expanded as

$$J_z(P') = \sum_{n=1}^{n=N} p_n^J(P') J_{zn} \quad (7a)$$

$$M_i(P') = \sum_{n=N+1}^{n=2N} p_n^M(P') M_{i,n} \quad (7b)$$

where  $p_n^I(P')$  and  $p_n^M(P')$  are the unit pulse functions which can also serve as the testing functions  $r^E(P)$  and  $r^H(P)$  in the reduction procedure of the integral operators in (6a) and (6b) to a matrix form, i.e.,

$$r^E(p) = \sum_{m=1}^{m=M} p_m^j(p) \quad (8a)$$

$$r^H(f) = \sum_{m=M+1}^{m=2M} p_m^M(f) \quad (8b)$$

where (8a) and (8b) are used in taking the inner products with (6a) and (6b), respectively. The resulting system of the matrix equations, following testing and expansion, turns out to be

$$\begin{bmatrix} [Z_{mn}^E] & [Y_{mn}^E] \\ [Z_{mn}^H] & [Y_{mn}^H] \end{bmatrix} \begin{bmatrix} [J_{zn}] \\ [M_{sn}] \end{bmatrix} = \begin{bmatrix} [E_{zm}^i] \\ [H_{sm}^i] \end{bmatrix} \quad (9)$$

where the various elements of the system submatrices are defined below.

1) The elements of the impedance matrix of the  $E$  field equation:

$$[Z_{mn}^E] = \frac{k_0 \eta_0}{4} \int_{\Delta_n} \left[ \mu_1 H_0^{(1)}(k_1 R) + \frac{\gamma}{\sqrt{\mu_{xx} \mu_{yy}}} H_0^{(1)}(k_a R_m) \right] ds' \quad (10a)$$

2) The elements of the admittance matrix of the  $E$  field equation:

$$\begin{aligned} [Y_{mn}^E] = & \frac{1}{4i} \int_{\Delta_n} k_1 (\hat{n}' \cdot \hat{R}) H_1^{(1)}(k_1 R) ds' \\ & + \frac{1}{4i} \int_{\Delta_n} \frac{k_a}{\sqrt{\mu_{xx} \mu_{yy}}} [(\hat{n}' \cdot \hat{R}) + \mu_{xy} (\hat{s}' \cdot \hat{R}_m')] \\ & \cdot \frac{H_1^{(1)}(k_a R_m)}{R_m} ds'. \end{aligned} \quad (10b)$$

3) The elements of the impedance matrix of the  $H$  field equation:

$$\begin{aligned} [Z_{mn}^H] = & \frac{\eta_0}{k_0 i} \int_{\Delta_n} (\hat{n} \cdot \hat{R}) k_1 H_1^{(1)}(k_1 R) \\ & + \frac{\eta_0}{k_0 i} \int_{\Delta_n} \frac{k_a}{\sqrt{\mu_{xx} \mu_{yy}}} [(\hat{n} \cdot \hat{R}) - \mu_{xy} (\hat{s} \cdot \hat{R}_m')] \\ & \cdot \frac{H_1^{(1)}(k_a R_m)}{R_m} ds'. \end{aligned} \quad (10c)$$

4) The elements of the admittance matrix of the  $H$  field equation:

$$\begin{aligned} [Y_{mn}^H] = & \frac{\epsilon_1}{2} \int_{\Delta_n} \left[ \cos(\Phi_m - \Phi') H_0^{(1)}(k_1 R) \right. \\ & - \left( \sin \Phi_m \sin \Phi' \left( 1 - \frac{2(x_m - x')^2}{R^2} \right) \right. \\ & + \cos \Phi_m \cos \Phi' \left( 1 - \frac{2(y_m - y')^2}{R^2} \right) \\ & + \frac{2 \sin(\Phi_m + \Phi')(x_m - x')(y_m - y')}{R^2} \Big) \\ & \cdot H_2^{(1)}(k_1 R) \Big] ds' \\ & + \frac{\epsilon_{zz}}{\sqrt{\mu_{xx} \mu_{yy}}} \int_{\Delta_n} (\mu_{yy} \sin \Phi_m \sin \Phi' + \mu_{xx} \cos \Phi_m \cos \Phi' \\ & + \mu_{xy} \sin(\Phi_m - \Phi')) H_0^{(1)}(k_a R_m) ds' \\ & - \frac{\epsilon_{zz} \gamma}{2(\mu_{xx} \mu_{yy})^{3/2}} \int_{\Delta_n} \left[ (\mu_{yy} \sin \Phi_m \sin \Phi' \right. \end{aligned}$$

$$\begin{aligned} & + \mu_{xx} \cos \Phi_m \cos \Phi') H_0^{(1)}(k_a R_m) \\ & + \left( \mu_{yy} \sin \Phi_m \sin \Phi' \left( 1 - \frac{2(x_m - x')^2}{\mu_{xx} R_m^2} \right) \right. \\ & + \mu_{xx} \cos \Phi_m \cos \Phi' \left( 1 - \frac{2(y_m - y')^2}{\mu_{yy} R_m^2} \right) \\ & + \frac{2 \sin(\Phi_m + \Phi')(x_m - x')(y_m - y')}{R_m^2} \Big) \\ & \cdot H_2^{(1)}(k_a R_m) \Big] ds'. \end{aligned} \quad (10d)$$

5) The column excitation matrix of the  $E$  field equation:

$$[E_{zm}^i] = \hat{z} \cdot \mathbf{E}^i(\mathbf{r}_m). \quad (10e)$$

6) The column excitation matrix of the  $H$  field equation:

$$[H_{sm}^i] = \frac{4\eta_0}{k_0} \hat{s}(\mathbf{r}_m) \cdot \mathbf{H}^i(\mathbf{r}_m) \quad (10f)$$

and where  $[J_{zn}]$  and  $[M_{sn}]$  are the unknown surface electric and magnetic current column matrices along the tangential directions  $\hat{z}$  and  $\hat{s}$  of the contour  $C$ . In (10a)–(10d), the subscripts  $m$  and  $n$  refer to the observation and the integration points on the scatterer contour  $C$ , and in the above matrix elements,

$$\mathbf{R}_m = \frac{(x_m - x')\hat{x} + (y_m - y')\hat{y}}{\sqrt{\mu_{xx}}} \quad (11a)$$

$$\mathbf{R}_{m'} = \frac{(x_m - x')\hat{x} + (y_m - y')\hat{y}}{\mu_{xx}} \quad (11b)$$

$$\mathbf{R} = (x_m - x')\hat{x} + (y_m - y')\hat{y} \quad (11c)$$

with  $R_m$ ,  $R_{m'}$ ,  $R$  being their respective magnitudes, and with  $\hat{n}$ ,  $\hat{n}'$ ,  $\hat{s}$ ,  $\hat{s}'$  being the normal and the tangential unit vectors on the contour at either the observation or the integration points (see Fig. 1). These unit vectors are defined in the following manner:

$$(\hat{n}; \hat{n}') = \cos(\Phi; \Phi')\hat{x} + \sin(\Phi; \Phi')\hat{y} \quad (11d)$$

$$(\hat{s}; \hat{s}') = -\sin(\Phi; \Phi')\hat{x} + \cos(\Phi; \Phi')\hat{y} \quad (11e)$$

where  $\Phi$  and  $\Phi'$  are the angles between the normals  $\hat{n}$  and  $\hat{n}'$  and the  $x$  axis of the coordinate system.

It is evident from (10a)–(10d), that as a consequence of letting the various differential operations to be performed on the Green's function inside the integrals, results in the appearance of higher order Hankel functions, in particular  $H_2^{(1)}$ . Nevertheless, the complications arising in the evaluation of the system submatrices due to such an approach, are outweighed by the gain in the quicker convergence rate of the solution [13]. Otherwise, the evaluation of those submatrices is straightforward apart from the calculation of their singular values, which should be obtained asymptotically. A detailed mathematical analysis leading to the determination of the singular parts of the various integrals is presented in [15], and

only the final results are summarized in the following. First, for the anisotropic medium they are given by

$$I_1 = \int_{\Delta_m} H_0^{(1)}(k_a R_m) ds' = \Delta_m \int_0^1 H_0^{(1)}\left(\frac{(\beta \bar{\Delta}_m)s}{2}\right) ds \quad (12a)$$

which is a well-known integral and can be evaluated in numerous ways [14]. The singular values of integrals involving the first derivative of  $H_0^{(1)}$  are given by

$$I_2 = \frac{k_a \mu_{xy}}{4i \sqrt{\mu_{xx} \mu_{yy}}} \int_{\Delta_m} (\hat{s}' \cdot R_m) \frac{H_1^{(1)}(k_a R_m)}{R_m} ds' \rightarrow 0 \quad (12b)$$

$$I_3 = \frac{k_a}{4i \sqrt{\mu_{xx} \mu_{yy}}} \int_{\Delta_m} (\hat{n}' \cdot R) \frac{H_1^{(1)}(k_a R_m)}{R_m} ds' \rightarrow \frac{1}{2} \quad (12c)$$

where all of the vectors have been defined previously in (11a)–(11e), and it should also be noted that the values of these integrals are same irrespective of whether the medium is anisotropic or isotropic. The most complicated integrals contain the second derivatives of  $H_0^{(1)}$ , nevertheless they can be evaluated asymptotically to yield the following results:

$$I_4 = \int_{\Delta_m} \left(1 - \frac{2(x_m - x')^2}{\mu_{xx} R_m^2}\right) H_2^{(1)}(k_a R_m) ds' \\ = \frac{\bar{\Delta}_m (\cos^2 \bar{\Phi}_m - \sin^2 \bar{\Phi}_m)}{\sqrt{\mu_{yy} \sin^2 \bar{\Phi}_m + \mu_{xx} \cos^2 \bar{\Phi}_m}} \left[ \frac{(\beta \bar{\Delta}_m)^2}{96} + i \frac{16}{\pi (\beta \bar{\Delta}_m)^2} \right] \quad (12d)$$

$$I_5 = \int_{\Delta_m} \left(1 - \frac{2(y_m - y')^2}{\mu_{yy} R_m^2}\right) H_2^{(1)}(k_a R_m) ds' = -I_4 \quad (12e)$$

$$I_6 = \int_{\Delta_m} \left[ \frac{2 \sin(\bar{\Phi}_m + \bar{\Phi}') (x_m - x')^2 (y_m - y')^2}{R_m^2} \right] \\ \cdot H_2^{(1)}(k_a R_m) ds' \\ = -\frac{\sqrt{\mu_{xx} \mu_{yy}} (\bar{\Delta}_m \sin \bar{\Phi}_m \cos \bar{\Phi}_m)}{\sqrt{\mu_{yy} \sin^2 \bar{\Phi}_m + \mu_{xx} \cos^2 \bar{\Phi}_m}} \left[ \frac{(\beta \bar{\Delta}_m)^2}{96} + i \frac{16}{\pi (\beta \bar{\Delta}_m)^2} \right] \quad (12f)$$

where the angle  $\bar{\Phi}_m$  is defined in [15] and related to the real angle  $\Phi_m$  by

$$\tan \bar{\Phi}_m = \sqrt{\frac{\mu_{yy}}{\mu_{xx}}} \tan \Phi_m. \quad (12g)$$

The remaining terms  $\beta$  and  $\bar{\Delta}_m$  are given by

$$\beta = \frac{k_a}{\sqrt{\mu_{xx} \mu_{yy}}} \quad (12h)$$

$$\bar{\Delta}_m = \Delta_m \sqrt{\mu_{yy} \sin^2 \Phi_m + \mu_{xx} \cos^2 \Phi_m}. \quad (12i)$$

Secondly, the same equations (12a)–(12f) can be specialized for the isotropic medium by simply making appropriate

substitution of variables, i.e.,

$$\epsilon_{zz} \rightarrow \epsilon_1; \mu_{xx} = \mu_{yy} \rightarrow \mu_1; \mu_{xy} \rightarrow 0; \bar{\Phi} \rightarrow \Phi. \quad (12j)$$

Also, it should be pointed out that the value of  $I_3 \rightarrow -I_3$  when the external isotropic medium is considered. This is a direct consequence of the observation point approaching the contour in the limit from the opposite direction for the external medium, as opposed to the internal medium, considered above. The remaining integrals are independent of this fact, thus requiring no additional sign changes.

The matrix equations derived above ((9) and (10)) have been programmed on the IBM 370 computer using Fortran 77, and the various quantities of interest, such as the near surface current distributions and the far scattered fields, are calculated in order to analyze the electromagnetic behavior of two-dimensional anisotropic material objects.

#### IV. NUMERICAL RESULTS

In this section selected numerical results are presented regarding the computed near and far fields, as well as the CPU time required to obtain them based on the solution of the matrix equations (9). Two canonical cylindrical anisotropic geometries are considered, namely the circular and square cylinders excited by an external TM polarized plane wave. Both the near and the far fields are computed, and validated for each of the two geometries. The radar cross section of a circular anisotropic cylinder with  $k_0 a = \pi/2$ , where  $a$  is the radius of the cylinder, characterized by  $\epsilon_{zz} = 2$ ,  $\mu_{xx} = 1$ , and  $\mu_{yy} = 4$  is computed based on the surface integral equation formulation and is compared to the one obtained based on the plane wave superposition integral representation of the fields inside the anisotropic medium [7]. The two results are displayed in Fig. 3 and appear to be in an excellent agreement. Similarly, Fig. 4 illustrates the RCS computed for a circular cylinder of the same size, but with the following anisotropic medium parameters:  $\epsilon_{zz} = 2$ ,  $\mu_{xx} = 1$ ,  $\mu_{yy} = 4$ , and  $\mu_{xy} = -\mu_{yx} = 2$ . For both cases, the surface electric and magnetic currents were calculated as well, but are reported elsewhere [15]. The number of unknowns for each of the surface currents was 60, such that the total system matrix size is  $120 \times 120$  for the level of agreement shown in Fig. 3.

The next case analyzed numerically is a square anisotropic cylinder characterized by  $\epsilon_{zz} = 1.5$ ,  $\mu_{xx} = 1.5$ ,  $\mu_{yy} = 2$  whose electrical size is  $k_0 s = 10$ , where  $s$  is the side length of the square. Once again the RCS is computed based on the solution of the combined field equations and is shown in Fig. 5(a). These results are compared with those computed via the FD-TD [10]. The agreement between the RCS patterns calculated by the two methods is quite good except for a small angular range in the shadow region in the interval of  $200^\circ$ – $220^\circ$ . The magnitudes of the surface electric and magnetic currents for this square cylinder are displayed in Figs. 5(b) and 5(c). The level of agreement for the currents is also seen to be good except in the vicinity of the corners of the scatterer where the results of the two methods differ. This discrepancy deserves additional comments. Since the exact nature of the field behavior at the corners of the anisotropic

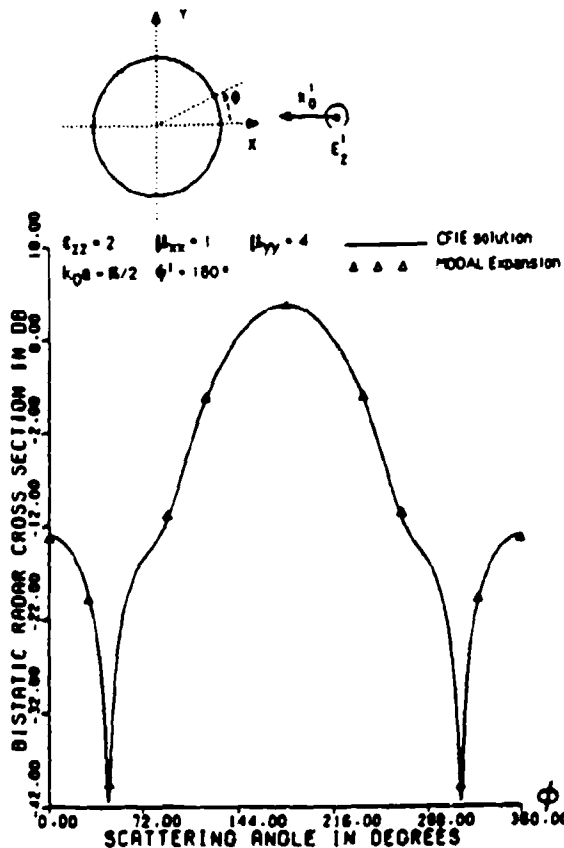


Fig. 3. Bistatic RCS of the circular anisotropic cylinder with only diagonal terms.

object is not yet known, it is difficult to say with absolute certainty which of the two methods gives the correct result. However, these corner regions are very small compared to the wavelength and since the far scattered fields are not expected to be greatly influenced by the currents over these localized corner regions, the RCS patterns may be more appropriate indicators of the agreement between the two methods. Also to be noted is the fact that in the FD-TD algorithm the fields are computed half a cell away from the actual physical boundary of the object, which may also be responsible for the discrepancies between the results. Since the fields do not vary greatly half a cell away from the object in regions far from surface discontinuities from their values computed directly on the object's surface, the agreement in the results calculated via both methods is expected to be good. However, in regions close to the bends the fields are expected to vary quite a bit between their values half a cell away from the contour and directly on it. This could possibly explain the differences in the results obtained via the two techniques in the vicinity of the corners of the square. The next example considered is a square cylinder having higher permeability values of the medium given by:  $\epsilon_{zz} = 2$ ,  $\mu_{xx} = 2$ ,  $\mu_{yy} = 4$ , and  $k_0a = 5$ . The RCS is computed and compared with that determined by FD-TD (see Fig. 6(a)). The corresponding magnitudes of the surface electric and magnetic currents for this scatterer are shown in Figs. 6(b) and 6(c), respectively. It is worth noting that in this case the results of both methods appear to predict similar behavior of  $M_z$  close to the bends in the contour, particu-

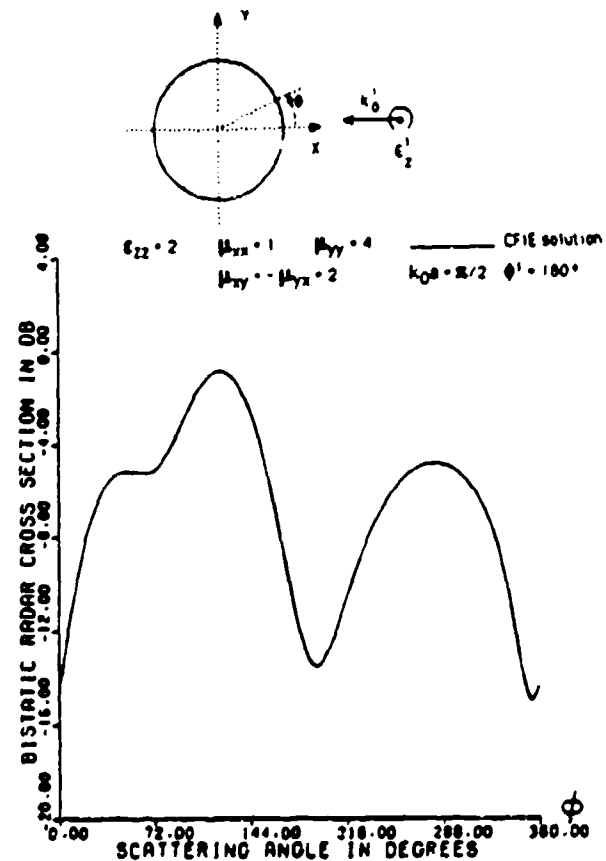


Fig. 4. Bistatic RCS of the circular anisotropic cylinder with mutual permeability terms.

larly, both indicate the dip in the magnitude of  $M_z$ , but not to the same extent. However, the discrepancy for the axial electric current is still present in those regions. This behavior may be attributed to the sparse sampling of the FD-TD algorithm, which in this case consisted in fifty cells per side of the square. It is believed that even further agreement in the results of the two methods could be achieved by increasing the sampling rate of the FD-TD. It is also worth mentioning that since both FD-TD and surface integral equation approach are based on methods of numerical analysis, it is not realistic to expect both of them to yield identical results. Additional examples for which both the surface currents and the RCS have been computed are available in [15]. The two square cylinders considered here are electrically large structures, especially the first one ( $k_0a = 10$ ) for which the number of current samples is such that the system matrix is  $592 \times 592$ . Nevertheless, the numerical solution is feasible, because most of the time is consumed by the system matrix inversion (which can be reduced for symmetric objects) and not for matrix filling. It should be pointed out that the symmetry of the structure has not been incorporated in the present algorithm. If the symmetry is incorporated into the algorithm, then substantial reduction in the CPU time for the matrix inversion can be achieved. Further savings in the CPU time can also be obtained if the inversion subroutine, based on the Gaussian elimination, is to perform partial pivoting instead of full pivoting.

In order to provide some idea of the time involved for the computations to obtain the results for the square cylinder dis-

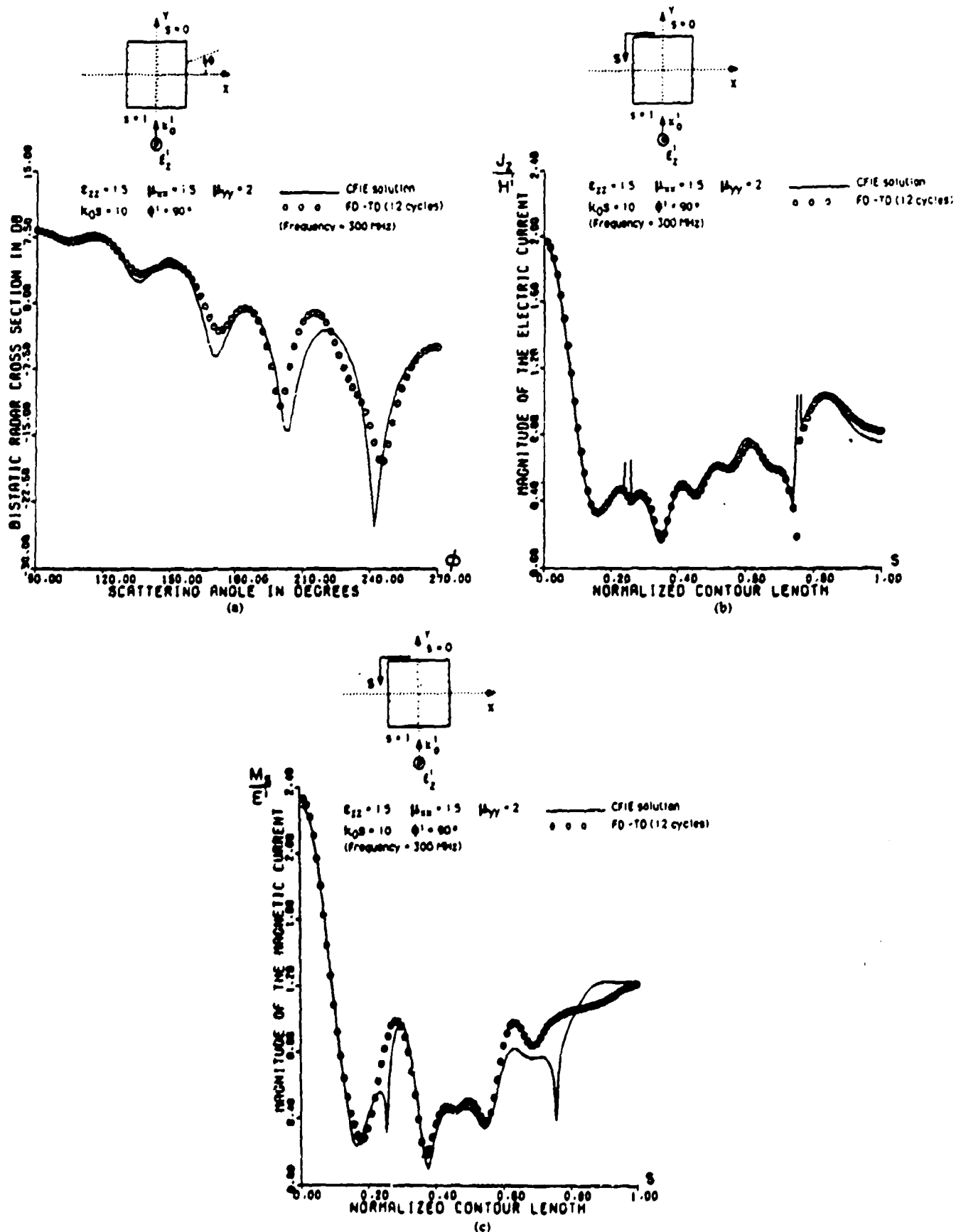


Fig. 5. (a) Bistatic RCS of the square anisotropic cylinder, low permeability case. (b) Surface electric current distribution of the square anisotropic cylinder, low permeability case. (c) Surface magnetic current distribution of the square anisotropic cylinder, low permeability case.



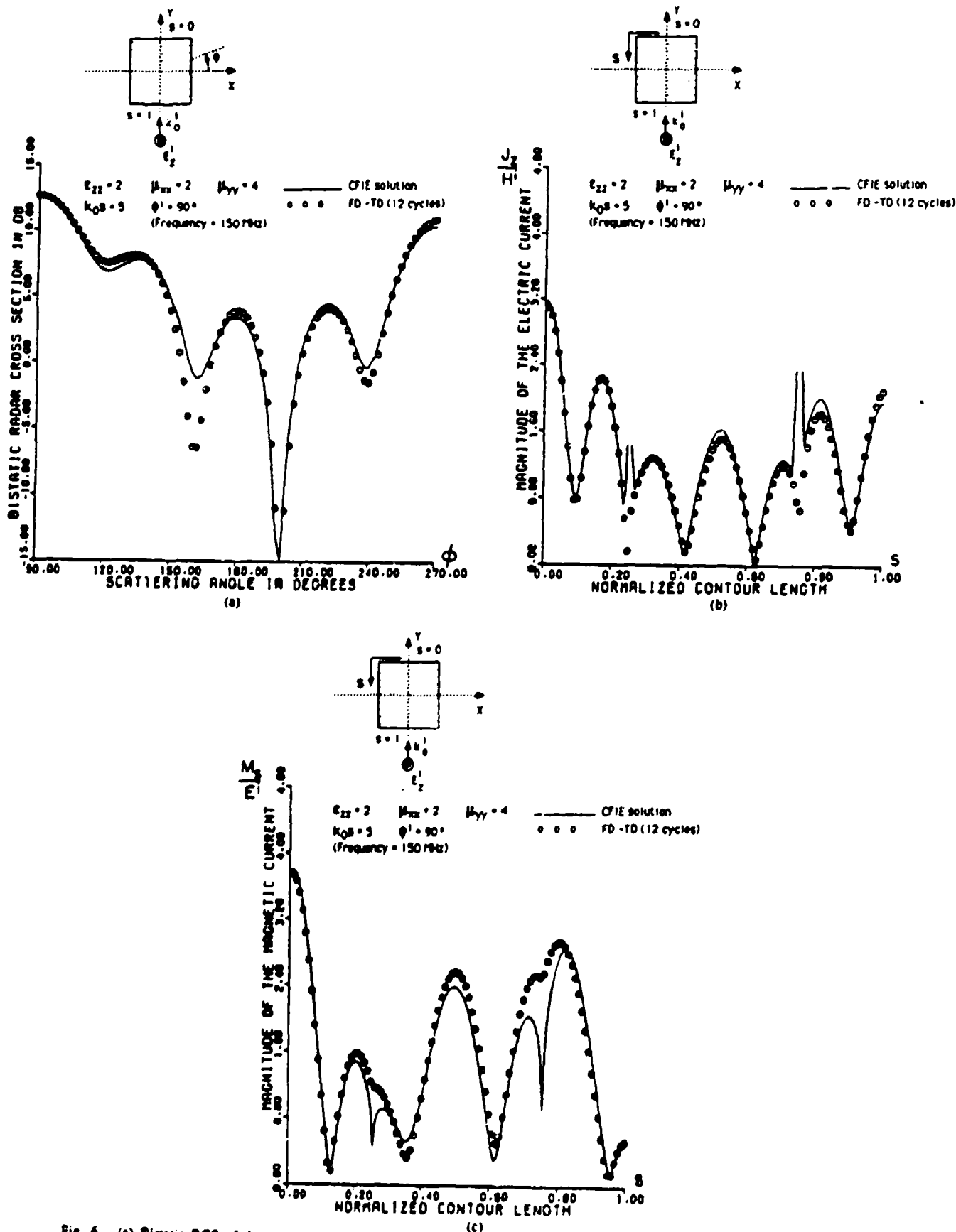


Fig. 6. (a) Bistatic RCS of the square anisotropic cylinder, high permeability case. (b) Surface electric current distribution of the square anisotropic cylinder, high permeability case. (c) Surface magnetic current distribution of the square anisotropic cylinder, high permeability case.

played in Fig. 5, the CPU time consumed by the algorithm was recorded. The actual time for all of the results to be calculated was found to be 1770.10 s on the IBM-370 mainframe. This indicates that consideration of electrically large anisotropic scatterers is quite feasible for the numerical solution.

#### V. SUMMARY

In this paper, a numerical solution of the combined field surface integral equations for the case of arbitrary shaped two-dimensional anisotropic scatterers has been presented. The computed results for the surface fields and the far scattered fields are validated by the currently available alternative methods, such as the FD-TD [2] and that of plane wave representation of fields in the anisotropic medium [7]. The discussion included a detailed account of the various aspects involved in the numerical solution, including the results of the singularity analysis for the integrals containing different orders of the Hankel functions for both anisotropic and isotropic media. The computer algorithm developed is applicable both for smooth contours and those with sharp edges.

#### REFERENCES

- [1] A. Taflové and M. E. Brodwin, "Numerical solution of steady-state electromagnetic scattering problems using the time dependent Maxwell's equations," *IEEE Trans. Microwave Theory Tech.*, vol. MTT-23, no. 8, pp. 623-630, Aug. 1975.
- [2] A. Taflové and K. R. Umashankar, "Radar cross section of general three-dimensional scatterers," *IEEE Trans. Electromagn. Comput.*, vol. EMC-25, no. 4, pp. 433-440, Nov. 1983.
- [3] R. D. Graglia, "Integral equations for anisotropic scatterers," Ph.D. dissertation, Univ. Illinois, Chicago, 1983.
- [4] R. D. Graglia and P. L. E. Uslenghi, "Electromagnetic scattering from anisotropic materials. Part I: General theory," *IEEE Trans. Antennas Propagat.*, vol. AP-32, no. 4, pp. 867-869, Aug. 1984.
- [5] —, "Electromagnetic scattering from anisotropic materials. Part II: Computer code and numerical results in two-dimensions," *IEEE Trans. Antennas Propagat.*, vol. AP-35, no. 2, pp. 225-232, Feb. 1987.
- [6] R. B. Wu and C. H. Chen, "Variational reaction formulation of scattering for anisotropic dielectric cylinders," *IEEE Trans. Antennas Propagat.*, vol. AP-34, no. 5, pp. 640-646, May 1986.
- [7] J. C. Monzon and N. J. Damaskos, "Two-dimensional scattering by a homogeneous anisotropic rod," *IEEE Trans. Antennas Propagat.*, vol. AP-34, no. 10, pp. 1243-1249, Oct. 1986.
- [8] J. C. Monzon, "Three-dimensional scattering by an infinite homogeneous circular cylinder: A spectral approach," *IEEE Trans. Antennas Propagat.*, vol. AP-35, no. 6, pp. 670-682, June 1987.
- [9] B. Beker and K. R. Umashankar, "Analysis of electromagnetic scattering by arbitrary shaped two-dimensional anisotropic objects: Combined field surface integral equation formulation," *Electromagn.*, vol. 9, pp. 215-229, Jan. 1989.
- [10] K. R. Umashankar and A. Taflové, "Analytical models for electromagnetic scattering," *Electromagn. Sci. Div., RADC, Hanscom AFB, MA, Final Tech. Rep. June 1984.*
- [11] R. F. Harrington, *Time-Harmonic Electromagnetic Fields*. New York: McGraw-Hill, 1961, ch. 3.
- [12] D. R. Wilton and C. M. Butler, "Effective methods for solving integral and integro-differential equations," *Electromagn.*, vol. 1, no. 3, pp. 289-308, July-Sept. 1981.
- [13] B. Beker and K. R. Umashankar, "Numerical solution of the combined field surface integral equations for the analysis of electromagnetic scattering by arbitrary shaped two-dimensional structures," in *Proc. IEEE-API/RSI Int. Symp.*, Blacksburg, VA, June 1987, p. 253.
- [14] M. Abramowitz and A. I. Stegun, *Handbook of Mathematical Functions*. New York: Dover, 1970, p. 480.
- [15] B. Beker, "Analysis of electromagnetic scattering by arbitrary shaped anisotropic objects using combined field surface integral equation formulation," Ph.D. dissertation, Univ. Illinois, Chicago, 1988.
- [16] M. Kobayashi and R. Terakado, "New view on an anisotropic medium and its application to transformation from anisotropic to isotropic problems," *IEEE Trans. Microwave Theory Tech.*, vol. MTT-27, no. 9, pp. 769-775, Sept. 1979.

Benjamin Beker (S'83-M'83-M'88), for a photograph and biography please see page 1257 of the November 1987 issue of this TRANSACTIONS.

Korada R. Umashankar (S'69-M'75-SM'81), for a photograph and biography please see page 765 of the June 1986 issue of this TRANSACTIONS.

Allen Taflové (M'75-SM'84), for a photograph and biography please see page 766 of the June 1986 issue of this TRANSACTIONS.

# THE FINITE-DIFFERENCE TIME-DOMAIN METHOD FOR NUMERICAL MODELING OF ELECTROMAGNETIC WAVE INTERACTIONS

---

Allen Taflov, *Department of Electrical  
Engineering and Computer Science,  
McCormick School of Engineering,  
Northwestern University, Evanston,  
Illinois 60208, USA*

Korada R. Umashankar, *Department of Electrical  
Engineering and Computer Science,  
University of Illinois at Chicago,  
Chicago, Illinois 60680, USA*

## ABSTRACT

This paper succinctly reviews the background and formulation of the finite-difference time-domain (FD-TD) method for numerical modeling of electromagnetic wave interactions with arbitrary structures. Selected 3-D results are given showing comparisons with both measured data and other numerical modeling approaches. An assessment is made of the present horizon of FD-TD modeling capabilities, and possible future directions.

## 1. INTRODUCTION

Accurate numerical modeling of full-vector electromagnetic (EM) wave interactions with arbitrary structures is difficult. Typical structures of engineering interest have shapes, apertures, cavities, and material compositions that produce near fields that cannot be resolved into finite sets of modes or rays. Proper numerical modeling of such near fields requires sampling at sub-wavelength ( $\text{sub-}\lambda$ ) resolution to avoid aliasing of magnitude and phase information. The goal is to provide a self-consistent model of the mutual coupling of the electrically-small cells comprising the structure, even if the structure spans tens of  $\lambda$  in 3-D.

This paper reviews the formulation and applications of a candidate numerical modeling approach for this purpose: the finite-difference time-domain (FD-TD) solution of Maxwell's curl equations. FD-TD is very simple in concept and execution. However, it is remarkably robust, providing highly accurate modeling predictions for a wide variety of EM wave interaction problems. FD-TD is analogous to existing finite-difference solutions of scalar wave propagation and fluid flow problems in that the numerical model is based upon a direct, time-domain solution of the governing partial differential equation. Yet, FD-TD is a nontraditional approach to numerical electromagnetics for engineering applications where frequency-domain integral equation approaches have dominated for 25 years.

One of the goals of this paper is to demonstrate that recent advances in FD-TD modeling concepts and software implementation, combined with advances in computers, have expanded the scope, accuracy, and speed of FD-TD modeling to the point where it may be the best choice for large EM wave interaction problems. With this in mind, this paper will succinctly review selected 2-D and 3-D FD-TD modeling validations and examples:

1. EM wave penetration and coupling
  - a. Narrow slot in a thick screen (2-D, TE-polarized case)
  - b. Wires in free space and in a metal cavity (2-D and 3-D)

2. Scattering and radar cross section (RCS)
  - a. T-shaped conducting target, multiple monostatic looks (3-D)
  - b. Trihedral corner reflector, both bare metal and with absorbing coating (3-D)
  - c. Wing-like structure, conformally modeled (2-D, TM-polarized case)
  - d. Jet engine inlet, conformally modeled (3-D)

Finally, this paper will conclude with an assessment of the present horizon of FD-TD modeling capabilities, and possible future directions.

## 2. GENERAL CHARACTERISTICS OF FD-TD

FD-TD is a direct solution of Maxwell's time-dependent curl equations. It employs no potentials. Instead, it applies simple, second-order accurate central-difference approximations [1] for the space and time derivatives of the electric (E) and magnetic (H) fields directly to the differential operators of the curl equations. This achieves a sampled-data reduction of the continuous EM field in a volume of space over a period of time. Space and time discretizations are selected to bound errors in the sampling process and to ensure numerical stability of the algorithm [2]. Overall, FD-TD is a marching-in-time procedure which simulates the continuous actual waves by sampled-data numerical analogs propagating in a computer data space. The system of equations to update E and H is fully explicit, so that there is no need to solve simultaneous equations. Thus, the required computer storage and running time is dimensionally low, proportional only to  $N$ , where  $N$  is the number of EM field unknowns in the volume modeled.

Fig. 1a illustrates the time-domain wave tracking concept of the FD-TD method. A region of space having initially zero fields is selected for field sampling in space and time. At  $t=0$ , it is assumed that an incident plane wave enters the region. Propagation of this wave is modeled by time-stepping, i.e., simply implementing the finite-difference analog of the curl equations. Time-stepping continues as the numerical analog of the incident wave strikes the modeled target embedded within the sampling region. All outgoing scattered wave analogs ideally propagate through the lattice truncation planes with negligible reflection to exit the region. Phenomena such as induction of surface currents, scattering

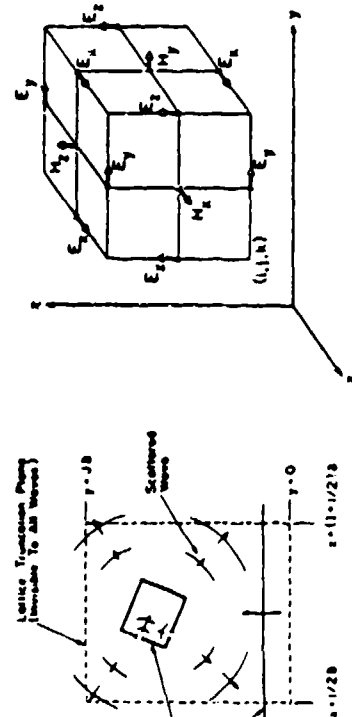


Fig. 1. Basic elements of the FD-TD space lattice.  
(a) Time domain wave tracking concept. (b) Lattice unit cell in Cartesian coordinates.

and multiple scattering, aperture penetration, and cavity excitation are modeled time-step by time-step by the action of the curl equations analog. Self-consistency of these modeled phenomena is generally assured if their spatial and temporal variations are well resolved by the space and time sampling process.

Time-stepping is continued until the desired late-time pulse response or steady-state behavior is observed. An important example of the latter is the sinusoidal steady state, wherein the incident wave is assumed to have a sinusoidal dependence, and time-stepping is continued until all fields in the sampling region exhibit sinusoidal repetition. This is a consequence of the limiting amplitude principle [3]. Extensive numerical experimentation with FD-TD has shown that the number of complete cycles of the incident wave required to be time-stepped to achieve the sinusoidal steady state is a function of two (possibly related) factors:

- 1) **Target electrical size.** Numerical wave analogs must be permitted time to propagate in the FD-TD grid to causally connect the physics of all regions of the target. For many targets, this requires a number of time steps sufficient to permit at least two front-to-back-to-front traverses of the target by a wave analog. For example, assuming a target spanning  $10\lambda$ , at least 40 cycles of the incident wave should be time-stepped to approach the sinusoidal steady state. For a grid resolution of  $\lambda/10$ , this corresponds to 800 time steps.
- 2) **Target Q factor.** Targets having well-defined low-loss cavities or low-loss dielectric compositions may require the number of complete cycles of the incident wave to be time-stepped to approach the Q factor of the resonance. Because Q can be large even for electrically moderate size cavities, this can dictate how many time steps the FD-TD code must be run.

In the RCS area, target electrical size may often be the dominant factor. Cavities for RCS problems (such as engine inlets) tend to be open, and therefore moderate Q; and the use of radar-absorbing material (RAM) serves further to reduce the Q factors of structures.

Fig. 1b illustrates the positions of the E and H vector components about a unit cell of the FD-TD lattice in Cartesian coordinates [1]. Note that each H component is surrounded by four circulating E components, and vice versa. This arrangement permits not only a centered-difference analog to the space derivatives of the curl equations, but also a natural geometry for implementing the integral form of Faraday's Law and Ampere's Law at the space-cell level. This integral interpretation permits a simple but effective modeling of the physics of thin-slot coupling, thin-wire coupling, and smoothly curved target surfaces, as will be seen in Section 4.

An arbitrary 3-D scatterer can be embedded in an FD-TD lattice simply by assigning desired values of electrical permittivity and conductivity to each lattice E component, and magnetic permeability and equivalent loss to each H component. These are interpreted by the FD-TD program as local coefficients for the time-stepping algorithm. Specification of media properties in this component-by-component manner results in a staircase approximation of curved surfaces, and assures continuity of tangential fields at the interface of dissimilar media with no need for special field matching. In the 1970's through mid-1980's, the staircase approximation of curved surfaces was found to be adequate in FD-TD modeling problems involving EM wave interactions with biological issues [4], [5], penetration into cavities [6], [8], and pulse interactions with structures [9], [11]. However, recent interest in wide dynamic range models of scattering has prompted the development of fully surface-conforming FD-TD approaches. One such approach is summarized in Section 4c.

## 3. BASIC FD-TD ALGORITHM DETAILS

## a. Time-Stepping Algorithm

Table 1 lists the six coupled equations for  $E$  and  $H$  that comprise Maxwell's equations in Cartesian coordinates, and the central-difference approximations to the space and time partial derivatives of these equations, using a sampled-field notation.

$$\begin{aligned}\frac{\partial H_x}{\partial t} &= \frac{1}{\mu} \left( \frac{\partial E_z}{\partial y} - \frac{\partial E_y}{\partial z} - \rho' H_x \right) \\ \frac{\partial H_y}{\partial t} &= \frac{1}{\mu} \left( \frac{\partial E_x}{\partial z} - \frac{\partial E_z}{\partial x} - \rho' H_y \right) \\ \frac{\partial H_z}{\partial t} &= \frac{1}{\mu} \left( \frac{\partial E_y}{\partial x} - \frac{\partial E_x}{\partial y} - \rho' H_z \right) \\ \frac{\partial E_x}{\partial t} &= \frac{1}{\epsilon} \left( \frac{\partial H_z}{\partial y} - \frac{\partial H_y}{\partial z} - \sigma E_x \right) \\ \frac{\partial E_y}{\partial t} &= \frac{1}{\epsilon} \left( \frac{\partial H_x}{\partial z} - \frac{\partial H_z}{\partial x} - \sigma E_y \right) \\ \frac{\partial E_z}{\partial t} &= \frac{1}{\epsilon} \left( \frac{\partial H_y}{\partial x} - \frac{\partial H_x}{\partial y} - \sigma E_z \right)\end{aligned}$$

where:

$E_x, E_y, E_z$  = Cartesian components of electric field, volts/meter  
 $H_x, H_y, H_z$  = Cartesian components of magnetic field, volts/meter  
 $\epsilon$  = electric permittivity, farads/meter  
 $\sigma$  = electric conductivity, siemens/meter  
 $\mu$  = magnetic permeability, henrys/meter  
 $\rho'$  = equivalent magnetic loss, ohms/meter

$$\begin{aligned}(i, j, k) &= (i \Delta x, j \Delta y, k \Delta z) \\ F^n(i, j, k) &= F(i \Delta x, j \Delta y, k \Delta z, n \Delta t) \\ \frac{\partial F^n(i, j, k)}{\partial x} &= \frac{F^n(i + \frac{1}{2}, j, k) - F^n(i - \frac{1}{2}, j, k)}{\Delta x} + \text{order}(\Delta x^2) \\ \frac{\partial F^n(i, j, k)}{\partial t} &= \frac{F^{n+1}(i, j, k) - F^{n-1}(i, j, k)}{\Delta t} + \text{order}(\Delta t^2)\end{aligned}$$

For a cubic space lattice,  $\Delta x = \Delta y = \Delta z \equiv \delta$

Table 1. Maxwell's equations and central-difference approximations.

Upon substituting the central-difference approximations for the space and time derivatives into Maxwell's equations, six coupled finite-difference time-stepping expressions arise for the Cartesian components of  $E$  and  $H$ . These expressions permit a progressive time integration of the Maxwell's equations suitable for the solution of an initial-value problem. The following is a sample time-stepping expression for an electric field component:

$$E_x^{n+1}(i, j, k + 1/2) = \frac{1 - \frac{\sigma(i, j, k + 1/2) \Delta t}{2\epsilon(i, j, k + 1/2)}}{1 + \frac{\sigma(i, j, k + 1/2) \Delta t}{2\epsilon(i, j, k + 1/2)}} E_x^n(i, j, k + 1/2) + \frac{1}{1 + \frac{\sigma(i, j, k + 1/2) \Delta t}{2\epsilon(i, j, k + 1/2)}} \times \left[ \frac{\Delta t}{2\epsilon(i, j, k + 1/2)} \left( H_y^{n+1/2}(i + \frac{1}{2}, j, k + \frac{1}{2}) - H_y^{n+1/2}(i - \frac{1}{2}, j, k + \frac{1}{2}) \right) + \right. \\ \left. - \frac{\Delta t}{2\epsilon(i, j, k + 1/2)} \left( H_z^{n+1/2}(i, j - \frac{1}{2}, k + \frac{1}{2}) - H_z^{n+1/2}(i, j + \frac{1}{2}, k + \frac{1}{2}) \right) \right] \quad (1)$$

Time-stepping expressions for the other electric field components follow by analogy. For the magnetic field components, the magnetic permeability  $\mu$  and equivalent loss  $\rho'$  simply appear in place of the electric permittivity  $\epsilon$  and conductivity  $\sigma$ .

The time-stepping system represented by (1) is fully explicit. That is, the new value of a field vector component at any lattice point depends only on its previous value and on previous values of the other field. Therefore, at any given time step, the updating of a field vector can proceed one point at a time; or, if  $p$  parallel processors are employed concurrently,  $p$  points at a time.

To insure the stability of the time-stepping algorithm exemplified by (1),  $\Delta t$  is chosen to satisfy the inequality [2],[8]

$$\Delta t \leq \frac{1}{c_{\max} \left( \frac{1}{\delta^2} + \frac{1}{\delta^2} + \frac{1}{\delta^2} \right)^{1/2}} \quad (2)$$

where  $c_{\max}$  is the maximum EM wave phase velocity within the media being modeled. Note that the corresponding stability criterion in [1, Eqs. (7) and (8)] is incorrect [2],[8].

## b. Numerical Dispersion

The numerical algorithm for Maxwell's curl equations represented by (1) causes dispersion of the simulated wave modes in the computational lattice. That is, the phase velocity of numerical modes in the FD-TD lattice can vary with modal wavelength, direction of propagation, and lattice discretization. Since numerical dispersion can lead to non-physical results such as pulse distortion, anisotropy, and refraction, it is a factor in FD-TD modeling that must be accounted to understand the operation of the algorithm and its accuracy limits.

Following the analysis in [8], it can be shown that the numerical dispersion relation for the 3-D case represented by (1) is given by

$$\left(\frac{1}{c\Delta t}\right)^2 \omega \Delta t^2 \left(\frac{\omega \Delta t}{2}\right) = \frac{1}{\Delta x^2} \omega \Delta t^2 \left(\frac{k_x \Delta x}{2}\right) + \frac{1}{\Delta y^2} \omega \Delta t^2 \left(\frac{k_y \Delta y}{2}\right) + \frac{1}{\Delta z^2} \omega \Delta t^2 \left(\frac{k_z \Delta z}{2}\right) \quad (3)$$

where  $k_x$ ,  $k_y$ , and  $k_z$  are, respectively, the  $x$ ,  $y$ , and  $z$  components of the wavevector;  $\omega$  is the wave angular frequency; and  $c$  is the speed of light in the homogeneous material being modeled.

In contrast to the numerical dispersion relation, the analytical dispersion relation for a plane wave in a continuous, lossless medium is just

$$\omega^2/c^2 = k_x^2 + k_y^2 + k_z^2 \quad (4)$$

for the 3-D case. We can easily show that (3) reduces to (4) in the limit as  $\Delta t$ ,  $\Delta x$ ,  $\Delta y$ , and  $\Delta z$  all go to zero. Qualitatively, this suggests that numerical dispersion can be reduced to any degree that is desired if we only use a fine-enough FD-TD gridding.

To quantitatively illustrate the dependence of numerical dispersion upon FD-TD grid discretization, we shall take as an example the 2-D case ( $\Delta z = \infty$ ), assuming for simplicity square unit cells. Fig. 2 provides results for this case showing the variation of numerical wave phase velocity with wave propagation angle in the grid [8].

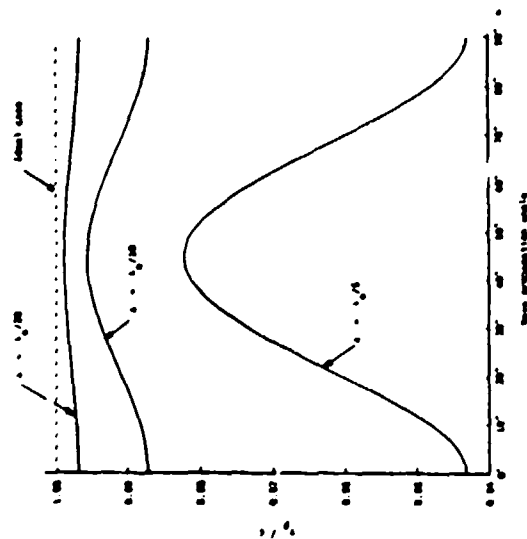


Fig. 2. Variation of FD-TD numerical wave phase velocity with wave propagation angle in the grid for three different grid discretizations.

In Fig. 2, three different grid resolutions of the propagating wave are examined:  $\lambda/5$ ,  $\lambda/10$ , and  $\lambda/20$ . For each resolution, the relation  $c\Delta t = \delta/2$  is maintained. This relation is commonly used in 2-D and 3-D FD-TD codes to satisfy the numerical stability criterion of (2) with an ample safety margin. It is seen that the numerical phase velocity is maximum at  $15^\circ$  (oblique incidence) and minimum at  $0^\circ$  and  $90^\circ$  (incidence along either Cartesian grid axis) for all grid resolutions. This represents a numerical anisotropy that is inherent in the Yee algorithm. However, the velocity error diminishes quadratically with grid resolution, so that the worst-case velocity error is  $\sim 1.3\%$  for  $\lambda/10$  grid resolution, but only  $\sim 0.31\%$  for  $\lambda/20$  resolution.

In addition to numerical phase velocity anisotropy and pulse distortion effects, numerical dispersion could lead to non-physical refraction of propagating modes if the cell size is a function of position in the grid. This is because the modal phase velocity distribution would vary with position in the grid, just as in an inhomogeneous medium. The error level would depend upon the magnitude and abruptness of the changes of the phase velocity distribution, and could be estimated by using conventional theory for wave refraction at dielectric interfaces.

### c. Lattice Zoning and Plane Wave Source Condition

The numerical algorithm for Maxwell's curl equations defined by the finite-difference system reviewed above has a linear dependence upon the components of the EM field vectors. Therefore, this system can be applied with equal validity to either the incident field, the scattered field, or the total field vector components. Present FD-TD codes utilize this property to divide the numerical lattice into two distinct zones, a total field zone and a scattered field zone, as shown in Fig. 3a. The zones are separated by a

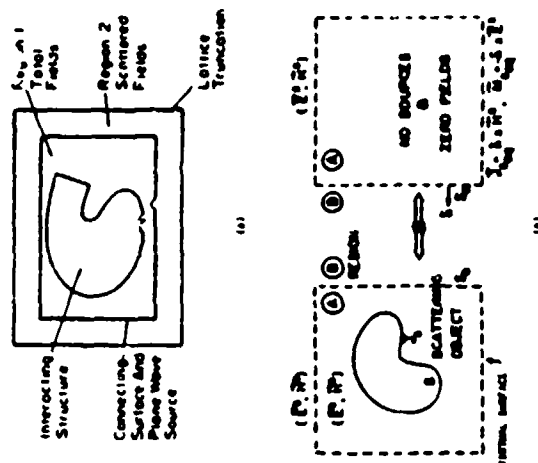


Fig. 3. Zones of the FD-TD lattice. (a) Total-field and scattered-field regions. (b) Near-to-far field integration surface located in the scattered-field region.

rectangular virtual surface which serves to connect the fields in each region [12],[13]. The interacting structure of interest is embedded within the total-field zone.

The total-field/scattered field lattice zoning shown in Fig. 3a provides a number of key features which enhance the computational flexibility and dynamic range of the FD-TD method:

- 1) *Arbitrary incident wave.* The connecting condition provided at the interface of the inner, and outer regions, which assures consistency of the numerical space derivative operations across the interface, simultaneously generates an arbitrary incident plane wave in Region 1 having a user-specified time waveform, angle of incidence, and angle of polarization. This connecting condition, discussed in [8], almost completely confines the incident wave to Region 1 and yet is transparent to outgoing scattered wave modes which are free to enter Region 2.
- 2) *Simple programming of homogeneous structures.* Embedding the modeled structure in the total-field region permits a natural satisfaction of tangential field continuity across media interfaces without having to compute the incident field at possibly tens of thousands of points along complicated media-interface loci that are unique to each structure. The zoning arrangement of Fig. 3a requires computation of the incident field only along the rectangular connecting surface between total-field and scattered-field regions. This surface is fixed, i.e., independent of the shape or composition of the enclosed modeled structure. A substantial benefit in computer running time accrues as a result, one that increases as the complexity of the target increases.
- 3) *Large near-field computational dynamic range.* Because the modeled structure is embedded in the total-field region, low total-field levels in shadow regions or within shielding enclosures are computed directly without suffering subtraction noise (as would be the case if scattered fields in such regions were time-stepped, and then added to a canceling incident field to obtain the low total-field levels). Avoidance of subtraction noise is the key to obtaining near-field computational dynamic ranges exceeding 60 dB.
- 4) *Systematic computation of bistatic RCS.* The provision of a well-defined scattered-field region in the FD-TD lattice permits the near-to-far field transformation illustrated in Fig. 3b [13]. The dashed virtual surface shown in Fig. 3b can be located along convenient lattice planes in the scattered-field region of Fig. 3a. Tangential scattered E and H fields computed via FD-TD at this virtual surface can then be weighted by the free-space Green's function and integrated (summed) to provide the far-field response and RCS (full bistatic response for the assumed illumination angle) [13],[15]. The near-field integration surface has a fixed rectangular shape independent of the composition of the enclosed modeled structure.

#### d. Lattice Truncations

The fields at the outermost lattice planes cannot be computed using central differences because of the absence of known field data at points outside of the lattice. Therefore, an auxiliary lattice truncation condition is necessary. This condition must permit an outgoing scattered-wave numerical analog to exit the lattice without appreciable nonphysical reflection.

It has been shown that the required lattice truncation condition is really a radiator condition in the near field [16],[19]. A successful second-order-accurate finite-difference approximation of the exact radiation condition in Cartesian coordinates was introduced in [12]. This was subsequently used in a variety of 2-D and 3-D FD-TD scattering codes [13],[15], yielding excellent results for both near and far fields (including those of this paper). However, recent interest in improved models of scattering has prompted research in higher-order near-field radiation conditions [19],[21]. The

goal is to reduce numerical noise due to imperfect lattice truncations by at least one order of magnitude (20 dB) relative to that achieved by [12].

#### 4. CONTOUR PATH INTERPRETATION

The original FD-TD algorithm was devised to directly approximate the pointwise derivatives of Maxwell's time-dependent curl equations by numerical central differences [1]. While this thinking is useful for understanding how FD-TD models wave propagation in free space, it sheds little light on what modifications are needed to model the physics of free structural features such as wires and slots requiring sub-cell spatial resolution.

Recent work has indicated that FD-TD modeling can be extended by starting with a more macroscopic description based upon Ampere's Law and Faraday's Law in integral form, implemented on an array of electrically small, spatially orthogonal contours. These contours mesh in the manner of links in a chain, filling the FD-TD modeled space. It can be easily shown that the original pointwise and new contour path interpretations are equivalent for the free-space case [22]. Further, it can be shown that wires, slots, and curved surfaces can be modeled by incorporating appropriate field behavior into the contour and surface integrals implementing Ampere's Law and Faraday's Law at selected meshes, and by deforming contour paths as required to conform with surface curvature.

##### a. Example 1: Application to the Thin Slot

To illustrate how the contour path interpretation provides the basis for FD-TD modeling of line geometrical features requiring sub-cell spatial resolution, we first consider the thin slot in a planar conducting screen (TE case) [22]. Fig. 4 illustrates the slot geometry and the Faraday's Law contour paths,  $C_1$ ,  $C_2$ , and  $C_3$ , used to derive special FD-TD algorithms for the longitudinal magnetic field components,  $H_z$ , located immediately adjacent to the screen.

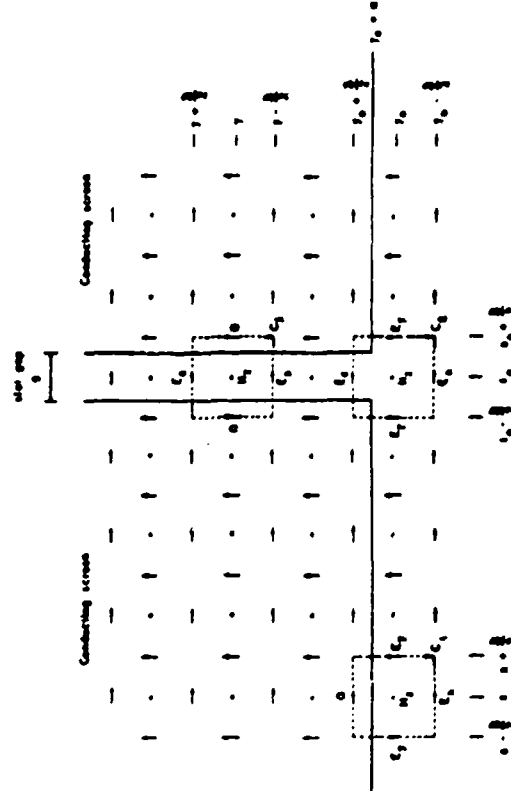


Fig. 4. Faraday's Law contour paths for the planar conducting screen with narrow straight slot (TE case).

Very simple assumptions are made regarding the field behavior near the slotted screen:

- 1) At contour  $C_1$ ,  $H_z$  and  $E_y$  have no variation in  $y$ . Evaluated at the  $x$  midpoint of  $C_1$ ,  $H_z$  and  $E_x$  represent the average values of their respective fields over the full  $x$  interval.
- 2) At contour  $C_2$ ,  $H_z$  is the average value of the magnetic field over the free-space part of  $S_2$ .  $E_y$  has no variation in  $y$ , and  $E_x$  is the average value over the full  $x$  interval.
- 3) At contour  $C_3$ ,  $H_z$  is the average value of the magnetic field over the full  $y$  interval, and  $H_x$  and  $E_x$  have no variation in the  $x$  direction (across the slot gap).

After applying Faraday's Law for the three contours subject to the above assumptions, the following special FD-TD time-stepping relations are obtained for  $H_z$  components [22]:

Away from the slot (contour  $C_1$ )

$$\frac{B_z^{n+1/2}(x, y) - B_z^{n-1/2}(x, y)}{\Delta t} = \frac{[E_y^n(x - \frac{1}{2}\Delta x) - E_y^n(x + \frac{1}{2}\Delta x)] \cdot (\frac{1}{2} + \alpha) - E_x^n(x, y - \frac{1}{2}) \cdot \delta}{\mu_0(\frac{1}{2} + \alpha)} \quad (5a)$$

At the opening (aperture) of the slot (contour  $C_2$ )

$$\frac{B_z^{n+1/2}(x_0, y) - B_z^{n-1/2}(x_0, y)}{\Delta t} = \frac{\left( \frac{E_y^n(x_0, y + \frac{1}{2}) \cdot g - E_y^n(x_0, y - \frac{1}{2}) \cdot \delta + [E_y^n(x_0 - \frac{1}{2}\Delta x) - E_y^n(x_0 + \frac{1}{2}\Delta x)] \cdot (\frac{1}{2} + \alpha)}{\mu_0 \cdot [H(\frac{1}{2} + \alpha) + H(\frac{1}{2} - \alpha)]} \right)}{\quad} \quad (5b)$$

Within the slot (contour  $C_3$ )

$$\frac{B_z^{n+1/2}(x_0, y) - B_z^{n-1/2}(x_0, y)}{\Delta t} = \frac{E_y^n(x_0, y + \frac{1}{2}) \cdot g - E_y^n(x_0, y - \frac{1}{2}) \cdot g}{\mu_0 g} \quad (5c)$$

No  $H$  or  $E$  components in the FD-TD grid other than these  $H_z$  components immediately adjacent to the screen require modified time-stepping relations.

## FINITE-DIFFERENCE TIME-DOMAIN METHOD

### b. Example 2: Application to the Thin Wire

The contour path interpretation is next applied to model coupling to a sub-cell diameter wire [23]. Fig. 5 illustrates the Faraday's Law contour path used to derive the special FD-TD algorithm for the circumferential  $H$  immediately adjacent to the wire.

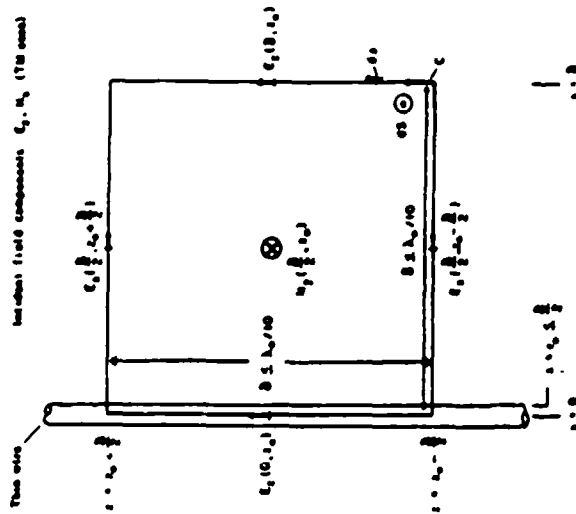


Fig. 5. Faraday's Law contour path for thin-wire model.

Although only  $H_y$  and  $E_x$  are shown, the analysis is easily generalized for the other adjacent looping  $H$  ( $H_x$ ) and radial  $E$  ( $E_y$ ). Very simple assumptions are made regarding the field behavior near the wire:

- 1) The scattered circumferential  $H$  and the scattered radial  $E$  components vary as  $1/r$ , where  $r$  is the distance from the wire center. (In Fig. 5,  $1/r$  is interpreted as  $1/\lambda$ .)
- 2) With  $r$  constrained to be less than  $\lambda/10$  at any point in  $C$  by FD-TD spatial resolution requirements, the  $1/r$  singularity behavior of the scattered circumferential  $H$  and radial  $E$  dominates the respective incident fields, so that the total circumferential  $H$  and total radial  $E$  also take on the  $1/r$  singularity.
- 3) The total circumferential  $H$  and the total longitudinal  $E$ , evaluated at the  $z$  midpoint of the contour, represent the average values of their respective fields over the full  $z$  interval.

Using these assumptions, we now apply Faraday's Law along contour  $C$ . The  $1/r$  variations in  $H_y$  and  $E_x$  yield natural logarithms upon integration. This yields the following [23]:

$1/h$



$$\frac{E_z^{n+1}(j, z_0) - E_z^n(j, z_0)}{\Delta t} = \frac{(E_z^n(j, z_0) - E_z^n(j, z_0)) + \frac{1}{2} \ln \left( \frac{z_0}{z_0} \right) + E_z^n(j, z_0)}{2 \frac{1}{2} \ln \left( \frac{z_0}{z_0} \right)} \quad (6)$$

where  $r_0$  (assumed to be less than  $\delta/2$ ) is the wire radius. Isolation of  $H_y^{n+1/2}(\delta/2, z_0)$  on the left hand side of (9) yields the required modified time-stepping relation. No H or E components in the FD-TD lattice other than the circumferential H components immediately adjacent to the wire require modified time-stepping relations.

### c. Example 3: Application to Curved Surfaces

The contour path interpretation is best applied to model scattering by targets having curved surfaces [24]. Fig. 6 depicts the embedding of such a target in a 2-D TE grid. Faraday's Law can be used to define integration contours that either split or stretch selected grid cells in a manner to conform with the curved target surface. Very simple assumptions are made regarding the field behavior at these special cells:

- 1) Each  $H_z$  component is evaluated at its usual grid position, and is the average value within the patch bounded by the deformed cell contour.
- 2) Each  $E_x$  or  $E_y$  component is evaluated at its usual grid position, and is the average value over its respective straight portion of the cell contour.
- 3) Where possible,  $E_z$  and  $E_y$  are calculated by finite-differencing adjacent  $H_z$ 's. Where such differencing would cut across the target surface,  $E_x$  or  $E_y$  is obtained simply by taking the value of its nearest co-linear  $E_x$  or  $E_y$  neighbor located on the same side of the target surface.

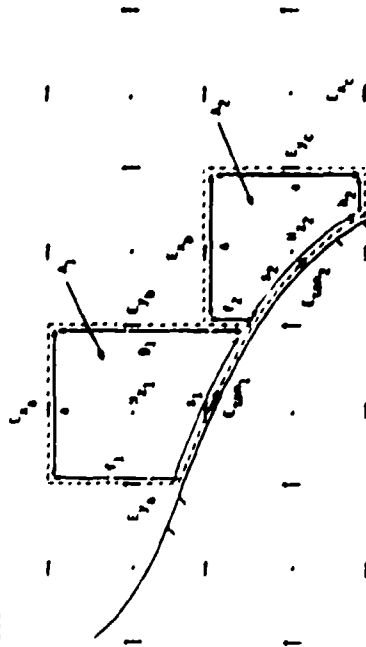


Fig. 6. Faraday's Law contour paths for conformal FD-TD modeling of a curved target.

4) An auxiliary field,  $E_{tan}$ , defined along the portion of the deformed cell contour that conforms to the target surface, represents the average value of the surface tangential E. For conducting targets having surface resistivity,  $E_{tan}$  can be easily related to the local tangential magnetic field by the surface resistivity,  $R_s$ .

5) For dielectric targets,  $E_{tan}$  is calculated by line-stepping using an Ampere's Law contour path that pierces the surface at a right angle. Exterior and interior  $H_z$ 's needed for this time-stepping are obtained via linear interpolation of stored  $H_z$ 's at standard grid locations.

Using these assumptions, we now apply Faraday's Law about the contours of Fig. 6 to obtain modified time-stepping relations for  $H_z$  suitable for conducting structures [24]:

Standard surface-conforming cell (contour  $C_1$ )

$$H_{z1}^{n+1} = C_1 \cdot H_{z1}^n + D_1 \cdot [E_{x1}^n \cdot \delta_1 - E_{y1}^n \cdot g_1 + E_{tan}^n \cdot \delta_1] \quad (7a)$$

where, assuming that  $R_{s1}$  is the local surface resistivity,

$$C_1 = \frac{(\frac{\delta_1}{\Delta t} - \frac{s_1^R}{2})}{(\frac{\delta_1}{\Delta t} + \frac{s_1^R}{2})} ; D_1 = \frac{1}{(\frac{\delta_1}{\Delta t} + \frac{s_1^R}{2})} \quad (7b)$$

Non-standard surface-conforming cell (contour  $C_2$ )

$$H_{z2}^{n+1} = C_2 \cdot H_{z2}^n + D_2 \cdot [E_{x2}^n \cdot \delta_2 - E_{y2}^n \cdot g_2 + E_{tan}^n \cdot \delta_2 - E_{tan}^n \cdot h_2] \quad (8a)$$

where, assuming that  $R_{s2}$  is the local surface resistivity,

$$C_2 = \frac{(\frac{\delta_2}{\Delta t} - \frac{s_2^R}{2})}{(\frac{\delta_2}{\Delta t} + \frac{s_2^R}{2})} ; D_2 = \frac{1}{(\frac{\delta_2}{\Delta t} + \frac{s_2^R}{2})} \quad (8b)$$

This procedure allows the conformal modeling of arbitrary curved targets essentially as easily and as quickly as the original stepped-surface FD-TD code, but with substantially better accuracy. No H or E components in the FD-TD space grid other than the  $H_z$  components immediately adjacent to the object surface require modified time-stepping relations.

## 5. FD-TD MODELING VALIDATIONS FOR PENETRATION AND COUPLING

## a. EMI Wave Penetration Through a Narrow Slot

The accuracy of the contour path model for sub-cell-gap slots (Section 4a) will now be illustrated for the case of a straight slot in a thick conducting screen [22].

Fig. 7 depicts modeling results for a  $\lambda/10$ -thick conducting screen that extends  $\lambda/2$  to each side of a straight slot which has a gap of  $\lambda/40$ . Broadside TE illumination is assumed. Three types of predictive data are compared: (a) A  $\lambda/10$  FD-TD model using the contour path approach to treat the slot as a 1/4-cell gap; (b) A high-resolution ( $\lambda/40$ ) FD-TD model treating the slot as a 1-cell gap; and (c) A very-high-resolution ( $\lambda/400$ ) sampling in the slot frequency-domain electric field integral equation (EFIE) model solved via M-M.

From Fig. 7, we see that there is excellent agreement between all three sets of predictive data in both magnitude and phase. It is seen that  $\lambda/10$  FD-TD gridding can accurately model the physics of wave penetration through sub-cell slots with the contour path approach. This can substantially reduce computer resource requirements for FD-TD models of complex structures.

## b. EMI Wave Coupling to Thin Wires and Bundles

The accuracy of the contour path technique for modeling EMI wave coupling to sub-cell-diameter wires (Section 4b) will now be illustrated for: (1) An infinitely long wire (over a wide range of radius); (2) A thin dipole; and (3) A wire-pair within a metal cavity [23].

Fig. 8a graphs the scattered azimuthal H field at a fixed distance of  $\lambda/20$  from the center of an infinitely long wire having a radius ranging between  $\lambda/30,000$  and  $\lambda/30$ .

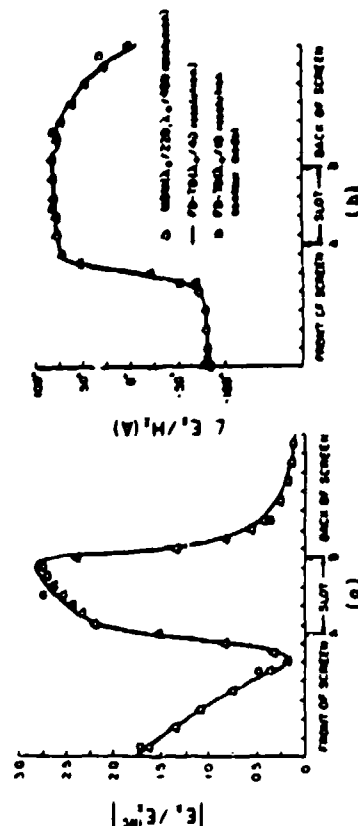


Fig. 7. Comparison of FD-TD and MoM solutions for the gap electric field distribution: (a) magnitude; (b) phase.

TM illumination is assumed. There is excellent agreement between the exact series solution and the  $\lambda/10$  FD-TD contour path model over the entire 3-decade range of wire radius. Fig. 8b graphs the scattered azimuthal H distribution along a  $2.0\lambda$  (antiresonant) wire of radius  $\lambda/200$ . Broadside TM illumination is assumed, and the field is observed at a fixed distance of  $\lambda/20$  from the wire center. There is excellent agreement between an EFIE MoM solution sampling the wire current at  $\lambda/80$  increments and the  $\lambda/10$  FD-TD contour path model.

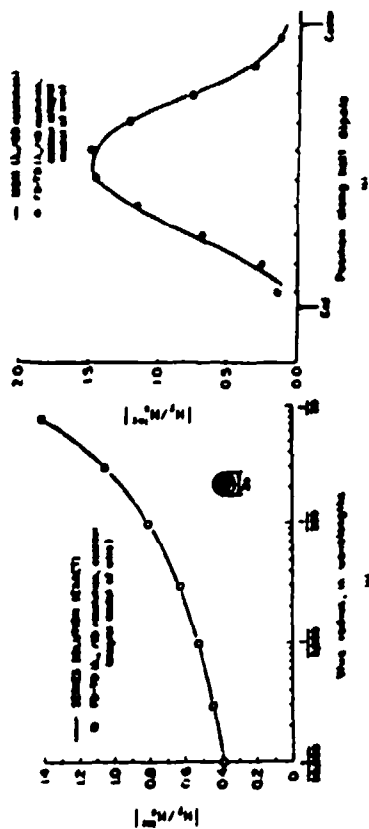


Fig. 8. Comparison of FD-TD and benchmark frequency-domain solutions for the scattered circumferential magnetic field: (a) infinite wire; (b)  $2.2\lambda$  wire.

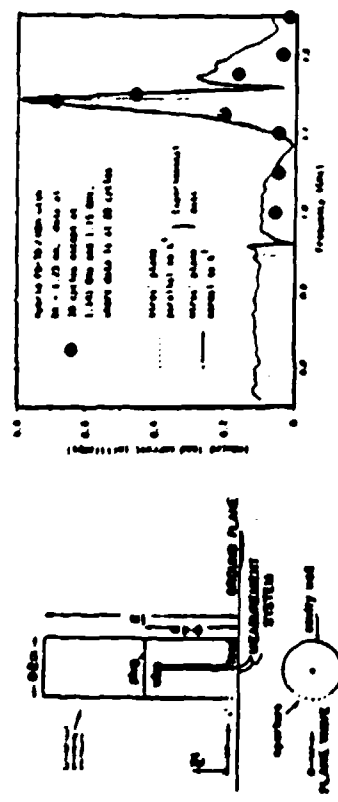


Fig. 9. Comparison of FD-TD and experimental data for coupling to a wire pair in a cavity.

The FD-TD contour path model for single thin wires can be extended to treat thin wire bundles [23]. Fig. 9 shows the geometry and test results for such a model involving a wire pair centered within a 3-D cylindrical metal cavity. The cavity, referenced to a large ground plane, is 1.6-m high, 20-cm diameter, and has an internal shorting plug located 40 cm above the ground plane. Approximate plane wave illumination in the band 0.75 - 1.25 GHz is provided by an electrically-large conical monopole. Wave penetration into the cavity is through a circumferential slot (12.5 cm arc length, 1.25 cm gap) at the ground plane. The internal pair is formed by two parallel wires (30-cm long, 0.495-mm radius) spaced 1 cm apart, with, respectively, 50- $\Omega$  and 0- $\Omega$  terminations to the ground plane.

From Fig. 9, we see that the predicted and measured wire load currents agree well. This test is challenging since the Q factor of the coupling response is quite high, about 75. Indeed, it is found that the FD-TD code has to be stepped through 80 cycles to approximately reach the sinusoidal steady state for illumination frequencies near the resonant peak [23].

#### a. FD-TD MODELING VALIDATIONS FOR SCATTERING AND RCS

Many analytical code-to-code, and experimental validations have been obtained for FD-TD modeling of EM wave scattering and RCS. Selected validations will be reviewed here.

##### a. T-shaped Conducting Target, Multiple Monostatic Looks

We first consider the monostatic RCS pattern of a 3-D T-shaped conducting target [15] consisting of a  $30 \times 10 \times 0.33$  cm main plate and a  $10 \times 10 \times 0.33$  cm bisecting fin (Fig. 10). The illumination is a 9.0-GHz plane wave at  $0^\circ$  elevation angle and TE polarization relative to the main plate. Thus, the main plate spans  $9.0\lambda$  and the fin  $3.0\lambda$ . Note that look-angle azimuths between  $90^\circ$  and  $180^\circ$  exhibit the complicated physics of back-to-back corner reflectors.

For this target, the FD-TD model uses a uniform cell size of  $0.3125$  cm ( $\lambda/10.667$ ), forming the main plate by  $96 \times 32 \times 1$  cells and the bisecting fin by  $32 \times 32 \times 1$  cells. The radiation boundary is located only 6 cells from this target, so that the lattice has  $112 \times 48 \times 48$  cells containing 1,548,288 unknown field components ( $212.6 \lambda^3$ ). Starting with zero fields, 661 time steps are used (31 cycles of the incident wave).

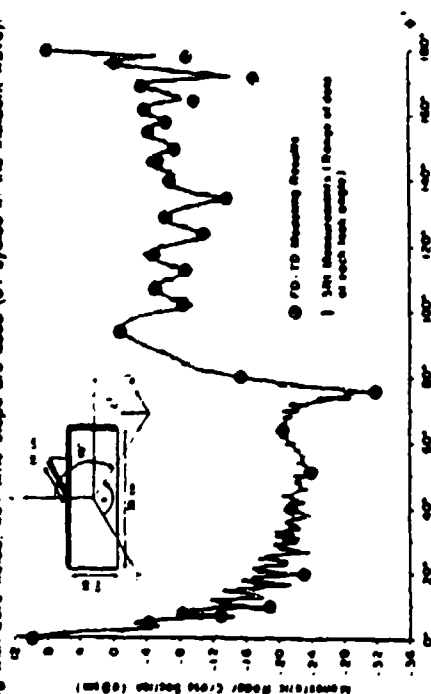


Fig. 10. Comparison of FD-TD and test data for monostatic RCS of the T-shaped target.

Fig. 10 compares the FD-TD predicted monostatic RCS values to measured data at 32 key look angles that define the major peaks and nulls of the pattern. The agreement is excellent: in amplitude, within 1 dB over a 40-dB dynamic range; and in azimuth, within  $1^\circ$ . Computer running time is about 12 seconds per monostatic angle on the Cray Y-MP.

##### b. Trifurcated Corner Reflector, Both Bare Metal and RAM Coated

We next consider the monostatic RCS pattern of a 3-D conducting trifurcated corner reflector, both uncoated and with commercial RAM coating. The reflector consists of three, thin,  $15 \times 15$  cm flat plates mounted at mutual  $90^\circ$  angles (Fig. 11a). The illumination is a 10-GHz plane wave at  $45^\circ$  azimuth angle and  $\theta$ -directed E-field. Thus, the reflector spans  $5 \times 5 \times 5 \lambda$ . For the coated case, the RAM is assumed to be Emerson & Cuming Type AN-73 (0.9525 cm thick, consisting of 3 distinct lossy layers of equal thickness).

For this target, the FD-TD cell size is  $0.25$  cm ( $\lambda/12$ ), with each plate spanned by  $60 \times 60$  cells. The radiation boundary is located only 12 cells from the target, so that the lattice has  $84 \times 84 \times 84$  cells containing 3,556,224 unknown field components ( $343 \lambda^3$ ). Starting with zero fields, 720 time steps are used (30 cycles of the incident wave).

Fig. 11b compares the FD-TD computed monostatic RCS pattern in the  $\theta$  plane ( $\phi$  fixed at  $45^\circ$ ) with predictions made by the shooting and bouncing ray (SBR) code developed by S. W. Lee of the University of Illinois at Urbana. Excellent agreement is seen for the uncoated target case. For the RAM-coated case, both codes predict substantial reduction of the RCS response. It is seen that the predicted RCS patterns for this case are in good qualitative agreement. Computer running time is about 30 seconds per monostatic angle on the Cray Y-MP.

##### c. Wing-Like Target, Conformally Modeled

To help evaluate the accuracy of the conformal curved surface model (Section 4c) for monostatic RCS, we last consider a conducting wing-like target. The target, shown in

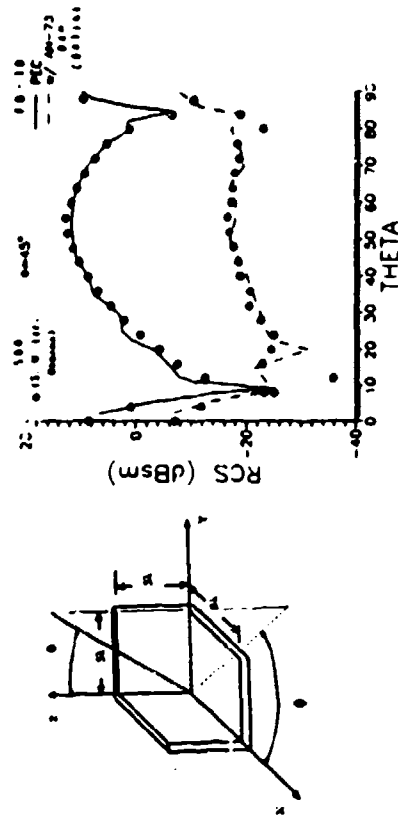


Fig. 11. FD-TD vs. SBR data for monostatic RCS of a trifurcated corner reflector.

Fig. 12, consists of a  $10^\circ$  by  $12^\circ$  metal plate, flat on one side and having steeply sloped sides with a central  $6^\circ$ -radius chamfer on the other. The plane-wave illumination is at  $10$  GHz with the incident wave electric field polarized vertically (parallel to the  $12^\circ$  edge). Viewing the  $12^\circ$  edge of the plate as the  $z$  axis,  $\theta_{inc} = 90^\circ$ , and the monostatic RCS pattern is obtained as the azimuth angle is varied from  $-90^\circ$  (broadside to the flat side of the target) to  $+90^\circ$  (broadside to the chamfer).

To permit direct code-to-code validation of FD-TD versus an existing, well-characterized 2-D Moli program, it was decided that all numerical modeling runs should be in 2-D (effectively letting the  $12^\circ$  dimension of the plate go to infinity). This allows acceptable Moli matrix size at  $10$  GHz, where the  $10^\circ$  side of the target spans  $8.47\lambda$ . In addition, both the FD-TD and Moli predictions were compared to anechoic chamber measurements (although, of course, these data were obtained for the original 3-D target, not the 2-D idealizations).

Fig. 12 graphs comparative Moli, FD-TD, and measured monostatic RCS data for the wing-like target. The FD-TD and Moli data visually overlay each other for observation angles between  $+60^\circ$  and  $+80^\circ$ , where the chamfer is being directly illuminated and conformal target surface modeling is essential to obtain the proper RCS. Excellent agreement is also noted for observation angles between  $-90^\circ$  and  $-30^\circ$ , where the flat side is being directly illuminated. There is some disagreement of the predictive and measured data at grazing. However, the disagreement at these relatively low RCS levels is likely a consequence of the idealized 2-D models versus the 3-D physics actually being measured in the anechoic chamber.

#### d. Jet Engine Inlet, Conformally Modeled

To illustrate the emerging potential of FD-TD to achieve 3-D conformal models of electrically large structures, we first consider a curved jet engine inlet illuminated by a plane wave at  $10$  GHz. The inlet is assumed to be embedded within a conducting box coated with Type AN-73 RAM (see Example 6b above) to eliminate wave reflections from the outside of its curved sidewalls. With the box dimensions set at  $30^\circ \times 10.5^\circ \times 10^\circ$ , the overall inlet-box target configuration spans  $25.4\lambda \times 8.86\lambda \times 8.47\lambda$ . For this target, the

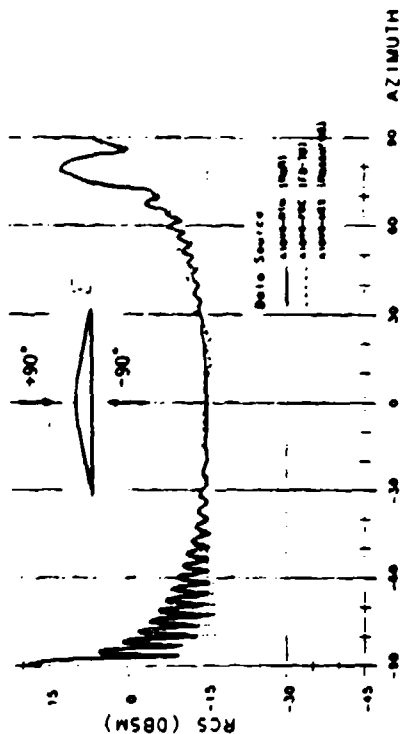


Fig. 12. Comparison of FD-TD, Moli, and measured RCS data for the wing-like target.

FD-TD cell size is  $1/8^\circ$  ( $\lambda/9.43$ ), and the overall lattice has  $270 \times 122 \times 118$  cells containing 23,321,520 unknown field components ( $4.608 \lambda^3$ ). Starting with zero-field initial conditions, 1800 time steps are used (95.25 cycles of the incident wave). Computer running time is about 8 minutes per monostatic angle on the Cray Y-MP.

Fig. 13 depicts the instantaneous distribution of the total electric field in a 2-D observation plane cutting through the center of the 3-D engine inlet. (This black and white photograph is derived from a color videotape display of the propagating electric field penetrating the inlet, generated directly by the FD-TD time-stepping.) The display is taken late in the time-stepping when the internal field is settled into a repetitive sinusoidal oscillation (standing wave). Light and dark bands indicate the positive and negative values of the field at one point in time of the standing wave. The incident wave is assumed to propagate from right to left, and is polarized so that its electric field points across the narrow dimension of the inlet. The aperture of the inlet is located at the right, and the inlet is scored by a conducting wall representing the turbine assembly at the far left.

Clearly, in addition to simple data for the RCS pattern, FD-TD modeling provides details of the complex standing wave pattern within the engine inlet, especially when visualized in the time domain using color video technology. The latter visualization shows that a general putting of the field pattern within the inlet occurs in the sinusoidal steady state, emitting backscattered energy in a regular series of bursts. It may be possible to use this highly detailed time-domain near-field information to better design such articles in the future.

We note, in comparison, that if the frequency-domain Moli were applied to this engine inlet, a linear system involving approximately 450,000 equations in 450,000 unknowns would have to be set up and solved. This assumes the standard triangular surface patching implementation of the electric field integral equation, with the  $1500 \lambda^2$  area of the engine inlet discretized at 10 divisions per  $\lambda$ . Using an optimized out-of-memory subroutine for LU decomposition developed by Cray Research, the Cray Y-MP running time for this matrix would be about  $2.6 \times 10^3$  s, with the Y-MP running essentially at top speed (2.1 Gflops). This compares to about 8 minutes per monostatic observation angle for FD-TD, equivalent to 28 days for 5000 monostatic angles. Additional problems involved in error accumulation in the LU decomposition and reliability of the computer system over the multi-year solution time probably would combine to render a traditional Moli solution useless for this target and those of similar or larger electrical sizes. We note also that the Moli solution does not directly provide details of the penetrating near-field distribution.

#### 7. PRESENT STATUS AND FUTURE DIRECTIONS OF FD-TD

At present, 3-D FD-TD conformal models of electrically large structures spanning more than  $30\lambda$  are being developed. These are apparently the largest detailed computational EM models ever attempted. Unresolved issues at this time include: (1) Automated FD-TD lattice generation for conformal modeling in 3-D; (2) Development of sub-cell models for thin-layer coatings of structure surfaces; (3) Understanding the accuracy limitations caused by numerical artifacts (such as lattice model phase velocity dispersion and unpurified radiation boundary conditions) at this unprecedented modeling scale; (4) Understanding the time-domain convergence properties of electrically large 3-D structures, especially those having reentrant or cavity-like features; (5) Efficiently incorporating the dispersive nature of material electrical properties in the time-marching algorithm; and (6) Developing highly efficient multi-processing software for computer types represented by the Cray 3, Cray Y-MP, and Thinking Machines CM-2 (on the latter two machines, especially for large "out-of-memory" problems).

By 1995, it is almost certain that 10-Gbit computers having 10 Gwords of fast memory will be routinely available to the academic and engineering communities. These would permit in-memory 3-D FD-TD models of structures spanning 100 - 300  $\lambda$  (depending upon the precise shape) to be run. At 10 GHz, this would imply 3-D structure sizes of 3 - 10 m (up to 30 feet in span) to be modeled with a uniform spatial resolution of 3 mm (1/8 inch). Advanced out-of-memory FD-TD software should enable even larger structures to be modeled in their entirety with uniform fine spatial resolution. Thus, for microwave frequencies up to about 10 GHz, the era of the "entire airplane in the grid" would be opened. Automated FD-TD geometry generation would permit the EMI modeling to utilize structure databases developed by non-EMI engineers, leading to design cost reduction and the possibility of innovative design optimizations.

### 8. CONCLUSION

This paper has reviewed the basic formulation of the FD-TD numerical modeling approach for Maxwell's equations. A number of examples of FD-TD modeling of electromagnetic wave interactions with structures were provided to indicate the accuracy and breadth of FD-TD applications. In all cases studied to date where rigorous analytical, code-to-code, or experimental validations were possible, FD-TD predictive data for penetrating and scattered near fields as well as RCS are in excellent agreement with benchmark data. With continuing advances in FD-TD modeling theory and continuing advances in supercomputer technology, it is likely that FD-TD numerical modeling will occupy an important place in high-frequency engineering electromagnetics in the 1990's.

### ACKNOWLEDGEMENTS

The authors wish to acknowledge the support of National Science Foundation Grant ASC-8811273; Office of Naval Research Contract N00014-88-K-0475; General Dynamics PO-4059045; Cray Research Inc.; and the National Center for Supercomputing Applications.

### REFERENCES

- [1] Yee, K. S., "Numerical solution of initial boundary value problems involving Maxwell's equations in isotropic media," *IEEE Trans. Antennas Propagat.*, AP-14, 302-307, May 1966.
- [2] Taflov, A., and M. E. Brodwin, "Numerical solution of steady-state electromagnetic scattering problems using the time-dependent Maxwell's equations," *IEEE Trans. Microwave Theory Tech.*, MTT-23, 623-630, August 1975.
- [3] Krigsmann, G. A., "Exploiting the limiting amplitude principle to numerically solve scattering problems," *Wave Motion*, 4, 371-380, 1982.
- [4] Taflov, A., and M. E. Brodwin, "Computation of the electromagnetic fields and induced temperatures within a model of the microwave-irradiated human eye," *IEEE Trans. Microwave Theory Tech.*, MTT-23, 889-896, Nov. 1975.
- [5] D. T. Bonup, D. M. Sullivan, and O. P. Gandhi, "Comparison of the FFT conjugate gradient method and the finite-difference time-domain method for the 2-D absorption problem," *IEEE Trans. Microwave Theory Tech.*, MTT-35, 383-385, April 1987.
- [6] Taflov, A., "Application of the finite-difference time-domain method to structural steady state electromagnetic penetration problems," *IEEE Trans. Electron. Comput.*, EMC-32, 191-202, Aug. 1980.
- [7] Taflov, A., and K. R. Umashankar, "A hybrid moment method/finite-difference time-domain approach to electromagnetic coupling and aperture penetration into complex geometries," *IEEE Trans. Antennas Propagat.*, AP-38, 617-627, July 1992.

Fig. 13. FD-TD computed instantaneous distribution of the total electric field in a 2-D observation plane cutting through the center of the 3-D engine inlet.



- [8] Taflove, A., and K. R. Umashankar, "Advanced numerical modeling of microwave penetration and coupling for complex structures," Final Rept. No. UCRL-15960, Contract 6599805, Lawrence Livermore Nat. Lab., 1987.
- [9] Holland, R., "Threde: A free-field EMP coupling and scattering code," *IEEE Trans. Nuclear Sci.*, NS-24, 2416-2421, Dec. 1977.
- [10] Kunz, K. S., and K. M. Lee, "A three-dimensional finite-difference solution of the external response of an aircraft to a complex transient EM environment: Part I, The method and its implementation," *IEEE Trans. Electromagn. Compat.*, EMC-20, 328-333, May 1978.
- [11] Merewether, D. E., R. Fisher, and F. W. Smith, "On implementing a numeric Huygens' source scheme in a finite-difference program to illuminate scattering bodies," *IEEE Trans. Nuclear Sci.*, NS-27, 1819-1833, Dec. 1980.
- [12] Mur, G., "Absorbing boundary conditions for the finite-difference approximation of the time-domain electromagnetic field equations," *IEEE Trans. Electromagn. Compat.*, EMC-23, 377-382, Nov. 1981.
- [13] Umashankar, K. R., and A. Taflove, "A novel method to analyze electromagnetic scattering of complex objects," *IEEE Trans. Electromagn. Compat.*, EMC-24, 397-405, Nov. 1982.
- [14] Taflove, A., and K. R. Umashankar, "Radar cross section of general three-dimensional scatterers," *IEEE Trans. Electromagn. Compat.*, EMC-25, 433-440, Nov. 1983.
- [15] Taflove, A., K. R. Umashankar, and T. G. Jurgens, "Validation of FD-TD modeling of the radar cross section of three-dimensional structures spanning up to nine wavelengths," *IEEE Trans. Antennas Propagat.*, AP-33, 662-666, June 1985.
- [16] Engquist, B., and A. Majda, "Absorbing boundary conditions for the numerical simulation of waves," *Math. Comp.*, 31, 629-651, July 1977.
- [17] Trefethen, L. N., and L. Halpern, "Well-posedness of one-way wave equations and absorbing boundary conditions," *Inst. Comput. Appl. Sci. and Engrg. (ICASE)*, NASA Langley Res. Ctr., Hampton, VA, Rept. 85-30, 1985.
- [18] Bayliss, A., and E. Turkel, "Radiation boundary conditions for wave-like equations," *Commun. Pure. Appl. Math.*, 33, 707-725, 1980.
- [19] Moore, T. G., J. G. Blaschak, A. Taflove, and G. A. Kriegsmann, "Theory and application of radiation boundary operators," *IEEE Trans. Antennas Propagat.*, 36, 1797-1812, Dec. 1988.
- [20] Blaschak, J. G., and G. A. Kriegsmann, "A comparative study of absorbing boundary conditions," *J. Computational Physics*, 77, 109-139, July 1988.
- [21] J. Fang and K. K. Mei, "A super-absorbing boundary algorithm for solving electromagnetic problems by time-domain finite-difference method," in *Proc. 1988 IEEE AP-S Int. Symp.* (Syracuse, NY, June 1988), 472-475.
- [22] Taflove, A., K. R. Umashankar, B. Beker, F. Harfoush, and K. S. Yee, "Detailed FD-TD analysis of electromagnetic fields penetrating narrow slots and lapped joints in thick conducting screens," *IEEE Trans. Antennas Propagat.*, AP-36, 247-257, Feb. 1988.
- [23] Umashankar, K. R., A. Taflove, and B. Beker, "Calculation and experimental validation of induced currents on coupled wires in an arbitrary shaped cavity," *IEEE Trans. Antennas Propagat.*, AP-35, 1248-1257, Nov. 1987.
- [24] Jurgens, T. G., A. Taflove, T. G. Moore, and K. R. Umashankar, "FD-TD conformal modeling of curved surfaces," submitted to *IEEE Trans. Antennas Propagat.*

# Time-Domain Synthesis of Broad-Band Absorptive Coatings for Two-Dimensional Conducting Targets

MARK A. STRICKEL, MEMBER, IEEE, AND ALLEN TAFLOVE, FELLOW, IEEE

**Abstract**—A new time-domain synthesis approach is introduced for broad-band absorptive coatings suitable for radar cross section (RCS) management. The new algorithm involves a finite-difference time-domain (FD-TD) forward-scattering representation of Maxwell's curl equations in a numerical feedback loop with the Levenberg-Marquardt (L-M) nonlinear optimization routine. L-M is used to adjust many geometric and constitutive parameters that characterize a target, while FD-TD is used to obtain the broad-band bistatic RCS response for each target adjustment. A recursive improvement process is established to minimize the broad-band RCS response over a selected range of bistatic angles using the available engineering degrees of freedom. The solution is valid over the potentially broad bandwidth (frequency decade or more) of the illuminating pulse used in the FD-TD computational model. Examples of this method are provided in the area of RCS management for canonical two-dimensional conducting targets.

## 1. INTRODUCTION

**SYNTHESIS PROBLEMS** are of fundamental importance in electrical engineering. In electromagnetics, essentially all the existing synthesis approaches utilize frequency-domain forward data, i.e., sinusoidal steady-state values for radiated or scattered fields, reflection coefficients, etc. Synthesis over a broad frequency band, therefore, requires calculations spread over the desired band and over the range of the engineering degrees of freedom in the design. In the area of radar cross section (RCS) management, this synthesis approach has driven research in reducing computer resource burdens involved in executing frequency-domain forward-scattering codes.

This paper introduces a new time-domain synthesis approach for broad-band absorptive coatings suitable for RCS management. The new algorithm involves a finite-difference time-domain (FD-TD) forward-scattering representation of Maxwell's curl equations [1] in a numerical feedback loop with the Levenberg-Marquardt (L-M) nonlinear optimization routine [2]. L-M is used to adjust many geometric and constitutive parameters that characterize a target, while FD-TD is used to obtain the broad-band bistatic RCS response for each target adjustment. A recursive improvement process is

established to minimize the broad-band RCS response over a selected range of bistatic angles using the available engineering degrees of freedom. The solution is valid over the potentially broad bandwidth (frequency decade or more) of the illuminating pulse used in the FD-TD computational model.

Because the FD-TD forward element is a direct solution of Maxwell's curl equations, it models in a straightforward manner a wide variety of electromagnetic wave scattering and interaction phenomena. The accuracy of FD-TD modeling is equivalent to that of the widely used, frequency-domain method of moments (MM), with essentially equivalent results of the two methods for arbitrary conducting and penetrable targets (the latter having media properties as complex as diagonalizable tensors) [1], [3], [4]. However, the explicit nature of the FD-TD algorithm leads to computer storage and running time burdens that are dimensionally low compared to those of MM for targets that are either electrically large or have a complex, inhomogeneous material composition. The accuracy and efficiency of FD-TD, combined with its time-domain formulation which allows direct modeling of broad-band phenomena, makes FD-TD the algorithm of choice for the forward-scattering element of the new time-domain synthesis approach.

The L-M algorithm [2], selected for use in the feedback path, is also considered to be robust and one of the best optimization methods for nonlinear least-squares problems. A good example of the utility of L-M optimization as opposed to possible alternatives such as the quasi-Newton method and the conjugate gradient method is given in [5], which reports the synthesis of near-field patterns using linear arrays of point dipoles. It is shown in [5] that L-M is the most effective synthesis algorithm in this application.

This paper describes the new FD-TD/L-M synthesis method, and provides examples of its application to synthesize absorptive coatings for broad-band RCS management of canonical two-dimensional (2-D) conducting targets. The new method is used to synthesize both isotropic and anisotropic coatings for three target shapes: 1) the infinite, flat metal plate illuminated at normal incidence; 2) the infinite right-angle metal wedge; and 3) the infinitely long circle-capped (rounded) metal strip of finite thickness. In each example, the synthesized absorptive coating is assumed to be nondispersive. However, it appears possible to incorporate canonical dispersions into the FD-TD element. This will be a subject of later work.

Manuscript received March 2, 1989; revised June 21, 1989. This work was supported in part by National Science Foundation Grant ASC-8811273 and by the Office of Naval Research under Contract N00014-88-K-0475.

M. A. Strickel is with Geldermann, Inc., 440 South LaSalle, Chicago, IL 60605.

A. Taflov is with the Electrical Engineering and Computer Engineering Department, McCormick School of Engineering, Northwestern University, Evanston, IL 60208-3118.

IEEE Log Number 9035920.

## II. FD-TD/L-M ALGORITHM

In this section, we discuss the application of the FD-TD/L-M algorithm to the synthesis of broad-band absorptive coatings for RCS management. For simplicity, we shall consider a target of fixed shape and size, although the synthesis algorithm is so general that optimization of target geometrical features can be incorporated in a straightforward manner.

We first observe that the properties of a target's coating can be described by a set of key parameters. These parameters might include the number of layers in the coating, the thickness of each layer, the components of the constitutive tensors of each layer (electrical permittivity and conductivity, as well as magnetic permeability and loss), and finally the variation of the previous properties with position along the target surface. It is clear that the number  $N$  of key parameters can be large: effectively, there are  $N$  degrees of freedom. For purposes of this synthesis approach, it is very useful to consider the state of the overall coating as a single point in an  $N$ -dimensional space defined by a coordinate value for each degree of freedom. The optimum coating can be synthesized by efficiently searching  $N$ -space for the set of points (hopefully not the empty set) that satisfies the engineering criteria.

The FD-TD/L-M synthesis algorithm begins with an initial guess for the target coating properties, i.e., a starting point in the  $N$ -space discussed above. The FD-TD element computes scattered field-versus-time waveform at the desired set of physical locations in the near or far field. (The latter are calculated using a time-domain analog of the near-to-far-field transformation discussed in [6].) FD-TD computations of the scattered transient responses at the locations of interest are compared to the desired field waveforms at these points. For comparison points in the backscatter direction, RCS management goals may dictate that the desired scattered field waveform is simply zero, and the mere presence of a calculated transient scattered response at these points comprises an error signal. More generally, the FD-TD calculated scattered pulse responses at all observation points of interest are compared to the desired time profiles, and a weighted, composite error signal is generated, which is sent to the L-M nonlinear optimization feedback element, as shown in Fig. 1(a). The L-M routine adjusts the position of the operating point in the coating  $N$ -space in a direction to reduce the error signal in the least-squares sense. With the calculation process in the time domain, causality can be exploited in the optimization process to modify only the coating properties causally connected to the physical observation points, thereby windowing desired target features.

With the version of the L-M algorithm used here, the  $N$ -space search per iteration through the FD-TD/feedback loop is conducted in two phases. In Phase 1, the search direction is established by calculating partial derivatives of the error signal with respect to each of the  $N$  dimensions (degrees of freedom). If central differences are used, two forward FD-TD runs are required per degree of freedom for this purpose, so that this phase entails  $2N$  FD-TD runs. In Phase 2, a line search is conducted along the calculated search direction to determine the distance that the operating point moves in the

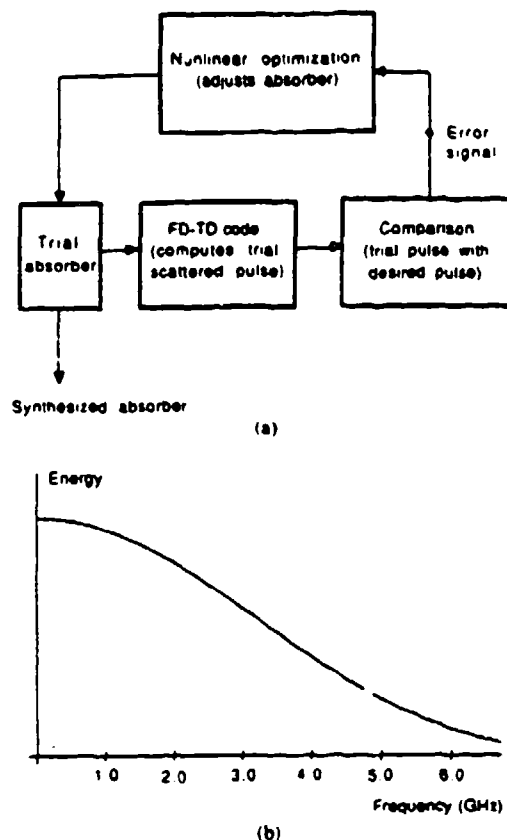


Fig. 1. FD-TD/feedback method for electromagnetic absorber synthesis. (a) Block diagram. (b) Energy spectral density of the one-half cycle, 3-GHz sinusoidal pulse used as the illuminating waveform.

$N$ -space. Numerical experiments indicate that approximately ten additional forward FD-TD runs are needed for this phase. At this juncture in the algorithm, the new operating point in the coating  $N$ -space has been established.

This process is repeated until the error signal drops to some minimum value which shows no further reduction upon additional iterations. Effectively, the procedure traces out a path in the coating  $N$ -space from the initial guess or starting point to the final coating state. The recursive improvement process established for the coating in this manner leads at worst to a local minimization of the error, that is, local in the sense of the coating  $N$ -space. Without much doubt, there may exist a number of such local minima, and possibly even a global error minimum for the entirety of the  $N$ -space. A challenging aspect of the nonlinear optimization process is to develop efficient means to perform a global search of the coating  $N$ -space. One possible approach is the use of advanced multiprocessing computers such as the Connection Machine to implement concurrently a large number of search trajectories in the coating  $N$ -space, seeded by a like number of starting points. Research in this area is commencing.

With the L-M optimization algorithm providing an efficient means of searching through the coating  $N$ -space, it becomes possible to either: 1) add additional degrees of freedom, i.e., dimensions to the  $N$ -space, to permit the target shape to be optimized as well; or 2) to define forbidden zones in the  $N$ -space through which search trajectories cannot pass due to



constraints imposed by manufacturing costs, material availability, or any other factors. Thus, the optimization for electromagnetic properties can be treated as a subset of a more general optimization wherein systems-type considerations can be imposed.

### III. SYNTHESIS EXAMPLE IN ONE DIMENSION

This section provides a simple example of the use of the FD-TD/L-M method: synthesis of a broad-band, two-layer absorbing coating to mitigate reflection of a normally incident plane wave by an infinite, planar, perfectly conducting sheet. For this (and subsequent) examples, it is desired merely to indicate the potential of this approach without actually completing an engineering design for scattering mitigation, so the number of design degrees of freedom is kept small. Further, artificial constraints are imposed upon the constitutive parameters of the absorber to avoid undue realism. For this example, the following constraints are imposed:

- 1) Overall absorber thickness—10 mm
- 2) Number of absorber layers—two
- 3) Properties of inner layer (next to conducting sheet)
  - thickness—7.5 mm
  - free-space permittivity
  - finite electric and magnetic conductivities,  $\sigma_e$  and  $\sigma_m$
  - electrical conductivity equal to that of the outer layer
- 4) Properties of outer layer
  - thickness—2.5 mm
  - free-space permittivity and permeability
  - only electric loss is present, and this is equal to that of the inner layer.

Thus, it is seen that the coating  $N$ -space has a dimensionality of only three, with the inner/outer layer electric loss, inner-layer magnetic permeability, and inner-layer magnetic loss the only design degrees of freedom available.

The absorber-coated conducting sheet is synthesized using a 50-cell, one-dimensional FD-TD grid having a uniform cell size of 0.5 mm. The broad-band excitation is a one-half cycle 3-GHz sinusoidal pulse having the energy spectral density shown in Fig. 1(b). Note that the exciting pulse has substantial energy content from dc to over 5 GHz, and that minimization of the reflected time-domain waveform in the least-squares sense amounts to a very broad-band mitigation of scattering.

To begin the synthesis process, the point ( $\sigma_e \approx 0.5$  S/m,  $\mu_r = 2.0$ ,  $\sigma_m = 0.5\eta_0^2$   $\Omega$ /m) in the coating three-space is selected arbitrarily as an initial guess, where  $\eta_0$  is the characteristic impedance of free space. While tracing out a trajectory in the coating three-space from this starting point, the FD-TD/feedback algorithm is constrained to keep the electric and magnetic conductivity values nonnegative and the permeability greater than or equal to one. For this example, causality is not exploited in the optimization and the entirety of the reflected pulse is considered as the error signal to be minimized in the least-squares sense. It is found that six-passes through the FD-TD/feedback system are needed for convergence, with each pass requiring 16 FD-TD runs (each 350 time steps). At the conclusion of this process, which involves a total CPU time of 2 min on the VAX 11/780, the operat-

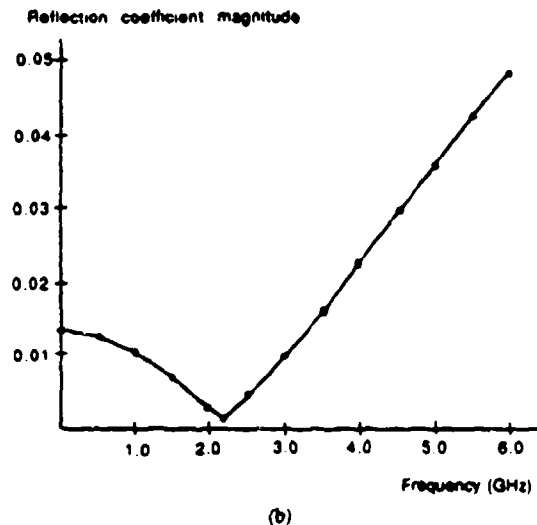
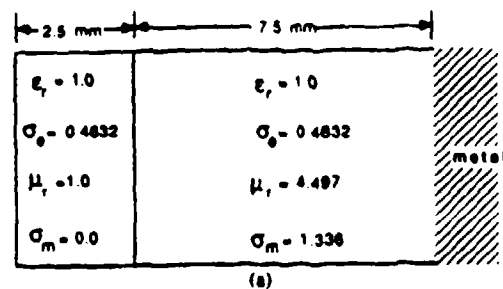


Fig. 2. Synthesis example in one dimension. (a) Final coating state after convergence of the synthesis algorithm. (b) Reflection coefficient magnitude versus frequency for the synthesized coating over metal.

ing point in the coating three-space has shifted to (0.4632, 4.497, 1.336 $\eta_0^2$ ), and the error signal (energy in the reflected time-domain waveform) has been reduced by a factor of 134:1 from that of the initial guess for the coating.

Fig. 2(a) shows the final coating state after convergence of the synthesis algorithm. (For notational simplicity in this and later examples, the listed value of magnetic conductivity is the actual value divided by  $\eta_0^2$ .) Validation of the effectiveness of this procedure is provided in Fig. 2(b), which plots as a function of frequency the usual sinusoidal-wave reflection coefficient for the coated conducting sheet, calculated using standard impedance-transformation formulae applied to the synthesized coating. Over the frequency range 0–6 GHz, this reflection coefficient is less than 0.05 (–26 dB), achieving a minimum value of 0.0014 (–57 dB) at 2.2 GHz.

### IV. SYNTHESIS OF ABSORPTIVE COATINGS FOR THE INFINITE METAL WEDGE

In this section, the FD-TD/feedback method is used to synthesize absorbing coatings for an important canonical two-dimensional structure, the infinite, perfectly conducting, right-angle wedge subject to transverse magnetic (TM) plane-wave illumination. As in the previous example, constraints are placed upon the synthesis to indicate the potential of the approach without completing an actual engineering design.

Fig. 3 shows the constraints imposed upon the problem to meet the above goals. The wedge, shown as the shaded region

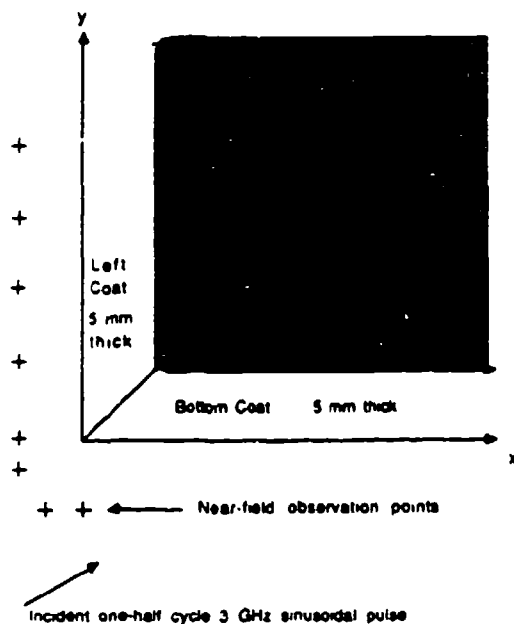
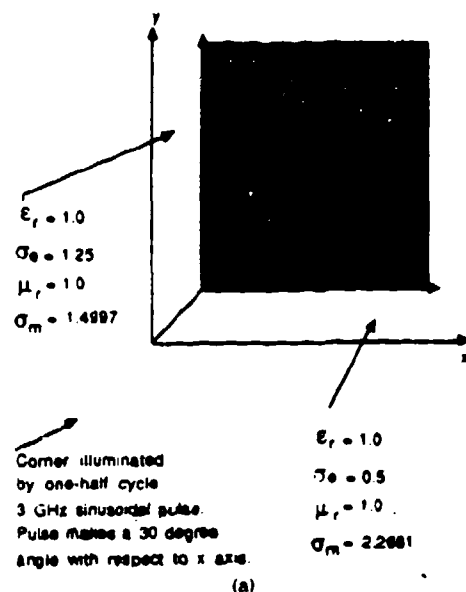


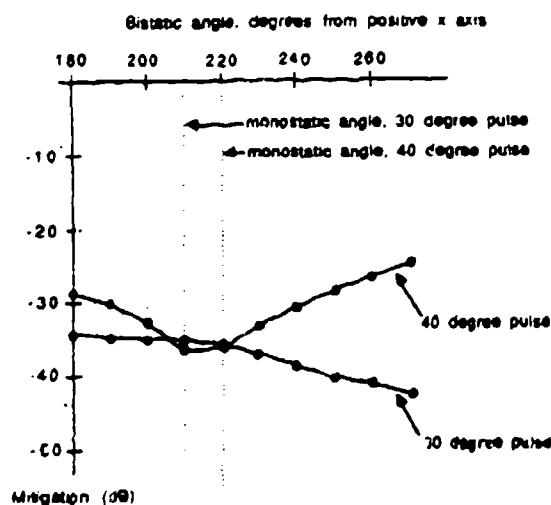
Fig. 3. Assumed geometry for the synthesis of absorbing coatings on an infinite, perfectly conducting, right-angle wedge.

extending an infinite distance along the  $+x$  and  $+y$  axes, is assumed coated with two distinct, homogeneous absorbers: a 5-mm thick "left" coat along the  $+y$ -axis; and a 5-mm thick "bottom" coat along the  $+x$ -axis. The two coats are in contact at the wedge vertex and form a miter joint. Two different coating pairs are synthesized. In Case 1, the left and bottom coats are isotropic; while in Case 2, the left and bottom coats have diagonal tensor anisotropy for the magnetic loss. For both cases, the relative permittivity and permeability of the coats is assumed fixed at 1.0 (a scalar value); the left-coat electrical conductivity is fixed at 1.25 S/m (scalar); and the bottom-coat electrical conductivity is fixed at 0.5 S/m (scalar). Thus, for Case 1, the coating  $N$ -space has a dimensionality of only two (the left- and bottom-coat scalar magnetic losses being the only degrees of freedom); while for Case 2, the coating  $N$ -space has four dimensions (the two diagonal tensor components of magnetic loss for each of the two coats).

The coated wedge is synthesized using a  $200 \times 300$  2D two-dimensional FD-TD grid having a uniform cell size of 0.5 mm. The broad-band excitation is again a one-half cycle, 3-GHz sinusoidal pulse, TM polarized, and having an incident wavevector oriented at  $30^\circ$  with respect to the  $+x$ -axis. Time waveforms of the scattered electric near field are observed at eight points located 5 mm from the coated wedge, denoted by "+" signs in Fig. 3. By properly selecting the FD-TD grid and wedge size, as well as the number of time steps, the observation points are causally isolated from diffraction effects at the rear of the wedge for a length of time sufficient to permit the observed fields to decay as they would for an infinite wedge. (In effect, the time-domain formulation of the forward-scattering element is exploited to permit effective simulation of an infinite wedge by time-gating spurious diffraction effects due to finite actual wedge size [7].) The error signal input to the optimizer consists of the square of the sum of the absolute values of the FD-TD computed time samples at the eight



(a)



(b)

Fig. 4. Synthesis results for the conducting right-angle wedge, isotropic coating case. (a) Final coating state after convergence of the synthesis algorithm. (b) Mitigation of the broad-band scattered pulse in the far field versus bistatic angle.

observation points, accumulated time-step by time-step until the essential decay of the computed fields at the observation points.

To begin the synthesis process for the isotropic coatings of Case 1, the point ( $\sigma_{m_{\text{left}}} = 1.25$ ,  $\sigma_{m_{\text{bot}}} = 5.0$ ) in the coating two-space is selected arbitrarily as the initial guess. It is found that six passes through the FD-TD/feedback system are needed for convergence, with each pass requiring 14 FD-TD runs (each 350 time steps). At the conclusion of this process, which involves a total CPU time of 2 min on a single processor of the Cray X-MP, the operating point in the coating two-space has shifted to (1.50, 2.266), and the error signal has been reduced by a factor of 2.9:1 from that of the initial guess for the coating.

Fig. 4(a) shows the final coating state for Case 1 after convergence of the synthesis algorithm, and Fig. 4(b) shows the corresponding mitigation of the broad-band scattered pulse in

the far field. The mitigation, shown over the bistatic angular range  $180^\circ$ – $270^\circ$ , is a broad-band figure of merit defined here as the ratio of the peak amplitudes of the computed scattered pulses for the absorber-coated and uncoated wedge. From Fig. 4(b), we see that the calculated bistatic mitigation for the  $30^\circ$  incident pulse used in the synthesis is fairly flat (ranging from  $-35$  to  $-42$  dB), with a mitigation of  $-37$  dB for the broad-band monostatic return at  $210^\circ$ . To illustrate the sensitivity of the mitigation to the illumination angle, Fig. 4(b) also shows results for the same coating state but with the incident pulse rotated by  $10^\circ$  in azimuth (propagating at  $40^\circ$  with respect to the  $+x$ -axis). The new monostatic return at  $220^\circ$  shows little change from the previous value. However, there appears to be somewhat degraded bistatic mitigation at angles to either side of  $220^\circ$ .

To begin the synthesis process for the anisotropic coatings of Case 2, the point ( $\sigma_{m, \text{left}} = 0.1$ ,  $\sigma_{m, \text{left}} = 1.34$ ,  $\sigma_{m, \text{bot}} = 6.92$ ,  $\sigma_{m, \text{bot}} = 0.5$ ) in the coating four-space is selected arbitrarily as the initial guess. It is found that 15 passes through the FD-TD/feedback system are needed for convergence, with each pass requiring 18 FD-TD runs (each 350 time steps). At the conclusion of this process, which involves a total CPU time of 6.4 min on a single processor of the Cray X-MP, the operating point in the coating four-space has shifted to (0.01, 1.604, 2.24, 0.0174), and the error signal has been reduced by a factor of 205:1 from that of the initial guess for the coating.

Fig. 5(a) shows the final coating state for Case 2 after convergence of the synthesis algorithm, and Fig. 5(b) shows the corresponding mitigation of the broad-band scattered pulse in the far field. From Fig. 5(b), we see that the calculated bistatic mitigation for the  $30^\circ$  incident pulse used in the synthesis varies in the range  $-44$  dB to  $-60$  dB, with a mitigation of  $-53$  dB for the broadband monostatic return at  $210^\circ$ . This is an improvement of 16 dB relative to the isotropic coatings of Case 1. However, the sensitivity of the mitigation to illumination angle appears increased for Case 2 relative to Case 1. This is indicated by the results shown in Fig. 5(b) for the same anisotropic coating state but with the incident pulse rotated by  $10^\circ$  in azimuth to propagate at  $40^\circ$  with respect to the  $+x$ -axis. The new monostatic return at  $220^\circ$  is degraded to a  $-43$  dB mitigation, and the remainder of the bistatic mitigation pattern generally is degraded even more.

In viewing the results for Case 2, one might conclude that anisotropic coatings present some difficulties with respect to scattering mitigation over a useful range of illumination angles. However, this conclusion is not warranted. Case 2 shown here was purposefully selected to represent a coating space of low dimensionality (no layering, no variation of permittivity or permeability, etc.). Our preliminary work has shown that synthesis of scattering mitigation over a specified range of illumination angles is possible for Case 2 simply by permitting more degrees of freedom.

#### V. SYNTHESIS OF ABSORPTIVE COATINGS FOR THE ROUNDED METAL STRIP

In this section, the FD-TD/feedback method is used to synthesize absorbing coatings for a second canoni-

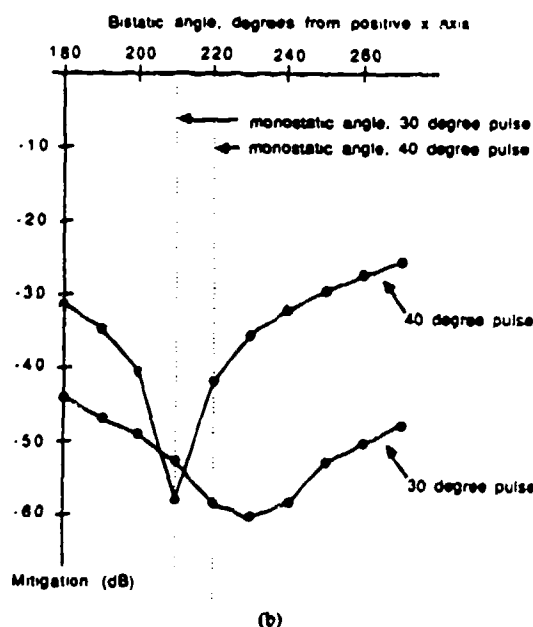
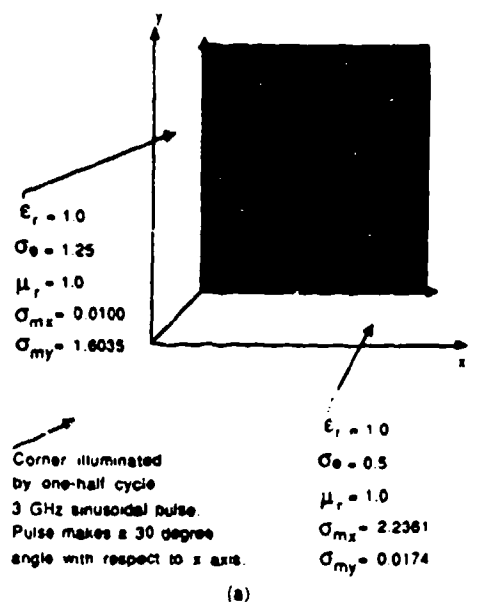


Fig. 5. Synthesis results for the conducting right angle wedge, anisotropic coating case. (a) Final coating state after convergence of the synthesis algorithm. (b) Mitigation of the broad-band scattered pulse in the far field versus bistatic angle.

cal two-dimensional structure, the infinitely long, perfectly conducting strip of finite thickness having a semicircular rounded edge. (This is the two-dimensional analog of the infinitely-long, sphere-capped cylinder.) As in the previous examples, the dimensionality of the coating space is deliberately kept low.

Fig. 6 shows the constraints imposed upon the problem to meet the above goal. The rounded strip, shown as the shaded region extending an infinite distance and centered along the  $+x$ -axis, is assumed to be 10 mm thick and coated with a 5-mm thick absorber. The absorber is assumed to be comprised of distinct 0.5-mm thick layers, with each layer parallel to the  $x$ -axis and having homogeneous material properties. Even symmetry of the absorber properties is assumed about the  $x$ -

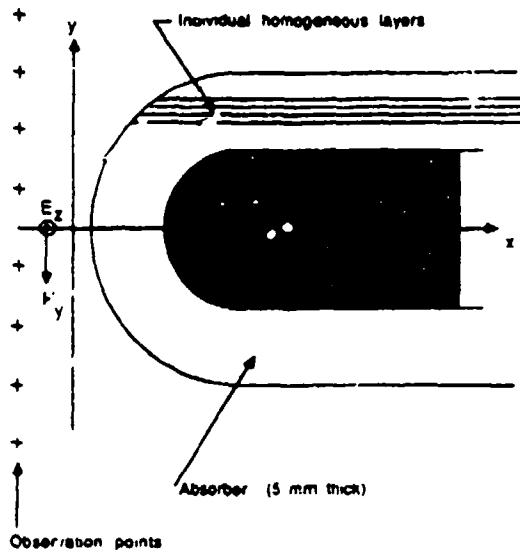


Fig. 6. Assumed geometry for the synthesis of absorbing coatings on an infinite, perfectly conducting strip of finite thickness with rounded edge.

axis. For notational simplicity, the coating layers to either side of the  $x$ -axis are assigned the indices  $j = 0, 1, 0.2, \dots, 2.0$ , where the  $j = 2.0$  layer is farthest from the  $x$ -axis. Given this arrangement, two different coatings are synthesized.

**Case 1:** Each coating layer is assumed to be isotropic, and the electric and magnetic conductivities are assumed to be separate, nonnegative, quadratic functions of the " $j$ " index of the layer, defined by:

$$\sigma_e(j) = |a_0 + a_1j + a_2j^2|;$$

$$\sigma_m(j) = \sigma_{m_r}(j) = |b_0 + b_1j + b_2j^2|.$$

**Case 2:** Each coating layer is assumed to be anisotropic, with the electric and magnetic conductivities defined as a function of the layer " $j$ " index by the nonnegative quadratic functions

$$\sigma_e(j) = \sigma_{m_r}(j) = |c_0 + c_1j + c_2j^2|;$$

$$\sigma_m(j) = |d_0 + d_1j + d_2j^2|.$$

For both cases, the relative permittivity and permeability for each coating layer is assumed to be one. Thus, despite the large number of layers in the absorber for each case, the coating  $N$ -space has a dimensionality of only six because there are only six degrees of freedom implied by the three coefficients for each of two quadratic functions used to describe the overall absorber electrical characteristics.

The coated, rounded strip is synthesized using a  $200 \times 100$  cell two-dimensional FD-TD grid having a uniform cell size of 0.5 mm. The broad-band excitation is again a one-half cycle, 3-GHz sinusoidal pulse, TM polarized, and having an incident wavevector oriented at  $0^\circ$  with respect to the  $+x$ -axis. Time waveforms of the scattered electric near field are observed at the eight points denoted by "+" signs in Fig. 6. Similar to the infinite wedge case, these observation points are causally isolated from diffraction effects at the rear of the strip by proper selection of the size of the FD-TD grid and strip, as well as the number of time steps. This permits the observed fields to decay as they would for an infinitely long

strip. Again, the error signal input to the optimizer consists of the square of the sum of the absolute values of the FD-TD computed time samples at the observation points, accumulated until the decay of the computed fields at these points.

To begin the synthesis process for the isotropic coating layers of Case 1, the point ( $a_0 = 1, a_1 = -0.4, a_2 = 0, b_0 = 1, b_1 = 1, b_2 = 0$ ) in the coating six-space is selected arbitrarily as the initial guess. It is found that seven passes through the FD-TD/feedback system are needed for convergence, with each pass requiring 22 FD-TD runs (each 350 time steps). At the conclusion of this process, which involves a total CPU time of 1.2 minutes on a single processor of the Cray X-MP, the operating point in the coating 6-space has shifted to (0.95522, 1.6156, -1.1627, 0.7785, -0.8257, 1.9198), and the error signal has been reduced by a factor of 22:1 from that of the initial guess for the coating.

Fig. 7(a) shows the final coating state for Case 1 after convergence of the synthesis algorithm by plotting the isotropic electric and magnetic conductivity profiles versus layer " $j$ " index. Fig. 7(b) shows the corresponding mitigation of the broad-band scattered pulse in the far field over the bistatic angular range  $90^\circ$ - $270^\circ$ . From Fig. 7(b) we see a moderate level of mitigation, about -20 dB, that is only a weak function of bistatic angle. We also note that the mitigation does not deteriorate appreciably when the incident pulse is rotated by  $10^\circ$  in azimuth.

To begin the synthesis procedure for the anisotropic coating layers of case 2, the point ( $c_0 = 1, c_1 = 0, c_2 = 0, d_0 = 1, d_1 = 0, d_2 = 0$ ) in the coating six-space is selected arbitrarily as the initial guess. It is found that six passes through the FD-TD/feedback system are needed for convergence, with each pass requiring 22 FD-TD runs (each 350 time steps). At the conclusion of this process, which involves a total CPU time of 1.0 min on a single processor of the Cray X-MP, the operating point in the coating six-space has shifted to (1.0299, 0.1299, -0.3277, 4.6508, 4.3234, 6.1330), and the error signal has been reduced by a factor of 240:1 from that of the initial guess for the coating.

Fig. 8(a) shows the final coating state for Case 2 after convergence of the synthesis algorithm by plotting the anisotropic electric and magnetic conductivity profiles versus layer " $j$ " index. Fig. 8(b) shows the corresponding mitigation of the broad-band scattered pulse in the far field over the bistatic angular range  $90^\circ$ - $270^\circ$ . From Fig. 8(b), we see that the use of coating anisotropy substantially increases the level of mitigation to the range -35 dB to -38 dB, with the mitigation remaining only a weak function of the bistatic angle. However, similar to the wedge coated with the low-dimensional anisotropic absorber, the sensitivity of the bistatic mitigation to a  $10^\circ$  rotation of the illumination angle (with coating properties fixed at the original synthesized state) is increased relative to the isotropic absorber case. We note, however, that mitigation of the new broad-band nonstatic return at  $190^\circ$  improves slightly to -42 dB.

## VI. CONCLUSION

This paper introduced a new time-domain synthesis approach for broad-band absorptive coatings suitable for RCS

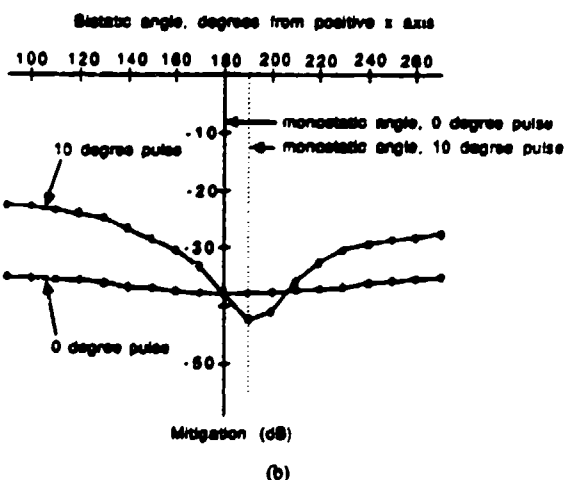
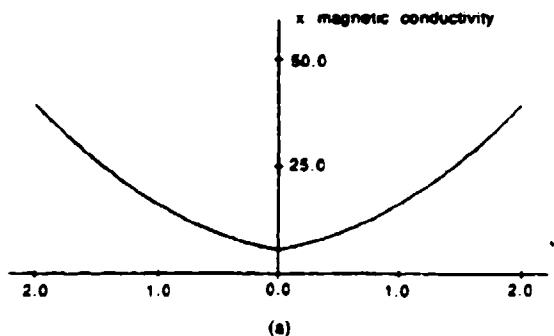
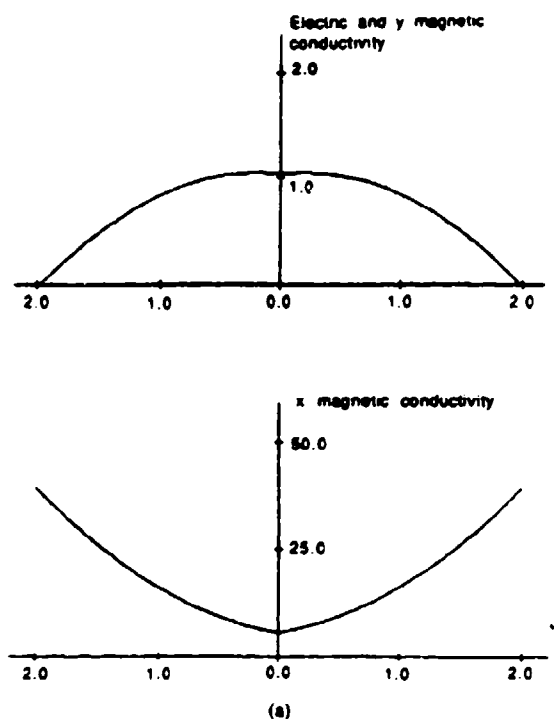
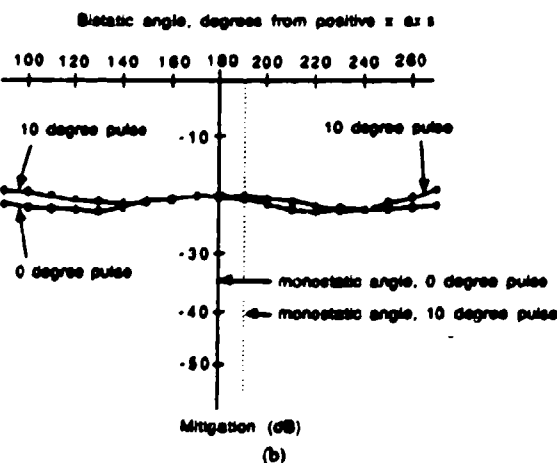
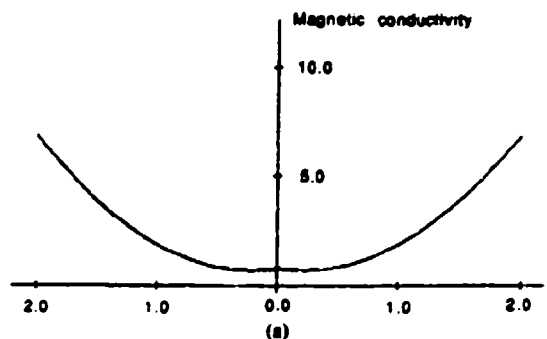
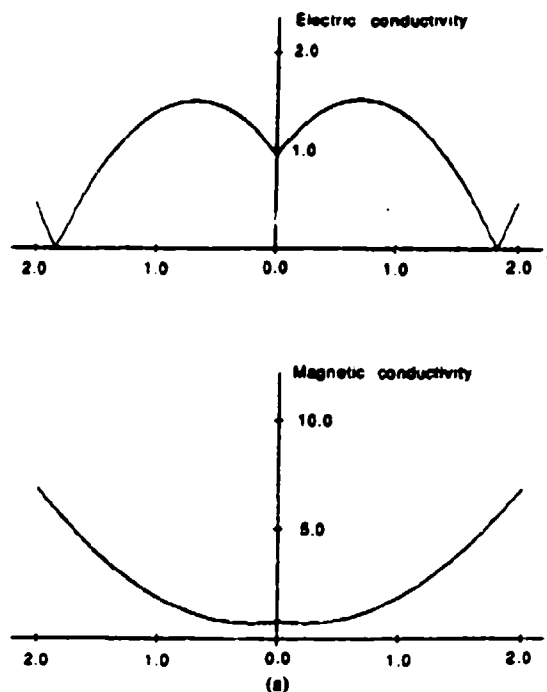


Fig. 7. Synthesis results for the rounded conducting strip, isotropic coating case. (a) Final coating state after convergence of the synthesis algorithm. (b) Mitigation of the broad-band scattered pulse in the far field versus bistatic angle.

management. The new FD-TD/L-M synthesis algorithm has a number of attractive features. First, the synthesis achieved is just as accurate, flexible, and computationally efficient as the forward-scattering FD-TD element used in the algorithm. Second, the synthesis is broad-band, depending upon the pulsed illumination used, due to the time-domain nature of FD-TD. Third, the synthesis is automated, capable of finding at least locally-optimum coatings in situations where the designer might be faced with many degrees of freedom. Evolution of large-scale concurrent processing, for example using the Connection Machine, to implement efficiently both the FD-TD and nonlinear optimization elements of the algorithm, may permit efficient searches of high-dimensional coating spaces that include manufacturing and economic constraints as well as technical.

Fig. 8. Synthesis results for the rounded conducting strip, anisotropic coating case. (a) Final coating state after convergence of the synthesis algorithm. (b) Mitigation of the broad-band scattered pulse in the far field versus bistatic angle.

#### ACKNOWLEDGMENT

The authors wish to acknowledge the contributions of Prof. Korada R. Umashankar of the University of Illinois at Chicago in related research involving the formulation of FD-TD/feedback methods for inverse scattering.

#### REFERENCES

- [1] A. Taflov, "Review of the formulation and applications of the finite-difference time-domain method for numerical modeling of electromagnetic wave interactions with arbitrary structures," *Wave Motion*, vol. 10, no. 6, pp. 547-582, Dec. 1988.
- [2] D. W. Marquardt, "An algorithm for least-squares estimation of non-

- linear parameters." *J. Soc. Indust. Appl. Math.*, vol. 11, no. 2, pp. 431-441, June 1963.
- [3] A. Taflové and K. R. Umashankar, "Review of FD-TD numerical modeling of electromagnetic wave scattering and radar cross section," *Proc. IEEE*, vol. 77, pp. 682-699, May 1989.
  - [4] B. Beker, K. R. Umashankar, and A. Taflové, "Numerical analysis and validation of the combined field surface integral equations for electromagnetic scattering by arbitrary shaped two-dimensional anisotropic objects," *IEEE Trans. Antennas Propagat.*, vol. 37, pp. 1573-1581, Dec. 1989.
  - [5] M. S. Narasimhan and B. Philips, "Synthesis of near-field patterns of a nonuniformly spaced array," *IEEE Trans. Antennas Propagat.*, vol. AP-35, pp. 1189-1198, Nov. 1987.
  - [6] K. R. Umashankar and A. Taflové, "A novel method to analyze electromagnetic scattering of complex objects," *IEEE Trans. Electromagn. Compat.*, vol. EMC-24, pp. 397-405, Nov. 1982.
  - [7] T. G. Moore, A. Taflové, K. R. Umashankar, and B. Beker, "Edge-field behavior for the infinite dielectric wedge: Detailed numerical studies," *IEEE Trans. Antennas Propagat.*, to be submitted.



Mark A. Strickel (S'87-M'88) was born in Chicago, IL, on August 13, 1955. He received the B.S. degree in electrical engineering from the Illinois Institute of Technology, Chicago, in 1983, and the M.S. and Ph.D. degrees in electrical engineering from Northwestern University, Evanston, IL, in 1984 and 1989, respectively.

Between August 1988 and March 1990 he was on the staff of the Institutional Financial Futures and Options Division of Drexel Burnham Lambert. In March 1990, he left Drexel to form his own profit center within Geldermann, Inc., Chicago, IL. His research interests are the development of speculative strategies and financial risk-management techniques using futures and options.

Dr. Strickel is a member of Eta Kappa Nu.

Allen Taflové (M'75-SM'84-F'90), for a photograph and biography please see page 1812 of the December 1988 issue of this TRANSACTIONS.

## Numerical Implementation of Relativistic Electromagnetic Boundary Conditions in a Laboratory-Frame Grid\*

FADY HARFOUSH

*Fermi National Accelerator Laboratory, Batavia, Illinois 60510*

AND

ALLEN TAFLOVE AND GREGORY A. KRIEGSMANN

*Northwestern University, Evanston, Illinois 60208*

Received June 6, 1988; revised January 24, 1989

A new method for modeling moving, perfectly conducting surfaces is analyzed using a numerical technique based on the finite-difference time domain (FD-TD) method. Contrary to any other method, the numerical technique used does not require a system transformation where the object is at rest but gives a solution to the problem directly in the laboratory frame. The central idea of this new technique is the direct finite difference implementation of the relativistic boundary conditions at a moving surface. The electromagnetic wave scattering properties of a uniformly moving and vibrating rectangular cylinder are analyzed, first in one dimension and then in two dimensions. Results obtained are in excellent agreement with published analytical results. The new approach provides a method to analyze different problems of moving perfectly conducting scatterers where alternative analytical means are not available. Moreover, the time evolution of the fields are directly observable in the laboratory frame. © 1990 Academic Press, Inc.

### 1. INTRODUCTION

The analysis of electromagnetic wave interactions with moving surfaces is of importance in studies of moving-target detection, generation of high-power microwave energy by moving dense plasmas, and astrophysical phenomena. Such problems can generally be divided in two categories: low-velocity effects (moving solid targets) and high-velocity effects (relativistic moving plasmas, astrophysics). Problems involving low velocities can be simplified by considering only first order terms in  $v/c$  ( $c$  being the velocity of light in free space). Problems involving relativistic velocities are more difficult to solve analytically and increasingly are being approached via numerical techniques.

In most cases, analytical approaches for the electrodynamics of moving bodies employ a system transformation wherein the object is at rest. Such a transformation is well defined for uniformly moving and is known as the Lorentz transformation [1].

\* This work was supported in part by National Foundation Grant ASC-8811273 and office of Naval Research Contract N00014-88-K-0475.

However, for non-uniform motion, a calculation using tensors is required to define a system where the object is relatively at rest [2]. Such calculations can become very complicated since the characteristics of the problem in the observer frame (field polarization, media parameters) are changed in the moving frame. Numerical simulation of such problems has followed the same pattern [3].

A direct way of approaching a moving-surface problem without using a system transformation involves the application of relativistic boundary conditions at the moving surface. For a moving material interface, these conditions are given by [4]:

$$\mathbf{n} \times (\mathbf{E}_2 - \mathbf{E}_1) - (\mathbf{n} \cdot \mathbf{v})(\mathbf{B}_2 - \mathbf{B}_1) = 0 \quad (1)$$

$$\mathbf{n} \cdot (\mathbf{B}_2 - \mathbf{B}_1) = 0 \quad (2)$$

$$\mathbf{n} \cdot (\mathbf{D}_2 - \mathbf{D}_1) = \rho, \quad (3)$$

$$\mathbf{n} \times (\mathbf{H}_2 - \mathbf{H}_1) + (\mathbf{n} \cdot \mathbf{v})(\mathbf{D}_2 - \mathbf{D}_1) = \mathbf{J}, \quad (4)$$

where  $\mathbf{E}_i$ ,  $\mathbf{D}_i$ ,  $\mathbf{H}_i$ , and  $\mathbf{B}_i$  are, respectively, the electric field, electric flux density, magnetic field, and magnetic flux density in medium  $i$ ;  $\rho$ , and  $\mathbf{J}$ , denote the surface-charge and current densities;  $\mathbf{v}$  is the velocity of the surface boundary (assumed to be uniform), and  $\mathbf{n}$  is the unit vector normal to the surface.

Note that (1), (2), and the radiation condition provide the complete problem physics, assuming that we initially have no surface charge and current density. It is also important to note from (1), (4) that a scatterer motion transverse to the surface plane (perpendicular to the surface normal) results in boundary conditions similar to that of a fixed object, simply because the term  $\mathbf{n} \cdot \mathbf{v}$  is now equal to 0. Further, (1) implies that the tangential  $\mathbf{E}$ -field at the surface of a perfectly conducting moving boundary can be finite. However, this does not result in an infinite surface current density because the usual expression,  $\mathbf{J} = \sigma \mathbf{E}$ , for current density in a material of conductivity,  $\sigma$ , is no longer valid. Instead, for a uniformly moving object, the total induced current is the result of a conduction current plus a convection current. Defining  $\beta$  as the ratio  $v/c$ ,  $c$  being the velocity of light in free space, the total current is given by

$$\mathbf{J} = \sigma(\mathbf{E} + \mathbf{v} \times \mathbf{B}) \frac{1}{\sqrt{1 - \beta^2}} \quad (5)$$

where, for a perfect conductor,  $\mathbf{E} + \mathbf{v} \times \mathbf{B} = 0$  from (1); and therefore the surface current density  $\mathbf{J}_s$  remains finite. In many references, only small velocities are considered and the term  $\beta^2$  is neglected compared to 1.

In the derivation of the above equations, no assumption is made on the speed  $v$  relative to the speed of light  $c$ , hence the designation relativistic boundary conditions. The only assumption made is that the speed  $v$  is uniform. However, the same relativistic boundary conditions derived for uniform  $v$  have been widely applied to study accelerating bodies, under certain conditions where the acceleration is sufficiently low [5]. Here, a new reference frame called the "co-moving

frame" or "instantaneous frame" is introduced [2]. The difference is that now the velocity  $\mathbf{v}$  in (1), (4) represents the instantaneous velocity instead of the uniform velocity. The term "Doppler approximation" [6] is also used to denote analyses wherein it is assumed that the instantaneous velocity equals a uniform velocity. It is not within the scope of this paper to discuss the details of this theory. Its validity in rotating coordinates has been investigated by Shiozawa [5]. The reader can also refer to the presentation given in [4, 2].

In this paper, we discuss a new numerical technique that appears novel in that it uses no system transformation. Instead it applies relativistic boundary conditions to provide the solution directly in the laboratory frame. It exploits the detailed modeling characteristics of the finite-difference time-domain (FD-TD) technique and has the potential to permit accurate numerical modeling of moving/vibrating rigid body problems of substantially more complexity than existing analytical approaches.

FD-TD is a direct solution of Maxwell's time-dependent curl equations using finite differences. Since its introduction [7-11], the method has been applied to a wide range of problems involving electromagnetic wave interactions with stationary two- and three-dimensional conducting, dielectric, and anisotropic structures. A recent review is given in [12]. Due to the time-domain nature of FD-TD, it is, in principle, applicable to direct modeling of wave interaction with time-varying surfaces. Our initial work in this area involved wave scattering from a half-space media having time-varying conductivity [13]. We subsequently considered wave scattering from relativistically moving perfectly conducting surfaces [14], using relativistic boundary conditions (1) in a laboratory frame grid. Boundary condition (1) relates the  $\mathbf{E}$  field and  $\mathbf{H}$  field linearly at the same point in space and time. This makes it impossible to implement in the FD-TD code, since there the  $\mathbf{E}$  field and the  $\mathbf{H}$  field are computed in a leapfrog manner at half-step intervals in time and space. It is therefore necessary to derive an equivalent form of (1) wherein implementation in the FD-TD code is possible. In [14], this derivation assumed that the reflected waves from the moving mirror act like plane waves. Such an assumption is exact for normal incidence and/or uniform motion but not for oblique incidence on a vibrating mirror. In this paper, we provide an improved model of relativistic motion which eliminates the need for such an assumption. The validity of this new method will be verified by considering again several cases of uniformly moving or vibrating infinite plane mirrors.

In the next section, we first briefly review the models used in [14] to numerically implement the required relativistic electromagnetic field boundary conditions. We then present an improved technique for achieving the same goal. Section 3 discusses validation studies for the uniformly moving and vibrating infinite mirror at normal incidence using the improved technique. Section 4 studies the case of a vibrating infinite mirror at oblique incidence again using the improved technique. Last, Section 5 provides the summary and conclusions.



## 2. RELATIVISTIC BOUNDARY CONDITIONS IN AN FD-TD CODE

## 2.1. Brief Description of the Earlier Methods

## 2.1.1. Quasi-stationary Method

This is the most simple approach to model a moving boundary and is widely used analytically to obtain a first approximation of the reflected field [1, 6]. For a uniformly moving mirror, this method gives the proper shift in frequency but leaves the amplitude of the reflected field unchanged. For the vibrating mirror case, the method predicts the generation of sidebands having amplitudes proportional to a zero-order Bessel function, similar to an FM-tone modulation. The modeling of the quasi-stationary method in the FD-TD code is relatively simple, with the mirror actually moving in the grid. The total tangential  $E$ -field at the mirror surfaces satisfies the boundary condition of a stationary perfectly conducting surface, i.e., is set equal to zero. Similarly, the total tangential  $H$ -field at the mirror surface is set equal to twice the incident  $H$  field. To compute the  $E$  and  $H$  fields next to the mirror surface, we use a contour integral model [14, 15].

## 2.1.2. Semi-relativistic Method

This method utilizes an equivalent relativistic boundary condition for the total tangential  $E$  or  $H$  field at the moving boundary surface based on the plane-wave assumption discussed earlier. In [14], the electric field is selected. This yields an equivalent relativistic boundary condition that relates the total tangential  $E$  field at the moving surface to the incident tangential  $E$  field. A contour integral model is used to compute the  $H$  field adjacent to the moving surface. Reference [14] shows that this model provides excellent agreement with published analytical results for scattered fields generated by an infinite conducting surface undergoing uniform translation or vibration. For the vibration cases considered, the dominant propagating modes act together almost like a plane wave, fulfilling the basic assumption of the model.

## 2.1.3. Fully-relativistic Method

This approach is similar to the semi-relativistic method except that now the equivalent relativistic boundary condition is implemented for both the  $E$  and the  $H$  fields. This approach is actually simpler to implement than the semi-relativistic model because it does not require a contour integral. Again, Reference [14] shows excellent agreement of the model with published analytical results.

## 2.2. The Improved Model

We now propose a new, more robust approach, where the plane-wave assumption used in our earlier models is removed. This permits accurate modeling of more general relativistic motion by arbitrary conducting bodies where it is not

clear a priori that the combined action of the dominant propagating modes approximates a plane wave. In this new model, we attempt to directly implement condition (1) and (2). In using (1) to calculate the tangential  $E$  field at the moving surface, there is no restriction on the time-varying velocity. However, a potential singularity problem arises when using (1) to calculate the tangential  $H$  field at the moving surface, since now  $v$  shows up in the denominator and may equal zero at particular times. We need an alternate relation for the tangential  $H$  field that does not have the singularity problem at  $v=0$ . Starting from (1), it is possible to derive such a relation that is suitable for FD-TD implementation at the moving object surface. Details of the derivation are given in the Appendix. The result is

$$\mu \frac{dH}{dt} = \frac{(v^2 - c^2)}{(v^2 + c^2)} \frac{\partial E}{\partial y} - \frac{1}{(v^2 + c^2)} \frac{dv}{dt} E, \quad (6)$$

where  $\mu$  is the free space permittivity and  $E$  and  $H$  represent the total tangential electric and magnetic fields, respectively, at the moving boundary surface. At  $v=0$ , (6) reduces to a form identical to Maxwell's curl  $E$  equation, clearly with no singularities. Equation (6) is suitable for the FD-TD algorithm because it can be computed every time step in parallel with  $H$  field computation. Note that because the  $E$  field has a step change from a non-zero value at the moving object surface to a zero value inside the perfectly conducting object the partial space derivative in (6) represents a one-sided derivative.

Our new model thus consists of condition (1) applied to the moving surface tangential  $E$  field, (2) applied to the moving surface tangential  $H$  field, and (6) applied to the moving-surface total tangential  $H$  field. We obtain

$$E_m^n = v^n \cdot \mu \cdot H_m^n, \quad (7)$$

where the subscript  $m$  denotes a total tangential field value exactly at the object surface and the surface  $H$ -field value at time  $n$  is computed by linearly extrapolating the  $H$ -field values at times  $n-1/2$  and  $n-3/2$  as follows:

$$H_m^n = 1.5 \cdot H_m^{n-1/2} - 0.5 \cdot H_m^{n-3/2}. \quad (8)$$

Condition (2) yields

$$H_{\text{normal}}^n = 0 \quad \text{for all } n. \quad (9)$$

Finally, for (6), we obtain

$$\mu \frac{H_m^{n+1/2} - H_m^{n-1/2}}{dt} = \frac{(v^2 - c^2)}{(v^2 + c^2)} \frac{E_m^n - E_m^{n-1}}{dy} - \frac{1}{(v^2 + c^2)} \frac{dv}{dt} E_m^n. \quad (10)$$

Here, the symbol  $E$  with no subscript denotes the non-zero total tangential electric field value at the grid point adjacent to the object surface, and  $dy'$  is the

corresponding distance from the mirror to this grid point. In all above equations (7)-(10) the mirror has a position corresponding to the time step at which the field is computed. This position, denoted by  $y_0(t)$  in Fig. 1a, is computed separately in the code and is necessary to calculate  $dy$ . Equations (7) and (8) provide us with the required field values at the mirror surface. Combining these equations with a contour integral model [14], we compute the fields adjacent to the surface. From the "co-moving" frame theory the velocity  $v$  in (1) or in (6) can be assumed to be time-varying.

### 3. NORMAL INCIDENCE ON A MOVING, INFINITE CONDUCTING SHEET

#### 3.1. Case of a Uniform Velocity

In our 1D model, a sinusoidal plane wave of frequency  $\omega$ , (illumination (frequency) and unit amplitude is normally incident on a uniformly moving, or vibrating mirror of frequency  $\omega$ . Referring to Fig. 1a, a positive mirror velocity,  $v$ , means that the mirror is receding from the incident wave, and a negative mirror velocity means that the mirror is advancing toward the incident wave. The scattered field from a uniformly moving mirror is given by [2]

$$E_s(y, t) = - \left[ \frac{1 - v/c}{1 + v/c} \right] \exp j \left[ \left( \frac{1 - v/c}{1 + v/c} \right) (\omega_0 t - ky) + 2\pi \left( \frac{r_0 - vt_0}{1 - v/c} \right) \right] \quad (11)$$

where  $y_0(t) = v(t - t_0) + r_0$  is the position of the mirror boundary with respect to a reference point, and  $r_0$  and  $t_0$  are some initial values. (For simplicity, we set both  $r_0$  and  $t_0$  equal to 0.) A "double-Doppler" effect is apparent from (11) in that both the frequency and amplitude of the scattered field are transformed by the same multiplying factor defined as  $\alpha = (1 - v/c)/(1 + v/c)$ .

Numerical results for double-Doppler shifts obtained with the new relativistic

TABLE I

Double-Doppler Shifts for Uniformly Moving Mirror as Obtained by FD-TD and Analytic

Velocity $v$	Frequency shift		Amplitude shift	
	Analytical	FD-TD	Analytical	FD-TD
$-c/3$	$2\omega$	$2\omega$	$2E_0$	$2.0377 E_0$
$-c/5$	$1.5\omega$	$1.5\omega$	$1.5E_0$	$1.5125 E_0$
$-c/7$	$1.33\omega$	$1.33\omega$	$1.33E_0$	$1.332 E_0$
$+c/2$	$0.33\omega$	$0.33\omega$	$0.33E_0$	$0.329 E_0$
$+c/3$	$0.5\omega$	$0.5\omega$	$0.5E_0$	$0.499 E_0$
$+c/5$	$0.66\omega$	$0.66\omega$	$0.66E_0$	$0.664 E_0$
$+c/7$	$0.75\omega$	$0.75\omega$	$0.75E_0$	$0.748 E_0$

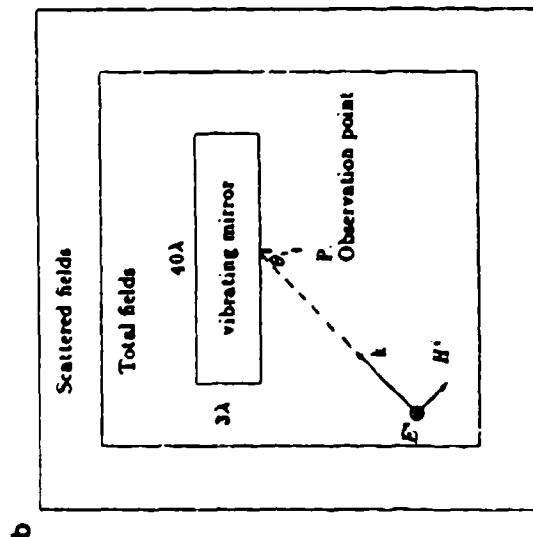
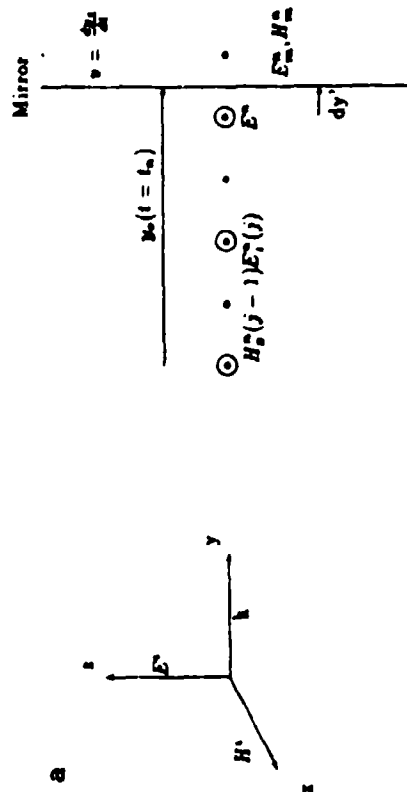


FIG. 1. (a) Schematic of a Moving Mirror in a 1D FD-TD Grid. (b) Vibrating Mirror in a 2D FT-TD Grid

model are summarized in Table I for different approach and recession velocities. In all cases, the new model provides highly accurate results in both frequency shift and amplitude shift (within 2%).

### 3.2. Case of a Sinusoidal Velocity

For a vibrating mirror, the scattered field is given by a set of two equations [16],

$$t = t_0 + \frac{d}{c} \sin(\omega_s t_0) - \frac{y}{c} \quad (12)$$

$$E_z(y, t) = -\frac{1 - \beta \cos(\omega_s t_0)}{1 + \beta \cos(\omega_s t_0)} \cos(\omega_s t_0 - k d \sin(\omega_s t_0)), \quad (13)$$

where  $\omega_s$  is the frequency of the incident wave;  $y_0 = d \sin(\omega_s t)$  describes the displacement of the mirror vibrating with a frequency,  $\omega_s$ , and  $\beta = \omega_s(d/c) = v_{\text{osc}}/c$ . Equation (13) can also be written in a Fourier series expansion,

$$E_z(y, t) = -\text{Re} \sum_{m=-\infty}^{\infty} J_{-m}(\alpha_m) \left( 1 + \frac{m}{m + 2(\omega_s/\omega_i)} \right) e^{j(\omega_s - m\omega_i)t + j\alpha_m y}, \quad (14)$$

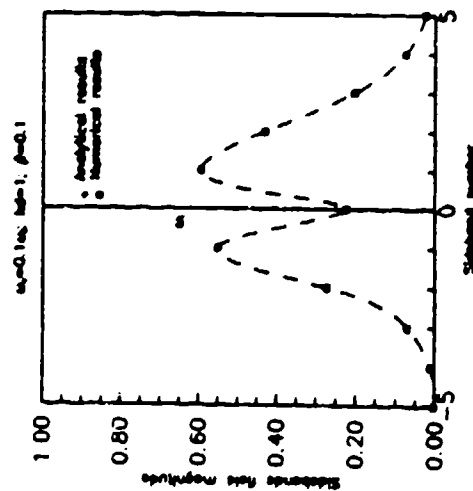


FIG. 2. Major sidebands of the reflected field spectrum as obtained both numerically and analytically.

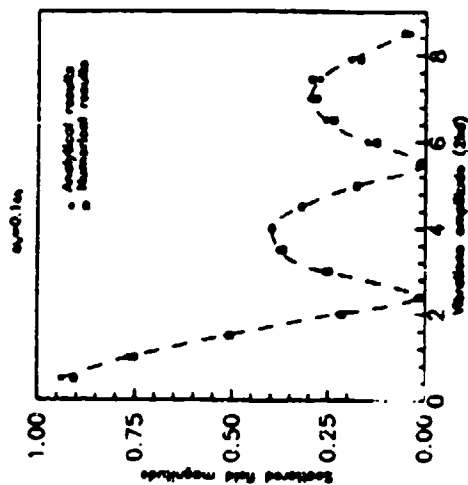


FIG. 3. Variations of the scattered field amplitudes at the illumination frequency for different vibration amplitudes ( $d$ ) of the mirror.

where

$$\alpha_m = m\beta + 2kd = \beta \left( m + 2 \frac{\omega_s}{\omega_i} \right). \quad (15)$$

The scattered field spectrum thus contains the incident frequency  $\omega_i$  and an infinity of sidebands located at  $\omega_i + m\omega_s$ , generated by the vibration of the mirror.

Figure 2 shows the magnitudes of the distinct sideband components of the reflected field spectrum for a mirror having a vibration frequency  $\omega_s = 0.1\omega_i$  and  $\beta = 0.1$ . The spectrum is obtained by taking a discrete fast Fourier transform (FFT) of the time-domain data. To obtain a correct representation of the reflected field spectrum the sampling rate was selected such that any sideband component in the spectrum is located at exactly a discrete point. The exact values are computed using (14). The correspondence between the exact and FD-TD numerical data is so close that the stars and open squares appear as closed squares. As a further test of the new model, Fig. 3 plots the variation of the scattered field amplitude at the illumination frequency for a fixed  $\omega_s = 0.1\omega_i$  and variable  $\beta$ . The exact solution is obtained from (14) by setting  $m = 0$  which leads to a zero-order Bessel function. Again, excellent agreement is demonstrated. Note that the model exactly detects the nulls of the Bessel function response.

\* The dashed line is used to indicate the general shape of the spectrum and not a continuous spectrum.

## 4. OBLIQUE INCIDENCE ON A MOVING, INFINITE CONDUCTING SHEET

## 4.1. Problem Description

Consideration of an infinite planar conducting surface for moving-interface problems simplifies the problem because of the absence of edge effects. Diffraction by an isolated uniformly moving edge has been analytically considered by Tsandoulis, [17] with respect to the far field. Also high and low frequency diffraction by a uniformly moving conducting strip has been considered respectively in [18, 19]. But to our knowledge, the analytical solution of an infinite vibrating strip or wedge has not yet been reported.

The model problem considered here is shown in Fig. 1b. A thin rectangular conducting slab is placed at the center of a two-dimensional FD-TD code. A plane wave strikes the surface of the slab at an oblique incident angle defined in the code. The goal here is to reconstruct published analytical results for reflection of obliquely incident waves by an infinite, vibrating, perfectly conducting planar surface, thereby validating the new numerical model. The form of the numerical relativistic equations (7) and (8) derived for the 1D problem are still valid for the 2D problem. It should be noted that the finite-size slab in the FD-TD grid introduces edge effects. To reduce or eliminate these effects via causal isolation, we obtain the early-time response for a sufficiently long slab. It is observed that as the incident angle becomes more grazing, we need to further increase the length of the slab for this purpose.

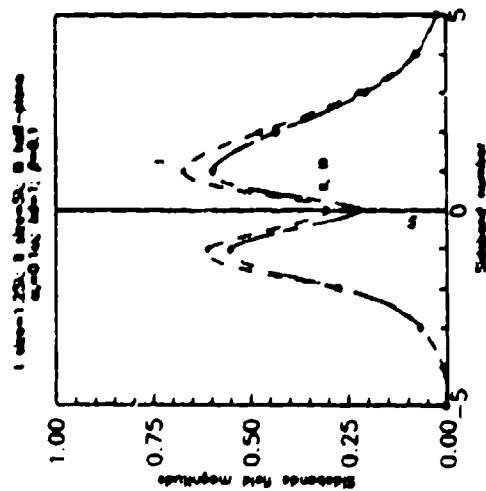


Fig. 4. Convergence of Numerical results to analytical results as the size of the cylinders approaches that of a half-plane mirror.

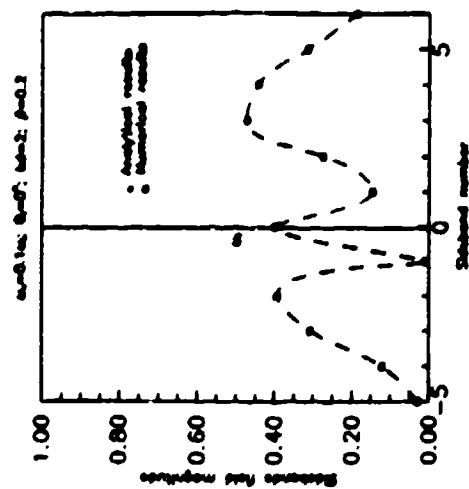


Fig. 5. Major subbands of the reflected field spectrum as obtained both externally and analytically.

## 4.2. Comparative Results

The first question considered is the minimum slab length necessary to approximately model an infinite mirror. Figure 4 presents an appropriate convergence study. Here, numerical data for the scattered subband spectrum are compared to the analytical results as the length of the slab increases. The case selected is similar to the 1D case, where  $Ld = 0.1$ ,  $\beta = 0.1$ , and  $\theta = 0^\circ$ . Clearly, the FD-TD results converge to the analytical results as the slab length increases from 50 cells (1.25  $\lambda$ ) to 200 cells (5  $\lambda$ ). The results for 100 cells (2.5  $\lambda$ ), not shown here, are identical to the 200-cell results, which imply that a slab of that size is sufficiently long to simulate an infinite mirror in a bounded FD-TD grid for the normal incidence case. As will be seen below, the slab length must be increased as the angle of incidence increases, to isolate edge effects.

At oblique incidence, we have much more complicated physics because the scattered wave has a spread both in frequency and angle of reflection. The analytical solution form, described in [20], solves a set of algebraic equations given by<sup>2</sup>

$$\sum_{n=-\infty}^{\infty} \beta_n A_n J_{n-1}(\gamma_n d) = J_{-1} \pi (k d \cos \theta_i), \quad (16)$$

<sup>2</sup> Table 1 of [20] reports values of  $A_n$  obtained from (16) for  $\theta_i = 45^\circ$ . We need to multiply each  $A_n$  term in this table by  $(k + n\beta)/k$  to get the desired Fourier spectral components. The coefficients designated by  $A_n$  in this table are really normalized amplitudes, in other words they are really  $k A_n$ , where  $k = 1$ .

where

$$\gamma_{\pm} = (k + mK) \left[ 1 - \frac{k^2 \sin^2 \theta_i}{(k + mK)^2} \right]^{1/2} \quad (17)$$

and  $K = \omega/c$ .

To validate our method we numerically solved (16) for angles of incidence between  $0^\circ$  and  $50^\circ$  for the case  $kd = 2$ , and  $\beta = 0.2$ . Figures 5-7 are graphs of the reflected sideband spectra corresponding to these angles of incidence. For each incident angle we note that the shape of the spectrum is quite different. Yet, the numerical model provides the proper sideband structure as given by the analytical theory. It is noted that the selected size of the slab at oblique incidence is greater than for the normal incidence case to minimize edge effects. It was also noted, during our test runs, that the model is correctly sensitive to a small  $5^\circ$  change in the angle of incidence.

Following the analysis in [20] it can be shown that the scattered field magnitude at the illumination frequency varies closely as

$$J_0(2kd \cos \theta_i) \quad (18)$$

In Fig. 8 we have plotted the above Bessel function versus illumination angle together with the results obtained from (16) and the FD-TD model. It is clearly seen that (18) constitutes a good approximation to the series solution obtained

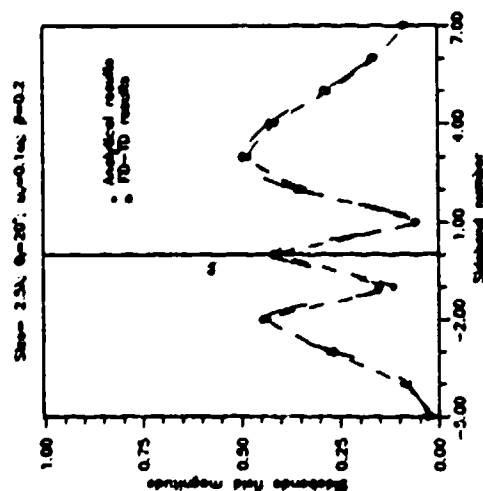


FIG. 6 Major propagating sidebands of the reflected field spectrum as obtained by FD-TD and analytically

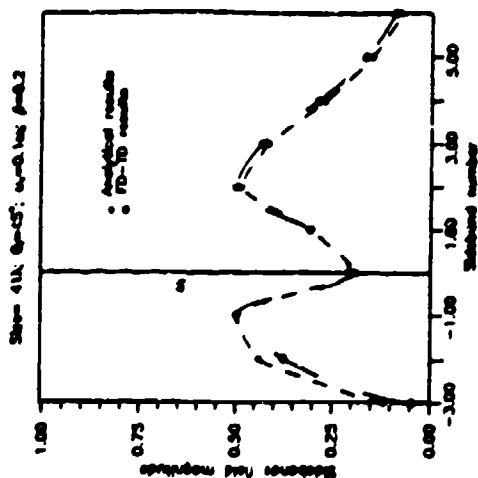


FIG. 7 Major propagating sidebands of the reflected field spectrum as obtained by FD-TD and analytically.

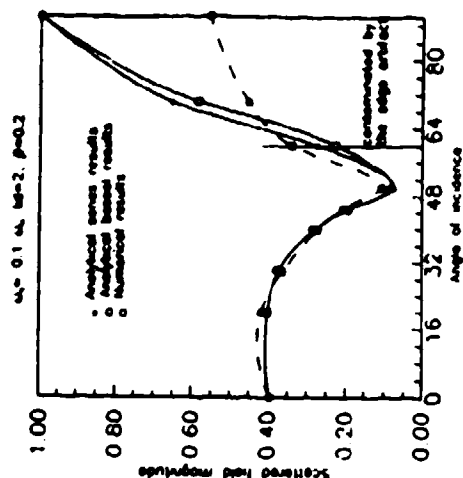


FIG. 8 Variations of the scattered field amplitude at the illumination frequency  $\omega$ , for different angles of incidence  $\theta_i$ .

from (16) over the entire angular range. Also, the correspondence between analytical and numerical results is very good up to almost  $60^\circ$ . At larger angles, the correspondence becomes less exact because of the edge effect. The analytically predicted value of 1 at  $\theta_s = 90^\circ$  (grazing) arises because the vibration of the mirror is insensitive to the incident wave and acts like a stationary surface.

### 5. SUMMARY AND CONCLUSION

We have presented a new method to incorporate relativistic boundary conditions at the surface of a moving conductor in a 1D and 2D numerical wave propagation codes. The model proposed is an exact one which eliminates the plane-wave assumption necessary in our earlier models. Two types of relativistic mirror motion have been considered: translation and vibration. Numerical results obtained were compared against the exact analytical solution, and uniformly good agreement was demonstrated. The numerical technique reported is unique in that it requires no system transformation, contrary to other methods where the problem is first solved in the moving frame and then transformed back to the rest frame. The method can be directly adapted to model other types of relativistic moving boundary problems involving two- and three-dimensional perfectly-conducting bodies of finite size and arbitrary shape. Extension to penetrable material bodies should be feasible as well. The new method promises to be a powerful tool to model electromagnetic wave interactions with complex moving obstacles where the analysis would be virtually intractable.

### APPENDIX

Following is the derivation of Eq. (6). We shall assume a TM wave of components  $(E_z, H_x, H_y)$ . The relativistic boundary condition (1) is now written as

$$E_z = v \cdot B_x \quad (19)$$

Assuming  $v$  to be time dependent, by total differentiating both sides we obtain

$$\frac{dB_x}{dt} = \frac{1}{v} \left( \frac{dE_z}{dt} - \frac{dv}{dt} \cdot B_x \right) \quad (20)$$

From Maxwell's equation we have

$$\frac{\partial E_z}{\partial y} = - \frac{\partial B_x}{\partial t} \quad (21)$$

which, together with

$$\frac{dB_x}{dt} = \frac{\partial B_x}{\partial t} + v \cdot \frac{\partial B_x}{\partial y} \quad (22)$$

lead, after simple manipulations, to

$$\mu \frac{dH_x}{dt} = \frac{v^2 - c^2}{v^2 + c^2} \frac{\partial E_z}{\partial y} - \frac{1}{v^2 + c^2} \frac{dv}{dt} \cdot E_z \quad (A.1)$$

The term associated with  $\partial B_x / \partial x$  is removed because the normal B component to the moving surface is equal to zero, from (2). Equation (A.1) corresponds to (6).

### REFERENCES

1. W. PAULI, *Theory of Relativity* (Pergamon, New York, 1958).
2. J. VAN BLADEL, *Relativity and Engineering* (Springer-Verlag, New York, 1984).
3. S. L. RAY AND R. W. ZOUKOWSKI, in *Proceedings, URSI Radio Science Meeting, Blacksburg, VA, 1987*.
4. J. VAN BLADEL, *Proc. IEEE* 64, 30 (1976).
5. T. SUGIYAMA, *Proc. IEEE* 61, 1694 (1973).
6. J. COOPER, *IEEE Trans. Antennas Propagat.* AP-28, 791 (1980).
7. K. S. YEH, *IEEE Trans. Antennas Propagat.* AP-14, 302 (1966).
8. A. TARLOVE AND M. E. BUCKWORTH, *IEEE Trans. Microwave Theory Tech.* MTT-23, 623 (1975).
9. R. HOLLAND, *IEEE Trans. Nucl. Sci.* NS-24, 2426 (1977).
10. K. S. KUNZ AND K. M. LEE, *IEEE Trans. Electromagn. Comput.* EMC-20, 328 (1978).
11. D. E. MUMFERTH, R. FLEISCH, AND F. W. SMITH, *IEEE Trans. Nucl. Sci.* NS-27, 1819 (1980).
12. A. TARLOVE, G. A. KRIEGSMANN, AND A. TARLOVE, in *Proceedings, URSI Radio Science Meeting, Blacksburg, VA 1987*.
13. F. HABPOUSH, A. TARLOVE, AND G. A. KRIEGSMANN, *IEEE Trans. Antennas Propagat.* AP-37, (1989).
14. F. HABPOUSH, A. TARLOVE, AND K. S. YEH, *IEEE Trans. Antennas Propagat.* AP-36, 1983.
15. A. TARLOVE, K. R. UMASHANKAR, B. BUCKER, F. HABPOUSH, AND K. S. YEH, *IEEE Trans. Antennas Propagat.* AP-36, 1983.
16. R. E. KUMMER, *IEEE Trans. Antennas Propagat.* AP-27, 344 (1979).
17. G. N. THANDRILAS, *Radio Sci.* 9 (1968).
18. J. D. HORTER, *IEEE Trans. Antennas Propagat.* (1972).
19. G. N. THANDRILAS, *J. Opt. Soc. Amer.* 59 (1969).
20. D. DE ZUTTER, *IEEE Trans. Antennas Propagat.* AP-30, 898 (1982).

# Extension of On-Surface Radiation Condition Theory to Scattering by Two-Dimensional Homogeneous Dielectric Objects

STEPHEN ARENDT, STUDENT MEMBER, IEEE, KORADA R. UMASHANKAR, SENIOR MEMBER, IEEE,  
ALLEN TAFLOVE, FELLOW, IEEE AND GREGORY A. KRIEGSMANN

**Abstract**—The recent new analytical formulation of electromagnetic wave scattering by perfectly conducting two-dimensional objects using the on-surface radiation boundary condition approach is conveniently extended to the case of two-dimensional homogeneous convex dielectric objects. The existing classical solution for the scattering and penetration analysis of dielectric objects is based upon coupled field formulation with the external and internal fields directly coupled together through the electromagnetic surface boundary conditions. It is shown here that a substantial simplification in the analysis can be obtained by applying the out-going radiation boundary condition on the surface of the convex homogeneous dielectric object. This analysis procedure decouples the fields in the two regions to yield explicitly a differential equation relationship between the external incident field excitation and the corresponding field distribution in the interior of dielectric object. The interior fields can be obtained by solving the differential equation using either an analytical approach or a suitable numerical method. Two dimensional scattering examples along with validations are reported showing the near surface field distributions for a homogeneous circular dielectric cylinder and an elliptic dielectric cylinder each with transverse magnetic plane wave excitation. The resulting surface currents are compared with good agreement to those obtained from the integral equation solution.

## I. INTRODUCTION

RECENTLY A NOVEL analytical technique based on the on-surface radiation condition (OSRC) theory [1] was introduced for modeling high-frequency electromagnetic wave scattering. For two-dimensional analysis of electromagnetic scattering by convex conducting objects, the OSRC approach has demonstrated substantial simplification of the usual integral equation for the induced surface currents through the application of a radiation boundary operator [2], [3] directly on the object surface. This method has been shown to give reasonable results for two-dimensional perfectly conducting

objects having either transverse magnetic (TM) or transverse electric (TE) plane wave excitation [1] and also has been applied to various reactively loaded acoustic scattering problems [4]. The main purpose of this paper is to demonstrate further an extension and application of this novel OSRC analytical technique to the analysis of electromagnetic scattering and penetration by homogeneous convex dielectric objects.

Over the past several years, there has been substantial investigation in the development of expansions for local radiation boundary conditions of higher order than the Sommerfeld condition [5], [6]. The goal has been to achieve nearly reflection-free truncations of space grids used to model wave interactions with structures via direct finite-difference [7], [8] or finite-element simulations of the governing partial differential field or wave equations. The boundary operators, containing mixes of both space and time partial derivatives, principally exploit the asymptotic behavior of the scattered field in either cylindrical or spherical coordinate systems. While the radiation boundary operators have been successfully applied to the scattered field away from the specific scatterer of interest, the OSRC concept was prompted by the observation that the outer boundaries of finite-difference time-domain space grids [7] employing the second-order radiation boundary operator, could be brought very close to a scatterer without adversely affecting the far-field results. In a limit, if the radiation boundary condition is applied directly on a two-dimensional conducting scatterer surface, the original integral equation for the scattered field can be reduced to merely a line integral of known fields around the surface for the TM case, or an ordinary differential equation to be solved around the surface for the TE case, whereby analytical expressions for the induced surface current distribution can be obtained [1]. Interestingly enough, elaborate finite-difference numerical simulation schemes are no longer required which seems to depend on the accuracy needed. In order to extend the general applicability of the OSRC technique to the case of scattering and penetration involving re-entrant and other related cavity type interaction problems, a detailed study is reported in this paper concerning the electromagnetic scattering and interaction analysis of homogeneous convex dielectric objects. In fact, the formulation is applicable in the low frequency, resonant frequency, and also high frequency regimes. Specifically for the case of high frequency regimes

Manuscript received August 19, 1988; revised March 9, 1990. This work was supported in part by the Office of Naval Research under grant N00014-88-K-0475 to Northwestern University and the University of Illinois at Chicago.

S. Arendt was with the Department of Electrical Engineering and Computer Science, University of Illinois, Chicago, IL. He is now with the Department of Physics, University of Chicago, Chicago, IL 60637.

K. R. Umashankar is with the Department of Electrical Engineering and Computer Science, University of Illinois at Chicago, Chicago, IL 60680.

A. Taflov is with the Department of Electrical Engineering and Computer Science, Northwestern University, Evanston, IL 60208.

G. A. Kriegsmann is with the Department of Engineering Sciences and Applied Mathematics, Northwestern University, Evanston, IL 60208.

IEEE Log Number 9037626.

[4], an asymptotic expansion in terms of the wavenumber  $k$  can also be used in the derivation of the near and far scattered fields.

For the analysis of homogeneous dielectric objects [9], use of the dielectric boundary conditions in the OSRC differential equation yields a relation between the electric field and its normal derivative on the surface of the scatterer. As the OSRC equation is only valid over the boundary surface, one needs an additional relation between the electric field and its normal derivative on the scatterer contour to completely solve the problem. In this study, a functional form for the interior field distribution is specified, immediately providing the required additional relation through differentiation. Specifically, the interior electric field is represented by a modal expansion with unknown coefficients. For the case of general dielectric scatterer application, the functional form of differential equation can be analyzed based on an appropriate numerical method. For a circular dielectric cylinder, a direct substitution of this modal expansion into the OSRC equation followed by an enforcement of the orthogonality of the angular eigenfunctions gives a solution for the unknown coefficients. However, for a general dielectric cylinder, such a procedure is not applicable because a modal series defined in an arbitrary dielectric object is not guaranteed convergence at points everywhere on the scatterer contour, so that the boundary conditions cannot be applied to this expansion. To surmount this difficulty, an analytic continuation method is used [10], [11]. In this scheme, the interior field modal expansions are analytically continued throughout the scatterer interior in order to obtain series expansions which are valid on the contour of the dielectric scatterer. Once this is done, the OSRC differential equation can be used to apply the boundary conditions, yielding a matrix equation for the unknown expansion coefficients.

In the following, the application of the OSRC method to the case of homogeneous dielectric objects is outlined briefly beginning with the general dielectric OSRC equation and the solution for a homogeneous circular dielectric cylinder. A brief outline of the analytical continuation formulation, which is required only inside the scatterer, is then presented and applied to the case of a homogeneous dielectric elliptic cylinder. Numerical results for the surface electric and magnetic current distributions are presented for both the dielectric circular and elliptic cylinders having TM plane wave excitation. The TE excitation case is not reported here since it forms a trivial dual case. For the canonical dielectric case studies reported, good validations have been obtained based on the regular eigenfunction solution and the combined field coupled integral equation numerical solution [8], [12].

## II. GENERAL FORMULATION

Let us consider a two-dimensional, convex, homogeneous dielectric scatterer excited normally by a TM polarized plane wave as shown in Fig. 1. The dielectric scatterer is assumed to be uniform in the  $z$ -coordinate direction. The cross section of the arbitrary convex cylinder is contained in region 2 and is bounded by a contour  $C$ . Outside region 2 is region 1 representing an isotropic free space medium. Referring to

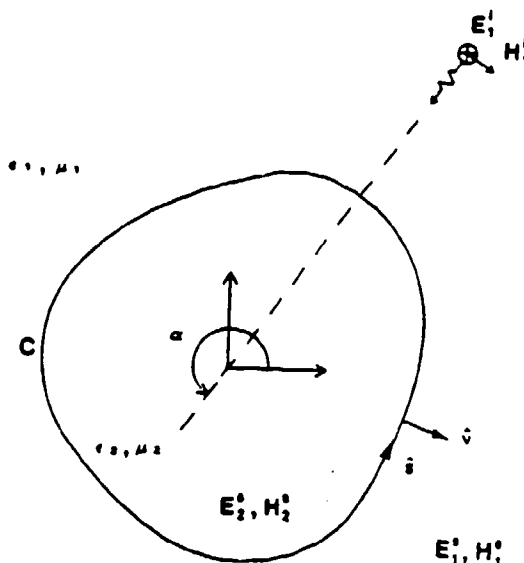


Fig. 1. Two-dimensional homogeneous dielectric scatterer.

Fig. 1, let

- $\epsilon_1, \mu_1$  permittivity and permeability of the free space region;
- $\epsilon_2, \mu_2$  permittivity and permeability of the dielectric material scatterer;
- $(\vec{E}_1^s, \vec{H}_1^s)$  electric and magnetic scattered fields in region 1;
- $(\vec{E}_2^s, \vec{H}_2^s)$  electric and magnetic scattered fields in region 2;
- $(\vec{E}_1^i, \vec{H}_1^i)$  electric and magnetic incident fields in region 1.

In the classical approach, the expressions for the scattered fields in regions 1 and 2 are obtained in terms of the surface electric and magnetic fields or in terms of the corresponding equivalent magnetic and electric currents on the contour  $C$ , by invoking the electromagnetic equivalence principle [8]. In the application of OSRC method for the electromagnetic scattering by the dielectric object, a higher order radiation boundary condition is enforced on the contour  $C$  of the convex scatterer itself. According to this approach, for the case of a TM excited two-dimensional smooth convex cylinder, the  $z$ -component of the scattered electric field in region 1 should satisfy the following radiation boundary condition [1]:

$$B_z E_1^s = O(R^{-2m-1/2}) \quad (1a)$$

$$B_z = \frac{\partial}{\partial \nu} + \frac{\xi}{2} + jk - \frac{1}{2(\xi + jk)} \left( \frac{\partial^2}{\partial s^2} + \frac{\xi^2}{4} \right) \quad (1b)$$

$$k = \omega [\mu_1 \epsilon_1]^{1/2} \quad (1c)$$

where  $R$  is the radius of large circle,  $k$  is the propagation factor in the free space region,  $\omega$  is the frequency,  $\partial/\partial \nu$  is the normal derivative,  $\xi$  and  $s$  are the curvature and arc length, respectively, along the contour  $C$ . Further, across the boundary contour  $C$  of the homogeneous dielectric cylinder,



the  $z$  component of the electric fields and the transverse component of the magnetic fields are continuous, yielding the regular surface boundary conditions

$$E_1^i + E_1^s = E_2^i \quad (2a)$$

$$\hat{s} \cdot (\bar{H}_1^i + \bar{H}_1^s) = \hat{s} \cdot \bar{H}_2^i \quad (2b)$$

where  $\hat{s}$  is a tangential vector to the contour  $C$ , and in terms of normal derivatives the expression (2b) takes the form

$$\frac{1}{\mu_1} \left( \frac{\partial E_1^i}{\partial \nu} + \frac{\partial E_1^s}{\partial \nu} \right) = \frac{1}{\mu_2} \frac{\partial E_2^i}{\partial \nu} \quad (2c)$$

On substituting the boundary conditions (2a) and (2c) into the OSRC boundary operator (1),

$$\frac{\mu_1}{\mu_2} \frac{\partial E_2^i}{\partial \nu} + AE_2^i + B \frac{\partial^2 E_2^i}{\partial s^2} = \frac{\partial E_1^i}{\partial \nu} + AE_1^i + B \frac{\partial^2 E_1^i}{\partial s^2} \quad (3a)$$

where the coefficients  $A$  and  $B$  are given by

$$A = jk + \frac{\xi}{2} + \frac{j\xi^2}{8(k - j\xi)} \quad (3b)$$

$$B = \frac{j}{2(k - j\xi)} \quad (3c)$$

The right-hand side of (3a) is simply equal to  $B_2 E_1^i$ , and, being a function of the incident field only, is completely known. For convenience, a second operator  $B_2^+$  is introduced to represent the operation on  $E_2^i$  in the left side of (3a). This operator differs from the  $B_2$  operator only in the permeability ratio multiplying the normal derivative. For the case of lossy materials, the permittivity and permeability parameters of the dielectric scatterer are redefined in terms of their effective values to take into account the conductivity parameter. It is known that the total electric field evaluated on the contour  $C$  is proportional to the equivalent magnetic surface current on  $C$ , and that the normal derivative of the electric field on  $C$  is proportional to the equivalent electric surface current on  $C$ . Thus, (3a) provides a relation between the equivalent electric and magnetic currents on the surface of the dielectric scatterer. Since (3a) is a relation between two unknowns, it alone is not enough to solve the scattering problem; an additional relation between the total electric field and its normal derivative on  $C$  is also necessary. If a functional form is assumed for the interior scattered electric field, the second required relation is immediately provided through differentiation. In the following section, the interior electric field of a circular cylinder will be represented by an eigenfunction expansion having unknown coefficients. This single expansion, when substituted into the relationship (3a), is enough to yield the unknown scattering coefficients. Once the electric field is known along the contour  $C$ , the corresponding scattered magnetic field along the contour  $C$  can be obtained by taking the normal derivative of the scattered electric field.

### III. SCATTERING BY A DIELECTRIC CIRCULAR CYLINDER

Consider the case of homogeneous dielectric circular cylinder of radius  $a$  illuminated by a TM polarized normally incident plane wave. In the regular dielectric scatterer analysis, one uses the electric and magnetic field boundary conditions (2a) and (2b) along with modal expansions for the interior and exterior scattered fields. However, in the OSRC analysis, one needs only an interior field modal expansion, and the expression (3a) which serves as a boundary condition for the interior field. For the case of circular cylindrical geometry, substituting  $\nu = r$  and  $s = r\phi$ , (3a) takes the form

$$\frac{\mu_1}{\mu_2} \frac{\partial E_2^i}{\partial r} + AE_2^i + \frac{B}{r^2} \frac{\partial^2 E_2^i}{\partial \phi^2} = \frac{\partial E_1^i}{\partial r} + AE_1^i + \frac{B}{r^2} \frac{\partial^2 E_1^i}{\partial \phi^2} \quad (4a)$$

and the coefficients  $A$  and  $B$  are given by

$$A = jk + \frac{1}{2r} + \frac{j}{8r^2(k - j/r)} \quad (4b)$$

$$B = \frac{j}{2(k - j/r)} \quad (4c)$$

A TM polarized normally incident plane wave having unit amplitude and propagating in the  $x$  direction can be written in terms of an infinite sum over cylindrical modes, and is given by

$$E_1^i(r, \phi) = e^{-jkx} = \sum_{m=-\infty}^{\infty} j^{-m} J_m(kr) e^{jm\phi} \quad (5a)$$

For the dielectric region the interior  $E_2^i$  can be similarly written as

$$E_2^i(r, \phi) = \sum_{m=-\infty}^{\infty} P_m J_m(k_2 r) e^{jm\phi} \quad (5b)$$

$$k_2 = \omega[\mu_2 \epsilon_2]^{1/2} \quad (5c)$$

where  $J_m$  is the Bessel function of first kind and of order  $m$ ,  $P_m$  are the unknown scattering modal coefficients for the interior fields, and  $k_2$  is the propagation constant for the dielectric region. By substituting the modal expansions (5a) and (5b) into the OSRC relationship (4a) and by invoking the orthogonality properties with respect to the angular variable  $\phi$  on both sides of the expression, the various modal coefficients  $P_m$  can be determined

$$P_m = \frac{j^{-m} \left[ kJ'_m(ka) - \left\{ \frac{Bm^2}{a^2} - A \right\} J_m(ka) \right]}{\left[ \frac{\mu_1}{\mu_2} k_2 J'_m(k_2 a) - \left\{ \frac{Bm^2}{a^2} - A \right\} J_m(k_2 a) \right]} \quad (6)$$

In fact, using the electric field boundary condition, expression (2a), the modal coefficients for the exterior fields can also be determined, if required. Similarly, the transverse magnetic field can be obtained by taking the normal derivative of the electric field. In fact, the electric and the magnetic fields along the contour  $C$  can be converted into the corre-



yields the following set of linear equations:

$$\sum_{n=-M}^M \sum_{m=-N}^N b_n j^{n-m} J_{m-n}(k_2 r'_0) e^{j(n-m)\phi_0} B_2^+ \cdot [j^{-m} J_m(k_2 r') e^{jm\phi}] = B_2 E_1^i(\bar{r}), \quad \text{for } \bar{r} = \bar{r}_i, \bar{r}' = \bar{r}_i. \quad (10)$$

It is noted that the differentiation in the  $B_2$  and  $B_2^+$  operators is with respect to the unprimed coordinate system, while the expansion (10) is a function of the primed coordinates, so that care is taken to include the coordinate transformation when determining the required derivatives. The expression (10) is repeated for all the secondary expansions yielding a system of  $W$  linear equations, where  $W$  is the number of contour sampling points. Selecting  $W$  to be equal to  $2N + 1$ , where  $N$  is the primary series truncation index, results in a completely determined set of linear equations for the primary expansion coefficients  $b_n$ . Hence the following matrix equation is obtained

$$\bar{L}\bar{B} = \bar{F} \quad (11a)$$

where

$$B_i = b_n \quad (11b)$$

$$F_i = B_2 E_1^i(\bar{r})|_{r=r_i} \quad (11c)$$

$$L_{in} = \sum_{m=-M}^M \sum_{n=-N}^N j^{n-m} J_{m-n}(k_2 r'_0) e^{j(n-m)\phi_0} B_2^+ \cdot [j^{-m} J_m(k_2 r') e^{jm\phi}]|_{r=r_i}. \quad (11d)$$

Once the unknown primary expansion coefficients have been determined, the expression (9c) can be utilized to obtain the secondary expansion coefficients for each  $\bar{r}'_0$ . This gives the required axial electric field at each contour point  $\bar{r}$ , as

$$E_2^i(\bar{r}_i) = \sum_{m=-M}^M \sum_{n=-N}^N b_n j^{n-m} J_{m-n}(k_2 r'_0) e^{j(n-m)\phi_0} \cdot [j^{-m} J_m(k_2 r'_i) e^{jm\phi_i}]. \quad (12)$$

As mentioned earlier, the electric field on  $C$  obtained in (12) represents the magnetic surface current, and the normal derivative of the electric field on  $C$  represents the corresponding electric surface current distribution. Once the complete field distributions are known at the boundary contour  $C$ , the interior and the exterior field distributions including the far field distributions can be easily calculated [1], [8].

Returning to the question of truncation indices, in order to determine the index at which truncation of a field expansion is permissible, the electrical size of the region of validity of the series expansion is examined. For a given argument, the Bessel functions of the first kind of integer order decrease approximately for orders greater than the argument. Hence, the Bessel functions in field expansions (7) and (8) become negligible for orders greater than their maximum possible argument. Since the primary field expansion (7) is valid inside the  $R_m$  circle, its truncation index is given by

$$N = k_2 r_m \quad (13a)$$

where  $r_m$  is the radius of the  $R_m$  circle. Similarly, the secondary field expansion (8) is valid only inside the circle centered at  $\bar{r}'_0$ , so that its truncation index is given by

$$M = k_2 |\bar{r}_i - \bar{r}'_0|. \quad (13b)$$

The limits stated in (13a) and (13b) are the minimum required, somewhat larger truncation indices than those above are selected.

It has been mentioned previously that it is not always possible to determine a suitable point  $\bar{r}'_0$  for every contour sampling point  $\bar{r}_i$ . This difficulty can be skirted by making successive continuations of the interior fields. Since the objective of the analytic continuation procedure is to obtain an inside scattered field expansion valid on the contour and related to the primary expansion, one can simply use more than one secondary field expansion to get from the  $R_m$  circle to the specific contour point of interest as discussed in [9]. For such objects, the analysis follows in an analogous fashion, and a similar matrix equation (11a) is obtained with the corresponding modified coefficient matrix elements given by

$$L_{in} = \sum_{p=-P}^P \sum_{m=-M}^M j^{n-m} J_{m-n}(k_2 r'_0) e^{j(n-m)\phi_0} \cdot \{ j^{m-p} J_{p-m}(k_2 r'_i) e^{j(m-p)\phi_i} \} \cdot B_2^+ [j^{-p} J_p(k_2 r') e^{jp\phi}]|_{r=r_i}. \quad (14)$$

The elaborate analysis details including discussion on the evaluation of matrix elements can be found in [9]. Still more elongated objects will require more than one of these auxiliary continuations, so that the matrix element expression for such objects will contain additional summations.

## V. NUMERICAL RESULTS

Based on the analysis discussed above for the electromagnetic scattering and interaction by homogeneous convex dielectric objects, numerical results and their validations for the surface electric current and magnetic current distributions are presented for the case of a circular dielectric cylinder and an elliptic dielectric cylinder.

### A. Homogeneous Circular Dielectric Cylinder

Fig. 3(a) show the magnitude and phase distribution of the surface electric current on a homogeneous circular dielectric cylinder based on both the OSRC formulation and the 'exact' eigenfunction series solution. These results are obtained by calculating the modal coefficients of (6), and then substituting the modal coefficients into the interior field expression 5(b). The dielectric cylinder has a relative permittivity of  $\epsilon_r = 2$  and a relative permeability of  $\mu_r = 2$ . The radius of the circular cylinder is  $a = 2.5$ , and the frequency of excitation of the incident plane wave is such that the free space propagation constant  $k_0 = 1$ . Since the surface electric current distribution is symmetrical with respect to the direction of excitation, only the distribution for the range  $\phi = 0$  to  $180$  is shown in the Fig. 3(a). For the same circular dielectric cylinder, Fig. 3(b) shows the magnitude and phase distribution of the surface magnetic currents. The OSRC results

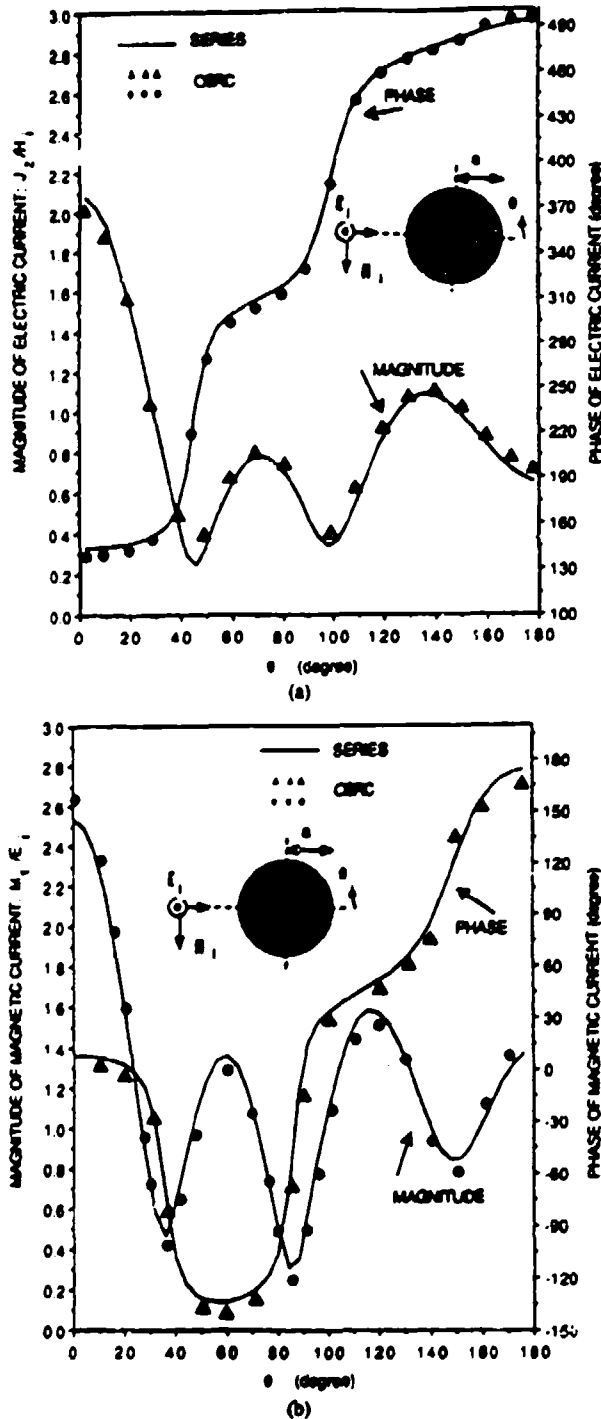


Fig. 3. (a) Magnitude and phase of electric current for dielectric circular cylinder ( $k_0 = 1$ ,  $a = 2.5$ ,  $\epsilon = 2\epsilon_0$ ,  $\mu = 2\mu_0$ ). (b) Magnitude and phase of magnetic current for dielectric circular cylinder ( $k_0 = 1$ ,  $a = 2.5$ ,  $\epsilon = 2\epsilon_0$ ,  $\mu = 2\mu_0$ ).

show good correspondence with the "exact" eigenfunction series solution.

### B. Homogeneous Elliptic Dielectric Cylinder

The OSRC numerical result for the elliptic dielectric cylinder is obtained by solving the matrix equation (11a) for the various modal coefficients of (11b), and then the modal coefficients are substituted into the interior field expression

(12). To effect such a solution, the coefficient matrix elements of (11d) are determined first. This involves applying the  $B_2^+$  operator to the  $m$ th eigenfunction. Denoting these eigenfunctions as  $G$  in the unprimed rectangular coordinate system, and  $F$  in the primed cylindrical coordinate system, we have

$$G(x, y) = F(r', \phi') = [j^{-m} J_m(k_2 r') e^{jm\phi'}] \quad (15a)$$

$$r' = [(x - x_0)^2 + (y - y_0)^2]^{1/2} \quad (15b)$$

$$\phi' = \tan^{-1} \left( \frac{y - y_0}{x - x_0} \right) \quad (15c)$$

In order to consider arbitrary cross sections, if  $X$  and  $Y$  are the  $x$  and  $y$  components, respectively, of the normal vector on the elliptic scatterer, then the normal and second tangential derivatives contained in the  $B_2^+$  operator can be calculated from

$$\frac{\partial}{\partial \nu} = X \frac{\partial}{\partial x} + Y \frac{\partial}{\partial y} \quad (16a)$$

$$\frac{\partial^2}{\partial s^2} = \left\{ \frac{dx}{ds} \right\}^2 \left[ \frac{\partial^2}{\partial x^2} + 2 \frac{dy}{dx} \frac{\partial^2}{\partial x \partial y} + \left\{ \frac{dy}{dx} \right\}^2 \frac{\partial^2}{\partial y^2} + \frac{d^2 y}{dx^2} \frac{\partial}{\partial y} \right] + \frac{d^2 x}{ds^2} \left[ \frac{\partial}{\partial x} + \frac{dy}{dx} \frac{\partial}{\partial y} \right] \quad (16b)$$

To calculate the derivatives given by (16a) and (16b), all the first- and second-order derivatives of  $G$  with respect to  $x$  and  $y$  are calculated using the chain rule and the coordinate transformation equations (15b) and (15c). The resulting expressions are then substituted into the  $B_2^+$  operator and the matrix element expression (11d). After inclusion of the terms dependent on the scatterer geometry, the coefficient matrix is then completely specified. The general equations derived above can be specialized to the case of the elliptic dielectric cylinder [9].

Fig. 4(a) shows the magnitude and phase distribution of the surface electric current on a homogeneous dielectric cylinder based on the OSRC formulation. The elliptic dielectric cylinder has a relative permittivity of  $\epsilon_r = 2$  and a relative permeability of  $\mu_r = 1$ . The semimajor axis of the elliptic cylinder is  $k_0 a = 1$ , and the semiminor axis is  $k_0 b = 0.52$ . The frequency of excitation of the incident plane wave is such that the free space propagation constant  $k_0 = 2\pi$ . Since the surface electric current distribution is symmetrical with respect to the direction of excitation as shown in the figure, only the distribution for the range  $\phi = 90$  to  $270$  is shown in the Fig. 4(a). The OSRC results for the surface electric current distribution is compared with respect to the "exact" solution obtained based on the coupled combined field integral equation and method of moments technique [8]. For the same elliptic dielectric cylinder, Fig. 4(b) shows the magnitude and phase distribution of the surface magnetic currents. These results show good correspondence to the combined field integral equation solution. Once the surface electric and magnetic currents are known, the far-field distribution can be easily calculated [8], [9].

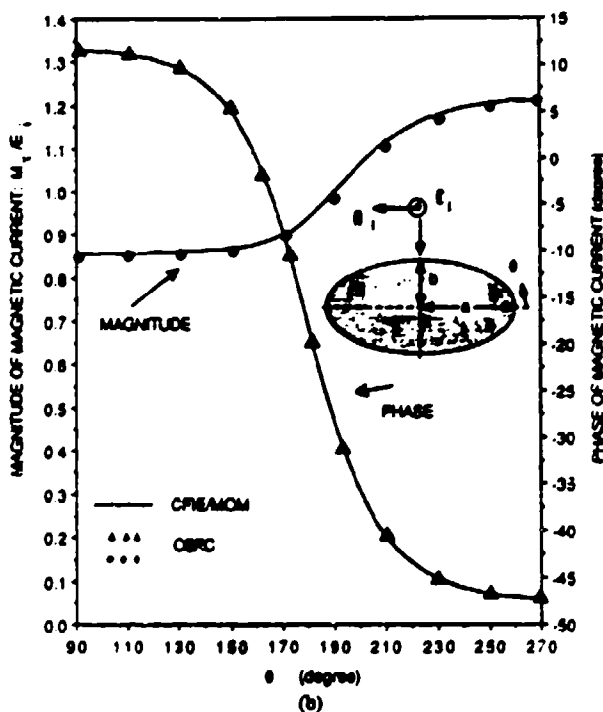
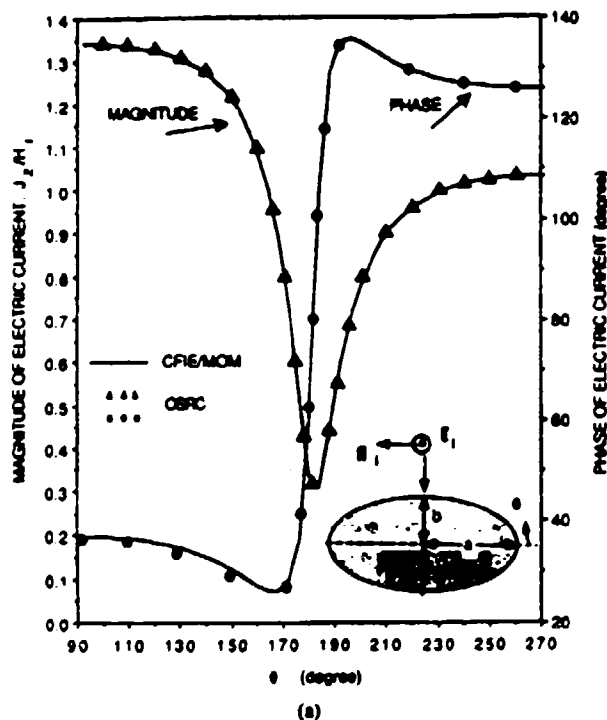


Fig. 4. (a) Magnitude and phase of electric current for dielectric elliptic cylinder ( $k_0 = 2\pi$ ,  $a = 1/2\pi$ ,  $b = 0.52/2\pi$ ,  $\epsilon = 2\epsilon_0$ ,  $\mu = \mu_0$ ). (b) Magnitude and phase of magnetic current for dielectric elliptic cylinder ( $k_0 = 2\pi$ ,  $a = 1/2\pi$ ,  $b = 0.52/2\pi$ ,  $\epsilon = 2\epsilon_0$ ,  $\mu = \mu_0$ ).

## VI. CONCLUSION


The recent new analytical formulation of electromagnetic wave scattering by perfectly conducting two dimensional objects using the on-surface radiation boundary condition approach is successfully extended and validated for the case of two dimensional homogeneous convex dielectric objects.

The classical scattering and penetration study of dielectric object is generally based upon the coupled field formulation with the external and internal fields directly coupled together. However, it is shown here that substantial simplification in the analysis can be obtained by applying the out-going radiation boundary condition directly on the surface of the convex homogeneous dielectric object. This approach decouples the fields in the two regions to yield explicitly a differential equation relationship between the external incident field excitation and the corresponding field distribution in the interior of the dielectric object. The interior fields are obtained by first solving the differential equation, using either an analytical approach or using a suitable numerical method. This technique can also be applied to conducting geometries with reentrant features and will be reported separately. Two-dimensional scattering examples along with validations are reported showing the near surface field distributions for a homogeneous circular dielectric cylinder and an elliptic dielectric cylinder with transverse magnetic plane wave excitation. The formulation and the corresponding results for the transverse electric polarization can be obtained based on the electromagnetic duality principle and are not reported here. The resulting surface electric and magnetic currents are compared and found in good agreement to those obtained from the coupled combined field integral equation solution.

## REFERENCES

- [1] G. A. Kriegsmann, A. Taflov, and K. Umashankar, "A new formulation of electromagnetic wave scattering using an on-surface radiation boundary condition," *IEEE Trans. Antennas and Propagat.*, vol. AP-35, pp. 153-161, Feb. 1987.
- [2] G. A. Kriegsmann and C. Morawetz, "Solving the Helmholtz equation for exterior problems with variable index of refraction: I," *SIAM J. Sci. Stat. Comput.*, vol. 1, pp. 371-385, Sept. 1980.
- [3] A. Baylis and E. Turkel, "Radiation boundary conditions for wave-like equations," *Commun. Pure Appl. Math.*, vol. 33, pp. 707-725, 1980.
- [4] G. A. Kriegsmann and T. G. Moore, "An application of the on-surface radiation condition to the scattering of acoustic waves by a reactively loaded sphere," *Wave Motion*, vol. 10, pp. 277-284, 1988.
- [5] G. Mur, "Absorbing boundary conditions for the finite-difference approximation of the time-domain electromagnetic field equations," *IEEE Trans. Electromagn. Comput.*, vol. EMC-23, pp. 377-382, Nov. 1981.
- [6] L. N. Trefethen and L. Halpern, "Well-posedness of one-wave wave equations and absorbing boundary conditions," *Inst. Comput. Appl. Sci. and Eng.*, NASA Langley Res. Cen., Hampton, VA, Rep. 85-30, June 1985.
- [7] K. Umashankar and A. Taflov, "A novel method to analyze electromagnetic scattering of complex objects," *IEEE Trans. Electromagn. Comput.*, vol. EMC-24, pp. 397-405, Nov. 1982.
- [8] —, "Analytical models for electromagnetic scattering," RADC/Hanscom AFB, MA, Final Tech. Rep. F19628-82-C-0140, June 1984.
- [9] S. Arendt, "Application of the on-surface radiation condition method to two-dimensional electromagnetic scattering problems," M.S. thesis, Univ. Illinois, Chicago, IL, Apr. 1988.
- [10] D. Wilton and R. Mittra, "A new numerical approach to the calculation of electromagnetic scattering properties of two-dimensional bodies of arbitrary cross section," *IEEE Trans. Antennas Propagat.*, vol. AP-20, pp. 310-317, May 1972.
- [11] C. R. Mullin, R. Sandburg, and C. O. Telline, "A numerical technique for the determination of scattering cross sections of infinite cylinders of arbitrary geometrical cross section," *IEEE Trans. Antennas Propagat.*, vol. AP-13, pp. 141-149, 1965.
- [12] A. J. Poggio and E. K. Miller, "Integral equation solutions of three dimensional problems," in *Computer Techniques for Electromagnetics*, R. Mittra, Ed. London: Pergamon, 1963, ch. 4.

- [13] G. N. Watson, *A Treatise on the Theory of Bessel Functions*. Cambridge, MA: The University Press, 1966.



Stephen Arendt (S'85) received the B.S. and M.S. degrees in electrical engineering from the University of Illinois, Chicago, IL, in 1986 and 1988, respectively. He is currently pursuing the Ph.D. degree in physics at the University of Chicago, Chicago, IL.

Mr. Arendt is a member of Tau Beta Pi and Eta Kappa Nu.

Kerada R. Umashankar (S'69-M'75-SM'81), for a photograph and biography please see pages 765 and 766 of the June 1986 issue of this TRANSACTIONS.

Allen Taflov (S'75-SM'84-F'90), for a photograph and biography please see page 1812 of the December 1988 issue of this TRANSACTIONS.

Gregory A. Kriegsmann, for a photograph and biography please see page 161 of the February 1987 issue of this TRANSACTIONS.

# Large-scale methods in computational electromagnetics

Daniel S. Katz and Allen Taflov, Northwestern University, Evanston, Illinois  
Jeffrey P. Brooks and Evans Harnagan, Cray Research, Inc.

The numerical modeling of electromagnetic wave phenomena can be a computationally intensive task. To date, the design and engineering of aerospace vehicles has been the primary application driving the development of large-scale methods in computational electromagnetics (CEM). Efforts in this area have been aimed primarily at minimizing the radar cross section (RCS) of aerospace vehicles. RCS minimization enhances the survivability of vehicles that are subjected to precision-targeted ordnance. The physics of RCS is determined by Maxwell's equations and the constitutive properties of a vehicle's materials. As a result, the interesting situation arises in which the effectiveness and cost of state-of-the-art aerospace systems in part depends on the ability to develop an efficient engineering understanding of 120-year-old equations that describe the propagation and scattering of electromagnetic waves.

Two algorithms are of primary interest in this field: the robust, traditional, full-matrix, frequency-domain integral equation method of moments (MoM); and emerging time-domain, grid-based direct solutions of Maxwell's curl equations. Both types of algorithm make efficient use of Cray Research hardware and software capabilities.

## Full-matrix MoM field computations at 2 GFLOPS

In the MoM area, one group of important codes originated with the Rao-Wilton-Glisson triangular surface patch technique for RCS analysis of arbitrarily shaped three-dimensional conducting structures.<sup>1</sup> Cray Research analysts determined that the primary task here involves the solution of very large, dense, complex-valued matrices (10K by 10K and larger) that exceed the available central memory. A strategy evolved to develop a complex-valued lower-upper matrix decomposition program that utilizes an efficient out-of-memory scheme and is adaptable to multiple CPU usage. The result was CLUD — Complex Lower-Upper Decomposition, with versions developed for the CRAY-2,

CRAY X-MP and CRAY Y-MP computer systems. This work rapidly gained popularity among MoM users, and Cray Research scientists have provided assistance to members of the CEM community in adapting these matrix solvers to many MoM codes.

Another group of important MoM codes originated with the Newman ESI-3 rectangular surface patch technique for RCS analysis of arbitrarily shaped three-dimensional conducting structures. Cray Research

analysts adapted their out-of-memory scheme for this code and subsequently developed an out-of-memory solver suitable for simultaneous solution of the monostatic RCS at a large number of illumination angles (right-hand sides). In fact, the number of right-hand sides could be in the thousands, approximating the order  $N$ , of the MoM matrix. Subsequently, a parallel-processing version of the "N right-hand-sides" code was developed.

Although CLUD works well, two drawbacks had to be addressed for very large problems.

- The input/output (I/O) for CLUD is either synchronous to disks or synchronously staged from disk to Cray Research's SSD solid-state storage device. If the matrix is scaled to fit entirely in an SSD, this is not troublesome, and near-peak performance is achieved on the CRAY X-MP and CRAY Y-MP systems. However, a 20K-by-20K complex-valued MoM matrix requires an 800 Mword SSD, which is not currently available. In CLUD, very large problems of this size require synchronous I/O between disks and SSD, which reduces overall performance.
- The CLUD algorithm is based on a SAXPY type kernel that works on individual columns. This kernel runs at peak performance on the CRAY X-MP and CRAY Y-MP systems, but not on the CRAY-2 system because of a high ratio of memory operations to computation.

Because the Cray Research mathematical software group had optimized the BLAS-3 Basic Linear Algebra Subroutines to run at near-peak performance on all Cray Research computer systems, an improved algorithm was developed that was based on these kernels. A block-oriented method was adapted from LAPACK to run out-of-memory by Jeffrey Brooks of Cray Research's benchmarking department. The routine CGETRF made use of two BLAS-3 kernels, CGEMM (complex matrix multiply) and CTRSM (complex triangular backsolve).

To adapt CGETRF to run out-of-memory, the matrix is divided into slabs. A slab is a matrix block consisting of a large number of adjacent columns of the matrix. The matrix is decomposed from left to right, one slab at a time. Computation works on pairs of slabs. To compute a new leading slab, all preceding slabs need to be brought into memory, one at a time, for computation. This is an I/O pattern similar to that

used in the existing CLUD code. However, three slab-sized memory buffers are used in the new code to allow for asynchronous I/O. The partial-pivoting scheme used in CGETRF is preserved in the new out-of-memory version.

A routine called CMXMA was written to take advantage of Golub's identity, which reduces the multiplication count for complex-number products. CMXMA converts complex matrix products to three real matrix multiplies and several matrix additions. (This routine is available as CGEMMS in SCILIB 6.0.) The Strassen's real matrix multiply (SGEMMS) was used to save further on operations. SGEMMS is a Strassen's algorithm extension to the standard BLAS-3 matrix multiply routine, SGEMM. SGEMMS was written by Cray Research's mathematical software group and is included in version 6.0 of Cray Research's UNICOS operating system.

When automatically multitasked to run on all eight processors on a CRAY Y-MP system, the new out-of-memory code ran at average computation rates exceeding 2.1 GFLOPS. Only 1.99 hours were required to process a 20K-by-20K matrix. During this run, 138 Gbytes of I/O were discharged to and from seven DD-40 disk drives. Yet, only 228 seconds (3.8 minutes) represented I/O wait time. In fact, 90 percent of the actual I/O operations were performed concurrently with the floating-point arithmetic by virtue of the asynchronous I/O scheme and therefore did not contribute to the observed wait time. As matrix size increased, the relative efficiency of the asynchronous scheme improved, with the I/O concurrency factor rising to 95 percent for a 40K matrix. Thus, the massive I/O associated with solving huge, dense, complex-valued MoM matrices could be buried almost completely.

### **Multiprocessing space-grid time-domain codes**

Although the LU decomposition strategy described here is highly efficient, the fundamental (order ( $N^3$ )) computational burden of LU decomposition remains dimensionally large. In fact, it is so large that there is virtually no prospect for using the traditional, full-matrix MoM to computationally model entire aerospace structures, such as fighter planes, at radar frequencies much above 150 MHz. Yet, radar frequencies of interest can greatly exceed 150 MHz, climb to 10 GHz and higher. Much research effort, therefore, has been invested in the development of alternative iterative frequency-domain approaches, including conjugate gradient and spectral methods, that preserve the rigorous boundary-integral formulation of MoM while realizing dimensionally reduced (order ( $N^2$ ) or less) computational burdens. Such methods would permit, in principle, the modeling of entire aircraft at radar frequencies above 1 GHz. However, these alternatives may not be as robust as the full-matrix MoM, insofar as they may not provide results of engineering value for a wide class of structures without the user having to wonder if the iterative algorithm has converged.

Problems involved in applying frequency-domain, full-matrix MoM technology to large scale RCS modeling have prompted much new interest in an alternative class of non-matrix approaches: direct space-grid, time-domain solvers for Maxwell's time-dependent curl equations. These approaches appear

**When automatically multitasked to run on all eight processors on a CRAY Y-MP system, the new out-of-memory code ran at average computation rates exceeding 2.1 GFLOPS.**

to be as robust and accurate as MoM, but have dimensionally-reduced computational burdens (approaching order ( $N$ )) such that whole-aircraft modeling for RCS can be considered in the near future. Currently, the primary approaches in this class are the finite-difference time-domain (FD-TD) and finite-volume time-domain (FV-TD) techniques.<sup>3,4</sup> These are analogous to existing mesh-based solutions of fluid-flow problems in that the numerical model is based upon a direct, time-domain solution of the governing partial differential equation. Yet, FD-TD and FV-TD are very nontraditional approaches to CEM for detailed engineering applications, where frequency-domain methods (primarily full-matrix MoM) have dominated.

FD-TD and FV-TD methods for Maxwell's equations are based on volumetric sampling of the unknown near-field distribution within and surrounding the structure of interest. The sampling is at sub-wavelength ( $\lambda_0$ ) resolution to avoid aliasing of the field magnitude and phase information. Overall, the goal is to provide a self-consistent model of the mutual coupling of all the electrically-small volume cells that comprise the structure and its near field, even if the structure spans tens of  $\lambda_0$  in three dimensions and there are tens of millions of space cells.

The primary FD-TD and FV-TD algorithms used today are fully explicit, second-order-accurate grid-based solvers that use highly vectorizable schemes for time-marching the six vector components of the electromagnetic near field at each of the volume cells. The explicit nature of the solvers is maintained either by leapfrog or predictor-corrector time-integration schemes. Present methods differ primarily in the set up of the space grid (almost-completely structured for FD-TD, body-fitted or unstructured for FV-TD) and the enforcement of EM field continuity at the interfaces of adjacent cells. As a result, the number of floating point operations needed to update a field vector component over one time step can vary by about 20 to 1 from one algorithm to another.

However, the choice of algorithm is not straightforward, despite this wide range of computational burdens. There is an important tradeoff decision to be made. Namely, a faster simpler solver such as FD-TD uses meshes that may not be compatible with those used in other aerospace engineering studies, computational fluid dynamics (CFD) studies in particular. As a result, there is much "homework" to be done as researchers learn to generate a new class of three-dimensional meshes specific to Maxwell's curl equations. On the other hand, the more complex FV-TD solvers can utilize existing CFD mesh generators, but require substantially more algorithmic computer arithmetic and storage. Both FD-TD and FV-TD algorithms are highly vectorized, having been benchmarked at over 200 MFLOPS on one processor of a CRAY Y-MP system for real models. However, the attainment of even higher MFLOPS rates may be hampered by the fact that the space grids have an unavoidable number of non-standard cells that require either scalar or odd-lot vector operations. These nonstandard cells result from the need to program a near-field radiation condition at the outermost grid boundary (simulating the grid continuing to infinity), and the need to stitch together varying types of meshes to accommodate complex structure shapes. Despite this, it has been found possible



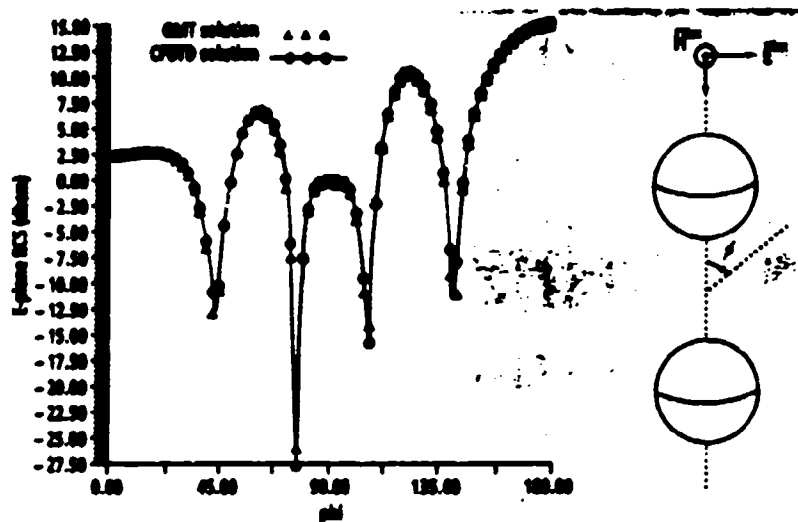


Figure 1. Agreement of FD-TD and generalized multipole technique (GMT) bistatic RCS within 1 dB over a 42-dB range for a pair of  $1-\lambda_0$  diameter conducting spheres separated by a  $1-\lambda_0$  air gap.

to achieve nearly 100 percent concurrent utilization of all eight processors on a CRAY Y-MP system using Cray Research's Autotasking automatic multitasking software feature for three-dimensional FD-TD and FV-TD codes. Only relatively minor modifications were required to the original single-processor Fortran code.

### Three-dimensional FD-TD validation example

Excellent validations of FD-TD have been obtained for three-dimensional problems that involve some of the key electromagnetic wave physics involved in RCS phenomena: near fields, monostatic RCS pattern, and bistatic RCS pattern. Here, we detail the results of a canonical, but difficult, bistatic RCS pattern validation.

Figure 1 shows the bistatic (side-scatter) RCS of a pair of  $1-\lambda_0$  diameter conducting spheres separated by a  $1-\lambda_0$  air gap.<sup>5</sup> The spheres are illuminated by a plane wave that propagates along a line connecting the centers of the spheres, and the bistatic pattern is observed in the plane of the incident electric field. (Note: when  $\phi = 0^\circ$ , the response is in the backscatter direction; that is, it is the monostatic RCS.) Here, the comparison is between FD-TD (using a mostly Cartesian, partially unstructured mesh to model conformally the spheres' surface curvatures) and an analytical approach well-suited for this problem, the generalized multipole technique (GMT).<sup>6</sup> Agreement between the two methods is excellent: within  $\pm 1$  dB (approximately  $\pm 25$  percent) over a wide 42-dB (16,000 to 1) range of RCS. This modeling accuracy occurs despite some tough electromagnetic field physics: the spheres interchange energy across the air gap in a tightly-coupled manner. For this problem, alternative FV-TD approaches using body-fitted meshes may introduce artifacts due to refraction and reflection of numerical waves propagating across global mesh distortions in the air-gap region. In fact, the two-sphere problem is a canonical example of difficult three-dimensional structures having substantial EM coupling between disjoint regions.

### Electrically-large FD-TD application: jet engine inlet

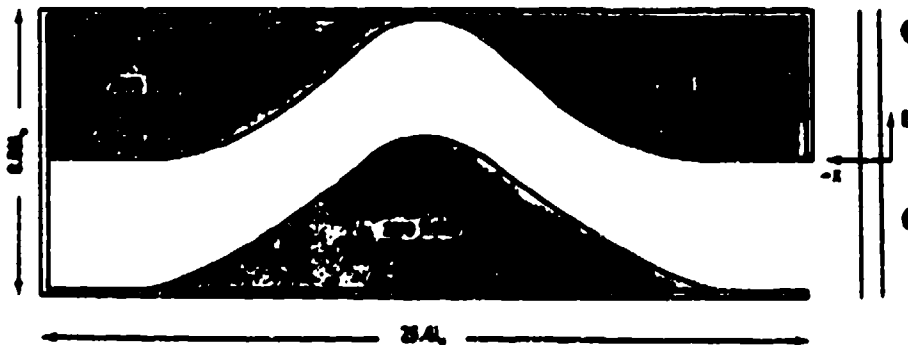
The multiprocessing in-memory FD-TD code was used to model the RCS properties of an

electrically large three-dimensional structure of engineering significance: a serpentine jet engine inlet (Figure 2). The overall system design problem involved sizing and shaping the engine inlet to meet specifications for both aerodynamics (thrust) and monostatic RCS at 10 GHz. The inlet was assumed embedded within a simple rectangular metal box coated with commercially available radar-absorbing material that provides approximately 30 dB (1000 to 1) suppression of electromagnetic wave reflections at 10 GHz. Thus, the FD-TD computed near-field and far-field electromagnetic response was primarily a function of the inside wall shaping of the inlet and not any exterior embedding.

As shown in Figure 2, the incident wave was assumed to propagate from right to left and be polarized with its electric field pointing across the narrow gap dimension (y direction) of the inlet. In this figure, the aperture of the inlet is located at the right, and the inlet is shorted by a conducting wall that represents the turbine assembly at the far left. With the box dimensions set at  $30'' \times 105'' \times 10''$ , the overall inlet and box target configuration spanned  $25.4\lambda_0 \times 8.89\lambda_0 \times 8.47\lambda_0$  at 10 GHz. For this target, the FD-TD space cell size was  $1/8''$  ( $\lambda_0/9.43$ ); and the overall lattice had  $270 \times 122 \times 118$  cells that spanned  $4608\lambda_0^3$  and contained 23,321,520 unknown vector field components. Starting with zero-field initial conditions, 1800 time steps were used (95.25 cycles of the incident wave) to march the field components to the sinusoidal steady state. The computer running time was only 3 minutes and 40 seconds per monostatic RCS calculation on the CRAY Y-MP system using automatic multiprocessing across eight processors (797/8 processor concurrency), yielding an average computation rate of 1.6 GFLOPS.

In addition to simple data for the RCS pattern, the FD-TD modeling provided details of the complex near field. Figure 3 shows the instantaneous distribution (positive and negative values) of the total gap ( $E_y$ ) electric field component in a two-dimensional observation plane that cuts through the center of the three-dimensional engine inlet. This photograph was derived from a color videotape display of the propagating electric field penetrating the inlet, generated directly by the FD-TD time-stepping. The display was taken late in the time-stepping when the field had settled into a repetitive sinusoidal oscillation (standing wave). It may be possible to use such highly detailed near-field information (very difficult to obtain from measurements) to improve future RCS designs. Comparatively, if MoM were applied to model the same engine inlet,

Figure 2. Geometry of engine inlet embedded in a rectangular metal box coated with commercial radar-absorbing material. The 10-GHz incident wave propagates from right to left.



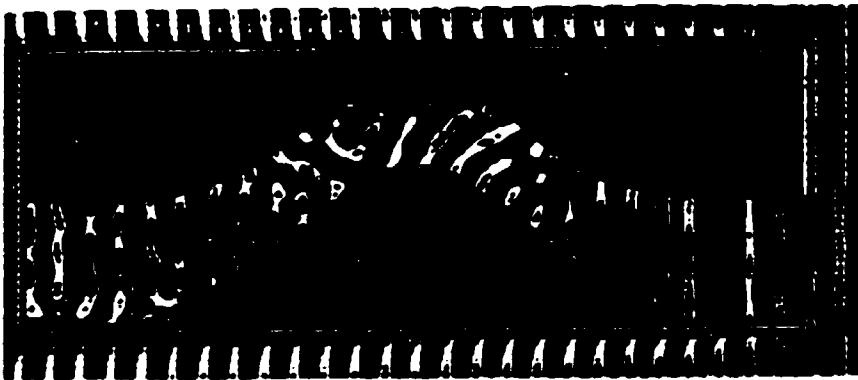


Figure 2. FD-TD computed map of the instantaneous distribution of the total  $E_z$  vector field component in a two-dimensional cut through the  $z$ -axis of the engine inlet geometry (in the dashed-line steady state).

a complex-valued linear system involving approximately 450,000 equations would have to be set up and solved. This assumes a standard triangular surface patching implementation of the electric field integral equation<sup>1</sup> with the  $1500\lambda^2$  surface area of the engine inlet discretized at 10 divisions per  $\lambda$ . Using the 2.1-GFLOPS out-of-memory subroutine for LU decomposition discussed earlier, the CRAY Y-MP system running time for this matrix would be about 2.6 years for 5000 monostatic angles. This compares to only about 12.7 days for FD-TD for the same number of monostatic angles, a speedup factor of 75. Additional problems involved in error accumulation in the LU decomposition and reliability of the computer system over the multiyear solution time probably would combine to render a traditional MoM solution useless for this target and those of similar or larger electrical sizes. We note also that MoM does not directly provide details of the penetrating near-field distribution.

#### Present work and future directions

At present, grid-based time-domain CEM models of three-dimensional structures that span more than  $30\lambda$  are being developed for the eight-processor CRAY Y-MP system. Work at this time addresses several areas:

- ☐ Automated mesh generation
- ☐ Multiprocessing out-of-memory software
- ☐ Subcell models for fine-grained structural features such as coatings
- ☐ Higher-order algorithms
- ☐ Application to nontraditional CEM areas, including design of ultra-high-speed electronic computer circuits, electro-optic components, and all-optical switches.

Extrapolating from benchmarks with the eight-processor CRAY Y-MP system, the next-generation CRAY Y-MP/16 system should provide a steady 10 to 13 GFLOPS computation rate for grid-based time-domain CEM codes when using automatic multitasking across 16 processors. The proverbial "billion-unknown" CEM problem (a three-dimensional computational volume of about  $150,000\lambda^3$ ) could be completed in as little as 40 minutes per monostatic RCS observation. Multiprocessing out-of-memory software should enable even larger volumes to be modeled in their entirety. Using such software, the era of the "entire airplane in the grid" would be opened for a number of important

aerospace systems for radar frequencies of 1 to 10 GHz. Automated geometry generation would permit CEM modelers to use structure databases developed by non-electromagnetics engineers, leading to lower design costs and the possibility of innovative design optimizations.  $\square$

#### Acknowledgments

Daniel S. Katz and Allen Taflovie were supported in part for this work by Cray Research, General Dynamics PO. 4039043, National Science Foundation Grant ASC-8811273, and Office of Naval Research Contract N00014-88-K-0475. Jeffrey P. Brooks and Evans Harrigan were primarily responsible for the MoM, FD-TD, and PV-TD code optimizations and benchmarks. Thomas G. Jurgens of Fermilab, Batavia, Illinois, implemented the double-sphere FD-TD model.

#### About the authors

Daniel S. Katz is a graduate student pursuing his Ph.D. degree in the Electrical Engineering and Computer Science Department, McCormick School of Engineering, Northwestern University. He served an internship in Cray Research's Industry, Science & Technology Department during the summers of 1989 and 1990.

Allen Taflovie is a professor of electrical engineering and computer science at Northwestern University. He recently was named an IEEE Fellow for his pioneering of FD-TD methods in CEM since 1973. He also is a national lecturer for the IEEE Antennas and Propagation Society and technical program chairman of the 1992 IEEE Antennas and Propagation Society International Symposium in Chicago.

Jeffrey P. Brooks is a manager of benchmark analysis in Cray Research's benchmarking department. He received an M.S. degree in mathematics and an M.B.A. degree from the University of Minnesota in 1985 and 1991, respectively. Before joining Cray Research in 1989, he was an instructor of mathematics at St. Olaf College in Minnesota and a technical representative at the Minnesota Supercomputer Center.

Evans Harrigan is a senior systems engineer at Cray Research, with 23 years of experience in supercomputing. He received a degree in mathematics from Michigan State University.

#### References

1. Rao, S. M., D. R. Wilson, and A. W. Glisson, "Electromagnetic Scattering by Surfaces of Arbitrary Shape," *IEEE Transactions on Antennas and Propagation*, Vol. 30, pp. 409-418, May 1982.
2. Newman, E. H. and D. M. Pozar, "Electromagnetic Modeling of Composite Wire and Surface Geometries," *IEEE Transactions on Antennas and Propagation*, Vol. 26, pp. 784-789, November 1978.
3. Taflovie, A., "Review of the Formulation and Applications of the Finite-Difference Time-Domain Method for Numerical Modeling of Electromagnetic Wave Interactions with Arbitrary Structures," *Wave Motion*, Vol. 10, pp. 347-382, December 1988.
4. Shariatz, V., A. H. 14oharizadian, and W. F. Hall, "A Time-Domain Finite-Volume Treatment for Maxwell's Equations," *Electromagnetics*, Vol. 10, pp. 127-145, January-June 1990.
5. Jurgens, T. G., "Conformal Finite-Difference Time-Domain Modeling," Ph.D. dissertation, Northwestern University, EECS Dept., 1990.
6. Ludwig, A. C., General Research Corp., Santa Barbara, California, private communication with T. G. Jurgens.

# Scattering of Electromagnetic Waves by a Material Half-Space with a Time-Varying Conductivity

Fady A. Harfoush, *Member, IEEE*, and Allen Taflov, *Fellow, IEEE*

**Abstract**—This paper analyzes for the first time electromagnetic wave penetration and scattering interactions for a material half-space having sinusoidally time-varying conductivity. Two limiting cases are considered. The first assumes that the material conductivity is almost a constant with a small temporal perturbation. The problem is accordingly attacked with first-order perturbation methods. The second exploits a large dimensionless parameter and yields an asymptotic expansion of the field inside a highly conducting material undergoing sinusoidal time variations. Illustrative examples are given which agree well with numerically obtained finite-difference time-domain (FDTD) results.

## I. INTRODUCTION

ELECTROMAGNETIC wave propagation and scattering interactions with media having time-varying parameters has been extensively studied. However, most published work considers only time-varying permittivity or permeability [1]–[4], and not time-varying conductivity. Yet, time-varying volumetric conductivity resulting from a nuclear burst, atmospheric fluctuations, or other environmental changes can markedly affect wave propagation. Further, time-varying surface conductivity can affect the fields that are radiated and scattered from objects. These phenomena can be exploited for engineering benefit if appropriate understanding could be developed.

Scattering problems involving media with temporally and/or spatially varying permittivity have been analyzed using Mathieu functions [1] and Floquet representations [5], [6]. Although a general Floquet representation is possible for a medium with time-varying conductivity, the resulting recursive relation describing the modal amplitudes is very complicated and difficult to solve. Here, it is no longer possible to obtain a Mathieu type differential equation, regardless of the assumed conductivity variation.

In this paper, we consider the scattering and propagation problem for a material half-space whose conductivity is a periodic function of time alone. The emphasis is on the mathematical tools utilized to obtain an approximate solution.

Manuscript received May 9, 1989; revised September 6, 1990. This work was supported in part by National Science Foundation Grant ASC-8811273 and by the Office of Naval Research under Contract N00014-88-K-0475.

F. A. Harfoush is with the Fermi National Accelerator Laboratory, MS 345, P.O. Box 500, Batavia, IL 60510.

A. Taflov is with the Department of Electrical Engineering and Computer Science, Technological Institute, Northwestern University, Evanston, IL 60208.

IEEE Log Number 9100556.

A physical interpretation of the final results is also presented. To verify our analytical results, comparison is made whenever possible, against purely numerical results generated by a finite-difference time-domain (FDTD) method [7]. Finally, and to further verify our results, the analysis is checked in the limit of constant conductivity both analytically and numerically. The incident radiation is a step-modulated time-harmonic plane wave of frequency  $\omega$ . To enable an approximate mathematical result, we analyze two different cases and limits. In Case 1, the conductivity is given by  $\sigma(t) = \sigma_0(1 + \epsilon f(t))$ , where  $\sigma_0$  is a reference conductivity,  $\epsilon$  is the amplitude of the modulation, and  $f(t)$  is a periodic function of time with period  $\omega_p$ . We develop an asymptotic approximation of the fields in the limit as  $\epsilon \rightarrow 0$  with  $\sigma_0$  and  $\omega_p$  held fixed. This results in simple expressions that agree well with FDTD results.

In Case 2, the conductivity is given by  $\sigma(t) = \sigma_0/[1 + \epsilon f(t)]$ , but now  $\epsilon$  and  $\omega_p$  are fixed while  $\sigma_0 \rightarrow \infty$ . Here, the material half-space is highly conductive with a substantial time variation. We develop two asymptotic schemes for analyzing this limit. To obtain the scattered field, we apply a boundary layer analysis for the material region close to the interface. To obtain the fields within the material, we apply (with some modifications) a method developed by Lewis [8] to study the short-term behavior of parabolic equations. In the present context, we assume that the fields within the material are proportional to the product of a slowly changing amplitude and a rapidly decaying exponential. The determination of the exponent and the amplitude parallels classical geometrical optics in as much as a nonlinear first-order partial differential eikonal equation determines the exponent and a "transport" equation determines the amplitude. We obtain space-time rays, which carry the wave into the half-space. This representation breaks down near the interface. However, this nonuniformity can be removed by matching the "ray" solution to the boundary layer solution mentioned above [12].

The remainder of the paper is organized as follows. Section II defines the problem and introduces the dimensionless quantities of interest. Section III analyzes Case 1, the half-space with slightly modulated conductivity. Section IV presents the two analyses for Case 2 and determines the scattered field in the large-conductivity limit. Section V describes the matching of the asymptotic solutions of Case 2. Finally, Section VI summarizes the various results and conclusions.

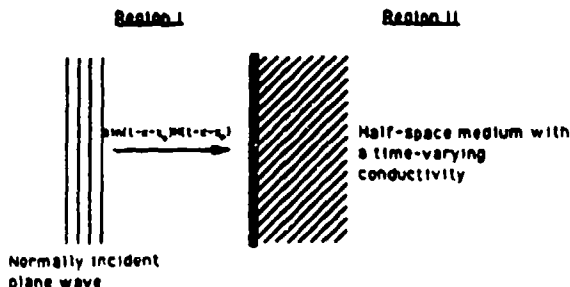


Fig. 1. Plane wave incident on a half-space media with a time-varying conductivity.

## II. PROBLEM DEFINITION

A plane electromagnetic wave traveling in the  $+x$  direction is normally incident on a material half-space with a time-varying conductivity  $\sigma(t) = \sigma_0 f(\nu t)$  (see Fig. 1). The partial differential equation describing the normalized wave electric field in the medium,  $\Omega = E_z/E_0$ , is given by

$$\Omega_{xx} = \Omega_{tt} + \alpha(\Omega f), \quad x > 0, \quad (1)$$

where  $x$  and  $t$  are dimensionless variables defined by  $x = kx'$ ,  $t = \omega_1 t'$ ;  $k$  and  $\omega_1$  are, respectively, the free space wavenumber and the incident wave frequency, and where  $\alpha$  and  $\nu$  are dimensionless parameters defined by  $\alpha = \sigma_0/\epsilon_0\omega_1$ ,  $\nu = \omega_0/\omega_1$ . Here, the primes denote the dimensioned quantities and  $E_0$  is the amplitude of the incident wave. Parameter  $\alpha$  is denoted as the material dissipation factor.

We assume that the total field in free space,  $x < 0$ , is given by

$$\vec{E} = E_0 \{ U(t-x) H(t-x-x_0) + U^s(x,t) \} \vec{z}, \quad (2)$$

identifying  $H$  as the Heaviside step function,  $U^s = U(t-x)H(t-x-x_0)$  as the incident field, and  $U^s$  as the scattered field. Throughout this paper, we assume a sinusoidal dependence of the incident wave,

$$U(t-x) = \sin(t-x-x_0). \quad (3)$$

The required continuity of the tangential  $E$  and  $H$  fields at the medium interface and the form of (2) gives the following boundary condition for  $\Omega$  at  $x = 0$ :

$$\Omega_t(0,t) - \Omega_x(0,t) = 2 \frac{\partial U^s(t)}{\partial t} = g(t). \quad (4)$$

In addition to (4),  $\Omega$  must be an outgoing wave at  $x = \infty$  and satisfy the initial conditions

$$\Omega(x > 0, 0) = \Omega_t(x > 0, 0) = 0. \quad (5)$$

These initial conditions are due to the Heaviside step function present in the incident field, and imply that the wavefront is at  $x = -x_0$  at time  $t = 0$ .

The initial boundary value problem (1)-(5) has no closed-form solution for any time-periodic conductivity. We shall, therefore, develop asymptotic approximations to the fields for the two separate cases described in the introduction, and validate these approximations using the purely numerical FDTD method.

## III. CASE 1: PERTURBATION ANALYSIS FOR THE LOW-AMPLITUDE CONDUCTIVITY VARIATION

In this section, we consider half-space conductivity variations of the form

$$\sigma(t) = \sigma_0(1 + \epsilon \sin(\nu t + \psi)) \quad (6)$$

where  $\epsilon \ll 1$  and  $\psi$  is a phase shift. We first assume that  $\Omega$  is given inside the medium by the regular perturbation expansion

$$\Omega(x,t) = \Omega_0 + \epsilon \Omega_1 + \epsilon^2 \Omega_2 + \dots, \quad x > 0. \quad (7)$$

Inserting this expansion into (1), (4), and (5) and equating to zero the coefficients of the powers of  $\epsilon$ , we obtain an infinite set of differential equations, boundary conditions, and initial data which sequentially determine the  $\Omega_n$ . The zero-order problem is given by

$$\Omega_{0xx} = \Omega_{0tt} + \alpha \Omega_{0t}, \quad x > 0 \quad (8)$$

$$\Omega_{0t} - \Omega_{0x} = 2H(t-x_0) \cos(t-x_0), \quad x = 0 \quad (9)$$

$$\Omega_0 = \Omega_{0t} = 0, \quad t = 0. \quad (10)$$

The complete solution of this problem can be obtained by transform methods because the conductivity bias  $\sigma_0$  is constant. The transient solution is given by the integral

$$-\frac{2\alpha}{\pi} \int_0^1 \frac{e^{-\alpha u} \sqrt{u-u^2}}{1+\alpha^2 u^2} du \quad (11)$$

where the interval  $[0, 1]$  defines a branch cut in the complex plane of integration. The "steady-state" solution as  $t \rightarrow \infty$  is given by

$$\Omega_0 = \frac{2}{[(1-\gamma_r)^2 + \gamma_i^2]^{1/2}} \cos(t + \gamma_r x + \varphi) \quad (12)$$

where  $\gamma = \gamma_r + j\gamma_i = \sqrt{j\alpha - 1}$  is the complex propagation constant. The phase shift  $\varphi$  is introduced by the complex nature of  $\gamma$ .

The first-order problem for  $\Omega_1$  is given by

$$\Omega_{1xx} = \Omega_{1tt} + \alpha \Omega_{1t} + \alpha \sin \nu t \Omega_{0t} + \nu \alpha \cos \nu t \Omega_0 \quad (13)$$

$$\Omega_{1t} - \Omega_{1x} = 0, \quad x = 0 \quad (14)$$

$$\Omega_1 = \Omega_{1t} = 0, \quad t = 0 \quad (15)$$

which now has a forced term due to  $\Omega_0$  and the presence of the modulated conductivity. Again, this problem can be solved completely by transform techniques. The steady-state result can be shown to be

$$\Omega_1 = \frac{\alpha}{2} \text{Re} \{ [k_1 e^{\gamma x} + A e^{\delta x}] e^{j(\nu+1)t} + [k_2 e^{\gamma x} + B e^{\delta x}] e^{j(1-\nu)t} \} \quad (16)$$

where

$$k_1 = \frac{\alpha \nu}{2} \frac{\nu+1}{(\gamma^2 - \delta^2)} \quad (17)$$

$$A = \frac{[j(\nu+1) - \gamma]}{\gamma^2 - \delta^2} \frac{k_1}{[\delta - j(\nu+1)]} \quad (18)$$

$$k_2 = \frac{\alpha\tau}{2} \frac{\nu-1}{(\gamma^2 - \beta^2)} \quad (19)$$

$$B = \frac{[j(1-\nu) - \gamma]}{\gamma^2 - \beta^2} \frac{k_2}{[\beta - j(1-\nu)]} \quad (20)$$

and

$$\delta = \sqrt{j\alpha(\nu+1) - (\nu+1)^2},$$

$$\beta = \sqrt{j\alpha(1-\nu) - (1-\nu)^2},$$

and  $\text{Re}$  denotes the real part of a complex number. The new variable  $\tau$  is the transmission coefficient due to a constant bias  $\sigma_0$ , and is equal to  $2/[1 + \sqrt{j\alpha - 1}]$ .

To find the scattered field, we assume again a solution of the form

$$U^s = U_0^s + \epsilon U_1^s + \epsilon^2 U_2^s + \dots \quad (21)$$

From the continuity of the field at the boundary and the fact that each  $U_n^s$  term satisfies a homogeneous wave equation in free space, the zero-order steady-state scattered field can be shown to be

$$U_0^s = \text{Re } \rho e^{j(\tau+x)} \quad (22)$$

where  $\rho$  is the reflection coefficient due to the constant bias  $\sigma_0$ .

$$\rho = \frac{1 - \sqrt{j\alpha - 1}}{1 + \sqrt{j\alpha + 1}} \quad (23)$$

The first-order steady-state scattered field can be shown to equal

$$U_1^s = \frac{\alpha}{2} \text{Re} \{ [k_1 + A] e^{j(\tau+1)(x+\tau)} + [k_2 + B] e^{j(1-\nu)(x+\tau)} \} \quad (24)$$

where  $k_1$ ,  $A$ ,  $k_2$ ,  $B$  are defined above.

We now compare the total scattered field amplitude obtained (to order  $\epsilon^2$ ) from (21)–(24) to purely numerical results obtained using FDTD. Fig. 2 shows the variation of the scattered-field amplitude at the illumination frequency versus the initial phase shift ( $\psi$ ) between the incident wave and the time-varying conductivity for  $\sigma_0 = 1$ ,  $\epsilon = 0.2$ , and  $\nu = 2$  and 3. The first-order approximation is seen to agree very well with the FDTD results. We also see that for  $\nu = 2$ , i.e.,  $\omega_s = 2\omega_i$ , there exists an amplitude dependence on the initial phase shift. (The same behavior will also be observed in Section IV with the asymptotic result.) For  $\nu = 3$  and other values of  $\nu \neq 2$  (not shown here), there is no amplitude dependence on phase shift. This is found to be true even for values quite close to 2, as for example  $\nu = 2.1$ . This strongly suggests an interference effect that occurs only for conductivity variations at twice the incident frequency. Such an effect at  $\nu = 2$  is plausible since the scattered field at the boundary involve a zero-order term like  $\cos(\tau + \psi)$  and a first-order term like  $\cos((\nu - 1)\tau)$ . For  $\nu = 2$  these two terms can then add up to result in a reflected field amplitude at the illumination frequency that varies with the phase  $\psi$  and is  $2\pi$  periodic.

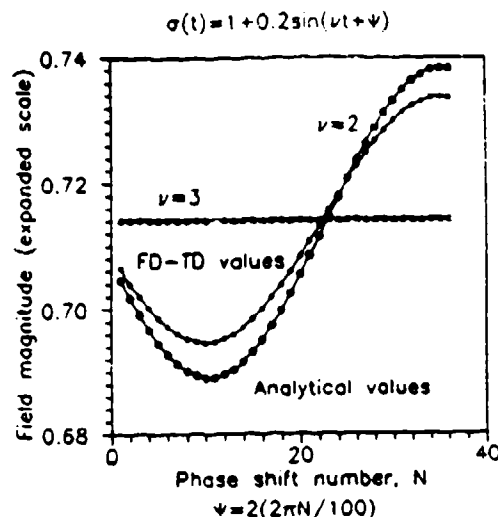


Fig. 2. Reflected field amplitude at the illumination frequency versus the initial phase shift  $\psi$  as obtained both by FDTD and the first-order perturbation analysis.

#### IV. CASE 2: BOUNDARY LAYER ANALYSIS FOR THE TIME-VARIABLE HIGHLY CONDUCTING HALF-SPACE

In this section, we consider half-space conductivity variations of the form  $\sigma(t) = \sigma_0/1 + \epsilon \sin(\nu t + \psi)$  in the limit of large conductivity; i.e.,  $\sigma_0 \rightarrow \infty$  with  $\nu$  and  $\epsilon$  fixed. If we wish only to determine the scattered field, the required information can be obtained by analysis of the structure of the half-space field within the first few skin depths. In terms of the dimensionless distance  $x$ , this corresponds to  $x \approx 1/\sqrt{\alpha}$ . The analysis of this "boundary-layer" is carried out in Section IV-A.

If, on the other hand, we require detailed knowledge of the field penetrating the time varying conductor, a different type of field expansion is needed. In Section IV-B, an asymptotic approximation is constructed which is strictly valid for  $x \gg 1/\sqrt{\alpha}$  and  $t \gg 1/\alpha$ . This approximation becomes invalid near  $x = 0$  for all time, where the boundary layer expansion of Section IV-A becomes valid. However, both representations are valid in a small region, and this permits the expansions to be matched.

Finally, we observe that both field expansions become invalid near  $x = t = 0$ . In Section V, we will perform a local analysis and show that it matches into the other representations.

##### A. The Boundary Layer Near $x = 0$

We begin by introducing the stretched (or boundary layer) variable  $\bar{x} = \sqrt{\alpha} x$  (which we take to be of order unity) into (1) and (4). We obtain

$$\Omega_{\bar{x}\bar{x}} = (\Omega f)_{\bar{x}} + \frac{1}{\alpha} \Omega_{\bar{x}\bar{x}}, \quad \bar{x} > 0 \quad (25)$$

$$\Omega_{\bar{x}} - \sqrt{\alpha} \Omega_x = g(\bar{x}), \quad \text{at } \bar{x} = 0. \quad (26)$$

For large  $\alpha$ , we assume that  $\Omega$  has the asymptotic representation

$$\Omega = \sum_{m=1}^{\infty} \frac{1}{\sqrt{\alpha^m}} \Omega_m(\bar{x}, t). \quad (27)$$

Substituting this ansatz in (25) and (26) and equating to zero the coefficients of the powers of  $\sqrt{\alpha}$ , we obtain an infinite set of boundary value problems which sequentially determine the  $\Omega_m$ . Since we are only interested in a leading-order term, we restrict our attention to  $\Omega_1$ . It satisfies

$$\Omega_{1,xx} = (\Omega_1 f)_x \quad (28)$$

$$\Omega_{1,x} = g(x) \quad (29)$$

$$\Omega_1(\bar{x}, 0) = \Omega_{1,x}(\bar{x}, 0) = 0 \quad (30)$$

where (30) follows from (5) and (27). By performing the following change of variables

$$\Omega_1(\bar{x}, t) f(t) = V_1(\bar{x}, t) \quad (31)$$

$$\xi = \int_0^t \frac{dt}{f(t)} \quad (32)$$

we transform (28)–(30) to

$$V_{1,xx} = V_{1,\xi}, \quad \bar{x} > 0, \xi > 0 \quad (33)$$

$$V_{1,x} = h(\xi), \quad \bar{x} = 0, \xi > 0 \quad (34)$$

$$V_1 = 0, \quad \text{at } \xi = 0 \quad (35)$$

where  $h(\xi) = g(t(\xi))f(t(\xi))$  and  $t(\xi)$  is given by the inverse of (32). This is a diffusion equation and we have accordingly only prescribed one homogeneous piece of initial data, (35). The solution to (33) can not satisfy the second condition in (30), namely  $V_{1,\psi} = 0$  at  $\psi = 0$ . This gives rise to a nonuniformity in (27) which we resolve in Section V. It is therefore seen that for large  $\alpha$  the equation takes the form of a diffusion equation. This is in accordance with the general approach to solve Maxwell's equations with large  $\alpha$ . Here the displacement current is neglected with respect to the conduction current. This leads to a diffusion equation in electric field. The ambiguity as to how can we match a propagating wave solution in region I to a diffusing (nonpropagating) wave solution in region II will become clear later. As mentioned in the beginning of Section IV this solution is valid only in a region of order  $1/\alpha$  and breaks down at  $x = t = 0$ .

The solution of (33) is readily found by transform or Green's function techniques [9]

$$V_1(\bar{x}, \xi) = \frac{-1}{\sqrt{\pi}} \int_0^\xi \frac{h(\xi')}{\sqrt{\xi - \xi'}} e^{-\frac{\bar{x}^2}{4(\xi - \xi')}} d\xi'. \quad (36)$$

When  $\bar{x} \gg 1$ , so that we are beginning to penetrate several skin depths into the material, (36) reduces to

$$V_1(\bar{x}, \xi) = \frac{\xi^{3/2}}{\bar{x}^2} e^{-\frac{\bar{x}^2}{4\xi}} \quad (37)$$

as we can show by integrating (36) by parts. Thus, for a fixed  $t$  (and hence  $\xi$ ), the field decays as a Gaussian distribution. The value of  $V_1$  at  $\bar{x} = 0$  is given by

$$V_1(0, \xi) = \frac{-1}{\sqrt{\pi}} \int_0^\xi \frac{h(\xi')}{\sqrt{\xi - \xi'}} d\xi' \quad (38)$$

and is needed to determine the scattered field. Its evaluation can be done, in principle, by numerical quadrature. However, if  $\nu$  is an integer, or the reciprocal of an integer (so that  $\omega_s$  and  $\omega_i$  are harmonically related frequencies), we can proceed further with our analysis. In this case  $h(\xi)$  is a periodic function of  $\xi$  and can be written as

$$h(\xi') = \sum_{n=-\infty}^{\infty} c_n e^{j \frac{2\pi n \xi'}{\zeta}} \quad (39)$$

where the coefficients  $c_n$  are defined by

$$c_n = \frac{2}{\zeta} \int_0^\zeta h(\xi) e^{-j \frac{2\pi n \xi}{\zeta}} d\xi. \quad (40)$$

The parameter  $\zeta$  is a period of  $h(\xi)$ . By introducing  $t$  as the variable of integration via (32), (40) becomes

$$c_n = \frac{2}{T} \int_0^T \cos(t) e^{-j \frac{2\pi n t(t)}{T}} dt \quad (41)$$

where  $T$  is the period of  $h$  as a function of  $t$ .

We now introduce (39) into (38) and interchange the order of integration and summation. We obtain after a change of variables in the integral

$$V_1(0, \xi) = \sum_{n=-\infty}^{\infty} c_n e^{2\pi n j \frac{\xi}{\zeta}} F\left(2\pi n \frac{\xi}{\zeta}\right) \sqrt{\frac{2\xi}{n\pi}} \quad (42)$$

where  $F$  is the Fresnel integral defined here by

$$F(s) = \int_0^{\sqrt{s}} e^{-j p^2} dp. \quad (43)$$

Since the conductivity function  $f(t)$  is positive,  $\xi(t)$  monotonically increases with  $t$ , a fact that we have taken implicitly in the statement of (33). Thus, as  $t \rightarrow \infty$  we have  $\xi \rightarrow \infty$ . Now, in this limit, (42) simplifies to

$$V_1(0, t) = 4 \sum_{n=1}^{\infty} \sqrt{\frac{\xi}{2n\pi}} c_n \sin\left(\frac{2\pi n \xi}{\zeta} + \frac{\pi}{4}\right) \quad (44)$$

because

$$F(\infty) = \frac{\sqrt{\pi}}{2} e^{-j \frac{\pi}{4}}. \quad (45)$$

It should be noted here that at  $x = 0$  and  $t \rightarrow \infty$  the solution form for  $V_1$  given by (44) is oscillating in time. This oscillation is necessary to match the propagating solution to the diffusive equation at the boundary  $x = 0$  between the two regions. Finally, we combine (44), (27), (28), and (2) with the fact that  $\vec{E}$  is continuous at  $x = \bar{x} = 0$  to obtain

$$U^s(0, t) = -\sin t + \frac{1}{\sqrt{\alpha}} \frac{V_1(0, \xi(t))}{f(t)} + O(1/\alpha) \quad (46)$$

where  $O(1/\alpha)$  denotes the remaining terms in (27). Since the scattered field satisfies the wave equation for  $x < 0$ , it must be a function of the argument  $x + t$ . Thus, the scattered field is given for large time and for  $x < 0$  by (46) with  $t$  replaced by  $(t + x)$ .

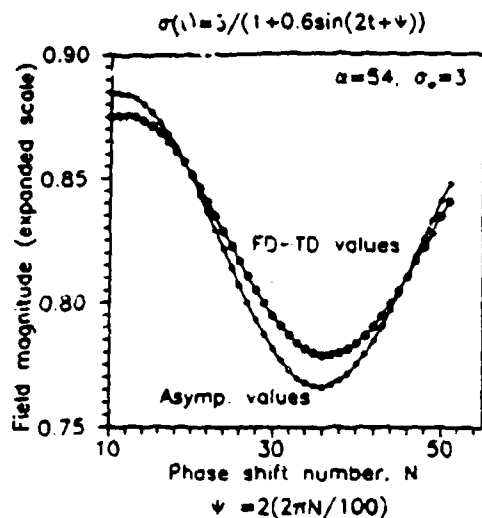


Fig. 3. Reflected field amplitude at illumination frequency versus initial phase shift  $\psi$  as obtained both asymptotically and by FDTD for  $\nu = 2$ ,  $\sigma_0 = 3$ , and  $\alpha = 54$ .

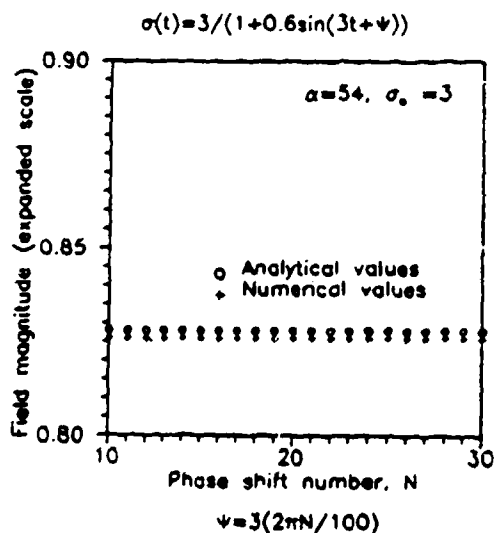


Fig. 4. Reflected field amplitude at illumination frequency versus initial phase as obtained both asymptotically and by FDTD for  $\nu = 3$ ,  $\sigma_0 = 3$ , and  $\alpha = 54$ .

To illustrate how these results can be applied to a specific problem, we shall consider the special case where

$$f(t) = \frac{1}{1 + \epsilon \sin(\beta t + \psi)} \quad (47)$$

For this particular choice of  $f(t)$ , the variable  $\xi$  defined in (32) is given explicitly by

$$\xi = 1 + \frac{\epsilon}{\beta} (\cos \phi - \cos(\beta t + \psi)). \quad (48)$$

This can be inserted into (41) to determine the  $c_n$ . The integrals are reminiscent of Bessel functions and can be numerically integrated. Combining these results with (44) we can deduce the surface value of the scattered field.

Figs. 3 and 4 show the results obtained by both FDTD and the above analysis with  $\epsilon = 0.6$  and  $\nu = 2$  and 3. The Fourier series summation given by (44) was computed nu-

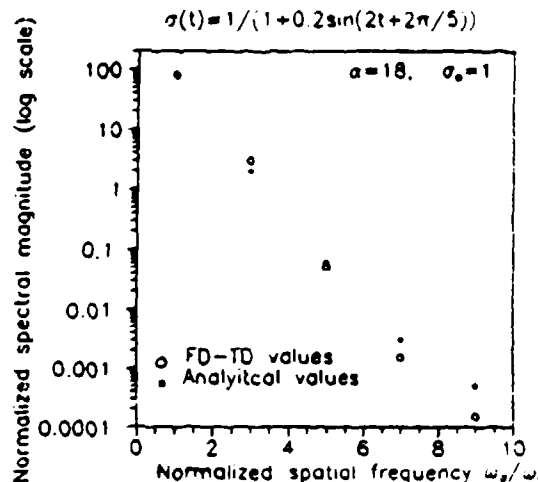


Fig. 5. Reflected field spectrum as obtained both asymptotically and by FDTD for  $\nu = 2$ ,  $\sigma_0 = 1$ , and  $\alpha = 18$ .

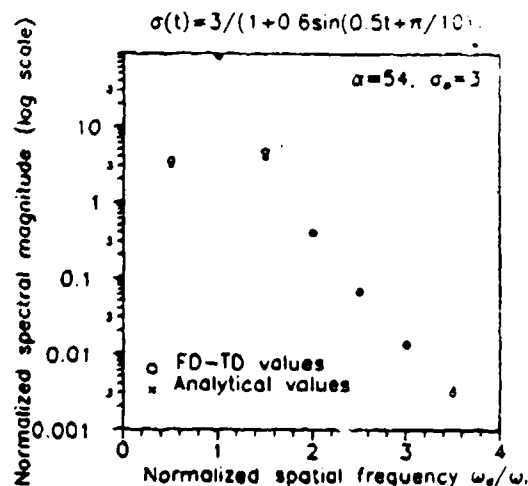


Fig. 6. Reflected field spectrum as obtained both asymptotically and by FDTD for  $\nu = 0.5$ ,  $\sigma_0 = 3$ , and  $\alpha = 54$ .

merically by taking up to 50 terms. The coefficients  $c_n$  are computed from integrating (41) using Simpson's rule. We observe again from Fig. 4 the interference effect occurring at only  $\nu = 2$ .

Figs. 5 and 6 compare the scattered field spectrum sidebands as obtained by FDTD and the above analysis for two different values of  $\nu$  and  $\alpha$ . Here, the field magnitude is given in percentage. As  $\alpha$  increases, the correspondence between both results improves. This is to be expected for an asymptotic large- $\alpha$  solution.

Tables I-III list the amplitude of the scattered field spectrum sidebands for fixed values of  $\alpha = 54$ ,  $\nu = 1$ , and three different values of amplitude modulations  $\epsilon = 0.2, 0.6, 0.8$ . In all cases, a good agreement is shown between the analytical and FDTD numerical results. The degree of agreement is seen to be independent of the choice of  $\epsilon$ .

### B. Deeper Penetration Into the Time-Variable Half-Space

Fig. 7 is a schematic diagram of the different boundary layers present in space-time coordinates for our problem. In the previous section, we solved for the field in a thin layer

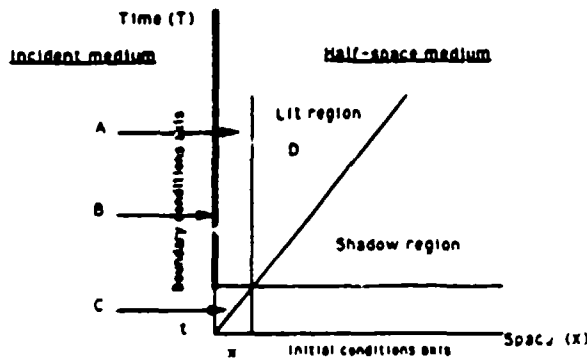


Fig. 7. Boundary-layers in a media with a time-varying conductivity. A: Diffusion solution, B: oscillating solution, C: propagating solution, D: large parameter solution.

TABLE I

FOURIER COMPONENTS OF THE REFLECTED SIGNAL FOR  $\epsilon = 0.8$ ,  $\sigma_0 = 3$ ,  $\alpha = 54$  AND  $\nu = 1$  AS OBTAINED ANALYTICALLY AND NUMERICALLY

Frequency	Analytical Value	FDTD Value
$\omega_i$	84.772	84.717
$\omega_i + 1\omega_e$	6.3494	7.8026
$\omega_i + 2\omega_e$	0.9818	0.9974
$\omega_i + 3\omega_e$	0.2184	0.2252
$\omega_i + 4\omega_e$	0.0565	0.0626
$\omega_i + 5\omega_e$	0.0162	0.0196
$\omega_i + 6\omega_e$	0.0062	0.0074

TABLE II

FOURIER COMPONENTS OF THE REFLECTED SIGNAL FOR  $\epsilon = 0.6$ ,  $\sigma_0 = 3$ ,  $\alpha = 54$  AND  $\nu = 1$  AS OBTAINED ANALYTICALLY AND NUMERICALLY

Frequency	Analytical Value	FDTD Value
$\omega_i$	83.951	83.923
$\omega_i + 1\omega_e$	4.2760	5.2934
$\omega_i + 2\omega_e$	0.4478	0.4397
$\omega_i + 3\omega_e$	0.0687	0.0668
$\omega_i + 4\omega_e$	0.0123	0.0126
$\omega_i + 5\omega_e$	0.0257	0.0274

TABLE III

FOURIER COMPONENTS OF THE REFLECTED SIGNAL FOR  $\epsilon = 0.2$ ,  $\sigma_0 = 3$ ,  $\alpha = 54$  AND  $\nu = 1$  AS OBTAINED ANALYTICALLY AND NUMERICALLY

Frequency	Analytical Value	FDTD Value
$\omega_i$	82.961	83.116
$\omega_i + 1\omega_e$	1.2882	1.6106
$\omega_i + 2\omega_e$	0.0421	0.0401
$\omega_i + 3\omega_e$	0.0197	0.0191
$\omega_i + 4\omega_e$	0.0002	0.0001

around  $x = 0$ . This is represented in Fig. 7 by the region labeled as A. Here the form of solution is diffusive. Enclosed in region A is the boundary region, labeled B, where the solution is oscillating in time. Still, both regions A and B do not result in a propagating solution. But, a propagating solution in the conductive region is seen to originate from region C next to the space time origin where the solution

form in regions A and B are not valid. In this section, we shall seek a solution for the fields in region D, away from the thin layer, where  $x > 0$ . Later, in Section V, we will match the solution forms in regions C and D.

To obtain an accurate approximation of the exponentially small fields in this region, we employ an analysis similar to that found in geometrical optics. We assume that the field is of the form

$$\Omega = e^{-\alpha\psi(x,t)} \left[ A(x,t) + O\left(\frac{1}{\alpha}\right) \right]. \quad (49)$$

As  $\alpha \rightarrow \infty$ . This representation is formally valid except in boundary layers and near caustics, if they exist. We note here the similarity with a ray analysis or high-frequency method, where instead of the wavenumber  $k$ , we now have  $\alpha$ .

Substituting (49) into (1) and equating coefficients of like powers of  $\alpha$ , we obtain to two orders in  $\alpha$

$$\psi_x^2 - \psi_t^2 + \psi_t f = 0 \quad (50)$$

$$2A_x\psi_x + A\psi_{xx} - 2A_t\psi_t + A\psi_{tt} - (Af)_t = 0 \quad (51)$$

which are the analogs of the eikonal and transport equations respectively. Equation (50) is a nonlinear first-order partial differential equation, with a time-varying coefficient which can be solved by the method of characteristics [10], [11]. Accordingly we begin by defining the following variables:

$$p = \psi_x(x,t); \quad q = \psi_t(x,t) \quad (52)$$

$$H(p, q, t) = p^2 - q^2 + qf = 0. \quad (53)$$

We now introduce a family of curves called characteristics (the analogs of rays) which are everywhere orthogonal to the surface defined by  $H = \text{constant}$ . Denoting by  $\tau$  the parameter which parameterizes a curve, i.e.,  $x = x(\tau)$  and  $t = t(\tau)$ , the orthogonality condition leads to

$$\frac{dx}{d\tau} = \frac{\partial H}{\partial p} = 2p \quad (54)$$

$$\frac{dt}{d\tau} = \frac{\partial H}{\partial q} = f - 2q. \quad (55)$$

From these equations we obtain

$$\frac{d\psi}{d\tau} = -qf. \quad (56)$$

It can also be shown that [10], [11]

$$\frac{dp}{d\tau} = 0 \quad (57)$$

$$\frac{dq}{d\tau} = -\frac{\partial H}{\partial t} = -qf_t, \quad (58)$$

because  $H$  does not depend explicitly upon  $\psi$ .

The data needed to solve the initial-value problem (54)-(58) requires knowledge of  $x$ ,  $q$ ,  $p$  and  $\psi$  along a curve which is not a characteristic, in the  $x-t$  plane. For the given problem, the curve degenerates into a point, the origin, as this is the "source" of the field (see Section V). The characteristics emanating from the origin are labeled by



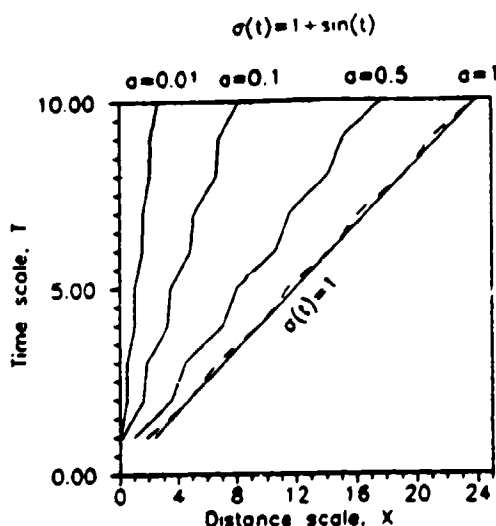


Fig. 8. Rays tracing in  $(x, t)$  space for a given time-modulated conductivity and different firing angles.

$p(0) = p_0$ , as  $p$  remains a constant by (57) along each curve. The values of  $x(0)$  and  $t(0)$  are both zero and  $q(0)$  is determined from (53). If we write

$$p_0 = \frac{f(0)}{2} \sinh \theta \quad (59)$$

then  $q(0)$  is given by (53) as

$$q(0) = q_0 = \pm \frac{\cosh \theta}{\sinh \theta}. \quad (60)$$

Finally, the value of  $\psi(0)$  is unknown at this stage and will be determined in Section V. Solving the equation  $H = 0$  for  $q$ , inserting this expression into (55) and noting that  $p = p_0$  we obtain

$$t(s) = \int_0^s \frac{ds}{\sqrt{f^2(s) + 4p_0^2}}. \quad (61)$$

Combining (55), (59), (61) and the fact that  $p = p_0$ , we find that  $x$  is given by

$$x(t) = f(t) \sinh \theta \int_0^t \frac{ds}{\sqrt{f^2(s) + f^2(0) \sinh^2 \theta}} \quad (62)$$

where  $\theta$  is now the new label of a ray. We now have a formula for the characteristics (or rays) in the space time coordinates given by the integral solution for  $x(t)$ .

Fig. 8 shows several characteristics for different values of  $\theta$  where  $\alpha = f(0) \sinh(\theta)$ . Therefore each variable  $\alpha$  in Fig. 8 represents a particular angle  $\theta$  referred to as firing angle. All the curves are confined to the region  $t > x$ , showing that the solution is causal. For vertically launched rays ( $\theta \rightarrow 0$ ), the modulation is less apparent and the ray acts more like a straight line. Moreover, this region is devoid of any geometrical singularity such as caustics (bending rays) or foci (intersecting rays). Finally, we observe that (56) can be integrated in principle to determine the phase, yielding

$$\psi = \psi(0) - \int_0^t q(\tau) f(t(\tau)) d\tau. \quad (63)$$

By introducing  $\tau$  and  $\theta$  as new independent variables in (51), we find that  $A$  satisfies

$$A_\tau + \left( \frac{J_\tau}{2J} + \frac{f_\tau}{2} \right) A = 0 \quad (64)$$

where  $J$  is the Jacobian given by

$$x_\tau t_\theta - x_\theta t_\tau. \quad (65)$$

The solution of (64) is

$$A(\tau) = \frac{C(\theta)}{\sqrt{J}} e^{-\int_0^\tau \frac{f_\tau}{2} d\tau}. \quad (66)$$

We observe that the Jacobian vanishes at the origin, so that (49) is invalid there. The local analysis required to remove this nonuniformity is presented in the next section. The constant  $C(\theta)$  will be computed there.

## V. MATCHING OF THE ASYMPTOTIC AND BOUNDARY LAYER SOLUTIONS

We shall first illustrate how the results obtained in the previous section are applied by considering the case of a fixed half-space conductivity  $\sigma_0$ . Under such circumstances, it is found that

$$J(x, t) = -\frac{2(t^2 - x^2)}{t} \quad (67)$$

$$\psi(x, t) = -\frac{\sigma_0}{2} (\sqrt{t^2 - x^2} - t). \quad (68)$$

This leads to

$$\Omega(x, t) = \frac{C\sqrt{t}}{\sqrt{2(t^2 - x^2)}} e^{-\frac{\sigma_0}{2}(t - \sqrt{t^2 - x^2})}. \quad (69)$$

The line  $x = t$  defines a caustic, or more precisely, the boundary of the Fresnel region that separates the "lit" region from the "shadow" region. The solution given by (69) reduces to the diffusion solution obtained earlier, as we approach the thin boundary layer strip at  $x = 0$ . A matching of the results of (36) and (69) leads to

$$C = -4\sqrt{\frac{2}{\pi}} \frac{f_1(0)}{\alpha^{3/2}} \left( \frac{t}{x} \right)^2. \quad (70)$$

This matching procedure is based on the assumption that the regions where (36) and (69) are valid overlap. Matching is performed by comparing the asymptotic expansion of (69) as  $x \rightarrow 0$  with the solution of (36) as  $x \rightarrow \infty$ . It is noted that  $C$  is a function of  $x/t$ . This is an expected result because for small  $x$ ,  $p_0 = x\sigma_0/2t$  so  $C(p_0)$  becomes  $C(x/t)$ . The field description around the origin can be found with the change of variables  $x \rightarrow \alpha x$  and  $t \rightarrow \alpha t$ . By retaining terms of order  $\alpha^2$ , we obtain

$$\Omega_{xx} = \Omega_{tt} + \sigma_0 \Omega. \quad (71)$$

Using the Laplace transform and a contour integral around the branch cuts, it can be shown that the steady-state response

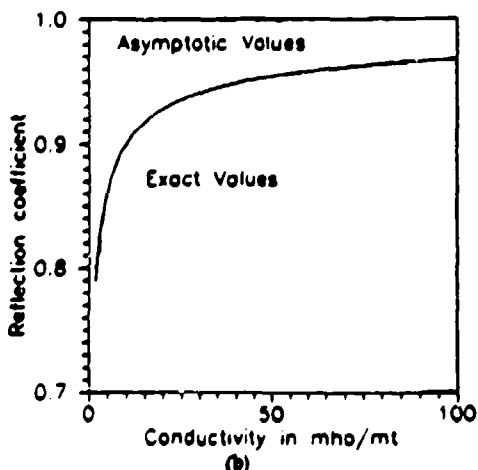
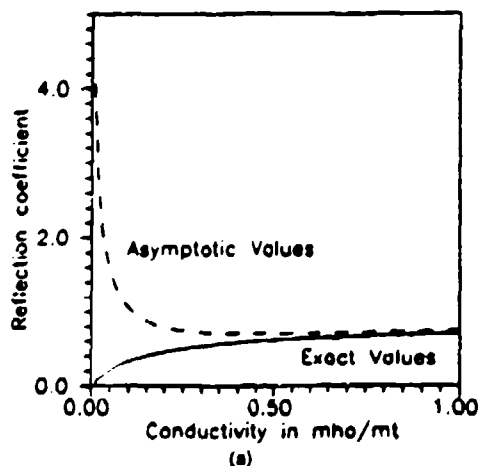


Fig. 9. Variations of the reflected field amplitude versus fixed conductivity  $\sigma_0$  as obtained both exactly and asymptotically.

is given by

$$- \operatorname{Im} \frac{2e^{-i\sqrt{\alpha}x} e^{-it}}{\sqrt{\alpha} e^{i\frac{\pi}{4}}} \quad (72)$$

At  $x = 0$  the above equation can be written as

$$Q(0, t) = \frac{2}{\sqrt{\alpha}} \sin \left( t + \frac{\pi}{4} \right). \quad (73)$$

This corresponds exactly to the solution that would be obtained by using (44) and (46) with a fixed conductivity. To have an idea on the range of  $\alpha$  satisfying the definition of "large" the reflected field magnitude is calculated using the asymptotic solution (46) for fixed conductivity and rewritten as

$$U^m(0, t) = \sqrt{\frac{2}{\alpha-1}} \sin t + \sqrt{\frac{2}{\alpha}} \cos t. \quad (74)$$

The amplitude of the reflected field is defined as the square root of the sum of the square coefficients multiplying the sin and cos terms. This latter is compared against the exact formula of the reflection coefficient given as

$$\rho = \left| \frac{1 - \sqrt{\alpha-1}}{1 + \sqrt{\alpha+1}} \right|. \quad (75)$$

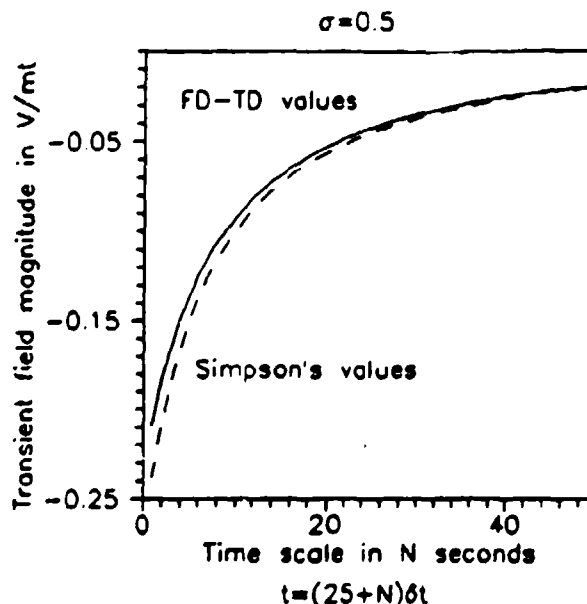


Fig. 10. Transient response in the reflected field from a material with a constant conductivity  $\sigma_0$  as obtained by numerical integration and FDTD.

Results are plotted in Fig. 9. The transient response is given by the integral

$$T = -2 \frac{\alpha}{\pi} \int_0^1 \frac{e^{-\alpha v}}{1 + \alpha^2 v^2} \cdot [-v \sin(\alpha \beta x) + \beta \cos(\alpha \beta x)] dv \quad (76)$$

where  $\beta = \sqrt{v - v^2}$ . Equation (76) reduces to (11) for  $x = 0$ . This integral can be evaluated numerically and compared against the FDTD results. Such a comparison for  $x = 0$  is shown in Fig. 10. For a fixed  $x$  and  $t$ , it can be shown the results given by (72) and (76) reduce to the result derived from (36) as  $\alpha \rightarrow \infty$ . It can also be shown that by fixing  $(x, t)$  and letting  $\alpha \rightarrow \infty$ , these results converge to the geometrical optics result given by (69). The resulting expression for  $C$  obtained by matching both results along a ray defined by  $t = mx$ , where  $m$  is large, reduces to the same expression for  $C$  defined in (70).

It has been shown the results obtained so far are valid for the constant-conductivity case. We shall now reconsider the case of a time-varying conductivity. The results describing our amplitude and phase functions are, in general, impossible to solve exactly because of the difficulty in solving for  $\tau$  and  $p_0$  in terms of  $x$  and  $t$ . However, we can consider limiting cases. Our interest is in finding a solution in the narrow strip next to the boundary. As  $p_0 \rightarrow 0$  it can be shown that

$$\psi(\xi) = \frac{x^2}{4\xi} \quad (77)$$

$$A(\xi) = \frac{C(p_0)}{\sqrt{2\xi} f(\xi)} \quad (78)$$

where again

$$\xi = \int_0^t \frac{d\tau}{f(\tau)}. \quad (79)$$

Therefore,

$$\Omega(x, \xi) = \frac{C(p_0)}{\sqrt{2\xi f(\xi)}} e^{-\frac{\pi x^2}{4\xi}} \quad (80)$$

A matching of (80) with (36) leads to

$$C(p_0) = -\frac{4\sqrt{2}}{\alpha^{3/2}\sqrt{\pi}} h(0) \left(\frac{\xi}{x}\right)^2 \quad (81)$$

which is similar in form to (70). The next limiting case is when  $\tau \rightarrow 0$ . This case leads to results similar to the fixed-conductivity case, where  $\sigma_0$  in (69) is replaced by  $f(0)$ , and where  $f(t)$  behaves like  $f(0)$  next to the origin where  $t = 0$ .

## VI. SUMMARY AND CONCLUSION

We have presented in this paper a detailed analysis of electromagnetic wave interactions with a material half-space having time-varying conductivity. At each stage, the results were verified by considering limiting cases. We also performed a matching of the different solution regions. Three different analysis methods were utilized: a simple first-order regular perturbation method; a large-parameter asymptotic analysis; and a large-parameter analysis similar to geometrical optics. A purely numerical FDTD code was used to obtain comparative results. Numerical and analytical results for the two types of conductivity variations considered were found to be in good agreement.

Our results indicate the presence of sidebands in the scattered field spectrum and an interference effect occurring when the material conductivity varies at twice the illuminating frequency. The characteristics inside the half-space are modulated as they propagate inside the material, and are seen to emanate from the origin in the  $x-t$  coordinate system. No intersection of rays (focusing effect) is detected. With the introduction of boundary layers, it becomes clear how the propagating and nonpropagating dissipative solutions are generated inside a conductive material.

Finally, the FDTD method has been shown to provide in a straightforward manner numerical predictions for scattering by the time-varying half-space that closely agree with the data obtained from the detailed analysis. We note that the FDTD model is restricted to the limiting cases of material conductivity variation required to make the detailed analysis tractable. Therefore, extension of the FDTD numerical model of time-varying media to two dimensions appears to be feasible. This would permit simulation of compact material targets having time-varying volumetric or surface constitutive parameters generating unusual electromagnetic phenomena. It may be possible to exploit these phenomena for engineering to achieve real-time control of target radiation and scattering properties.

## REFERENCES

- (1) D. E. Holdberg and K. S. Kuntz, "Parametric properties of fields in a slab of time-varying permittivity," *IEEE Trans. Antennas Propagat.*, vol. AP-14, pp. 183-194, Mar. 1966.
- (2) R. L. Fante, "On the propagation of electromagnetic waves through a time-varying dielectric layer," *Appl. Sci. Res.*, vol. 27, pp. 341-354, Apr. 1973.
- (3) —, "Optical propagation in space-time media using many-space-scale perturbation theory," *J. Opt. Soc. Am.*, vol. 62, pp. 1052-1060, Sept. 1972.
- (4) F. R. Morgenthaler, "Velocity modulation of electromagnetic waves," *IRE Trans. Microwave Theory Tech.*, vol. MTT-6, pp. 167-172, Apr. 1958.
- (5) A. Hessel and A. A. Oliner, "Wave propagation in a medium with a progressive sinusoidal disturbance," *IRE Trans. Microwave Theory Tech.*, vol. MTT-9, pp. 337-339, July 1961.
- (6) J. C. Simon, "Action of a progressive disturbance on a guided electromagnetic wave," *IRE Trans. Microwave Theory Tech.*, vol. MTT-14, pp. 18-22, Jan. 1966.
- (7) A. Taflov, "Review of the formulation and applications of the finite-difference time-domain method for numerical modeling of electromagnetic wave interactions with arbitrary structures," *Wave Motion*, vol. 10, Dec. 1988.
- (8) J. K. Cohen and R. M. Lewis, "A ray method for the asymptotic solution of the diffusion equation," *J. Inst. Math. Appl.*, no. 3, pp. 266-290, 1967.
- (9) H. S. Carslaw and J. C. Jaeger, *Conduction of Heat in Solids*. Oxford: Clarendon, 1959.
- (10) N. Bleistein, *Mathematical Methods for Wave Phenomena*. New York: Academic, 1984.
- (11) J. Fritz, *Partial Differential Equations*. New York: Springer-Verlag, 1978.
- (12) F. Harfoush, "Analysis and numerical modeling of electromagnetic waves scattering from time varying surfaces in one and two dimensions," Ph.D. dissertation, Northwestern Univ., Evanston, IL, Aug. 1988.

Fady A. Harfoush (S'85-M'87-S'87-M'88) was born in Beirut, Lebanon, on January 16, 1957. He received the B.S. degree in electrical engineering from Bogazici University, Istanbul, Turkey, in 1981, and the M.S. and Ph.D. degrees in electrical engineering from Northwestern University, Evanston, IL, in 1984 and 1988, respectively.

From 1984 to 1988, while at Northwestern, he worked on the scattering and penetration of electromagnetic waves using both the finite difference time domain techniques and analytical methods. In

1988 he joined the Fermi National Accelerator Laboratory, Batavia, IL, where his research activities include the area of computational electromagnetics for the modeling of static and time dependent electromagnetic problems in accelerator physics.

Allen Taflov (M'75-SM'84-F'90) was born in Chicago, IL, on June 14, 1949. He received the B.S. (with highest distinction), M.S., and Ph.D. degrees in electrical engineering from Northwestern University, Evanston, IL, in 1971, 1972, and 1975, respectively.

From 1975 to 1984, he was a staff member in the Electronics Division, IIT Research Institute, Chicago, IL, holding the positions of Associate Engineer, Research Engineer, and Senior Engineer. During this time, he was principal investigator on a number of externally funded research programs, including five that contributed to the early development of the finite-difference time-domain method for computational modeling of electromagnetic wave interactions with complex structures. He was also a key contributor to large-scale programs involving the application of radio-frequency heating to produce oil in place (without mining) from deposits of oil shale, tar sands, and heavy oil; to accelerate oil production from slowly producing conventional wells; and to decontaminate large sections of the ground permeated with toxic chemical wastes. In this technical area, he has been awarded 10 U.S. patents to date. In 1984, he returned to Northwestern University where he is currently Professor of Electrical Engineering and Computer Science. He is actively pursuing supercomputing computational electromagnetics modeling of a broad variety of phenomena and technologies, including radiation and scattering, high-speed digital electronics, microwave/millimeter wave circuits, and optical pulse propagation and switching. He also co-originated and is active in Northwestern's innovative Honors Program in Undergraduate Research, wherein extremely bright high school graduates participate in an accelerated, research-oriented curriculum leading to the Ph.D. in as little as six years.

Dr. Taflov is a member of Tau Beta Pi, Eta Kappa Nu, Sigma Xi, Commission B of URSI, and the Electromagnetics Academy. During 1990-1991, he was a Distinguished National Lecturer for the IEEE Antennas and Propagation Society, and he is Chairman of the Technical Program of the 1992 IEEE Antennas and Propagation Society International Symposium to be held in Chicago. He is co-author of the Best Paper at the 1983 IEEE International EMC Symposium, Washington, DC.

# FDTD Analysis of Electromagnetic Wave Radiation from Systems Containing Horn Antennas

Daniel S. Katz, *Student Member, IEEE*, Melinda J. Picket-May, *Student Member, IEEE*, Allen Taflov, *Fellow, IEEE*, and Korada R. Umashankar, *Senior Member, IEEE*

**Abstract**—The application of the finite-difference time-domain (FDTD) method to various radiating structures is considered. These structures include two- and three-dimensional waveguides, flared horns, a two-dimensional parabolic reflector, and a two-dimensional hyperthermia application. Numerical results for the horns, waveguides, and parabolic reflectors are compared with results from method of moments (MM). The results for the hyperthermia application are shown as extensions of the previously validated models. This new application of the FDTD method is shown to be useful when other numerical or analytic methods cannot be applied.

## I. INTRODUCTION

THIS paper will attempt to validate the finite-difference time domain (FDTD) code when used for the modeling of both two- and three-dimensional radiating structures. It will use waveguides, flared horns, and parabolic reflectors as examples that will be validated against method of moments (MM) codes. There are no published examples of previous use of the FDTD method to solve problems involving a radiating object.

Previously, for work such as this, high-frequency approximations and MM have been used. Most high-frequency methods are based on the geometric theory of diffraction (GTD), which was introduced by Keller [1], [2] in the late 1950's. GTD has also been used recently to study a pyramidal horn, as part of a complex system in which the horn fed an offset reflector [3]. The horn was modeled using GTD, and asymptotic physical optics (APO) was used to model the reflector illuminated by the GTD-produced far fields of the horn.

Russo *et al.* [4] soon developed edge diffraction theory (EDT) as an approximation applied in solving for backscattering of horns. The diffraction coefficients of GTD were shown to be inadequate for treatment of the horn antenna, and the theory was modified to use diffraction of cylindrical waves at the edges of thin metal sheets. GTD was also modified to solve diffraction from thick edges. EDT gave solutions that were substantially better than those of GTD.

For parabolas, APO has been used to solve for far fields, with various correction factors. Knop and Ostertag [5] showed that APO gave good results compared with experimental data, except in the backscattering region, and that the disagreements were caused by faulty edge-current approximations. They corrected the diffraction coefficients and showed that these corrections had negligible effects in the forward-scattering region, and greatly improved the results in the rear region.

Another method that has been used is the uniform asymptotic theory (UAT). Menendez and Lee [6] used UAT to model simple, two-dimensional radiating structures. UAT generally agrees with GTD, and may be viewed as another refinement, which gives better results under some conditions. Sanyal and Bhattacharyya [7] further refined UAT to give slightly better results than had been previously reported.

In general, high-frequency asymptotic methods work well for modeling electromagnetic wave interactions with electrically large, perfectly conducting structures. However, these approaches are difficult to apply when the structures have reentrant features supporting multiple regions, or material compositions and surface treatments. For these types of structures, the use of other more robust methods is suggested.

It has been shown that MM and FDTD are equally valid methods for finding far-field patterns and radar cross section (RCS) due to scatterers [8], but in the case of very large structures, MM is limited by the amount of computer time and memory available and the possible error accumulation of the matrix solution. Even though MM problems of a large size can be solved with the supercomputers available today, the matrix inversion contained in MM can be a fundamental limit on the use of this method.

One aspect of both FDTD and MM that is only now being studied for the first time is that of dynamic range. The examination of the radiation patterns of the antennas in this paper form a study of dynamic range for objects with a broad angular region of low response. Studies have been done that show that FDTD and MM can both pick up sharp nulls in radiation patterns that are caused by cancellation of field values, but the antennas studied herein are completely different. The low-response region of these antennas is both very broad and is also very gradual. In a region such as this, where the far fields are 50 dB down from peak values, power levels are a factor of  $10^{-3}$  down. This implies accuracy in

Manuscript received October 1, 1990; revised March 1, 1991.

D. S. Katz, M. J. Picket-May, and A. Taflov are with the Department of Electrical Engineering and Computer Science, Robert R. McCormick School of Engineering and Applied Science, Northwestern University, Evanston, IL 60208.

K. R. Umashankar is with the Department of Electrical Engineering, University of Illinois at Chicago, Chicago, IL 60680.

IEEE Log Number 9101995.

the electric and magnetic fields must be approximately 0.3%, to effectively model these low fields emanating in this direction.

Modeling this huge dynamic range is currently becoming important in many areas: specifically, in two. The first is the design of antennas where sidelobe suppression can be important, and the second is for the design of aerospace vehicles intended to scatter an extremely low fraction of the power of the incident field over a broad angular range. In some cases, especially in the second area, the problems to be solved cannot be studied in the open literature, so it is important to have canonical problems that permit us to examine the important aspects of physics and computational methodology. The horn antenna systems are good canonical problems, because they naturally have this desired broad range of low response in the backward direction.

The results shown here also have applications to other systems of partial differential equations where the desired solutions are required to be accurate to similar levels: namely, one part in three hundred. One example of a system of this type may be found in computational fluid dynamics. In solving the problem of turbulence in air flow near a wing, it may be necessary to have accuracies of one part in one thousand relative to a unit average flow around the wing. A difference of one one-thousandth may make the difference between the flow separating or not. To solve any system with this level of accuracy is a challenge to most numerical methods.

## II. FDTD FORMULATION

### A. Standard FDTD (Stepped-Edge)

Finite-differencing was introduced by Yee in the mid-1960's as an efficient way of solving Maxwell's time-dependent curl equations [9]. His method involved sampling a continuous electromagnetic field in a finite region at equidistant points in a spatial lattice, and also at equidistant time intervals. Spatial and time intervals have been chosen to avoid aliasing and to provide stability for the time-marching system [10]. The propagation of waves from a source, assumed to be turned on at time  $t = 0$ , is computed at each of the spatial lattice points by using the finite difference equations to march forward in time. This process continues until a desired final state has been reached (usually the steady state). This method has been demonstrated to be accurate for solving for hundreds of thousands of field unknowns in a relatively efficient manner on a vector-processing computer [11].

The FDTD method has advantages over other methods in that the required computer memory and required running time are proportional to the number of field components in the finite volume of space being analyzed. In other words, the FDTD method is  $O(m)$ , where  $m$  is the number of field components in the region of space being modeled. The method of moments, which involves a matrix inversion step, is  $O(m^2)$  in storage and  $O(m^3)$  in running time, where  $m$  is the size of the matrix.

Initial problems that were overcome in the early 1980's included the termination of the spatial grid while retaining the approximation of the larger size of real space without the

addition of reflections from the grid edges [12], [13], the simulation of an arbitrary incident wave [14], and the calculation of the far fields given near-field data over a number of time steps [14]–[16]. The FDTD method is also very straightforward and very robust. However, some problems have existed which have slowed the general acceptance and usage of this method.

One problem, which was simply overcome by the march of technology, was computer resources. Today's computers make it possible to solve for scattering by objects which would have been too large just a few years ago. A second problem is that of visualization, but this is gradually being solved by ongoing work of the authors. Other groups are also making progress in this area. A third problem with the FDTD method for solving practical engineering problems is that of automated geometry generation, but this as well should soon be solved.

The fourth problem, which has recently been solved, is the question of objects that do not fit directly into the standard grid, and that of objects which are smaller than one grid cell. The current FDTD code uses a regularly spaced Cartesian grid with deformed contours along the surface of the modeled object [17]. This is called the contour FDTD method, as opposed to the older, stepped-edge method.

### B. Contour FDTD Method

This method involves applying Ampere's and Faraday's laws in those cells where Yee's algorithm is insufficient to describe the geometry of the modeled object, i.e., cells where the intersection of the object's edge and the cell is not along one of the edges or diagonally through the center of the cell. Fig. 1 shows examples of the application of this method. The contour method has been shown to be equivalent to the Yee algorithm in free space [11], and for completeness, this equivalence is demonstrated here for one field component as shown in Fig. 1(a).

By applying Ampere's law along contour  $C_1$  and assuming that the average value of a field component along one side of a contour is equal to the value of that component at the midpoint of that side, one may obtain:

$$\frac{\partial}{\partial t} \int_{S_1} \mathbf{D} \cdot d\mathbf{S}_1 = \oint_{C_1} \mathbf{H} \cdot d\mathbf{l}_1 \quad (1)$$

$$\begin{aligned} \frac{\partial}{\partial t} \int_{S_1} \epsilon_0 E_z(l, j, k) dS_1 &= H_x \left( l, j - \frac{1}{2}, k \right) \Delta x \\ &\quad + H_y \left( l + \frac{1}{2}, j, k \right) \Delta y \\ &\quad - H_x \left( l, j + \frac{1}{2}, k \right) \Delta x \\ &\quad - H_y \left( l - \frac{1}{2}, j, k \right) \Delta y. \quad (2) \end{aligned}$$

Using the assumptions that  $E_z(l, j, k)$  equals the average value of  $E_z$  over the surface  $S_1$ ,  $\Delta x = \Delta y = \delta$ , and time derivatives may be evaluated through a central difference

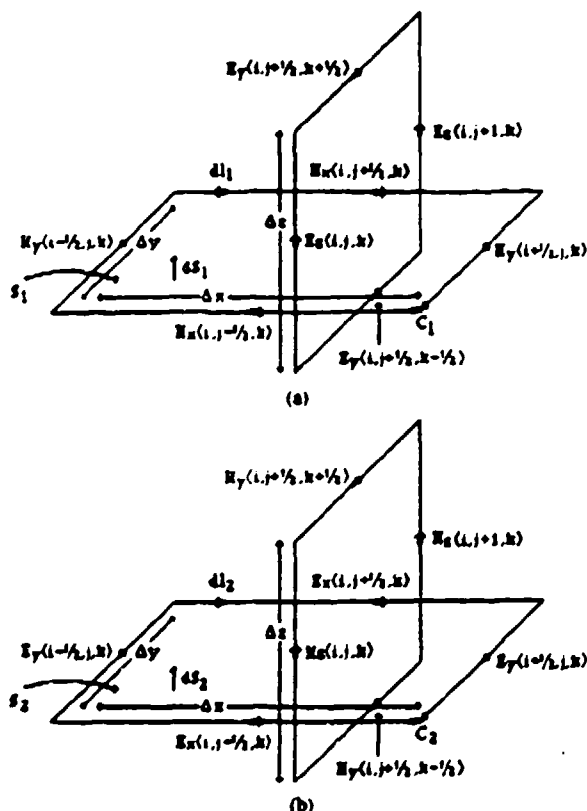


Fig. 1. Examples of spatially orthogonal contours in free space. (a) Ampere's law for  $E_z$ . (b) Faraday's law for  $H_z$ .

expression, (2) reduces to:

$$\epsilon_0 \delta^2 \left[ \frac{E_z^{n+1}(i, j, k) - E_z^n(i, j, k)}{dt} \right] = \left[ H_x^{n+1/2} \left( i, j - \frac{1}{2}, k \right) - H_x^{n+1/2} \left( i, j + \frac{1}{2}, k \right) + H_y^{n+1/2} \left( i + \frac{1}{2}, j, k \right) - H_y^{n+1/2} \left( i - \frac{1}{2}, j, k \right) \right] \delta \quad (3)$$

where the superscripts indicate the time step for each field value. Solving for  $E_z^{n+1}(i, j, k)$  leads to the equation in the Yee algorithm, which may also be derived from the  $\nabla \times \mathbf{H}$  equation.

An example of how this may be applied in a two-dimensional transverse electric (TE) case is shown in Fig. 2. Contour  $C_1$  is a normal contour, but Contours  $C_2$  and  $C_3$  are deformed along the dotted lines. The algorithms for the three  $H_z$  points within the contours follow, where  $H_z$  implies the value inside the contour,  $E_{x-}$  and  $E_{x+}$  indicate the values of the  $E_x$  components on the left and right sides of the  $H_z$  point,  $E_{y-}$  and  $E_{y+}$  indicate values of  $E_y$  components on the top and bottom of the  $H_z$  point, and  $D_a$  and  $D_b$  are constants dependant on the media of the contour:

$$H_z^{n+1} = D_a \cdot H_z^n + D_b \cdot (E_{x-}^{n+1/2} - E_{x+}^{n+1/2} + E_{y-}^{n+1/2} - E_{y+}^{n+1/2}) \quad (4)$$

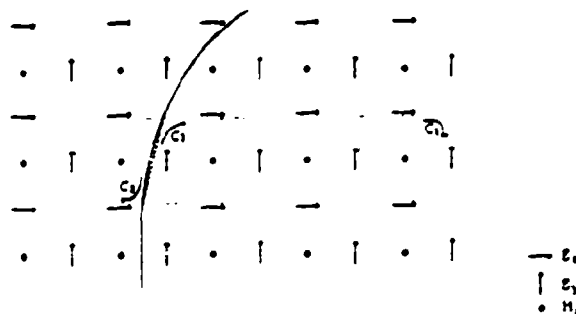


Fig. 2. Example of contour FDTD method, TE case.

$$H_z^{n+1} = D_a \cdot H_z^n + \frac{D_b}{\text{area}(C_2)} \cdot (l_l \cdot E_{x-}^{n+1/2} - l_r \cdot E_{x+}^{n+1/2} + l_t \cdot E_{y-}^{n+1/2} - l_b \cdot E_{y+}^{n+1/2}) \quad (5)$$

$$H_z^{n+1} = D_a \cdot H_z^n + \frac{d_b}{\text{area}(C_3)} \cdot (l_l \cdot E_{x-}^{n+1/2} - l_r \cdot E_{x+}^{n+1/2} - l_t \cdot E_{y-}^{n+1/2} + l_b \cdot E_{y+}^{n+1/2}) \quad (6)$$

assuming that the curved figure is a perfect electric conductor and that  $l_l$ ,  $l_r$ ,  $l_t$ , and  $l_b$  indicate lengths along the respective (left, right, top, and bottom) sides of the contour, normalized to lengths of exactly 1.0 for the standard contour ( $C_1$ ).

As may be seen from (4)–(6), the differences between the last two equations for the deformed contours and the first equation for the standard contour are minimal. Thus, it is a simple matter to transform the stepped-edge model of a scatterer into a true contour model, as long as the number of special cells are small in comparison to the total number of cells in the grid. This is analogous to saying that the number of surface components must be smaller than the number of volume components, which is always true for a reasonably large object.

The rationale behind this approach is that it is more robust and more stable to have a simple algorithm, valid over most of the grid with a slight modification at a few points, than to have a complex algorithm which may be used over the entire grid. The authors believe that this method will lead to reduced computer storage and reduce running times over body-fitted grids and other nonregular grids.

### C. Winglike Object (Using Contour FDTD)

As an example of the contour method, a winglike object was modeled. This object was suggested by General Dynamics, Inc. as a test of the accuracy of the contour FDTD method. Fig. 3(a) shows a cross section of the object. The length of the wing is 10 in, and its height is slightly less than 1 in at the center. The object extends 12 in in the third dimension.

To permit direct code-to-code validation of FDTD versus an existing, well-characterized 2-D MM program, it was decided that all numerical modeling runs should be in 2-D (effectively letting the 12-in dimension of the object go to infinity.) This allows an acceptable MM matrix size. In addition, both the FDTD and MM predictions are compared

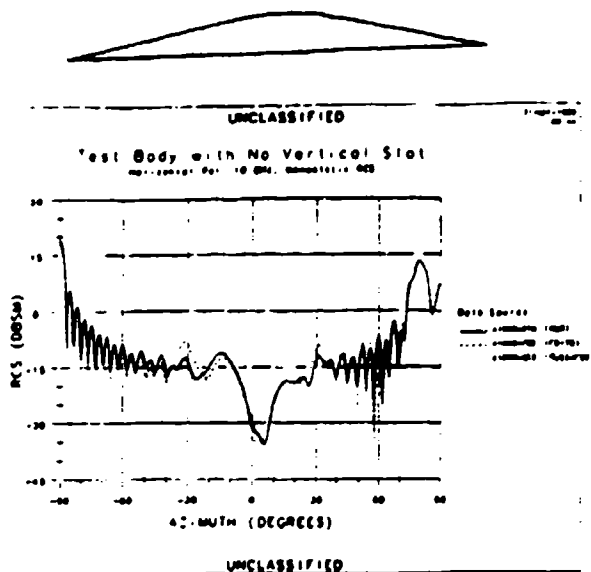


Fig. 3. General Dynamics' test object.

to anechoic chamber measurements (although, of course, this data was obtained for the original 3-D target, not the 2-D idealization).

Fig. 3(b) shows the RCS over a range of angles for the H/H polarization at 10 GHz, and includes the MM data in addition to the FDTD and chamber data. It is clear that the FDTD and MM data virtually overlay each other for observation angles between  $+60^\circ$  and  $+90^\circ$ , where the smooth curve is being directly illuminated and conformal surface modeling is essential to obtain the proper RCS. Excellent agreement is also noted for observation angles between  $-90^\circ$  and  $-30^\circ$ , where the flat side is being directly illuminated. There is some disagreement of the predicted and measured data at grazing illumination. However, the disagreement at these relatively low RCS levels is likely a consequence of the idealized 2-D models versus the 3-D physics actually being modeled in the anechoic chamber.

### III. MODELS AND VALIDATIONS

#### A. Structures Modeled by FDTD

The work in FDTD modeling of radiating structures begins with a 2-D rectangular waveguide excited by a point source. Next a flare of either  $45^\circ$  or  $26.6^\circ$  is added; these horns are validated against MM for both the aperture fields and the far fields. Next the flared horn is used to excite a parabolically-shaped reflector, and the resulting far-field pattern is examined and compared with a far-field pattern generated from MM. Finally, two 3-D structures are modeled: a rectangular waveguide, and the same waveguide flared into a  $H$ -plane sectoral horn. The far-field pattern of the waveguide is compared against an MM model. The far-field pattern of the horn is shown. In addition, a third-dimensional waveguide is used in a hyperthermia application, and a validation is given.

#### B. Waveguides and Horns in Two Dimensions

The initial object to be modeled is a simple 2-D waveguide. This is one of the simplest radiating objects that can be

simulated through the FDTD method, because the rectangular shape leads to a natural stepped-edge model. The waveguide modeled has a width of  $\lambda_0$ , and a length of  $5\lambda_0$ . A line source is centered within the guide  $\lambda_0/2$  from the closed end. Fig. 4(a) shows a contour map of the fields inside the guide and also emerging from the guide. This picture is clearly the same as any found in an elementary textbook on electromagnetic fields and waves. Fig. 4(b) is a plot of the far-field pattern compared to that obtained using MM. Discrepancies between the two sets of results at levels 35 dB or more below the main lobe are similar to those for the horns discussed in some detail later.

To create the two horn antennas, flares are added to the initial waveguide, adding  $\lambda_0$  to the total length, with a slope of either 1 or 1/2, corresponding to flare angles of  $45^\circ$  and  $26.6^\circ$  respectively. The  $45^\circ$  horn is not much of a challenge, because of the manner in which a  $45^\circ$  line passes through a square grid. A portion of this model is shown in Fig. 5(a), which demonstrates that by setting the media parameter of the  $E_z$  points along the flare to have the properties of metal, the standard FDTD algorithm may be used with no modification.

Fig. 6 shows the agreement between the FDTD results for normalized aperture and phase of the electric field, and results from MM for the  $45^\circ$  horn. It is apparent that these two methods give results which are virtually identical to the human eye.

For the  $26.6^\circ$  horn, which has a flare sloped at 1/2 as seen in Fig. 5(b), only two types of special cells exist (one for the upper flare and one for the lower flare), and the algorithm for these cells may be easily determined by slightly altering the location of the  $H_z$  point through which the metal flare passes. The  $E_z$  point directly above this becomes a point which is ignored in further computations, but the  $H_z$  point above that and the  $H_z$  point to its left also become special points. Finally, the  $H_z$  point to the right of the  $E_z$  point is also ignored in further computations. A similar process will apply to the bottom flare. The algorithm for these special cells is repeated from the end of the waveguide to the end of the horn, along the full length of the flare.

Fig. 7 demonstrates the aperture field agreement of magnitude and phase data between the two methods for the  $26.6^\circ$  horn. As the aperture fields appear the same, the next item of interest was the far-field patterns. This comparison (Fig. 8) showed some agreement in the main lobe, but not anywhere else. This was a matter which caused mild consternation when it was first discovered, because conventional wisdom in this area suggests that near fields which are even slightly different will produce similar far fields, due to the fact that going from near fields to far fields involves an integration, which should average out small errors. Here, however, this is not the case. Extremely close near fields are producing rather distinct far-field patterns.

The first question to be asked is which far-field pattern is correct, if either. The MM model uses 10 sample points per wavelength, and a pulse-current expansion with point matching. Under the assumption that this formulation was suitable for this problem, the number of sample points per wave-

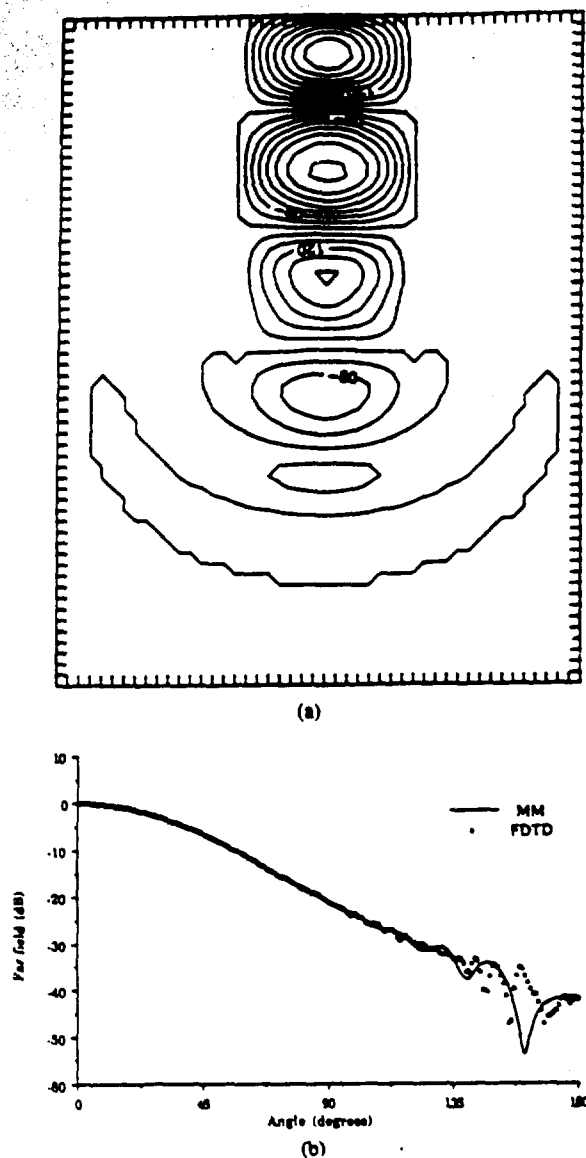


Fig. 4. TM parallel plate wave guide. (a) Near fields. (b) Far fields.

length was varied to 20, 30, and 40. The results of this examination are shown in Fig. 9. It is clear that this variation has little if any effect in the main lobe, but the sampling rate has a definite effect on the sidelobes, and further, the area of the pattern which is affected moves to the sides and down as the number of samples increases. Thus, it has been concluded that the dynamic range of MM is highly dependent on the number of samples per wavelength, and for modeling of objects such as this, 10 samples is not enough, and 40 must be used. In addition, it is possible that other choices of MM current-expansion and weighting functions could give somewhat different results, especially in the low-radiated field region.

For the FDTD model, more possibilities exist to be studied. First, what is the effect of the radiation boundary conditions (RBC's)? For a time-marching code, this is simple to determine by increasing the size the grid in such a manner that the earliest possible reflections from the boundary cannot reach the portion of the grid that is of interest in the number of time steps for which the code is run. This can be consid-

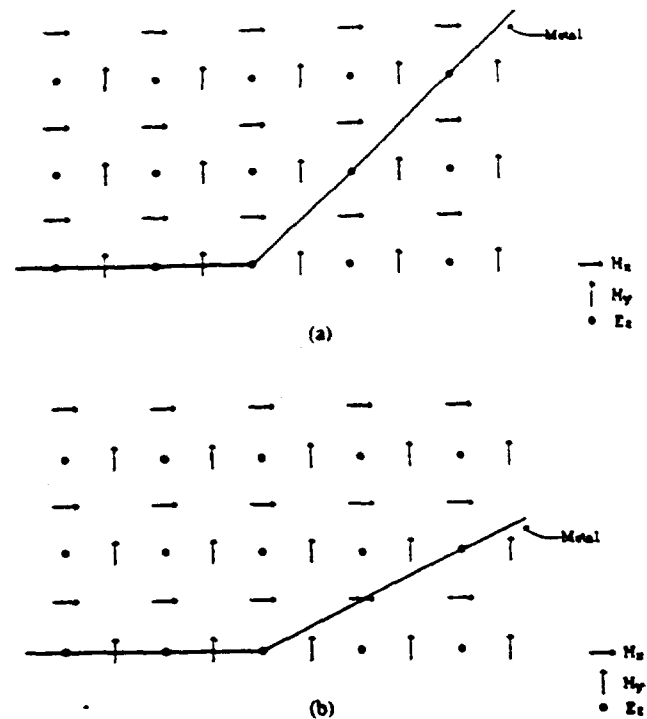


Fig. 5. A portion of the FDTD grid for the TM horns. (a) 45° horn. (b) 26.6° horn.

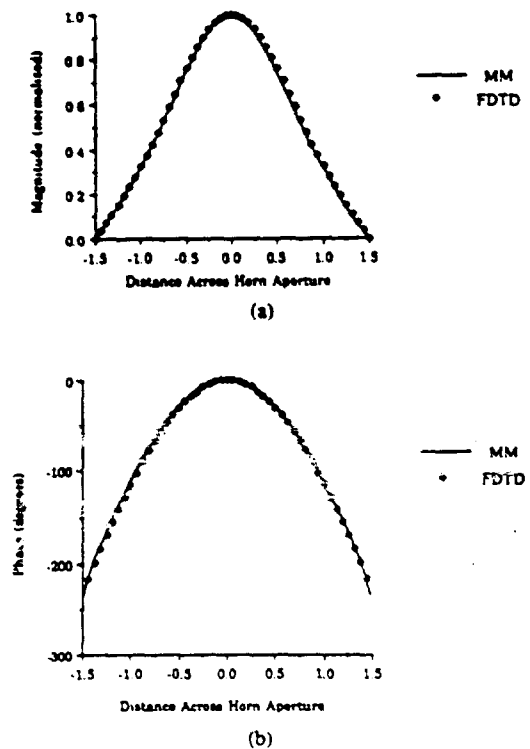


Fig. 6. Normalized aperture data for the 45° horn, TM case. (a) Magnitude. (b) Phase.

ered time-gating out the RBC's. Fig 10(a) shows the results of this time-gating. It is clear that the RBC's perturb the computed pattern, particularly at levels of -40 dB and lower compared to the main beam.

The next change was to move the contour of integration farther from the object while maintaining the time-gating of



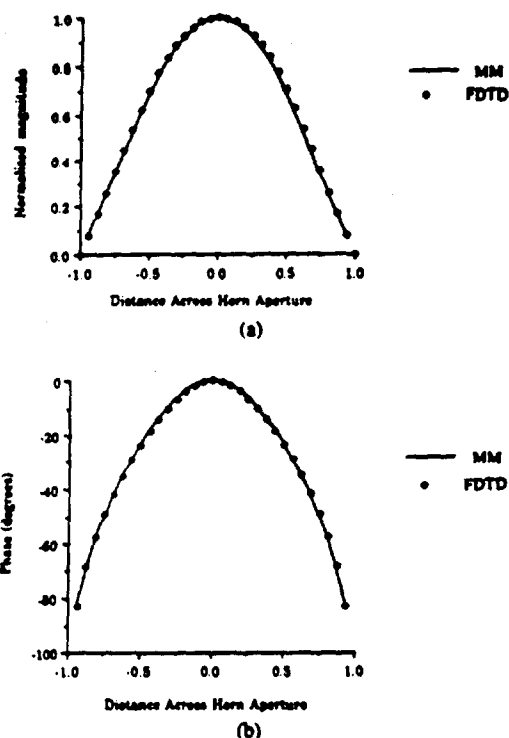


Fig. 7. Normalized aperture data for the 26.6° horn, TM case. (a) Magnitude. (b) Phase.

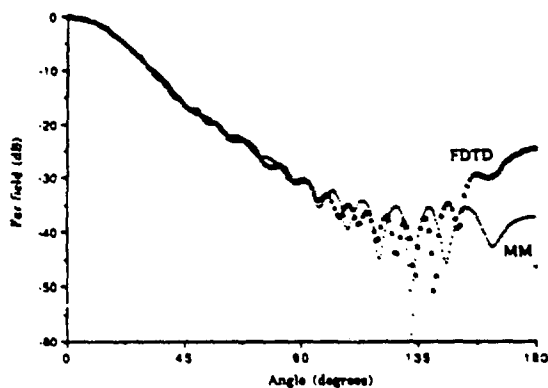


Fig. 8. Initial Comparison for far-field data for the 26.6° horn.

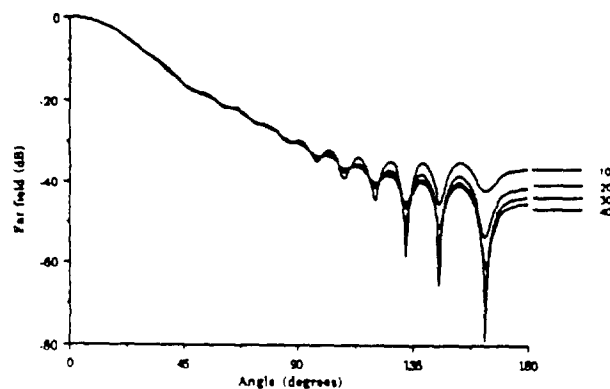


Fig. 9. Far-field data for the 26.6° horn, TM case, MM patterns versus number of samples per  $\lambda$ .

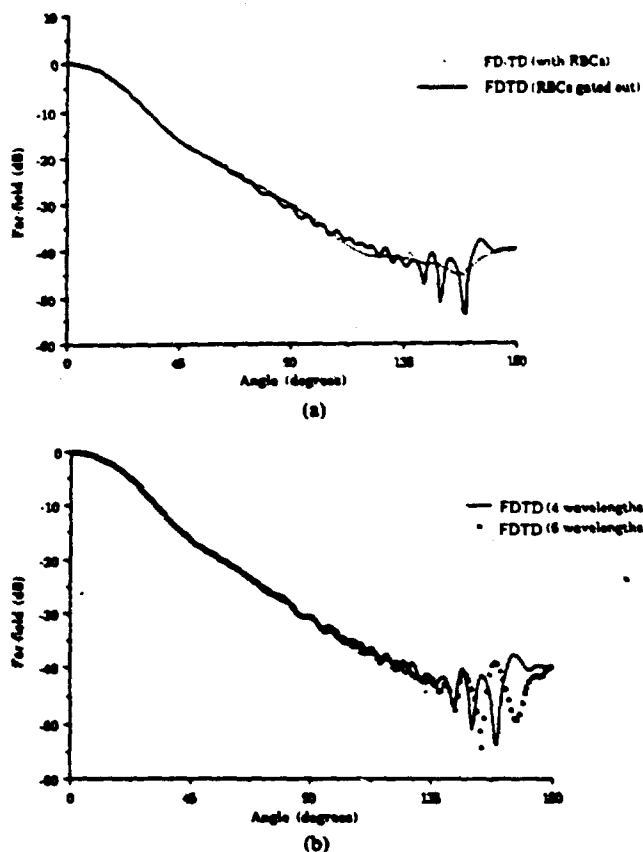


Fig. 10. Far-field data for the 26.6° horn, TM case. (a) FDTD patterns showing effects of RBC's. (b) Patterns showing varied distance from  $S_p$  plane to RBC.

the RBC's. In a standard FDTD code which produces good results in most cases, this contour is at least one wavelength away from the object. Fig. 10(b) shows the variation in the far-field pattern, as this distance is increased. It is clear that the placement of the integration contour can also perturb the computed pattern at levels of  $-40$  dB and below.

Fig. 11 compares the most accurate MM and FDTD patterns. There is a substantial improvement over the initial attempt, but there are still differences in the range of the pattern with low-level fields. A change of method of integration of the FDTD near fields was investigated, from trapezoidal rule to Simpson's rule, but this did not make any appreciable difference in the patterns.

Since the possibilities of error in going from the near field to far field have been eliminated by the changes discussed, the next item to examine is the near fields themselves. It has been shown that FDTD requires a grid spacing of 10 cells per wavelength [10], and the models to this point have used a spacing of 16 cells per wavelength. If MM requires a higher spatial sampling rate for this type of model, perhaps FDTD does as well. This is left for future investigation.

### C. Horn-Fed Parabolic Antennas in Two Dimensions

After reasonable certainty of the results of the 2-D horns was achieved, the 26.6° horn was placed in two systems containing both a horn and a parabolic reflector. The difference between the systems is the distance between the phase

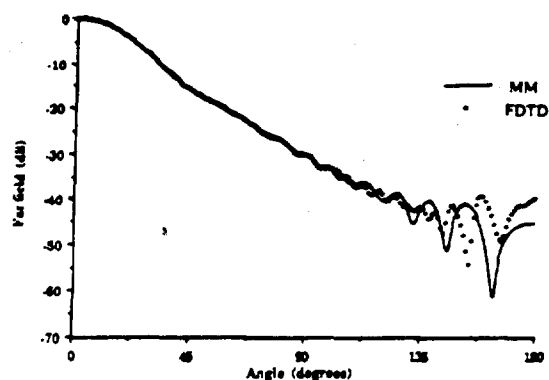


Fig. 11. Far-field data for the 26.6° horn, TM case, FD-TD versus MM, final comparison.

center of the horn and the parabola. This phase center of the horn is located at the focus of the parabola in the first system, and in the second system it is one wavelength closer than the focus. Each system features a parabola with an opening width of  $50 \lambda_0$ . The two systems, including both the horns and the parabolas, were modeled using the contour method, described above.

The parabola run on a single processor of a Cray 2 used approximately 50 min of CPU time for the FDTD version, and 150 min for the MM version at 40 current sources per wavelength. The latter was shown to be required by a convergence study, as seen in Fig. 12(b).

The far-field plots for these two systems are shown in Fig. 13. The variation in far fields appears most noticeable in the main lobe of the pattern. It appears that placing the horn such that its phase center is slightly closer to the parabola than the focal point (Fig. 13(b)) gives a roughly flat region behind the horn, and only a small amount of scattering behind the parabola.

#### D. Waveguides and Horns in Three Dimensions

FDTD modeling of two 3-D radiating structures, an open-ended waveguide and a horn antenna, is now considered. The horn is developed from the waveguide, which has the following dimensions. The cross section is  $2\lambda_0/3$  in the  $y$  direction and  $\lambda_0/3$  in the  $z$  direction. The length in the  $x$  direction is  $2\lambda_0$ . A line source (monopole) oscillates sinusoidally  $\lambda_0/3$  from closed end in the  $x$  direction, centered in the  $y$  direction, and extending from the top to bottom in the  $z$  direction. The horn adds a flare perpendicular to the  $x$ - $y$  plane, at an angle of  $45^\circ$  to the sides of the waveguide, and extending the full  $z$  height of the structure.

Validation of the FDTD model was accomplished by comparison of the computed far-radiated fields with results obtained from a triangular surface patching MM code. The resolution of the MM code was varied from 10 patches per wavelength up to a maximum of 20 patches per wavelength. Little change was noted in comparison with the MM results from lower-resolution models. It is apparent from Fig. 14(b) that MM and FDTD results agree reasonably well for this simple waveguide. Running times for the two codes were also comparable. Fig. 15(b) shows the FDTD computed far-field pattern of the horn.

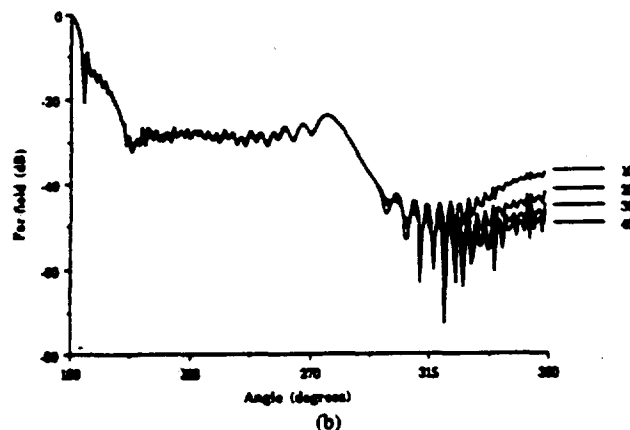
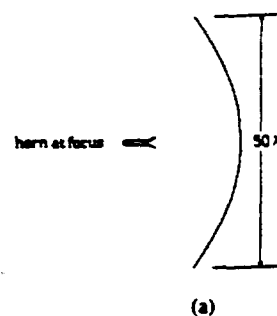


Fig. 12. Far-field data for parabola of  $50 \lambda_0$  width, horn fed at focus, MM patterns for various number of patches per wavelength.

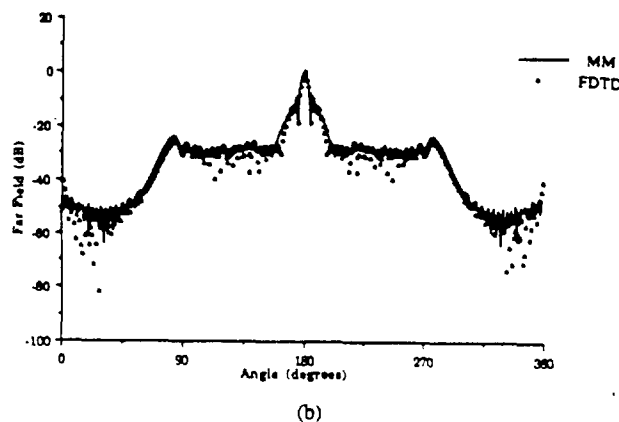
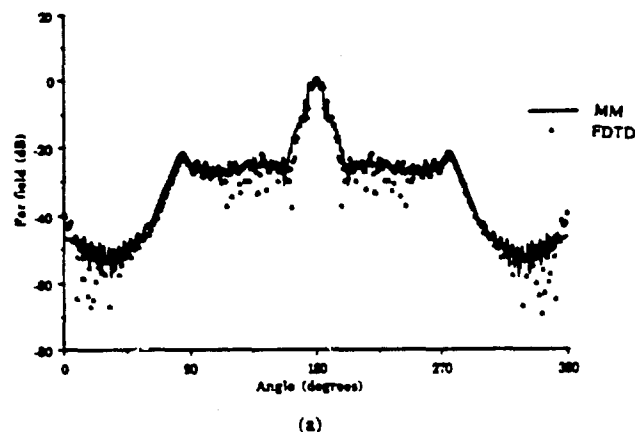


Fig. 13. Far-field data for parabola of  $50 \lambda_0$  width. (a) Horn fed at focus. (b) Horn fed  $\lambda_0$  closer than focus.

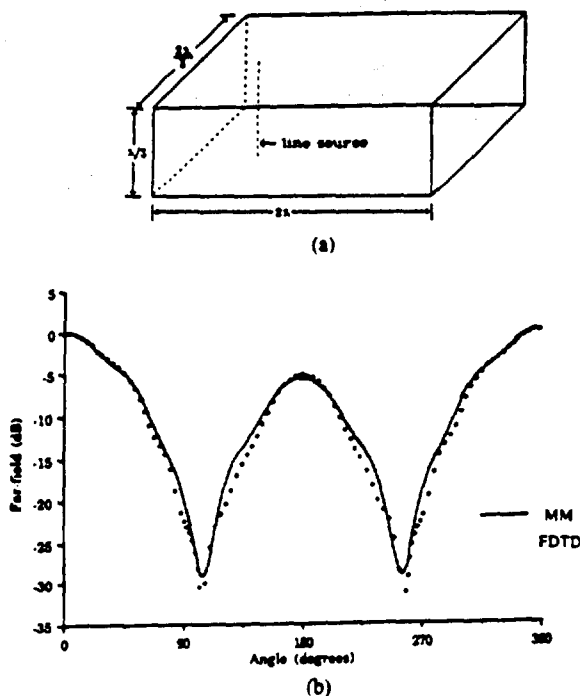


Fig. 14. Three-dimensional waveguide, far fields,  $\phi$  sweep,  $\theta = 90^\circ$ ,  $E_z$  polarization.

#### E. Hyperthermia Application

Hyperthermia is the use of heat to elevate the temperature of a tumor to greater than  $42^\circ\text{C}$ . In combination with radiation or chemotherapy it has shown promising results in the treatment of small surface tumors. Major problems which exist in clinical hyperthermia are: maximizing the therapeutic effects of tumor temperature distribution, minimizing normal tissue damage, and ensuring deposited power is confined to the target tumor volume. Power is applied through electromagnetic (EM) applicators, which can take the form of dielectrically loaded waveguides.

A semi-automated, real-time, patient-specific hyperthermia model has been developed using computer vision system technology and FDTD analysis. [18] Through the use of computer vision, a patient's computed tomography (CT) scans are analyzed to reconstruct a complex, 3-D tissue geometry [19], [20]. These data are transformed into a form suitable for the FDTD method. Luckily, biologic tissue is lossy enough that a stepped-edge geometry is sufficient for good accuracy. The EM applicator is then inserted into the FDTD grid, and the program is run to give an accurate picture of the power deposition. The correct applicator and incident power can then be selected on the basis of this run to provide the desired localization and uniform heat in the tumor volume.

In three dimensions, a water-loaded rectangular waveguide is used to illuminate a tissue structure similar to that modeled by a University of Athens group [21] through an integral equation approach. Fig. 16(a) shows the geometry of the model. In the Athens group's problem, the tissue structure is a layered half-space with 0.5 cm of skin, 1.0 cm of fat, and an infinite layer of muscle. The  $5.6 \times 2.8 \times 2.8 \text{ cm}^3$  waveguide is excited by a line source at 432 MHz, which creates an incident power of 1 W on the tissue structure. The FDTD

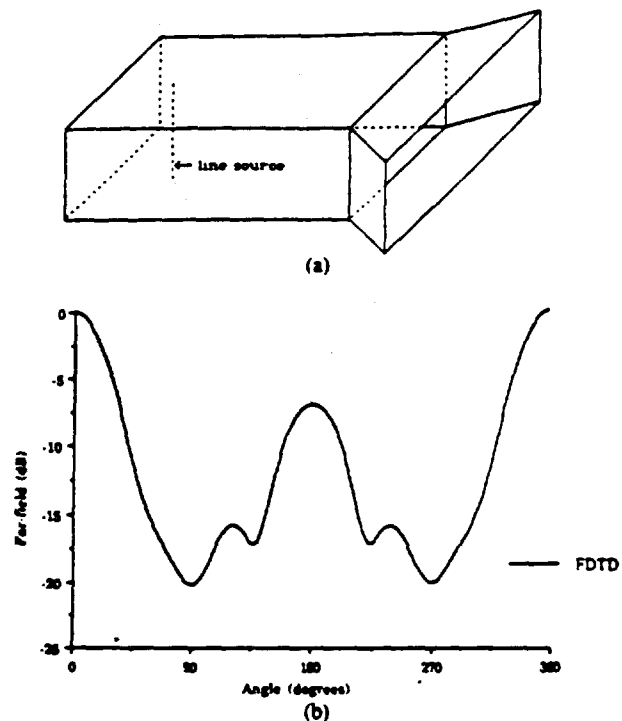


Fig. 15. Three-dimensional flared horn, far fields,  $\phi$  sweep,  $\theta = 90^\circ$ ,  $E_z$  polarization.

model assumes the infinite dimensions of the structure may be modeled by half a skin depth in any direction.

Figs. 16(b) and 16(c) show a comparison of the FDTD results and those of the integral equation solver for penetrating electric field contours at the skin-fat interface, and at the fat-muscle interface, respectively. Because of symmetry, only a quadrant of the field distribution is shown.

#### IV. SUMMARY AND CONCLUSION

This paper has demonstrated that the FDTD method is valid for use in modeling of radiating structures. Based on this validity, the contour FDTD method has been proven to be a new and useful tool for modeling various reflector systems and some biologic problems. While it is recognized that this method has some limitations, the authors can foresee a time in the future when these problems will have been solved, and FDTD will be a standard tool for the analysis of electromagnetic interactions involving large objects.

There are several important issues affecting computational dynamic range. From the discussion of the  $26.6^\circ$  horn, it is clear that neither MM nor current FDTD methods can be blindly applied to antennas or scatterers which have a broad angular range of far fields lower than  $-40 \text{ dB}$  relative to the main lobe or the incident beam. Changing the FDTD gridding to a finer spatial sampling, using brute-force methods to eliminate the effects of the RBC's, and calculating the best integration from the near-field points seem to be ways to achieve more accurate results, and hence, greater dynamic range. However, this reasoning is only valid in two dimensions.

In three dimensions, many things change. The MM matrix size increases by an order of magnitude, which causes the inversion or solution time to increase by three orders of magnitude. For the FDTD code, time-gating out the RBC

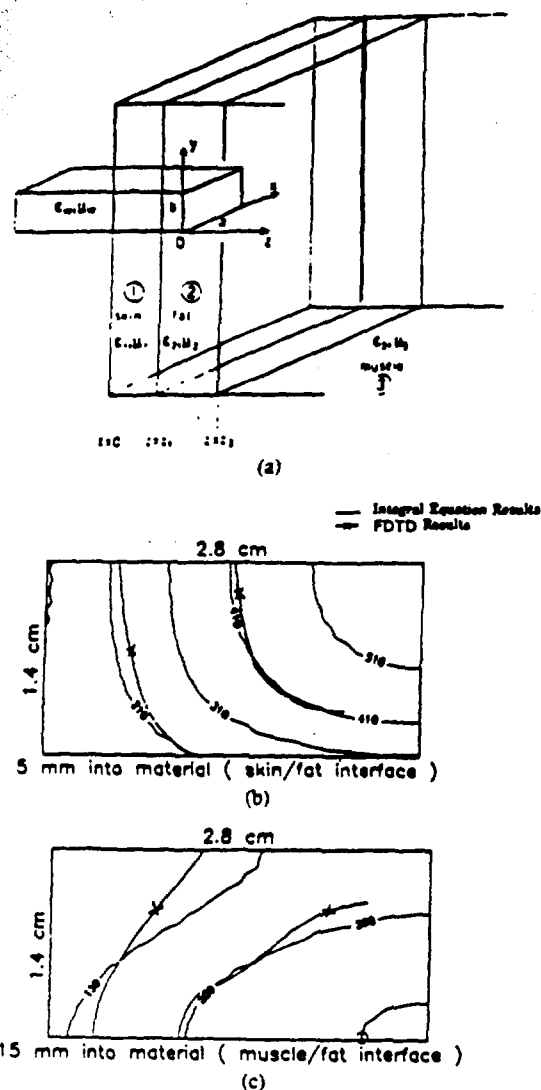


Fig. 16. Hyperthermia application.

reflections is impractical, because it increases the volume of space in which the time marching takes place, which is much worse than simply increasing the area in two dimensions. The fields themselves also change in three dimensions, going from an  $r^{-0.5}$  dependence to an  $r^{-1}$  dependence. Perhaps this will reduce the negative effects of the RBC's because the fields will be weaker upon reaching the grid boundaries. An important point to note is that for antenna problems, FDTD and MM are similar in that after one large solution is worked out (time marching of fields or matrix inversion,) finding the antenna pattern is simply a matter of a number of integrations or a number of matrix multiplies.

Improved RBC's exist, and these must be examined in both two and three dimensions in the context of problems of this class. In addition, the standard second-order Yee differencing algorithm may itself be unsuitable for problems such as these. It may be necessary to use a fourth-order scheme to achieve the requisite accuracy while maintaining  $0.1 \lambda_0$  (relatively coarse) spatial resolution. This also must be examined in both two and three dimensions.

Finally, assuming these modifications are sufficient, large 3-D problems may be attempted. These models will have to

be verified experimentally, as the MM equivalent models will be too large to run on today's computers in a reasonable amount of time.

#### ACKNOWLEDGMENT

The authors wish to thank John Baldauf and S. W. Lee of the University of Illinois at Urbana-Champaign for the validations of the aperture fields for the two-dimensional horns. Thanks also go to Evans Harrigan and Kent Misegades of Cray Research, Inc. for computer resources used for some of the FDTD runs.

#### REFERENCES

- [1] J. B. Keller, "Diffraction by an aperture," *J. Appl. Phys.*, vol. 28, pp. 426-444, Apr. 1957.
- [2] —, "Geometric theory of diffraction," *J. Opt. Soc. Am.*, vol. 52, pp. 116-130, Feb. 1962.
- [3] J. Huang, Y. Rahmat-Samii, and K. Woo, "A GTD study of pyramidal horns for offset reflector antenna applications," *IEEE Trans. Antennas Propagat.*, vol. AP-31, pp. 305-309, Mar. 1983.
- [4] P. M. Russo, R. C. Rudduck, and L. Peters, Jr., "A method for computing E-plane patterns of horn antennas," *IEEE Trans. Antennas Propagat.*, vol. AP-13, pp. 219-244, Mar. 1965.
- [5] C. M. Knop and E. L. Ostertag, "A note on the asymptotic physical optics solution to the scattered fields from a paraboloidal reflector," *IEEE Trans. Antennas Propagat.*, vol. AP-25, pp. 531-534, July 1977.
- [6] R. C. Menendez and S. W. Lee, "Analysis of rectangular horn antennas via uniform asymptotic theory," *IEEE Trans. Antennas Propagat.*, vol. AP-30, pp. 241-250, Mar. 1982.
- [7] S. Sanyal and A. K. Bhattacharyya, "UAT analysis of E-plane near and far-field patterns of electromagnetic horn antennas," *IEEE Trans. Antennas Propagat.*, vol. AP-31, pp. 817-819, Sept. 1983.
- [8] A. Taflov, K. R. Umashankar, and T. G. Jurgens, "Comparative time and frequency domain solutions of Maxwell's equations for modeling radar cross section," presented at the Fifth IMACS Symp. Comput. Methods for Partial Differential Equations, Bethlehem, PA, June 19-21, 1984.
- [9] K. S. Yee, "Numerical solution of initial boundary value problems involving Maxwell's equations in isotropic media," *IEEE Trans. Antennas Propagat.*, vol. AP-14, pp. 302-307, May 1966.
- [10] A. Taflov and M. E. Brodwin, "Numerical solution of steady-state electromagnetic scattering problems using the time-dependent Maxwell's equations," *IEEE Trans. Microwave Theory Tech.*, vol. MTT-23, pp. 623-630, Aug. 1975.
- [11] A. Taflov, K. R. Umashankar, B. Beker, F. Harfoush, and K. S. Yee, "Detailed FD-TD analysis of electromagnetic fields penetrating narrow slots and lapped joints in thick conducting screens," *IEEE Trans. Antennas Propagat.*, vol. 36, pp. 247-257, Feb. 1988.
- [12] B. Engquist and A. Majda, "Radiation boundary conditions for acoustic and elastic wave calculations," *Commun. Pure Appl. Math.*, vol. 32, pp. 313-357, 1979.
- [13] G. Mur, "Absorbing boundary conditions for finite-difference approximation of the time-domain electromagnetic field equations," *IEEE Trans. Electromagn. Compat.*, vol. EMC-23, pp. 1073-1077, Nov. 1981.
- [14] K. R. Umashankar and A. Taflov, "A novel method to analyze electromagnetic scattering of complex objects," *IEEE Trans. Electromagn. Compat.*, vol. EMC-24, pp. 397-405, Nov. 1982.
- [15] A. Taflov and K. R. Umashankar, "Radar cross section of general three-dimensional scatterers," *IEEE Trans. Electromagn. Compat.*, vol. EMC-25, pp. 433-440, Nov. 1983.
- [16] A. Taflov, K. R. Umashankar, and T. G. Jurgens, "Validation of FD-TD modeling of the radar cross section of three-dimensional structures spanning up to 9 wavelengths," *IEEE Trans. Antennas Propagat.*, vol. AP-33, pp. 662-666, June 1985.
- [17] T. G. Jurgens, A. Taflov, K. R. Umashankar, and T. G. Moore, "Finite-difference time-domain modeling of curved surfaces," *IEEE Trans. Antennas Propagat.*, to appear.
- [18] M. J. Picket, A. Taflov, W. C. Lin, D. S. Katz, V. Sathiseelan, and B. B. Mital, "Computational modeling of electromagnetic hyperthermia: Three-dimensional and patient specific," *IEEE Trans. Biomed. Eng.*, to appear.

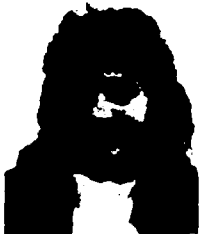
- [19] W. C. Lin, C. C. Liang, and C. T. Chen, "Dynamic elastic interpolation for 3-D object reconstruction from serial cross-sectional images," *IEEE Trans. Medical Imaging*, vol. 7, pp. 225-232, 1989.
- [20] W. C. Lin, S. Y. Chen, and C. T. Chen, "A new surface interpolation technique for reconstructing 3-D objects from serial cross sections," *Comput. Vision, Graphics, and Image Processing*, vol. 48, pp. 124-128, 1989.
- [21] K. S. Nikita and N. K. Uzunoglu, "Analysis of the power coupling from a waveguide applicator into a three-layered tissue model," *IEEE Trans. Microwave Theory Tech.*, vol. 37, pp. 1794-1801, Nov. 1989.



Daniel S. Katz (S'88) was born in Belleville, IL, on September 11, 1966. He received the B.S.E.E. and M.S. degrees in electrical engineering, both from Northwestern University, Evanston, IL, in 1988 and 1990, respectively.

Currently he is pursuing the Ph.D. degree in the Department of Electrical Engineering at Northwestern University, where he works as a Research Assistant. His research interests include computational modeling of electromagnetic wave propagation, radiation, and scattering.

Mr. Katz is a member of Tau Beta Pi and Eta Kappa Nu.



Melinda J. Pilket-May (S'89) was born in Kalamazoo, MI, on July 9, 1965. She received the B.S.E.E. degree from the University of Illinois, Urbana, in 1988, and the M.S. degree in electrical engineering from Northwestern University, Evanston, IL, in 1990.

She is currently pursuing the Ph.D. degree in the Department of Electrical Engineering at Northwestern University, where she works as a Research Assistant. Her research interests include numerical modeling of electromagnetic phenomena with application to VLSI and biomedical problems.

Allen Tallone (M'75-SM'84-F'90), for a photograph and biography please see page 906 of the July 1991 issue of this Transactions.



Korada R. Umashankar (S'69-M'75-SM'81) received the B.E. degree from Mysore University, India, in 1962, the M.E. degree from the Indian Institute of Science, Bangalore, India, in 1964, and the Ph.D. degree from the University of Mississippi, University, in 1974, all in electrical engineering.

From 1964 to 1969, he was Assistant Professor and Head of the Department of Electrical Engineering, Karnatak University, Hubli, India. During 1974 and 1975, he was a Postdoctoral Research

Associate, and from 1975 to 1977, Assistant Professor of Electrical Engineering at the University of Mississippi. From 1977 to 1979, he was the National Research Council Visiting Fellow at the U.S. Air Force Weapons Laboratory, Kirtland AFB, New Mexico. During 1979 to 1984, he was Senior Engineer at IIT Research Institute, Chicago, IL. During 1984, he joined the faculty of the Department of Electrical Engineering and Computer Science, University of Illinois at Chicago, Chicago, where he is currently a full Professor. His primary research is in the development of analytical and numerical techniques in electromagnetic field theory, EMP/EMC interactions. He has extensively published in open literature research investigations dealing with EM simulation of complex material objects using integral equation methods, finite-difference time-domain techniques, and has been involved in the development of large scale numerical algorithms for super computer applications. He has authored the textbook, *Introduction to Engineering Electromagnetic Fields*, (World Scientific) and has contributed several book chapters in edited research monographs.

Dr. Umashankar is a member of Eta Kappa Nu, Sigma Xi, and URSI Commission B. He is co-chairman of the Technical Committee, the 1992 International APS/URSI, and the NEM Symposium, Chicago, IL.

# Direct time integration of Maxwell's equations in linear dispersive media with absorption for scattering and propagation of femtosecond electromagnetic pulses

Rose M. Joseph, Susan C. Hagness, and Allen Taflov

Department of Electrical Engineering and Computer Science, McCormick School of Engineering, Northwestern University, Evanston, Illinois 60208-3118

Received May 29, 1991

We report the initial results for femtosecond pulse propagation and scattering interactions for a Lorentz medium obtained by a direct time integration of Maxwell's equations. The computational approach provides reflection coefficients accurate to better than 6 parts in 10,000 over the frequency range of dc to  $3 \times 10^{16}$  Hz for a single 0.2-fs Gaussian pulse incident upon a Lorentz-medium half-space. New results for Sommerfeld and Brillouin precursors are shown and compared with previous analyses. The present approach is robust and permits two-dimensional and three-dimensional electromagnetic pulse propagation directly from the full-vector Maxwell's equations.

A pulse propagating in a dispersive medium such as an optical fiber exhibits complicated behavior. It is of interest to have an accurate numerical model for this behavior as well as for other electromagnetic interactions with frequency-dependent materials.

The finite-difference time-domain (FD-TD) method is a numerical technique for direct time integration of Maxwell's equations.<sup>1-4</sup> It is a computationally efficient approach to modeling sinusoidal or impulsive electromagnetic interactions with arbitrary three-dimensional structures consisting of linear, possibly anisotropic, lossy dielectric and permeable media with frequency-independent parameters. It has been used for predicting electromagnetic wave scattering, penetration, and radiation for a variety of problems.<sup>5</sup> Recently, the range of FD-TD modeling applications has been substantially expanded to include ultra-high-speed signal lines,<sup>6</sup> subpicosecond electro-optic switches,<sup>7</sup> and linear optical directional couplers.<sup>8</sup>

Attempts have been made to extend FD-TD to frequency-dependent materials. Chromatic dispersion can be expressed in the time domain as a convolution integral involving the electric field and a causal susceptibility function. This convolution integral can be efficiently incorporated into the FD-TD algorithm for a first-order (Debye) dispersion.<sup>9</sup> In this Letter we present a more general approach that permits modeling of media having arbitrary-order dispersions. Our approach is based on a suggestion by Jackson (Ref. 10, p. 331) to relate the electric displacement  $D(t)$  to the electric field  $E(t)$  through an ordinary differential equation in time.

We consider a one-dimensional problem with field components  $E_z$  and  $H_y$  propagating in the  $x$  direction. If we assume first that the medium is nonpermeable, isotropic, and nondispersive, Maxwell's curl equations in one dimension are

$$\frac{\partial H_y}{\partial t} = \frac{1}{\mu_0} \frac{\partial E_z}{\partial x}, \quad (1a)$$

$$\frac{\partial D_z}{\partial t} = \frac{\partial H_y}{\partial x}. \quad (1b)$$

Here  $D_z = \epsilon E_z$ , where the permittivity  $\epsilon$  is independent of frequency. Using central differencing in time and space,<sup>1</sup> we can express the curl equations in finite-difference form as the following second-order accurate leapfrog algorithm:

$$H_y^{n+1/2}(i + \frac{1}{2}) = H_y^{n-1/2}(i + \frac{1}{2}) + \frac{\Delta t}{\mu_0 \Delta x} [E_z^n(i+1) - E_z^n(i)], \quad (2a)$$

$$E_z^{n+1}(i) = E_z^n(i) + \frac{\Delta t}{\epsilon \Delta x} [H_y^{n+1/2}(i + \frac{1}{2}) - H_y^{n-1/2}(i - \frac{1}{2})], \quad (2b)$$

where  $E_z^n(i)$  denotes the electric field sampled at space point  $x = i \Delta x$  and time point  $t = n \Delta t$ . (Please refer to Ref. 2 for the proper numerical stability criterion.)

For many dispersive media of interest, however,  $\epsilon = \epsilon(\omega)$ . We propose to include this frequency dependence in the FD-TD model by concurrently integrating an ordinary differential equation in time that relates  $D_z(t)$  to  $E_z(t)$ . As suggested by Jackson, this equation is derived by taking the inverse Fourier transform of the complex permittivity expression,

$$\epsilon(\omega) = \frac{D_z(\omega)}{E_z(\omega)}. \quad (3)$$

For an order- $M$  dispersion, the computational model now becomes a three-step recursive process that re-

tains the fully explicit nature of the original dispersionless FD-TD formulation,

$$H_y^{n+1/2}(i + \frac{1}{2}) = H_y^{n-1/2}(i + \frac{1}{2}) + \frac{\Delta t}{\mu_0 \Delta x} [E_x^n(i+1) - E_x^n(i)], \quad (4a)$$

$$D_x^{n+1}(i) = D_x^n(i) + \frac{\Delta t}{\Delta x} [H_y^{n+1/2}(i + \frac{1}{2}) - H_y^{n-1/2}(i - \frac{1}{2})], \quad (4b)$$

$$E_x^{n+1}(i) = f(D_x^{n+1}, \dots, D_x^{n-M+1}; E_x^n, \dots, E_x^{n-M+1}). \quad (4c)$$

At any time step  $n$ , this method requires storage of  $M$  previous values of  $D_x$  and  $M-1$  previous values of  $E_x$  beyond the current field values. The approach will be made clear by the following examples:

**Example 1:** A first-order (Debye) dispersion can be specified by

$$\epsilon(\omega) = \epsilon_\infty + \frac{\epsilon_s - \epsilon_\infty}{1 - j\omega\tau} = \frac{D_s(\omega)}{E_s(\omega)}, \quad (5)$$

where  $\epsilon_s = \epsilon(0)$ ,  $\epsilon_\infty = \epsilon(\infty)$ , and  $\tau$  is the Debye relaxation time constant. If we take the inverse Fourier transform of Eq. (5) as defined by

$$f(t) = \int_{-\infty}^{\infty} f(\omega) \exp(-j\omega t) d\omega, \quad (6)$$

the result is a first-order differential equation in time relating  $D_s$  and  $E_s$ ,

$$D_s + \tau \frac{dD_s}{dt} = \epsilon_s E_s + \tau \epsilon_\infty \frac{dE_s}{dt}. \quad (7)$$

This differential equation can be easily differenced to solve for  $E_s^{n+1}$  in terms of known values of  $E_s$  and  $D_s$  for insertion into Eq. (4c),

$$E_s^{n+1}(i) = \frac{\Delta t + 2\tau}{2\tau\epsilon_\infty + \epsilon_s \Delta t} D_s^{n+1}(i) + \frac{\Delta t - 2\tau}{2\tau\epsilon_\infty + \epsilon_s \Delta t} D_s^n(i) + \frac{2\tau\epsilon_\infty - \epsilon_s \Delta t}{2\tau\epsilon_\infty + \epsilon_s \Delta t} E_s^n(i). \quad (8)$$

**Example 2:** A second-order (Lorentz) dispersion can be specified by

$$\epsilon(\omega) = \epsilon_\infty - \frac{\omega_0^2(\epsilon_s - \epsilon_\infty)}{\omega^2 + 2j\omega\delta - \omega_0^2} = \frac{D_s(\omega)}{E_s(\omega)}, \quad (9)$$

where  $\epsilon_s = \epsilon(0)$ ,  $\epsilon_\infty = \epsilon(\infty)$ ,  $\omega_0$  is the resonant frequency, and  $\delta$  is the damping coefficient. Figure 1 shows the relative permittivity curve for a Lorentz medium that has the following parameters:

$$\epsilon_s = 2.25\epsilon_0, \quad \epsilon_\infty = \epsilon_0, \quad \omega_0 = 4.0 \times 10^{16} \text{ rad/s}, \\ \delta = 0.28 \times 10^{16} \text{ s}^{-1}.$$

Inverse Fourier transformation of Eq. (9) results in the following second-order differential equation relating  $D_s$  and  $E_s$ :

$$\omega_0^2 D_s + 2\delta \frac{dD_s}{dt} + \frac{d^2 D_s}{dt^2} = \omega_0^2 \epsilon_s E_s + 2\delta \epsilon_\infty \frac{dE_s}{dt} + \epsilon_\infty \frac{d^2 E_s}{dt^2}. \quad (10)$$

This differential equation can be easily differenced to solve for  $E_s^{n+1}$  in terms of known values of  $E_s$  and  $D_s$  for insertion into Eq. (4c),

$$E_s^{n+1} = [(\omega_0^2 \Delta t^2 + 2\delta \Delta t + 2)D_s^{n+1} - 4D_s^n + (\omega_0^2 \Delta t^2 - 2\delta \Delta t + 2)D_s^{n-1} + 4\epsilon_\infty E_s^n - (\omega_0^2 \Delta t^2 \epsilon_s - 2\delta \Delta t \epsilon_\infty + 2\epsilon_\infty)E_s^{n-1}] / (\omega_0^2 \Delta t^2 \epsilon_s + 2\delta \Delta t \epsilon_\infty + 2\epsilon_\infty). \quad (11)$$

We first demonstrate the accuracy of this method by computing the wideband reflection coefficient for a planar interface between vacuum and a half-space made of the Lorentz medium of Fig. 1. A single 0.2-fs duration Gaussian pulse (between the 1/e points) is normally incident upon the interface. This pulse has a spectrum that covers the full range from dc to  $3 \times 10^{16}$  Hz. Data are taken every time step ( $\Delta t = 2.0 \times 10^{-19}$  s) at a fixed observation point on the vacuum side of the interface. The FD-TD computed complex-valued reflection coefficient is obtained by taking the ratio of the discrete Fourier transforms of the reflected and incident pulses. Figure 2 compares the magnitude and phase of this

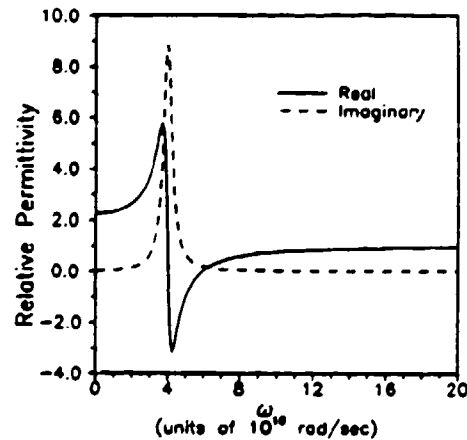


Fig. 1. Complex permittivity of the Lorentz medium with parameters  $\epsilon_s = 2.25\epsilon_0$ ,  $\epsilon_\infty = \epsilon_0$ ,  $\omega_0 = 4.0 \times 10^{16}$  rad/s, and  $\delta = 0.28 \times 10^{16} \text{ s}^{-1}$ .

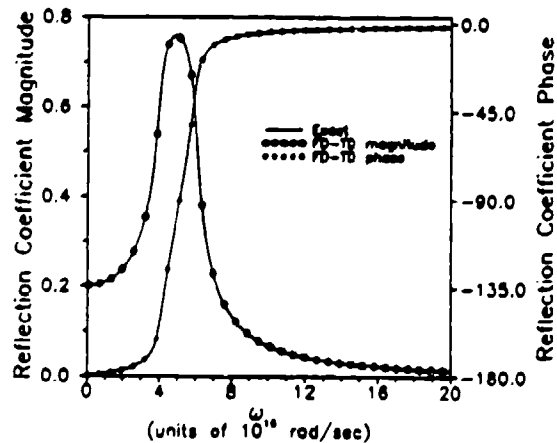


Fig. 2. Comparison of FD-TD and exact results from dc to  $3 \times 10^{16}$  Hz for the magnitude and phase of the reflection coefficient of a half-space made of the Lorentz medium of Fig. 1.

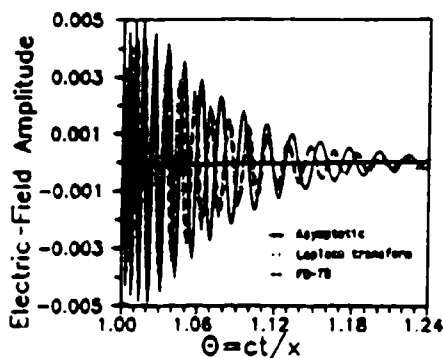


Fig. 3. Comparison of FD-TD, asymptotic,<sup>13</sup> and Laplace-transform<sup>14</sup> results for the Sommerfeld precursor observed at  $x = 1 \mu\text{m}$  in the Lorentz medium of Fig. 1 for a unit-step modulated sinusoidal excitation ( $\omega_c = 1.0 \times 10^{14}$  rad/s) at  $x = 0$ .

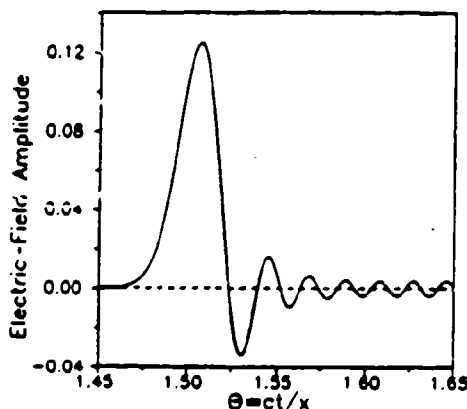


Fig. 4. FD-TD results for the total signal (including the Brillouin precursor) at  $x = 10 \mu\text{m}$  in the Lorentz medium of Fig. 1 for the unit-step modulated sinusoidal excitation.

reflection coefficient as a function of frequency to the exact solution (Ref. 10, p. 282). The deviation from the exact solution over the complete range of dc to  $3 \times 10^{14}$  Hz is less than 6 parts in 10,000. (This 6/10,000 error occurs at the peak of the reflection magnitude curve.)

The time integration of Maxwell's equations permits the computation of a pulse propagating in a dispersive medium at any space-time point. Historically, such pulse dynamics have been obtained only by asymptotic analyses, notably by Sommerfeld<sup>11</sup> and Brillouin<sup>12</sup> in 1914. More recently, advances in uniform asymptotic analysis for such problems have been made by Oughstun and Sherman<sup>13</sup> and in Laplace transform analysis by Wyns *et al.*<sup>14</sup>

To demonstrate the integration of Maxwell's equations to obtain pulse dynamics, we now use the FD-TD method to compute the precursor fields for a unit-step modulated sinusoidal signal propagating in the Lorentz medium discussed in Figs. 1 and 2. Now the signal source is located at  $x = 0$ . The carrier frequency  $\omega_c$  is  $10^{14}$  rad/s. Figure 3 compares the FD-TD computed Sommerfeld precursor ob-

served at  $x = 1 \mu\text{m}$  to the asymptotic<sup>13</sup> and Laplace-transform<sup>14</sup> predictions. Much closer agreement with the Laplace-transform calculation is noted. Extensive numerical convergence studies of the FD-TD results indicate that the zero crossings of the precursor converge quickly (at relatively coarse grid resolutions), while the envelope converges more slowly to a limiting distribution. Overall, we believe that the FD-TD computed envelope distribution shown in Fig. 3 is within 3% of the limiting distribution obtained at infinitely fine grid resolution.

For completeness, Fig. 4 shows the total signal at  $x = 10 \mu\text{m}$  in the Lorentz medium computed with the FD-TD method. This includes the Brillouin precursor. These results are again somewhat different from the asymptotic results reported in Ref. 13, yet the FD-TD calculations here exhibit at least the same degree of convergence as those of Fig. 3.

The method of this Letter should be directly applicable to full-vector electromagnetic pulse propagation and scattering effects for inhomogeneous dispersive media in two and three dimensions. We foresee the possibility of incorporating material nonlinearity to obtain the dynamics of soliton propagation and scattering directly from the time-dependent Maxwell's equations.

This research was supported in part by U.S. Office of Naval Research contract N00014-88-K-0475, NASA-Ames University Consortium Joint Research Interchange no. NCA2-562, and Cray Research, Inc. We thank K. E. Oughstun for providing graphical results of his precursor analyses<sup>13,14</sup> and P. Goorjian of NASA-Ames for suggesting the improved time-stepping scheme of Eq. (11).

## References

1. K. S. Yee, *IEEE Trans. Antennas Propag.* AP-14, 302 (1966).
2. A. Taflov and M. E. Brodwin, *IEEE Trans. Microwave Theory Tech.* MTT-23, 623 (1975).
3. G. Mur, *IEEE Trans. Electromagn. Comput.* EC-23, 377 (1981).
4. K. R. Umashankar and A. Taflov, *IEEE Trans. Electromagn. Comput.* EC-24, 397 (1982).
5. A. Taflov, *Wave Motion* 10, 547 (1988).
6. G. C. Liang, Y. W. Liu, and K. K. Mei, *IEEE Trans. Microwave Theory Tech.* MTT-37, 1949 (1989).
7. E. Sano and T. Shibata, *IEEE J. Quantum Electron.* 26, 372 (1990).
8. S. T. Chu and S. K. Chaudhuri, *IEEE J. Lightwave Technol.* 7, 2033 (1989).
9. R. Luebbers, F. P. Hunsberger, K. S. Kunz, R. B. Standler, and M. Schneider, *IEEE Trans. Electromagn. Comput.* EC-32, 222 (1990).
10. J. D. Jackson, *Classical Electrodynamics*, 2nd ed. (Wiley, New York, 1975).
11. A. Sommerfeld, *Ann. Phys.* 44, 177 (1914).
12. L. Brillouin, *Ann. Phys.* 44, 203 (1914).
13. K. E. Oughstun and G. C. Sherman, *J. Opt. Soc. Am. A* 6, 1394 (1989).
14. P. Wyns, D. P. Foty, and K. E. Oughstun, *J. Opt. Soc. Am. A* 6, 1421 (1989).



# Simple Analytical Solution to Electromagnetic Scattering by Two-Dimensional Conducting Object with Edges and Corners: Part I— TM Polarization

Korada Umashankar, *Senior Member, IEEE*, Wan Chun, *Student Member, IEEE*, and Allen Taflove, *Fellow, IEEE*

**Abstract**—A simple and approximate analytical solution is presented by invoking on-surface radiation condition (OSRC) theory for the analysis of electromagnetic scattering by a perfectly conducting two-dimensional object. The scattering object is assumed to be placed in a free space medium and is excited by a time harmonic plane wave having transverse magnetic (TM) polarization. The closed form analytical result for the monostatic as well as bistatic radar cross section is approximate and is useful in many engineering studies. It is applicable only for the case of a convex shaped conducting object having arbitrary two dimensional cross section with arbitrary edges and corners. Canonical scattering objects, such as a triangular shaped scatterer and a thin strip scatterer are analyzed for the transverse magnetic excitation to evaluate usefulness of the analytical results reported in this paper. Numerical data for the monostatic as well as the bistatic radar cross section are also presented by comparing them with respect to the numerical solution obtained by solving an electric field integral equation based on the method of moments technique.

## I. INTRODUCTION

THERE exist numerous analytical and numerical approaches for analyzing the electromagnetic scattering by a perfectly conducting object [1]–[7]. Generally, the formulation of the scattering problem is accomplished in terms of either a differential equation or an integral equation by treating it as a boundary value problem. The analytical approach is limited in its application to canonical objects, and for analyzing practical scattering geometries the numerical approaches based on the matrix method [3], the finite element or the finite difference method [7] are widely used. Even though many analytical and numerical methods are widely reported [2], [7] in the literature for various class of material and scattering geometries, still in many engineering applica-

tions involving electromagnetic scattering studies, there exists a need for simple analytical tools for the induced electric current and the corresponding radar cross section of arbitrary shaped conducting object. The purpose of this paper is to report a possible approach to obtain simple and approximate solution (yet form an useful tool for many engineering applications) of the electromagnetic scattering by a perfectly conducting object having arbitrary edges and corners. The study reported in the following section is limited to the two-dimensional scattering object placed in a free space medium which is excited by a time harmonic plane wave having transverse magnetic (TM) polarization. The analysis is accomplished by invoking the on-surface radiation condition (OSRC) theory [8]. It can be noted that the OSRC approach basically utilizes an additional boundary relationship for the normal derivative of the scattered electric field which is proportional to the scattered magnetic field by implementing, in a limit, a higher order near field radiation boundary condition [9], [10] directly on the surface of scattering object. In fact, for the study of scattering by two-dimensional convex conducting object, the OSRC has exposed [11], [14] substantial simplification of the usual integral equation for the induced surface electric current distribution, and it is interesting to note that elaborate numerical approaches are no longer required.

A preliminary OSRC study using the first- and second-order operators is reported in [8] for the electromagnetic scattering by a two-dimensional circular conducting scatterer for TM and transverse electric (TE) plane wave excitations. The validation data for the induced surface current and the bistatic radar cross section with the application of second-order OSRC operator show agreement in the illuminated region for both the TM and TE excitations. But the results are inconclusive with respect to very low level field distribution in the deep shadow region for the TM excitation, and similarly, are inconclusive to predict creeping wave fields deep in the shadow region for the TE excitation. In fact, using the third and fourth higher order OSRC operators a detailed study is assessed in [14] for the OSRC analysis of scattering by a circular conducting object for both TM and TE excitations. Even though a third- or a fourth-order differential equation is to be solved for the application of higher order OSRC operators, the investigation [14] predicts the distribution of

Manuscript received January 10, 1990; revised August 12, 1991. This work was supported in part by Office of Naval Research (ONR) grant N00014-88-K-0475 and by National Science Foundation (NSF) Grant ASC-8811273.

K. Umashankar and W. Chun are with the Department of Electrical Engineering and Computer Science, University of Illinois, Chicago, IL 60680.

A. Taflove is with the Department of Electrical Engineering and Computer Science, McCormick School of Engineering, Northwestern University, Evanston, IL 60208.

IEEE Log Number 9104567.

low level fields with the TM excitation, and similarly, predicts behavior of creeping wave fields deep in the shadow region with the TE excitation. In a separate study, the application of second-order OSRC is also extended for the analysis of electromagnetic scattering and penetration by a homogeneous convex dielectric object [11], [12]. Further, in the OSRC study reported in [8] for the cases of thin strip and square scatterer, the dominant effect of the singular electric currents at the geometric corners are not considered, but only the physical optics type currents are taken into account in the calculation of radar cross section.

For considering application to engineering oriented problems, this paper presents a simple and approximate analysis to include the additional effects due to radiation from the sharp corners [4], [6], [14] so that arbitrary cross-sectional convex geometries consisting of arbitrary edges and corners can be systematically analyzed. For the scattering geometries considered, it is shown that the second-order OSRC result for the induced electric current has a some relevance to the electric currents of the physical theory of diffraction. Two canonical conducting objects, such as a triangular shaped scatterer and a thin strip scatterer are analyzed for the plane wave excitation with TM polarization to evaluate the simple and approximate analytical results reported in this paper. Comparative data for the monostatic as well as the bistatic radar cross section are also presented by comparing the second-order OSRC results with respect to the numerical solution obtained by solving the electric field integral equation based on the method of moments technique [3]. Similar analytical study [14] can also be considered for a plane wave excitation with TE polarization, and is reported separately.

## II. FORMULATION—TM POLARIZATION

Let us consider a two-dimensional, convex, conducting scatterer having an arbitrary cross section with arbitrary edges and corners. It is excited normally by a TM polarized plane wave as shown in Fig. 1. The scatterer is assumed to be uniform in  $z$  coordinate direction and the various electric and magnetic field quantities are independent of the  $z$  coordinate variation. The cross section of the arbitrary conducting scatterer is contained in region 2 and is bounded by a contour  $C_s$ . Outside region 2 is region 1 representing an isotropic free space medium. Referring to Fig. 1, let

$(E_z^s, \bar{H}^s)$ : scattered electric and magnetic fields in region 1  
 $(E_z^i, \bar{H}^i)$ : incident electric and magnetic fields in region 1.

For the TM polarized excitation, the  $z$  component of the incident plane wave electric field can be written as

$$E_z^i(\rho, \phi) = E_0 e^{-jk\rho \cos(\phi - \phi^i)} \quad (1)$$

where

$k$ : propagation constant of the free space medium

$\phi^i$ : incident angle of the exciting TM plane wave.

Further, the  $z$  component of scattered electric field [1], [2] in the regions 1 is obtained by

$$E_z^s(\bar{\rho}) = \oint_{C_s} [\mathcal{J}(\bar{\rho}, \bar{\rho}') + \mathcal{J}(\bar{\rho}, \bar{\rho}')] ds' \quad (2a)$$

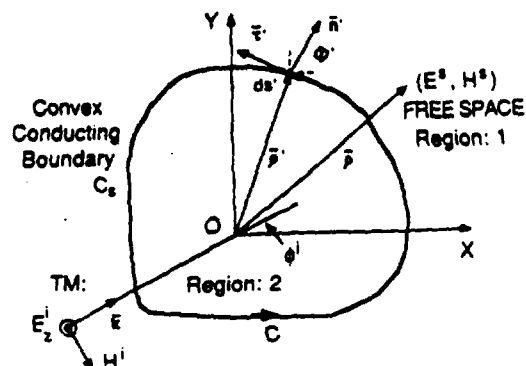


Fig. 1. Two-dimensional arbitrary shaped convex conducting scatterer—TM excitation.

$$\mathcal{J}(\bar{\rho}, \bar{\rho}') = G(\bar{\rho}, \bar{\rho}') \frac{\partial E_z^s(\bar{\rho}')}{\partial n'} \quad (2b)$$

$$\mathcal{J}(\bar{\rho}, \bar{\rho}') = -E_z^s(\bar{\rho}') \frac{\partial G(\bar{\rho}, \bar{\rho}')}{\partial n'} \quad (2c)$$

where the two-dimensional Green's function

$$G(\bar{\rho}, \bar{\rho}') = \frac{1}{4j} H_0^{(2)}(k|\bar{\rho} - \bar{\rho}'|). \quad (2d)$$

$H_0^{(2)}$  is the Hankel function of second kind and zero order

On the scatterer boundary contour  $C_s$ ,  $n'$  and  $s'$  represent the normal and the tangential variables along the corresponding unit vectors given by

$$\hat{n}' = \hat{x}' \cos \Phi' + \hat{y}' \sin \Phi' \quad (3a)$$

$$\hat{s}' = -\hat{x}' \sin \Phi' + \hat{y}' \cos \Phi'. \quad (3b)$$

$\Phi'$  is the angle of the normal unit vector with respect to  $x$  coordinate axis

On referring to (2a), the scattered electric field at any point outside the conducting scatterer can be calculated, if the scattered electric field and the normal derivative of the scattered electric field are known along the boundary contour  $C_s$ . To determine these two unknown field quantities, the following two near-field boundary relationships are utilized. The relationship for the scattered electric field is obtained by enforcing the regular conducting boundary condition that the tangential  $z$  component of the total electric field is equal to zero on the boundary contour  $C_s$

$$E_z^s(\bar{\rho}') = -E_z^i(\bar{\rho}'), \quad \bar{\rho}' \text{ on } C_s. \quad (4)$$

The relationship for the normal derivative of scattered electric field is obtained by (invoking directly on the boundary contour  $C_s$ ) the second-order on-surface radiation boundary condition [8], [10], [14] for the outgoing scattered cylindrical waves. According to the OSRC approach [8], the axial component of the scattered electric field at a radial distance  $\rho$  should satisfy the following outgoing radiation boundary condition in terms of radial coordinate variables

$$\begin{aligned} \mathcal{B}_2 E_z^s = & -\frac{1}{\rho^2} \frac{\partial^2}{\partial \phi^2} E_z^s + \left[ 2jk + \frac{2}{\rho} \right] \frac{\partial}{\partial \rho} E_z^s \\ & + \left[ -2k^2 + \frac{3jk}{\rho} + \frac{3}{4\rho^2} \right] E_z^s = O(\rho^{-9/2}). \end{aligned} \quad (5a)$$

The above second-order OSRC boundary operator yields a relationship for the normal derivative of scattered electric field on the conducting scatterer and is given by

$$\frac{\partial E_z^s(\vec{\rho})}{\partial n'} = \left[ \frac{\xi(s')}{2} + jk + \frac{j\xi^2(s')}{8[k - j\xi(s')]} \right] E_z^i(\vec{\rho}) + \frac{j}{2[k - j\xi(s')]} \frac{\partial^2 E_z^i(\vec{\rho})}{\partial s'^2}. \quad (5b)$$

$\xi(s')$  is the curvature of the osculating circle at location  $s'$  on contour  $C_r$ ,

$$\frac{\partial^2 E_z^i(\vec{\rho})}{\partial s'^2} = -k^2 [\sin^2 \Phi' \cos^2 \phi' + \cos^2 \Phi' \sin^2 \phi' - 2 \sin \Phi' \cos \Phi' \cos \phi' \sin \phi'] E_z^i(\vec{\rho}). \quad (5c)$$

The two boundary conditions (4) and (5b) for the scattered electric field and its normal derivative on the contour  $C_r$  are now substituted into expressions (2b) and (2c), and the scattered electric near-field distribution in region 1, expression (2a), can be calculated for a given arbitrary boundary contour  $C_r$ . Further, for the case of TM excitation, the  $z$  directed induced electric current on the conducting scatterer is directly proportional to the normal derivative of the total electric field and is given by

$$J_z(\vec{\rho}) = \frac{-j}{\eta k} \left[ \frac{\partial E_z^s(\vec{\rho})}{\partial n'} + \frac{\partial E_z^i(\vec{\rho})}{\partial n'} \right] \quad (6)$$

where  $\eta$  is the intrinsic impedance of region 1. The far-field distribution can also be derived using the expression (2a) with the two-dimensional Green's function term (2d) replaced with its large argument approximation.

### III. CONDUCTING TRIANGULAR SCATTERER

To illustrate a procedure to analyze an arbitrary convex conducting scatterer with edges and corners, and to obtain a simple analytical solution by performing the integration along the close boundary contour  $C_r$ , a triangular scattering geometry of Fig. 2, with three straight edges and three wedge type corners is considered. At the sharp corners, there exists a geometrical discontinuity and thus the curvature of the osculating circle for the corner region is undefined. In order to overcome this difficulty, the sharp corners of the scattering geometry are rounded off [13], [14] by smooth contours, for example, small circular regions are inserted with a limiting radius  $\epsilon$  and centered at the corners. A virtual boundary contour  $C_v$  is now drawn enclosing the conducting scatterer such that it is always parallel to the original boundary contour  $C_r$  and is also drawn tangential to each of the small limiting circles located at the geometrical sharp corners as shown in Fig. 2. In a limit as the radius  $\epsilon$  tends to zero, the virtual boundary contour  $C_v$  exactly coincides with the original boundary contour  $C_r$  of the conducting scattering object. On referring to expression (2) and Fig. 2, the  $z$  component of scattered electric field at any point in the region 1 is given by

$$E_z^s(\vec{\rho}) = \lim_{\epsilon \rightarrow 0} \oint_{C_v} [\mathcal{S}(\vec{\rho}, \vec{\rho}') + \mathcal{J}(\vec{\rho}, \vec{\rho}')] ds'. \quad (7)$$

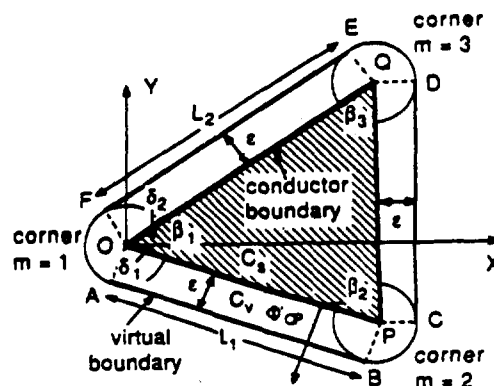


Fig. 2. Geometry of triangular conducting scatterer—TM excitation.

$C_r$  are contour segments  $FA + AB + BC + CD + DE + EF$  where the virtual contour  $C_v$  enclosing the triangular scatterer, is split into six segments. The terms in integrand of the integral expression (7) are completely known in terms of the geometrical parameters of the scattering object and the plane wave incident field. Since the radius of the limiting circle located around the corners,  $m = 1, 2$ , and  $3$ , is very small and in a limit tends to zero, it is assumed that the integrand of (7) does not vary along the arc length of the limiting circle. Hence, the integral expression for the scattered electric field distribution in region 1 simplifies to the sum of two specific terms consisting of the three smooth edge contributions and the three corner contributions with explicit dependence on the angle of incidence of TM plane wave excitation, and is given by

$$E_z^s(\vec{\rho}) = \left[ \int_{OP} + \int_{PQ} + \int_{QO} \right] [\mathcal{S}(\vec{\rho}, \vec{\rho}') + \mathcal{J}(\vec{\rho}, \vec{\rho}')] ds' + \sum_{m=1}^3 \frac{3E_0}{32j} (\pi - \beta_m) H_0^{(2)} \cdot (k|\vec{\rho} - \vec{\rho}'_m|) e^{-jk\rho'_m \cos(\phi'_m - \phi)}. \quad (8)$$

By taking the large argument approximation for the Green's function (2d), expression (8) can be conveniently simplified to obtain an analytical solution for the scattered electric far field distribution. Hence, in the far-field region, (8) yields

$$E_z^s(\rho, \phi) = \frac{e^{-j\pi/4}}{\sqrt{8\pi k}} \left[ A_0 + \sum_{m=1}^3 C_m \right] E_0 \frac{e^{-jk\rho}}{\sqrt{\rho}} \quad (9a)$$

$$A_0 = \left[ \int_{OP} + \int_{PQ} + \int_{QO} \right] \cdot \left[ \frac{\partial E_z^s(\vec{\rho}')}{\partial n'} + jk \cos(\phi - \Phi') E_z^i(\vec{\rho}') \right] \cdot e^{jk\rho' \cos(\phi - \Phi')} ds' \quad (9b)$$

$$= jk \{ T_{OP} + \cos(\phi - \Phi'_{OP}) \} \left[ \frac{e^{j\gamma_{OP} L_1} - 1}{j\gamma_{OP}} \right] + jk \{ T_{PQ} + \cos(\phi - \Phi'_{PQ}) \} \cdot \left[ \frac{e^{j\gamma_{PQ} L_2 \sin \delta_2} - e^{-j\gamma_{PQ} L_1 \sin \delta_1}}{j\gamma_{PQ}} \right] e^{j\alpha_{PQ} L_1}$$

$$+jk\{T_{QO} + \cos(\phi - \phi'_{QO})\} \cdot \left[ \frac{1 - e^{-j\gamma_{QO}L_1}}{j\gamma_{QO}} \right] \quad (9c)$$

and

$$C_m = \frac{3}{8}(\pi - \beta_m) e^{-jk\rho'_m[\cos(\phi'_m - \phi') - \cos(\phi'_m - \phi)]} \quad (9d)$$

where the various angular terms are given by

$$T_{OP} = 1 - \frac{1}{2} \{ \sin^2 \phi'_{OP} \cos^2 \phi' + \cos^2 \phi'_{OP} \sin^2 \phi' - 2 \sin \phi'_{OP} \cos \phi'_{OP} \cos \phi' \sin \phi' \} \quad (10a)$$

$$\gamma_{OP} = k[-\cos(\phi'_{OP} - \phi') + \cos(\phi'_{OP} - \phi)] \quad (10b)$$

$$T_{PQ} = 1 - \frac{1}{2} \sin^2 \phi' \quad (11a)$$

$$\gamma_{PQ} = k[-\sin \phi' + \sin \phi] \quad (11b)$$

$$\alpha_{PQ} = k[-\cos \phi' + \cos \phi] \cos \delta_1 \quad (11c)$$

$$T_{QO} = 1 - \frac{1}{2} \{ \sin^2 \phi'_{QO} \cos^2 \phi' + \cos^2 \phi'_{QO} \sin^2 \phi' - 2 \sin \phi'_{QO} \cos \phi'_{QO} \cos \phi' \sin \phi' \} \quad (12a)$$

$$\gamma_{QO} = k[\cos(\phi'_{QO} - \phi') - \cos(\phi'_{QO} - \phi)] \quad (12b)$$

The radar cross section of the conducting triangular scatterer can now be calculated using the far-field expression (9a)

$$RCS = \lim_{\rho \rightarrow \infty} 2\pi\rho \left| \frac{E_z^s(\phi)}{E_z^i(\phi)} \right|^2 \quad (13)$$

Similar to the treatment in physical theory of diffraction [4], [6], the scattered electric field distribution can be viewed as the contribution from the induced electric currents on the triangular shaped conducting scatterer. It consists of the contribution due to currents on the three smooth edges and the localized currents due to the three corner effects. As can be seen, the distribution of the electric current due to corner effects is only approximate. In the context of presenting a simple and an approximate analytical solution, the corner effects are considered only due to the dominant curvature effect, but the remaining minor contribution [15] due to slope of the radius of curvature is excluded. The  $z$  directed induced electric current distribution at any point along the triangular edge  $OP$  is given by

$$J_z(\vec{\rho}') = J_z(\vec{\rho}')|_{\text{edge effect}} + J_z(\vec{\rho}')|_{\text{corners}}, \quad \vec{\rho}' \text{ on } OP. \quad (14a)$$

Using (1), (5b), and (6), the electric current due to edge effect is given by

$$J_z(\vec{\rho}')|_{\text{edge } OP} = \frac{-j}{\eta k} \left[ \frac{\partial E_z^i(\vec{\rho}')}{\partial n'} + \frac{\partial E_z^i(\vec{\rho}')}{\partial n'} \right], \quad \vec{\rho}' \text{ on } OP \quad (14b)$$

$$= \frac{1}{\eta} \left[ 1 - \frac{1}{2} \{ \sin^2 \phi'_{OP} \cos^2 \phi' + \cos^2 \phi'_{OP} \sin^2 \phi' - 2 \sin \phi'_{OP} \cos \phi'_{OP} \cos \phi' \sin \phi' \} - \cos(\phi'_{OP} - \phi') \right] E_z^i(\vec{\rho}_{OP}). \quad (14c)$$

Further, in (8), the scattered electric field distribution due to the three wedge type corners can be viewed as the contribution due to the localized electric current distributions which principally exist at the three corners  $m = 1, 2$ , and  $3$  of the scatterer in the form of isolated line sources with weighted amplitudes corresponding to the internal wedge angle  $\beta_m$  and the angle of TM incident excitation.

Based on (9a) and (13), Fig. 3(a) shows the monostatic radar cross section in decibels for the case of a perfectly conducting triangular scatterer as a function of monostatic angle  $\phi = \pi + \phi'$ . For the triangular scatterer, the dimensions are selected as  $kL_1 = kL_2 = 10$  and the angle  $\beta_1 = \pi/3$  which corresponds to an equilateral triangular scatterer. The OSRC result for the radar cross section shown in Fig. 3(a) is also compared with an alternative numerical solution obtained based on the electric field integral equation [3] for a two-dimensional conducting scatterer. The electric field integral equation is solved using the method of moments numerical scheme with a resolution of 20 pulse samples for every half-wavelength. Two types of monostatic comparison data are presented in Fig. 3(a). If the three corner effects are excluded, the comparison between OSRC and integral equation monostatic data is poor for certain incident angles. With the three corner effects included, a better comparison is obtained for various excitation angles including broadside and grazing angles of incidence. Similarly, Fig. 3(b) shows comparative result for the bistatic radar cross section in decibels for the same triangular scatterer with broad side excitation on one edge.

#### IV. CONDUCTING THIN STRIP SCATTERER

In order to illustrate further the application of the integral expression (7) and to obtain a simple analytical solution by performing the integration along the close boundary contour  $C_s$ , a thin strip scattering geometry of Fig. 4 with one straight edge and two corners is considered. Again, the two sharp corners of the thin strip scattering geometry are rounded off [13], [14] by inserting small circular regions with a limiting radius  $\epsilon$  and centered at the corners. A virtual boundary contour  $C_v$  is now drawn enclosing the thin strip scatterer such that it is always parallel to the original boundary contour  $C_s$  and is also drawn tangential to each of the small limiting circles. Referring to the Fig. 4, in a limit as the radius  $\epsilon$  tends to zero, the virtual boundary contour  $C_v$  exactly coincides with the original boundary contour  $C_s$  of the scattering object. Now, the axial component of scattered electric field at any point in region 1 is given by

$$E_z^s(\vec{\rho}) = \lim_{\epsilon \rightarrow 0} \oint_{C_v} [\mathcal{S}(\vec{\rho}, \vec{\rho}') + \mathcal{J}(\vec{\rho}, \vec{\rho}')] ds'. \quad (15)$$

$C_v$  are contour segments  $DA + AB + BC + CD$  and where the virtual contour  $C_v$  enclosing the thin strip scatterer, is

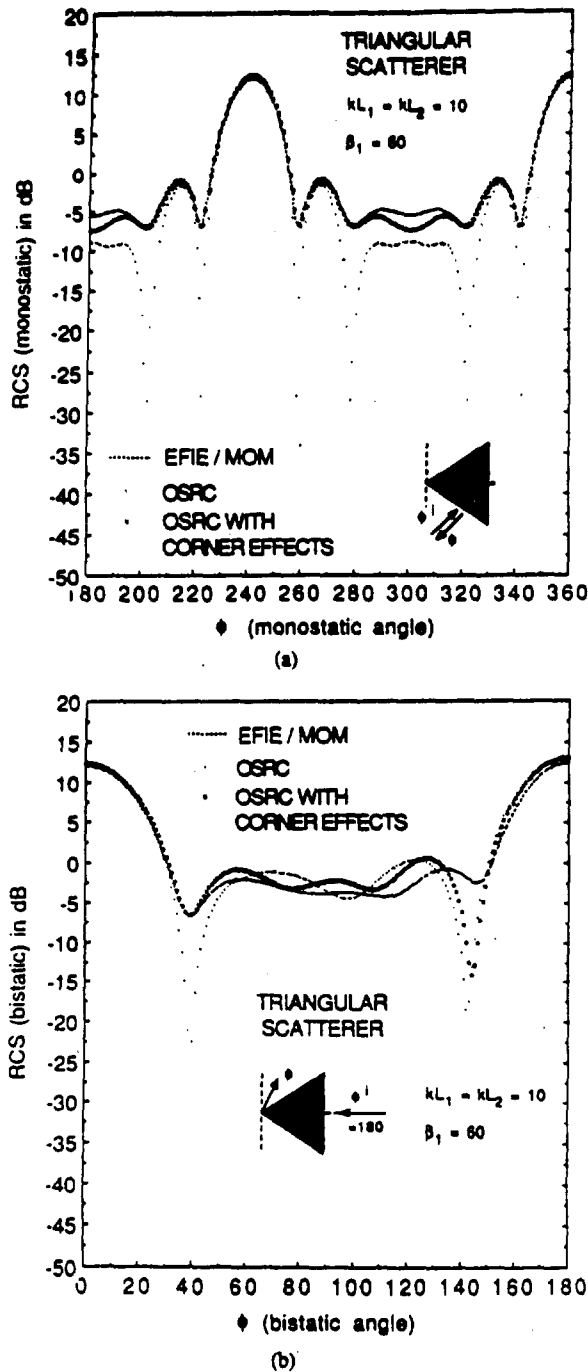


Fig. 3. Monostatic radar cross section of triangular conducting scatterer using second-order OSRC—TM excitation. (b) Bistatic radar cross section of triangular conducting scatterer using second-order OSRC—TM excitation,  $\phi' = 180$ .

split into four segments. The terms in integrand of the integral expression (15) are completely known in terms of the geometrical parameters of the thin strip and the plane wave incident field. Since the radius of the limiting circle located around a corner is very small and in a limit tends to zero, again it is assumed that the integrands of (15) do not vary along the arc length of the limiting circle. Hence, the integral expression for the scattered electric field distribution in region 1 simplifies to the sum of two specific terms consisting of the smooth edge contribution and the two corner contribu-

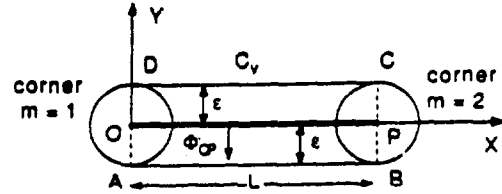


Fig. 4. Geometry of thin strip conducting scatterer—TM excitation.

tions,  $m = 1$  and  $2$ , and is given by

$$E_z^s(\bar{\rho}) = \left[ \int_{OP} + \int_{PO} \right] [\mathcal{S}(\bar{\rho}, \bar{\rho}') + \mathcal{J}(\bar{\rho}, \bar{\rho}')] ds' + \frac{3E_0}{32j} \pi H_0^{(2)}(k\rho) + \frac{3E_0}{32j} \pi H_0^{(2)}(k|\bar{\rho} - \bar{\rho}_2|) e^{-jkL \cos \phi'}. \quad (16)$$

By taking the large argument approximation for the Green's function (2d), (16) can be conveniently simplified to obtain an analytical solution for the scattered electric far field distribution. Hence, in the far-field region, (16) yields

$$E_z^s(\rho, \phi) \sim \frac{e^{-j\pi/4}}{\sqrt{8\pi k}} [A_0 + C_1 + C_2] E_0 \frac{e^{-jk\rho}}{\sqrt{\rho}} \quad (17a)$$

$$A_0 = \left[ \int_{OP} + \int_{PO} \right] \cdot \left[ \frac{\partial E_z^s(\bar{\rho}')}{\partial n'} + jk \cos(\phi - \phi') E_z^s(\bar{\rho}') \right] \cdot e^{jk\rho' \cos(\phi - \phi')} ds' \quad (17b)$$

$$= jk \{ T_{OP} - \sin \phi \} \left[ \frac{e^{j\gamma_{OP}L} - 1}{j\gamma_{OP}} \right] + jk \{ T_{PO} + \sin \phi \} \left[ \frac{1 - e^{-j\gamma_{PO}L}}{j\gamma_{PO}} \right] \quad (17c)$$

and

$$C_1 = \frac{3}{8} \pi \quad (17d)$$

$$C_2 = \frac{3}{8} \pi e^{-jkL[\cos \phi' - \cos \phi]} \quad (17e)$$

where the various angular terms are given by

$$T_{OP} = 1 - \frac{1}{2} \cos^2 \phi' \quad (18a)$$

$$\gamma_{OP} = k[-\cos \phi' + \cos \phi] \quad (18b)$$

$$T_{PO} = 1 - \frac{1}{2} \cos^2 \phi' \quad (19a)$$

$$\gamma_{PO} = k[\cos \phi' - \cos \phi]. \quad (19b)$$

The radar cross section of the conducting thin strip scatterer can now be calculated using (13). A similar monostatic radar cross section result is also reported in [13] using elliptic

coordinates where the virtual contour  $C_v$  is selected as an elliptic boundary and the thin strip scatterer is simulated by taking the limit as the minor axis of the ellipse tending to zero and the major axis tending to length of the thin strip scatterer. It is interesting to note that the analytical result obtained in this section for the thin strip scatterer also can be verified based on the analytical result of the triangular scatterer, (8)–(12), by substituting the side lengths  $L_1 = L_2 = L$ , the angles  $\delta_1 = 0$  and  $\delta_2 = 0$ . The  $z$  directed induced electric current distribution at any point on the strip is given by

$$J_z(\vec{\rho}') = \{J_{z-}(\vec{\rho}') - J_{z+}(\vec{\rho}')\} |_{\text{edge effect}} + J_z(\vec{\rho}') |_{\text{corners}} \quad (20a)$$

$\vec{\rho}'$  on strip.

Again, the scattered electric field distribution can be viewed as the contribution from the induced electric currents on the thin strip conducting scatterer. It consists of the contribution due to currents on two sides of the smooth edge and the currents due to the two corner effects. As discussed earlier, in the context of presenting a simple and an approximate analytical solution, the corner effects are considered only due to the dominant curvature effect, but the remaining minor contribution [15] due to slope of the radius of curvature is excluded. Using (1), (5b), and (6), the electric current distribution on the thin strip scatterer is calculated as the difference between the induced current on the bottom contour AB and the top contour CD in a limit as  $\epsilon$  tends to zero, and is given by

$$J_z(\rho') |_{\text{edge OP}} = \frac{-j}{\eta k} \left[ \frac{\partial E_z^s(\vec{\rho}')}{\partial n'} + \frac{\partial E_z^i(\vec{\rho}')}{\partial n'} \right],$$

$\vec{\rho}'$  on  $OA_{z-} + OA_{z+}$

$$= \frac{2E_0}{\eta} \sin \phi' e^{-jk\rho' \cos \phi'}. \quad (20b)$$

In (16), the scattered electric field distribution due to the two wedge type corners can be viewed as the contribution due to the electric current distribution which principally exists at the two corners  $m = 1$  and  $2$  of the scatterer in the form of isolated line sources with weighted amplitudes corresponding to the internal wedge angles and the angle of TM incident excitation. Based on (13) and (17a), Fig. 5(a) shows the monostatic radar cross section in decibels for the case of a perfectly conducting thin strip scatterer as a function of monostatic angle  $\phi = \pi + \phi'$ . The dimension of the strip scatterer is selected as  $kL = 10$  and the angle  $\beta_1 = 0$ . The OSRC result for the radar cross section shown in the Fig. 5(a) is also compared with the numerical solution obtained based on the electric field integral equation [3]. The electric field integral equation is solved using the method of moments numerical scheme with a resolution of 20 pulse samples for every half-wavelength. Two types of monostatic comparison data are presented in Fig. 5(a). If the two corner effects are excluded, the comparison between OSRC and integral equation monostatic data is poor for certain incident angles. With the two corner effects included, a better comparison is obtained for various excitation angles including broadside and grazing angles of incidence. Similarly, Fig. 5(b) shows com-

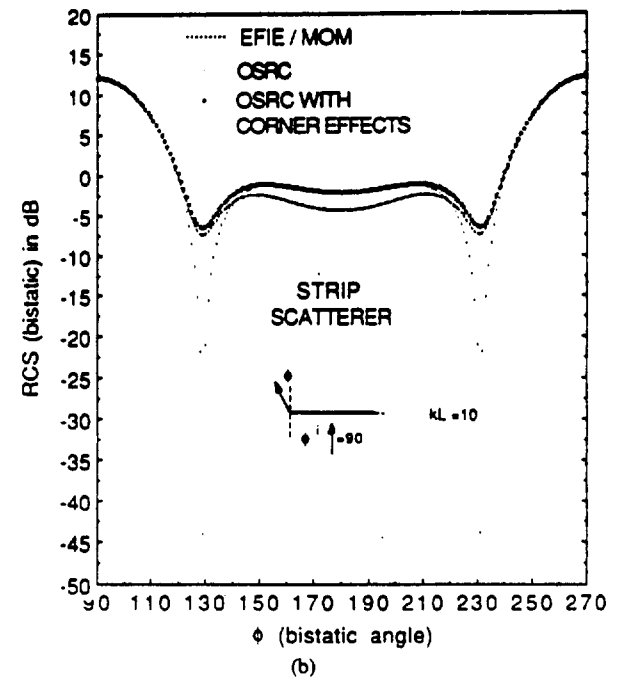
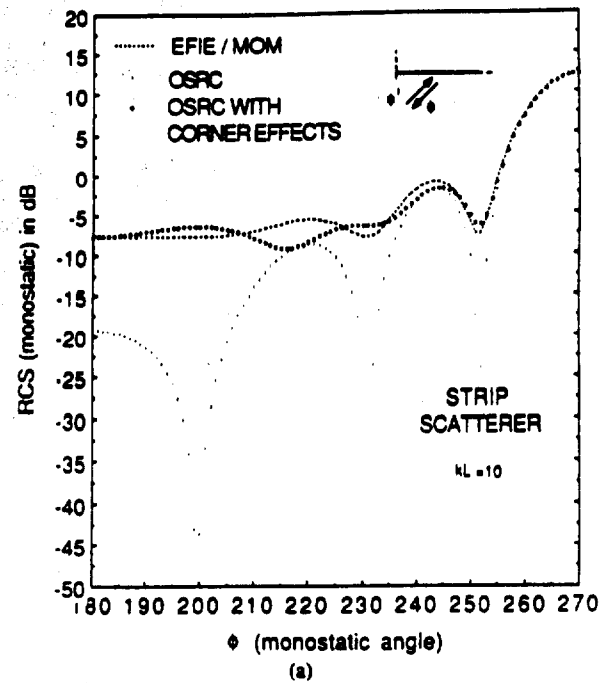


Fig. 5. Monostatic radar cross section of thin strip conducting scatterer using second-order OSRC—TM excitation. (b) Bistatic radar cross section of thin strip conducting scatterer using second-order OSRC—TM excitation,  $\phi' = 90$ .

parative result for the bistatic radar cross section in decibels for the same thin strip scatterer with broad side excitation.

## V. CONCLUSION

With engineering applications in mind, this paper presented a simple and an approximate analytical solution for the analysis of electromagnetic scattering by a perfectly conducting two dimensional object by invoking on-surface radiation condition theory. The close form analytical result for the induced electric current distribution and the radar cross sec-

tion is applicable to the case of a convex conducting object having two dimensional cross section with arbitrary edges and corners. Canonical scattering objects, such as, a triangular shaped scatterer and a thin strip scatterer are analyzed, and numerical data concerning both the monostatic and the bistatic radar cross section for the transverse magnetic excitation are presented with comparison to assess usefulness of the results. Similar study of the two dimensional conducting scatterer is also undertaken for the transverse electric excitation and is reported separately.

#### ACKNOWLEDGMENT

The authors wish to thank Dr. Arthur Jordan of NRL for helpful discussion during the course of this investigation.

#### REFERENCES

- [1] J. Bowman, T. B. A. Senior, and P. L. E. Uslenghi, *Electromagnetic and Acoustic Scattering by Simple Shapes*. Amsterdam: North Holland, 1969.
- [2] A. J. Poggio and E. K. Miller, "Integral equation solutions of three-dimensional scattering problems," in *Computer Techniques for Electromagnetics*, R. Mittra, Ed. Elmsford, NY: Pergamon, 1973.
- [3] K. Umashankar, "Numerical analysis of electromagnetic wave scattering and interaction based on frequency-domain integral equation and method of moments techniques," *Wave Motion*, no. 10, pp. 493-525, Dec. 1988.
- [4] R. G. Kouyoumijan, "Asymptotic high-frequency methods," *Proc. IEEE*, vol. 53, pp. 864-876, Aug. 1965.
- [5] R. C. Hansen, Ed., "Geometric theory of diffraction," Selected Preprint Series, IEEE Press, 1981.
- [6] R. G. Kouyoumijan and P. H. Pathak, "A uniform geometrical theory of diffraction of an edge in a perfectly conducting surface," *Proc. IEEE*, vol. 62, pp. 1448-1461, Nov. 1974.
- [7] A. Taflové and K. Umashankar, "Review of FD-TD Numerical Modeling of Electromagnetic Wave Scattering and Radar Cross Section," *Proc. IEEE*, Special Issue on Radar Cross Section, vol. 77, pp. 682-699, May 1989.
- [8] G. A. Kriegsmann, A. Taflové, and K. Umashankar, "A new formulation of electromagnetic wave scattering using an on-surface radiation boundary condition," *IEEE Trans. Antennas Propagat.*, vol. AP-35, pp. 153-161, 1987.
- [9] A. Bayliss and E. Turkel, "Radiation boundary conditions for wave-like equations," *Commun. Pure Appl. Math.*, vol. 33, pp. 707-725, 1980.
- [10] T. G. Moore, J. G. Blaschak, A. Taflové, and G. A. Kriegsmann, "Theory and application of radiation boundary operators," *IEEE Trans. Antennas Propagat.*, vol. 36, pp. 1797-1812, Dec. 1988.
- [11] S. Arendt, K. Umashankar, A. Taflové, and G. A. Kriegsmann, "Extension of on-surface radiation condition theory to scattering by two-dimensional homogeneous dielectric objects," *IEEE Trans. Antennas Propagat.*, vol. 38, pp. 1551-1558, Oct. 1990.
- [12] S. Arendt, "Application of the on-surface radiation condition method to two dimensional electromagnetic scattering problems," M.S. thesis, Univ. of Illinois, Chicago, IL, Apr. 1988.
- [13] I. D. King, "Application of on-surface radiation condition to electromagnetic scattering by conducting strip," *Electron. Lett.*, vol. 25, no. 1, pp. 56-57, Jan. 1989.
- [14] K. Umashankar and W. Chun, "Investigation of the on-surface boundary operators for electromagnetic scattering by conducting object," Tech. Rep. Office of Naval Research (ONR) under Grant N00014-88-K-0475, June 1991.
- [15] D. S. Jones, "Surface radiation conditions," *J.I.M.A.*, vol. 41, pp. 21-29, 1988.

Korada Umashankar (S'69-M'75-SM'81), for a photograph and biography please see page 1212 of the August 1991 issue of this TRANSACTIONS.



Wan Chun (S'90) was born in Seoul, Korea. He received the B.S.E.E. degree from Korea University in 1980 and the M.S.E.E. degree from the University of Illinois, Chicago, in 1987, where he is currently working toward the Ph.D. degree.

Since 1987, he has been working as a Research Assistant in the Department of Electrical Engineering and Computer Science. His research interests are in the area of analytical and numerical methods for electromagnetic field scattering and interaction.

Allen Taflové (M'75-SM'84-F'90), for a photograph and biography please see page 906 of the July 1991 issue of this TRANSACTIONS.

# Direct time integration of Maxwell's equations in nonlinear dispersive media for propagation and scattering of femtosecond electromagnetic solitons

Peter M. Goorjian

National Aeronautics and Space Administration, Ames Research Center, Mail Stop 258-1, Moffett Field, California 94036

Allen Taflove

Department of Electrical Engineering and Computer Science, McCormick School of Engineering, Northwestern University, Evanston, Illinois 60208-3118

Received October 18, 1991

We report the initial results for femtosecond electromagnetic soliton propagation and collision obtained from first principles, i.e., by a direct time integration of Maxwell's equations. The time integration efficiently implements linear and nonlinear convolutions for the electric polarization and can take into account such quantum effects as Kerr and Raman interactions. The present approach is robust and should permit the modeling of two- and three-dimensional optical soliton propagation, scattering, and switching from the full-vector Maxwell's equations.

This Letter introduces a direct solution to Maxwell's vector-field equations suitable (in principle) for modeling the propagation and scattering of optical pulses, including solitons, in inhomogeneous nonlinear dispersive media. We believe that this approach will eventually provide a modeling capability for millimeter-scale integrated optical circuits beyond that of existing techniques that use the generalized nonlinear Schrödinger equation (GNLSE).

In Ref. 1, we discussed an efficient finite-difference time-domain (FD-TD) numerical approach for the direct time integration of Maxwell's equations to model linear media that have arbitrary-order chromatic dispersions. The approach was based on a suggestion by Jackson<sup>2</sup> to relate  $D(t)$  to  $E(t)$  with an ordinary differential equation in time integrated concurrently with the Maxwell equations. In this manner, we computed reflection coefficients accurate to better than 6 parts in 10,000 over the frequency range of dc to  $3 \times 10^{16}$  Hz for a single 0.2-fs Gaussian pulse incident upon a Lorentz half-space and obtained new results for the Sommerfeld and Brillouin precursors.

In this Letter, we report a generalization of the above to deal with the nonlinear terms of the electric polarization. The FD-TD direct time integration of Maxwell's equations can now incorporate nonlinear instantaneous and nonlinear dispersive effects as well as linear dispersive effects, thereby permitting the modeling of optical solitons that have large instantaneous bandwidths.

We again consider a one-dimensional problem with field components  $E_z$  and  $H_y$ , propagating in the  $x$  direction. Assuming that the medium is nonpermittable and isotropic, we see that Maxwell's equations in one dimension are written as

$$\frac{\partial H_y}{\partial t} = \frac{1}{\mu_0} \frac{\partial E_z}{\partial x}, \quad (1a)$$

$$\frac{\partial D_z}{\partial t} = \frac{\partial H_y}{\partial x}, \quad (1b)$$

$$E_z = \frac{D_z - (P_{zL} + P_{zNL})}{\epsilon_0}. \quad (1c)$$

Here we assume that the polarization consists of two parts: a linear part  $P_{zL}$  and a nonlinear part  $P_{zNL}$ .  $P_{zL}$  is given by a linear convolution of  $E_z(x, t)$  and the susceptibility function  $\chi^{(1)}$ ,

$$P_{zL}(x, t) = \epsilon_0 \int_{-\infty}^{\infty} \chi^{(1)}(t - t') E_z(x, t') dt', \quad (2a)$$

and  $P_{zNL}$  is given by a nonlinear convolution of  $E_z(x, t)$  and the third-order susceptibility  $\chi^{(3)}$ ,

$$P_{zNL}(x, t) = \epsilon_0 \int_{-\infty}^{\infty} \int_{-\infty}^{\infty} \int_{-\infty}^{\infty} \chi^{(3)}(t - t_1, t - t_2, t - t_3) \times E_z(x, t_1) E_z(x, t_2) E_z(x, t_3) dt_1 dt_2 dt_3. \quad (2b)$$

This provides the physics of a nonlinearity with time retardation or memory, i.e., a dispersive nonlinearity that can occur because of quantum effects in silica at time scales of 1–100 fs. Note that  $\chi^{(3)}$  may differ from  $\chi^{(1)}$  in physical properties such as resonances and dampings.

We consider a material having a Lorentz linear dispersion characterized by the following  $\chi^{(1)}$ :

$$\begin{aligned} \chi^{(1)}(t) &= \frac{\omega_p^2}{\omega_0} e^{-\gamma t/2} \sin \omega_0 t \\ &= F^{-1}[\chi^{(1)}(\omega)] \\ \rightarrow \epsilon(\omega) &= \epsilon_\infty + \frac{\omega_0^2(\epsilon_s - \epsilon_\infty)}{\omega_0^2 - j\delta\omega - \omega^2}, \end{aligned} \quad (3)$$



where  $\omega_p^2 = \omega_0^2(\epsilon_s - \epsilon_\infty)$  and  $\nu_0^2 = \omega_0^2 - \delta^2/4$ . Further, the material nonlinearity is assumed to be characterized by the nonlinear single time convolution for  $P_{NL}$ ,

$$P_{NL}(x, t) = \epsilon_0 \chi^{(3)} E_s(x, t)$$

$$\times \int_{-\infty}^{\infty} [\alpha \delta(t - t') + (1 - \alpha) g_R(t - t')] E_s^2(x, t') dt'. \quad (4)$$

Here  $\chi^{(3)}$  is the nonlinear coefficient,  $\delta(t)$  models Kerr nonresonant virtual electronic transitions on the order of about 1 fs or less,  $g_R(t) = [(\tau_1^2 + \tau_2^2)/\tau_1\tau_2] e^{-t/\tau_2} \sin(t/\tau_1)$  and models transient Raman scattering, and  $\alpha$  parameterizes the relative strengths of the Kerr and Raman interactions. Effectively,  $g_R(t)$  models a single Lorentzian line that is centered on the optical phonon frequency  $1/\tau_1$  and has a bandwidth of  $1/\tau_2$  (the reciprocal phonon lifetime).

We now describe a system of coupled nonlinear ordinary differential equations to characterize the physics of Eqs. (3) and (4). Assuming zero initial conditions at  $t = 0$ , we define the functions  $F(t)$  and  $G(t)$ , respectively, as the linear and nonlinear convolutions,

$$F(t) = \epsilon_0 \int_0^t \chi^{(1)}(t - t') E_s(x, t') dt', \quad (5)$$

$$G(t) = \epsilon_0 \int_0^t g_R(t - t') E_s^2(x, t') dt'. \quad (6)$$

Then,  $F$  and  $G$  satisfy the following coupled system of nonlinear ordinary differential equations:

$$\frac{1}{\omega_0^2} \frac{d^2 F}{dt^2} + \frac{\delta}{\omega_0^2} \frac{dF}{dt} + \left[ 1 + \frac{\epsilon_s - \epsilon_\infty}{\epsilon_\infty + \alpha \chi^{(3)} E^2} \right] F + \frac{(\epsilon_s - \epsilon_\infty)(1 - \alpha) \chi^{(3)} EG}{\epsilon_\infty + \alpha \chi^{(3)} E^2} = \frac{(\epsilon_s - \epsilon_\infty) D}{\epsilon_\infty + \alpha \chi^{(3)} E^2}, \quad (7)$$

$$\frac{1}{\bar{\omega}_0^2} \frac{d^2 G}{dt^2} + \frac{\bar{\delta}}{\bar{\omega}_0^2} \frac{dG}{dt} + \left[ 1 + \frac{(1 - \alpha) \chi^{(3)} E^2}{\epsilon_\infty + \alpha \chi^{(3)} E^2} \right] G + \frac{EF}{\epsilon_\infty + \alpha \chi^{(3)} E^2} = \frac{DE}{\epsilon_\infty + \alpha \chi^{(3)} E^2}, \quad (8)$$

where  $\bar{\delta} = 2/\tau_2$  and  $\bar{\omega}_0^2 = (1/\tau_1)^2 + (1/\tau_2)^2$ . Equations (7) and (8) are first solved simultaneously for  $F$  and  $G$  at the latest time step by using a second-order-accurate finite-difference scheme that operates on data for the current value of  $D$  and previous values of  $D$ ,  $E$ ,  $F$ , and  $G$ . Only two time levels of storage are required with this approach. Then, the latest value of  $E$  can be obtained by means of Newton's iteration of the following equation, using the new values of  $D$ ,  $F$ , and  $G$ :

$$E = \frac{D - F - (1 - \alpha) \chi^{(3)} EG}{\epsilon_0(\epsilon_\infty + \alpha \chi^{(3)} E^2)}. \quad (9)$$

The algorithm for the system of Eqs. (7), (8), and (9) is inserted to implement Eq. (1c). This, combined with the usual FD-TD realization of Eqs. (1a) and (1b),<sup>1</sup> makes up the complete solution method.

We now demonstrate the integration of Maxwell's equations to obtain soliton dynamics. A pulsed optical signal source is assumed to be located at  $x = 0$ . The pulse is assumed to have unity amplitude of its sinusoidal-carrier electric field, a carrier frequency

$f_c = 1.37 \times 10^{14}$  Hz ( $\omega_c = 8.61 \times 10^{14}$  rad/s), and a hyperbolic-secant envelope function with a characteristic time constant of 14.6 fs. Approximately seven cycles of the carrier are contained within the pulse envelope, and the center of the pulse coincides with a zero crossing of the sinusoid. To achieve soliton formation over short propagation spans of less than 200  $\mu\text{m}$ , we scale values of group-velocity dispersion  $\beta_2$  and nonlinear coefficient  $\chi^{(3)}$ . For example, let  $\epsilon_s = 5.25\epsilon_0$ ,  $\epsilon_\infty = 2.25\epsilon_0$ ,  $\omega_0 = 4.0 \times 10^{14}$  rad/s,  $\delta = 2.0 \times 10^8$  s<sup>-1</sup>,  $\chi^{(3)} = 7 \times 10^{-2}$  (V/m)<sup>-2</sup>,  $\alpha = 0.7$ ,  $\tau_1 = 12.2$  fs, and  $\tau_2 = 32$  fs. (The last three values are from Ref. 4.) This results in  $\beta_2$  varying widely over the spectral width of the pulse; i.e., from  $-7$  to  $-75$  ps<sup>2</sup>/m over the range  $(1.37 \pm 0.2) \times 10^{14}$  Hz. Finally, by choosing a uniform FD-TD space resolution of 5 nm ( $\approx \lambda_0/300$ ), the numerical phase velocity error is limited to approximately 1 part in  $10^5$ , small compared with that of the physical dispersions being modeled.

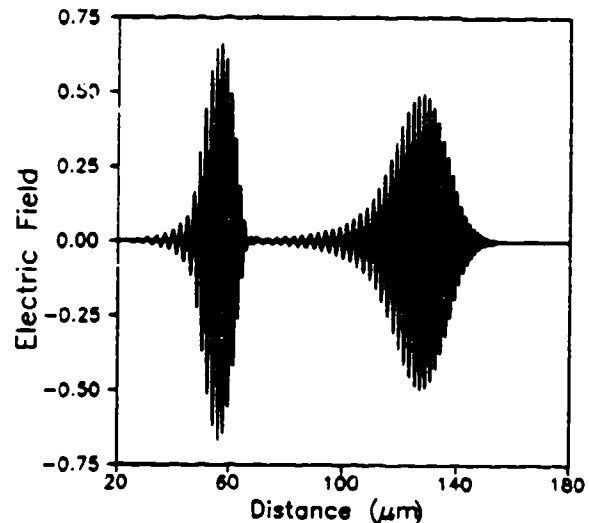


Fig. 1. Finite-difference time-domain results for the optical carrier pulse (linear case) after it has propagated 55  $\mu\text{m}$  and 126  $\mu\text{m}$  in the Lorentz medium.

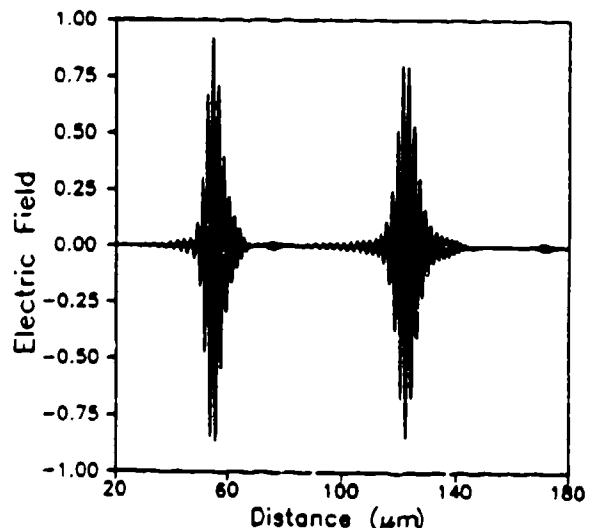


Fig. 2. Finite-difference time-domain results for the optical soliton carrier pulse that correspond to the observation locations of Fig. 1.

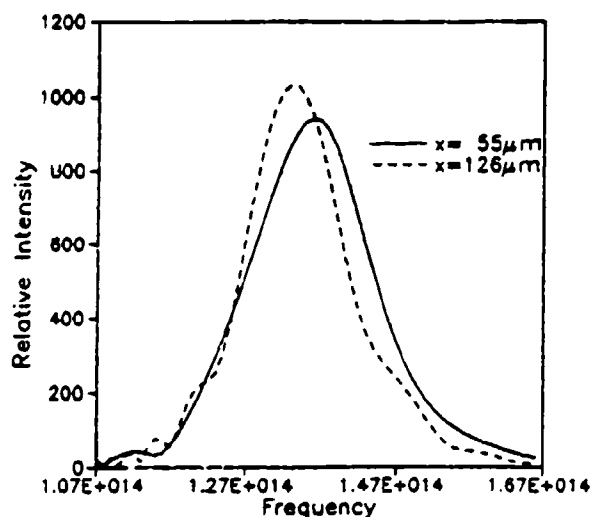


Fig. 3. Red shift of the Fourier spectrum of the main propagating soliton of Fig. 2.

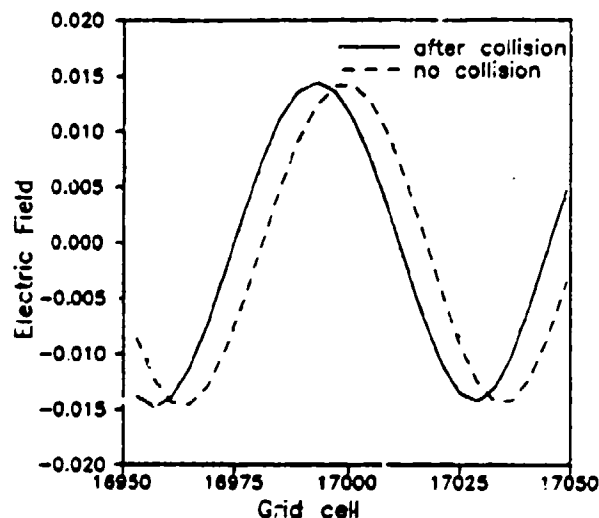


Fig. 4. Phase lag of the rightward-moving daughter soliton as a result of collisions with counterpropagating solitons.

Figure 1 depicts the FD-TD computed propagating pulse for the linear case [ $\chi^{(3)} = 0$ ] observed at  $n = 2 \times 10^4$  and  $4 \times 10^4$  time steps, corresponding to propagation to  $x = 55 \mu\text{m}$  and  $126 \mu\text{m}$ . Note pulse broadening, diminishing amplitude, and carrier frequency modulation ( $> f_c$  on the leading side and  $< f_c$  on the trailing side), which cause an asymmetrical shifting of the envelope, a higher-order dispersive effect. These qualitative features of the effect of anomalous dispersion have been predicted<sup>6</sup> but until now have not been computed by directly integrating Maxwell's equations.

In Fig. 2, we set  $\chi^{(3)} = 7 \times 10^{-2} (\text{V/m})^{-2}$ , which yields a soliton that retains its amplitude and width. However, a second, low-amplitude soliton is seen to move out and ahead of the main soliton. The carrier frequency of this daughter soliton is upshifted to  $\approx 4.9 \times 10^{14} \text{ Hz}$ , approximately 3.6 times that of the main soliton. From GNLSE theory, the appearance of the daughter soliton is predicted because of the assumed higher-order dispersive and nonlinear effects.<sup>2</sup> However, GNLSE theory does not easily

predict the carrier frequency shift that we have computed for this pulse. Also, in both cases depicted in Figs. 1 and 2, by observing a video of the pulse evolution, it was noted that the phase velocity of the carrier was substantially greater than the group velocity of the envelope.

Figure 3 depicts the Fourier spectrum of the main solitons shown in Fig. 2. The figure shows a 4-THz red shift and a sharpening of the spectrum as the pulse propagates. From GNLSE theory, the red shift is predicted because of the Raman effect's<sup>3,4</sup> occurring as a higher-order dispersive nonlinearity modeled by the function  $g_R(t)$  in the kernel of Eq. (4).

Last, we consider the collision of two counter-propagating solitons. They are identical and have all the parameters of the above case. As is characteristic of colliding solitons,<sup>6</sup> after the collisions, both main and daughter pulses separate and move apart without changing their general appearances. However, there are lagging phase shifts due to the collision:  $12^\circ$  for the carrier in the main solitons and  $31^\circ$  for the carrier in the daughters. To illustrate this, in Fig. 4 we plot the space dependence of the central part of the rightward-moving daughter for the original uncollided case and the collided case, with both curves at exactly 30,000 time steps of the algorithm. Such phase shifts, not easily detected by GNLSE, may be a basis for optical switching devices.

The approach of this Letter assumes nothing about the homogeneity or isotropy of the optical medium, the magnitude of its nonlinearity, the nature of its  $\omega$ - $\beta$  variation, and the shape or duration of the optical pulse. By retaining the optical carrier, the new method solves for fundamental quantities, the optical electric and magnetic fields in space and time, rather than a nonphysical envelope function. Thus it is extendable to full-vector optical fields in two and three dimensions to permit rigorous boundary-value problem studies of nonlinear vector-wave polarization, diffraction, scattering, and interference effects.

The authors acknowledge the assistance of Rose Joseph in this research, including many helpful discussions, performance of some of the calculations, and preparation of the figures. A. Taflové was supported in part by NASA-Ames University Consortium Joint Research Interchange grants NCA2 561 and 562, Office of Naval Research contract N00014-89-K-0475, and Cray Research, Inc.

## References

1. R. M. Joseph, S. C. Hagness, and A. Taflové, *Opt. Lett.* **16**, 1412 (1991).
2. J. D. Jackson, *Classical Electrodynamics*, 2nd ed. (Wiley, New York, 1975).
3. G. P. Agrawal, *Nonlinear Fiber Optics* (Academic, New York, 1989).
4. K. J. Blow and D. Wood, *IEEE J. Quantum Electron.* **25**, 2665 (1989).
5. T. E. Bell, *IEEE Spectrum* **27**(8), 56 (1990).
6. D. Marcuse, *Theory of Dielectric Optical Waveguides*, 2nd ed. (Academic, New York, 1991).

# Initial Results for Automated Computational Modeling of Patient-Specific Electromagnetic Hyperthermia

Melinda J. Piket-May, *Student Member, IEEE*, Allen Taflove, *Fellow, IEEE*, Wei-Chung Lin, *Member, IEEE*, Daniel S. Katz, *Student Member, IEEE*, V. Sathiaselalan, *Member, IEEE*, and B. B. Mittal

**Abstract**—Developments in finite-difference time-domain (FD-TD) computational modeling of Maxwell's equations, super-computer technology, and computed tomography (CT) imagery open the possibility of accurate numerical simulation of electromagnetic (EM) wave interactions with specific, complex, biological tissue structures. One application of this technology is in the area of treatment planning for EM hyperthermia. In this paper, we report the first highly automated CT image segmentation and interpolation scheme applied to model patient-specific EM hyperthermia. This novel system is based on sophisticated tools from the artificial intelligence, computer vision, and computer graphics disciplines. It permits CT-based patient-specific hyperthermia models to be constructed without tedious manual contouring on digitizing pads or CRT screens. The system permits in principle near real-time assistance in hyperthermia treatment planning. We apply this system to interpret actual patient CT data, reconstructing a 3-D model of the human thigh from a collection of 29 serial CT images at 10 mm intervals. Then, using FD-TD, we obtain 2-D and 3-D models of EM hyperthermia of this thigh due to a waveguide applicator. We find that different results are obtained from the 2-D and 3-D models, and conclude that full 3-D tissue models are required for future clinical usage.

## I. INTRODUCTION

Much evidence has emerged from clinical studies that hyperthermia, i.e., heating of tumors to temperatures greater than 42°C, has efficacy as an adjuvant to radiation therapy in the treatment of localized superficial malignancies [1]–[5]. However, a recent study by the Radiation Therapy Oncology Group has cast a shadow over the earlier promising results by showing no significant difference between complete response rates obtained with and without hyperthermia [6]. The principal reason for these poor results seems to be inadequate heating of the tumors, especially those larger than 3 cm in diameter due

to poor coverage with external microwave applicators. In hyperthermia applications, adequacy of tumor coverage can reasonably be related to the extent to which the tumor is enclosed by surfaces of 50% iso-SAR (specific absorption rate, the absorbed power density in watts/kg) produced by the applicators.

The objective is to heat all tumor tissues of a patient to a uniform desired temperature without overheating surrounding normal tissues. However, this is difficult because current equipment and techniques produce poorly localized nonuniform heating in both tumor and normal tissues. This is further complicated by the cooling produced by significantly varying blood perfusion rates within the heated volumes. At present, heating techniques using electromagnetic (EM) energy are commonly employed in the clinic to produce therapeutic temperatures in tumors [7]. A number of factors influence the SAR patterns from commonly used EM applicators. Significant among these are: 1) the effect of relative applicator positioning with respect to the defined treatment volume; 2) the means of coupling the energy from the applicator(s) to the patient's surface; and 3) the complex, patient-specific tissue geometry. It is very difficult to either intuitively visualize or measure these effects, especially for deep tumor treatments where the SAR patterns are strongly affected by internal tissue structures.

Clearly, accurate patient-specific computer modeling of hyperthermia treatments to predict SAR distributions would be very useful for pretreatment evaluation of EM applicator setups. For example, Sathiaselalan *et al.* [8] used a 2-D numerical EM model to investigate the effect of phase steering with an annular phased array applicator system. The results of this numerical study were then used in the clinic to devise phase steering techniques to change the SAR patterns to improve the quality of treatments and reduce toxicity [9]. Also, patient-specific numerical simulation would enable parametric treatment studies to be performed quickly and inexpensively so that sensitive and insensitive parameters could be identified. These studies would also help to evaluate applicator-array systems now being developed.

Manuscript received July 20, 1990; revised August 1, 1991. This work was supported in part by American Cancer Society (Illinois Division) Grant 90-52, National Science Foundation Grant ASC-8811273, Office of Naval Research Contract N00014-88-K-0475, and Cray Research, Inc.

M. J. Piket-May, A. Taflove, W.-C. Lin, and D. S. Katz are with the Department of Electrical Engineering and Computer Science, McCormick School of Engineering, Northwestern University, Evanston, IL 60208.

V. Sathiaselalan and B. B. Mittal are with the Radiation Oncology Center, Northwestern Memorial Hospital, 250 East Superior, Room 44, Chicago, IL 60611.

IEEE Log Number 9105589.

A key step in realizing a computerized, patient-specific hyperthermia treatment planning involves the development of an accurate, efficient means for acquiring detailed 3-D anatomical tissue data for each patient. Regardless of the power of the EM analysis method, the modeling results can be no better than the tissue geometry data input. In principle, the advent of computed tomography (CT) has made the acquisition of accurate, patient-specific tissue geometry data feasible. However, processing the information from the CT data base to generate the corresponding 3-D dielectric medium data for the EM model can be difficult, especially if automation is desired to achieve speed. Problems include: 1) interpretation of the individual CT images to determine tissue and organ types and locations in each cross-section cut; and 2) interpolation or connection between adjacent CT images to reconstruct the original 3-D tissue geometry. The first issue is very complex, currently requiring the intervention of a human expert.

This paper describes progress made by our interdisciplinary group in both the EM modeling and CT-image interpretation problems. Section II reports the first analytical validations for 3-D computational EM models based on the finite-difference time-domain (FD-TD) method [10] for aperture-type hyperthermia applicators. These validations involve radiated fields from open-ended waveguides and horns, with benchmark data provided by the frequency-domain method of moments (MM). The validated FD-TD models of aperture sources are used later in Section IV for the patient-specific hyperthermia studies.

Section III describes the first automated CT image processing system to reconstruct patient-specific, 3-D tissue geometries for EM hyperthermia from serial CT image data. This novel system is based on sophisticated tools from the artificial intelligence, computer vision, and computer graphics disciplines [11]-[14]. It permits CT-based patient-specific hyperthermia models to be constructed without tedious manual contouring on digitizing pads or CRT screens. The system permits in principle near real-time assistance in hyperthermia treatment planning.

Section IV illustrates the entire process by describing automated 2-D and 3-D patient-specific models of EM hyperthermia of a human thigh due to a waveguide applicator. Here, the thigh tissue geometry data base is derived by combining 29 serial CT images of the patient. The FD-TD modeling results are shown as contour plots of the penetrating electric field and SAR. We find that different results are obtained from the 2-D and 3-D FD-TD models, and conclude that full 3-D tissue models are required for future clinical usage.

For completeness, we note that two distinct physical modeling problems are involved in the patient-specific computer simulation of hyperthermia treatments: 1) computation of the absorbed EM power distribution in tissue; and 2) the prediction of resulting temperature distribu-

tions using a suitable thermal model. These are two complex problems requiring different theoretical bases and different tissue property and physiological data. In this paper, only the patient-specific EM modeling problem is considered.

## II. FD-TD MODELING VALIDATIONS FOR APERTURE HYPERTHERMIA SOURCES

The important EM issues addressed in this paper are: 1) FD-TD modeling validations for aperture hyperthermia sources; and 2) 2-D versus 3-D modeling quantification. This section will focus on the first issue, while Section IV will consider the second. These are key areas to be investigated to ensure that EM modeling provides clinically meaningful answers, and to advance modeling progress in hyperthermia.

### A. Background of EM Modeling

In the 1970's and early 1980's, 3-D predictive models of EM wave absorption by biological tissue structures were based largely on the frequency-domain method of moments (MM) using space-filling cubic [15] and tetrahedral [16] elements. Yet, because MM leads to systems of linear equations having dense, full, complex-valued coefficient matrices, the required computer resources prevented modeling of arbitrary 3-D structures spanning more than a few wavelengths. In fact, the literature indicates that the basic MM treatment of whole-body human tissue structures culminated in models having in the order of several hundred space cells, each of multicentimeter scale [17]. This resolution is inadequate to provide the details of internal tissue structure needed for patient-specific hyperthermia treatment planning.

Theoretical efforts therefore shifted to alternative formulations of MM which promise a dimensional reduction of computer resources. One such formulation [18] exploits the convolutional nature of the volume integral equation based on polarization currents to permit use of the fast Fourier transform (FFT). Although this extends MM modeling to structures having thousands of space cells, it may provide errors in SAR calculations for EM excitations having transverse electric field components [19]. This would greatly impede the application of FFT/MM approaches to the important 3-D tissue case.

An alternative to frequency-domain MM formulations was the FD-TD method introduced by Taflovie in 1975 [20], [21], based in part on an algorithm published by Yee [22] in 1966. FD-TD is a direct finite-difference solution of Maxwell's time-dependent curl equations implementing a marching-in-time procedure which simulates the actual propagating EM waves by sampled data numerical analogs. There is no need to set up or solve a system of linear equations. Thus, FD-TD computational resources are dimensionally low compared to MM. Furthermore, unlike the FFT/MM approaches, which also have dimen-

sionally low computer burdens, FD-TD has been shown to be robust, providing accurate modeling predictions for a wide variety of EM wave interaction problems in 2-D and 3-D [19]. A subset of these includes biological tissue interactions [19], [21], [23], including detailed (order 1-cm resolution) whole-human-body dosimetry under plane-wave illumination [24], and detailed partial- or whole-body hyperthermia modeling [25]–[27].

The increasing availability of Crays to the engineering EM community has permitted application of FD-TD to model EM wave interactions with arbitrary 3-D structures approximately ten times larger in electrical size than MM (1000 times larger in volume). At present, the largest and fastest reported 3-D FD-TD model is the jet engine inlet modeled by Katz and Tafove [28] for radar cross section. This model, implemented on the Cray Y-MP/8, spans  $30 \lambda_0$  in 3-D, has a uniform  $0.1 - \lambda_0$  resolution, and solves for 23-million unknown vector field components. The Cray Y-MP/8 running time is only 3 min, 40 s per illumination angle (1800 time steps—100 cycles of the incident wave—to the sinusoidal steady state).

In the area of EM wave interactions with biological tissue structures, the literature also indicates work in finite-element modeling [29], [30]. The goals of this work involve nearly conformal modeling of tissue structures using well-characterized finite-element geometry generation software. (FD-TD theory is also progressing in this area with the advent of accurate, fully conformal surface models based upon local Faraday's Law and Ampere's Law contour paths [31].) However, detailed studies [19], [23] have shown that simple FD-TD surface staircasing of cylindrical and spherical tissue structures is sufficient to permit calculation of the penetrating internal fields with a high degree of accuracy compared to the exact solutions. It is observed that FD-TD calculated fields penetrating a lossy dielectric structure show little sensitivity to the nature of the surface approximation of the structure. This observation permits effective use of simple staircasing FD-TD models for computing penetrating fields in tissue structures. These sacrifice little accuracy and have small computer burdens compared to the finite-element approaches.

### B. FD-TD Validation Studies

At present, there exists only a limited set of validations of FD-TD models for clinically used hyperthermia applicators [25]–[27]. In this section, this paper provides the first analytical validations of FD-TD for generic aperture sources: open-ended waveguides and horns, including details of the waveguide probe excitation. Benchmark data are obtained from detailed frequency-domain integral equation and MM numerical results. These validation studies are relevant in that the patient-specific, FD-TD hyperthermia models to be discussed in Section IV employ similar 2-D and 3-D aperture sources; and it is clearly desirable to have confidence in the numerical EM model

before drawing conclusions based upon the model (as we will).

Consider first the validation studies for the generic microwave aperture sources. Validation here consists of comparing the magnitude and phase of radiated near fields predicted by FD-TD and MM, and determining the level of disagreement. For example, Fig. 1a depicts the geometry of a 2-D waveguide-fed horn antenna, excited by a monopole probe, used for comparison of FD-TD and MM computed aperture electric field distributions. As seen in Fig. 1(b) and (c), the FD-TD and MM computations of radiated near fields agree within about 1% in magnitude and about  $2^\circ$  in phase. (This level of agreement has been found consistently for a variety of 2-D aperture sources.) This implies that the FD-TD predictions are, for engineering purposes, just as useful as those of MM.

Two analytical validation studies are considered for the 3-D FD-TD aperture source model. The first validation involves a simple rectangular waveguide radiating in free space. The waveguide is assumed to have a  $2\lambda_0/3 \times \lambda_0/3$  cross section, and a  $2\lambda_0$  length. A sinusoidally excited line source is assumed to be located  $\lambda_0/3$  from the closed end, centered in the waveguide, and extending from the top to the bottom of the guide. The FD-TD computations for radiated far-fields are compared to those obtained using a standard electric field integral equation, triangular surface patching MM code with three different meshings, with results shown in Fig. 2. It is seen that the FD-TD predicted far-fields are "bracketed" by the various MM results, indicating a substantial code-to-code validation.

The second 3-D validation study compares FD-TD results to a recently published integral equation solution [32] for an infinitely long rectangular waveguide heating a planar layered tissue medium. The waveguide of [32] is water-loaded ( $\epsilon_w = 81\epsilon_0$ ), has a  $5.6 \times 2.8$  cm cross-section, and is excited at 432 MHz. The tissue medium is comprised of a 0.5-cm skin layer ( $\epsilon_s = (42 - j25)\epsilon_0$ ), a 1.0-cm fat layer ( $\epsilon_f = (5 - j10)\epsilon_0$ ), and a muscle half-space ( $\epsilon_m = (42 - j25)\epsilon_0$ ). For the FD-TD model, the waveguide is assumed to have finite length, 19.3 cm ( $2.5\lambda_w$ ), with a line source located 1.9 cm ( $0.25\lambda_w$ ) from the closed end. To maintain a reasonable FD-TD grid size, the infinite extent of the tissue structure is approximated by extending it only one-half skin depth in all directions from the waveguide. Overall, using a uniform 1.0-mm space resolution, the FD-TD grid size is  $280 \times 134 \times 106$  cubic cells (23.9-million vector field components).

Fig. 3 compares the FD-TD and integral equation results for penetrating electric field contours at the skin-fat interface 0.5 cm into the layered tissue structure. Because of symmetry in the  $x$  and  $y$  direction, only a single quadrant of the electric field distribution is shown for each  $z = \text{constant}$  plane. The agreement is quite good considering the truncated (noninfinite) tissue layers used in the FD-TD modeling.

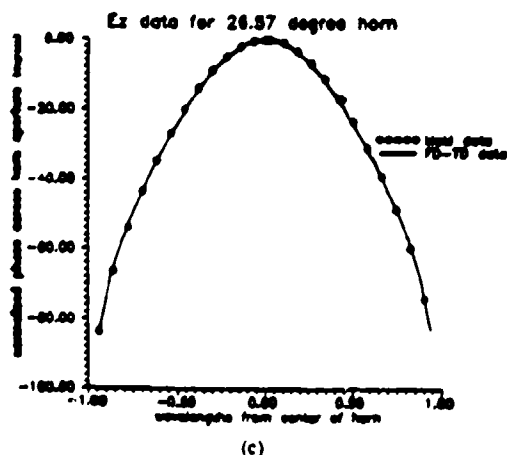
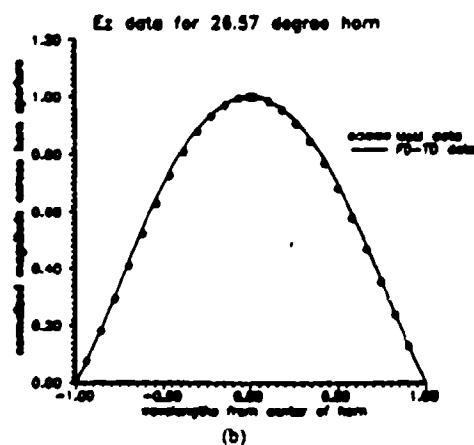
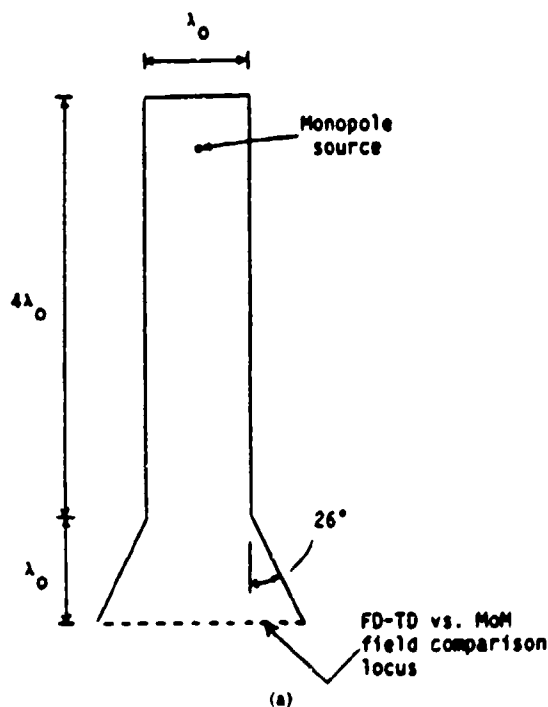


Fig. 1. 2-D waveguide-fed horn antenna: (a) Geometry, (b) electric field magnitude distribution at aperture, (c) electric field phase distribution at aperture.

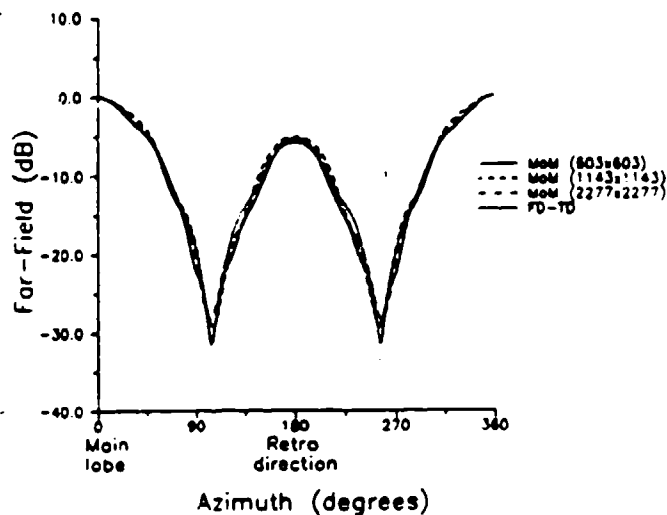


Fig. 2. Comparison of FD-TD and MM triangular surface patching results for the *H*-plane radiated far-field pattern of the short open-ended 3-D waveguide (various MM spatial resolutions).

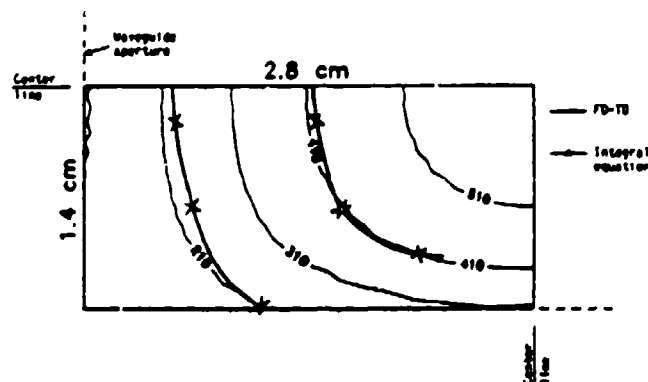


Fig. 3. Comparison of FD-TD and integral equation results [32] for penetrating electric field contours in a 3-layer tissue model due to a waveguide applicator. Location of map: 0.5 cm into the tissue (at the skin/fat interface); only one quadrant of the map is shown because of symmetry.

### III. AUTOMATED CT IMAGE ANALYSIS AND RECONSTRUCTION

#### A. Background

To reconstruct the 3-D tissue structure from serial CT cross-sectional image data, an image analysis system must perform two basic functions: 1) image segmentation/correspondence establishment; and 2) interpolation. *Image segmentation* is the process of dividing a CT image into regions that correspond to physical objects or parts [33]–[36]. After the meaningful entities in each slice have been identified (and their contours extracted), the next step is to establish the correspondence among them. By doing so, the information about the start contour in one slice and the corresponding goal contour(s) in adjacent slices can be obtained. There is no existing system that can perform fully automated medical image segmentation and correspondence establishment in a practical problem domain. *Interpolation* [11], [34], [37]–[39] ideally permits the re-

construction of the original tissue structure by filling the empty space between contours in adjacent CT slices derived by the segmentation process.

Much progress has been made during the past decade in addressing a similar problem in radiation treatment planning. Sophisticated computerized 3-D treatment planning systems based on CT and magnetic resonance imaging systems have been developed [40]–[44]. All of these systems use a combination of automatic and manual contouring methods to delineate tissue regions, i.e., segment images, in each CT slice. Edge-detection techniques have been used successfully to delineate structures that have significantly different Hounsfield numbers from those of adjacent tissues [44], [45]. A threshold CT value is selected and then the computer automatically traces a contour which separates points above and below the threshold.

However, for the spinal cord, brain stem, kidney, liver, stomach, heart, and other tissue structures embedded in fat or muscle tissue, the task is not straightforward. The Hounsfield CT numbers of these organs are sufficiently close to those of the surrounding tissue to make edge-detection algorithms useless, necessitating the use of a manual system. Here, the structures are outlined by skilled personnel having specific knowledge about the location of these organs, their shape, and their progression through the scanned volume as one moves from slice to slice through the CT data. Outlining is accomplished using a track-ball device or digitized pen system that controls the cursor on the computer screen.

Despite the development of graphical aids, manual generation of contours to delineate tissue structures can be tedious and labor-intensive, requiring many manhours to prepare the data for treatment planning. New approaches to define low-contrast tissues automatically or interactively have to be developed. This is an active area of research, and recently a technique for outlining regions where object CT values overlap has been reported [46]. However, to more fully automate this process, it will be necessary to use knowledge-based and other symbolic reasoning software tools.

Knowledge-based (expert) systems are an attempt to represent the knowledge, experience, and insight of the "expert" in a computer-based environment. These software tools have opened new paths for the use of computers in radiation oncology and diagnostic radiology [47]. For example, Pizer *et al.* [48] have recently developed a hierarchical figure-based shape description system with promising applications in defining low-contrast objects. Extension of these techniques to the needs of hyperthermia treatment planning offers the potential for new tools for tumor localization and extraction of anatomical features.

### B. Our Approach

In this paper, we report the first highly automated CT image segmentation and interpolation scheme applied to

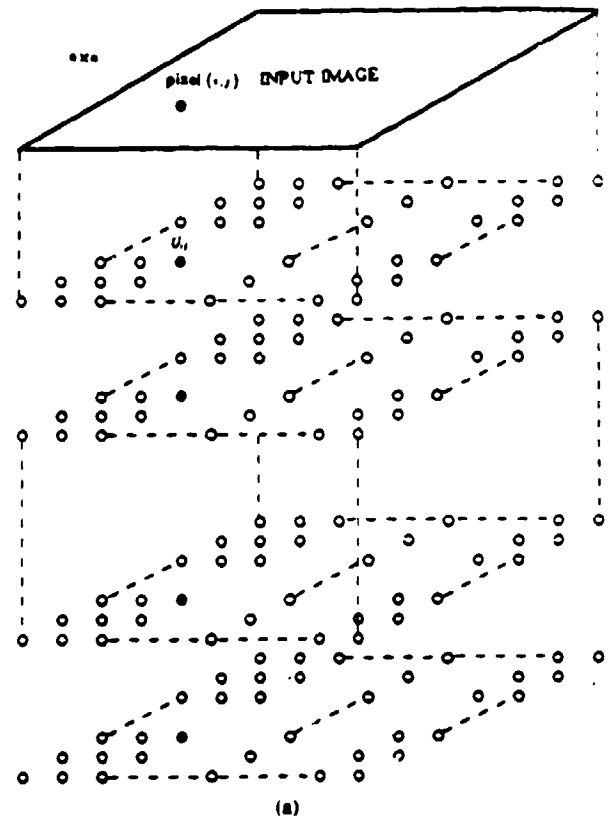


Fig. 4. Example of usage of constraint satisfaction neural network technique for automated segmentation of CT images: (a) Topology of the neural network, (b) CT image of pelvic cross section, (c) segmented image [14].

model patient-specific EM hyperthermia. The method is based on the following:

1) *Image Segmentation Using a Neural Network Approach:* We report a constraint satisfaction neural

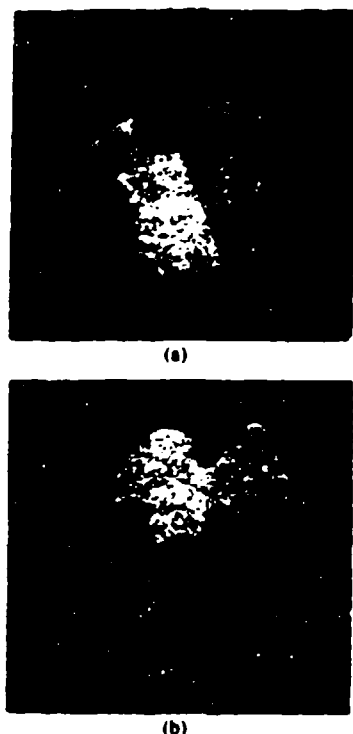


Fig. 5. Examples of usage of dynamic elastic surface interpolation technique for automated reconstruction of canonical 3-D branched objects from serial cross-sectional contours: (a) two branches, (b) three branches [11].

network<sup>1</sup> (CSNN) technique which enables, in principle, automatic segmentation of complex images [14]. In CSNN, each neuron corresponds to a pixel in an  $n \times n$  image. Suppose that each pixel is to be assigned one of  $m$  labels. Then, the CSNN consists of  $n \times n \times m$  neurons, and can be conceived as a 3-D array. The topology of the CSNN is shown in Fig. 4(a). The CSNN has been developed for image segmentation as the first step toward automated object reconstruction. Fig. 4(b) and (c) show an example of the use of the CSNN technique to automatically segment a CT image of a pelvic cross section [14] with results comparable to conventional techniques.

2) *Interpolation*: We also report the development of a dynamic elastic surface interpolation (DESI) scheme [11]–[13]. The central idea of DESI is to identify the geometric difference between the start and the goal contours, and derive force vectors that can be applied to the start contour to distort it to match the goal contour. The algorithm provides a mechanism to generate iteratively a series of intermediate contours for filling the gaps between the start and goal contours. A 3-D object is reconstructed by stacking up the start, intermediate, and goal contours. The major advantage of this method is its superior capability in handling the branching situation where a contour in one

2-D cut splits into several contours in adjacent cuts, or where several contours merge into one contour. DESI is simple and has the advantage that pairwise interpolation can be performed simultaneously with a parallel architecture. Fig. 5(a) and (b) show examples of the use of DESI to reconstruct canonical branched 3-D objects from serial cross-sectional contours [11].

#### IV. APPLICATION TO PATIENT-SPECIFIC EM HYPERTHERMIA

We have applied the above techniques for the first time to interpret actual patient CT data for modeling EM hyperthermia. Specifically, we reconstructed a 3-D model of the human thigh from a collection of 29 serial CT images at 10 mm intervals. Two typical slices are shown in Fig. 6. Each slice consists of four different tissue structures: fat, muscle, bone, and bone marrow. In the reconstruction process, we assumed that we had the following prior knowledge:

- 1) Image content—each image contains a left and a right thigh.
- 2) Tissues types and spatial relationships—there are four types of tissues in each image, and if we draw a line from outside the whole region to its centroid, the order of regions encountered is always fat, muscle, bone, and then bone marrow.
- 3) Average intensity levels of the regions of different tissue types—used in thresholding operation.
- 4) Expected boundary between fat and muscle—should be smooth and closed, even though the muscle region may actually consist of many disconnected regions or may have bay-like (or crack-like) areas.

The four regions of interest corresponding to the four tissue types of the left thigh were obtained by the following semiautomatic procedure. First, the touching points of the two thighs were detected by locating the points with the maximum curvatures. Then, a line was drawn between the two points to separate the left thigh from the right thigh. The right thigh was blackened out and a  $128 \times 128$  image [shown in Fig. 7(a)] containing only the left thigh was extracted. After manually analyzing this image to select three threshold values (see point 3), the pixels in the image were classified into groups by a thresholding operation. Fig. 7(b) shows the result of performing this operation on the image in Fig. 7(a). The boundaries between these regions were then obtained by automatic contour tracing methods [50]. Some heuristics were also applied<sup>2</sup> to obtain a closed and smooth boundary between fat and muscle (see point 4). After all the boundaries were detected, the four regions were labeled with distinct integers. Fig. 8 shows the results of Fig. 7 after boundary

<sup>1</sup>A neural network is composed of many interconnected processing elements that operate in parallel, and a weighted matrix of interconnections that allows the network to "learn" and "remember" [49]. Artificial neural networks are being used for a variety of applications including image and signal processing and pattern recognition. The parallel nature of a neural network permits, in principle, rapid concurrent processing of complex image data.

<sup>2</sup>In our experiments, in an attempt to automate the boundary detection process, we also applied some well-recognized "signal-based" image segmentation algorithms such as split-and-merge [51] to this set of images. Although the algorithm had some success on some slices, it is not powerful enough to handle all the slices in our data set with a uniform set of parameters.





Fig. 6. Two typical CT images (slices) of the thighs of a patient.



(a)



(b)

Fig. 7. Results of automated thresholding and pixel classification for the patient's left thigh of Fig. 6: (a) extraction of the left thigh. (b) results of processing.

detection and region labeling. The DESI method was then applied to each consecutive pair of slices for generating intermediate slices. After the pairwise interpolation, 28 intermediate slices were generated. Fig. 9 shows the result of stacking up the 57 slices.



Fig. 8. Results of Fig. 7(b) after tissue boundary detection and region labeling.



Fig. 9. Reconstructed 3-D thigh model (29 segmented CT images plus 28 intermediate slices generated using dynamic elastic surface interpolation).

#### A. 2-D Study

It was desired first to implement the prototype automated EM hyperthermia analysis system in 2-D. Using the CT-scan data of a human thigh, the tissue structure (fat, muscle, bone, and bone marrow) was automatically deduced as described above. A prototype automatic interface was constructed to take the data output of the CT analysis system and feed it into a Compaq 386/25/Weitek lab computer used for the 2-D FD-TD EM model. The model simulated a monopole-excited 2-D waveguide aperture source operating at 915 MHz as the hyperthermia applicator for the thigh with and without a  $1/4$ -wavelength slab used for impedance matching. (Previous studies discussed in Section II had validated the FD-TD model of the monopole-excited waveguide source.)

Fig. 10 depicts the 2-D geometry of the thigh and the  $10 \times 33.5$  cm parallel-plate waveguide hyperthermia source operated at 915 MHz. A  $150 \times 300$  cell FD-TD grid having a uniform resolution of 1.602 mm, the exact resolution of the CT data, was used for the model. The waveguide was assumed filled with a dielectric having  $\epsilon_r = 6.0$  (except for a possible matching section having  $\epsilon_r = 16.0$ ), and excited in the  $TE_1$  mode by a line source centered within the guide 6.7 cm from the closed end. This provided an incident electric field parallel to the

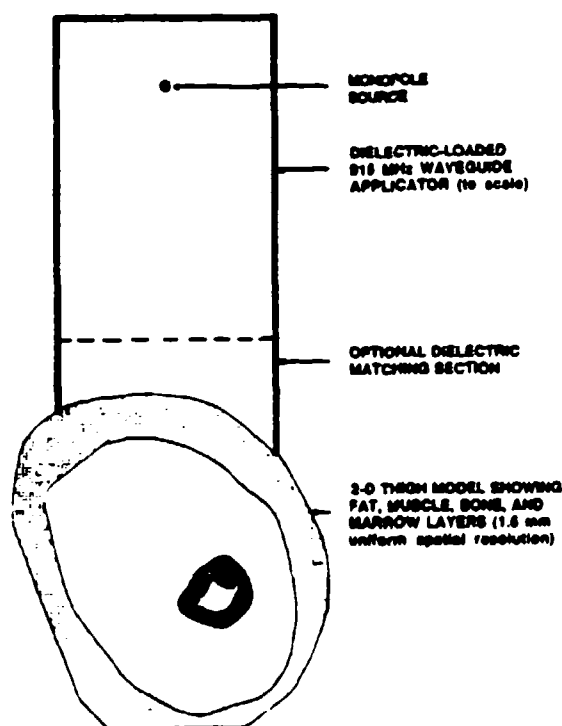


Fig. 10. Geometry of 2-D hyperthermia model, showing monopole-excited waveguide applicator and patient-specific thigh model, all contained within the FD-TD space grid.

thigh. Fig. 11(a) and (b) graph contour maps of the SAR distribution within the thigh for the unmatched and matched cases, respectively, normalized to 1000 W/m incident power. All data were obtained after time stepping eleven periods of the incident wave at 915 MHz (2 h run time on the Compaq). The figures clearly depict the matching action of the waveguide dielectric insert in enhancing EM heating within the thigh, and show an intense hot spot at the fat-muscle interface.

### B. 3-D Study

Using the automated CT image analysis system to process 29 serial, patient-specific CT scans for the human thigh, we constructed a 3-D dielectric media data base which was automatically interfaced to a Cray-2 for the FD-TD model. (See Fig. 9 for the final 3-D thigh model.) The FD-TD grid resolution used here was 5 mm ( $\lambda_d/27$ ). This resolution was chosen because it is the vertical distance between the interpolated CT layers. For the dielectric-loaded, TE<sub>10</sub> mode waveguide hyperthermia applicator (dimensions 10 × 10 × 33.5 cm), the same metal and dielectric parameters as in the previous 2-D waveguide model were used, as well as the same excitation frequency. A line source, assumed to be centered in the guide 6.7 cm from the closed end, generated an incident electric field parallel to the thigh.

With the thigh in place, the FD-TD code solved for 2.4 million EM field components per time step. All data were obtained after time-stepping eleven periods of the incident wave at 915 MHz. (Eleven periods permits reasonable

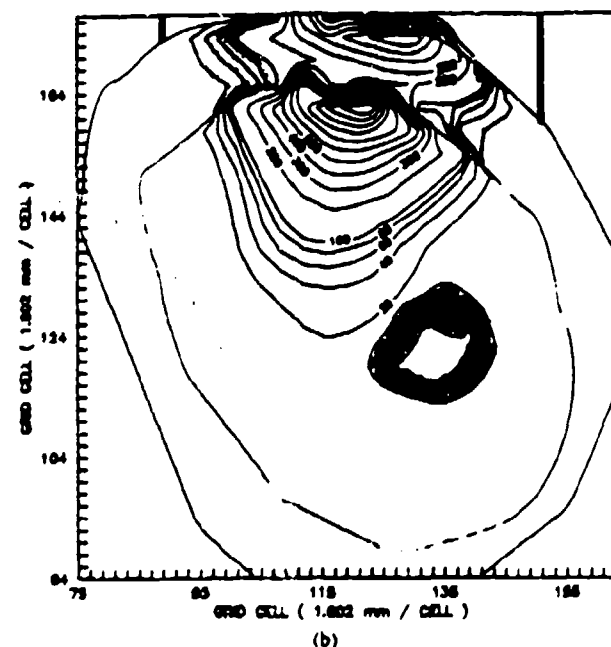
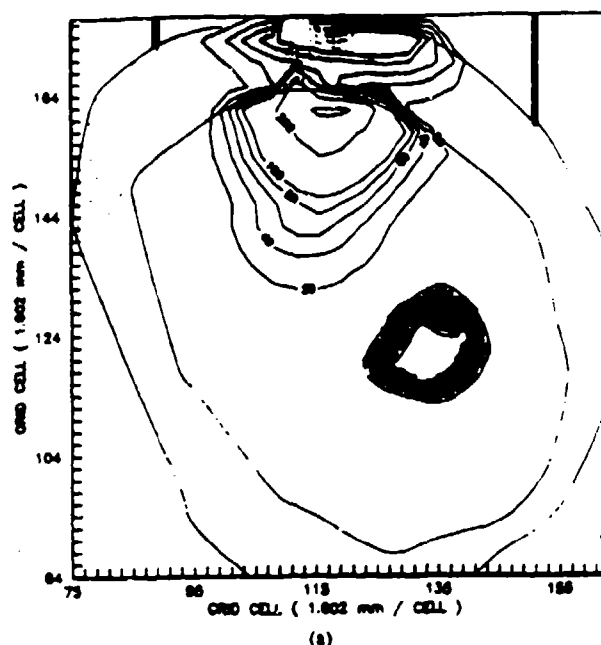


Fig. 11. FD-TD computed SAR distribution in the 2-D thigh model of Fig. 10, normalized to 1000 W/m incident power: (a) with no dielectric matching section, (b) with dielectric matching section.

convergence to the sinusoidal steady state for this case. During this time, a numerical wave can undergo one complete front-back-front traverse of the grid, taking into account the velocity-slowness effect of the high-permittivity tissue media.) This required 10 minutes of single-processor Cray-2 time per 3-D run. The previous 2-D model was also reworked in the same coarser resolution (5 mm) grid so that the 2-D and 3-D results could be directly compared. Fig. 12(a) shows the FD-TD computed SAR contour pattern penetrating into the 3-D model along a central horizontal cut, while Fig. 12(b) shows the corresponding FD-TD SAR contour pattern for the 2-D model.

We observe some interesting results which emphasize

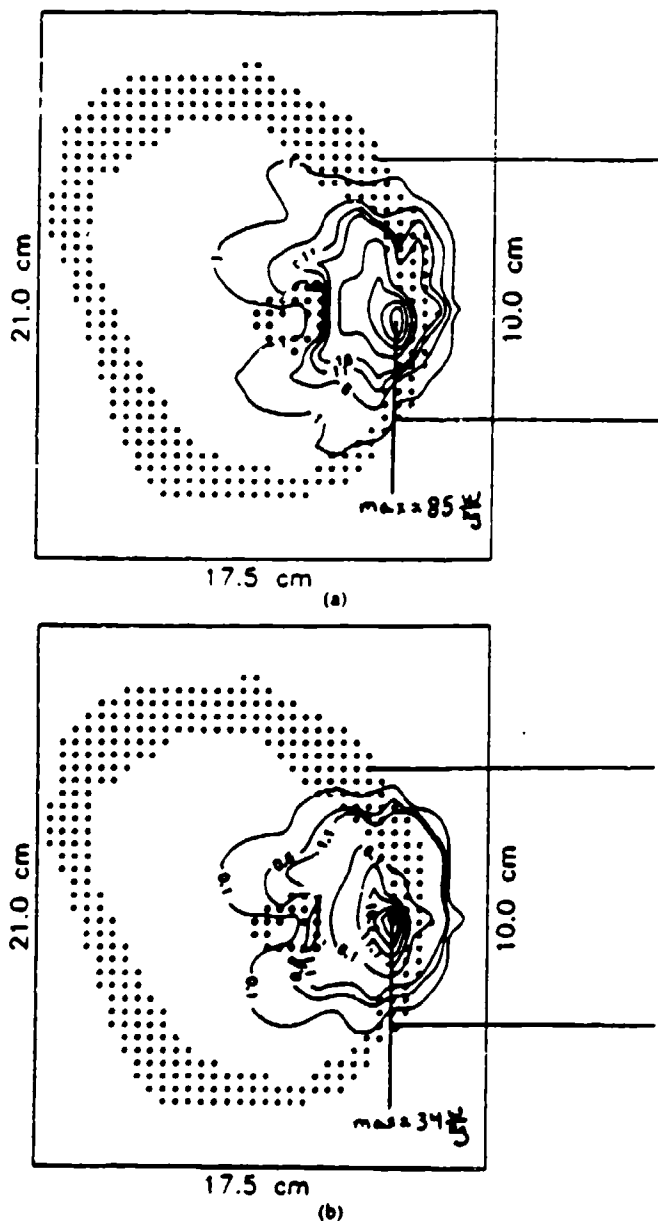


Fig. 12. PD-TD computed SAR distribution in the patient-specific thigh model, normalized to 1000 V/m incident waveguide field: (a) 3-D model, (b) 2-D model.

the need for 3-D EM modeling. With the same normalized incident electric field, deeper penetration is seen in the 3-D case. Note that the maximum SAR in the 3-D graph is 85 W/kg, whereas the maximum SAR in the 2-D graph is only 34 W/kg. If one compares the position of the 16 W/kg contour line in the 3-D and the 2-D graphs, the difference in penetration is clear. This contour almost penetrates the bone in the 3-D SAR graph, but is close to the fat-muscle interface in the 2-D SAR graph. This is perhaps one of the first comparisons of detailed computational modeling for EM absorption in 3-D versus 2-D.

To help explain the possibly counter-intuitive result that the 3-D model exhibits deeper penetration than the 2-D model, the electric field distribution through a vertical ( $z$ )

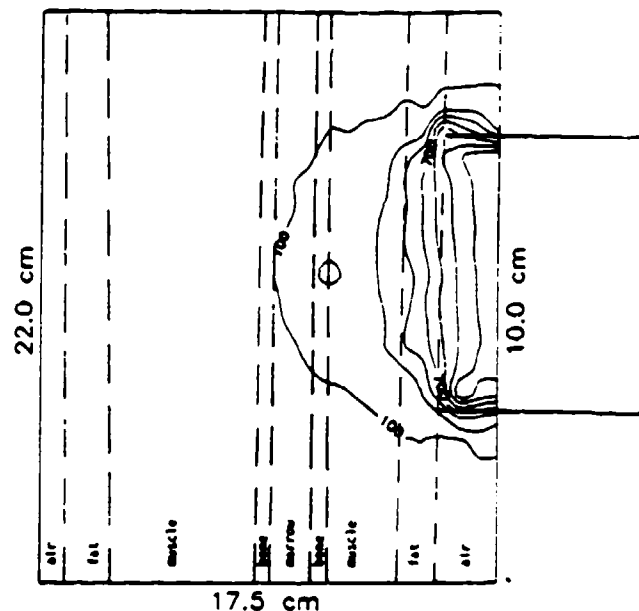


Fig. 13. FD-TD computed electric field map along a vertical slice of the 3-D patient-specific thigh model, at the waveguide center line (normalized to 1000 V/m incident waveguide field).

cut of the 3-D thigh geometry is shown in Fig. 13. Note the second curvature of the electric field contours in the third dimension,  $z$ . There is now a double curvature of the penetrating electric field, a sort of "bubble." This apparently bends the electric fields deeper into the thigh structure and sets up deeper heating.

## V. CONCLUSION

This paper described progress by our group in automated computational modeling of patient-specific EM hyperthermia. We reported the first analytical validations of 3-D FD-TD models of aperture-type hyperthermia applicators. We also reported the first highly automated CT image segmentation and interpolation scheme applied to model patient-specific EM hyperthermia. We applied this technique to interpret actual patient CT data, reconstructing a 3-D model of the human thigh from a collection of 29 serial CT images at 10 mm intervals. Using FD-TD, we obtained 2-D and 3-D models of EM hyperthermia of this thigh due to a waveguide applicator. We found that different results are obtained from the 2-D and 3-D models, and concluded that full 3-D tissue models are required for future clinical usage.

## REFERENCES

- [1] G. Arcangeli, J. Overgaard, D. G. Gonzalez, and P. N. Shrivastava, "Hyperthermia trials," *Int. J. Radiation Oncol. Biol. Physics*, vol. 14, suppl. 1, pp. S93-S109, 1988.
- [2] R. Valdagni, F. Liu, and D. S. Kapp, "Important prognostic factors influencing outcome of combined radiation and hyperthermia," *Int. J. Radiation Oncol. Biol. Phys.*, vol. 15, pp. 959-972, 1988.
- [3] J. L. Meyer, "The clinical efficacy of localized hyperthermia," *Cancer Res.*, vol. 44, pp. 4745S-4751S, 1984.
- [4] J. Overgaard, "The current and potential role of hyperthermia in radiotherapy," *Int. J. Radiation Oncol. Biol. Phys.*, vol. 16, pp. 535-549, 1989.

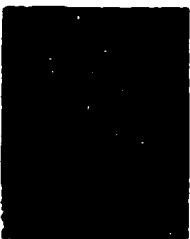
- [5] C. A. Perez and B. N. Emami, "Clinical trials with local (external and interstitial) irradiation and hyperthermia. Current and future perspectives," in *The Radiologic Clinics of North America*, R. A. Steeves, Ed., Philadelphia, PA: R. A. Saunders, vol. 27, 1989, pp. 525-542.
- [6] C. A. Perez, B. Gillespie, T. Pajak, N. B. Hornback, B. N. Emami, and P. Rubin, "Quality assurance problems in clinical hyperthermia and their impact on therapeutic outcome: A report by the Radiation Therapy Oncology Group," *Int. J. Radiation Oncol. Biol. Phys.*, vol. 16, pp. 551-558, 1989.
- [7] J. W. Hand and J. R. James, Eds., *Physical Techniques in Clinical Hyperthermia*. Research Studies Press, Letchworth, Herts., England, 1986.
- [8] V. Sathiaselan, M. F. Iskander, G. C. Howard, and N. M. Bleehen, "Theoretical analysis and clinical demonstration of the effect of power pattern control using the annular phased array hyperthermia system," *IEEE Trans. Microwave Theory Tech.*, vol. 34 (special issue on phased arrays), pp. 514-519, 1986.
- [9] G. C. Howard, V. Sathiaselan, G. A. King, A. K. Dixon, A. Anderson, and N. M. Bleehen, "Regional hyperthermia for extensive pelvic tumors using an annular phased array applicator: A feasibility study," *Brit. J. Radiol.*, vol. 59, pp. 1995-1201, 1986.
- [10] A. Taflov, "Review of the formulation and applications of the finite-difference time-domain method for numerical modeling of electromagnetic wave interactions with arbitrary structures, (Invited Paper)," *Wave Motion*, vol. 10, pp. 547-582, 1988.
- [11] W.-C. Lin, C.-C. Liang, and C.-T. Chen, "Dynamic elastic interpolation for 3-D object reconstruction from serial cross-sectional images," *IEEE Trans. Med. Imag.*, vol. 7, pp. 225-232, 1988.
- [12] W.-C. Lin, S.-Y. Chen, and C.-T. Chen, "A new surface interpolation technique for reconstructing 3-D objects from serial cross-sections," *Comp. Vis., Graph., Image Process.*, vol. 48, pp. 124-143, 1989.
- [13] S.-Y. Chen, W.-C. Lin, C.-C. Chen, and C.-T. Chen, "Improvement on dynamic elastic interpolation for 3-D object reconstruction from serial cross-sectional images," *IEEE Trans. Med. Imag.*, vol. 9, pp. 71-83, 1990.
- [14] W.-C. Lin, C.-K. Tsao, and C.-T. Chen, "Constraint satisfaction neural networks for image segmentation," *IEEE Trans. Neural Networks*, 1990.
- [15] D. E. Livesay and K. M. Chen, "Electromagnetic fields induced inside arbitrarily shaped biological bodies," *IEEE Trans. Microwave Theory Tech.*, vol. 22, pp. 1273-1280, 1974.
- [16] D. H. Schaubert, D. R. Wilton, and A. W. Glisson, "A tetrahedral modeling method for electromagnetic scattering by arbitrarily shaped inhomogeneous dielectric bodies," *IEEE Trans. Antennas Propag.*, vol. 32, pp. 77-85, 1984.
- [17] J. F. DeFord, O. P. Gandhi, and M. J. Hagmann, "Moment-method solutions and SAR calculations for inhomogeneous models of man with large number of cells," *IEEE Trans. Microwave Theory Tech.*, vol. 31, pp. 848-851, 1983.
- [18] D. T. Borup and O. P. Gandhi, "Fast Fourier transform method for calculation of SAR distributions in finely discretized inhomogeneous models of biological bodies," *IEEE Trans. Microwave Theory Tech.*, vol. 32, pp. 355-360, 1984.
- [19] D. T. Borup, D. M. Sullivan, and O. P. Gandhi, "Comparison of the FFT conjugate gradient method and the finite-difference time-domain method for the 2-D absorption problem," *IEEE Trans. Microwave Theory Tech.*, vol. 35, pp. 383-395, 1987.
- [20] A. Taflov and M. E. Brodwin, "Numerical solution of steady-state electromagnetic scattering problems using the time-dependent Maxwell's equations," *IEEE Trans. Microwave Theory Tech.*, vol. 23, pp. 623-630, 1975.
- [21] —, "Computation of the electromagnetic fields and induced temperatures within a model of the microwave-irradiated human eye," *IEEE Trans. Microwave Theory Tech.*, vol. 23, pp. 888-896, 1975.
- [22] K. S. Yee, "Numerical solution of initial boundary value problems involving Maxwell's equations in isotropic media," *IEEE Trans. Antennas Propag.*, vol. 14, pp. 302-307, 1966.
- [23] D. M. Sullivan, D. T. Borup, and O. P. Gandhi, "Use of the finite-difference time-domain method in calculating EM absorption in human tissues," *IEEE Trans. Biomed. Eng.*, vol. 34, pp. 148-157, 1987.
- [24] D. M. Sullivan, O. P. Gandhi, and A. Taflov, "Use of the finite-difference time-domain method in calculating EM absorption in man models," *IEEE Trans. Biomed. Eng.*, vol. 35, pp. 179-186, 1988.
- [25] R. W. Lau, R. J. Sheppard, G. Howard, and N. M. Bleehen, "The modeling of biological systems in three dimensions using the time-domain finite-difference method: I. The implementation of the model; II. The application and experimental evaluation of the method in hyperthermia applicator design," *Phys. Med. Biol.*, vol. 31, pp. 1247-1266, 1986.
- [26] C.-Q. Wang and O. P. Gandhi, "Numerical simulation of annular phased arrays for anatomically based models using the FD-TD method," *IEEE Trans. Microwave Theory Tech.*, vol. 37, pp. 118-126, 1989.
- [27] D. Sullivan, "Three-dimensional computer simulation in deep regional hyperthermia using the finite-difference time-domain method," *IEEE Trans. Microwave Theory Tech.*, vol. 38, pp. 204-211, 1990.
- [28] D. S. Katz and A. Taflov, "FD-TD visualization of electromagnetic wave interactions with three-dimensional objects," in *Proc. 1990 Int. Symposium, IEEE Antennas and Propagation Society/Int. Union of Radio Science*, Dallas, TX, May 1990.
- [29] K. D. Paulsen, D. R. Lynch, and J. W. Strohbehn, "Three-dimensional finite, boundary, and hybrid element solutions of the Maxwell equations for lossy dielectric media," *IEEE Trans. Microwave Theory Tech.*, vol. 36, pp. 682-693, 1988.
- [30] K. D. Paulsen and D. R. Lynch, "Time-domain solution of the Maxwell's equations by finite elements for electromagnetic hyperthermia," in *Abstracts of Papers for the Ninth Annu. Meet. North Amer. Hyperthermia Group*, Seattle, WA, Mar. 18-23, 1989, Abstract A4-10.
- [31] T. G. Jurgens, A. Taflov and K. R. Umashankar, "FD-TD conformal modeling of smoothly curved targets," *IEEE Trans. Antennas Propag.*, to be published.
- [32] K. S. Nikita and N. K. Uzunoglu, "Analysis of the power coupling from a waveguide applicator into a three-layered tissue model," *IEEE Trans. Microwave Theory Tech.*, vol. 37, pp. 1794-1801, 1989.
- [33] R. M. Haralick and L. G. Shapiro, "Survey: Image segmentation techniques," *Computer Vis., Graph., Image Process.*, vol. 29, pp. 100-132, 1985.
- [34] K. S. Fu and J. K. Mui, "A survey on image segmentation," *Pattern Recognit.*, vol. 13, pp. 3-16, 1981.
- [35] E. M. Riseman and M. A. Arbib, "Survey: Computational techniques in the visual segmentation of static scenes," *Computer Graph. Image Process.*, vol. 67, pp. 253-261, May 1979.
- [36] R. Nevatia, "Image segmentation," in *Handbook of Pattern Recognition and Image Processing*, vol. 29, T. Y. Young and K. S. Fu, Eds., 1985, pp. 100-132.
- [37] H. Fuchs, Z. M. Kedem, and S. P. Uselton, "Optimal surface reconstruction from planar surface contours," *Commun. ACM*, vol. 20, pp. 693-702, 1977.
- [38] H. N. Christiansen and T. W. Sederberg, "Conversion of complex contour line definitions into polygonal element mosaics," *Computer Graphics*, vol. 12, pp. 187-192, 1978.
- [39] J. D. Boissonnat, "Surface reconstruction from planar cross-sections," in *Proc. IEEE Conf. Computer Vision and Pattern Recognition*, San Francisco, CA, June 1985, pp. 393-397.
- [40] P. Bloch and J. K. Udupa, "Application of computerized tomography to radiation therapy and surgical planning," *Proc. IEEE*, vol. 71, pp. 351-355, 1983.
- [41] R. Mohan, O. Barest, L. J. Brewster, C. S. Chui, G. J. Kutcher, J. S. Laughlin, and Z. Fuks, "A comprehensive three-dimensional radiation treatment planning system," *Int. J. Radiation Oncol. Biol. Phys.*, vol. 15, pp. 481-495, 1988.
- [42] B. A. Fraass and D. L. McShan, "3-D treatment planning: I. Overview of a clinical planning system," in *Proc. Ninth Conf. on the Use of Computers in Radiation Therapy*, Scveningen, Netherlands. North Holland: Elsevier Science, 1987, pp. 273-276.
- [43] J. A. Purdy, J. Wong, W. B. Harms et al., "Three-dimensional radiation treatment planning," in *Proc. Ninth Conf. on the Use of Computers in Radiation Therapy*, Scveningen, Netherlands. North Holland: Elsevier Science, 1987, pp. 277-279.
- [44] M. Goitein and M. Abrams, "Multi-dimensional treatment planning: I. Delineation of anatomy," *Int. J. Radiation Oncol. Biol. Phys.*, vol. 9, pp. 777-787, 1983.
- [45] J. K. Udupa, "Interactive segmentation and boundary surface formation for 3-D digital images," *Computer Graphics and Image Processing*, vol. 18, pp. 213-235, 1982.
- [46] J. N. Roy, P. Steiger and C. C. Ling, "Overlap detection and contour-tracking algorithms for critical organs—application to kidney," *Computerized Med. Imag. Graph.*, vol. 13, pp. 153-161, 1990.

- [47] S. Zink, "The promise of a new technology: Knowledge-based systems in radiation oncology and diagnostic radiology," *Computerized Med. Imag. Graph.*, vol. 13, pp. 282-293, 1990.
- [48] S. M. Pizer, W. R. Oliver, J. M. Gauch, and S. H. Bloomberg, "Hierarchical figure-based shape description for medical imaging," in *Proc. NATO Advanced Science Institute on Mathematics and Computer Science in Medical Imaging*. New York: Springer-Verlag, 1988, pp. 365-387.
- [49] J. L. McClelland and D. E. Rumelhart, *Explorations in Parallel Distributed Processing*. Cambridge, MA: MIT Press, 1987.
- [50] T. Pavlidis, *Algorithms for Graphics and Image Processing*. Rockville, MD: Computer Science Press, 1982.
- [51] S. L. Horowitz and T. Pavlidis, "Picture segmentation by a tree traversal algorithm," *J. Assoc. Comput. Mach.*, vol. 23, pp. 368-388, 1976.



Melinda J. Piket-May (S'89) was born in Kalamazoo, MI, on July 9, 1965. She received the B.S.E.E. degree from the University of Illinois, Urbana, in 1988, and the M.S. degree in electrical engineering from Northwestern University, Evanston, IL, in 1990.

She is currently pursuing the Ph.D. degree in the Department of Electrical Engineering at Northwestern University, where she works as Research Assistant. Her research interests include numerical modeling of electromagnetic phenomena with application to VLSI and biomedical problems.



Allen Taflové (M'75-SM'84-F'90) was born in Chicago, IL, on June 14, 1949. He received the B.S. (with highest distinction), M.S., and Ph.D. degrees in electrical engineering from Northwestern University, Evanston, IL, in 1971, 1972, and 1975, respectively.

From 1975 to 1984, he was a staff member in the Electronics Division, IIT Research Institute, Chicago, IL, holding the positions of Associate Engineer, Research Engineer, and Senior Engineer. During this time, he was principal investigator

on a number of externally funded programs, including five that contributed to the early development of the finite-difference time-domain method for computational modeling of electromagnetic wave interactions with complex structures. He was also a key contributor to large-scale programs involving the application of radio-frequency heating to produce oil in place (without mining) from deposits of oil shale, tar sands, and heavy oil; to accelerate oil production from slowly producing conventional wells; and to decontaminate large sections of the ground permeated with toxic chemical wastes. In this technical area, he has been awarded ten U.S. patents. He also authored a major EPRI report on electromagnetic field coupling effects of 60-Hz power transmission and distribution lines upon adjacent utilities. In 1984, he returned to Northwestern University where he is currently Professor of Electrical Engineering and Computer Science. He is actively pursuing supercomputing computational electromagnetics modeling of a broad variety of phenomena and technologies, including radiation and scattering, microwave/millimeter wave circuits, picosecond digital electronics, and femtosecond optical pulse propagation and switching. He also cooriginated and is active in Northwestern's innovative Honors Program in Undergraduate Research, wherein extremely bright high school graduates participate in an accelerated, research-enriched curriculum leading to the Ph.D. in as little as six years. In May 1991, he was honored as Adviser of the Year in the McCormick School of Engineering.

Dr. Taflové is a member of Tau Beta Pi, Eta Kappa Nu, Sigma Xi, Commission B of URSI, and the Electromagnetics Academy. During 1990-1991, he was a Distinguished National Lecturer for the IEEE Antennas and Propagation Society, and he is Chairman of the Technical Program of the 1992 IEEE Antennas and Propagation Society International Symposium to be held in Chicago. He is coauthor of the Best Paper at the 1983 IEEE International EMC Symposium, Washington, DC. He presented a one-hour invited talk at the AIAA 30th Aerospace Sciences Meeting, Reno, NV, Jan. 1992.



Wei-Chung Lin (S'80-S'84) received the B.S. degree in electrical engineering from the National Taiwan University, Taiwan, R.O.C., in 1975, the M.B.A. degree from the National Cheng-chi University in 1977, the M.S. degree in computer science from Michigan State University, East Lansing, in 1980, and the Ph.D. degree in electrical engineering from Purdue University, West Lafayette, IN, in 1984.

From 1984 to 1986, he was a Project Engineer in the R&D Center of the Standard Oil Company, Ohio. He is currently Assistant Professor of Electrical Engineering and Computer Science at Northwestern University and Faculty Member of the Center for Imaging Science at the University of Chicago. His current research activities include building computer vision systems for automated three-dimensional object recognition, expert vision systems for medical image understanding, and neural network systems for machine vision.

Dr. Lin is a member of AAAI, ACM, IEEE, INNS, SPIE, Classification Society of North America, and Pattern Recognition Society.



Daniel S. Katz (S'81) was born in Belleville, IL, on September 11, 1966. He received the B.S.E.E. and M.S. degrees in electrical engineering, both from Northwestern University, Evanston, IL, in 1988 and 1990, respectively.

Currently he is pursuing the Ph.D. degree in the Department of Electrical Engineering at Northwestern University, where he works as a Research Assistant. His research interests include computational modeling of electromagnetic wave propagation, radiation, and scattering.

Mr. Katz is a member of Tau Beta Pi and Eta Kappa Nu.



Vythilingam Sathiaselvan (M'86) was born in Sri Lanka in 1952. He received the B.Sc. degree in electronics engineering from the University of Sri Lanka, Katubadde Campus in 1976 with First Class honors and the Ph.D. degree in microwave engineering from the University of Bradford in 1982.

From 1982 to 1986, he was a Research Scientist with the Medical Research Council's Clinical Oncology and Radiotherapeutics Unit in Cambridge, England. He was an Assistant Professor in the Washington University School of Medicine, Mallinckrodt Institute of Radiology in St. Louis, USA from 1986 to 1988. He is currently employed by the Northwestern Memorial Hospital as Hyperthermia Engineer in the Radiation Oncology Center. He also holds an appointment as an Assistant Professor in Clinical Radiology in the Department of Radiology, Division of Radiation Oncology, Northwestern University Medical School. He is also a member of the Cancer Center, Northwestern University. His main research focuses on the development of improved electromagnetic techniques for heating deep-seated and superficial tumors and numerical modeling of electromagnetic interaction with biological objects.



Bharat B. Mittal was born in India in 1952. He received the B.S. degree in 1969 from Meerut University, India, and the M.B.B.S. degree from the Christian Medical College, Ludhiana, India in 1973.

He was a resident in Internal Medicine at the Christian Medical College, Ludhiana, India from 1975 to 1976 and in Radiation Oncology at the Northwestern University, Chicago, Illinois from 1977 to 1980. He had a Fellowship in Radiation Oncology from 1980 to 1981 at the Mallinckrodt

Institute of Radiology, Washington University School of Medicine, St. Louis, Missouri and was an Instructor of Radiation Oncology from 1981 to 1982 at the same institute. From 1982 to 1985 he was an Assistant Professor of Radiology, University of Pittsburgh, Pittsburgh, Pennsylvania. In 1985 he joined the Department of Radiology, Division of Radiation Oncology, Northwestern University Medical School, Chicago as a Clinical Assistant Professor of Radiology and became an Associate Professor in

1989. He is also a member of the Cancer Center, Northwestern University. He is a member of the attending medical staff of Northwestern Memorial Hospital, where he directs the hyperthermia program. His research involves management of head and neck cancers, lymphoid malignancies, and the use of hyperthermia with irradiation and/or chemotherapy in the treatment of a variety of malignant tumors.

Dr. Mittal is certified by the American Board of Radiology

# Finite-Difference Time-Domain Modeling of Curved Surfaces

Thomas G. Jurgens, *Member, IEEE*, Allen Taflové, *Fellow, IEEE*  
Korada Umashankar, *Senior Member, IEEE*, and  
Thomas G. Moore, *Member, IEEE*

**Abstract**—In this paper the finite-difference time-domain (FDTD) method is generalized to include the accurate modeling of curved surfaces. This generalization, the contour path (CP) method, accurately models the illumination of bodies with curved surfaces, yet retains the ability to model corners and edges. CP modeling of two-dimensional electromagnetic wave scattering from objects of various shapes and compositions is presented.

## I. INTRODUCTION

A significant flaw in previous finite-difference time-domain (FDTD) models of structures with smooth curved surfaces has been to use stepped edge (staircase) approximations of the actual structure surface. Although not a serious problem for modeling wave penetration and scattering for low- $Q$  metal cavities, recent FDTD studies have shown that stepped approximations of curved walls and aperture surfaces can shift center frequencies of resonant responses by 1 to 2% for  $Q$  factors of 30 to 80, and can possibly introduce spurious nulls [1]. In the area of scattering by complex shapes, the use of stepped surface approximations has limited the application of FDTD for the modeling of the important target class where surface roughness, exact curvature, and dielectric or permeable loading is important in determining the radar cross section. This paper reports on a generalization of the FDTD method, the contour path (CP) method, where grid cells local to structure surfaces are deformed.

Recently, three different types of FDTD conformable surface models have been proposed and examined for scattering problems.

1) *Locally distorted grid models*. These preserve the basic Cartesian grid arrangement of field components at all space cells except those immediately adjacent to the structure surface. Space cells adjacent to the structure surface are

deformed to conform with the surface locus. Slightly modified time stepping expressions for the field components adjacent to the surface are obtained by applying either a modified finite volume technique [2] or the CP technique.

2) *Globally distorted grid models, body fitted*. These employ available numerical mesh generation schemes to construct non-Cartesian grids which are continuously and globally stretched to conform with smoothly shaped structures. In effect, the Cartesian grid is mapped to a numerically generated coordinate system wherein the structure surface contour occupies a locus of constant equivalent "radius." Time-stepping expressions are adapted either from the Cartesian FDTD case [3] or from a characteristics based method used in computational fluid dynamics [4].

3) *Globally distorted grid models, unstructured*. These employ available numerical mesh generation schemes to construct non-Cartesian grids comprised of an unstructured array of space filling cells. Structure surface features are appropriately fit into the unstructured grid, with local grid resolution and cell shape selected to provide the desired geometric modeling aspects. An example of this class is the control region approach discussed in [5].

Research is ongoing for each of these types of conformable surface models. Key questions concerning the usefulness of each model include the following:

- 1) computer resources involved in mesh generation;
- 2) severity of numerical artifacts introduced by grid distortion, which includes numerical instability, dispersion, and nonphysical wave reflection, and subtraction noise;
- 3) limitation of the near-field computational range due to subtraction noise;
- 4) comparative computer resources for running realistic scattering models, especially for three-dimensional targets spanning lengths or more.

## II. REVIEW OF THE FDTD METHOD

In this section the analytical basis of the FDTD method will be briefly described first, since the CP method is a generalization of it. Detailed descriptions of the FDTD method can be found elsewhere [6]–[10].

The traditional FDTD algorithm is a direct solution of Maxwell's time dependent curl equations, which are shown in Table I(a). The algorithm applies a second-order accurate finite difference approximation to the space and time deriva-

Manuscript received October 20, 1989; revised September 30, 1991. The work of A. Taflové was supported in part by National Science Foundation Grant ASC-8811273, the Office of Naval Research under Contract N00014-88-K-0475, and General Dynamics P.O. 4059045.

T. G. Jurgens is with the Fermi National Accelerator Laboratory, Mail Stop 308, Batavia, IL 60510.

A. Taflové is with the Department of Electrical Engineering and Computer Science, McCormick School of Engineering, Northwestern University, Evanston, IL 60208.

K. Umashankar is with the Department of Electrical Engineering and Computer Science, University of Illinois, Chicago, IL 60680.

T. G. Moore is at the Massachusetts Institute of Technology Lincoln Laboratory, Boston, MA 02173.

IEEE Log Number 91C5997.

TABLE I  
(a) MAXWELL'S CURL EQUATIONS IN CARTESIAN COORDINATES

$$\frac{\partial H_z}{\partial t} = \frac{1}{\mu} \left( \frac{\partial E_y}{\partial z} - \frac{\partial E_z}{\partial y} - \rho' H_z \right) \quad (1)$$

$$\frac{\partial H_y}{\partial t} = \frac{1}{\mu} \left( \frac{\partial E_z}{\partial x} - \frac{\partial E_x}{\partial z} - \rho' H_y \right) \quad (2)$$

$$\frac{\partial H_x}{\partial t} = \frac{1}{\mu} \left( \frac{\partial E_x}{\partial y} - \frac{\partial E_y}{\partial x} - \rho' H_x \right) \quad (3)$$

$$\frac{\partial E_x}{\partial t} = \frac{1}{\epsilon} \left( \frac{\partial H_z}{\partial y} - \frac{\partial H_y}{\partial z} - \sigma E_x \right) \quad (4)$$

$$\frac{\partial E_y}{\partial t} = \frac{1}{\epsilon} \left( \frac{\partial H_x}{\partial z} - \frac{\partial H_z}{\partial x} - \sigma E_y \right) \quad (5)$$

$$\frac{\partial E_z}{\partial t} = \frac{1}{\epsilon} \left( \frac{\partial H_y}{\partial x} - \frac{\partial H_x}{\partial y} - \sigma E_z \right) \quad (6)$$

where

$E_x, E_y, E_z$  Cartesian components of electrical field, v/m  
 $H_x, H_y, H_z$  Cartesian components of magnetic field, v/m  
 $\epsilon$  electric permittivity, F/m  
 $\sigma$  electric conductivity, S/m  
 $\mu$  magnetic permeability, H/m  
 $\rho'$  equivalent magnetic loss,  $\Omega/\text{m}$

(b) CENTRAL DIFFERENCE APPROXIMATION TO SPACE AND TIME PARTIAL DERIVATIVES

$$(i, j, k) = (i\Delta x, j\Delta y, k\Delta z) \quad (7)$$

$$F^n(i, j, k) = F(i\Delta x, j\Delta y, k\Delta z, n\Delta t) \quad (8)$$

$$\frac{\partial F^n(i, j, k)}{\partial x} = \frac{F^n(i + \frac{1}{2}, j, k) - F^n(i - \frac{1}{2}, j, k)}{\Delta x} + \text{order}(\Delta x^2) \quad (9)$$

$$\frac{\partial F^n(i, j, k)}{\partial t} = \frac{F^{n+1/2}(i, j, k) - F^{n-1/2}(i, j, k)}{\Delta t} + \text{order}(\Delta t^2) \quad (10)$$

for a cubic space lattice,  $\Delta x = \Delta y = \Delta z = \delta$

TABLE II  
EXAMPLES OF FINITE-DIFFERENCE EQUATIONS DERIVED FROM MAXWELL'S EQUATIONS

$$H_x^{n+1/2}(i, j + 1/2, k + 1/2) = H_x^{n-1/2}(i, j + 1/2, k + 1/2) + \frac{\Delta t}{\mu(i, j + 1/2, k + 1/2)} \left[ \frac{1}{\Delta z} (E_y^n(i, j + \frac{1}{2}, k + 1) - E_y^n(i, j + \frac{1}{2}, k)) + \frac{1}{\Delta y} (E_z^n(i, j, k + \frac{1}{2}) - E_z^n(i, j + 1, k + \frac{1}{2})) \right] \quad (11)$$

$$E_x^{n+1}(i, j, k + 1/2) = \frac{1 - \frac{\sigma(i, j, k + 1/2)\Delta t}{2\epsilon(i, j, k + 1/2)}}{1 + \frac{\sigma(i, j, k + 1/2)\Delta t}{2\epsilon(i, j, k + 1/2)}} E_x^n(i, j, k + 1/2) + \frac{1}{1 + \frac{\sigma(i, j, k + 1/2)\Delta t}{2\epsilon(i, j, k + 1/2)}} \times \frac{\Delta t}{\epsilon(i, j, k + 1/2)} \left[ \frac{1}{\Delta x} (H_y^{n+1/2}(i + \frac{1}{2}, j, k + \frac{1}{2}) - H_y^{n+1/2}(i - \frac{1}{2}, j, k + \frac{1}{2})) + \frac{1}{\Delta y} (H_z^{n+1/2}(i, j, -\frac{1}{2}, k + \frac{1}{2}) - H_z^{n+1/2}(i, j + \frac{1}{2}, k + \frac{1}{2})) \right] \quad (12)$$



tives of each cartesian field component. These central difference approximations are displayed in Table I(b).

The above equations combined with the constitutive relations result in a set of difference equations, examples of which are given in Table II. The constitutive relations are:

$$\vec{D} = \epsilon \vec{E} \quad (13)$$

$$\vec{B} = \mu \vec{H} \quad (14)$$

$$\vec{J}_c = \sigma \vec{E} \quad (15)$$

where  $\epsilon$ ,  $\mu$ , and  $\sigma$  are the permittivity, permeability, and conductivity, respectively. All quantities on the right-hand side of each difference equation are known from computations performed at previous time steps. This results in a fully explicit system of difference equations whereby chronological values of the electric and magnetic field components at each location are obtained in a temporal leapfrog manner. Spatially, the computations are dependent on nearby field components, which enhances the method's ability to be computed on parallel architecture machines [11]. Fig. 1(b) illustrates the resulting spatial relationship between the field components.

Now that the structure of an individual FDTD cell has been described, the structure of the complete FDTD lattice will be discussed. The lattice is partitioned into two volumes, a total field region and a scattered field region, as illustrated in Fig. 1(c). Inside the total field region both incident and scattered waves exist. This region also encompasses the entire scattering body. No boundary condition needs to be applied at the body's surface, the medium changes implicitly with the cell to cell change of material characteristics ( $\sigma$ ,  $\epsilon$ ,  $\mu$ ). The overwhelming majority of lattice cells are in the total field region, a percentage that increases with the lattice size. The scattered field region surrounds the total field region. The scattered field region is necessary in order to utilize an accurate radiation boundary condition introduced by Mur [12]. The basis of this radiation condition is a two-term Taylor series approximation of a one-way wave equation [13]. The existence of a scattered field region also permits the implementation of a near- to far-field transformation [14], based upon the electromagnetic field equivalence principle [15].

At this point it is worthwhile to remark that some FDTD codes do not divide their lattices into total and scattered field regions explicitly. In these codes, only scattered fields exist external to an object, while total fields are in the interior. The incident field is introduced by applying an appropriate boundary condition on an object's surface. For example, a perfectly conducting body would have the condition  $E_{\text{tan}} = -E_{\text{tan}}$  applied to  $E$ -field components tangent to the body's surface. This methodology becomes quite cumbersome for materially complex heterogeneous objects. In addition, these codes suffer from accuracy problems in modeling the interior of shielded cavities and shadow regions [16], [17].

### III. ANALYTICAL BASIS OF THE CONTOUR PATH METHOD

#### A. Introduction

The CP algorithm is based on Ampere's and Faraday's laws, shown below:

$$\oint_C \vec{H} \cdot d\vec{l} = \int_S (\vec{J}_c + \vec{J}_s) \cdot d\vec{S} + \frac{\partial}{\partial t} \int_S \vec{D} \cdot d\vec{S} \quad (16)$$

$$\oint_C \vec{E} \cdot d\vec{l} = - \frac{\partial}{\partial t} \int_S \vec{B} \cdot d\vec{S} \quad (17)$$

where  $\vec{E}$ ,  $\vec{D}$ ,  $\vec{H}$ ,  $\vec{B}$ ,  $\vec{J}_c$ , and  $\vec{J}_s$  denote the electric field, electric flux density, magnetic field, magnetic flux density, conduction current and source current, respectively, and the  $C$  contours enclose the  $S$  surfaces. The contours of Ampere's and Faraday's laws intersect each other's enclosed surface in much the same way as the links in a chain intersect. Fig. 1(a) illustrates this relationship, where the coordinates ( $u$ ,  $v$ ,  $w$ ) are any cyclical permutation of  $x$ ,  $y$ , and  $z$ . Implementing (16), the value of the  $E_u$  field component at time step  $n$  is calculated from the two  $H_v$  and the two  $H_w$  field components at time step  $n - 1/2$  and the value of the  $E_u$  component at time step  $n - 1$ . Then implementing (17), the value of  $H_u$  at time step  $n + 1/2$  is calculated from the two  $E_v$  and  $E_w$  components at time step  $n$  and the value of  $H_u$  at time step  $n - 1/2$ . In this leap frog manner the CP algorithm progresses with its calculations. For contours not near a media interface, the contour shape is rectangular and the CP difference equations are identical to the traditional FDTD difference equations. For example, this is a CP Faraday difference equation not near a media interface:

$$\begin{aligned} H_x^{n+1/2}(i, j + 1/2, k + 1/2) &= H_x^{n-1/2}(i, j + 1/2, k + 1/2) \\ &+ \frac{\Delta t}{A\mu(i, j + 1/2, k + 1/2)} \\ &\times \left[ l_3 E_y^n(i, j + \frac{1}{2}, k + 1) - l_1 E_y^n(i, j + \frac{1}{2}, k) \right. \\ &\left. + l_4 E_z^n(i, j, k + \frac{1}{2}) - l_2 E_z^n(i, j + 1, k + \frac{1}{2}) \right] \end{aligned} \quad (18)$$

In this equation,  $A = \Delta y \Delta z$ ,  $l_1 = l_3 = \Delta z$  and  $l_2 = l_4 = \Delta y$ . Thus, this equation is identical to the FDTD equation (11). Consequently, the CP method need only be applied to cells near a material interface, with the traditional FDTD method applied to the remaining cells. The total field-scattered field lattice partition, the near- to far-field lattice truncation and the absorbing boundary condition are unaffected by this inclusion of CP cells in the traditional FDTD grid.

Both the CP and the traditional FDTD methods have the same capabilities regarding time stepping and waveform modeling. The results presented here are obtained by illuminating the objects with a step sinusoid and waiting for the fields to reach steady state. Subtraction noise problems have never been observed with the traditional FDTD methodology and do not occur with the CP method either.

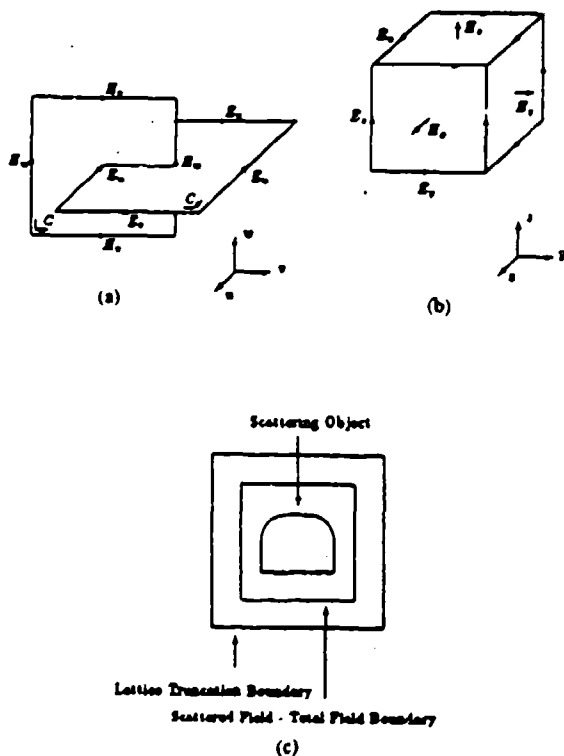


Fig. 1. (a) The CP Ampere and Faraday contour relationship. (b) A unit cell of the FDTD lattice. (c) The FDTD lattice structure.

### B. Perfectly Conducting Objects, TE Illumination

In this section the CP modeling of the TE illumination of perfectly conducting objects is discussed. First, the normally rectangular Faraday contours surrounding each  $H$  component near the object are deformed so as to conform to its surface. Each  $H$  component is assumed to represent the average value of the magnetic field within the patch bounded by the distorted contour. The electric field,  $E_{\text{tan}}$ , on the distorted contour at the object surface is zero. Along the remaining straight portions of the contour, the electric field components are assumed to have no variation along their respective contour segments. Where possible these electric field components are calculated using rectangular Ampere contours from adjacent  $H$  components. The Ampere contours are not deformed. Also, calculations of Ampere contours which cross the media boundary are not used, necessitating that the  $E$ -field along the corresponding Faraday contour segments, if needed, are computed in some other way. These Faraday segments which intersect the object's surface, but are not tangent to it, have their  $E$ -field computed in one of two ways.

In the first way, the normal  $E$  approximation shown in Fig. 2(a), the projection onto the Faraday contour segment, of the  $E$ -field value at the intersection of the segment and the surface, is used. The  $E$ -field at this intersection point ( $E_n$ ) is normal to the object's surface.  $E_n$  is calculated by setting up an auxiliary Ampere's law contour computation along the surface. The  $H$ -field values needed for the auxiliary computation are interpolated from  $H$ -field components near the surface.

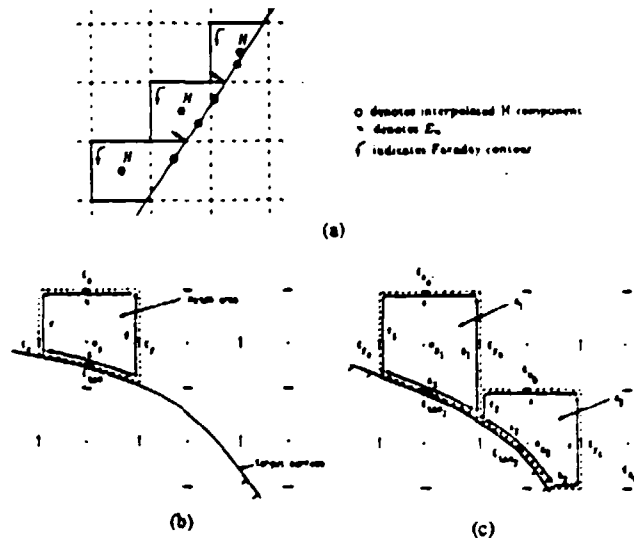


Fig. 2. CP TE methodology for perfectly conducting surfaces. (a) Normal  $E$  approximation. (b), (c) Nearest neighbor approximation.

The second way, the nearest neighbor approximation shown in Figs. 2(b) and 2(c), uses the near field component that is collinear with the Faraday contour segment, of the same type ( $E_x$ ,  $E_y$ , etc.) and on the same side of the media interface as the Faraday segment. After applying Faraday's law for the three illustrative contours of Figs. 2(b) and 2(c), the following special FDTD time stepping relations are obtained for the  $H_z$  components immediately adjacent to the object surface, as listed below.

Standard Subcell - Fig. 2(b):

$$\begin{aligned} H_z^{n+1/2}(i+1/2, j+1/2) &= C \cdot H_z^{n-1/2}(i+1/2, j+1/2) \\ &+ D \cdot [E_y^n(i, j+1/2) \cdot f - E_y^n(i+1, j+1/2) \cdot g \\ &+ E_x^n(i+1/2, j+1) \cdot \delta] \end{aligned} \quad (19)$$

where

$$C = \left( \frac{\mu_0 A}{\delta t} - \frac{sZ_s}{2} \right) / \left( \frac{\mu_0 A}{\delta t} + \frac{sZ_s}{2} \right) \quad (20)$$

$$D = 1 / \left( \frac{\mu_0 A}{\delta t} + \frac{sZ_s}{2} \right) \quad (21)$$

Standard Stretched Cell - Fig. 2(c), component  $H_z$ :

$$\begin{aligned} H_z^{n+1/2}(i+1/2, j+1/2) &= C_1 \cdot H_z^{n-1/2}(i+1/2, j+1/2) \\ &+ D_1 \cdot [E_y^n(i, j+1/2) \cdot f_1 \\ &- E_y^n(i+1, j+1/2) \cdot g_1 \\ &+ E_x^n(i+1/2, j+1) \cdot \delta] \end{aligned} \quad (22)$$

where

$$C_1 = \left( \frac{\mu_0 A_1}{\delta t} - \frac{s_1 Z_{s1}}{2} \right) / \left( \frac{\mu_0 A_1}{\delta t} + \frac{s_1 Z_{s1}}{2} \right) \quad (23)$$

$$D_1 = 1 / \left( \frac{\mu_0 A_1}{\delta t} + \frac{s_1 Z_{s1}}{2} \right). \quad (24)$$

*Non-standard Subcell* – Fig. 2(c), component  $H_{zj}$ :

$$\begin{aligned} H_{zj}^{n+1}(i+1/2, j+1/2) \\ = C_2 \cdot H_{zj}^{n-1}(i+1/2, j+1/2) + D_2 \\ \cdot \left[ \begin{aligned} &E_{y2}^n(i, j+1/2) \cdot \delta_2 - E_{y2}^n(i+1, j+1/2) \cdot \delta \\ &+ E_{x2}^n(i+1/2, j+1) \cdot \delta - E_{x2}^n(i+1/2, j+1) \cdot h_2 \end{aligned} \right] \end{aligned} \quad (25)$$

where

$$C_2 = \left( \frac{\mu_0 A_2}{\delta t} - \frac{s_2 Z_{s2}}{2} \right) / \left( \frac{\mu_0 A_2}{\delta t} + \frac{s_2 Z_{s2}}{2} \right) \quad (26)$$

$$D_2 = 1 / \left( \frac{\mu_0 A_2}{\delta t} + \frac{s_2 Z_{s2}}{2} \right). \quad (27)$$

In the above equations, we note that the only data needed to describe a distorted contour are:

- 1) the area of the patch,  $A$ , within the contour;
- 2) intercept points of the object surface contour with grid lines;
- 3) the subtended arc length,  $s$ , of the object surface;
- 4) knowledge of whether  $E$  components along the contour are calculable using the regular Yee algorithm; and
- 5) variation of the surface impedance,  $Z_s$ , with position along the object surface contour.

The distorted contour and field approximation information, obtained from a suitable geometry generation preprocessor, allows the CP code to process the conformably modeled object surface contour as easily and quickly as the FDTD code, but with substantially better accuracy, as will be demonstrated shortly. However, the choice of the nearest neighbor or normal  $E$  approximations provide equal levels of accuracy. For completeness, we note that no magnetic or electric field components in the FDTD space lattice, other than the  $H_z$  components immediately adjacent to the object surface, require modified time stepping relations.

### C. Perfectly Conducting Objects, TM Illumination

In the modeling of the TM illumination of perfectly conducting objects, the Faraday contours surrounding each  $H$  component located near the object are deformed so as to conform to its surface, as illustrated in Fig. 3. The Ampere contours which cross the media boundary are not used. Each such magnetic field component is assumed to represent the average value of the magnetic field within the patch bounded by the truncated contour.  $Z_s$  is the surface impedance of the object. The electric field,  $E_{\text{tan}}$ , located on the truncated contour at the object's surface, is equal to  $Z_s$  times the local azimuthal magnetic field,  $H_\phi$ .  $H_\phi$  is collocated with  $E_{\text{tan}}$  and is obtained by interpolating the known  $H_x$  and  $H_y$

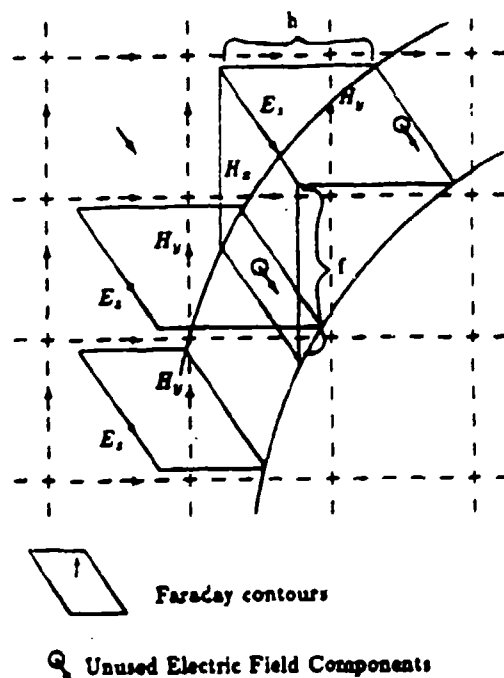


Fig. 3. Examples of modified Faraday's Law contour paths for the TM curved object.

components at this location and then adding their projections in the tangent direction.

For this study, consider only the case of  $Z_s = 0$  (perfectly conducting object). This eliminates the need to calculate a local surface azimuthal magnetic field via interpolation and vectorial addition. Then, applying Faraday's law to the contours of Fig. 3,

$$H_x^{n+1}(i, j+1/2) = H_x^{n-1}(i, j+1/2) - \frac{\delta t}{\mu_0 \delta} \cdot E_z^n(i, j+1) \quad (28)$$

$$H_y^{n+1}(i+1/2, j) = H_y^{n-1}(i+1/2, j) + \frac{\delta t}{\mu_0 h} \cdot E_z^n(i, j) \quad (29)$$

where it is noted that the  $E_z$  component at the object surface is zero. Here, only the intercept point of the object surface contour with the grid lines need to be known. This is substantially less geometry data needed than for the TE illumination cases discussed earlier. The Faraday segments which lie along the object's surface are assigned an  $E$ -field value of zero, since the tangential electric field at a perfect conductor's surface is zero.

### D. Dielectric Objects

For the modeling of dielectric objects, Faraday contours are deformed while the Ampere contours are not. Referring to Fig. 4, the Faraday contours are distorted so as to have them conform to the object's surface. Each  $H$  component is assumed to represent the average value of the magnetic field within the patch bounded by the distorted contour. The electric field,  $E_{\text{tan}}$ , on the distorted contour at the object surface is calculated via an auxiliary Ampere contour. Along

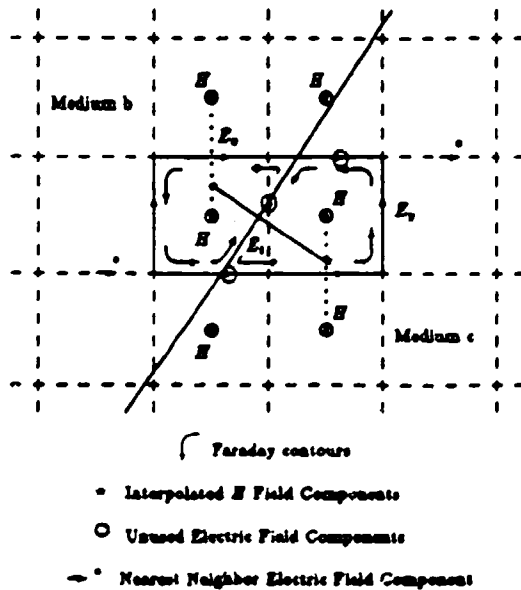


Fig. 4. Contour path TE Tangential  $E$ -field approximation for dielectric objects.

the remaining straight portions of the contour, the electric field components are assumed to have no variation along their respective contour segments. Where possible these electric field components are calculated using rectangular Ampere contours from adjacent  $H$  components. Also, calculations of Ampere contours which cross the media boundary are not used, necessitating that the  $E$ -field along the corresponding Faraday contour segments, if needed, is computed using the nearest neighbor approximation, as described above.

The Faraday's law difference equation for contours near the surface is:

$$\begin{aligned}
 H^{n+1}(i + 1/2, j + 1/2) \\
 = H_{E_1}^{n+1}(i + 1/2, j + 1/2) \\
 + D \cdot \left[ \begin{aligned} &E_y^n(i, j + \frac{1}{2})\delta y - E_x^n(p) \cdot l_1 \\ &+ E_x^n(i + \frac{1}{2}, j + 1) \cdot l_3 - E_x^n(i + \frac{1}{2}, j) \cdot l_1 \end{aligned} \right] \quad (30)
 \end{aligned}$$

where

$$D = \frac{\delta t}{\mu_0 \mu_{rel} A} \quad (31)$$

and  $l_1$  is the length of the contour segment along the media interface,  $l_1$  and  $l_3$  are the lengths of the bottom and top contour segments,  $\delta y$  is the length of the left contour segment and  $p$  is the  $E_{\text{int}}$  index.

The Ampere's law difference equation for the auxiliary tangential  $E$ -field components is:

$$E_{E_1}^{n+1}(p) = E_{E_1}^n(p) + \delta t$$

$$\begin{aligned}
 \times \left[ \begin{aligned} &(b_1 \cdot H^{n+1}(i + \frac{1}{2}, j + \frac{1}{2}) + b_2 \cdot H^{n+1}(i + \frac{1}{2}, j + \frac{1}{2}))/A_b \epsilon_b(i + \frac{1}{2}, j) - \\ &(c_1 \cdot H^{n+1}(i + 1\frac{1}{2}, j + \frac{1}{2}) + c_2 \cdot H^{n+1}(i + 1\frac{1}{2}, j - \frac{1}{2}))/A_c \epsilon_c(i + 1\frac{1}{2}, j) \end{aligned} \right] \quad (32)
 \end{aligned}$$

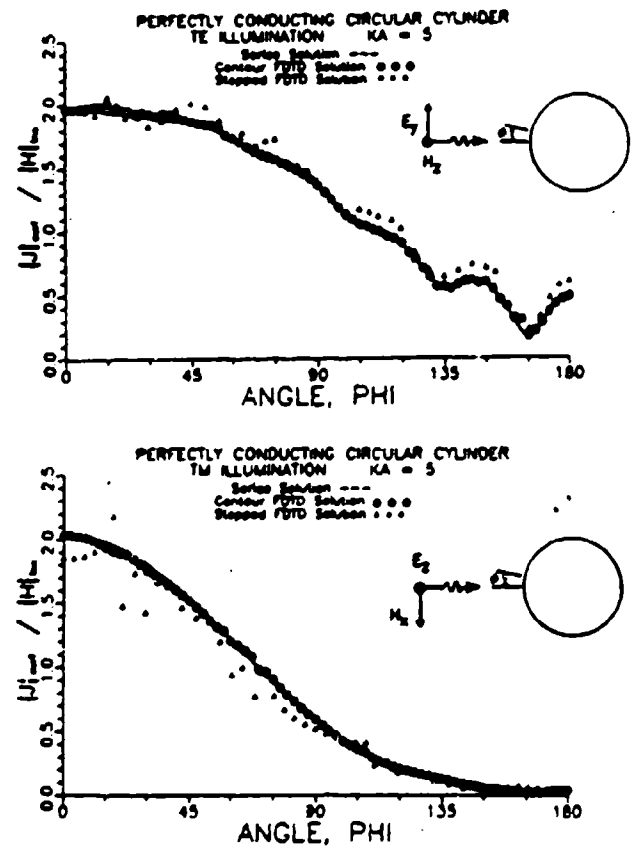


Fig. 5. Comparison of traditional FDTD, contour FDTD, and exact summed eigenmodes solutions for surface current induced on a circular conducting cylinder. (a) TE illumination. (b) TM illumination ( $\delta x = \lambda_0/20$  resolution).

where  $A_b$  and  $A_c$  are areas of the left and right portion of the Ampere's contour, respectively, and  $b_1$ ,  $b_2$ ,  $c_1$  and  $c_2$  are the coefficients for the  $H$ -field linear interpolation.

For the CP modeling of dielectric objects, TM illumination is the dual of TE illumination. That is, switching the roles of the magnetic field and the electric field, the permeability,  $\mu$ , and the permittivity,  $\epsilon$ , and the magnetic current and the electric current means that solving a TE illumination problem automatically provides data for a dual TM illumination problem.

### E. Anisotropic Objects

The CP modeling of anisotropic dielectric objects is a direct extension of isotropic dielectric objects. For axially anisotropic dielectric media the relationship between the  $\vec{D}$  and  $\vec{E}$  fields is

$$\vec{D} = \begin{pmatrix} \epsilon_{xx} & 0 \\ 0 & \epsilon_{yy} \end{pmatrix} \vec{E}. \quad (33)$$

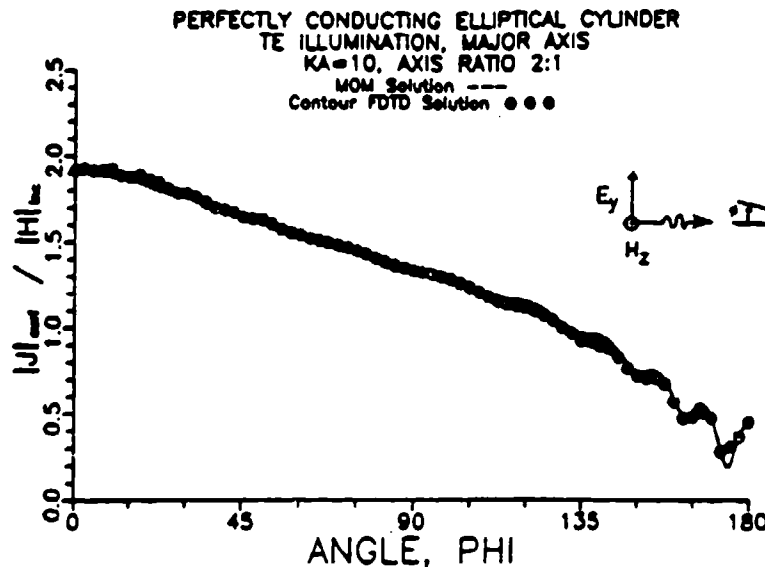


Fig. 6. Comparison of contour FDTD and method of moments solutions for surface current induced on an elliptical conducting cylinder, TE illumination ( $\delta x = \lambda_0/20$  resolution).

This tensor relationship results in an Ampere's law difference equation which is a slight modification of (32).

The next shape considered is an elliptical cylinder, subjected to TE illumination along its major axis. The circumference of the cylinder is 10 wavelengths and its axis ratio is

$$E_i^{n+1}(\rho) = E_i^n(\rho) + \delta t \times \left[ \begin{aligned} &(b_1 \cdot H^{n+1/2}(i + \frac{1}{2}, j + \frac{1}{2}) + b_2 \cdot H^{n+1/2}(i + \frac{1}{2}, j - \frac{1}{2})) / A_b \epsilon_b (i + \frac{1}{2}, j) \\ &- (c_1 \cdot H^{n+1/2}(i + \frac{1}{2}, j + \frac{1}{2}) + c_2 \cdot H^{n+1/2}(i + \frac{1}{2}, j - \frac{1}{2})) / A_c K \end{aligned} \right] \quad (34)$$

where  $A_b$  and  $A_c$  are areas of the left and right portion of the Ampere's law contour, respectively, and  $b_1, b_2, c_1$  and  $c_2$  are the coefficients for the  $H$ -field linear interpolation, and

$$K = \epsilon_{xx} \cos^2 \phi + \epsilon_{yy} \sin^2 \phi \quad (35)$$

where  $\phi$  is the angle  $E_{\text{inc}}$  makes with the positive  $x$ -axis. The Faraday's law difference equation for this case is identical to the isotropic case (30). As in the isotropic case, TM illumination is the dual of TE illumination.

#### IV. NUMERICAL RESULTS

In this section analytical and numerical data validations of the CP method are presented. Objects of various shapes and compositions are analyzed.

##### A. Perfectly Conducting Objects

The first shape considered is a  $k_0 a = 5$  circular cylinder, subjected to TE and TM illumination. Fig. 5 is a plot of the CP predicted surface current and the traditional (stepped) FDTD predicted surface current compared to the series solution. The CP method achieves an accuracy of 1% or better at most surface points resulting in accurate modeling of the peak and null structure of the current distribution. This figure also shows that the CP method is a significant improvement over the traditional FDTD method.

2:1. Fig. 6 is a plot of the CP predicted surface current compared to the method of moments solution. Once again, the CP method achieves accurate modeling of the peak and null structure of the current distribution.

The final shapes in this category are wing-like bodies, depicted in Fig. 7. It consists of a 10 in  $\times$  12 in metal plate, having steeply sloped sides with a central six inch radius chamfer on one side and either flat on the other side or having a symmetrically positioned V-shaped vertical slot on the other side. The measured data to be presented are for these three dimensional shapes, while the numerical data (the CP method and method of moments) are for the two dimensional shapes which result from allowing the 12 in dimension to go to infinity. Fig. 8(a) shows the monostatic radar cross section of the plate with the flat side. It is illuminated with a 10 GHz TM polarized wave. Fig. 8(b) shows the monostatic radar cross section of the plate with the V-slotted side. It is illuminated with a 16 GHz TE polarized wave. There is generally good agreement between the three sets of RCS data. In the low RCS regime near grazing incidence Fig. 8(b) shows that the CP method provides substantially better agreement with the measurements than MM. The residual disagreement between the CP and measured data is a consequence of the difference between the idealized 2-D computational model and the actual 3-D physical measured target.

For a given grid density, the CP method permits an object to be modeled more accurately than the traditional FDTD

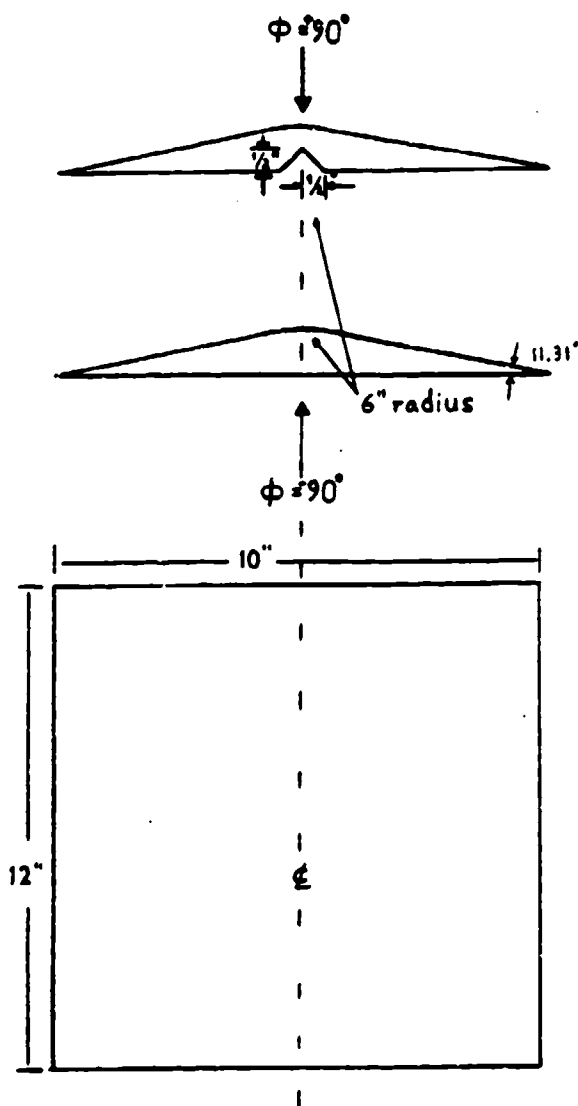


Fig. 7. Mechanical description of the wing-like body.

method. Both TE and TM cases are shown. Studies for the wing-like object indicate that  $1/20\lambda_0$  gridding with CP surface modeling provides monostatic RCS accuracy better than with  $1/80\lambda_0$  traditional (staircased) FDTD. This effect is most pronounced for incident angles near  $90^\circ$  as shown in Fig. 8(b). This is a *very large* advantage: in 2-D, more than 16:1 in storage and 64:1 in run time and in 3-D, more than 64:1 in storage and 256:1 in run time.

### B. Dielectric Objects

The first shape considered is a TE illuminated  $k_0 a = 5$  circular cylinder, with  $\epsilon_r = 4$ . Fig. 9 is a plot of the CP predicted electric and magnetic surface current compared to the series solution. The CP method achieves an accuracy of 1% or better at most surface points resulting in accurate modeling of the peak and null structure of the current distributions.

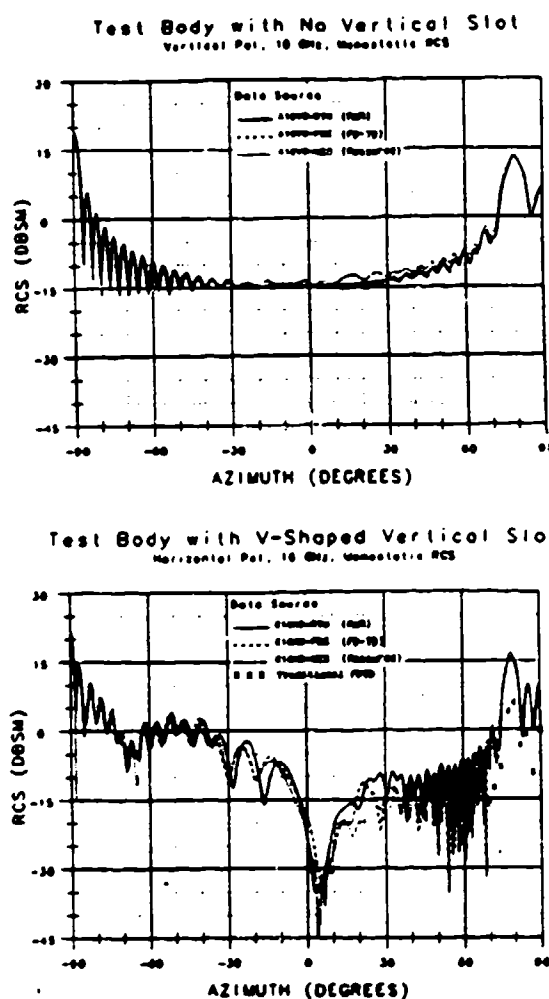


Fig. 8. Comparison of contour FDTD, method of moments and measured data for the radar cross section of a wing-like body. (a) TM illumination with no slot, (b) TE illumination with a V-shaped slot.

The final shape in this category is a TE illuminated  $k_0 a = 2.5$  anisotropic circular cylinder. The dielectric and magnetic coefficients for this object are  $\epsilon_{xx} = 2\epsilon_0$ ,  $\epsilon_{yy} = 4\epsilon_0$  and  $\mu = 2\mu_0$ . Fig. 10 is a plot of the CP predicted magnetic surface current compared to the combined field integral equation (CFIE) MM solution [18]. The CP method agrees with the MM results to 1% or better at most surface points resulting in accurate modeling of the peak and null structure of the current distributions.

### V. CONCLUSION

This paper has introduced a generalization of the FDTD method, the contour path method. Examples of CP modeling of two dimensional electromagnetic wave scattering are presented. Objects of various shapes and compositions are analyzed. The method accurately models the illumination of bodies with curved surfaces, yet retains the ability to model corners and edges. The CP modeling of three-dimensional objects is presently being investigated.

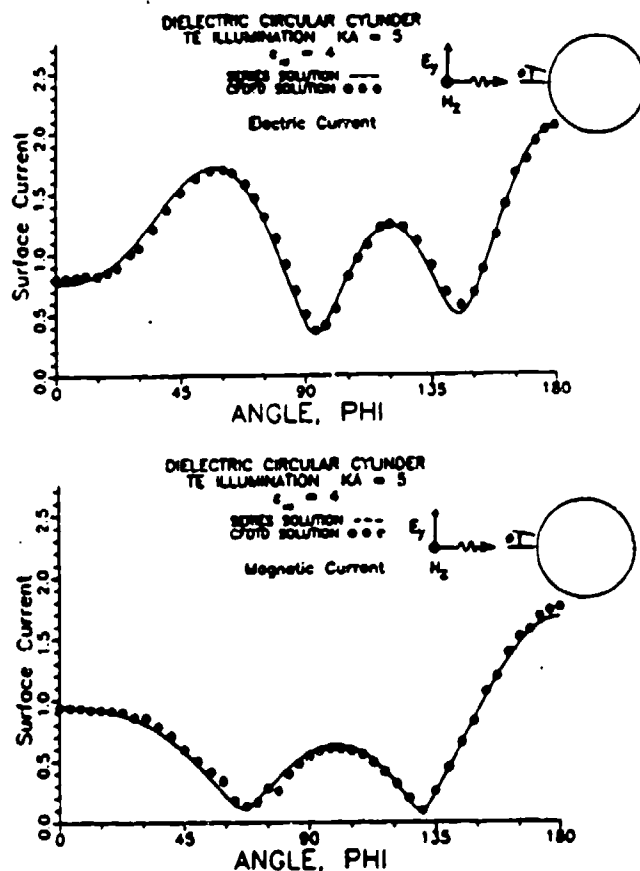


Fig. 9. Comparison of contour FDTD and exact summed eigenseries solutions for TE surface current induced on a dielectric circular cylinder. ( $\delta x = \lambda_y/20$  resolution).

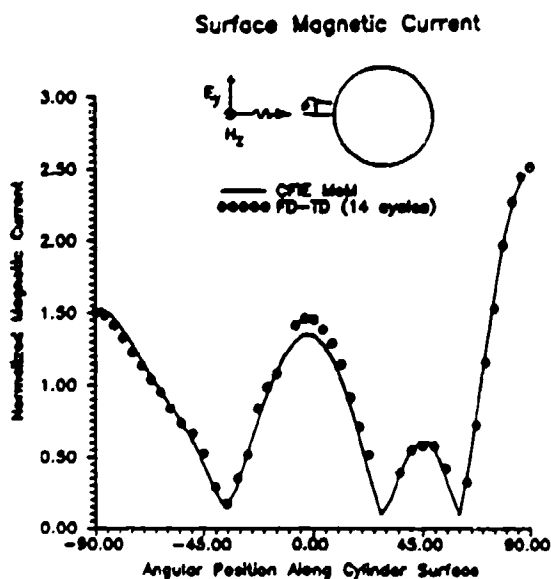


Fig. 10. Comparison of contour FDTD and method of moments solutions for TE surface current induced on an anisotropic circular cylinder with  $\epsilon_{xx} = 2\epsilon_0$ ,  $\epsilon_{yy} = 4\epsilon_0$  and  $\mu = 2\mu_0$ .

## REFERENCES

- [1] K. R. Umashankar, A. Taflov, B. Beker, and K. Yee, "Calculation and experimental validation of induced currents on coupled wires in an arbitrary-shaped cavity," *IEEE Trans. Antennas Propagat.*, vol. AP-35, pp. 1248-1257, Nov. 1987.
- [2] N. Madsen and R. Ziolkowski, "Numerical solution of Maxwell's equations in time domain using irregular nonorthogonal grids," *Wave Motion*, vol. 10, pp. 583-596, Dec. 1988.
- [3] M. Fusco, "FDTD algorithm in curvilinear coordinates," *IEEE Trans. Antennas Propagat.*, vol. 38, pp. 76-89, Jan. 1990.
- [4] V. Shankar, W. Hall, and A. H. Mohammadian, "A three-dimensional Maxwell's equation solver for computation of scattering from layered media," *IEEE Trans. Magn.*, vol. 25, pp. 3098-3103, July 1989.
- [5] B. J. McCartin and J. F. DiCello, "Three-dimensional finite difference frequency domain scattering using the control region approximation," *IEEE Trans. Magn.*, vol. 25, pp. 3092-3094, July 1989.
- [6] A. Taflov and K. R. Umashankar, "The finite difference time domain (FD-TD) method for electromagnetic scattering and interaction problems," *J. Electromagn. Waves Appl.*, 1(4):363-387, 1987.
- [7] A. Taflov and K. Umashankar, "Radar cross section of general three-dimensional scatterers," *IEEE Trans. Electromagn. Compat.*, vol. EMC-25, pp. 433-440, Nov. 1983.
- [8] K. Umashankar and A. Taflov, "Analytical models for electromagnetic scattering," *Hanscom Air Development Center, Hanscom AFB, MA, Tech. Rep.*, June 1984.
- [9] A. Taflov, K. R. Umashankar, and T. G. Jurgens, "Validation of FD-TD modeling of the radar cross section of three-dimensional scatterers," *IEEE Trans. Antennas Propagat.*, vol. AP-33, pp. 662-666, June 1985.
- [10] K. S. Yee, "Numerical solution of initial boundary value problems involving Maxwell's equations in isotropic media," *IEEE Trans. Antennas Propagat.*, vol. AP-14, pp. 302-307, May 1966.
- [11] A. T. Perlik, T. Opasch, and A. Taflov, "Predicting scattering of electromagnetic fields using FDTD on a connection machine," *IEEE Trans. Magn.*, vol. 25, pp. 2910-2912, July 1989.
- [12] G. Mur, "Absorbing boundary conditions for the finite-difference approximation of time-domain electromagnetic field equations," *IEEE Trans. Electromagn. Compat.*, vol. 23, pp. 377-382, Nov. 1981.
- [13] T. G. Moore, J. G. Blachak, O. A. Kriegsmann, and A. Taflov, "Theory and application of radiation boundary operators," *IEEE Trans. Antennas Propagat.*, vol. 36, pp. 1797-1812, Dec. 1988.
- [14] K. R. Umashankar and A. Taflov, "A novel method to analyze electromagnetic scattering of complex objects," *IEEE Trans. Electromagn. Compat.*, vol. EMC-24, pp. 397-405, Nov. 1982.
- [15] S. A. Schelkunoff, "Kirchoff formula, its vector analogue and other field equivalence theorems," *Comm. Pure Appl. Math.*, vol. 4, pp. 43-59, June 1951.
- [16] A. Taflov, K. R. Umashankar, and T. G. Jurgens, "Comparative time and frequency domain solutions of Maxwell's equations for modeling radar cross section," in *Advances in Computer Methods for Partial Differential Equations - V*, June 1984, pp. 406-414.
- [17] R. Holland and J. W. Williams, "Total field versus scattered field finite difference codes: a comparative assessment," *IEEE Trans. Nucl. Sci.*, vol. NS-30, pp. 4583-4588, Dec. 1983.
- [18] B. Beker, K. R. Umashankar, and A. Taflov, "Numerical analysis and validation of the combined field surface integral equations for electromagnetic scattering by arbitrarily shaped two dimensional anisotropic objects," *IEEE Trans. Antennas Propagat.*, vol. 37, pp. 1573-1581, Dec. 1989.



Thomas G. Jurgens (M'83) received the B.S.E.E. and M.S.E.E. degrees from the University of Illinois, Chicago, in 1980 and 1985, respectively, and the Ph.D. degree in electrical engineering from Northwestern University, Evanston, IL, in 1990.

He was with Northrop Corporation Rolling Meadows, IL from 1980-1982 and with UT Research Institute from 1982-1985. From 1985 to 1987 he worked as a research assistant at Northwestern University. Since 1987 he has been at Fermi National Accelerator Laboratory, Batavia,

IL. His research activities have included the study of EMP interaction, electromagnetic scattering, particle accelerator field analysis and semiconductor device modeling.

Allen Taflov (M'75-SM'84-F'90), for a photograph and biography please see page 906 of the July 1991 issue of this TRANSACTIONS.

Korada Umashankar (S'69-M'75-SM'81), for a photograph and biography please see page 1212 of the August 1991 issue of this TRANSACTIONS.

Thomas G. Moore (S'84-M'89) received the B.S., M.S., and Ph.D. degrees from Northwestern University, Evanston, IL, in 1986, 1987, and 1989, respectively.

After receiving the Ph.D. degree, he joined the technical staff in the radar imaging group at MIT Lincoln Laboratory. While at Lincoln Laboratory he has worked on problems involving electromagnetic scattering and radar imaging. His research interests include computational electromagnetics, electromagnetic theory and nonlinear wave propagation.

Dr. Moore is a member of Tau Beta Pi and Eta Kappa Nu.



# Numerical Analysis of Electromagnetic Scattering by Electrically Large Objects Using Spatial Decomposition Technique

Korada R. Umashankar, *Senior Member, IEEE*, Sainath Nimmagadda, *Student Member, IEEE*, and Allen Taflov, *Fellow, IEEE*

**Abstract**—The boundary value integral equation and method of moments numerical technique is widely utilized for the study of electromagnetic scattering by arbitrary shaped conducting and penetrable objects. Even though this direct approach is elegant as far as its application to analyze electrically large object is concerned, it inherently suffers from a wide range of computational difficulties. The method of moments system matrix is, in general, full and dense, requiring impractical demand on computer resources. In addition to operational numerical errors and ill-conditioning involved in the solution of large scale matrix equation, the direct numerical technique bears progressive degradation of accuracy of the near-field solution as the size of the system matrix increases. The apparent computational difficulties with the direct integral equation and method of moments has prompted an alternative numerical solution procedure based on the spatial decomposition technique. Using rigorous electromagnetic equivalence, the spatial decomposition technique virtually divides an electrically large object into a multiplicity of subzones. It permits the maximum size of the method of moments system matrix that need be inverted to be strictly limited, regardless of the electrical size of the large scattering object being modeled. The requirement on the computer resources is of order  $(N)$ , where  $N$  is the number of spatial subzones and each subzone is electrically small spanning in the order of a few wavelengths. Numerical examples are reported along with comparative data and relative error estimation to expose applicability and limitation of the spatial decomposition technique for the two-dimensional scattering study of electrically large conducting and dielectric objects.

## I. INTRODUCTION

THE frequency domain analysis of electromagnetic scattering, penetration and interaction by arbitrary shaped conducting and dielectric objects can be conveniently formulated using the boundary value integro-differential equations.

The boundary value equations, such as the electric field, the magnetic field and the combined field integral equations [1]–[3] have been extensively utilized to model various electromagnetic interactions associated with arbitrary shaped two and three dimensional objects. Generally, the near surface electric and magnetic fields or the corresponding equivalent magnetic and electric current distributions are treated as unknowns in the integral equations, and are solved by applying straight forward method of moments numerical technique [3]–[6]. Invariably, the numerical technique based on the method of moments converts the operator type of linear integral equation into an equivalent matrix equation by expanding the unknown current distributions in terms of a linearly independent set of expansion functions and testing the integral equation by a suitable set of weighting functions. This direct technique appears to be an elegant means for modeling and analyzing electromagnetic scattering and interaction by both canonical and arbitrary shaped conducting and dielectric objects. In fact, a large class of both two- and three-dimensional problems has been studied and reported extensively in the literature [3], [6]–[9]. However, there are key limitations and relative error estimations which render the direct integral equation and method moments technique unattractive beyond low and resonant frequencies.

The direct integral equation and method of moments technique generate a system of linear equations having dense, complex valued, full coefficient matrices. For a conventional matrix approach, the required computer storage is of the order  $O(P^2) + C_p P$  where  $P$  is the number of surface patches and  $C_p$  is a constant which depends upon the scatterer geometry and desired display of the numerical solution. Similarly, the execution time is of the order of  $O(P^2) + C_q P$  to  $O(P^3) + C_r P$ , where  $C_q$  and  $C_r$  are constants which depend upon numerical model adapted to generate the system matrix, and further, solve for the unknown surface currents. With a spatial resolution requirement in the order of  $\lambda/5$ – $\lambda/10$  to avoid aliasing of vital near-field magnitude and phase informa-

Manuscript received July 31, 1990; revised March 25, 1992. This work was supported in part by National Science Foundation Grant ASC-8811273 and by Office of Naval Research Grant N00014-88-K-0475.

K. R. Umashankar and S. Nimmagadda are with the Department of Electrical Engineering and Computer Science, University of Illinois, Chicago, IL 60680.

A. Taflov is with the Department of Electrical Engineering and Computer Science, McCormick School of Engineering, Northwestern University, Evanston, IL 60208.

IEEE Log Number 9201665.

tion implies that arbitrary three-dimensional structures spanning more than  $5\lambda$  would exhaust most existing and planned mainframe computer resources [7], [10]. The dimensionally large computer resource requirement has, in fact, served to place such a "cap" on problem applications.

The large system matrix (of electrically large object) generated by the direct integral equation and method of moments numerical technique tends to become highly ill-conditioned. This potentially degrades the accuracy of the computed results [11]. The accuracy of the numerical solution may also be due to floating point word-length used in the computer and numerical procedure used for computing individual elements and inversion of the system matrix. Accumulating errors of these types can be troublesome, especially when hundreds of millions of matrix elements/floating point operations are involved in one modeling problem.

The computational difficulties with the direct integral equation and method of moments solution technique have prompted a number of alternative approaches, such as combining the method of moments and a high frequency technique to obtain a hybrid formulation [12], [13] and also its related iterative variations [14], [15]. In addition, iterative matrix solution methods including conjugate gradient, spectral iterative approaches [16], [17] have been investigated as tools to study electrically large scattering problems. It is not yet clear that the hybrid and iterative approaches proposed to date for electrically large objects possess the broad applicability and excellent accuracy that the full matrix method of moments approach evidences for the case of electrically small objects.

This paper presents preliminary findings of a novel methodology, which has been reported recently [3], [18], [19], [26], specifically referred to as the *spatial decomposition* technique (SDT) for the integral equation and method of moments that shows promise in significantly reducing both the dimensionality and ill-conditioning of the computational burden. In fact, the spatial decomposition permits the maximum size of the method of moments system matrix that need be inverted to be strictly limited, regardless of the electrical size of the electromagnetic scattering target being modeled. Using rigorous electromagnetic equivalences [20], the spatial decomposition technique allows one to divide an electrically large arbitrary shaped material object into a multiplicity of subzones. The individual subzones, in fact, are separated by virtual surfaces across which cancelling tangential electric and magnetic virtual currents are postulated. The subzones are defined as distinct scattering targets having fully enclosing surfaces with additional unknown virtual electric and magnetic currents introduced as needed to define the interfaces. The electromagnetic field boundary conditions are well preserved by simulating across the interface separating two subzones by requiring that the tangential virtual currents on one side of the interface must be equal but opposite to the tangential virtual currents on the other side. By sequentially implementing the integral equation

and method of moments solution for each subzone, effectively "scanning" the original target subzone by subzone, a rapidly convergent iterative process is established.

This paper reports a preliminary study of the spatial decomposition technique to analyze electromagnetic scattering by arbitrary shaped electrically large two-dimensional perfectly conducting and dielectric scatterers. Numerical results of the near surface currents and radar cross section along with comparative validation data and relative error estimation based on matrix condition number [21], [22] are reported in this paper to expose applicability and limitation of the SDT for electromagnetic scattering by an electrically large perfectly conducting thin strip scatterer, perfectly conducting rectangular and wedge type scatterers and homogeneous dielectric rectangular scatterer.

## II. SPATIAL DECOMPOSITION TECHNIQUE

Fig. 1 illustrates an arbitrary shaped two-dimensional isotropic homogeneous dielectric scattering object. It is excited externally by a transverse magnetic (TM) polarized plane wave propagating in a direction normal to the  $z$ -coordinate axis. As shown in Fig. 1, axially directed equivalent electric currents  $J_z(\bar{\rho}')$  and transverse directed equivalent magnetic currents  $M_\tau(\bar{\rho}')$  reside on a virtual boundary conforming to the physical surface of dielectric scatterer. This scattering object, in fact, is appropriate for formulating a set of coupled combined field integral equations (CFIE) by invoking the electromagnetic equivalence principle [2], [7], [20] and by treating the two surface electric and magnetic currents as initially unknown distributions. Further, the method of moments numerical technique can be implemented (for the scatterer taken as a whole) to solve for the two unknown surface currents as discussed in [3], [6], [9]. There exist only the following components of electric and magnetic field distributions:

- $E_z(\rho, \phi)\hat{z}$  total axial component of electric field distribution
- $H_\nu(\rho, \phi)\hat{\nu}$  total normal component of magnetic field distribution
- $H_\tau(\rho, \phi)\hat{s}$  total tangential component of magnetic field distribution.

Referring to Fig. 1,

$$\bar{J}_{eq}(\bar{\rho}') = \hat{z}'J_z(\bar{\rho}') \quad (1a)$$

$$= \hat{\nu}' \times \hat{s}'H_\tau(\rho', \phi'), \quad \bar{\rho}' \text{ on } C \quad (1b)$$

$$\bar{M}_{eq}(\bar{\rho}') = \hat{s}'M_\tau(\bar{\rho}') \quad (2a)$$

$$= -\hat{\nu}' \times \hat{z}'E_z(\rho', \phi'), \quad \bar{\rho}' \text{ on } C. \quad (2b)$$

For the TM normal excitation, based on the above components of unknown electric and magnetic current distributions, the  $z$ -component of scattered electric field

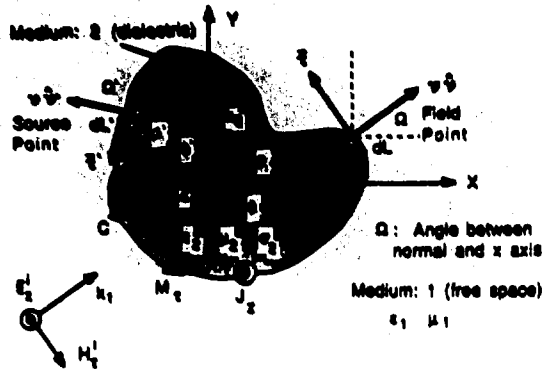


Fig. 1. Geometry of homogeneous, lossy, dielectric scatterer.

and  $r$ -component of scattered magnetic field are obtained by

$$\pm E_{mz}'(\bar{\rho}) = -\hat{z} \cdot j\omega \bar{A}_m(\bar{\rho}, \omega) - \hat{z} \cdot \nabla_r \times \frac{1}{\epsilon_m} \bar{F}_m(\bar{\rho}, \omega) \quad (3a)$$

$$\pm H_{mr}'(\bar{\rho}) = -\hat{r} \cdot j\omega \bar{F}_m(\bar{\rho}, \omega) - \frac{\partial}{\partial s} \Psi_m(\bar{\rho}, \omega) + \hat{s} \cdot \nabla_r \times \frac{1}{\mu_m} \bar{A}_m(\bar{\rho}, \omega) \quad (3b)$$

where on the left-hand side, the positive sign is selected for the region ( $m = 1$ ) outside the dielectric scatterer with  $\bar{\rho}$  on or outside the boundary contour  $C$ , and the negative sign is selected for the region ( $m = 2$ ) inside the dielectric scatterer with  $\bar{\rho}$  on or inside the boundary contour  $C$ . The vector and scalar potential integrals in (3a) and (3b) are given

$$\bar{A}_m(\bar{\rho}) = \frac{\mu_m}{4j} \int_C \hat{z}' J_z(\bar{\rho}') H_0^{(2)}(k_m |\bar{\rho} - \bar{\rho}'|) dL(\bar{\rho}') \quad (4a)$$

$$\bar{F}_m(\bar{\rho}) = \frac{\epsilon_m}{4j} \int_C \hat{s}' M_r(\bar{\rho}') H_0^{(2)}(k_m |\bar{\rho} - \bar{\rho}'|) dL(\bar{\rho}') \quad (4b)$$

$$\Psi_m(\bar{\rho}) = \frac{1}{4\omega\mu_m} \int_C [\nabla_r' \cdot \hat{s}' M_r(\bar{\rho}')] \cdot H_0^{(2)}(k_m |\bar{\rho} - \bar{\rho}'|) dL(\bar{\rho}'),$$

for  $m = 1$ ,  $\bar{\rho}$  on or outside  $C$  (free space medium)

for  $m = 2$ ,  $\bar{\rho}$  on or inside  $C$  (dielectric medium) (4c)

and

$$H_0^{(2)}(k_m |\bar{\rho} - \bar{\rho}'|)$$

Green's function for the two-dimensional case—

Hankel function of zero-order and second kind

$k_m$ : propagation constant for  $m = 1$  and  $m = 2$  regions

$$= \omega \sqrt{\mu_m \epsilon_m} \quad (4d)$$

The complete derivation of the coupled combined field integral equations can be found in [2], [3], [7], [6], and [9] by invoking the electromagnetic equivalences for regions

1 and 2, and the boundary conditions that the tangential components of total electric and magnetic fields are continuous across the boundary  $C$ . Only a summary of the relevant CFIE expressions which are useful for development of the spatial decomposition technique are given below

$$E_z^i(\bar{\rho}) = \sum_{m=1}^2 \mathcal{L}_m^{II}[J_z(\bar{\rho}')] + \sum_{m=1}^2 \mathcal{L}_m^{IM}[M_r(\bar{\rho}')], \quad \bar{\rho} \text{ on } C \quad (5a)$$

$$H_r^i(\bar{\rho}) = \sum_{m=1}^2 \mathcal{L}_m^{MI}[J_z(\bar{\rho}')] + \sum_{m=1}^2 \mathcal{L}_m^{MM}[M_r(\bar{\rho}')], \quad \bar{\rho} \text{ on } C \quad (5b)$$

where the CFIE partial integral operators [3], [6], [9] for the two-dimensional case are

$$\mathcal{L}_m^{II} = \int_C \left[ \frac{\omega \mu_m}{4} H_0^{(2)}(k_m R) \right] dL' \quad (6a)$$

$$\mathcal{L}_m^{IM} = \int_C \left\{ \frac{x-x'}{R} \cos \Omega' + \frac{y-y'}{R} \sin \Omega' \right\} \cdot \left[ \frac{k_m}{4j} H_0^{(2)'}(k_m R) \right] dL' \quad (6b)$$

$$\mathcal{L}_m^{MI} = \int_C \left\{ \frac{x-x'}{R} \cos \Omega + \frac{y-y'}{R} \sin \Omega \right\} \cdot \left[ \frac{k_m}{4j} H_0^{(2)'}(k_m R) \right] dL' \quad (6c)$$

$$\mathcal{L}_m^{MM} = \int_C \cos(\Omega - \Omega') \left[ \frac{\omega \epsilon_m}{4} H_0^{(2)}(k_m R) \right] dL' + \frac{\partial}{\partial s} \int_C dL' \left[ \frac{1}{4\omega \mu_m} H_0^{(2)}(k_m R) \right] \frac{\partial}{\partial s'}, \quad m = 1, 2. \quad (6d)$$

In (5a) and (5b),  $E_z^i$  represents the TM polarized axial component of the incident plane wave electric field excitation and  $H_r^i$  represents corresponding transverse component of the incident magnetic field excitation. In the case of direct method of moments solution [4]–[7], the axial electrical current  $J_z$  and the transverse magnetic current  $M_r$  distributions are expanded in terms of suitable expansion functions, such as, staggered pulse expansion functions discussed in [7]. Further, the coupled CFIE expressions (5a) and (5b) are tested on both sides by the weighting functions chosen to be same as the expansion functions in order to reduce the coupled set of integral equations to their equivalent partitioned matrix equation. Based on the direct method of moments numerical solution, extensive numerical data for the near surface current distributions and the radar cross section results are reported in the literature [5]–[9] both for the electrically

small and the resonant size conducting and dielectric scattering objects. As the electrical size of the scatterer increases, this direct solution technique puts impractical demand on the computer resources, in addition to various unsettled numerical accuracy and ill-conditioning problems of the large system matrix associated with the electrically very large object.

In order to circumvent high demand on the computer resources and also reduce numerical difficulties, the formulation of the boundary value problem is modified still retaining all the physics of electromagnetic scattering and interaction as depicted schematically in Figs. 2(a) and 2(b). Fig. 2(a) represents a rectangular homogeneous dielectric scatterer geometry with unknown surface electric and magnetic current distributions on a virtual boundary. An identical geometry is repeated in Fig. 2(b), but the virtual boundary contour is modified to define (in this case) two distinct spatial subzones. A key point to note is that at the virtual interface separating the two subzones, the tangential virtual currents on one side of the interface must be equal, but opposite to the tangential virtual currents on the other side of the interface. In fact, the scatterer can be divided into an arbitrary number of  $N$  distinct spatial subzones in this manner (in Fig. 2(b),  $N = 2$ ). Now, the usual combined field integral equation and method of moments technique is used to compute the electric and magnetic currents along the enclosing surface of one subzone. In effect, the subzone is treated as a distinct scatterer. It should be noted that a part of the subzone's surface is the virtual interface separating it from the adjacent subzone. The excitation for this subzone consists of the original incident plane wave and additional excitation due to the electric and magnetic currents residing on the surfaces on the remaining spatial subzones and radiating into the free space. Initially, the additional excitation due to the currents on the remaining spatial subzones is not known. But, these can be conveniently approximated to a zeroth-order using either the physical optics (PO) [23] or possibly a first-order better approximation based on the on-surface radiation condition (OSRC) theory [24], [25]. Hence, for subzone 1, the CFIE takes the form

$$F_z^i(\bar{\rho}) = \sum_{m=1}^2 \mathcal{L}_m^{JJ} [J_{z1}(\bar{\rho}')] + \sum_{m=1}^2 \mathcal{L}_m^{JM} [M_{\tau 1}(\bar{\rho}')] \quad (7a)$$

$$G_\tau^i(\bar{\rho}) = \sum_{m=1}^2 \mathcal{L}_m^{MJ} [J_{z1}(\bar{\rho}')] + \sum_{m=1}^2 \mathcal{L}_m^{MM} [M_{\tau 1}(\bar{\rho}')],$$

for subzone 1,  $\bar{\rho}$  on  $C_1$  (7b)

$J_{z1}(\bar{\rho}')$  unknown electric current distribution for the subzone 1

$M_{\tau 1}(\bar{\rho}')$  unknown magnetic current distribution for the subzone 1

where the boundary contour  $C_1$  encloses completely the spatial subzone 1. The total excitation for the spatial subzone 1 is given by plane wave excitation and additional

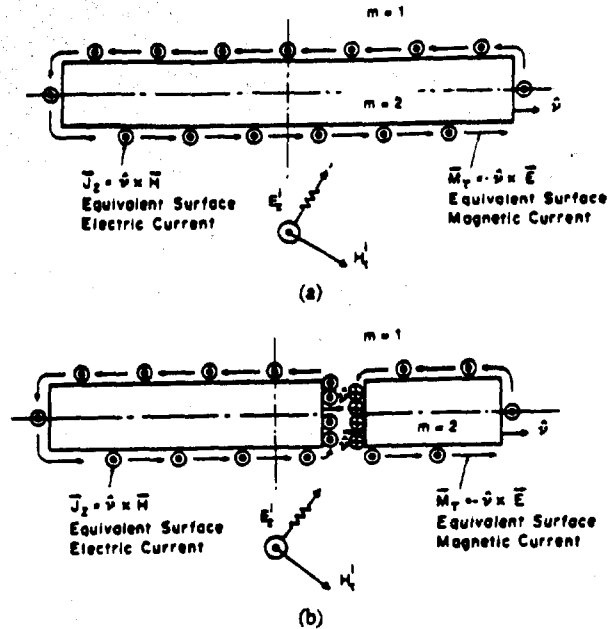


Fig. 2. (a) Distribution of equivalent electric and magnetic currents on a virtual surface. (b) Distribution of equivalent electric and magnetic currents on a modified virtual surface for the spatial decomposition technique.

excitation due to the remaining spatial subzones,  $n = 2, 3, 4, \dots, N$

$$F_z^i(\bar{\rho}) = E_z^i(\bar{\rho}) - \sum_{n=2}^N \mathcal{L}_1^{JJ} [J_{zn}(\bar{\rho}_n')] - \sum_{n=2}^N \mathcal{L}_1^{JM} [M_{\tau n}(\bar{\rho}_n')] \quad (8a)$$

$$G_\tau^i(\bar{\rho}) = H_\tau^i(\bar{\rho}) - \sum_{n=2}^N \mathcal{L}_1^{MJ} [J_{zn}(\bar{\rho}_n')] - \sum_{n=2}^N \mathcal{L}_1^{MM} [M_{\tau n}(\bar{\rho}_n')],$$

for subzone 1, and

$$\bar{\rho}_n' \text{ on } n\text{th subzone boundary } C_n. \quad (8b)$$

The analysis is now shifted to the next adjacent subzone. The excitation for this subzone consists of the original plane wave and additional excitation due to the currents on the surfaces of the remaining subzones, including the updated currents on the first subzone. In this manner, the step-by-step analysis approach can be sequentially implemented for rest of the subzones, effectively scanning the original scatterer subzone by subzone, always using the incident plane wave and the latest surface currents as the excitation for the subzone of interest. This iterative process appears to differ from any yet proposed in that: 1) subzones are used rather than the complete structure at a time, and 2) the subzones are not completely related to individual blocks of the original full matrix problem; rather, the subzones are defined as distinct targets having fully enclosing boundary surfaces with additional virtual electric and magnetic current unknowns (still maintaining the boundary conditions) introduced as needed to define the virtual interface consistently between the subzones.

Thus, the SDT provides means to implement the existing integral equation and method of moments technique with a computer memory and execution time requirement of  $O(N)$ , where  $N$  is the number of spatial subzones. Since each subzone is electrically small, spanning few wavelengths either in the two- or three-dimensional scattering problems, it is expected that conditioning of the method of moments system matrix resulting for each subzone is acceptable for numerical processing with limited demand on computer resources. In the following, several scattering case studies are presented along with relative error estimation based on the matrix condition number [21], [22] to expose preliminary studies of the SDT to analyze electromagnetic scattering by two-dimensional perfectly conducting and dielectric scatterers. Numerical results of the surface electric current and radar cross section data along with comparison based on the direct Gauss-Seidel algorithm are reported in this paper for the perfectly conducting thin strip scatterer, perfectly conducting rectangular and wedge type scatterers and homogeneous dielectric rectangular scatterer.

### III. PERFECTLY CONDUCTING SCATTERER—TM CASE

In order to illustrate the spatial decomposition technique, the electromagnetic scattering by a perfectly conducting thin strip and a rectangular scatterer are considered. Referring to Fig. 2(a), the conductivity of the scatterer is assumed to be infinite in a limit, and the thickness of the rectangular geometry is reduced to zero. For the case of TM normal excitation, there exists only an axially directed electric current along the length of thin strip scatterer given by the difference between the top and bottom current distributions. Referring to (5a) and (6a), the electric field integral equation (EFIE) for the two-dimensional perfectly conducting case is given by [1]–[3]

$$E_z^i(\bar{\rho}) = \mathcal{J}_1^{II}[J_z(\bar{\rho}')], \quad \bar{\rho} \text{ on thin strip} \quad (9a)$$

where for the TM excitation

$$\mathcal{J}_1^{II} = \int_C \left[ \frac{\omega \mu_1}{4} H_0^{(2)}(k_1 R) \right] dL' \quad (9b)$$

and the incident plane wave electric field can be written as

$$E_z^i(\rho, \phi) = E_0 e^{-jk_1 \rho \cos(\phi - \phi^i)} \quad (9c)$$

$\phi^i$  incident angle of the TM polarized plane wave excitation.

The distribution of the electric current on the thin strip scatterer can be directly obtained by applying the method of moments numerical technique [4] by using a pulse expansion set for representing the unknown electric current distribution, and also testing the EFIE expression (9a) by the same pulses. Fig. 3(a) shows a plot of the magnitude of electric current on a thin strip scatterer of total length,  $L = 25\lambda$ , excited at an angle of incidence  $\phi^i = 90^\circ$ . This result is obtained using a full matrix of size

$(250 \times 250)$  with a current resolution of 10 pulse samples per wavelength. In order to apply the spatial decomposition technique, the thin strip scatterer is divided, for example, into five subzones,  $N = 5$ . Maintaining the same current resolution of 10 samples per wavelength, the matrix size is now only  $(50 \times 50)$  for each subzone modeling. Referring to (7a) and (8a), the EFIE for the first subzone has the form

$$E_z^i(\bar{\rho}) - \sum_{n=2}^5 \mathcal{J}_1^{II}[J_{zn}(\bar{\rho}_n')] = \mathcal{J}_1^{II}[J_{z1}(\bar{\rho}')], \quad \bar{\rho} \text{ on subzone 1.} \quad (10)$$

On the left-hand side of the SDT expression (10), the total excitation for the spatial subzone 1 is given by the plane wave excitation and additional excitation due to the electric currents on remaining spatial subzones,  $n = 2, 3, 4$  and 5. But, the distributions of the electric current on the remaining subzones,  $n = 2, 3, 4$  and 5, are not known initially. However, they can be obtained approximately based on either the PO [23] or the OSRC approach [24], [25]. An approximate distribution of the electric current on a perfectly conducting scatterer is obtained using the normal derivative of the total electric field, and for subzones  $n = 2, 3, 4$  and 5 is given by

$$J_{zn}(\bar{\rho}') = \frac{-j}{\eta_1 k_1} \left[ \frac{\partial E_z^i(\bar{\rho}')}{\partial \nu'} + \frac{\partial E_z^i(\bar{\rho}')}{\partial \nu'} \right] \quad (11)$$

where  $\eta_1$  is the intrinsic impedance of the free space medium. Using the second-order OSRC boundary operator [22], an approximate relationship for the normal derivative of axially directed scattered electric field on the perfectly conducting convex scatterer can be obtained as

$$\frac{\partial E_z^i(\bar{\rho}')}{\partial \nu'} = \left[ \frac{\xi(s')}{2} + jk_1 + \frac{j\xi^2(s')}{8[k_1 - j\xi(s')]} \right] E_z^i(\bar{\rho}') + \frac{j}{2[k_1 - j\xi(s')]} \frac{\partial^2 E_z^i(\bar{\rho}')}{\partial s'^2} \quad (12a)$$

$\xi(s')$  curvature of an osculating circle drawn tangential to the boundary contour

$s'$  tangential coordinate variable along the boundary contour, and

$$\frac{\partial^2 E_z^i(\bar{\rho}')}{\partial s'^2} = -K^2 [\sin^2 \Omega' \cos^2 \phi^i + \cos^2 \Omega' \sin^2 \phi^i - 2 \sin \Omega' \cos \Omega' \cos \phi^i \sin \phi^i] E_z^i(\bar{\rho}'). \quad (12b)$$

With the normal broadside excitation,  $\phi^i = 90^\circ$ , the above OSRC expression yields an initial current distribution, which is a flat current, with no current singularities at the thin strip scatterer ends. In fact, the goal of the SDT is to sequentially update this initial current for each subzone. The analysis is now shifted to the adjacent subzone  $n = 2$ . The excitation for this subzone 2 consists of the original plane wave plus additional excitation due

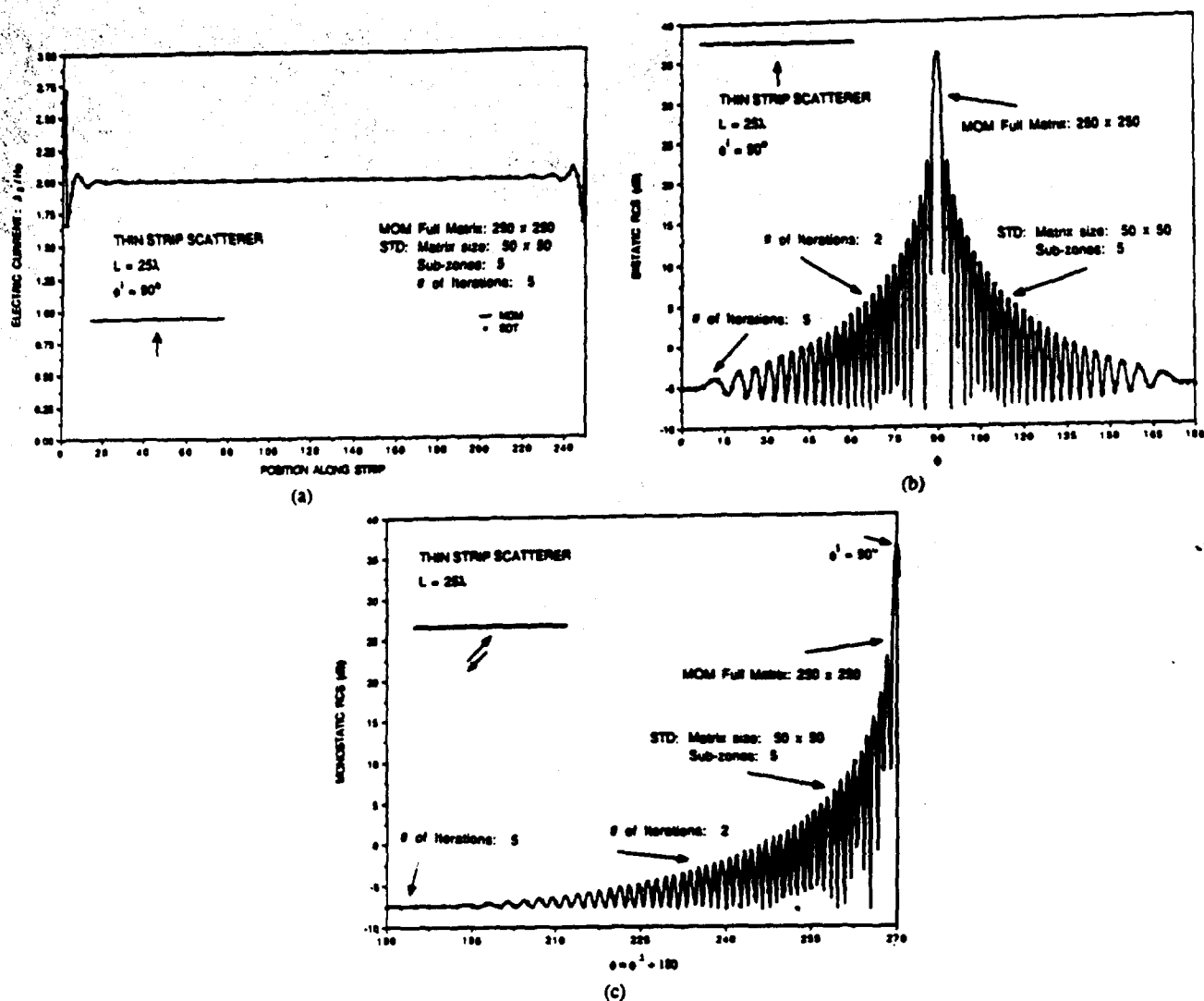


Fig. 3. (a) Distribution of the equivalent electric current on the thin strip scatterer—TM normal excitation. (b) Bistatic radar cross section of the thin strip scatterer—TM normal excitation. (c) Monostatic radar cross section of the thin strip scatterer—TM normal excitation.

to the approximate currents on the surface of the remaining subzones,  $n = 3, 4$  and  $5$  including the updated current along the first subzone. This step-by-step analysis approach is sequentially implemented in an iterative sweep for each subzone from one end of the scatterer to the other end. Once the first sweep is completed, a first-order approximate distribution of the electric current on the thin strip scatterer is numerically simulated. It is noted here that no additional boundary conditions are enforced in the application of SDT. Better approximation of the distribution of magnitude and phase of the electric current on the thin strip scatterer can be obtained by more iterative sweeps. In Fig. 3(a) is shown the distribution of the magnitude of electric current calculated based on the SDT (with five spatial subzones,  $N = 5$ ) on the thin strip scatterer excited with an angle of incidence  $\phi^i = 90^\circ$ . The results shown are obtained for five sweeps with less than 1% error in the region separating two adjacent subzones. It should be noted that the electric currents are valid only for the specified angle of incidence and the SDT iterative

process is to be repeated if the numerical data for other angles of incidence is required. The distribution of the electric current can now be utilized for calculating either the near electric and magnetic field distributions or the bistatic radar cross-section data. In fact, the number of successive iterative sweeps is determined based on the degree of convergence required of the electric current or the radar cross-section data. The far-field distribution and the radar cross-section data can be derived using (3a), (4a), and (9b) with the two-dimensional Green's function term replaced with its large argument approximation. Fig. 3(b) shows a plot of the bistatic radar cross section obtained using SDT compared with the direct method of moments (MM) solution. In the angular range of  $\phi = 30^\circ$  to  $150^\circ$ , the bistatic radar cross section converges in two sweeps with less than 1% error, but for the grazing angles more sweeps are required, and for the results shown five sweeps are utilized. Fig. 3(c) shows a plot of the monostatic radar cross section obtained using SDT compared with respect to the direct (MM) solution.

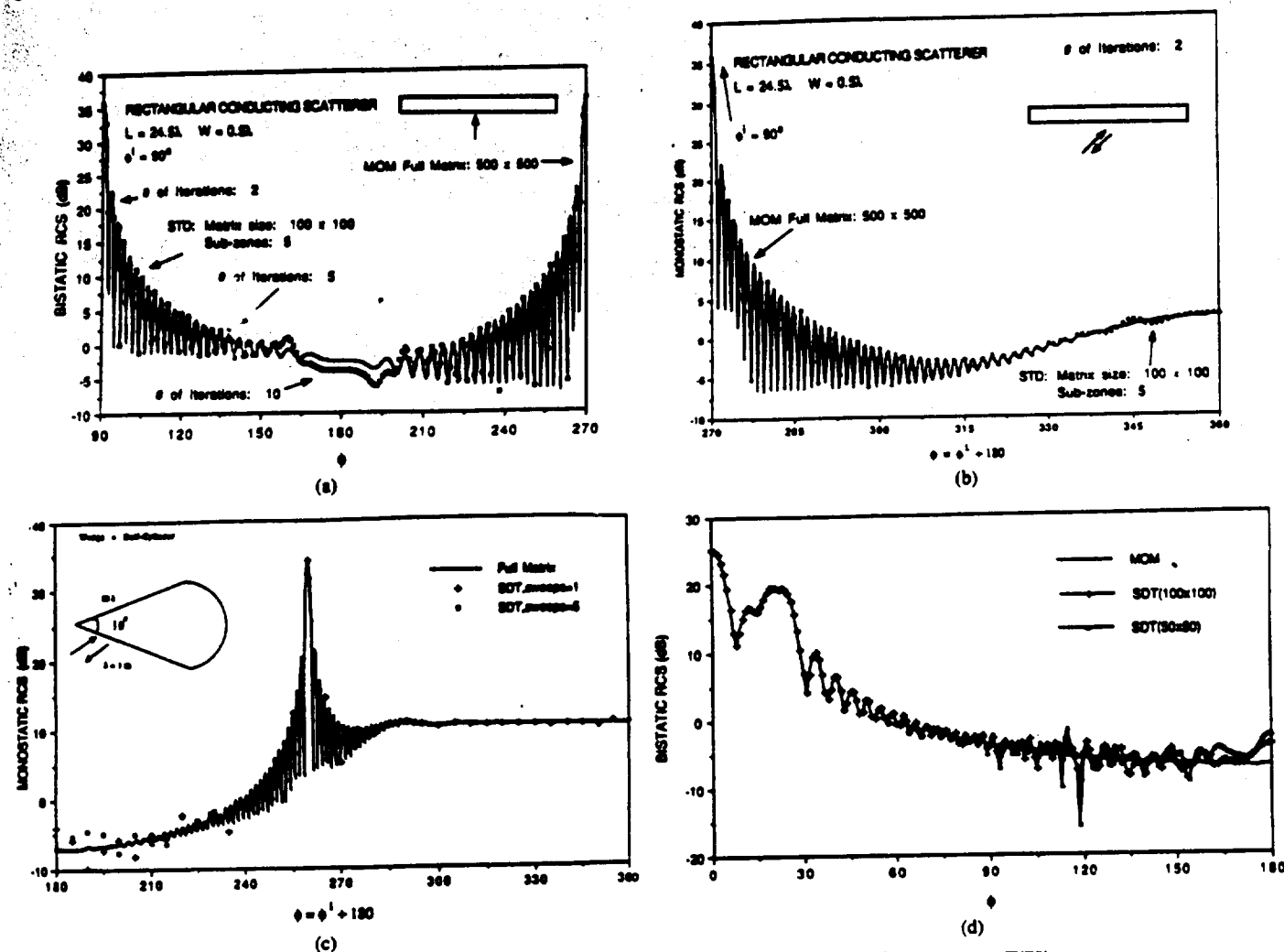


Fig. 4. (a) Bistatic radar cross section of the rectangular conducting scatterer—TM normal excitation. (b) Monostatic radar cross section of the rectangular conducting scatterer—TM normal excitation. (c) Monostatic radar cross section of the wedge with half-cylinder—TM excitation. (d) Bistatic radar cross section of the wedge with half-cylinder—TM excitation.

In fact, numerical studies indicate smaller subzone sizes [18] can be adapted with even lower computer resources, but require more iterative sweeps for the same degree of convergence. Tables I, II, and III show computer resources required on a Sun 4.0 Workstation as a function of subzone size and number of iterative sweeps. The representative case of thin strip scatterer of total length  $L = 10\lambda$  excited at an angle of incidence,  $\phi^i = 90^\circ$ , is considered with a finer current resolution of 20 pulse samples per wavelength. The results reported here are based on a general unoptimized computer algorithm with Gauss-Seidel numerical inversion. The run times reported in the tables, in fact, are higher than many standard optimized algorithms [3], [7].

Similar convergence behavior is observed for other bistatic and monostatic angles. The above studies using SDT can be easily extended for the case of electromagnetic scattering by a perfectly conducting rectangular and wedge type scatterers. Fig. 4(a) shows a plot of bistatic radar cross section of a rectangular scatterer of total length  $L = 24.5\lambda$  and width  $W = 0.5\lambda$  which is excited at

TABLE I  
DIRECT MM SOLUTION

Full Matrix Size Total	Bistatic RCS in decibels Observation Angle, $\phi = 90^\circ$	Run Time in Seconds
200	27.971437	205.2

TABLE II  
SDT SOLUTION—VARIATION OF NUMBER OF SUBZONES  
(NUMBER OF SWEEPS = 1)

Subzone Matrix Size	Number of Subzones	Bistatic RCS in decibels Observation Angle, $\phi = 90^\circ$	Run Time in Seconds
20	10	27.95345306	10.0
25	8	27.97183609	12.6
40	5	27.96068573	23.9
50	4	27.97832870	34.1
100	2	27.96839523	121.0

an angle of incidence  $\phi^i = 90^\circ$ . This result is obtained using a full matrix of size  $(500 \times 500)$  for the direct MM solution. Similar to the thin strip case discussed earlier, in

TABLE III  
SDT SOLUTION—VARIATION OF NUMBER OF SWEEPS  
(SUBZONE MATRIX SIZE = 50 AND NUMBER OF SUBZONES = 4)

Number of Sweeps	Bistatic RCS in decibels Observation angle, $\phi = 90^\circ$	Run Time in Seconds
1	27.97832870	34.1 per sweep
2	27.97790012	
3	27.97251701	
4	27.97248459	
5	27.97203225	
6	27.97153854	
7	27.97137260	
8	27.97138977	
9	27.97143173	
10	27.97144699	

order to apply the spatial decomposition technique, the scatterer is divided into five subzones,  $N = 5$ , and the matrix size is chosen with the same uniform resolution for each subzone modeling. Fig. 4(a) also shows a plot of the bistatic radar cross section obtained using SDT compared with the direct MM solution. Both forward and back scattering data in the angular range  $\phi = 90^\circ$  to  $120^\circ$  converge with only two iterative sweeps, and for the angular range  $\phi = 120^\circ$  to  $150^\circ$  convergence is obtained with five sweeps with less than 1% error. However, for the grazing angles more sweeps are required, and for the bistatic results shown 10 sweeps are utilized. The monostatic data, on the other hand, converges rapidly with only two iterative sweeps. Fig. 4(b) shows a plot of the monostatic radar cross section obtained using SDT with two sweeps compared with the direct MM solution. The monostatic study has been extended even for the case of a conducting wedge type scatterer. Fig. 4(c) shows a plot of the monostatic radar cross section obtained for a two-dimensional finite length wedge with half-cylinder. Fig. 4(d) shows bistatic radar cross sections obtained using subzones of  $(100 \times 100)$  and  $(50 \times 50)$  matrix systems. TM normal excitation with  $\phi' = 0^\circ$  is assumed to be incident on the tip of the wedge. In Figs. 4(c) and 4(d), the SDT numerical results are compared with the direct MM solution.

#### IV. ERROR ANALYSIS BASED ON MATRIX CONDITION NUMBER

It is evident that the SDT offers substantial savings in computer storage and time as compared to the direct integral equation and method of moments solution. From error analysis and estimation point of view, the SDT deals with only smaller matrices arising due to division of the large scatterer into multiplicity of subzones. The Gauss-Seidel inversion of matrices inevitably introduces round-off errors, the extent of which essentially depends on the sophistication of computing device and its word-length. In fact, round-off errors are fairly random in nature and do not cancel out in a given computation, but rather tend to accumulate if later calculations are based on the earlier ones. A detailed discussion concerning relative error analysis and estimation of the degree

ill-conditioning associated with typical method of moments scattering problems is addressed in [21] and [22] using a qualitative figure, such as, the matrix condition number. A convenient measure of the condition of a matrix can be assessed in defining

$$\text{cond}([Z]) = \|Z\| \cdot \|Z^{-1}\| \quad (13a)$$

where considering the infinite norm, the maximum row sum of the matrix

$$\|Z\| = \|Z\|_\infty \quad (13b)$$

In solving the matrix equation, the condition number of matrix represents an upper bound on the relative uncertainty in determining the electric current distribution. Just in the numerical inversion alone, the direct method requires arithmetic operations proportional to third power of the matrix size. But, in the SDT only very small matrices are dealt with proportional to electrical size of subzones. Fig. 5 shows variation of worst-case condition number with number of subzones for the strip and rectangle cases studies discussed above. Thus, the submatrices corresponding to the subzones are better conditioned than the large matrix of the direct method. The condition of the subzone matrix improves as it becomes smaller, however, this improvement cannot be extracted indefinitely in view of the stronger coupling and interaction with very small subzones.

#### V. PERFECTLY CONDUCTING SCATTERER—TE CASE

The preliminary study of the spatial decomposition technique is reported for the case of perfectly conducting thin strip scatterer with transverse electric (TE) excitation. For the case of TE normal excitation, there exists only a tangentially directed electric current along the boundary of scatterer. Referring to (5b) and (6d), and considering its dual representation for the induced electric current, the EFIE is given by [1]–[3]

$$E_z(\bar{\rho}) = \int_C \cos(\Omega - \Omega') J_z(\bar{\rho}') \left[ \frac{\omega \mu_1}{4} H_0^{(2)}(k_1 R) \right] dL' \\ + \frac{\partial}{\partial s} \int_C \frac{\partial}{\partial s'} J_z(\bar{\rho}') \left[ \frac{1}{4\omega \epsilon_1} H_0^{(2)}(k_1 R) \right] dL', \quad (13)$$

$\bar{\rho}$  on thin strip.

Again, the distribution of the electric current on the thin strip scatterer can be directly obtained by using a pulse expansion set for representing the unknown electric current distribution, and also testing the EFIE expression (13) by the same pulses. Fig. 6(a) shows a plot of the magnitude of electric current on a thin strip scatterer of total length,  $L = 25\lambda$ , excited at an angle of incidence  $\phi' = 90^\circ$ . This result is obtained using a full matrix of size  $(250 \times 250)$  with a current resolution of 10 pulse samples per wavelength. Similar to the TM case discussed earlier, in order to apply the spatial decomposition technique, the thin strip scatterer is divided into five subzones,  $N = 5$ . Providing the same resolution, the SDT matrix size is only



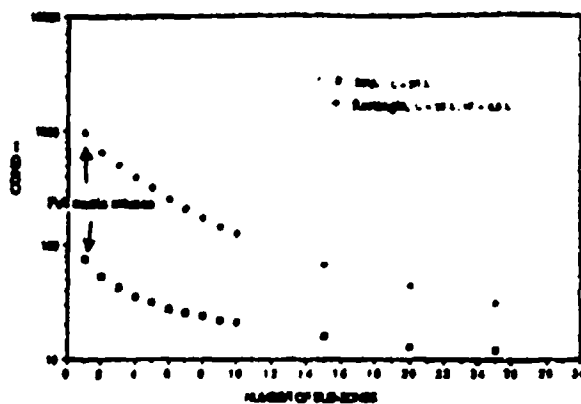


Fig. 5. Variation of worst-case condition number with number of subzones—strip and rectangular scatterers—TM excitation.

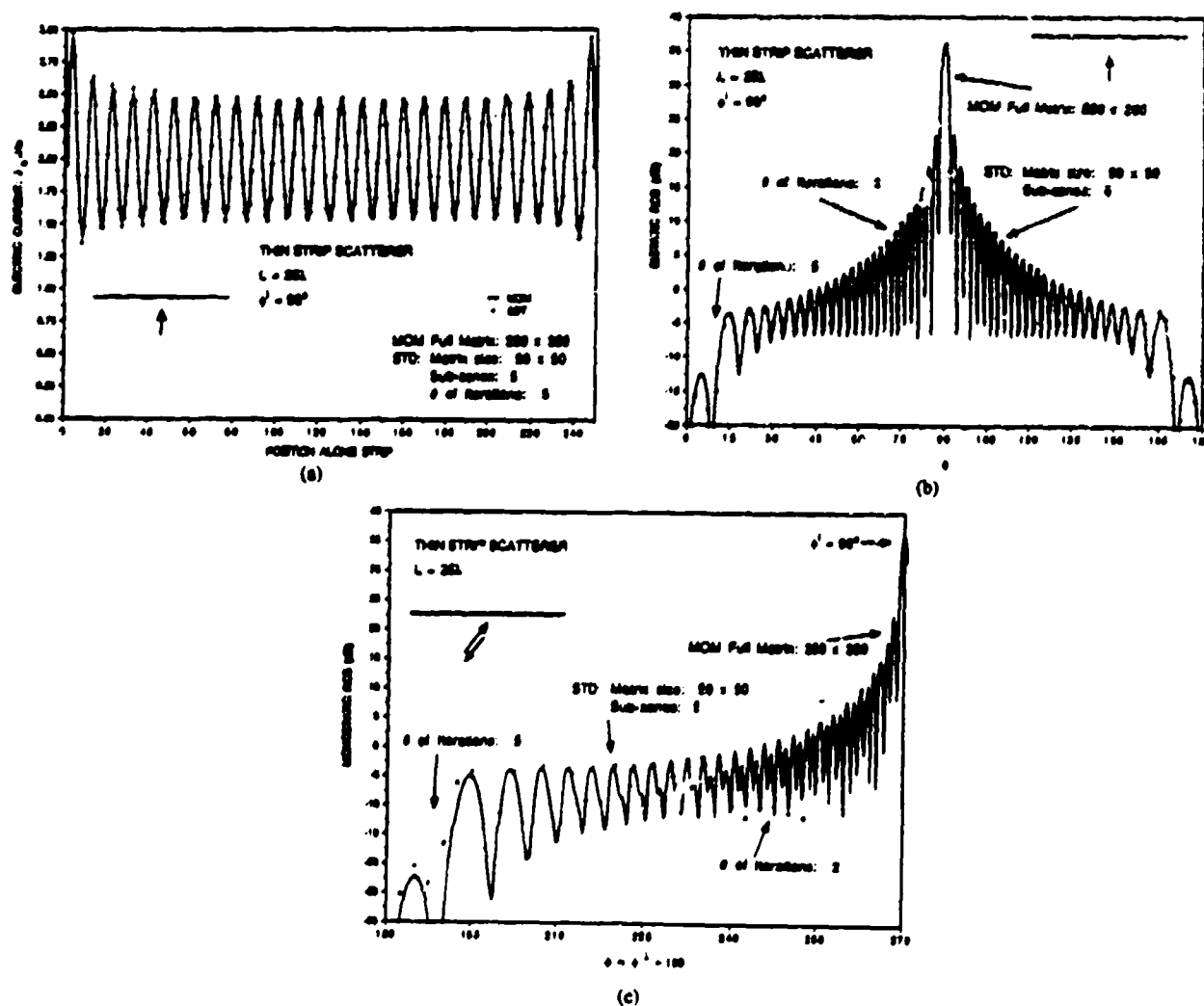


Fig. 6. (a) Distribution of the equivalent electric current on the thin strip scatterer—TE normal excitation. (b) Bistatic radar cross section of the thin strip scatterer—TE normal excitation. (c) Monostatic radar cross section of the thin strip scatterer—TE normal excitation.

(50 × 50) for each subzone modeling. Using the OSRC TE-boundary operator [24], an approximate relationship for the tangential electric current on the perfectly conducting convex scatterer is obtained

$$\hat{s}' J_t(\bar{\rho}') = \hat{\nu}' \times [\hat{z}' H_z'(\bar{\rho}') + \hat{z}' H_z'(\bar{\rho}')], \quad \bar{\rho}' \text{ on } C \quad (14a)$$

$$\frac{\partial H_z'(\bar{\rho}')}{\partial \nu'} = - \left[ \frac{\xi(s')}{2} + jk_1 + \frac{j\xi^2(s')}{8[k_1 - j\xi(s')]} \right] H_z'(\bar{\rho}') \quad (14b)$$

$$E_z'(\bar{\rho}') = \frac{1}{j\omega\epsilon} \frac{\partial}{\partial \nu'} H_z'(\bar{\rho}'). \quad (14c)$$

With normal excitation, the above OSRC expression yields an initial current distribution, which is a flat current, with no standing wave distribution along the thin strip scatterer. In fact, the process of the SDT is to sequentially update this initial current for each subzone. In Fig. 6(a) is also shown the magnitude distribution of electric current calculated based on the SDT (with five spatial subzones,  $N = 5$ ). The result shown is obtained for five sweeps with less than 1% error in the region separating adjacent subzones. Fig. 6(b) shows a plot of the bistatic radar cross section obtained using SDT compared with the direct MM solution. In the angular range of  $\phi = 30^\circ$  to  $150^\circ$ , the bistatic radar cross section converges in two sweeps with less than 1% error, but for the grazing observation angles more sweeps are required, and for the result shown five sweeps are utilized. Fig. 6(c) shows a plot of the monostatic radar cross section obtained using SDT compared with the direct MM solution.

## VI. HOMOGENEOUS DIELECTRIC SCATTERER—TM CASE

Referring to Figs. 2(a) and 2(b), the spatial decomposition technique presented in Section II is now applied for the case of isotropic, homogeneous, lossless dielectric rectangular scatterer of length  $L = 10\lambda$  and width  $W = 0.25\lambda$  (where  $\lambda$  is the free space wavelength) with TM excitation. The angle of incidence is  $\phi' = 90^\circ$ , and the relative permittivity and permeability of the lossless dielectric scatterer are selected as  $\epsilon_r = 2.56$  and  $\mu_r = 1.0$ . Applying the CFIE discussed in Section II and using a full matrix of size (420 × 420), the electric and magnetic current distributions are calculated first, and then the bistatic radar cross section is obtained as shown in Fig. 7. In order to apply the spatial decomposition technique, the dielectric rectangular scatterer is divided into five subzones,  $N = 5$ , and the SDT matrix size is chosen with same uniform resolution for each subzone modeling. The initial distributions of the axial electric current and tangential magnetic current on the dielectric scatterer are obtained using the first-order OSRC boundary operator [23]. The two current distributions are sequentially updated using the SDT. Fig. 7 also shows a plot of the bistatic radar cross section obtained using SDT compared with the

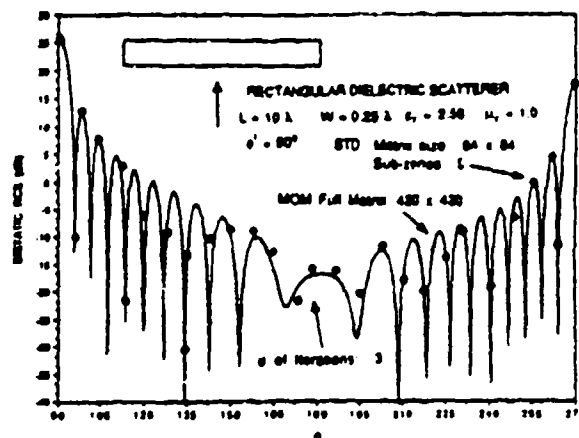


Fig. 7. Bistatic radar cross section of the rectangular dielectric scatterer—TM normal excitation.

TABLE IV  
COMPUTER RESOURCES: DIRECT MM VERSUS SDT

### a) Bistatic Radar Cross Section of Thin Strip

Excitation	Strip Size (λ)	Direct MM Matrix Size	MM Run Time (s)	SDT Matrix Size	SDT(*) Run Time (s)
TM	10	200	205	50	34
TM	25	500	3175	50	83
TE	10	200	282	50	45
TE	25	500	4210	50	109

### b) Bistatic Radar Cross Section of Wedge with Half-Cylinder

Excitation	Direct MM Matrix Size	MM Run Time (s)	SDT Matrix Size	SDT(*) Run Time (s)
TM	500	4137	100	167
			50	55

direct MM solution. The bistatic radar cross section converges in one or two sweeps for broad side angles and takes more sweeps for grazing incident angles. The SDT numerical data is obtained with three sweeps with less than 1% error.

## VI. REMARKS

Using rigorous electromagnetic equivalence, the spatial decomposition technique divides an electrically large object into a multiplicity of subzones. The technique permits limiting the size of the method of moments system matrix that need be inverted regardless of the electrical size of the large scattering object being modeled. Several numerical scattering case studies have also been reported along with comparison and relative error estimation based on condition numbers to expose possible applicability of the spatial decomposition technique to the two-dimensional scattering study of electrically large conducting and dielectric objects. Details of the computational burden to obtain bistatic radar cross section of 1) two thin perfectly

conducting strips of lengths  $10\lambda$  and  $25\lambda$  and 2) wedge with half-cylinder structure using the direct MM technique and the SDT are reported for the TM and TE excitations.

It can be inferred from Table IV that the spatial decomposition technique can provide order (100:1) savings in computer resources over the direct MM solution for electrically large geometries. This comparative savings appears to increase with the size of the scatterer. In fact, as the MM matrix size increases by a factor of  $R$  and the direct MM run time increases by  $R^3$ , the SDT run time increases only by  $R$ . This may be quite significant.

### REFERENCES

- [1] A. J. Poggio and E. K. Miller, "Integral equation solutions of three dimensional scattering problems," in *Computer Techniques for Electromagnetics*, R. Mittra, Ed. Elmsford, NY: Pergamon, 1973, ch. IV.
- [2] J. R. Mautz and R. F. Harrington, "A combined-source solution for radiation and scattering from a perfectly conducting body," *IEEE Trans. Antennas Propagat.*, vol. AP-27, pp. 445-454, 1979.
- [3] K. Umashankar, "Numerical analysis of electromagnetic wave scattering and interaction based on frequency domain integral equation and method of moments techniques," *Wave Motion*, no. 10, pp. 493-525, Dec. 1988.
- [4] R. F. Harrington, *Field Computation by Moment Methods*. New York: MacMillan, 1968.
- [5] B. J. Strait, Ed., *Applications of the Method of Moments to Electromagnetic Fields*. SCSEE Press, 1981.
- [6] A. W. Glisson, "On the development of numerical techniques for treating arbitrary-shaped surfaces," Ph.D. dissertation, Univ. Mississippi, University, MS, 1978.
- [7] K. Umashankar and A. Taflov, "Analytical models for electromagnetic scattering," *Hanacom Air Force Base, MA, Final Tech. Rep. F19628-82-C-0140, RADC/ESD*, June 1984.
- [8] S. M. Rao, D. R. Wilton, and A. W. Glisson, "Electromagnetic scattering by surfaces of arbitrary shape," *IEEE Trans. Antennas Propagat.*, vol. AP-30, pp. 409-418, 1982.
- [9] K. Umashankar, A. Taflov, and S. M. Rao, "Electromagnetic scattering by arbitrary shaped three dimensional homogeneous lossy dielectric objects," *IEEE Trans. Antennas Propagat.*, vol. AP-34, pp. 758-766, June 1986.
- [10] T. K. Sarkar, K. Siarkiewicz, and R. Stratton, "Survey of numerical methods for solution of large systems of linear equations for electromagnetic field problems," *IEEE Trans. Antennas Propagat.*, vol. AP-29, pp. 847-856, 1981.
- [11] R. Mittra and C. A. Klein, "Stability and convergence of methods of moments solutions," in *Numerical and Asymptotic Techniques in Electromagnetics*, R. Mittra, Ed. New York: Springer-Verlag, 1975, pp. 129-133.
- [12] W. L. Ko and R. Mittra, "A new approach based on combination of integral equation and asymptotic techniques for solving electromagnetic scattering problems," *IEEE Trans. Antennas Propagat.*, vol. AP-25, pp. 187-197, 1977.
- [13] W. D. Burnside, C. L. Yu, and R. J. Marhefka, "A technique to combine the geometrical theory of diffraction and the method of moment method," *IEEE Trans. on Antennas Propagat.*, vol. AP-23, pp. 551-557, 1975.
- [14] T. J. Kim and G. A. Thiele, "A hybrid diffraction technique—General theory and applications," *IEEE Trans. Antennas Propagat.*, vol. AP-30, pp. 888-897, 1982.
- [15] L. N. Medgyesi-Mitschang and D. Wang, "Hybrid solutions for scattering from perfectly conducting bodies of revolution," *IEEE Trans. Antennas Propagat.*, vol. AP-31, pp. 570-583, July 1983.
- [16] T. K. Sarkar, X. Yang, and E. Arvas, "A limited survey of various conjugate gradient methods for solving complex matrix equations arising in electromagnetic wave interactions," *Wave Motion*, no. 10, pp. 527-546, Dec. 1988.
- [17] R. Mittra and T. S. Li, "A spectral domain approach to the numerical solution of electromagnetic scattering problems," *AEU Electron. and Commun.*, band 29, pp. 217-222, 1975.
- [18] K. R. Umashankar, S. Nimmagadda, and A. Taflov, "Application of integral equation and method of moments for electrically very large scatterers using spatial decomposition technique," in *1990 APS / URSI Int. Symp. Dig.*, vol. 1, pp. 76-79, Dallas, TX, May 1990.
- [19] K. Umashankar, "Analysis of the electromagnetic scattering by electrically very large objects based on the spatial decomposition technique," *Final Tech. Rep.*, Univ. Illinois, Chicago, Chicago, IL, Jan. 1988.
- [20] S. A. Schelkunoff, "Field equivalence theorems," *Comm. Pure Appl. Math.*, vol. 4, pp. 43-59, June 1951.
- [21] C. Klein and R. Mittra, "Stability of matrix equations arising in electromagnetics," *IEEE Trans. Antennas Propagat.*, vol. AP-31, pp. 902-905, Nov. 1973.
- [22] G. E. Forsythe and C. B. Moler, *Computer Solution of Linear Algebraic Systems*. Englewood Cliffs, NJ: Prentice-Hall, 1967.
- [23] R. G. Kouyoumijan and P. H. Pathak, "A uniform geometrical theory of diffraction of an edge in a perfectly conducting surface," *Proc. IEEE*, vol. 62, pp. 1448-1461, Nov. 1974.
- [24] G. A. Kriegsmann, A. Taflov, and K. Umashankar, "A new formulation of electromagnetic wave scattering using an on-surface radiation boundary condition," *IEEE Trans. Antennas Propagat.*, vol. AP-35, pp. 153-161, 1987.
- [25] S. Arendt, K. Umashankar, A. Taflov and G. A. Kriegsmann, "Extension of on-surface radiation condition theory to scattering by two-dimensional homogeneous dielectric objects," *IEEE Trans. Antennas Propagat.*, vol. 38, pp. 387-406, Dec. 1990.
- [26] K. R. Umashankar, S. Nimmagadda, and A. Taflov, "Numerical analysis of electromagnetic scattering by electrically large objects using spatial decomposition technique," in *1991 Progress in Electromagn. Res. Symp. Proc.*, Cambridge, MA, July 1991.

Korada R. Umashankar (S'69-M'75-SM'81), for a photograph and biography please see page 1212 of the August 1991 issue of this TRANSACTIONS.



Selaath Nimmagadda (S'89) was born in Kurnool, India. He received the B.S.E.E. degree from Jawaharlal Nehru Technological University, India, in 1979 and the M.S.E.E. degree from the Indian Institute of Technology, Kharagpur, India, in 1981. He is currently working toward the Ph.D. degree at the University of Illinois, Chicago.

During 1981-1988, he was an Assistant Professor at Bangalore University and Osmania University. Since 1988, he has been working as a Research Assistant in the Department of Electrical Engineering and Computer Science. His present research interests include numerical methods for electromagnetic field scattering and interaction, simulation of high-frequency, high-speed compound semiconductor devices, supercomputing of electromagnetic phenomena and 3-D visualization of transient fields.

Allen Taflov (M'75-SM'84-F'90), for a photograph and biography please see page 906 of the July 1991 issue of this TRANSACTIONS.

# Computational Modeling of Femtosecond Optical Solitons from Maxwell's Equations

Peter M. Goorjian, *Member, IEEE*, Allen Taflove, *Fellow, IEEE*, Rose M. Joseph, and Susan C. Hagness

**Abstract**—A new algorithm has been developed that permits, for the first time, the direct time integration of the full-vector nonlinear Maxwell's equations. This new capability permits the modeling of linear and nonlinear, instantaneous and dispersive effects in the electric polarization in material media. The modeling of the optical carrier is retained in this approach. The fundamental innovation of the present approach is to notice that it is possible to treat the linear and nonlinear convolution integrals, which describe the dispersion, as new dependent variables. Using this observation, a coupled system of nonlinear second-order ordinary differential equations can be derived for the linear and nonlinear convolution integrals, by differentiating them in the time domain. These equations, together with Maxwell's equations form the system that is solved to determine the electromagnetic fields in nonlinear dispersive media. Using this algorithm, results are presented of first-time calculations in one dimension of the propagation and collision of femtosecond electromagnetic solitons that retain the optical carrier. The nonlinear modeling takes into account such quantum effects as the Kerr and Raman interactions. The present approach is robust and should permit modeling 2-D and 3-D optical soliton propagation, scattering, and switching directly from the full-vector nonlinear Maxwell's equations for integrated optical structures having complex engineered inhomogeneities.

## I. INTRODUCTION

IN computational electromagnetics, there is a substantial activity in solving the linear Maxwell equations by finite-difference methods in the time domain (FD-TD), for applications to aeronautics, electronics, and biology [1], [2]. During the 1980's, the primary interest in Maxwell's equations solvers of all types centered on defense applications, primarily the prediction and mitigation of radar cross section (RCS). Grid-based Maxwell's solvers, implemented on supercomputers, are rapidly becoming this country's primary means of modeling the RCS of advanced aerospace vehicles [2]. The FD-TD method implements the spatial derivatives of the curl operators in Maxwell's equations by using finite differences on a regular Cartesian space mesh, and employs a simple leapfrog time integration scheme.

Manuscript received February 18, 1992; revised June 8, 1992. The work of A. Taflove was supported in part by NASA-Ames University Consortium Joint Research Interchange NCA2561 and 562, ONR Contract N00014-88-K-0475 and Cray Research, Inc.

P. M. Goorjian is with NASA Ames Research Center, Moffett Field, CA 94035.

A. Taflove, R. M. Joseph, and S. C. Hagness are with the Department of Electrical Engineering and Computer Science, McCormack School of Engineering, Northwestern University, Evanston, IL 60208.

IEEE Log Number 9202623.

Now, in the 1990's, initial efforts are being made to use the Maxwell's equations to explore the physics of devices having substantial commercial applications, especially ultrahigh-speed electronic, electrooptic, and all-optical devices, which are useful in the construction of advanced digital signal processors and computers. To date, these investigations are being conducted almost exclusively by using the FD-TD algorithm, which permits a means of combining the physics of the Maxwellian electromagnetic field and energy transport with the physics of electronic charge transport and volume-averaged quantum effects. Applications include modeling high-data-rate passive interconnects for digital circuits [3], active electronic devices [4] and all-optical devices [5].

However, these efforts use the linear Maxwell's equations. To adequately model optical switches, nonlinear effects in dielectric materials [6], [7] both instantaneous and dispersive, must be included. Experimental researchers have produced switches [6] capable of switching short (100 fs) optical pulses in nonlinear directional couplers. Also nonlinear responses in dielectric materials are important in the generation of very short, intense, fast-rise-time pulses. Such pulses are important in ultrawideband (UWB) technology [8] in aeronautics. These pulses have very high peak power and a frequency spectrum that extends from near-direct current to several gigahertz.

The nonlinear behavior of electromagnetic fields in materials is determined by solving the nonlinear Maxwell's equations. The equations become nonlinear because the electric polarization is now determined by a nonlinear relation to the electric field intensity. Up to now, these nonlinear Maxwell's equations have not been solved exactly. Rather, various approximations to the governing equations have been made. The least approximate methods solve nonlinear scalar equations for the slowly varying envelope of the optical pulses. This class of equations, known as the generalized nonlinear Schrödinger equations (GNLSE) [9], [10] has been solved by the split-step Fourier method [10] and by the Propagating beam method [11] (PBM). For example, the split-step Fourier method [10] is often used to simulate the propagation of optical pulses in low-loss fibers over very long optical distances, and the propagating beam method [11] has been used to model directional couplers.

However certain effects are neglected when Maxwell's equations are approximated by the GNLSE, including scattering and diffraction effects, and short pulse effects

in the 10 fs regime. For example, optical wave scattering and diffraction effects relevant to all-optical switches integrated in microchip form will be difficult or impossible to obtain with GNLSE because its formulation discards the optical carrier. Engineered inhomogeneities in nonlinear optical circuits should be fairly complicated. Very likely, these inhomogeneities will be at short distance scales in the order of 0.1–10 optical wavelengths, and all assumptions regarding slowly varying parameters (which run throughout GNLSE theory) will be unjustified. In fact, material inhomogeneities such as crossing optical paths critically affect optical pulse scattering even in the absence of nonlinearities. There is no preferred direction of scattering for general inhomogeneities, and the primary scattering physics occurs at the optical carrier time scale with the enforcement of vector electromagnetic field boundary conditions at all material interfaces. The only way to model this situation is to set up and solve Maxwell's vector-field equations for the material geometry of interest, rigorously enforcing the vector-field boundary conditions and the physics of nonlinear dispersion.

In this paper, a new approach will be presented for solving the nonlinear Maxwell equations. The nonlinear relation between the polarization and the electric field will be modeled by a nonlinear convolution relation [7]. This system of equations will be solved exactly, using finite-difference methods in the time domain (FD-TD). Wave scattering and diffraction effects that are not accounted for in the GNLSE approach are included here. Also, unlike the split-step Fourier method, the effects of nonlinearity and dispersion are not treated separately in this approach. The inclusion of some of the nonlinear terms in the algorithm for Maxwell's equations employs techniques that were developed in computational fluid dynamics for the solution of nonlinear equations [12]. However, the treatment of the nonlinear convolution integral has required the development of a new computational technique [13]–[15].

This approach will provide direct solutions to Maxwell's vector-field equations suitable for modeling the propagation and scattering of optical pulses, including solitons, in inhomogeneous nonlinear dispersive media. The modeling of the pulses will include the optical carrier. The study of solitons [9], [16] is of fundamental importance. Approximately one hundred different types of nonlinear partial differential equations have been found to have solitons or soliton-like solutions mathematically. Solitons are a fundamental feature of nonlinear equations in a manner similar to Fourier modes for linear equations. During the past two decades [17] the study of solitons has become a fundamental part of many different areas of nonlinear science, including optics, plasma waves, molecular biology, nerve conduction, nucleic acids, quantum gauge fields, and cosmology. For nonlinear optics, this approach has the potential to provide a modeling capability for millimeter-scale integrated optical circuits beyond that of existing techniques using the generalized nonlinear Schrödinger equation.

In Section II and III, the new formulation of the governing differential equations and the new finite-difference equations will be given, respectively. In Section IV, results of the calculations of propagating and colliding solitons will be presented. Finally, in Section V, concluding remarks will be given.

## II. GOVERNING EQUATIONS

An efficient FD-TD numerical approach has been developed [5] for the direct time integration of Maxwell's equations to model *linear* media having arbitrary-order chromatic dispersions. This approach was based upon a suggestion by Jackson [18] to relate  $\vec{D}(\vec{x}, t)$  the electric field displacement, to  $\vec{E}(\vec{x}, t)$ , the electric field intensity, via an ordinary differential equation in time. That equation is integrated concurrently with the Maxwell's equations. The differential equation that relates  $\vec{D}(\vec{x}, t)$  to  $\vec{E}(\vec{x}, t)$  is derived by taking the inverse Fourier transform of the complex permittivity relation,  $\epsilon(\omega) = \vec{D}(\vec{x}, \omega) / \vec{E}(\vec{x}, \omega)$ . Using that approach, initial calculations were made of femtosecond pulse propagation and scattering interactions for a Lorentz medium by a direct time integration of Maxwell's equations. The computed reflection coefficients [5] were accurate to better than 6 parts in 10 000 over the frequency range dc to  $3 \times 10^{16}$  Hz for a single 0.2 fs Gaussian pulse incident upon a Lorentz half space, and new results were obtained for the Sommerfeld and Brillouin precursors, agreeing very well with previous published Laplace transform theory.

In this paper, we report a generalization of the above approach to deal with the *nonlinear* terms of the electric polarization. The FD-TD direct time integration of Maxwell's equations can now incorporate nonlinear instantaneous and dispersive effects as well as linear instantaneous and dispersive effects, thereby permitting the modeling of optical solitons having very large instantaneous bandwidths.

As in [5], again consider a one-dimensional problem with electric and magnetic field intensities,  $E_z$  and  $H_y$ , respectively, propagating in the  $x$  direction. Assuming that the medium is nonpermeable and isotropic, Maxwell's equations in one dimension are written as

$$\frac{\partial \mu_0 H_y}{\partial t} = \frac{\partial E_z}{\partial x} \quad (1)$$

$$\frac{\partial D_z}{\partial t} = \frac{\partial H_y}{\partial x} \quad (2)$$

$$D_z = \epsilon_0 \epsilon_\infty E_z + P_z \quad (3)$$

Here  $\mu_0$  and  $\epsilon_0$  are the permeability and permittivity coefficients for free space,  $\epsilon_\infty$  is the relative material permittivity at infinite frequency,  $D_z$  is the electric field displacement, and  $P_z$  is the electric polarization.

Assume that the polarization  $P_z$  consists [10] of two parts: a linear part  $P_z^L$  and a nonlinear part  $P_z^{NL}$ .

$$P_z = P_z^L + P_z^{NL} \quad (4)$$

The linear polarization  $P_i^L$  is given by a linear convolution of  $E_i(x, t)$  and the first-order susceptibility function  $\chi^{(1)}$ :

$$P_i^L(x, t) = \epsilon_0 \int_{-\infty}^{\infty} \chi^{(1)}(t - \bar{t}) E_i(x, \bar{t}) d\bar{t} \quad (5)$$

and  $P_i^{NL}$  is given by a nonlinear convolution of  $E_i(x, t)$  and the third-order susceptibility function,  $\chi^{(3)}$ :

$$P_i^{NL}(x, t) = \epsilon_0 \int_{-\infty}^{\infty} \int_{-\infty}^{\infty} \int_{-\infty}^{\infty} \chi^{(3)}(t - \bar{t}_1, t - \bar{t}_2, t - \bar{t}_3) E_i(x, \bar{t}_1) E_i(x, \bar{t}_2) E_i(x, \bar{t}_3) d\bar{t}_1 d\bar{t}_2 d\bar{t}_3. \quad (6)$$

This last integral models the physics of a nonlinearity with retardation or memory, i.e., a dispersive nonlinearity that can occur due to quantum effects in silica at time scales of 1 to 100 fs. Note that  $\chi^{(3)}$  may differ from  $\chi^{(1)}$  in physical properties such as resonances and dampings.

We consider a material having a Lorentz linear dispersion characterized [18] by the following  $\chi^{(1)}$ :

$$\chi^{(1)}(t) = \left( \frac{\omega_p^2}{\nu_0} \right) \exp(-\delta t/2) \sin(\nu_0 t). \quad (7)$$

The corresponding linear permittivity as a function of frequency is

$$\epsilon(\omega) = \epsilon_\infty + \chi^{(1)}(\omega) = \epsilon_\infty + \frac{\omega_p^2(\epsilon_1 - \epsilon_\infty)}{\omega_0^2 - j\delta\omega - \omega^2} \quad (8)$$

where  $\omega_p^2 = \omega_0^2(\epsilon_1 - \epsilon_\infty)$  and  $\nu_0^2 = \omega_0^2 - \delta^2/4$ .

Further, the material nonlinearity is assumed to be characterized [7] by the following nonlinear single time convolution for  $P_i^{NL}$ :

$$P_i^{NL}(x, t) = \epsilon_0 \chi^{(3)} E_i(x, t) \int_{-\infty}^{\infty} g(t - \bar{t}) E_i^2(x, \bar{t}) d\bar{t} \quad (9)$$

where  $\chi^{(3)}$  is the nonlinear coefficient. The causal response function  $g(t - \bar{t})$  is normalized so that

$$\int_{-\infty}^{\infty} g(\bar{t}) d\bar{t} = 1. \quad (10)$$

Equation (9) only accounts for nonresonant third-order processes. The processes considered in (9) are phonon interactions and nonresonant electronic effects. The modeling [7] of those responses is given by the third-order response function  $g(t)$ , where

$$g(t) = \alpha \delta(t) + (1 - \alpha) g_R(t) \quad (11)$$

and

$$g_R(t) = \left( \frac{\tau_1^2 + \tau_2^2}{\tau_1 \tau_2} \right) \exp(-t/\tau_2) \sin(t/\tau_1). \quad (12)$$

In (11),  $\delta(t)$  is the instantaneous delta function response and models Kerr nonresonant virtual electronic transitions in the order of about 1 fs or less. The function  $g_R(t)$  models transient Raman scattering and  $\alpha$  parameterizes the relative strengths of the Kerr and Raman interactions. Effectively,

$g_R(t)$  models a single Lorentzian line centered on the optical phonon frequency  $1/\tau_1$  and having a bandwidth of  $1/\tau_2$  (the reciprocal phonon lifetime). See [7] for a more detailed explanation of the modeling of the nonlinear optical fiber.

We will now describe a solution procedure [15] for evolving the electric polarization in time by solving a system of coupled nonlinear ordinary differential equations. Equations (4) through (12) describe the electric polarization in the nonlinear medium. Those equations together with (1) to (3) will provide a system of equations for evolving the electromagnetic field in nonlinear media. The procedure will be a generalization of the approach that was used in [5]. However that approach used the complex permittivity relation in the frequency domain to obtain an ordinary differential equation that related  $E_i$  to  $D_i$ . Such an approach is not applicable to nonlinear polarizations. Nevertheless, the same ordinary differential equation can be derived by an alternative approach, which is to start in the time domain with (3) and differentiate it. The key property that is used in that derivation is the fact that the kernel function  $\chi^{(1)}(t)$ , as given by (7), satisfies a linear second-order ordinary differential equation. Note that the kernel function  $g_R(t)$  as given by (12) for the nonlinear convolution integral, also satisfies a linear second-order ordinary differential equation. The fundamental innovation of the present approach is to notice that those properties make it possible to treat the linear and nonlinear convolution integrals as new dependent variables. Using this observation, a coupled system of nonlinear second-order ordinary differential equations can be derived for the linear and nonlinear convolution integrals, by differentiating them in the time domain.

Those equations determine the polarization  $P_i$  by using (4). Since those equations are second-order ordinary differential equations, a solution procedure only requires two time levels of storage for each equation. By comparison, a direct evaluation of the convolution integrals in (4) would require the storage of the electromagnetic fields from an initial time to the current time and an evaluation of the integrals at each time level. As the following calculations will show, typical calculations require several tens of thousands of time levels of evolution. Hence the present method is more efficient both in storage and in operation count than a direct method. For a 2-D or 3-D full-vector nonlinear optics model, this improvement reduces the computer memory required for a first-principles computation from an impossible level of 100-1000 Gwords to a presently feasible level of 0.1-1 Gword.

We will now describe the differential equations that govern the evolution of the polarization, as given by (4) to (12). Assuming zero values of the electromagnetic field and the kernel functions for  $t \leq 0$ , define the functions  $F(t)$  and  $G(t)$  as respectively the linear and nonlinear convolutions:

$$F(t) = \epsilon_0 \int_0^t \chi^{(1)}(t - \bar{t}) E_i(x, \bar{t}) d\bar{t} \quad (13)$$

$$G(t) = \epsilon_0 \int_0^t g(t-i) E_i^2(x, i) di. \quad (14)$$

Then, by differentiating  $F$  and  $G$ , we have found that they satisfy the following coupled system of nonlinear ordinary differential equations:

$$\begin{aligned} \frac{1}{\omega_0^2} \frac{d^2 F}{dt^2} + \frac{\delta}{\omega_0^2} \frac{dF}{dt} + \left(1 + \frac{\epsilon_s - \epsilon_\infty}{\epsilon_\infty + \alpha \chi^{(3)} E_i^2}\right) F \\ + \left(\frac{(\epsilon_s - \epsilon_\infty)(1 - \alpha) \chi^{(3)} E_i}{\epsilon_\infty + \alpha \chi^{(3)} E_i^2}\right) G \\ = \left(\frac{(\epsilon_s - \epsilon_\infty)}{\epsilon_\infty + \alpha \chi^{(3)} E_i^2}\right) D_i \end{aligned} \quad (15)$$

$$\begin{aligned} \frac{1}{\bar{\omega}_0^2} \frac{d^2 G}{dt^2} + \frac{\bar{\delta}}{\bar{\omega}_0^2} \frac{dG}{dt} + \left(1 + \frac{(1 - \alpha) \chi^{(3)} E_i^2}{\epsilon_\infty + \alpha \chi^{(3)} E_i^2}\right) G \\ + \left(\frac{E_i}{\epsilon_\infty + \alpha \chi^{(3)} E_i^2}\right) F = \left(\frac{E_i}{\epsilon_\infty + \alpha \chi^{(3)} E_i^2}\right) D_i \end{aligned} \quad (16)$$

where  $\bar{\delta} = 2/\tau_2$  and  $\bar{\omega}_0^2 = (1/\tau_1)^2 + (1/\tau_2)^2$ . Equation (15) and (16) are first solved simultaneously for  $F$  and  $G$  at the latest time step by using a second-order accurate finite-difference scheme that operates on data for the current value of  $D_i$  and previous values of  $D_i$ ,  $E_i$ ,  $F$ , and  $G$ . Only two time levels of storage are required with this approach. Then, the latest value of  $E_i$  can be obtained via a Newton's iteration of the following equation, using the new values of  $D_i$ ,  $F$ , and  $G$ :

$$E_i = \frac{D_i - F - (1 - \alpha) \chi^{(3)} E_i G}{\epsilon_0 (\epsilon_\infty + \alpha \chi^{(3)} E_i^2)}. \quad (17)$$

This algorithm, as given by the system (15) to (17), determines values of  $E_i$  and  $P_i$  so that (3) is satisfied. This procedure, combined with the usual FD-TD realization [19] of (1) and (2), comprises the complete solution method.

### III. ALGORITHM

In this section, the finite-difference equations [20] will be described that are used to solve Maxwell's equations, (1) and (2), as well as the equations that account for the nonlinear and dispersive effects contained in the polarization, (15), (16), and (17). Let a region in space-time,  $x$ - $t$ , (one-dimensional), contain a lattice of points with coordinates  $(i, n)$  for  $D_i(x, t)$  and  $E_i(x, t)$  and  $(i + 1/2, n + 1/2)$  for  $H_i(x, t)$ . This computational grid will be used to implement the standard leapfrog algorithm [19], known as the FD-TD method.

Using the FD-TD approach, the finite-difference equations for (1) and (2) are given, respectively, by

$$\begin{aligned} \frac{\mu_0}{\Delta t} \left( H_i^{n+1/2}(i) - H_i^{n-1/2}(i) \right) \\ = \frac{1}{\Delta x} (E_i^n(i+1) - E_i^n(i)) \end{aligned} \quad (18)$$

$$\begin{aligned} \frac{1}{\Delta t} (D_i^{n+1/2}(i) - D_i^n(i)) \\ = \frac{1}{\Delta x} \left( H_i^{n+1/2}(i) \left( i + \frac{1}{2} \right) - H_i^{n-1/2}(i) \left( i - \frac{1}{2} \right) \right). \end{aligned} \quad (19)$$

These explicit equations are used in the solution procedure as follows. First (18) is used to determine  $H_i^{n+1/2}$  from the previous values  $E_i^n$  and  $H_i^{n-1/2}$ . Then (19) is used to determine  $D_i^{n+1/2}$  from the previous values  $H_i^{n+1/2}$  and  $D_i^n$ .

Next (15) and (16) are used to determine the values of the linear and nonlinear convolution integrals,  $F^{n+1}$  and  $G^{n+1}$  at the new time level  $n+1$ , using the new value of  $D_i^{n+1/2}$  and the previous values of  $D_i$ ,  $E_i$ ,  $F$ , and  $G$ . Note that the form of the coupling in (15) and (16) results in a finite discretization in which there is strong diagonal dominance in the resulting matrices. This feature is essential for a stable algorithm. A second-order accurate finite-difference scheme for the coupled (15) and (16) is given by the following.

$$\begin{aligned} \frac{1}{\omega_0^2} \left( \frac{F^{n+1}(i) - 2F^n(i) + F^{n-1}(i)}{(\Delta t)^2} \right) \\ + \frac{\delta}{\omega_0^2} \left( \frac{F^{n+1}(i) - F^{n-1}(i)}{2 \Delta t} \right) \\ + \left( 1 + \frac{\epsilon_s - \epsilon_\infty}{\epsilon_\infty + \alpha \chi^{(3)} (E_i^n(i))^2} \right) \cdot \left( \frac{F^{n+1}(i) + F^{n-1}(i)}{2} \right) \\ + \left( \frac{(\epsilon_s - \epsilon_\infty)(1 - \alpha) \chi^{(3)} E_i^n(i)}{\epsilon_\infty + \alpha \chi^{(3)} (E_i^n(i))^2} \right) \cdot \left( \frac{G^{n+1}(i) + G^{n-1}(i)}{2} \right) \\ = \left( \frac{(\epsilon_s - \epsilon_\infty)}{\epsilon_\infty + \alpha \chi^{(3)} (E_i^n(i))^2} \right) \left( \frac{D_i^{n+1/2}(i) + D_i^{n-1/2}(i)}{2} \right) \end{aligned} \quad (20)$$

$$\begin{aligned} \frac{1}{\bar{\omega}_0^2} \left( \frac{G^{n+1}(i) - 2G^n(i) + G^{n-1}(i)}{(\Delta t)^2} \right) \\ + \frac{\bar{\delta}}{\bar{\omega}_0^2} \left( \frac{G^{n+1}(i) - G^{n-1}(i)}{2 \Delta t} \right) \\ + \left( 1 + \frac{(1 - \alpha) \chi^{(3)} (E_i^n(i))^2}{\epsilon_\infty + \alpha \chi^{(3)} (E_i^n(i))^2} \right) \cdot \left( \frac{G^{n+1}(i) + G^{n-1}(i)}{2} \right) \\ + \left( \frac{E_i^n(i)}{\epsilon_\infty + \alpha \chi^{(3)} (E_i^n(i))^2} \right) \left( \frac{F^{n+1}(i) + F^{n-1}(i)}{2} \right) \\ = \left( \frac{E_i^n(i)}{\epsilon_\infty + \alpha \chi^{(3)} (E_i^n(i))^2} \right) \left( \frac{D_i^{n+1/2}(i) + D_i^{n-1/2}(i)}{2} \right). \end{aligned} \quad (21)$$

Finally, the new values  $D_t^{n+1}$ ,  $F^{n+1}$ , and  $G^{n+1}$  are used in (17) to determine  $E^{n+1}$ , by using an approximate Newton iteration procedure as follows.

$$E_t^{n+1} = \frac{D_t^{n+1} - F^{n+1} - (1 - \alpha)\chi^{(3)}E_t^p G^{n+1}}{\epsilon_0(\epsilon_\infty + \alpha\chi^{(3)}(E_t^p)^2)} \quad (22)$$

$p = 0, 1, 2, \dots$

Here  $E^p = E^n$  for  $p = 0$ . For the results shown in this paper, the iteration process was stopped at  $p = 1$ , since sufficient accuracy was obtained at that step. Having determined  $E^{n+1}$ , the solution process, given by (18) to (22) is iteratively repeated to advance the electromagnetic field to successive time levels.

## RESULTS

Now results [20], [21] of the integration of Maxwell's equations will be presented, including soliton dynamics. A pulsed optical signal source is assumed to be located at  $x = 0$  at the initial time  $t = 0$ . The pulse is assumed to have unity amplitude of its sinusoidal-carrier electric field, a carrier frequency  $f_c = 1.37 \times 10^{14}$  Hz, ( $\omega_c = 8.61 \times 10^{14}$  rad/s), and a hyperbolic secant envelope function with a characteristic time constant of 14.6 fs. Approximately 7 cycles of the carrier are contained within the pulse envelope, and the center of the pulse coincides with a zero-crossing of the sinusoid. To achieve soliton formation over short propagation spans of less than 200  $\mu$ , we scale values of the group velocity dispersion  $\beta_2$  and the nonlinear coefficient  $\chi^{(3)}$ . For example, let:  $\epsilon_\infty = 5.25$ ;  $\epsilon_\infty = 2.25$ ;  $\omega_0 = 4.0 \times 10^{14}$  rad/s;  $\delta = 2.0 \times 10^9$  s $^{-1}$ ;  $\chi^{(3)} = 7 \times 10^{-2}$  (V/m) $^{-2}$ ;  $\alpha = 0.7$ ;  $\tau_1 = 12.2$  fs; and  $\tau_2 = 32$  fs. (The last three values are from [7].) This results in  $\beta_2$  varying widely over the spectral width of the pulse, i.e., from  $-7$  to  $-75$  ps $^2$ /m over the range  $(1.37 \pm 0.2) \times 10^{14}$  Hz. Finally, by choosing a uniform FD-TD space resolution of 5 nm ( $\approx \lambda_0/300$ ), the numerical phase velocity error is limited to about 1 part in  $10^5$ , which is very small compared to the physical dispersions being modeled.

First a calculation was performed for the linear case ( $\chi^{(3)} = 0$ ), in which only the effects of dispersion would act on the pulse. As shown in [15], the results showed significant effects of dispersion after a propagation distance of 150  $\mu$ m. These effects included pulse broadening, diminishing amplitude, and carrier frequency modulation ( $>f_c$  on the leading side,  $<f_c$  on the trailing side) which causes an asymmetrical shifting of the envelope, a higher-order dispersive effect. These qualitative features of the effect of anomalous dispersion have been predicted [16], but until now have not been computed by directly integrating Maxwell's equations.

Fig. 1 shows the results for  $\chi^{(3)} = 7 \times 10^{-2}$  (V/m) $^{-2}$ . The pulse is plotted at  $n = 2 \times 10^4$  and  $4 \times 10^4$  time steps, corresponding to propagation to  $x = 55$   $\mu$ m and 126  $\mu$ m. The nonlinear effects balance the linear dispersive effects, yielding a rightward propagating soliton that re-

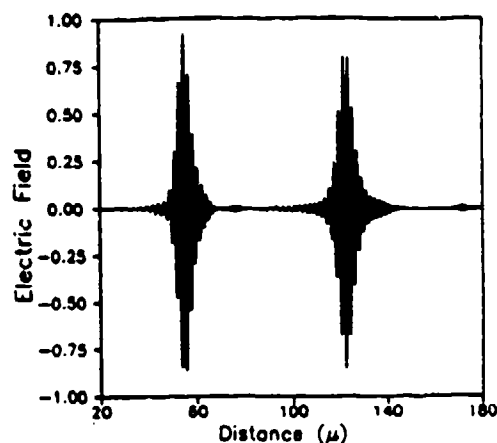


Fig. 1. FD-TD results for the optical soliton carrier pulse after propagating 55  $\mu$ m and 126  $\mu$ m.

tains its amplitude and width. Also, a second low-amplitude pulse is seen to move out ahead of the soliton. The carrier frequency of this "daughter" is upshifted to  $\approx 4.9 \times 10^{14}$  Hz, approximately 3.6 times that of the soliton. Also, in both the linear and nonlinear cases, by observing a video of the pulse evolution, it was noted that the phase velocity of the carrier was substantially greater than the group velocity of the envelope. In the video, waves would appear at the rear (left) side of the pulse, advance through the pulse and disappear from the front (right) side of the advancing pulse. Such observations of the carrier properties are readily observable in the present formulation.

To further verify that the main pulse in Fig. 1 had the characteristics of a soliton, in [15], a plot was presented of the Fourier spectrum of the main pulse at the two times that are shown in Fig. 1. The figure showed a 4 THz redshift and sharpening of the spectrum as the soliton propagates. From GNLSE theory, the redshift is predicted due to the Raman effect [7], [10] occurring as a higher-order dispersive nonlinearity modeled by the function  $g_R(t)$  in (12).

Last, we consider the collision of two counter-propagating solitons. Each is identical and has all of the parameters of the previous case. As is characteristic of colliding solitons [22], we find that after the collisions both main and daughter pulses separate and move apart without changing their general appearances. Fig. 2 shows the counter-propagating solitons at 20 000 time steps; at this time the two main pulses are approaching each other. Fig. 3 shows them at 25 000 time steps; at this time they are nonlinearly interacting. A video of the collision showed violent changes in the solitons during the interaction period, with severe increases and decreases in the amplitude of the combined pulse due to the nonlinear interference effects. Finally, Fig. 4 shows them at 30 000 time steps; at this time they have passed through each other and are separating. However, there are lagging phase shifts due to the collision: 12° for the carriers in the solitons, and 31° for the carriers in the daughters. (At 30 000 time steps, the phase shift due to numerical error is approxi-



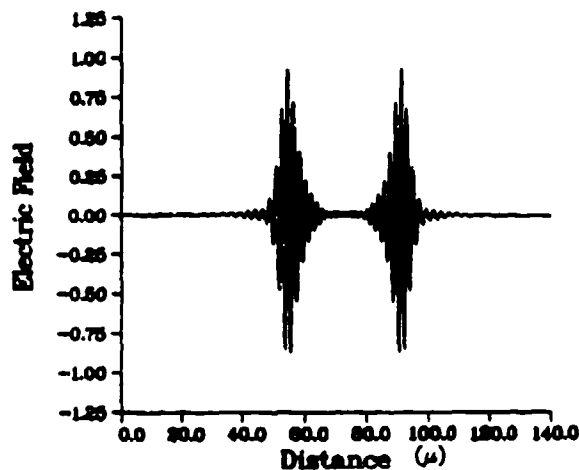


Fig. 2. Counter-propagating solitons at 20 000 time steps.

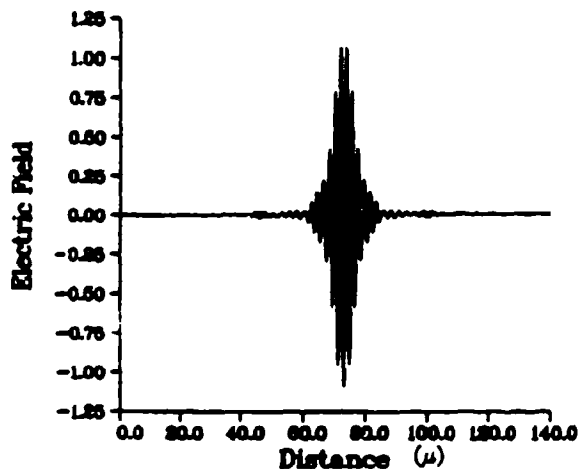


Fig. 3. Counter-propagating solitons at 25 000 time steps.

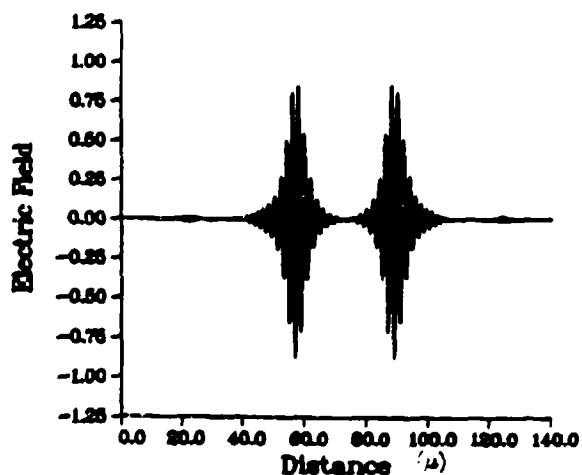


Fig. 4. Counter-propagating solitons at 30 000 time steps.

mately equal to one-third of a degree.) To illustrate the phase lag due to the interaction, in [15], a plot was presented of the space dependence of the central part of the rightward-moving daughter for the original uncollided

case and the collided case, with both curves at exactly 30 000 time steps of the algorithm. It clearly illustrated the phase shift of  $31^\circ$ . Such precise measurements of phase shifts, not easily obtained by GNLSE theory, are readily displayed by using results from the present formulation. Also if an amplification of these phase lags could be obtained by varying the parameters in this calculation, such a phase lag might form the basis for an optical switching device.

For these calculations, less than 350 s of CPU time were required on a Cray Y-MP8/832, which is a small amount of time. Hence significantly larger calculations are feasible on present-day computers. For example, the propagation of larger pulses, such as picosecond pulses, may be possible. The modeling of any pulse over long distances, such as meters or kilometers, may be possible by the use of scaling on the parameters that characterize the material. In the case considered in this article, the values of the linear group velocity dispersion  $\beta_2$  and the nonlinear coefficient  $\chi^{(3)}$  were scaled to values that are orders of magnitude larger than those that occur naturally in optical fibers. By use of these scalings, the effects of linear dispersion, nonlinear dispersion and nonlinear instantaneous response took place over the short distance of 200  $\mu\text{m}$ .

## V. CONCLUDING REMARKS

Optical switching, which is based on nonlinear optical responses, has become an intense area of research [6] following the advent of the laser. Currently, many materials are being investigated [23] for their nonlinear optical properties for various applications, including optical switching.

A new algorithm has been developed that permits, for the first time, the direct time integration of the full-vector, nonlinear Maxwell's equations. This new capability permits the modeling of linear and nonlinear, instantaneous and dispersive effects in the electric polarization in material media. The modeling of the optical carrier is retained in this approach. Using this algorithm, results are presented of first-time calculations in one dimension of the propagation and collision of femtosecond electromagnetic solitons that retain the optical carrier. The nonlinear modeling takes into account such quantum effects as the Kerr and Raman interactions at distance scales larger than about 5 nm.

The novel approach discussed here is a fine-grained direct time-domain numerical solution of Maxwell's equations that rigorously enforces the field vector boundary conditions at all interfaces of dissimilar media, whether or not the media are dispersive or nonlinear. The new approach is almost completely general. It assumes nothing about 1) the homogeneity or isotropy of the optical medium; 2) the magnitude of the nonlinearity; 3) the nature of the material's  $\omega - \beta$ ; or 4) the shape, duration, polarization, and numbers of the optical pulse(s).

By retaining the optical carrier, the new method solves

for fundamental quantities—the optical electric and magnetic fields in space and time—rather than a nonphysical envelope function. The present approach is robust and should permit modeling 2-D and 3-D boundary-value problems involving optical soliton propagation, scattering, and switching directly from the full vector, nonlinear Maxwell's equations. For nonlinear optics, this approach has the potential to provide a modeling capability for millimeter-scale integrated optical circuits beyond that of existing techniques using the generalized nonlinear Schrödinger equation.

## REFERENCES

- [1] A. Taflov, "Review of the formulation and applications of the finite-difference time-domain method for numerical modeling of electromagnetic wave interactions with arbitrary structures," *Wave Motion*, vol. 10, Amsterdam: North-Holland, pp. 547-582, 1988.
- [2] —, "Re-inventing electromagnetics: supercomputing solution of Maxwell's equations via direct time integration on space grids," presented at AIAA 30th Aerospace Sciences Meet., Reno, NV, Jan. 6-9, 1992, AIAA Paper 92-0333.
- [3] S. Maeda, T. Kashiwa, and I. Fukai, "Full wave analysis of propagation characteristics of a through hole using the finite-difference time-domain method," *IEEE Trans. Microwave Theory Tech.*, vol. 39, 1991.
- [4] E. Sano and T. Shibata, "Fullwave analysis of picosecond photoconductive switches," *IEEE J. Quantum Electron.*, vol. 26, pp. 372-377, 1990.
- [5] R. M. Joseph, S. C. Hagness, and A. Taflov, "Direct time integration of Maxwell's equations in linear dispersive media with absorption for scattering and propagation of femtosecond electromagnetic pulses," *Opt. Lett.*, vol. 16, pp. 1412-1414, 1991.
- [6] S. R. Friberg, A. M. Weiner, Y. Silberberg, B. G. Sfez, and P. S. Smith, "Femtosecond switching in a dual-core-fiber nonlinear coupler," *Opt. Lett.*, vol. 13, no. 10, pp. 904-906, Oct. 1988.
- [7] K. Blow and D. Wood, "Theoretical description of transient stimulated Raman scattering in optical fibers," *IEEE J. Quantum Electron.*, vol. 25, pp. 2665-2673, Dec. 1989.
- [8] W. Scott, "Ultra-wideband technology," *Aviation week and space Technol.*, pp. 18-22, Nov. 19, 1990.
- [9] A. Hasagawa, *Optical Solitons in Fibers*. New York: Springer-Verlag, 1990.
- [10] G. Agrawal, *Nonlinear Fiber Optics*. New York: Academic, 1990, Ch. 2.
- [11] M. Feit, and J. W. Fleck Jr., "Three-dimensional analysis of a directional coupler exhibiting a Kerr nonlinearity," *IEEE J. Quantum Electron.*, vol. 24, Oct. 1988.
- [12] P. M. Goorjian, and S. Obayashi, "A streamwise upwind algorithm applied to vortical flow over a delta wing," in *Notes on Numerical Fluid Mech.*, vol. 29, P. Wesseling, Ed. City: Vieweg, 1990, pp. 169-178.
- [13] P. M. Goorjian and A. Taflov, "FD-TD computational modeling of nonlinear electromagnetic phenomena using a nonlinear convolution approach," in *Proc., 1991 North American Radar Science Meet. and Int. IEEE/AP-S Symp.*, URSI, London, Ont., Canada, June 24-28, 1991, paper B60.1, p. 190.
- [14] A. Taflov, "Supercomputing simulation of femtosecond pulse propagation," presented at Superconducting Digital Circ. and Syst. Conf., George Washington Univ., Washington, DC, Sept. 11-13, 1991.
- [15] P. M. Goorjian and A. Taflov, "Direct time integration of Maxwell's equations in nonlinear dispersive media for propagation of femtosecond electromagnetic solitons," *Opt. Lett.*, vol. 17, no. 3, pp. 180-182, Feb. 1, 1992.
- [16] T. E. Bell, "Light that acts like 'Natural Bits,'" *IEEE Spectrum*, vol. 27, pp. 36-37, Aug. 1990.
- [17] J. A. Krumhansl, "Unity in the science of physics," *Phys. Today*, vol. 44, no. 3, pp. 33-38, Mar. 1991.
- [18] J. D. Jackson, *Classical Electrodynamics*, 2nd ed. New York: Wiley, 1975.
- [19] K. S. Yee, "Numerical solution of initial boundary value problems involving Maxwell's equations in isotropic media," *IEEE Trans. Antennas Propag.*, vol. AP-14, pp. 302-307, May, 1966.
- [20] P. M. Goorjian and A. Taflov, "Computational modeling of nonlinear electromagnetic phenomena," presented at AIAA 30th Aerospace Sci. Meet., Reno, NV, Jan. 6-9, 1992, paper 92-0457.
- [21] —, "Direct time integration of Maxwell's equations in nonlinear dispersive media for propagation and scattering of femtosecond electromagnetic solitons," *Integrated Photon. Res. Top. Meet., 1992 Tech. Dig.*, vol. 10. New Orleans, LA: Opt. Soc. Amer., April 13-15, 1992.
- [22] D. Marcuse, *Theory of Dielectric Optical Waveguides*, 2nd ed. New York: Academic, 1991.
- [23] D. F. Eaton, "Nonlinear optical materials," *Science*, vol. 253, pp. 281-287, July 19, 1991.

Peter M. Goorjian (M'89), photograph and biography not available at the time of publication.

Allen Taflov (M'75-SM'84-F'90), photograph and biography not available at the time of publication.

Ross M. Joseph, photograph and biography not available at the time of publication.

Steven C. Hagness, photograph and biography not available at the time of publication.

## RE-INVENTING ELECTROMAGNETICS: SUPERCOMPUTING SOLUTION OF MAXWELL'S EQUATIONS VIA DIRECT TIME INTEGRATION ON SPACE GRIDS

A. TAFLOVE

Department of Electrical Engineering and Computer Science, McCormick School of Engineering,  
Northwestern University, Evanston, IL 60208-3118, U.S.A.

**Abstract**—This paper summarizes the present state and future directions of applying finite-difference and finite-volume time-domain techniques for Maxwell's equations on supercomputers to model complex electromagnetic wave interactions with structures. Applications so far have been dominated by radar cross-section technology, but by no means are limited to this area. In fact, the gains we have made place us on the threshold of being able to make tremendous contributions to non-defense electronics and optical technology. Some of the most interesting research in these commercial areas is summarized.

### 1. INTRODUCTION

Defense requirements for aerospace vehicles having low radar cross-section (RCS) have driven the development of large-scale methods in computational electromagnetics. We have an anomaly that the effectiveness and cost of such state-of-the-art systems depends upon our ability to develop engineering understanding of century-old basic science, Maxwell's equations (ca 1870). Recently, direct space-grid time-domain Maxwell's solvers have been the subject of intense interest for this application, challenging previously dominant frequency-domain integral equation approaches.

This paper summarizes the history, present state, and possible future of applying space-grid time-domain techniques for Maxwell's equations to model complex electromagnetic wave interactions. As teraflop-class supercomputers permit structures of amazing complexity and size to be modeled, the old/new theme of Maxwell's equations/RCS design will be seen to recur in areas that cut a wide swath through the core of electrical engineering. We will consider:

- The state of the full-matrix method of moments.
- The history of space-grid time-domain techniques for Maxwell's equations.
- The state of existing algorithms and meshes: basis, primary types, predictive dynamic range.
- Scaling to problems of  $>10^9$  field unknowns.
- Future defense electromagnetics needs: 70 dB dynamic range; modeling of complex and composite materials; optimization of materials and shapes for RCS; integrated RCS and aerodynamics design and optimization; target identification.
- Future dual-use electromagnetics needs: antenna design; microwave and millimeter wave inte-

grated circuits; bio-electromagnetic systems; high-speed interconnects and packaging for electronic digital circuits; incorporation of models of active devices; all-optical devices, including femtosecond switches and logic gates.

Overall, advances in supercomputing solutions of Maxwell's equations based on their direct time integration on space grids place us on the threshold of being able to make large contributions to dual-use electronics and optical technology as well as RCS technology. In fact, I claim that solving Maxwell's equations at ultra-large scales will permit us to design devices having working bandwidths literally from d.c. to light.

### 2. THE STATE OF THE FULL-MATRIX METHOD OF MOMENTS

The modeling of engineering systems involving EM wave interactions has been dominated by frequency-domain integral equation techniques and high-frequency asymptotics. This is evidenced by the almost universal use of the method of moments (MoM)<sup>1,2</sup> to provide a rigorous boundary value analysis of structures and the geometrical theory of diffraction (GTD)<sup>3,4</sup> to provide an approximate analysis valid in the high-frequency limit. However, a number of important contemporary problems in EM wave engineering are not adequately treated by such models. Complexities of structure shape and material composition confound the GTD analysis; and structures of even moderate electrical size (spanning five or more wavelengths in three dimensions) present very difficult computer resource scaling problems for MoM.

The latter problem is particularly serious since MoM has provided virtually the only means of dealing with the non-metallic materials now

commonly used in aerospace design. Consider the following:

Define  $d_{\text{span}}$  as the characteristic span of a flat-configured target and  $\lambda_0$  as the wavelength of the impinging radar beam such that the electrical surface area of the target (in square wavelengths) is  $2(d_{\text{span}}/\lambda_0)^2$ . Assume a standard triangular surface patching implementation of the electric field integral equation with the surface area of the target discretized at  $R$  divisions per  $\lambda_0$ . Then, the number of triangular surface patches is given by  $4R^2(d_{\text{span}}/\lambda_0)^2$ ; and  $N$ , the number of field unknowns, is given by  $6R^2(d_{\text{span}}/\lambda_0)^2$ . In fact,  $N$  is the order of the MoM system matrix. With  $R$  usually taken as 10 or greater to properly sample the induced electric current distribution on the target surface, we see that  $N$  rises above 10,000 for  $d_{\text{span}}$  greater than  $4\lambda_0$ . Further, we see that  $N$  increases quadratically as  $\lambda_0$  drops (radar frequency increases) and the computational burden for LU decomposition increases as the sixth power of frequency (order of  $N^3$ ).

Let us see what this means in terms of program running time for the recently introduced CRAY C-90 supercomputer. First, assume that  $d_{\text{span}}$  is on the order of 10 m, perhaps typical of a jet fighter.  $N$  rises above 40,000 at a radar frequency of 240 MHz and the CRAY C-90 running time is projected to be less than 3 h, based upon much experience with the CRAY Y-MP/8 machine.<sup>9</sup> Up an octave to 480 MHz,  $N$  increases to 160,000 and the C-90 running time projects to be 8 days, a 64-fold ( $2^6$ ) increase. Up still another octave to 960 MHz,  $N$  increases to 640,000 and the C-90 running time projects to be 1 year, 5 months. The latter assumes that: (a) we have enough disk drives to store the trillion-word MoM matrix; (b) we find acceptable the error accumulation resulting from the million-trillion floating-point operations on MoM matrix elements having precisions of only perhaps 1 part in 10,000; and (c) the computer system stays up continuously for over 1 year.

It is quite clear that the traditional, full-matrix MoM computational modeling of an entire aerospace structure such as a fighter plane is at present impractical at radar frequencies much above 500 MHz, despite advances in supercomputer hardware and software. However, radar frequencies of interest go much higher than 500 MHz, in fact up to 10 GHz or more. Much research effort has been expended in deriving alternative iterative frequency-domain approaches (conjugate gradient, spectral, etc.) that preserve the rigorous boundary-integral formulation of MoM while realizing dimensionally reduced computational burdens. These would permit, in principle, entire aircraft modeling at radar frequencies well above 500 MHz. However, these alternatives may not be as robust as the full-matrix MoM, that is, providing results of engineering value for a wide class of structures without the user wondering if the algorithm is converged.

### 3. HISTORY OF SPACE-GRID TIME-DOMAIN TECHNIQUES FOR MAXWELL'S EQUATIONS

The problems involved in applying frequency-domain, dense-matrix MoM technology to large-scale RCS modeling have prompted a rapid recent expansion of interest in an alternative class of non-matrix approaches: direct space-grid time-domain solvers for Maxwell's time-dependent curl equations. The new approaches appear to be as robust and accurate as MoM, but have dimensionally-reduced computational burdens to the point where whole-aircraft modeling for RCS is becoming possible at frequencies above 1 GHz. They are analogous to existing mesh-based solutions of fluid-flow problems in that the numerical model is based upon a direct, time-domain solution of the governing partial differential equation. Yet, they are very non-traditional approaches to CEM for engineering applications, where frequency-domain methods (primarily MoM) have dominated.

Table I summarizes key developments and publications in the history of direct space-grid time-domain solvers for Maxwell's time-dependent curl equations. As can be seen, both the pace and range of applications of FD-TD and other time-domain grid-based models of Maxwell's equations are expanding rapidly. These efficient volumetric solutions in the time domain are making possible applications in areas far beyond those of the method of moments. In this regard, this paper seeks to explore selected areas of high promise.

### 4. STATE OF EXISTING ALGORITHMS AND MESHES

#### 4.1. Basis

FD-TD and FV-TD are direct solution methods for Maxwell's equations. They employ no potentials. Rather, they are based upon volumetric sampling of the unknown near-field distribution ( $E$  and  $H$  fields) within and surrounding the structure of interest, and over a period of time. The sampling in space is at a sub-wavelength (sub- $\lambda_0$ ) resolution set by the user to properly sample (in the Nyquist sense) the highest near-field spatial frequencies thought to be important in the physics of the problem. Typically, 10–20 samples per illumination wavelength are needed. The sampling in time is selected to insure numerical stability of the algorithm.

Overall, FD-TD and FV-TD are marching-in-time procedures which simulate the continuous actual EM waves by sampled-data numerical analogs propagating in a computer data space. Time-stepping continues as the numerical wave analogs propagate in the space grid to causally connect the physics of all regions of the target. All outgoing scattered wave analogs ideally propagate through the lattice truncation planes with negligible reflection to exit the region. Phenomena such as induction of surface currents, scattering and multiple scattering, aperture penetration and cavity excitation are modeled time

Table 1. Partial history of space-grid time-domain techniques for Maxwell's equations

1966	Yee <sup>4</sup> described the basis of the first space-grid time-domain technique, later called the finite-difference time-domain (FD-TD) method. FD-TD implements the spatial derivatives of the curl operators using finite-difference in regular interleaved (dual) Cartesian space meshes for the electric and magnetic fields. Simple leapfrog time integration is employed
1975	Taflov and Beker published the correct numerical stability criterion for Yee's algorithm and the first grid-based time-integration of a two-dimensional EM scattering problem all the way to the sinusoidal steady state, <sup>7</sup> as well as the first three-dimensional grid-based computational model of EM wave absorption in complex, inhomogeneous biological tissues <sup>8</sup>
1977	Holland <sup>9</sup> and Kunz and Lee <sup>10</sup> applied the Yee algorithm to electromagnetic pulse (EMP) interaction problems
1980	Taflov coined the term "FD-TD" and published the first validated FD-TD models of EM wave penetration of a three-dimensional metal cavity <sup>11</sup>
1981	Mur published an accurate and numerically stable second-order radiation boundary condition for the Yee grid <sup>12</sup>
1982, 1983	Umeshankar and Taflov published the first FD-TD EM wave scattering models computing near fields, far fields and RCS for two-dimensional structures <sup>13</sup> and three-dimensional structures <sup>14</sup>
1987, 1988	Kriegsmann and coworkers introduced modern radiation boundary condition theory to the engineering EM community <sup>15,16</sup>
1987-	Sullivan, Gandhi, Taflov and coworkers commenced publishing a series of articles applying FD-TD to model EM wave interactions, especially hyperthermia, with complex three-dimensional models of humans <sup>17-20</sup>
1987-	Taflov, Umashankar and coworkers introduced contour-path, subcell techniques to permit FD-TD modeling of EM wave coupling to thin wires and wire bundles, <sup>21</sup> EM wave penetration through cracks in conducting screens <sup>22</sup> and conformal surface treatments of curved structures <sup>23</sup>
1988-	Finite-element time-domain (FE-TD), body-fitted finite-volume time-domain (FV-TD) and unstructured or partially unstructured meshes for Maxwell's equations were introduced by Cangellaris <i>et al.</i> , <sup>24</sup> Shankar <i>et al.</i> , <sup>25</sup> McCartin <i>et al.</i> , <sup>26</sup> and Madsen and Ziolkowski <sup>27</sup>
1989-	FD-TD modeling of optical circuit interconnects and microstrips was introduced by Liang <i>et al.</i> , <sup>28</sup> Shibata and Sano, <sup>29</sup> Sbein <i>et al.</i> <sup>30</sup> and Ko and Mitta <sup>31</sup>
1990-	FD-TD modeling of frequency-dependent dielectric permittivity was introduced by Luebbers <i>et al.</i> , <sup>32</sup> and Joseph <i>et al.</i> <sup>33</sup>
1990-	FD-TD modeling of antennas was introduced by Maloney <i>et al.</i> , <sup>34</sup> Tirkas and Balanis <sup>35</sup> and Katz <i>et al.</i> <sup>36</sup>
1990-	FD-TD modeling of picosecond optoelectronic switches was introduced by Sano and Shibata <sup>27</sup> and El-Ghazaly <i>et al.</i> <sup>38</sup>
1991-	FD-TD modeling of the propagation of femtosecond optical pulses in non-linear dispersive media was introduced by Georgian and Taflov <sup>39</sup> and Ziolkowski and Judkins <sup>40</sup>
1992-	FD-TD modeling of lumped-circuit elements (resistors, inductors, capacitors, diodes and transistors) in a two-dimensional EM wave code was introduced by Sui <i>et al.</i> <sup>41</sup>

step by time step by the action of the curl equations analog. Self-consistency of these modeled phenomena is generally assured if their spatial and temporal variations are well resolved by the space and time sampling process. In fact, the goal is to provide a self-consistent model of the mutual coupling of all of the electrically-small volume cells comprising the structure and its near field, even if the structure spans tens of  $\lambda_0$  in three dimensions and there are tens of millions of space cells.

Time-stepping is continued until the desired late-time pulse response or steady-state behavior is observed. An important example of the latter is the sinusoidal steady state, wherein the incident wave is assumed to have a sinusoidal dependence and time-stepping is continued until all fields in the sampling region exhibit sinusoidal repetition. This is a consequence of the limiting amplitude principle. Extensive numerical experimentation has shown that the number of complete cycles of the incident wave required to be time-stepped to achieve the sinusoidal steady state is a function of:

(1) *Target electrical size.* For many targets, this requires a number of time steps sufficient to permit at least two front-to-back-to-front traverses of the target by a wave analog. For example, assuming

a target spanning  $10\lambda_0$ , at least 40 cycles of the incident wave should be time-stepped to approach the sinusoidal steady state. For a grid resolution of  $\lambda_0/10$ , this corresponds to 800 time steps for FD-TD.

(2) *Target Q factor.* Targets having well-defined low-loss cavities or low-loss dielectric compositions may require the number of complete cycles of the incident wave to be time-stepped to approach the Q factor of the resonance; because Q can be large even for electrically moderate size cavities, this can dictate how many time steps the FD-TD or FV-TD code must be run.

In the RCS area, target electrical size may often be the dominant factor. Cavities for RCS problems (such as engine inlets) tend to be open and therefore moderate Q; and the use of radar-absorbing material (RAM) serves further to reduce the Q factors of structures.

#### 4.2. Primary types

The primary FD-TD and FV-TD algorithms used today are fully explicit second-order accurate grid-based solvers employing highly vectorizable and concurrent schemes for time-marching the six vector components of the EM near field at each of the

volume cells. The explicit nature of the solvers is maintained by either leapfrog or predictor-corrector time integration schemes. Second-order accurate radiation boundary conditions are used to simulate the extension of the problem space to infinity, thereby minimizing error due to the artifactual reflection of outgoing numerical wave modes at the mesh outer boundary.

Present methods differ primarily in how the space grid is set up. In fact, gridding methods can be categorized according to the degree of structure or regularity in the mesh:

(1) *Almost completely structured.* Space cells more than one or two cells from the structure of interest are organized in a completely regular manner, for example, using a uniform Yee Cartesian mesh. Only the cells adjacent to the structure are modified in size and shape to conformally fit the structure surface.<sup>22,27</sup>

—Advantage: computationally efficient, because there are relatively few modified cells requiring special storage to locate the cells in the mesh and special computations to perform the field updates. In fact, the number of modified cells (proportional to the surface area of the structure) becomes arbitrarily small compared with the number of regular mesh cells as structure size increases. As a result, the computer memory and running time needed to implement a fully conformal model can be indistinguishable from that required for a stepped-surface model. Further, an ultra-fast, minimal memory, Yee-like algorithm can be used for the regular space cells.

—Advantage: mapping of the mesh onto a parallel-vector computer or massively parallel computer is straightforward.

—Advantage: artifacts due to refraction and reflection of numerical wave modes propagating across global mesh distortions are not present. This is especially important for three-dimensional structures having substantial EM coupling between electrically disjoint sections, or reentrant regions.

—Disadvantage: geometry generation software for this type of meshing has not reached the mature state achieved for other types. Considerable work remains.

—Disadvantage: thin target surface coatings do not conform to mesh boundaries. These are best modeled here using surface impedances.

(2) *Body-fitted.* The space grid is globally distorted to fit the shape of the structure of interest.<sup>24</sup> Effectively, a coordinate transformation between a non-Cartesian physical mesh and a Cartesian logical mesh is implemented.

—Advantage: well-developed geometry generation software is available from the CFD community. Aerodynamic shapes appropriate for the RCS problem are nicely handled.

—Advantage: thin target surface coatings naturally conform to mesh boundaries.

—Advantage: mapping of the logical mesh onto a parallel-vector computer or massively parallel computer is straightforward.

—Disadvantage: relative to the baseline Yee algorithm, extra computer storage must be allocated to account for the three-dimensional position and stretching factors of each space cell. Further, extra computer arithmetic operations must be performed to implement Maxwell's equations at each cell and/or to enforce EM field continuity at the interfaces of adjacent cells. As a result, the number of floating point operations needed to update the six field components at a space cell over one time step can exceed that of the Yee algorithm by as much as 20:1, thereby increasing running times by the same amount with respect to FD-TD.

—Disadvantage: artifacts due to refraction and reflection of numerical wave modes propagating across global mesh distortions will be present. These errors arise because the phase velocity of numerical wave modes propagating in the mesh is a function of position in the mesh, as well as angle of propagation. These artifacts are important for three-dimensional structures having substantial EM coupling between electrically disjoint sections, or reentrant regions, and may limit the predictive dynamic range (thereby limiting the ability to model low-observable structures).

(3) *Completely unstructured.* The space containing the structure of interest is completely filled with a collection of solid cells of varying sizes and shapes, but conforming to the structure surface.<sup>26</sup>

—Advantage: geometry generation software is available. This software is appropriate for modeling extremely complicated three-dimensional shapes possibly having volumetric inhomogeneities, for example inhomogeneous radar absorbing material.

—Disadvantages: the same as for the body-fitted meshes.

—Another disadvantage: mapping of the logical mesh onto a parallel-vector computer or massively parallel computer is not straightforward.

At present, the optimal choice of computational algorithm and mesh is not obvious. Clearly, there are important tradeoff decisions to be made. For the next several years, we can expect considerable progress in this area as various groups develop their favored approaches and perform validations.

#### 4.3. Predictive dynamic range

For computational modeling of the RCS of aerospace vehicles (especially low-observable vehicles) using space-grid time-domain codes, it is useful to define a predictive dynamic range,  $D$ , analogous to the "quiet zone" figure of merit for an experimental anechoic chamber:

$$D = 10 \log(P^{\text{max}}/P^{\text{min}}) \text{ decibels,}$$

where  $P^{\text{inc}}$  is the power density of a modeled incident plane wave in the space grid, and  $P^{\text{min,obs}}$  is the minimum observable local power density of a modeled scattered wave at any bistatic angle. At levels lower than this the accuracy of the computed scattered field degrades to poorer than 1 dB (or some other criterion).

This definition succinctly quantifies the reality that weak, physical numerical wave analogs propagating in the space grid exist in an additive noise environment due to the non-physical propagating wave analogs caused by the imperfect radiation boundary conditions. In addition to additive noise, the desired physical wave analogs undergo gradual progressive deterioration while propagating due to accumulating numerical dispersion artifacts, including phase velocity anisotropies and inhomogeneities within the mesh.

Since 1982, researchers have accumulated solid evidence for a predictive dynamic range of the order of 40 dB for the present class of second-order accurate space-grid time-domain codes when used to calculate monostatic and bistatic RCS. This value is reasonable if one considers the additive noise due to imperfect radiation boundaries to be the primary limiting factor, since existing second-order radiation boundary conditions yield effective reflection coefficients of about 1% (-40 dB), with an additional factor of perhaps -10 dB provided by the normal  $r^{-1/2}$  rolloff (in two dimensions) or  $r^{-1}$  rolloff (in three dimensions) experienced by the outgoing scattered waves before reaching the radiation boundaries. Figure 1 illustrates a typical result for bistatic RCS dynamic range when using Cartesian-grid FD-TD with automated local mesh contouring to conform to curved target surfaces. Here, the scattering geometry consists of two  $1\lambda_0$ -diameter metal spheres separated by  $1\lambda_0$  air gap, and the FD-TD grid has a uniform space resolution of  $0.05\lambda_0$ . The benchmark data are provided by a quasi-analytic frequency-domain approach, the generalized multipole technique (GMT).<sup>4</sup>

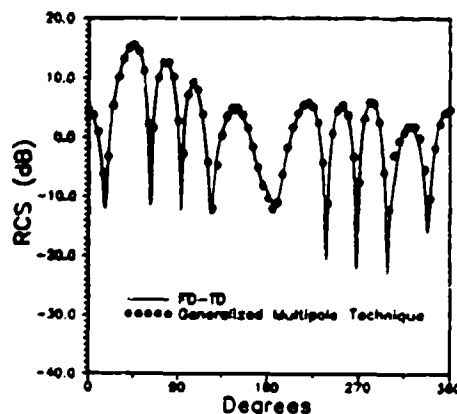


Fig. 1. Comparison of FD-TD and generalized multipole technique data for the bistatic RCS of two  $1\lambda$  diameter spheres separated by a  $1\lambda$  air gap, illuminated at oblique incidence.

Is more dynamic range needed? Certainly yes, if a better job is to be done in modeling specially shaped targets having low observability features. A good example of such a shape is the NASA almond,<sup>41</sup> which has been demonstrated to have monostatic RCS variations of 60 dB or more occurring over broad angular ranges. However, going from 40 to 60 or 70 dB will not be simple: We will require the development of advanced radiation boundary conditions having effective reflection coefficients of 0.1% or better, thereby reducing this contribution to the grid noise by 20 dB or more; and we will have to shift to space-sampling, time-integration algorithms having dimensionally better accuracy than the second-order procedures common today. A 20 dB reduction in the grid noise contribution due to dispersive effects accumulating on propagating numerical waves is needed to permit the use of grid resolutions no finer than those of today's algorithms.

### 5. SCALING TO PROBLEMS OF GREATER THAN $10^6$ FIELD UNKNOWNS

#### 5.1. Why this problem size is needed

Three-dimensional electromagnetic wave interaction problems modeled on volumetric space grids at the size level of  $10^6$  unknowns begin to have major engineering applications. For example, these might include: entire fighter planes illuminated by radar at 1 GHz and above; entire personal-computer-size multi-layer circuit boards modeled layer by layer for digital signal propagation, crosstalk and radiation; and entire microstrip circuits and antennas.

At this level, the goals are to achieve algorithm/computer architecture scaling such that for  $N$  field unknowns to be solved on  $M$  processors, we wish to approach an order  $(N/M)$  scaling of the computational modeling time.

#### 5.2. Algorithm scaling factors

Is there a "best" EM computational algorithm to approach the ideal order  $(N)$  scaling of the computational modeling time? A consensus appears to be emerging that the class of non-matrix, space-grid time-domain solvers has the most promise. If robust algorithms for spatial or domain decomposition<sup>42</sup> cannot be achieved, the class of matrix-based frequency-domain methods may fade as a viable alternative because of difficult computational and error propagation problems associated with any large matrix, whether dense or sparse.

Let us now consider the factors involved in determining the computational burden for the class of non-matrix, space-grid time-domain solvers.

(1) *Number of grid cells,  $N$ .* The six vector electromagnetic field components located at each grid cell must be updated at every time step. This yields by itself an order  $(N)$  scaling.

(2) *Number of time steps.* A completely self-consistent solution in the time domain mandates that

numerical wave analogs propagate over time scales sufficient to causally connect each portion of the structure of interest. Therefore, in three dimensions, it can be argued that the number of time steps increases as a characteristic electrical length of the structure and thus a fractional power function of  $N$  such as  $N^{1/2}$ . The number of time steps must also be adequate to march through "ring-up" and "ring-down" times of energy storage features such as cavities and cavity-backed apertures.

(3) *Cumulative propagation errors.* Additional computational burdens may arise due to the need for either progressive mesh refinement or progressively higher-accuracy algorithms to bound cumulative positional/phase errors for propagating numerical modes in progressively enlarged meshes. Any need for progressive mesh refinement would feed back to Factor 1.

It appears likely that for most RCS problems, Factors 2 and 3 will be weaker functions of the size of the modeled structure than Factor 1. This is because geometrical scattering features at increasing electrical distances from each other become more and more weakly coupled due to radiative and other losses acting on electromagnetic wave energy propagating between these features. However, at this time there is insufficient experience in the grid-based modeling community with three-dimensional structures in this electrically-large size regime to provide meaningful comment.

### 5.3. Computer architecture scaling factors

Is there a "best" computer architecture to approach the ideal  $1/\text{order}(M)$  scaling of the computational modeling time as the number of processors,  $M$ , increases? At present, the optimum connectivity of multi-processors is not clear. In 1993, the following manufacturers will offer massively parallel machines of varying architectures having claimed peak performances exceeding 100 Gflops (0.1 Tflop):

Intel:	Paragon
Cray Research:	MPP0
Thinking Machines:	CM-5.

In addition, Cray Research continues to develop its line of conventional general purpose vector-processing supercomputers descending from the CRAY Y-MP and C-90 machines. This will lead to a 100+ Gflop general purpose machine, the CRAY C-95, in 1994-1995.

### 5.4. Results to date

A number of groups have implemented large-scale grid-based Maxwell's equation solvers on vector-processing and massively parallel supercomputers.<sup>1,22,15-17</sup> Sufficient experience has been accumulated to justify the following statements:

(1) Concurrency very close to 100% (i.e. an algorithm speedup factor equal to eight if the number

of available processors equals eight) have been achieved with the CRAY Y-MP/8 under the CRAY autotasking (automatic multitasking) compiler for FD-TD and FV-TD. Average processing rates exceeding 1.6 Gflops were achieved for full FORTRAN programs. Performance scaling looks excellent at least through 16 high-performance (CRAY C-90 class) processors.

(2) Good to very good concurrencies for FD-TD can also be achieved using the JPL/Intel Hypercube. Performance scaling looks good into the hundreds of moderate-performance (Intel I-860 class) processors.

(3) For grid-based Maxwell's solvers, the CRAY Y-MP and JPL/Intel Hypercube machines were much easier to program and achieved substantially better fractions of their peak speeds than the CM-2 Connection Machine, when the CM-2 was programmed using the PARIS assembler.

(4) The volumetric space-grid time-domain solvers are already more efficient than surface-patching MoM. In one example,<sup>1,17</sup> FD-TD was used to conformally model an electrically large  $(25 \lambda_0 \times 10 \lambda_0 \times 10 \lambda_0)$  three-dimensional serpentine jet engine inlet. Here, the projected CRAY C-90 time is only 30 s per illumination angle (involving time-marching 23,000,000 vector field components over 1800 time steps), or 1.6 days for 5000 angles. In comparison, the standard full-matrix MoM set up a dense matrix of approximately 450,000 equations, assuming that the  $1500 \lambda_0^2$  area of the engine inlet is discretized at 10 divisions per  $\lambda_0$ . The projected CRAY C-90 running time for LU decomposition and backsolve of this matrix is about 4 months for 5000 angles. Overall, the speedup when using FD-TD would be at least 75:1, with speedup factors much larger than this if we account for the likelihood of using FD-TD to evaluate the inlet RCS simultaneously for many frequencies by using an impulsive excitation and discrete Fourier transformation of the scattered field.

### 5.5. The jet fighter model

Consider again modeling a jet fighter, but now in the context of FD-TD. Assuming dimensions of  $20 \times 20 \times 5$  m for the space grid and assuming a radar frequency of 1 GHz ( $\lambda_0 = 0.3$  m; resolution = 3 cm), the space grid would be of the order of 75,000  $\lambda_0^3$  (450,000,000 vector field components) and the FD-TD central memory requirement would be about 1.3 Gword. This central memory size is currently feasible with 1-4 billion-word memory options of the CRAY Y-MP series. Running time on the C-90 is projected to be in the range 20-25 min per illumination angle. Modeling of the fighter at radar frequencies of 2 GHz and higher would be possible using well-known asynchronous out-of-core techniques that permit I/O to and from multiple disk drives to be performed concurrently with the floating point operations.



#### 6. FUTURE DEFENSE ELECTROMAGNETICS NEEDS

Goals for computational electromagnetics modeling capabilities in the defense area have been and remain driven by the design of low-observable aircraft and missiles. Some of these goals are now summarized.

##### 6.1. 70 dB predictive dynamic range

As noise-cancelling anechoic chambers become more sophisticated and attain effective quiet zones deeper than  $-70$  dB, it is desired to extend numerical modeling capabilities to this dynamic range to balance theory and measurements. Clearly, larger predictive and measurement dynamic ranges permit structures of lower radar cross-section to be modeled and tested. Note that attainment of 70 dB predictive dynamic ranges is equivalent to the ability to suppress all sources of computational noise to amplitudes no larger than about  $10^{-4}$  that of the incident wave. This will be a very difficult challenge for any computational electromagnetics model.

With respect to space-grid time-domain algorithms, a primary challenge will occur in the area of advanced radiation boundary conditions (RBCs). In comparison with today's codes, a 40-dB (100:1) improvement is needed here in reducing the effective reflection coefficient of the outer grid boundaries relative to outward propagating numerical modes. It is not clear that this will be possible without a fundamental advance in RBC theory or direct numerical emulation of the noise cancellation used in the 70-dB anechoic chambers.

##### 6.2. Modeling of complex and composite materials

The usage of multilayer composites and cellular materials for structural and electromagnetic purposes in aerospace design has markedly increased. These materials can have inhomogeneities and anisotropies of their electric and magnetic properties at distance scales of a few microns, the thickness of one lamina in a composite sandwich. Further, the electric and magnetic properties can be functions of the frequency of radar illumination. Any conceivable electromagnetic analysis code will be very strongly challenged by the requirement to simultaneously model distance scales ranging over six orders of magnitude (from micrometers to meters) and frequencies ranging over three orders of magnitude (from megahertz to gigahertz).

In fact, it may be unfeasible in the time frame of the next decade to successfully attack the micrometers-to-meters distance-scale problem by direct modeling. Most likely, this problem will be approached by developing advanced electromagnetic field boundary conditions applied at the surface of complex composite media to nearly equivalence the field physics of the underlying media without having to refine the computational mesh beyond that used in the air region outside. If this is the case, the problem

of modeling composite media in meshes is one of fundamental electromagnetic theory rather than numerical methods.

##### 6.3. Optimization of materials and shapes for RCS

Analogous to CFD, the availability of increasingly sophisticated and accurate numerical analysis tools for RCS presents the possibility of optimizing target materials and shapes on the computer before any models are constructed. Space-grid time-domain models of scattering appear to be particularly useful for this purpose because of their potential for containing entire aircraft and their time-domain formulation. The latter permits modeling a very wideband [and even ultrawideband (UWB)] radar illumination in a single modeling run, as well as natural time-windowing of the scattering response to focus attention on the behavior of specific scattering centers.

For example, at least one published paper<sup>48</sup> reports an algorithm to automatically optimize the RCS of a structure using space-grid time-domain techniques. The algorithm of Ref. 48 optimizes broadband absorptive coatings for two-dimensional structures by embedding a FD-TD forward-scattering code in a numerical feedback loop with the Levenberg-Marquardt (LM) non-linear optimization routine. LM is used to adjust the many geometric and constitutive parameters that characterize the target, while FD-TD is used to obtain the broadband RCS response for each target adjustment. A recursive improvement process is established to minimize the broadband RCS response over a selected range of bistatic angles using the available engineering degrees of freedom. The solution is valid over the potentially broad bandwidth (frequency decade or more) of the illuminating pulse used in the FD-TD model.

This approach compactly treats the scatterer shape and coating specifications as a single point in an  $N$ -dimensional space ( $N$ -space) of geometrical and electrical parameters. By repeatedly recalculating the forward problem to obtain one or more figures of merit for the near or far-field response, this method implements a gradient-based search strategy in the  $N$ -space to obtain locally optimum monostatic or bistatic RCS reductions over the bandwidth of the illuminating plane wave pulse. More globally optimum searches can be conducted by seeding the algorithm with a variety of starting points in the  $N$ -space. The non-linear optimizer also permits adding constraints so that the search path in the  $N$ -space weights manufacturability and cost, and avoids possible forbidden zones.

Figure 2 illustrates the use of this method to synthesize an absorbing coating for a canonical two-dimensional structure, the infinite, perfectly conducting right-angle wedge subject to transverse magnetic (TM) illumination. As shown in Fig. 2a, the wedge coating is a single homogeneous 5 mm thick absorbing layer to the left and bottom of the wedge

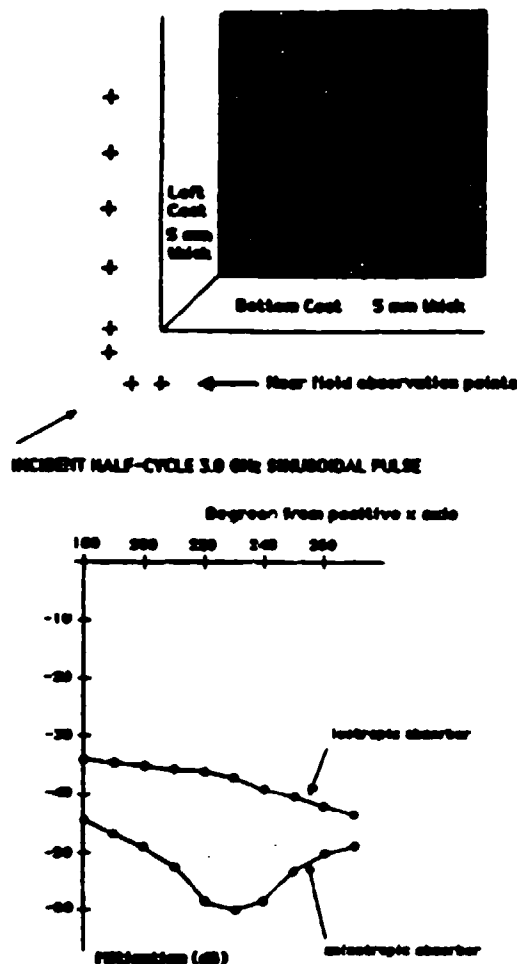


Fig. 2. FD-TD/LM synthesis of broadband absorbing coatings on an infinite conducting right-angle wedge, two-dimensional case: (a) wedge and coating geometry, showing the near-field observation points; (b) optimized mitigation of the broadband scattered pulses in the far field for bistatic angles bracketing the monostatic return, isotropic and anisotropic coating cases.

vertex, joined via a miter. In one case considered, the coating is assumed to be isotropic and independent of position, while in the other the coating is permitted to have an anisotropy of the magnetic loss that is dependent upon location (either in the left or bottom coat). The broadband illumination, a half-cycle 3.0 GHz sinusoidal pulse, is highly resolved everywhere by using a space discretization of  $\lambda_0/200$ . LM non-linear optimization is employed to minimize a weighted average of scattered near-field energy as observed at the eight near-field points indicated in Fig. 2a. From Fig. 2b, we see that the optimized broadband bistatic RCS mitigation in the far field (ratio of the peak scattered pulse power with coating to the peak scattered pulse power without coating) for bistatic angles bracketing the monostatic return is -34 to -42 dB for the isotropic coating and -44 to -60 dB for the anisotropic coating.

This case was purposefully selected to represent a coating  $N$ -space of low dimensionality, i.e. no coating layering was permitted. Given the simplicity of the coating examined here, it is likely that expanding the dimensionality of the automated search procedure would significantly increase the broadband RCS mitigation, increase the range of bistatic angles mitigated for RCS and decrease the sensitivity of the RCS mitigation to the illumination angle.

Methods such as the above appear to be ideal for implementation on massively parallel, multiple instruction multiple datastream (MIMD) computers. Here, systematic global searches of the  $N$ -space of interest could be implemented by assigning to each of the hundreds of processors (or groups of processors) a specific seed, or starting point, in the  $N$ -space. The searches could proceed independently of each other, culminating in an optimized engineering design for RCS.

#### 6.4. Integrated RCS and aerodynamics design and optimization

In principle, the above ideas can be taken a large step further by performing simultaneous, linked modeling and optimization of RCS and aerodynamic performance, since these separate engineering goals can strongly mutually interact and even directly conflict. Needless to say, automated, integrated RCS/aero design is an ambitious goal—a true grand challenge—well worthy of the teraflop computers and 70 dB dynamic range electromagnetic modelers hopefully to come by the year 1997.

An interesting issue here is: "Should we use the same computational mesh for both the RCS model and the aero model?" At first glance this appears to be desirable, since target geometry and meshing could then be shared by both disciplines and the non-linear optimization software would deal with only a single geometry data base. However, it is less clear that the extraordinary 70 dB dynamic range needed by the electromagnetics model can be achieved by "shoehorning" Maxwell's equations into current CFD meshes. The physics involved in the two disciplines may be sufficiently different to mandate a Maxwell-specific mesh for the electromagnetics model. The computer storage and running time of the electromagnetics code and complexity of the umbrella non-linear optimization software may also factor into the choice of mesh for the electromagnetics model.

#### 6.5. Target Identification

An interesting observation is that the technique of embedding a space grid time-domain Maxwell's solver within a non-linear optimization algorithm, considered above in the context of synthesizing scatterers having desired RCS properties, appears to be useful in reconstructing the shape (and even the composition) of a target from its broadband radar signature.<sup>49</sup>

Again, consider the FD-TD/LM non-linear optimization algorithm, but with the optimizer geared to replicate some finite measured impulsive scattering response rather than replicate a zero desired scattering response. Now, FD-TD generates a test pulse response for a parameterized trial target shape or composition, the test pulse is compared to the measured pulse, and an error signal is developed. Working on this error signal, the LM algorithm perturbs the original trial point in the  $N$ -space of parameters, effectively conducting a gradient search through this  $N$ -space. Upon repeated iterations, the trials ideally converge to the actual target geometry and composition. The advantage of working in the time domain is that causality can be exploited to permit progressive and cumulative target reconstruction as the incident pulse wavefront moves across the target. This reduces the complexity of reconstruction since only a portion of the target is being generated at each iteration.

Figure 3 provides examples of the ability of the FD-TD/LM non-linear optimization technique to exploit causality and reconstruct a dielectric J-shaped target from minimal two-dimensional TM near-field data contaminated by additive Gaussian noise.<sup>10</sup> Here, a single field observation point was assumed to be located approximately 10 target spans from the

front vertex of the J-target, with the incident plane wave pulse having a spatial width comparable with the J-target span and headed toward the front vertex of the J. The principal *a priori* information provided to the optimizer here is the target composition: lossless dielectric ( $\epsilon_r = 2.1$ ).

Figure 3 exemplifies hundreds of FD-TD/LM reconstruction attempts where varying samples of Gaussian noise (provided by a random number generator) are added to the simulated measured scattered waveform (a sequence of FD-TD-generated numbers). Using this technique, the probability of exact reconstruction of the J-shaped target has been estimated as a function of the signal-to-noise (S/N) power ratio. It has been found that the probability of exact reconstruction exceeds 0.9 when S/N ratios exceed 40 dB. For lower S/N ratios, the reconstruction process appears to degrade gracefully, as shown.

We see that space-grid time-domain Maxwell's solvers combined with non-linear optimizers that exploit causality hold promise for the classic inverse-scattering problem. Further progress awaits study of this problem by more groups in the Maxwell's equations gridding community. Perhaps this will occur in the next 5 years.

#### 7. FUTURE DUAL-USE ELECTROMAGNETICS NEEDS

By the mid-1990s, we will be implementing space-grid time-domain Maxwell's solvers on the 0.1–1 Tflop supercomputers of the day to model the radar cross-section of entire low-observable fighter aircraft at frequencies up to at least 2 GHz through dynamic ranges up to 70 dB; but, perhaps of more importance to the interests of society, we will be using these same Maxwell's solvers implemented on the same supercomputers to model electromagnetic wave problems that arise in cutting-edge commercial applications.

This discussion will start with extensions of existing commercial applications of electromagnetic wave interactions and proceed to highly innovative applications that best represent the dual-use nature of modeling Maxwell's equations on large scales.

##### 7.1. Antenna design

This area includes the design of UHF/microwave data links for worldwide personal wireless telephony, cellular communications, remote computing and advanced automotive electronics (particularly car location and navigation).

Here, we are seeing that space-grid time-domain Maxwell's solvers are permitting the modeling of complicated antennas, especially those having finite ground planes that cannot be analyzed using conventional frequency-domain analyses based upon the Green's function technique. Key recent examples include:

(1) Maloney *et al.*<sup>11</sup>—FD-TD models of body-of-revolution-type monopoles and conical monopoles over finite ground planes. Here, computed results

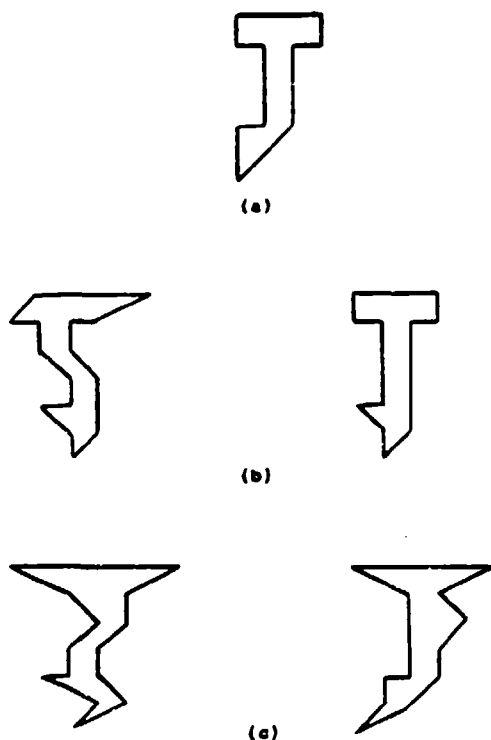


Fig. 3. Typical effects of Gaussian noise upon FD-TD/LM non-linear optimization inverse scattering reconstruction of a two-dimensional dielectric target having reentrant features: (a) S/N = 40 dB, exact reconstruction; (b) S/N = 30 dB, examples of imperfect reconstruction; (c) S/N = 25 dB, examples of imperfect reconstruction.

for the transient reflected waveforms in the feeding coaxial line and for the input impedances were found to agree with measurements to better than 1%.

(2) Katz *et al.*<sup>16</sup>—surface-conforming FD-TD models of two-dimensional waveguide-fed horn antennas and horn-excited parabolic reflectors. Here, the computed results for near-fields in the antenna apertures were found to agree with frequency-domain MoM numerical data to within 1% in magnitude and phase.

(3) Tirkas and Balanis<sup>17</sup>—surface-conforming FD-TD models of three-dimensional waveguide-fed horn antennas. Here, the computed results for far-field radiation patterns were found to agree very well with measurements over a 55-dB dynamic range.

(4) Thiele and Taflove<sup>18</sup>—in perhaps the most complex modeling so far, the authors are constructing three-dimensional FD-TD models of 6–18 GHz Vivaldi flares (tapered slot antennas) constructed from three-layer circuit board. Here, both single flares, double flares, quad elements comprised of perpendicular double-flares and arrays of up to eight quad elements are being modeled. The latter involve the solution of up to 60,000,000 vector field unknowns. Results are being obtained for radiation pattern and input impedance. The variation of the input impedance with phasing of the array of quad elements is also being studied.

As detailed FD-TD modeling proceeds in this area, it is possible that commercial application areas will include the design of mass-produced surface-conforming antennas for: homes (rooftop-mounted antennas for satellite reception); automobiles (rooftop-mounted antennas for two-way satellite communication, license-plate-mounted antennas for automated collision avoidance and programmed route-following); and laptop computers (computer-case-mounted antennas for two-way cellular and satellite communication).

#### 7.2. Microwave circuits

Stripline microwave circuits, including filtering elements and couplers, are being studied for the first time by applying grid-based time-domain Maxwell's solvers. Key recent examples include:

(1) Sheen *et al.*<sup>19</sup>—FD-TD models of microstrip interconnects.

(2) Ko and Mittra<sup>20</sup>—three-dimensional FD-TD models yielding the broadband *S*-parameters of microstrip filters, couplers and hybrids.

This work is leading to the modeling of microwave and millimeter wave integrated circuits (MIMIC) in regimes of electrical size and complexity that cannot be handled by any existing finite-element or boundary integral method.

#### 7.3. Bioelectromagnetic systems

Grid-based time-domain Maxwell's solvers are now being extensively applied in clinical settings for

patient-specific electromagnetic hyperthermia. This technology uses electromagnetic absorption at RF, UHF, or microwave frequencies to heat cancerous tumors inside the human body, thereby rendering the tumors more vulnerable to ionizing radiation or chemotherapy. Recent examples of work include:

(1) Sullivan<sup>19</sup>—three-dimensional FD-TD models of RF hyperthermia for human patients.

(2) Picket-May *et al.*<sup>20</sup>—three-dimensional FD-TD models of UHF hyperthermia specifically tailored to patients by using computed tomography (CT) imaging to establish a three-dimensional dielectric medium data base unique to each patient's tissue structure.

This work is leading to the routine clinical usage of electromagnetic hyperthermia for cancer treatment. Time-domain solution of Maxwell's equations on grids is essential to this process because it permits an efficient, individual modeling of each patient to accommodate the electromagnetic field physics unique to his or her tissue geometry and selection of field applicators.

#### 7.4. Packaging and metallic interconnect design for digital circuits

This area involves engineering problems in the propagation, crosstalk and radiation of electronic digital pulses, and has important implications in the design of the multi-layer circuit boards and multi-chip modules that are widely used in modern digital technology. Most existing computer-aided circuit design tools (primarily SPICE) are inadequate when digital clock speeds exceed about 250 MHz. These tools cannot deal with the physics of UHF/microwave electromagnetic wave energy transport (along metal surfaces like ground planes, or in the air away from metal paths) that predominate above 250 MHz. Effectively, electronic digital systems develop substantial analog wave effects when clock rates are high enough, and full-vector (full-wave) Maxwell's equations solvers become necessary for their understanding.

Key recent examples include:

(1) Liang *et al.*<sup>21</sup>—three-dimensional FD-TD modeling of picosecond pulse propagation along co-planar waveguides above gallium arsenide.

(2) Shibata and Sano<sup>22</sup>—three-dimensional FD-TD modeling of propagation along metal-insulator-semiconductor lines.

(3) Lam *et al.*<sup>23</sup>—three-dimensional FD-TD modeling of digital signal propagation and radiation for VLSI packaging.

(4) Maeda *et al.*<sup>24</sup>—three-dimensional FD-TD modeling of digital pulse propagation through vias in a three-layer circuit board.

(5) Picket-May *et al.*<sup>25</sup>—in perhaps the most complex modeling so far, the authors constructed three-dimensional FD-TD models of sub-nanosecond digital pulse propagation and crosstalk behavior in

### Z-Axis Connector System

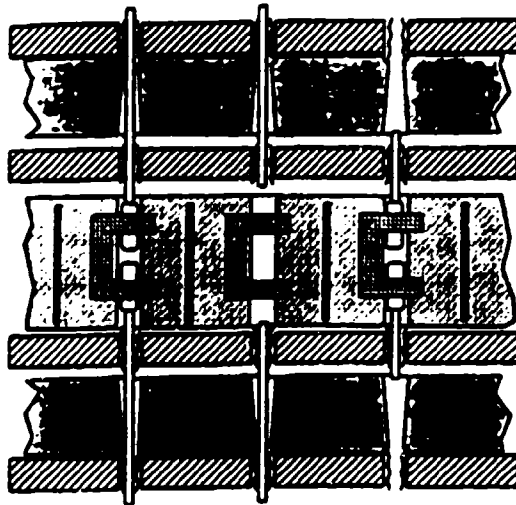


Fig. 4. Vertical cut through the four-circuit-board, three-connector geometry showing the via pins spaced 0.1 in apart.

modules consisting of four 22-layer circuit boards connected by three 100-pin connectors. The entire space was modeled with a uniform resolution of 0.004 in, permitting each layer, via and pin of the circuit boards and connectors to be modeled. A maximum of 60,000,000 vector field unknowns was solved per modeling run, a factor of perhaps 600 times larger than the capacity of the largest SPICE or finite-element CAD tool available. Color videos of digital signal propagation and crosstalk were constructed to vividly illustrate these phenomena.

Figure 4 depicts the geometry of the four-board, three-connector stack as seen in a vertical cut through the stack. Each 22-layer circuit board is shown as a cross-hatched horizontal slab, and each vertical via pin (spaced at a 0.1 in interval) is shown in proper relation to the surrounding boards and connectors. (Recall that each 0.004 in-thick metal-dielectric layer of each board is modeled.)

Figure 5 is a color plate showing the plan view of an outwardly propagating electromagnetic wave within a

single 22-layer board generated by the passage of a sub-nanosecond pulse down one of the via pins. Although the relatively intense magnetic field adjacent to the excited via (shown by the yellow color) is quite localized, moderate-level magnetic fields (shown by light blue) emanate throughout the entire transverse cross-section of the board and link all of the adjacent via pins, shown as dark dots in a diamond pattern. The complete color video of this phenomenon shows repeated bursts of outward propagating waves linking all points within transverse cross-sections of the board as the digital pulse passes vertically through the 22 metal-dielectric-metal layers of the board.

Figure 6 is a color plate showing the magnitude and direction of currents instantaneously flowing along the vertical cross-section of Fig. 4 for a sub-nanosecond digital pulse assumed to excite a single vertical via pin in the upper 22-layer board. The currents were calculated in a post-processing step by numerically evaluating the curl of the magnetic field obtained from the three-dimensional FD-TD model. The color red was selected to denote downward-directed current, while the color green was selected to denote upward-directed current. At the time of this visualization, current had proceeded down the excited via through all four boards and all three connectors; but upward-directed (green) current is seen to flow on the adjacent vias. This represents undesired ground-loop coupling to the digital circuits using these vias. Ironically, the far-left-hand and far-right-hand vias showing downward-directed (red) currents were designated by the designers of this structure to be the ground return pins and should have been the only pins carrying upward-directed (green) current. In other words, this interconnection module wound up working nearly in an opposite manner relative to what its designers had intended.

This work is leading to the direct time-domain Maxwell's equations modeling of the metallic interconnects and packaging of general-purpose digital circuits operating at clock speeds about 250 MHz. From the example shown, it is clear that the analog coupling effects for such devices can be so complex that there may be no way to design them—no way to make them work in a timely and reliable manner—without such modeling.



Fig. 5. Color plate showing the plan view of an outwardly propagating electromagnetic wave within a single circuit board of Fig. 4 generated by the passage of a sub-nanosecond pulse down one of the via pins. Color scale: yellow = maximum; green = moderate; dark blue = negligible.



Fig. 6. Color plate showing the magnitude and direction of currents instantaneously flowing along the vertical cross-section of Fig. 4 for a sub-nanosecond digital pulse assumed to excite a single vertical via pin in the upper 22-layer board. Color scale: red = net downward-directed current; green = net upward-directed current; dark blue = negligible.

#### 7.5. Incorporation of models of active devices

It is a short distance from modeling device packaging and interconnects, as discussed above, to including the active devices themselves. Work has begun in this area. The best examples are:

(1) Sano and Shibata<sup>37</sup>—incorporation of a self-consistent drift-diffusion charge-transport model of gallium arsenide in the three-dimensional FD-TD solver. This work modeled picosecond-regime pulse generation for an optically excited gallium arsenide device.

(2) El Ghazaly *et al.*<sup>38</sup>—incorporation of a self-consistent Monte Carlo charge-transport model of gallium arsenide in the three-dimensional FD-TD solver. This work also modeled picosecond-regime pulse generation for an optically excited gallium arsenide device.

(3) Sui *et al.*<sup>41</sup>—two-dimensional FD-TD modeling of lumped-circuit elements (resistors, inductors, capacitors, diodes and transistors).

By 1995, this work will probably lead to the incorporation of SPICE models of arbitrary linear and non-linear circuit elements into three-dimensional space-grid time-domain Maxwell's solvers. This will expand full-vector electromagnetic modeling of digital interconnects to include the voltage-current characteristics of the connected logic devices. It should result in a virtual replacement of SPICE for most problems involved in digital interconnect design above 250 MHz.

A recently initiated 3-year cooperative program between Cray Research and Los Alamos National Laboratory recognizes the possibility that the design of the digital microchips themselves will mandate

full-vector EM modeling, especially when clock speeds exceed 3 GHz. In this regime, wave propagation and coupling effects within the chips may render their operation just as problematic as that of today's circuit board modules operating at 300 MHz.

Subsequently, the Cray/Los Alamos program seeks to explore Maxwell's equations modeling of digital chips having clock speeds well above 10 GHz. The reasoning here is that when the logic pulse rise time becomes comparable with the charge transport time, existing approaches for modeling semiconductors which assume a quasi-static formulation for Maxwell's equations (the Poisson equation) will no longer have validity. In this regime, the simple circuit concept of a digital signal toggling a transistor may have to be considered at the most elemental level. Namely, the digital signal and transistor actually comprise a three-dimensional electromagnetic pulse scattering geometry: the digital signal is really a three-dimensional propagating field distribution having a specific temporal response and the transistor is really a three-dimensional charge density distribution that reacts non-linearly to the impinging electromagnetic pulse. Self-consistent Maxwell's equations field transport and semiconductor charge transport modeling are required to properly understand this non-linear scattering situation.

#### 7.6. Application to all-optical devices

Work has begun to appear on first-principles modeling of the propagation and switching of femtosecond optical pulses in non-linear dispersive media. Again, time-domain grid-based Maxwell's solvers are being used:

(1) Joseph *et al.*<sup>32</sup>—demonstrated and rigorously validated an efficient one-dimensional FD-TD analysis of femtosecond pulse propagation and reflection effects for a linear Lorentz (resonant dispersive) medium. This work pioneered direct Maxwell's equations modeling of second-order dispersion, providing extremely accurate physics over instantaneous bandwidths of literally d.c. to light for reflection coefficients and Sommerfeld and Brillouin impulsive precursors.

(2) Goorjian and Taflov<sup>33</sup>—demonstrated an efficient one-dimensional FD-TD analysis of femtosecond optical soliton propagation and collision in a second-order non-linear dispersive medium. This work obtained for the first time optical solitons from Maxwell's equations, with quantum physics such as the Kerr and Raman interactions incorporated into the Maxwell's equations at distance scales larger than about 10 nm.

(3) Ziolkowski and Juddins<sup>34</sup>—two-dimensional FD-TD analysis of femtosecond optical pulse propagation and self-focusing in a first-order non-linear dispersive medium.

Consider qualitatively the key results of Ref. 39. Fig. 7a depicts the FD-TD computed propagation of a 50 fs duration infrared optical pulse observed at

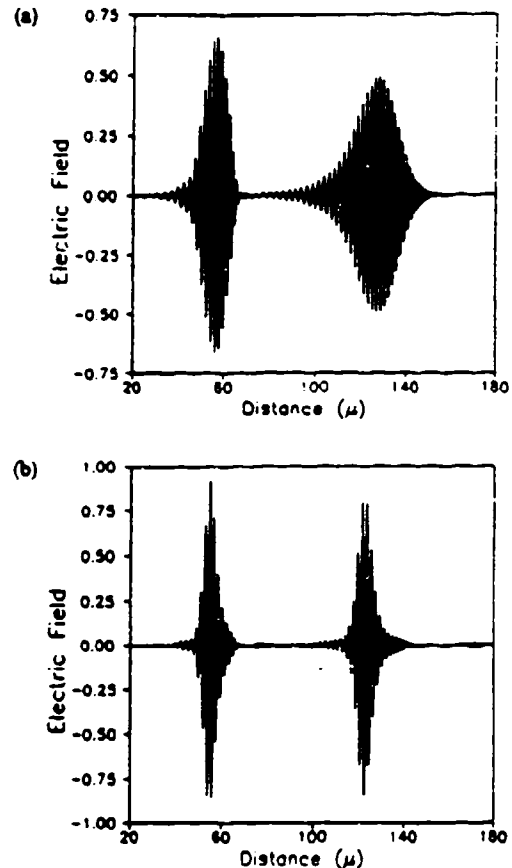


Fig. 7. FD-TD computed propagation of a 50 fs duration infrared optical pulse: observed at propagation distances of 55 and 126  $\mu$ m from the source in a medium having anomalous dispersion due to a single Lorentzian relaxation: (a) linear case, showing pulse attenuation, broadening, and frequency modulation; (b) dispersive non-linear case, showing the formation of a soliton pulse and precursor.

propagation distances of 55 and 126  $\mu$ m from the source in a linear medium having anomalous dispersion. Note pulse broadening, diminishing amplitude and carrier frequency modulation ( $>f_c$  on the leading side,  $<f_c$  on the trailing side) which causes an asymmetrical shifting of the envelope, a higher-order dispersive effect. In Fig. 7b, sufficient non-linearity is introduced to yield a soliton that retains its amplitude and width when observed at the same propagation distances as Fig. 7a. However, a low-amplitude precursor is seen to move out ahead of the soliton. The carrier frequency of this precursor is upshifted to approximately 3.6 times that of the main pulse.

Figure 8 depicts the Fourier spectrum of the solitons shown in Fig. 7b. The figure shows a red shift and sharpening of the spectrum as the pulse propagates. This red shift is predicted due to the Raman effect occurring as a higher-order dispersive non-linearity modeled by the non-linear Maxwell's equations solver.

Finally, Ref. 39 considers the collision of two counter-propagating solitons. Each is identical and

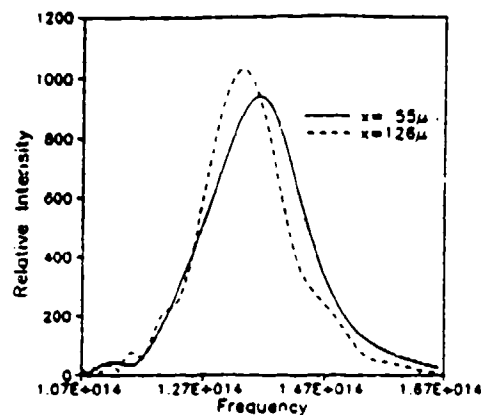


Fig. 8. Red shift of the Fourier spectrum of the propagating soliton of Fig. 7b.

has all of the parameters of the previous case. As is characteristic of colliding solitons, after the collisions the pulses separate without changing their general appearance. However, there are lagging phase shifts due to the collision, up to  $31^\circ$  for the carrier in the precursor. To illustrate this, Fig. 9 plots the space dependence of the central part of the precursor for the uncollided case and the collided case. Such phase shifts, not easily detected by previous theory, may be a basis for optical switching devices.

Unlike all previous soliton theory based upon the pulse-envelope approach, the direct Maxwell's equations model of Ref. 39 assumes nothing about the homogeneity or isotropy of the optical medium, the magnitude of its non-linearity, the nature of its  $\omega$ - $\beta$  variation, or the shape or duration of the optical pulse. By retaining the optical carrier, the new Maxwell's equations method solves for fundamental quantities—the optical electric and magnetic fields in space and time—rather than a non-physical envelope function. Thus, it is extendible to full-vector optical fields in two and three dimensions to permit rigorous boundary value problem studies of non-linear vector-wave polarization, diffraction, scattering and interference effects. This is being actively pursued.

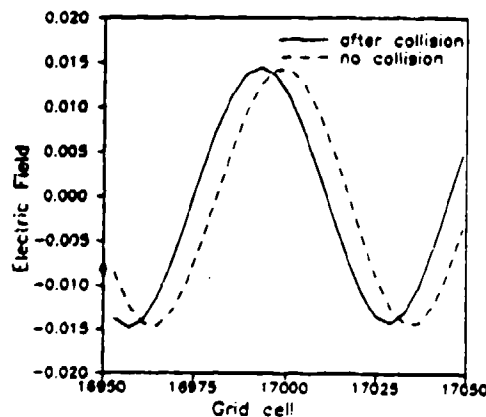


Fig. 9. Phase lag of the precursor pulse as a result of counterpropagating soliton-soliton collision.

This work may lead to the modeling of all-optical digital logic devices switching potentially in 10–50 fs at room temperature. This is about 1000 times faster than the best transistor today and 100 times faster than a Josephson junction operating under liquid helium. The implications may be profound for the realization of "optronics", a proposed successor technology to electronics in the 21st century that would integrate optical fiber interconnects and all-optical processors into systems of unimaginable information processing capability.

## 8. CONCLUSIONS

Supercomputers of the mid-1990s, which promise to achieve rates from 0.1 to 1 Tflop, will permit us to attack some "grand challenges" in electromagnetics. One such "challenge" remains from the RCS technology side—the airplane-in-the-grid. In fact, using the new class of machines and the new class of space-grid time-domain Maxwell's solvers, it will certainly be possible to obtain whole low-observable fighter-airplane models in the 1–3 GHz range and jet-engine-inlet models up to perhaps 5–10 GHz, with predictive dynamic ranges up to 70 dB. In addition, time-domain non-linear optimization algorithms will probably be used to achieve engineering goals with respect to observability and aerodynamics. But, of arguably more importance to society, the same algorithms implemented on the same computers could attack other "grand challenges" in electromagnetics:

- the satellite-antenna-in-the-grid;
- the cancer-patient-in-the-grid;
- the digital-microchip-module-in-the-grid;
- the microwave/millimeter wave integrated circuit-in-the-grid;
- the array-of-picosecond-transistors-in-the-grid;
- the femtosecond-all-optical-switch-in-the-grid, etc.

I assert that ultra-large-scale solution of Maxwell's equations using time-domain grid-based approaches may be fundamental to the advancement of our technology as we continue to push the envelope of the ultra-complex and the ultra-fast. Simply speaking, Maxwell's equations provide the physics of electromagnetic phenomena from d.c. to light and their accurate modeling is essential to understand high-speed signal effects having wave transport behavior. Let us aim for the computational unification of:

- full-vector electromagnetic waves in three dimensions;
- charge transport in transistors, Josephson junctions and electro-optic devices;
- surface and volumetric wave dispersions, including those of superconductors; and
- non-linearities due to quantum effects.

Then, we can attack some computational "grand challenges" to directly benefit our society.



**Acknowledgements**—The author acknowledges the invaluable assistance of his collaborators, Professor Korada Umashankar of the University of Illinois at Chicago, Dr Peter Goorjian of NASA Ames and Dr Evans Harrigan of Cray Research. He also acknowledges the assistance of his graduate students, Ross Joseph, Das Katz, Melinda Piket-May, Chris Reuter and Eric Thiele, as well as his undergraduate research students Peter Anvin, Susan Hagness and Ann Komaromi. The author was supported in part by NASA Ames University Consortium Joint Research Interchange Grants NCA2 561 and 562, Office of Naval Research Contract N00014-88-K-0475, and Cray Research, Inc.

## REFERENCES

1. R. F. Harrington, *Field Computation by Moment Methods*, Macmillan, New York, 1968.
2. K. R. Umashankar, "Numerical analysis of electromagnetic wave scattering and interaction based on frequency-domain integral equation and method of moments techniques," *Wave Motion* 10, 493 (1988).
3. J. B. Keller, "Geometrical theory of diffraction," *Journal of the Optical Society America* 52, 116 (1962).
4. R. G. Kouyoumjian and P. L. Pathak, "A uniform geometrical theory of diffraction for an edge in a perfectly conducting surface," *Proceedings of the IEEE* 62, 1448 (1974).
5. J. P. Brooks, K. K. Ghosh, E. Harrigan, D. S. Katz and A. Taflov, "Progress in Cray-based algorithms for computational electromagnetics," in *Progress in Electromagnetics Research (PIER)* edited by T. Cwik, Vol. 7, Elsevier, New York, 1992.
6. K. S. Yee, "Numerical solution of initial boundary value problems involving Maxwell's equations in isotropic media," *IEEE Transactions Antennas and Propagation* 14, 302 (1966).
7. A. Taflov and M. E. Brodwin, "Numerical solution of steady-state electromagnetic scattering problems using the time-dependent Maxwell's equations," *IEEE Transactions Microwave Theory Tech.* 23, 623 (1975).
8. A. Taflov and M. E. Brodwin, "Computation of the electromagnetic fields and induced temperatures within a model of the microwave-irradiated human eye," *IEEE Transactions Microwave Theory Tech.* 23, 888 (1975).
9. R. Holland, "Threde: a free-field EMP coupling and scattering code," *IEEE Transactions Nuclear Science* 24, 2416 (1977).
10. K. S. Kunz and K. M. Lee, "A three-dimensional finite-difference solution of the external response of an aircraft to a complex transient EM environment I: the method and its implementation," *IEEE Transactions Electromagnetic Compat.* 20, 328 (1978).
11. A. Taflov, "Application of the finite-difference time-domain method to sinusoidal steady-state electromagnetic penetration problems," *IEEE Transactions Electromagnetic Compat.* 22, 191 (1980).
12. G. Mur, "Absorbing boundary conditions for the finite-difference approximation of the time-domain electromagnetic field equations," *IEEE Transactions Electromagnetic Compat.* 23, 377 (1981).
13. K. R. Umashankar and A. Taflov, "A novel method to analyze electromagnetic scattering of complex objects," *IEEE Transactions Electromagnetic Compat.* 24, 397 (1982).
14. A. Taflov and K. R. Umashankar, "Radar cross section of general three-dimensional scatterers," *IEEE Transactions Electromagnetic Compat.* 25, 433 (1983).
15. G. A. Kriegsmann, A. Taflov and K. R. Umashankar, "A new formulation of electromagnetic wave scattering using an on-surface radiation boundary condition approach," *IEEE Transactions Antennas and Propagation* 35, 153 (1987).
16. T. G. Moore, J. G. Blaschak, A. Taflov and G. A. Kriegsmann, "Theory and application of radiation boundary operators," *IEEE Transactions Antennas and Propagation* 36, 1797 (1988).
17. D. T. Borup, D. M. Sullivan and O. P. Gandhi, "Comparison of the FFT conjugate gradient method and the finite-difference time-domain method for the 2-D absorption problem," *IEEE Transactions Microwave Theory Tech.* 35, 383 (1987).
18. D. M. Sullivan, O. P. Gandhi and A. Taflov, "Use of the finite-difference time-domain method in calculating EM absorption in man models," *IEEE Transactions Biomedical Engineering* 35, 179 (1988).
19. D. M. Sullivan, "Three-dimensional computer simulation in deep regional hyperthermia using the finite-difference time-domain method," *IEEE Transactions Microwave Theory Tech.* 38, 204 (1990).
20. M. J. Piket-May, A. Taflov, W.-C. Lin, D. S. Katz, V. Sarinasselan and B. Mittal, "Initial results for automated computational modeling of patient-specific electromagnetic hyperthermia," *IEEE Transactions Biomedical Engineering* 39, 226 (1992).
21. K. R. Umashankar, A. Taflov and B. Beker, "Calculation and experimental validation of induced currents on coupled wires in an arbitrary shaped cavity," *IEEE Transactions Antennas and Propagation* 35, 1248 (1987).
22. A. Taflov, K. R. Umashankar, B. Beker, F. Harfoush and K. S. Yee, "Detailed FD-TD analysis of electromagnetic fields penetrating narrow slots and lapped joints in thick conducting screens," *IEEE Transactions Antennas and Propagation* 36, 247 (1988).
23. T. G. Jurgens, A. Taflov, K. R. Umashankar and T. G. Moore, "Finite-difference time-domain modeling of curved surfaces," *IEEE Transactions Antennas and Propagation* 40, 357 (1992).
24. A. C. Cangellaris, C. C. Lin and K. K. Mei, "Point-matched time-domain finite element methods for electromagnetic radiation and scattering," *IEEE Transactions Antennas and Propagation* 35, 1160 (1987).
25. V. Shankar, A. H. Mohammadian and W. F. Hall, "A time-domain finite-volume treatment for the Maxwell equations," *Electromagnetics* 10, 127 (1990).
26. B. J. McCartin, L. J. Bahrmann and G. Meitz, "Application of the control region approximation to two dimensional electromagnetic scattering," in *Progress in Electromagnetics Research* (edited by M. A. Morgan), Vol. 2, Ch. 5, Elsevier, New York, 1990.
27. N. K. Madsen and R. W. Ziolkowski, "A three-dimensional modified finite volume technique for Maxwell's equations," *Electromagnetics* 10, 147 (1990).
28. G.-C. Liang, Y.-W. Liu and K. K. Mei, "Full-wave analysis of coplanar waveguide and slotline using the time-domain finite-difference method," *IEEE Transactions Microwave Theory Tech.* 37, 1949 (1989).
29. T. Shibata and E. Sano, "Characterization of MIS structure coplanar transmission lines for investigation of signal propagation in integrated circuits," *IEEE Transactions Microwave Theory Tech.* 38, 881 (1990).
30. D. M. Sheen, S. M. Ali, M. D. Abouzahra and J. A. Kong, "Application of the three-dimensional finite-difference time-domain method to the analysis of planar microstrip circuits," *IEEE Transactions Microwave Theory Tech.* 38, 849 (1990).
31. W. L. Ko and R. Mittra, "A combination of FD-TD and Prony's methods for analyzing microwave integrated circuits," *IEEE Transactions Microwave Theory Tech.* 39, 2176 (1991).
32. R. Luebbers, F. P. Hunsberger, K. S. Kunz, R. B. Standler and M. Schneider, "A frequency-dependent finite-difference time-domain formulation for dispersive materials," *IEEE Transactions Electromagnetic Compat.* 32, 222 (1990).

33. R. M. Joseph, S. C. Hagness and A. Taflove, "Direct time integration of Maxwell's equations in linear dispersive media with absorption for scattering and propagation of femtosecond electromagnetic pulses," *Optics Letters* 16, 1412 (1991).
34. J. G. Maloney, G. S. Smith and W. R. Scott, Jr., "Accurate computation of the radiation from simple antennas using the finite-difference time-domain method," *IEEE Transactions Antennas and Propagation* 38, 1059 (1990).
35. P. A. Tirkas and C. A. Balanis, "Finite-difference time-domain technique for radiation by horn antennas," 1991 *IEEE Antennas and Propagation Society International Symposium Digest*, Vol. 3, pp. 1750-1753, London, Ontario, Canada, 1991.
36. D. S. Katz, M. J. Piket-May, A. Taflove and K. R. Umashankar, "FD-TD analysis of electromagnetic wave radiation from systems containing horn antennas," *IEEE Transactions Antennas and Propagation* 39, 1203 (1991).
37. E. Sano and T. Shibata, "Fullwave analysis of picosecond photoconductive switches," *IEEE Journal Quantum Electronics* 26, 372 (1990).
38. S. M. El-Ghazaly, R. P. Joshi and R. O. Gredin, "Electromagnetic and transport considerations in subpicosecond photoconductive switch modeling," *IEEE Transactions Microwave Theory Tech.* 38, 629 (1990).
39. P. M. Goorjian and A. Taflove, "Direct time integration of Maxwell's equations in nonlinear dispersive media for propagation and scattering of femtosecond electromagnetic solitons," *Optics Letters* 17, 180 (1992).
40. R. W. Ziolkowski and J. B. Judkins, "Full-wave vector Maxwell equation modeling of the self-focusing of ultrashort optical pulses in a nonlinear Kerr medium exhibiting a finite response time," *Journal Optical Society of America B*, submitted.
41. W. Sui, D. A. Christensen and C. H. Durney, "Extending the two-dimensional FD-TD method to hybrid electromagnetic systems with active and passive lumped elements," *IEEE Transactions Microwave Theory Tech.* 40, 724 (1992).
42. A. C. Ludwig, General Research Corporation, private communication.
43. S. W. Lee (ed.), *High Frequency Scattering Data Book*, Electromagnetic Laboratory, University of Illinois at Urbana-Champaign, 1989.
44. K. R. Umashankar, S. Nimmagadda and A. Taflove, "Numerical analysis of electromagnetic scattering by electrically large objects using spatial decomposition technique," *IEEE Transactions Antennas and Propagation*, in press.
45. A. T. Perlik, T. Opsahl and A. Taflove, "Predicting scattering of electromagnetic fields using FD-TD on a Connection Machine," *IEEE Transactions Magnetics* 25, 2910 (1989).
46. J. E. Patterson, T. Cwik, R. D. Ferraro, N. Jacobi, P. C. Liewer, T. G. Lockhart, G. A. Lyzenga, J. W. Parker and D. A. Simoni, "Parallel computation applied to electromagnetic scattering and radiation analysis," *Electromagnetics* 10, 21 (1990).
47. D. S. Katz, A. Taflove, J. P. Brooks and E. Harrigan, "Large-scale methods in computational electromagnetics," in *Cray Channels*, Cray Research, 1991.
48. M. A. Strickel and A. Taflove, "Time-domain synthesis of broadband absorptive coatings for two-dimensional conducting targets," *IEEE Transactions Antennas and Propagation* 38, 1084 (1990).
49. M. A. Strickel, A. Taflove and K. R. Umashankar, "Finite-difference time-domain formulation of an inverse scattering scheme for remote sensing. Part II—Two-dimensional case: conducting and dielectric targets," *Journal of Electromagnetic Waves and Applications*, in press.
50. E. Thiele and A. Taflove, "FD-TD analysis of Vivaldi tapered slot antennas," in preparation.
51. C. W. Lam, S. M. Ali, R. T. Shin and J. A. Kong, "Radiation from discontinuities in VLSI packaging structures," *Proceedings of the Progress in Electromagnetics Research Symposium*, Boston, Massachusetts, p. 567, July 1991.
52. S. Maeda, T. Kachiwa and I. Fukai, "Full wave analysis of propagation characteristics of a through hole using the finite-difference time-domain method," *IEEE Transactions Microwave Theory Tech.* 39, 2154 (1991).
53. M. Piket-May and A. Taflove, "First-principles supercomputing simulation of crosstalk in high-speed digital interconnects," 1992 Joint Symposium, URSI Radio Science Meeting Digest, p. 451, Chicago, IL, 1992.

# Electrodynamics of visible-light interactions with the vertebrate retinal rod

Melinda J. Piket-May and Allen Taflové

*Department of Electrical Engineering and Computer Science, McCormick School of Engineering,  
Northwestern University, Evanston, Illinois 60208-3118*

John B. Troy

*Department of Biomedical Engineering, McCormick School of Engineering, Northwestern University, Evanston, Illinois 60208-3118*

Received December 21, 1992

We report the initial investigation of the electrodynamics of visible-light interaction with the outer segment of the vertebrate retinal rod based on detailed, first-principles computational electromagnetics modeling. The computational method employs a direct time integration of Maxwell's equations in a two-dimensional space grid for both transverse-magnetic and transverse-electric vector-field modes. Detailed maps of the optical standing wave within the retinal rod are given for three illumination wavelengths: 714, 505, and 475 nm. The standing-wave data are Fourier analyzed to obtain spatial frequency spectra. Except for isolated peaks, the spatial frequency spectra are essentially independent of the illumination wavelength.

For many years there has been interest in the optical properties of photoreceptors.<sup>1-6</sup> These studies addressed a variety of questions concerning the optical functioning of the photoreceptors. The goal of the research reported here differs from the earlier studies in at least one important aspect: We have sought to understand the interaction of the photoreceptor with light from a fundamental electrodynamics perspective. Our working hypothesis is that the detailed physical structure of a photoreceptor impacts the physics of its optical absorption and, thereby, vision. In this Letter we consider one such photoreceptor, the vertebrate retinal rod. The bulk structure of the retinal rod exhibits the physics of an optical waveguide, while the internal disk-stack periodic structure adds the physics of an optical interferometer. These effects combine to generate a complex optical standing wave within the rod, thereby creating a pattern of local intensifications of the optical field.

We employ a robust direct time-integration approach for Maxwell's vector-field equations, implemented on a two-dimensional space grid, to obtain the electrodynamics of the retinal rod at optical frequencies. The computational approach, designated as the finite-difference time-domain (FD-TD) method,<sup>7-10</sup> employs second-order accurate spatial central differences and leapfrog time stepping to implement the space and time derivatives of Maxwell's time-dependent curl equations. FD-TD is a highly efficient means to model full-vector impulsive or sinusoidal electromagnetic wave interactions with arbitrary one-, two-, or three-dimensional inhomogeneous material structures. Originating from defense applications in the radar cross-section area, FD-TD is becoming widely used for modeling radio frequency and microwave scattering, penetration, and radiation interactions with industrial and biomedical structures of realistic complexity.

Recently, the range of FD-TD modeling of electromagnetic wave interactions has been expanded to linear and nonlinear dispersive optical materials and structures, including linear optical-directional couplers<sup>11</sup> and femtosecond optical pulses and solitons.<sup>12,13</sup> The upper-frequency bound of FD-TD modeling (equivalently, the lower bound on grid cell size) is predicated by the proper incorporation of quantum effects into the macroscopic  $\chi^{(1)}$  susceptibility function that relates the Maxwell displacement flux  $D$  to the electric field  $E$  as a function of frequency  $\omega$ .

In our study we have implemented two separate two-dimensional models of the isolated outer segment of the retinal rod; a transverse-magnetic (TM) model and a transverse-electric (TE) model. The TM model involves the vector-field mode having  $H_z$  and  $H_x$  as the magnetic-field unknowns and  $E_z$  as the electric-field unknown, while the TE model involves the mode having  $E_z$  and  $E_x$  as the electric-field unknowns and  $H_z$  as the magnetic-field unknown. For both models, the optical excitation is a monochromatic incident plane wave propagating in the  $+y$  direction parallel to the major axis of the rod, which is assumed to be infinite and unchanging in the  $z$  direction. Three different free-space optical wavelengths  $\lambda_0$  have been investigated: 714 nm (red), 505 nm (green), and 475 nm (blue). The rod is assumed to have cross-section dimensions of  $2000 \text{ nm} \times 20,000 \text{ nm}$ ,<sup>14</sup> corresponding to  $(3.8-5.7\lambda_d) \times (38-57\lambda_d)$  over the range of wavelengths used in the model, where  $\lambda_d$  is the optical wavelength within the rod's dielectric media.

A uniform Cartesian space grid having  $5.0 \text{ nm} \times 5.0 \text{ nm}$  unit cells is utilized in the computational model. This provides a wavelength resolution of  $\lambda_d/70$  to  $\lambda_d/105$ , depending on the incident wavelength. The overall grid includes  $2.1 \times 10^6$  cells, corresponding to  $6.3 \times 10^6$  vector-field unknowns. Reliable

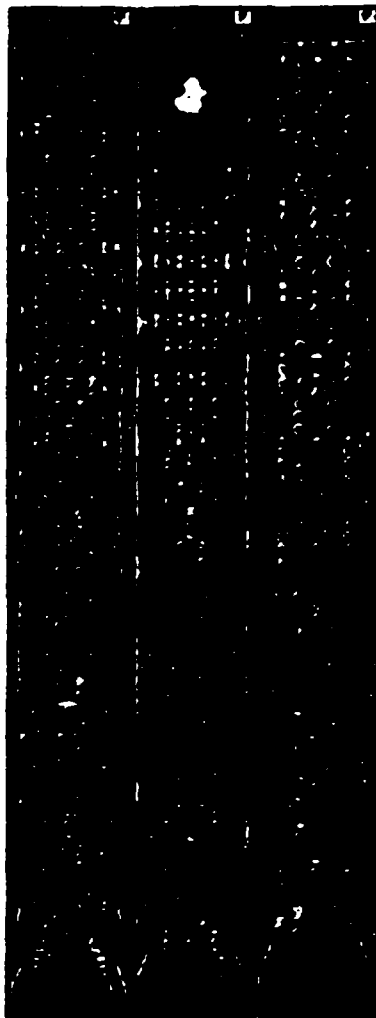


Fig. 1. Visualization of the magnitude of the electric-field values of the optical standing wave within the retinal rod for TM illumination relative to 1 V/m incident at 475, 505, and 714 nm. White areas, standing-wave peaks; dark areas, standing-wave nulls. The maximum simplification for the TM mode is 2.3.

second-order radiation boundary conditions<sup>9</sup> are implemented at the outer grid boundaries to simulate the rod embedded in an infinite fluid region. Thus any computed wave reflections are virtually exclusively due to interface effects within and at the surface of the rod. There is little contribution to the computed optical standing wave owing to reflections from the outer grid boundary.

The 5-nm resolution of the space grid permits detailed modeling of the 15-nm-thick outer wall membrane of the rod and the 15-nm-thick internal disk membranes.<sup>14</sup> There is assumed to be 799 of the latter distributed uniformly along the length of the rod, separated from each other by 10 nm of fluid and separated from the outer wall membrane by 5 nm of fluid. The index of refraction for the membrane  $n_m$  was chosen to be 1.43, and the index of refraction for the fluid  $n_f$  was chosen to be 1.36, in accordance with generally accepted physiological data.

The computational procedure involves launching a sinusoidal plane wave of the desired optical frequency in the +y direction and integrating Maxwell's equations in time as the wave penetrates the rod, propagates all the way to its back end (maximum y coordinate), rebounds, and propagates all the way to its front end (minimum y coordinate), rebounds again, and then repeats the front-to-back-to-front traversal one additional time. It should be understood that electromagnetic wave diffraction in all directions in the x-y plane is computed during this process in accordance with Maxwell's equations. At the conclusion of the time integration, the standing wave of the time-dependent optical electric field is obtained. Convergence studies involving extension of the integration period to allow a variable number of front-to-back-to-front traversals of the wave have been conducted and indicate that the sinusoidal steady state is essentially achieved after the first two complete traversals. Approximately 1.6 h of single-processor Cray Y-MP time is required to model one such integration at the 505-nm incident wavelength.

Figure 1 is a visualization of the computed magnitude of the normalized electric-field values of the optical standing wave within the retinal rod for TM polarization at  $\lambda_0 = 714, 505,$  and 475 nm. A similar visualization is observed for TE polarization. To assist our understanding of the physics of the retinal rod as a complex optical waveguiding structure, we performed the following reduction of the standing-wave magnitude data at each  $\lambda_0$ . First, at each transverse plane located at a given  $y_0$  in the rod, we integrated the electric-field values  $E(x, y_0)$  of the optical standing wave over the x coordinate to obtain a single number,  $E_m(y_0)$ . Second, we performed a discrete spatial Fourier transform of the resulting distribution  $E_m(y)$  over the y coordinate. The results are shown in Fig. 2 for the TM case and in Fig. 3 for the TE case. With the exception of isolated peaks unique to each  $\lambda_0$ , the spatial frequency spectra for each polarization are essentially independent of

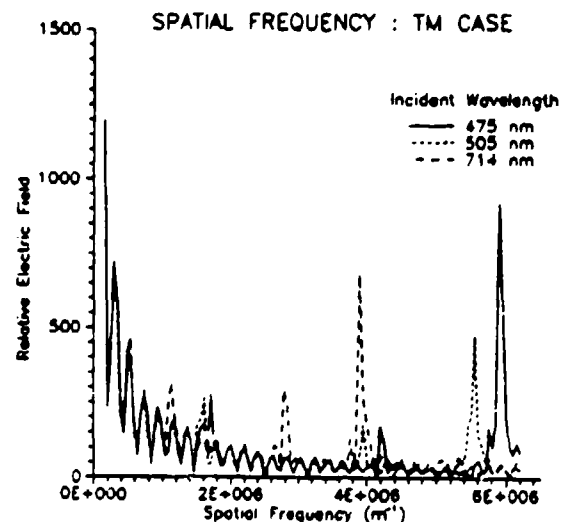


Fig. 2. Spatial frequency spectra of the transverse integrated optical standing wave for TM illumination at 714, 505, and 475 nm.

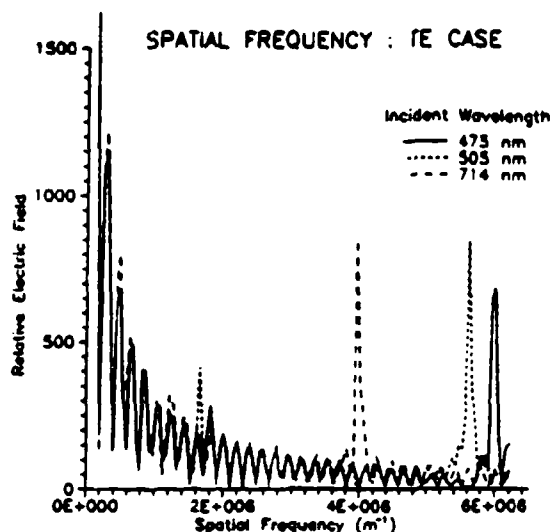


Fig. 3. Spatial frequency spectra of the transverse integrated optical standing wave for TE illumination at 714, 505, and 475 nm.

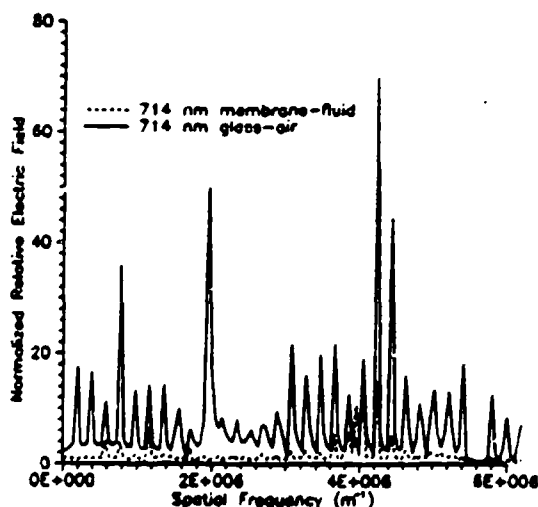


Fig. 4. Spatial frequency spectra for the membrane-fluid structure and the glass-air structure at 714 nm normalized to the spatial frequency spectrum of the respective structures at 505 nm.

the illumination wavelength. The retinal rod thus appears to exhibit a type of frequency-independent electrodynamic behavior.

The agreement of the spatial frequency spectra for the three incident wavelengths for each polarization was so remarkable that we tested our overall procedure for computational artifacts. The test involved perturbing the indices of refraction of the membrane and fluid from those of the vertebrate rod to those of glass and air. Figure 4 graphs the spatial frequency spectra at  $\lambda_i = 714$  nm for the membrane-fluid structure and the glass-air structure, as normalized to the spectrum of the respective structures at  $\lambda_i =$

505 nm. We see that the normalized glass-air spectrum exhibits little correlation, i.e., numerous sharp high-amplitude oscillations over the entire spatial frequency range considered. On the other hand, the normalized membrane-fluid spectrum varies in a tight range near unity through spatial frequencies of  $3.6 \times 10^6 \text{ m}^{-1}$ . We conclude that the agreement of the spatial frequency spectra for the vertebrate retinal rod indicates a real physical effect that is dependent on the proper definition of the indices of refraction of the components of the rod structure.

The observed independence of the spatial frequency spectrum of the optical standing wave within the retinal rod structure relative to  $\lambda_i$  supports the hypothesis that the electrodynamic properties of the rod contribute little if at all to the wavelength specificity of optical absorption.<sup>15</sup> From an electrical engineering standpoint, frequency-independent structures have found major applications in broadband transmission and reception of radio-frequency and microwave signals. There is a limited set of such structures, and it is always exciting to find a new one. We speculate that some engineering application of frequency-independent retinal-rod-like structures may eventually result for optical signal processing.

We thank M. Friedman for his initial suggestion to investigate computationally the electromagnetic properties of the vertebrate retinal rod. We thank P. Anvin for assisting in the visualization and A. Komaromi for assisting in the data reduction. This study was supported by National Science Foundation grant ASC-8811273, Office of Naval Research contract N00014-88-K-0475, and Cray Research, Inc.

## References

1. B. O'Brien, *J. Opt. Soc. Am.* **41**, 862 (1951).
2. J. Enoch, *J. Opt. Soc. Am.* **53**, 71 (1963).
3. M. L. Calvo, *Bio. Cybernet.* **54**, 201 (1986).
4. W. Wijngaard, *J. Opt. Soc. Am.* **61**, 1187 (1971).
5. A. W. Snyder and C. Pask, *Vision Res.* **13**, 1115 (1973).
6. P. M. Tannenbaum, *Vision Res.* **15**, 591 (1975).
7. K. S. Yee, *IEEE Trans. Antennas Propag.* **AP-14**, 302 (1966).
8. A. Taflov and M. E. Brodwin, *IEEE Trans. Microwave Theory Tech.* **MTT-23**, 623 (1975).
9. G. Mur, *IEEE Trans. Electromagn. Compat.* **EC-23**, 377 (1981).
10. A. Taflov, *Wave Motion* **10**, 547 (1988).
11. S. T. Chu and S. K. Chaudhuri, *IEEE J. Lightwave Technol.* **7**, 2033 (1989).
12. R. M. Joseph, S. C. Hagness, and A. Taflov, *Opt. Lett.* **16**, 1412 (1991).
13. P. M. Goorjian, A. Taflov, R. M. Joseph, and S. C. Hagness, *IEEE J. Quantum Electron.* **28**, 2416 (1992).
14. J. E. Dowling, *The Retina* (Harvard U. Press, Cambridge, Mass., 1987).
15. A. Fein and E. Z. Szuts, *Photoreceptors: Their Role in Vision* (Cambridge U. Press, Cambridge, UK, 1982), p. 84.